

Accurate multiscale simulation of wave-like systems

J. Divahar

August 21, 2022

*Thesis submitted for the degree of
Doctor of Philosophy
in
Applied Mathematics
at The University of Adelaide
Faculty of Engineering, Computer and Mathematical Sciences
School of Mathematical Sciences*



THE UNIVERSITY
of ADELAIDE

Contents

Signed Statement	v
Acknowledgements	vi
Dedication	viii
Abstract	ix
1 Introduction	1
1.1 <i>Equation-free patch schemes offer a flexible multiscale modelling approach</i>	3
1.2 <i>Patch schemes for wave-like systems are challenging</i>	6
1.3 <i>Staggered patch schemes are stable, accurate, consistent, and efficient for waves</i>	7
2 Extend staggered grids to multiscale modelling	11
2.1 <i>Staggered patches of staggered micro-grid for multiscale modelling</i> . . .	12
2.1.1 Staggered grids are best for full-domain waves-like systems . .	12
2.1.2 Extend the staggered grid to multiscale patch scheme	15
2.1.3 Multi-layer edge nodes for higher order spatial derivatives . .	23
2.2 <i>Patch coupling connects the scales</i>	25
2.2.1 Global spectral interpolation for patch coupling	26
2.2.2 A family of local polynomial interpolations for patch coupling	28
3 Staggered patch schemes accurately simulate general linear waves	46
3.1 <i>Full-domain microscale model and staggered patch schemes</i>	48
3.2 <i>Staggered patch schemes are accurate</i>	51
3.2.1 Eigenvalue analysis of the PDEs	54
3.2.2 Eigenvalue analysis of staggered grid full-domain model . . .	55
3.2.3 Analytic eigenvalue analysis of staggered patch schemes . . .	57
3.2.4 Compute numerical Jacobian of the full-domain model	65
3.2.5 Compute numerical Jacobian of the staggered patch schemes .	66
3.2.6 Staggered patch schemes are accurate for macroscale waves . .	67

3.3	<i>A method of wavenumber-wise scale separation for patch scheme eigenvalues</i>	91
3.4	<i>Staggered patch schemes are not sensitive to numerical roundoff errors</i>	95
3.5	<i>Staggered patch schemes are stable</i>	105
3.5.1	Patch scheme stability requires geometric symmetry	107
3.5.2	Spectral patch scheme is stable for a range of physical parameters	110
3.5.3	All five patch schemes are stable for a range of grid parameters	113
3.6	<i>Staggered patch schemes are consistent</i>	121
3.6.1	Spectral patch scheme is uniformly accurate	123
3.6.2	The four polynomial patch schemes are consistent	127
3.7	<i>Large computational savings in staggered patch scheme time simulation</i>	133
3.7.1	Patch schemes compute only within a small fraction of space	133
3.7.2	Patch schemes compute for a small number of state variables	134
3.7.3	Computational complexity of the staggered patch schemes	135
3.7.4	Staggered patch schemes simulate with small compute time	137
3.7.5	Staggered patch scheme time simulations of general linear waves	144
4	Patch schemes accurately simulate viscous shallow water flows	157
4.1	<i>PDEs, full-domain microscale model, and staggered patch schemes</i>	159
4.1.1	Non-dimensionalise the PDEs to keep same domain size	160
4.1.2	Full-domain microscale model for viscous shallow water flows	165
4.1.3	Staggered patch scheme for viscous shallow water flows	168
4.1.4	Selection of parameter regime for patch scheme exploration	173
4.2	<i>Staggered patch schemes are accurate</i>	174
4.2.1	Eigenvalue analysis of the PDEs	176
4.2.2	Eigenvalue analysis of staggered grid full-domain model	179
4.2.3	Analytic eigenvalue analysis of staggered patch schemes	181
4.2.4	Compute numerical Jacobian of the full-domain model	186
4.2.5	Compute numerical Jacobian of the staggered patch schemes	188
4.2.6	Staggered patch schemes are accurate for macroscale waves	189
4.3	<i>Staggered patch schemes are not sensitive to numerical roundoff errors</i>	208
4.4	<i>Staggered patch schemes are not artificially unstable for appropriate patch grids</i>	215
4.4.1	Spectral staggered patch scheme is not artificially unstable for a range of physical parameters	217
4.4.2	Dominant artificial instabilities are due to sub-patch microscale structure modulated over non-small macroscale wavenumbers	231
4.4.3	No artificial instability among the five staggered patch schemes for a range of grid parameters	238
4.5	<i>Staggered patch schemes are consistent</i>	244
4.5.1	Spectral patch scheme is uniformly accurate	246
4.5.2	The four polynomial patch schemes are consistent	252

4.6	<i>Staggered patch schemes are invariant to flow direction</i>	258
4.7	<i>Large computational savings via staggered patch schemes</i>	261
4.7.1	Patch schemes compute only within a small fraction of space	261
4.7.2	Patch schemes compute for a small number of state variables	262
4.7.3	Computational complexity of the staggered patch schemes	262
4.7.4	Staggered patch schemes simulate with small compute time	264
4.7.5	Patch scheme time simulations of viscous shallow water flows	271
4.7.6	Some practical issues in staggered patch scheme simulations of viscous shallow water flows	275
5	Patch schemes accurately simulate turbulent shallow water flows	282
5.1	<i>PDEs, Full-domain microscale model, and staggered patch schemes</i>	283
5.1.1	Non-dimensionalise the PDEs to keep same domain size	284
5.1.2	Full-domain microscale model and staggered patch schemes	287
5.1.3	Selection of parameter regime for patch scheme exploration	289
5.2	<i>Staggered patch schemes are accurate</i>	291
5.2.1	Eigenvalue analysis of the PDEs	292
5.2.2	Eigenvalue analysis of staggered grid full-domain model	293
5.2.3	Analytic eigenvalue analysis of staggered patch schemes	295
5.2.4	Staggered patch schemes are accurate for macroscale waves	296
5.3	<i>Staggered patch schemes are not artificially unstable for appropriate patch grids</i>	305
5.4	<i>Staggered patch schemes are consistent</i>	309
5.5	<i>Staggered patch scheme time simulations of turbulent shallow water flows</i>	310
6	Conclusion	314
6.1	<i>Multiscale staggered patch schemes enable accurate large-scale simula- tion of wave-like systems</i>	314
6.2	<i>Further research directions</i>	316
	Bibliography	319

Signed Statement

I certify that this work contains no material which has been accepted for the award of any other degree or diploma in my name, in any university or other tertiary institution and, to the best of my knowledge and belief, contains no material previously published or written by another person, except where due reference has been made in the text. In addition, I certify that no part of this work will, in the future, be used in a submission in my name, for any other degree or diploma in any university or other tertiary institution without the prior approval of the University of Adelaide and where applicable, any partner institution responsible for the joint award of this degree.

I give permission for the digital version of my thesis to be made available on the web, via the University's digital research repository, the Library Search and also through web search engines, unless permission has been granted by the University to restrict access for a period of time.

I acknowledge the support I have received for my research through the provision of an Australian Government Research Training Program Scholarship.

Signed: Date: 21 - Aug - 2022

Acknowledgements

I wish to sincerely thank the following people.

- My principal supervisor *Emeritus Professor Tony Roberts*, for inculcating in me many of the best scholarly practices and abilities, for his expert supervision, dedicated regular weekly meetings, PhD research directions, help with academic requirements, career advice, and the many detailed reviews of my writings; any errors/imperfections in this thesis will almost surely be the ones where I disagreed with him.
- My co-supervisors *Dr. Judith Bunder*, and *Dr. Trent Mattner* for their specific scholarly and career advice, supportive supervision, dedicated regular weekly meetings, help with academic requirements, detailed reviews of my thesis, and offering the opportunity to tutor and mark for two beautiful applied mathematics courses.
- Postgraduate coordinator *Associate Professor Benjamin Binder* for his help with academic requirements, travel grant applications, and his supportive advice, especially during tough times.
- My wife *Mrs. Malarkodi Kumar*, not even a single day of my PhD would have been possible without her dedicated and persistent help.
- My daughter *Kaviya* and son *Kathiravan* for their patience towards my inability to spend time with them or fix their toys during their important childhood times over the last four and a half years.
- My sister *Srimathi* and brother *Prabakar*, only holding our hands together and tight we raised against the gravity of poverty during the toughest parts of our early life.
- My friends, *Arun*, *Prasanna*, *Stimit*, *Sudhakar*, *Suresh*, and *Vinay* for the guidance in my PhD application when I had no idea about a PhD research proposal, the encouragement to persist, and other suggestions.

I also extend my sincere thanks to the following organisations.

- The school of mathematical sciences and The University of Adelaide, for providing me with this PhD opportunity, the facilities to carry

out this research work, and the support through the travel grants to participate in Amplify Ignite pitch competition, Mathematics In Industry Study Group, and the conferences of AustMS and ANZIAM.

- The Australian Government for the Research Training Program (RTP) Scholarship.

I also express my sincere thanks to the two anonymous reviewers for their detailed thesis examination and comments.

Dedication

I dedicate this PhD thesis to my mother *Mrs. Pankajam Jayaraman* and my father *Mr. Jayaraman Chandrakasu*.

During my childhood, we lived in a hut under a roof made of hay and holes, in an Indian village that is not connected by public transport even today. During rainy nights, we used to spread hay on the wet floor and sleep over a sheet on top. In many midnights my parents saved us from drenching by placing cooking vessels around us. In spite of many struggles, my parents educated all four of their kids into degree holders at the cost of sacrificing most of their life. My sister is the first woman degree holder of my village. Upon completion, I will be the first PhD holder of my village.

Amma and appa, I hope I live a meaningful life at least partly worthy of your struggles and sacrifices.

I also dedicate this work to the memory of my uncle *Mr. Murugu Rajangam*.

My uncle had been my most caring mentor and a constant source of motivation in many of my endeavours ranging from making my own toys in my childhood times to contributing to large aerospace projects in MNCs.

I still keep hearing your voices mama!

Abstract

Many important phenomena exhibit multiscale emergent behaviour that currently cannot be accurately modelled (e.g., many turbulent flows, floods, tsunamis, weather, sediment transport) due to the high computational effort to capture all the details spread over a large range of scales. To address this issue, many multiscale modelling techniques have been developed for dissipative systems. The flexible equation-free multiscale *patch schemes* accurately model emergent macroscale spatial dynamics using a given microscale model within small sparsely located coupled patches. Such multiscale patch schemes have been developed successfully for dissipative systems. But the small dissipation in wave-like systems poses significant challenges for developing multiscale patch schemes, especially in multiple dimensions. The recent works of Cao and Roberts (2013, 2015) extend the patch scheme to 1D wave-like systems. *This PhD thesis develops the equation-free multiscale patch schemes for 2D wave-like systems (small dissipation) and explores the schemes more thoroughly.*

For high accuracy and to preserve much of the wave characteristics, *we extend the concept of staggered grids in the full-domain modelling to multiscale modelling.* In contrast to the usual collocated patch grid, using staggered grids within the patches leads to many different arrangements of the patch edge nodes. We considered 83 520 staggered patch grids that are geometrically compatible for 2D wave-like systems. Almost all such staggered grids lead to unstable and/or inaccurate patch schemes. *We designed two staggered patch grids that constitute stable and accurate patch schemes for linear and nonlinear wave-like systems.*

Patch coupling provides a two-way connection between two scales: from microscale within patches to macroscale over the domain, and from macroscale to microscale. Depending upon the *patch coupling* methods, many variants of patch schemes are possible on a staggered patch grid; many such patch schemes are unstable and/or inaccurate. *We developed two novel families of equation-free multiscale staggered patch schemes for accurate large-scale simulation of wave-like systems: a spectral patch scheme, and four*

polynomial patch schemes. The spectral patch scheme is the best for accuracy, over simple geometry and periodic boundary conditions. Polynomial patch schemes are best for complex geometry and boundary conditions.

We show that the staggered patch schemes accurately simulate general linear waves, viscous shallow water flows, and turbulent shallow water flows. For these three wave models, we establish the stability and consistency of the staggered patch schemes for a wide range of physical and grid parameters via analytic eigenvalue analysis and numerical von Neumann analysis. *The eigenvalues of the patch scheme macroscale modes converge towards the corresponding eigenvalues of the full-domain model, with decreasing macro-grid interval (inter-patch distance).*

The staggered patch schemes are not sensitive to numerical roundoff errors, except when the patches are too small relative to inter-patch distance, and/or when the underlying microscale model is sensitive to numerical roundoff errors. Even for very small patches, we confirm the consistency of the patch schemes via arbitrary-precision floating-point implementation. We also show the accuracy of the patch scheme time simulations by comparing them with the full-domain simulation. Our work shows the robustness of the patch scheme simulation by recovering emergent macroscale waves from random initial perturbations.

Explicit analytic expressions quantify the computational complexity of the staggered patch schemes. *The staggered patch schemes accurately model the macroscale waves with large computational savings, via detailed microscale simulations only within the patches, that is, within a small fraction of the whole space. The staggered patch schemes compute only for a small number of dynamical state variables, as small as one-millionth of the number of state variables in the corresponding full-domain model. The measured compute times of the multiscale staggered patch schemes are up to 10^5 times smaller than the corresponding full-domain model.* Users can choose how much computational savings to achieve depending on the scales of interest in the modelling. The patch schemes' ability to accurately model macroscale waves with large computational savings is an enabling feature for accurate simulation and prediction of large-scale waves like floods and tsunamis.

Keywords: equation-free multiscale modelling; patch schemes; emergent dynamics; staggered grids; multiscale wave-like systems; large-scale waves; weather; floods; tsunamis; general linear wave; viscous shallow water flows; turbulent shallow water flows.

Chapter 1

Introduction

Many important phenomena exhibit multiscale emergent behaviour that currently cannot be accurately modelled (e.g., many turbulent flows, floods, tsunamis, weather, sediment transport) due to the high computational effort required to capture all the details spread over a large range of scales in space and time. Resolving a large range of scales requires very many degrees of freedom from spatial discretisation and very many function evaluations from time discretisation, leading to prohibitively high computational costs. The challenges of multiscale modelling are major obstacles to progress in many fields such as environmental and geosciences, climate, complex materials, heterogeneous media, combustion, high energy density physics, fusion, bioscience, and chemistry (e.g., see Dolbow et al. 2004).

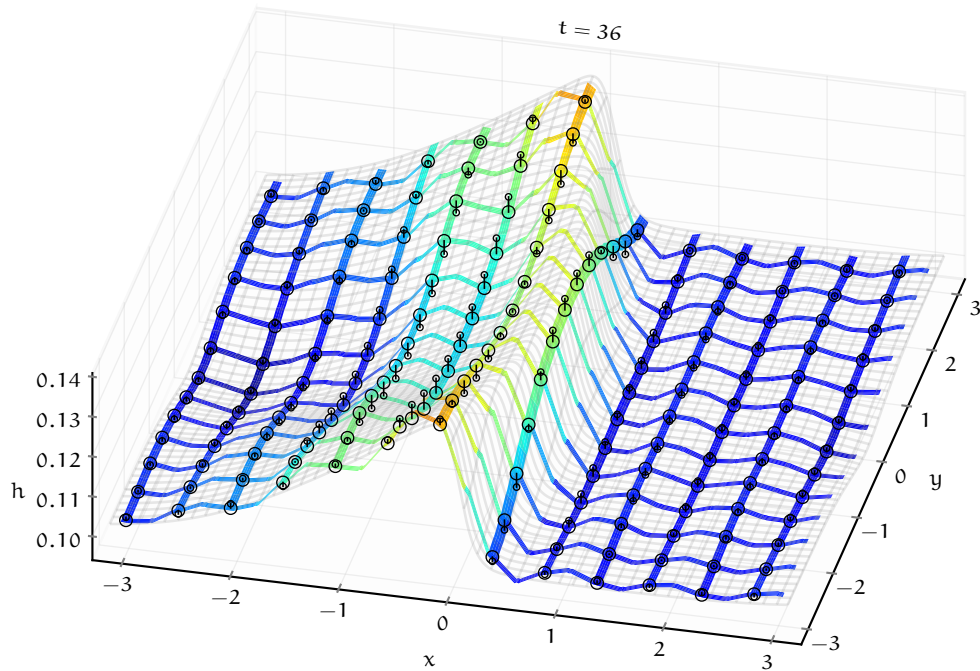
To address this issue, many multiscale modelling techniques have been developed. For example, mathematical homogenization (Berlyand and Rybalko 2018; Mei and Vernescu 2010), renormalization group based methods (Chorin and Stinis 2005; Ei et al. 2000; Mudavanhu and O'Malley 2003), two-stage finite element method (FE^2) of Feyel and Chaboche (2000) and Raju et al. (2021), Multiscale Finite Element Methods (MSFEM) (Hou and Efendiev 2009), generalized finite element methods (Babuška and Osborn 1983), Generalized Multiscale Finite Element Methods (GMSFEM) of Efendiev et al. (2013), variational multiscale (VMS) methods (Hughes et al. 1998), Localised Orthogonal Decomposition (LOD) of Målqvist and Peterseim (2014), wavelet-based numerical homogenization (Dorobantu and Engquist 1998), and Heterogeneous Multiscale Method (HMM) (E and Björn 2003, 2005; E et al. 2003). Nearly all of these multiscale modelling methods need to be specifically tailored for particular problems, within narrow application areas, using specific underlying models; not readily applicable for new problems. Several of those methods require a priori knowledge about the macroscale model. For example, E and Björn (2005, pp.105–106, §5) state

“... for the success of HMM, some information about the macroscale model is crucial. Without them, a blind application of HMM can give wrong results.”. Many such methods typically also require scale separation with a large spectral gap in the dynamics, as opposed to a continuous spread of scales which is the case in many turbulent and wave systems. On the other hand, the equation-free multiscale patch scheme is a general framework with high flexibility for many different application domains and different kinds of problems, without strong dependence on the underlying microscale model. Patch schemes are *equation-free* as connecting the scales is done through generic interpolation instead of explicit equations as done in homogenisation and similar other multiscale methods; that is, there is no derived equation to describe the macroscale model, the only information the macroscale model gets is the computational data (§1.1). Patch schemes have been developed for dissipative systems; but the small dissipation in wave-like systems poses significant challenges for developing multiscale schemes for wave-like systems, especially in multiple dimensions (§1.2). This PhD thesis develops the equation-free multiscale patch schemes for 2D wave-like systems (small dissipation).

Specifically, this work develops equation-free multiscale staggered patch schemes that *enable accurate simulation of macroscale waves for many specific application areas* over large space, yet computing only within small sparsely located patches. As a concrete example, the current work mainly focuses on water waves. For example, Fig. 1.0.1 shows the accurate patch scheme simulation (colour-coded ribbons) in comparison with the full-domain simulation (grey mesh) of a nearly discontinuous turbulent roll wave; §5.5 of Chapter 5 gives further details. *The regions where the colour-coded ribbons cross are patches*; the patches are much smaller than illustrated in the figure for visual clarity. *The staggered patch schemes compute only within patches*, a small fraction ranging from hundredths to several thousandths of the area of the full domain (§3.7 quantifies the computational savings).

The objective of the multiscale patch schemes is accurate macroscale simulation of a given microscale model/code. Hence, the main aim of this work is to establish that the multiscale staggered patch schemes accurately and efficiently simulate wave-like systems with small dissipation, *using a given microscale model*. For the models demonstrated in this work, one could reasonably accurately use a coarse spatial grid, without a strong need for multiscale modelling. But the aim is to use whatever microscale code is given, and anticipate the code to efficiently simulate where fine micro-grids are essential (e.g., heterogeneities and turbulence). In the context of flows in heterogeneous media, the multiscale behaviour is due to space-varying coefficients of the PDEs. In turbulent flows, due to turbulent cascading the

Figure 1.0.1. The emergent turbulent roll wave (height h at $t = 31$), from the initial condition of a moving Gaussian hump (5.5.1), using Square-p6 patch scheme (colour-coded ribbons, with $N = 22$, $n = 6$, and $r = 0.1$) agrees very closely with that of the fine-grid full-domain model (grey mesh). Black circles on h -centred patches show the discrepancy.

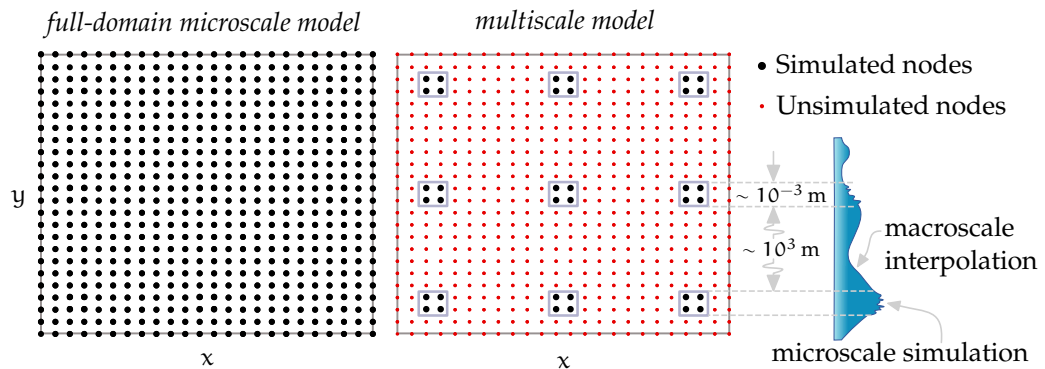


dynamics span over a large range of scales in time and space; hence a direct numerical simulation has to resolve a range of small length (sub-patch) scales. The particular physics and the characteristics of the governing PDEs and their coefficients are peripheral in this study.

1.1 Equation-free patch schemes offer a flexible multiscale modelling approach

In the fluid dynamics of Earth's atmosphere and oceans, the length scales range from a few millimetres to several thousands of kilometres (Grooms and Julien 2018, p. 3). We define *the full-domain microscale simulation* as the detailed full-scale simulation (of all/most scales) over the complete simulation domain. The main interest generally lies in the large-scale dynamics only, yet the effect of the smallest scales that give rise to the emergent large-scale dynamics needs to be accounted for. On the other hand, the detailed

Figure 1.1.1. Schematic of a typical multiscale model that simulates only within small coupled regions (grey squares) in the domain. Smooth waves on the right, over the unsimulated nodes, are interpolated over the large space without detailed simulation.



full-domain microscale simulation (of the fluid dynamics, e.g.) over such a large space is impractical. Hence, many multiscale modelling methods (e.g., Emereuwa 2020; Grooms and Julien 2018; Welsh et al. 2018) aim to accurately model the macroscale physics by computing only within small coupled regions in the domain as depicted in Fig. 1.1.1. The unsimulated nodes corresponding to the intermediate scales are interpolated from the small number of simulated nodes that are located sparsely over a large space. Hence, multiscale modelling of macroscale physics by computing only within small coupled regions located sparsely over large space offers enormous computational savings. Such large computational savings is an enabling powerful feature of multiscale modelling.

The *patch scheme* is an equation-free multiscale framework. A patch scheme performs detailed microscale simulations within small *patches* and couples the patches (*patch coupling*) via interpolation over the macroscale space (Hyman 2005; Kevrekidis et al. 2004; Kevrekidis and Samaey 2009). One can achieve arbitrarily high order of macroscale consistency for patch schemes via appropriate high order interpolation for patch coupling (Roberts and Kevrekidis 2005, 2007).

- Patch schemes are *equation-free* as connecting the scales is done through generic interpolation instead of explicit equations as done in homogenisation and similar other multiscale methods; that is, there is no derived equation that describes the macroscale model. The only information we obtain about the macroscale model is the computational data (Kevrekidis and Samaey 2009).
- A patch scheme, as a framework, is generally agnostic of the un-

derlying microscale model. One can use microscale mesh-based models (Bunder et al. 2020, 2017; Maclean et al. 2021b; Roberts and Kevrekidis 2007) like finite difference, finite volume, finite element or its recent variant of particle finite element (Franci et al. 2020); or meshless models (Cisternas et al. 2004; Kevrekidis et al. 2003; Makeev and Kevrekidis 2004; Siettos et al. 2012; Tsoumanis et al. 2010) like smoothed particle hydrodynamics, lattice–Boltzmann, Monte–Carlo, molecular dynamics, or other stochastic systems such as modelling of evolving diseases, and agent-based models.

Thus, the patch scheme is a general framework with high flexibility for many different application domains and different kinds of problems.

In patch schemes for stochastic systems, the patches contain stochastic microscale states. A patch scheme starts with a macroscale initial condition over the simulation domain. Then, a macroscale to microscale (*lifting*) operator gives stochastic sub-patch microscale states whose distribution is consistent with the macroscale variation over the simulation domain (Kevrekidis et al. 2004, p.1348; Samaey et al. 2009, pp. 4–5). Then, the microscale model evolves the sub-patch microscale states for one time step as dictated by some governing rules. Then, a microscale to macroscale (*restriction*) operator gives a macroscale value for a patch which is an aggregate statistic of the microscale states within that patch, typically low-order moments (Kevrekidis et al. 2004, p.1348; Samaey et al. 2009, p. 5). For the next iteration, the lifting operator gives new sub-patch microscale values, then the microscale states evolve, and then the cycle continues.

In patch schemes for grid-based discrete models of continuum problems (e.g., numerically solving PDEs over a finite grid of discrete points in space and time), the patches contain deterministic interior node values—the sub-patch microscale states (Bunder et al. 2020, 2017; Maclean et al. 2021b; Roberts and Kevrekidis 2007). A patch scheme starts with a microscale initial condition over the simulation domain, which assigns the values of all the sub-patch microscale nodes. Then, an *aggregation function* gives a *macroscale value* for a patch which is based on the sub-patch microscale states, typically the patch centre value or mean of all the sub-patch node values. This aggregation function for grid-based systems is analogous to the restriction operator of the patch schemes for stochastic systems in that it carries information from microscale to macroscale dynamics; but in terms of how it works aggregation is different from the restriction operator. Then, the *patch coupling* gives the values of the patch edge nodes by interpolating over the macroscale values of the neighbouring patches. This patch coupling macroscale interpolation for grid-based systems is

analogous to the lifting operator of the patch schemes for stochastic systems in that it carries information from macroscale to microscale dynamics; but in terms of how it works the patch coupling is different from the restriction operator. For example, Fig. 2.1.2 of §2.1.2 illustrates the process of patch coupling and aggregation. Then, the microscale model evolves the sub-patch microscale states (interior node values) for one time step, typically via discrete approximations of PDEs. For the next iteration, the aggregation function gives new macroscale values for the patches, and then the cycle continues.

1.2 Patch schemes for wave-like systems are challenging

Patch schemes have been developed and applied successfully for dissipative systems (Bunder et al. 2017; Maclean et al. 2021b; Roberts and Kevrekidis 2005, 2007). The weak inherent dissipation in wave-like systems poses significant challenges for developing patch schemes that are stable and accurate for wave-like systems, especially in multiple dimensions. The recent works of Cao and Roberts (2013, 2015) extend the patch scheme to 1D wave-like systems. *This PhD thesis develops the equation-free multiscale patch schemes for 2D wave-like systems (small dissipation) and explores the schemes more thoroughly.* The developed 2D staggered patch schemes should generalise straightforwardly to higher spatial dimensions.

Chapter 2 explains the challenges of the numerical schemes for wave-like (near Hamiltonian) systems with negligible dissipation in the context of both the full-domain and multiscale modelling. Section 2.1 introduces the staggered grid, a common strategy used in full-domain numerical simulation of wave-like systems. Section 2.1 extends the full-domain concept of staggered grids to multiscale modelling. As §2.1.2 shows, a total of 83 520 staggered patch grids are possible as geometrically compatible 2D discretisations for simulating multiscale wave physics. Yet, as §3.5.1 shows, the staggered patch schemes on very many such staggered grids are unstable and/or inaccurate. *We designed two staggered patch grids that constitute stable and accurate staggered patch schemes for wave-like systems.*

Patch coupling provides a two-way connection between two scales: from microscale within patches to macroscale over the domain, and from macroscale to microscale. Depending upon the patch coupling methods, many variants of patch schemes are possible on a staggered patch grid; many such patch schemes are unstable and/or inaccurate. *We developed two*

novel families of equation-free multiscale staggered patch schemes for accurate large-scale simulation of wave-like systems: a spectral patch scheme, and four polynomial patch schemes. A spectral patch scheme couples the patch edge values via macroscopic global 2D spectral interpolation. A family of polynomial patch schemes couple the patch edge values via macroscopic local 2D polynomial interpolations. A basic pilot study and an example implementation of the 2D staggered patch schemes developed in this thesis is published in the article by Bunder et al. (2020).

1.3 Staggered patch schemes are stable, accurate, consistent, and efficient for waves

The detailed analysis in [Chapters 3 to 5](#) establishes that the developed five staggered patch schemes (a spectral patch scheme, and four polynomial patch schemes) are stable, accurate, consistent with the given microscale model for increasingly finer patch grids, and computationally efficient for simulating macroscale wave-like systems (e.g., general linear wave, viscous shallow water flows, turbulent shallow water flows).

[Chapter 3](#) shows that the staggered patch schemes accurately simulate the macroscale dynamics of the 2D *general (dissipative) linear wave-like systems*, with linear drag and viscous diffusion. [Chapter 3](#) interprets the variables in the general linear waves in the context of water waves, but all the discussions and outcomes are generally applicable for many 2D *linear* wave phenomena. [Section 3.1](#) derives a discrete full-domain microscale model and a generic staggered patch scheme corresponding to the general linear wave PDEs. [Section 3.2](#) shows that the developed five staggered patch schemes are accurate for the general linear wave by comparing the eigenvalues of the staggered patch schemes with the eigenvalues of the full-domain microscale model. [Sections 3.2.1 to 3.2.5](#) derives the eigenvalues of the general linear wave PDEs, full-domain microscale model, and that of the staggered patch schemes. [Section 3.2.6](#) illustrates the structure of the patch scheme eigenvalues in the complex plane and explains the corresponding dynamical modes via eigenvector plots. The eigenvalue analysis in [§3.2.6](#) visually demonstrates the accuracy (in the complex plane eigenvalue plots) for a representative subset of the physical parameters and grid parameters. [Section 3.4](#) shows that the staggered the patch schemes are not sensitive to numerical roundoff errors for the general linear wave. [Section 3.5](#) demonstrates the stability of the staggered patch schemes and explores the dependence of the patch scheme stability on various aspects

like grid symmetry, physical parameters, and grid parameters. [Section 3.5.1](#) shows that among the 83 520 possible 2D staggered patch grids for wave-like systems, almost all lead to unstable and/or inaccurate patch schemes. [Section 3.6](#) shows that the staggered patch schemes are consistent with the given microscale model for increasingly finer patch grids. [Section 3.7](#) quantifies and demonstrates the large computational savings of the staggered patch schemes for the general linear wave. [Section 3.7.5](#) demonstrates the accuracy and effectiveness of the patch schemes via time simulation of the general dissipative linear waves for two example cases (simple progressive wave and moving Gaussian hump). Via random perturbation to the initial condition, [§3.7.5](#) also demonstrates the robustness of the patch schemes.

The impactful utility of the multiscale staggered patch schemes lies in modelling wave-like systems possessing complex physical processes such as nonlinear waves, turbulence, sediment transport etc. Nonlinear waves exhibit rich and complex characteristics (superposition does not hold, sensitive dependence on initial conditions, discontinuous solutions, etc.) that are not present in the linear waves, and pose additional challenges to the patch grid geometry and to the accuracy, stability and consistency of the patch schemes. First, as a prototype of nonlinear waves, [Chapter 4](#) explores the multiscale patch scheme simulation of laminar viscous shallow water flows. Specifically, [Chapter 4](#) shows that the staggered patch schemes accurately simulate the macroscale dynamics of viscous shallow water flows, using the PDEs derived by Roberts and Li (2006) as the microscale model within the patches. The nonlinearity in these viscous shallow water flows is primarily due to the advection and the height-dependent bed drag. Roberts and Li (2006) demonstrate the utility of their derived viscous shallow water PDEs for various thin-fluid flows such as drop formation on cylindrical fibres, wave transitions, three-dimensional instabilities, Faraday waves, viscous hydraulic jumps, flow vortices in a compound channel and flow down and up a step.

[Sections 4.1.2](#) and [4.1.3](#) derive a discrete full-domain microscale model and a generic staggered patch scheme respectively, corresponding to the viscous shallow water PDEs. [Section 4.2](#) shows that the developed five staggered patch schemes are accurate for viscous shallow water flows by comparing the eigenvalues of the staggered patch schemes with the eigenvalues of the full-domain microscale model. [Sections 4.2.1](#) to [4.2.5](#) derives the eigenvalues of the viscous shallow water PDEs, full-domain microscale model, and that of the staggered patch schemes. [Section 4.2.6](#) illustrates the structure of the patch scheme eigenvalues in the complex plane and explains the corresponding dynamical modes via eigenvector plots.

For the linear waves, due to superposition, it is sufficient to study the stability, accuracy and consistency for one initial condition. Due to nonlinearity in the viscous shallow water flows, [Chapter 4](#) establishes the stability, accuracy and consistency of the staggered patch schemes for a range of linearisation points (i.e., different mean flows). The eigenvalue analysis in [§4.2.6](#) visually demonstrates the accuracy (in the complex plane eigenvalue plots) for a representative subset of the physical parameters and grid parameters. [Section 4.5](#) on the consistency of the patch schemes establishes the accuracy over a wider range of parameters. [Section 4.3](#) shows that the staggered patch schemes are not sensitive to numerical roundoff errors for viscous shallow water flows.

In contrast to the general linear wave in [Chapter 3](#), the viscous shallow water flows have inherent physical instability. Hence, a good patch scheme must be stable as well as unstable in correspondence to the physical system depending upon the physical parameters (Reynolds number, mean flow), but without any additional/artificial instability. [Section 4.4](#) shows that the staggered patch schemes do not have any artificial instability for appropriate patch grids and explores the dependence of the patch scheme stability on various aspects like grid symmetry, physical parameters, and grid parameters. [Section 4.5](#) shows that the staggered patch schemes are consistent with the given microscale model for increasingly finer patch grids. [Section 4.7](#) quantifies and demonstrates the large computational savings of the staggered patch schemes for viscous shallow water flows. [Section 4.7.5](#) demonstrates the accuracy and effectiveness of the patch schemes via time simulation of a viscous roll wave. [Section 4.7.6](#) establishes the accuracy of the staggered patch scheme time simulations more quantitatively and explains some subtle details of the practical issues in the patch scheme simulations.

Nonlinear models are essential in the accurate simulation of environmental water waves and also for their pressure-based underwater measurements (e.g., [Constantin 2017](#)). As the second prototype of nonlinear waves, [Chapter 5](#) explores the multiscale patch scheme simulation of highly nonlinear turbulent shallow water flows using the PDEs derived by [Cao and Roberts \(2016\)](#) as the microscale model within the patches. There is a significant increase in the physical complexity of the turbulent shallow water PDEs of [Cao and Roberts \(2016\)](#), compared to the viscous shallow water PDEs of [Roberts and Li \(2006\)](#) in [Chapter 4](#). The viscous shallow water PDEs of [Roberts and Li \(2006\)](#) have only relatively weak nonlinearity primarily due to the advection and the height dependent bed drag. But in the turbulent shallow water PDEs, due to the rate dependent *eddy viscosity*, the strong nonlinearity arises in almost all terms. *This strong nonlinearity*

and the increased physical complexity in the turbulent shallow water flows pose even more challenges for the development of the multiscale patch schemes. For example, for viscous shallow water flows the minimal six sub-patch micro-grid intervals are generally sufficient, but turbulent shallow water flows require a minimum of ten sub-patch micro-grid intervals to avoid artificial instabilities for many parameter combinations. Unlike viscous shallow water flows, turbulent shallow water flows exhibit steeper discontinuities in solution (e.g., steeper roll waves) and stronger physical instabilities. Such issues lead to more pronounced artificial instabilities of the patch schemes, requiring more careful choices for the patch grid parameters. [Chapter 5](#) establishes that the patch schemes accurately simulate the macroscale dynamics of turbulent shallow water flows for appropriate grid parameters.

[Section 5.1](#) derives a discrete full-domain microscale model and a generic staggered patch scheme corresponding to the turbulent shallow water PDEs. [Section 5.2](#) shows that the developed five staggered patch schemes are accurate for turbulent shallow water flows by comparing the eigenvalues of the staggered patch schemes with the eigenvalues of the full-domain microscale model. [Sections 5.2.1](#) to [5.2.3](#) derive the eigenvalues of the turbulent shallow water PDEs, full-domain microscale model, and that of the staggered patch schemes respectively. [Section 5.2.4](#) illustrates the structure of the patch scheme eigenvalues in the complex plane and explains the corresponding dynamical modes via eigenvector plots. The eigenvalue analysis in [§5.2.4](#) visually demonstrates the accuracy (in the complex plane eigenvalue plots) for a representative subset of the physical parameters and grid parameters. [Section 5.4](#) on the consistency of the patch schemes establishes the accuracy over a wider range of parameters. [Section 5.3](#) shows that the staggered patch schemes do not have any artificial instability for appropriate patch grids and explores the dependence of the patch scheme stability on various aspects like grid symmetry, physical parameters, and grid parameters. [Section 5.4](#) shows that the staggered patch schemes are consistent with the given microscale model for increasingly finer patch grids. [Section 5.5](#) demonstrates the accuracy and effectiveness of the patch schemes via time simulation of a turbulent roll wave.

[Chapter 6](#) presents the conclusive summary and discusses the further research directions. [Section 6.1](#) concludes with some key details that the developed multiscale staggered patch schemes enable accurate large-scale simulation of wave-like systems. [Section 6.2](#) lists several impactful further research directions.

Chapter 2

Extend staggered grids to multiscale modelling

The numerical schemes for wave-like systems with negligible dissipation are often inaccurate and unstable due to truncation errors and numerical roundoff errors. Hence, numerical simulations of wave-like systems that ignore these numerical issues often fail to represent the physical characteristics of wave phenomena. This challenge gets even more intricate for the multiscale patch schemes, especially in multiple dimensions. The recent works of Cao and Roberts (2013, 2015) extend the patch scheme to 1D wave-like systems using *staggered grids* (§2.1 explains the staggered grids). *This PhD thesis develops the equation-free multiscale staggered patch schemes for 2D wave-like systems (small dissipation)* and explores the schemes more thoroughly.

Section 2.1 first introduces one of the common strategies used in full-domain numerical simulation of wave-like systems known as the staggered grid that gives accurate and robust numerical schemes for wave-like systems. Section 2.1 then extends the full-domain concept of staggered grids to multiscale modelling. We expect most characteristics of a staggered grid also hold for the multiscale wave-like simulations, which is established for three different wave-like systems each in separate subsequent chapters.

As §2.1.2 explains, a patch scheme's patch coupling provides a two-way connection between two scales: from microscale within patches to macroscale over the domain, and from macroscale to microscale. Section 2.2 explains two kinds of patch coupling which lead to two families of staggered patch schemes: a spectral patch scheme, and four polynomial patch schemes.

2.1 Staggered patches of staggered micro-grid for multiscale modelling

Section 2.1.1 introduces one of the common strategies used in full-domain numerical simulation of wave-like systems known as the staggered grid that gives accurate and robust numerical schemes for wave-like systems.

Section 2.1.2 explains how our research extends the full-domain concept of staggered grids to multiscale modelling, using staggered patches of a staggered “*micro-grid*” (fine microscale grid within the patches).

The discussion in §2.1.2 is for systems with only first-order derivatives in their governing equations. Section 2.1.3 explains extending the staggered grid to multiscale modelling for systems with higher order derivatives in their governing equations.

2.1.1 Staggered grids are best for full-domain waves-like systems

For wave-like (near Hamiltonian) systems with little or no dissipation, accurate numerical simulation is challenging for the usual full-domain numerical simulation itself, especially over long time, which gets even more intricate for the multiscale modelling. The numerical schemes for wave-like systems with negligible dissipation are often inaccurate and unstable due to numerical dissipation and numerical dispersion caused by truncation and numerical roundoff errors (Hinch 2020, p.136; Zikanov 2010, pp. 70–73; Anderson 1995, pp. 232–243). Hence, numerical simulations of wave-like systems without proper handling of these numerical issues often fail to represent the physical characteristics of wave phenomena. This subsection introduces one of the common strategies used in full-domain numerical simulation of wave-like systems known as the staggered grid which gives accurate and robust numerical schemes for wave-like systems.

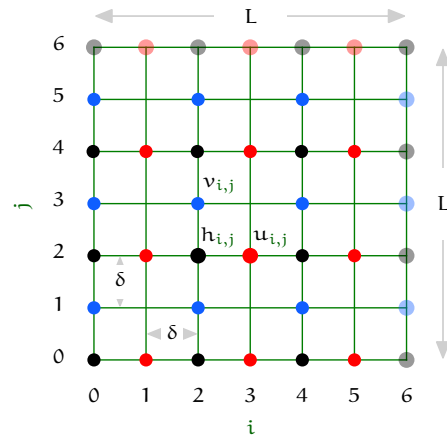
Consider a generic 2D wave-like system over the macroscale periodic spatial domain $[0, L] \times [0, L]$. Such systems in terms of $h(x, y, t)$, $u(x, y, t)$ and $v(x, y, t)$ are modelled as non-dimensional PDEs,

$$\frac{\partial h}{\partial t} = -\frac{\partial u}{\partial x} - \frac{\partial v}{\partial y} + f_0(h, u, v), \quad (2.1.1a)$$

$$\frac{\partial u}{\partial t} = -\frac{\partial h}{\partial x} + f_1(h, u, v), \quad (2.1.1b)$$

$$\frac{\partial v}{\partial t} = -\frac{\partial h}{\partial y} + f_2(h, u, v), \quad (2.1.1c)$$

Figure 2.1.1. Schematic of the full-domain microscale *staggered grid* where variables are simulated only on staggered/alternating discrete points, *nodes*, \bullet h for height, \bullet u , \bullet v for horizontal velocities along x and y directions respectively. Here we draw $n = 6$ grid intervals in the green grid, both in x and y directions. Transparent filled circles on the boundaries indicate the discrete n -periodic boundary values.



with the boundary conditions that the three non-dimensional fields h , u , and v are L -periodic in both x and y , and an appropriate initial condition $h(x, y, 0)$, $u(x, y, 0)$, and $v(x, y, 0)$. In the generic wave PDEs (2.1.1), the explicitly written terms (excluding the functions f_m) models the essence of wave phenomena. The functions f_m in PDEs (2.1.1) indicate other application-specific terms, potentially nonlinear and/or involving higher derivatives. The functions f_m could model additional physics in addition to the wave phenomena, such as bed drag, viscous/turbulent diffusion and surface tension. In the generic wave PDEs (2.1.1), dropping the additional terms denoted by f_m gives the PDEs for ideal wave. The dependent variables in PDEs (2.1.1) let us interpret the PDEs as a model of water wave with h as height and u, v as horizontal velocities along x and y directions respectively. But it is a generic model of many 2D wave phenomena.

In *staggered grids*, the state variables are interspersed at alternate discrete points (nodes) where green grid lines intersect. For example, in Fig. 2.1.1, the h, u nodes are horizontally alternating and the h, v nodes are vertically alternating. In contrast, the usual *collocated grids*, store all state variables at each and every discrete point. In the classification of Arakawa and Lamb (1977, Fig. 3, p.181), these collocated and staggered grids are A-grid and C-grid respectively. The staggered grid was first used in the Marker and Cell (MAC) method of Harlow and Welch (1965). The staggered grids were later used in the SIMPLE (Semi Implicit Method for Pressure Linked Equations) method of Patankar and Spalding (1972) and many others. For wave-like systems, staggered grids such as depicted in Fig. 2.1.1 lead to higher accuracy compared to that of a same-order scheme in collocated grids. Staggered grids preserve much of the wave characteristics (Fornberg and Christ 1999, Figs. 8 and 9; Fornberg 1990). Even though a central difference scheme on a collocated grid gives a second-order accuracy, the same second-

order accurate central difference scheme on a staggered grid is significantly less dispersive (Lauritzen et al. 2011, p. 46, §3.2; Ólafsson and Bao 2021, p. 55, §2.2.1). Also, the group velocity of the energy propagation in the numerical waves on a staggered grid is in the correct direction. Whereas for collocated grid schemes the group velocities for large wavenumbers are in the opposite direction to that of the correct solution (Lauritzen et al. 2011, p. 46, §3.2; Ólafsson and Bao 2021, p. 55, §2.2.1). Hence, staggered grids (e.g., Fig. 2.1.1) are simple and robust for full-domain numerical simulation of waves.

Figure 2.1.1 depicts a full-domain microscale staggered grid over the square domain $[0, L] \times [0, L]$, with microscale grid interval δ , for illustration shown with a very small number of grid intervals $n = 6$. Approximating the spatial derivatives in the generic wave PDEs (2.1.1) by central finite differences on the nodes (filled circles) in Fig. 2.1.1, gives the *full-domain microscale model* corresponding to the generic wave-like system (2.1.1)

$$\bullet \frac{dh_{i,j}}{dt} = -\frac{u_{i+1,j} - u_{i-1,j}}{2\delta} - \frac{v_{i,j+1} - v_{i,j-1}}{2\delta} + f_{0,i,j}^{\mu} \quad (2.1.2a)$$

for $i, j \in \{0, 2, 4, \dots, n-2\}$,

$$\bullet \frac{du_{i,j}}{dt} = -\frac{h_{i+1,j} - h_{i-1,j}}{2\delta} + f_{1,i,j}^{\mu} \quad (2.1.2b)$$

for $i \in \{1, 3, 5, \dots, n-1\}$, $j \in \{0, 2, 4, \dots, n-2\}$,

$$\bullet \frac{dv_{i,j}}{dt} = -\frac{h_{i,j+1} - h_{i,j-1}}{2\delta} + f_{2,i,j}^{\mu} \quad (2.1.2c)$$

for $i \in \{0, 2, 4, \dots, n-2\}$, $j \in \{1, 3, 5, \dots, n-1\}$.

Analogous to the PDEs (2.1.1), the three fields h, u, v are n -periodic in both i and j where $n = L/\delta$, with an appropriate initial condition $h_{i,j}(0)$, $u_{i,j}(0)$, and $v_{i,j}(0)$. The terms $f_{m,i,j}^{\mu}$ indicate full-domain discretisation of the additional application-specific terms f_m in the PDEs (2.1.1). The coloured bullets $\bullet, \bullet, \bullet$ in the full-domain microscale model (2.1.2) indicate respectively the $h, u,$ and v nodes.

The PDEs (2.1.1) inspire the microscale computational model (2.1.2). Hence occasionally we aim to compare the characteristics of the staggered patch scheme and full-domain microscale model with the characteristics of the PDEs. But, *it is the microscale computational model that the staggered patch scheme seeks to predict accurately, not the solutions of the PDEs*. Thus, how well the full-domain microscale model (2.1.2) predicts the solutions of the PDEs (2.1.1) is peripheral in this study.

Arranging the state variables of (2.1.2) that are defined over the staggered grid in Fig. 2.1.1, into a vector gives the state vector of the full-domain microscale model

$$\mathbf{x} = (\quad h_{0,0}, h_{0,2}, h_{0,4}, \dots, h_{2,0}, h_{2,2}, h_{2,4}, \dots, \\ \dots, u_{1,0}, u_{1,2}, u_{1,4}, \dots, u_{3,0}, u_{3,2}, u_{3,4}, \dots, \\ \dots, v_{0,1}, v_{0,3}, v_{0,5}, \dots, v_{2,1}, v_{2,3}, v_{2,5}, \dots). \quad (2.1.3)$$

For a full-domain staggered grid with $n \times n$ micro-grid intervals, the size of \mathbf{x} is $3n^2/4$. For example, for the staggered grid in Fig. 2.1.1 with $n = 6$, the state vector has 27 elements. In terms of the state vector \mathbf{x} , the full-domain microscale model (2.1.2) is represented as a dynamical system by the ODEs

$$\frac{d\mathbf{x}}{dt} = \mathbf{f}(\mathbf{x}), \quad (2.1.4)$$

where the microscale model \mathbf{f} is a vector function encapsulating the same finite difference discrete model as (2.1.2) for the generic wave-like system (2.1.1). The components of $\mathbf{f}(\mathbf{x})$ in ODEs (2.1.4) are the same as the RHS of the explicit ODEs (2.1.2), just listed in the index-order of the state vector \mathbf{x} (2.1.3).

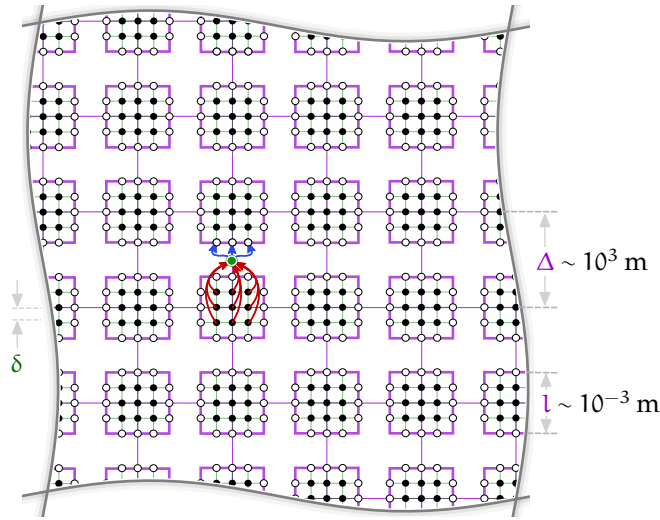
A full-domain microscale simulation is performed by numerical time-integration of the ODEs (2.1.2) on the nodes (filled circles in Fig. 2.1.1) of the full-domain microscale grid.

All the time simulations for this thesis (both the full-domain microscale model and the staggered patch scheme) are performed using the ODE integrator BS3 provided by `DifferentialEquations.jl` package (Rackauckas and Nie 2017) in the Julia programming language (Bezanson et al. 2017). BS3 is a non-stiff ODE integrator based on Bogacki–Shampine (2, 3) pair, similar to `ode23` of MATLAB (DifferentialEquations.jl 2021; L. F. Shampine and Reichelt 1997). We chose BS3 after a detailed exploration of various ODE solvers based on the accuracy and computation speed. We find that various higher order ODE integrators take significantly longer computational time yet provide only a small improvement in the time solutions. We use relative and absolute error tolerances of respectively 10^{-3} , 10^{-6} for all time simulations using the BS3 ODE integrator; higher error tolerances only increase the computational time with only negligible change in the computed solution.

2.1.2 Extend the staggered grid to multiscale patch scheme

This subsection explains how our research extends the full-domain concept of staggered grids to multiscale modelling, using staggered patches of a

Figure 2.1.2. Usual (collocated) patch grid, filled circles represent interior nodes and unfilled circles represent edge nodes that are computed by patch coupling (**compute macroscale patch values**, and **compute microscale edge values**). Patches are enlarged here for visual clarity, in practice patch size l is a few orders of magnitude smaller than the inter-patch distance Δ ; δ is sub-patch microscale grid interval.



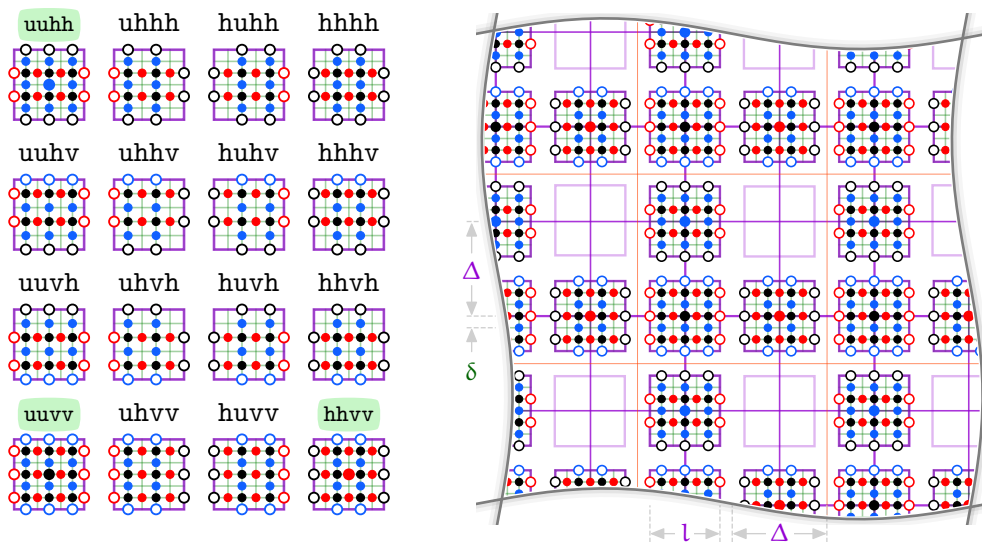
staggered “*micro-grid*” (fine microscale grid within the patches). We expect most characteristics of the full-domain staggered grid also hold for the multiscale staggered patch grid for the multiscale modelling of wave-like systems and also for any other multiscale modelling in general. But the particular focus of this thesis is on staggered patch schemes for accurate simulation of wave-like systems.

We adapt the usual (collocated) patch scheme for the dissipative systems (Fig. 2.1.2) to wave-like systems by appropriately incorporating the essential “wave-friendly” features of the staggered grids (§2.1.1). Fig. 2.1.2 shows the usual (collocated) patch grid, a non-staggered grid, with square patches. The following list defines the parameters for both collocated and staggered patch grids containing square patches over the square domain.

- Number of *macro-grid intervals* N is the number of **violet** grid intervals in the periodic domain x - and y -directions. In the rest of this thesis, for brevity, the “a patch grid with N macro-grid intervals” means “a patch grid with N macro-grid intervals in the x - and y -directions”, similarly for the other following parameters Δ , l , r , and n .
- *Inter-patch distance* Δ is the distance between two adjacent patch cen-

Figure 2.1.3. Possible micro-grids and the chosen staggered patch grid (patch size l , inter-patch distance Δ , sub-patch microscale grid interval δ). The nodes use the same colour coding as the full-domain microscale staggered grid in Fig. 2.1.1: \bullet h for height, \bullet u , \bullet v for horizontal velocities along x and y directions respectively.

- (a) All 16 possible staggered micro-grids compatible for PDEs of wave-like systems (2.1.2). The names indicate edge node type.
- (b) Chosen staggered patch grid uses micro-grids $uuvv$, $hhvv$ and $uuhh$, for stable and accurate patch schemes with minimal computational effort.



tres (size of the violet grid intervals) in x - and y -directions (uniformly spaced patches over a square domain is our focus).

- Patch size l is the side length of the square patch in x - and y -directions.
- Patch scale ratio $r = l/(2\Delta)$ quantifies the ratio of the simulated to the unsimulated space for each spatial dimension in a rectangular simulation domain.
- Number of sub-patch micro-grid intervals n is the number of green grid intervals within a patch in x - and y -directions.
- Sub-patch micro-grid interval δ is the distance between two adjacent micro-grid nodes (size of the green grid intervals) in x - and y -directions (uniformly spaced micro-grid nodes over a square patch is our focus).

In a patch scheme, at each time step, the edge values (by coupling the patches) and the interior node initial values (from previous time step)

are known. Given the edge values and the interior values at the current time step, an ODE integrator such as BS3 of `DifferentialEquations.jl` (Rackauckas and Nie 2017), computes the interior values at the next time step by computing time derivatives from the governing ODEs (2.1.2). In an usual patch scheme over the collocated patch grid, constructing and using a micro-grid within a patch is straightforward as there is only one way to arrange patch edge nodes, as depicted in Fig. 2.1.2. But when we use a staggered grid (depicted in Fig. 2.1.1) as the micro-grid within a patch, the heterogeneous nodes lead to different arrangements of the patch edge nodes. To have all the necessary edge nodes for calculating the required spatial derivatives at all the interior nodes for wave-like systems using ODEs (2.1.2), a total of 16 different kinds of micro-grid are possible within a 2D patch (Fig. 2.1.3a). We denote each micro-grid by the type of nodes on left, right, bottom and top edges respectively. For example, as illustrated in the left-bottom of Fig. 2.1.3a, `uuvv` means that the micro-grid has `u`-edge nodes on the left and right edges, and `v`-edge nodes on the bottom and top edge nodes. Among the 16 possible types, only three patch micro-grids `uuvv`, `hhvv` and `uuhh` (green highlighted in Fig. 2.1.3a) have a node at the centre of the patch, these types of patches are called *h-centred*, *u-centred* and *v-centred* patches respectively.

Consider a possible 2D staggered patch grid to be designed, comprising the cells (orange squares in Fig. 2.1.3b) each containing $2 \times 2 = 4$ patches (purple squares in Fig. 2.1.3b). Each of the four patches within a cell could be either empty or contain one of the 16 possible micro-grids of Fig. 2.1.3a. Thus the total number of possible 2D staggered patch grids (in a 2×2 cell configuration) is $(16 + 1)^4 - 1 = 83\,520$, excluding the all-empty case.

We define a staggered patch grid to be geometrically *compatible* when the patches have all the necessary edge nodes to calculate spatial derivatives of all the interior nodes using the governing ODEs (2.1.2). For example, the `uhvv` micro-grid (second in the bottom row of Fig. 2.1.3a) would not be compatible if the right edge contains `v`-nodes instead of `h`-nodes, as the `h`-nodes are necessary on the right edge to compute $\partial h / \partial x$ on the right most interior `u`-nodes.

Whereas all the possible 83 520 staggered patch grids are geometrically compatible 2D discretisations for simulating multiscale wave physics, most of them constitute unstable patch schemes (§3.5.1). As discussed in §3.5.1, patch grids containing any sub-patch micro-grid without a centre node (i.e., micro-grids other than the green highlighted ones in Fig. 2.1.3a), lead to unstable patch schemes. Among the staggered patch grids that have a centre node in each of the patches, from the stability analysis we found only two staggered patch grids over which the staggered patch schemes are

stable, they are plotted in Figs. 2.1.3b and 3.5.1b. From the two staggered patch grids that constitute stable patch schemes, we find the staggered patch grid depicted in Fig. 2.1.3b to be the best in terms of computational effort and accuracy (§3.5.1 discusses the details). Except §3.5.1, which discusses the choosing of the patch grid in Fig. 2.1.3b, all other discussions in this thesis are based on the staggered patch grid in Fig. 2.1.3b, with one or more layers of edge nodes (§2.1.3).

The chosen staggered patch grid in Fig. 2.1.3b, in addition to having the reflective symmetry, also has *self-similarity* among the micro- and macroscales: just as $\bullet\text{-}\bullet$ and $\bullet\text{-}\bullet$ nodes are staggered (alternating) along the x - and y -directions (horizontal and vertical in Fig. 2.1.3b) within the micro-grid, $\bullet\text{-}\bullet$ and $\bullet\text{-}\bullet$ centred patches are staggered for the macroscale.

Fig. 2.1.4 illustrates the following three kinds of indices we use to identify the patches and sub-patch micro-grid nodes in Fig. 2.1.3b:

- the pair $I, J \in \{0, 1, \dots, N-1\}$ is the global (macroscale) patch index;
- the pair p, q with $p = I \bmod 2$, $q = J \bmod 2$, is the local (macroscale) sub-cell patch index, that is, $p, q \in \{0, 1\}$ within each macro-cell (orange squares in Fig. 2.1.4b);
- (i, j) is the sub-patch micro-grid node index with $i, j \in \{1, \dots, n-1\}$ for interior nodes (filled circles \bullet , \bullet , \bullet in Figs. 2.1.4a and 2.1.5a) and $i, j \in \{0, n\}$ for patch edge nodes (unfilled circles \circ , \circ , \circ in Figs. 2.1.4a and 2.1.5a).

Using the microscale model (2.1.2) within the patches in a staggered patch grid (Fig. 2.1.3b) with N macro-grid intervals (i.e., total of $N/2 \times N/2$ macro-cells with each macro-cell containing 3 patches h -centred, u -centred and v -centred), where each patch consists of n sub-patch micro-grid intervals (e.g., Fig. 2.1.3b shows a staggered patch grid with $n = 6$), gives the *staggered patch scheme* for the microscale model (2.1.2) of a generic wave-like system as

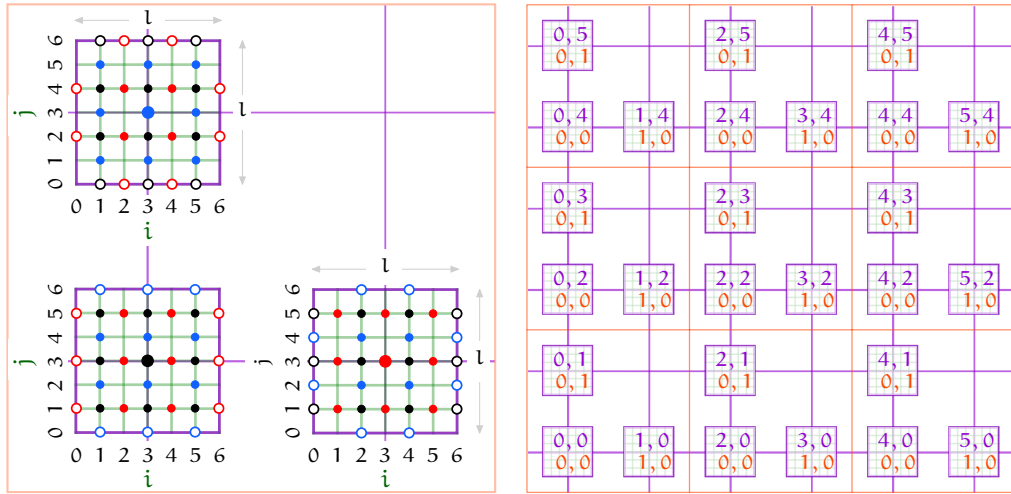
$$\bullet \frac{d}{dt} h_{i,j}^{I,J}(t) = -\frac{u_{i+1,j}^{I,J} - u_{i-1,j}^{I,J}}{2\delta} - \frac{v_{i,j+1}^{I,J} - v_{i,j-1}^{I,J}}{2\delta} + f_{0,i,j}^p(h, u, v), \quad (2.1.5a)$$

$$\begin{aligned} i \in \{1, 3, 5, \dots, n-1\}, \quad j \in \{1, 3, 5, \dots, n-1\} & \text{ for } p = 0, q = 0, \\ i \in \{1, 3, 5, \dots, n-1\}, \quad j \in \{2, 4, \dots, n-2\} & \text{ for } p = 0, q = 1, \\ i \in \{2, 4, \dots, n-2\}, \quad j \in \{1, 3, 5, \dots, n-1\} & \text{ for } p = 1, q = 0, \end{aligned}$$

$$\bullet \frac{d}{dt} u_{i,j}^{I,J}(t) = -\frac{h_{i+1,j}^{I,J} - h_{i-1,j}^{I,J}}{2\delta} + f_{1,i,j}^p(h, u, v), \quad (2.1.5b)$$

Figure 2.1.4. Index convention for the staggered patch grid with $N = 6$ macro-grid intervals in the **violet** grid, containing staggered patches of staggered micro-grids with $n = 6$ micro-grid intervals in the **green** grid.

- (a) Sub-patch micro-grid node index $i, j \in \{1, 2, \dots, n-1\}$ for the interior nodes (filled circles $\bullet, \bullet, \bullet$) and $i, j \in \{0, n\}$ for patch edge nodes (unfilled circles \circ, \circ, \circ).
- (b) Global (macroscale) patch index $I, J \in \{0, 1, \dots, N-1\}$; local sub-cell patch index $p, q \in \{0, 1\}$ within each macro-cell (**orange** squares).



$$\begin{aligned}
 i \in \{2, 4, \dots, n-2\}, \quad j \in \{1, 3, 5, \dots, n-1\} & \text{ for } p = 0, q = 0, \\
 i \in \{2, 4, \dots, n-2\}, \quad j \in \{2, 4, \dots, n-2\} & \text{ for } p = 0, q = 1, \\
 i \in \{1, 3, 5, \dots, n-1\}, \quad j \in \{1, 3, 5, \dots, n-1\} & \text{ for } p = 1, q = 0,
 \end{aligned}$$

$$\bullet \frac{d}{dt} v_{i,j}^{I,J}(t) = -\frac{h^{I,J}_{i,j+1} - h^{I,J}_{i,j-1}}{2\delta} + f_{2,i,j}^p(h, u, v), \quad (2.1.5c)$$

$$\begin{aligned}
 i \in \{1, 3, 5, \dots, n-1\}, \quad j \in \{2, 4, \dots, n-2\} & \text{ for } p = 0, q = 0, \\
 i \in \{1, 3, 5, \dots, n-1\}, \quad j \in \{1, 3, 5, \dots, n-1\} & \text{ for } p = 0, q = 1, \\
 i \in \{2, 4, \dots, n-2\}, \quad j \in \{2, 4, \dots, n-2\} & \text{ for } p = 1, q = 0,
 \end{aligned}$$

and a patch coupling (e.g., Square-p4) to compute the edge values

$\circ h_{i,j}^{I,J}, \circ u_{i,j}^{I,J}, \circ v_{i,j}^{I,J}$ for

$i \in \{0, n\}, j \in \{1, 2, \dots, n-1\}$ for left and right edges and

$i \in \{1, 2, \dots, n-1\}, j \in \{0, n\}$ for bottom and top edges, (2.1.5d)

$I \in \{0, 2, 4, \dots, N-2\}$ for h, v , $I \in \{1, 3, 5, \dots, N-1\}$ for u ,

$J \in \{0, 2, 4, \dots, N-2\}$ for h, u , $J \in \{1, 3, 5, \dots, N-1\}$ for v .

Analogous to the full-domain microscale model (2.1.2), the three fields $h, u,$

v are macroscale N -periodic in both \mathbf{I} and \mathbf{J} where $N = L/\Delta$, with an appropriate initial condition $h_{i,j}^{\mathbf{I},\mathbf{J}}(0)$, $u_{i,j}^{\mathbf{I},\mathbf{J}}(0)$, and $v_{i,j}^{\mathbf{I},\mathbf{J}}(0)$. The functions $f_{m,i,j}^p$ indicate patch grid discretisation of the additional application-specific terms corresponding to the terms $f_{m,i,j}^\mu$ in the full-domain microscale model (2.1.2). A specific patch coupling method computes patch edge nodes ($\circ h_{i,j}^{\mathbf{I},\mathbf{J}}$, $\circ u_{i,j}^{\mathbf{I},\mathbf{J}}$, $\circ v_{i,j}^{\mathbf{I},\mathbf{J}}$ in Fig. 2.1.5a) from the interior nodes of the neighbouring patches ($\bullet h_{i,j}^{\mathbf{I},\mathbf{J}}$, $\bullet u_{i,j}^{\mathbf{I},\mathbf{J}}$, $\bullet v_{i,j}^{\mathbf{I},\mathbf{J}}$ with $i = j = n/2$ in Fig. 2.1.5a), and provides the mechanism whereby patches influence each other. Section 2.2 discusses details of different patch coupling.

Arranging the patch interior values of (2.1.5), which are over the staggered patch grid in Fig. 2.1.4, into a vector gives the state vector \mathbf{x}^I of the staggered patch scheme, which is a dynamic state variable evolving in time. The superscript $(\cdot)^I$ is not an index or exponent, instead, a qualifier denoting the patch interior nodes. The general form of a staggered patch scheme state vector \mathbf{x}^I of size n_p^I containing all the interior values of all the patches is,

$$\mathbf{x}^I = \left(\begin{array}{l} h_{1,1}^{0,0}, h_{1,3}^{0,0}, \dots, u_{2,1}^{0,0}, u_{2,3}^{0,0}, \dots, v_{1,2}^{0,0}, v_{1,4}^{0,0}, \dots, \\ h_{1,2}^{0,1}, h_{1,4}^{0,1}, \dots, u_{2,2}^{0,1}, u_{2,4}^{0,1}, \dots, v_{1,1}^{0,1}, v_{1,3}^{0,1}, \dots, \\ h_{1,1}^{0,2}, h_{1,3}^{0,2}, \dots, u_{2,1}^{0,2}, u_{2,3}^{0,2}, \dots, v_{1,2}^{0,2}, v_{1,4}^{0,2}, \dots, \\ h_{2,1}^{1,0}, h_{2,3}^{1,0}, \dots, u_{1,1}^{1,0}, u_{1,3}^{1,0}, \dots, v_{2,2}^{1,0}, v_{2,4}^{1,0}, \dots, \\ h_{2,1}^{1,2}, h_{2,3}^{1,2}, \dots, u_{1,1}^{1,2}, u_{1,3}^{1,2}, \dots, v_{2,2}^{1,2}, v_{2,4}^{1,2}, \dots, \\ h_{1,1}^{0,2}, h_{1,3}^{0,2}, \dots, u_{2,1}^{0,2}, u_{2,3}^{0,2}, \dots, v_{1,2}^{0,2}, v_{1,4}^{0,2}, \dots \end{array} \right). \quad (2.1.6)$$

The total number of patch interior nodes, that is the size of the state vector \mathbf{x}^I ,

$$n_p^I = (N^2/4)(9n^2/4 - 4n + 2), \quad (2.1.7)$$

where N is the number of macro-grid intervals and n is the number of sub-patch micro-grid intervals. For example, for $N = 6, 10, 14, 18, 22, 26$ macro-grid intervals with $n = 6$ sub-patch micro-grid intervals, $n_p^I = 531, 1475, 2891, 4779, 7139, 9971$ respectively.

Arranging the patch edge values of (2.1.5) with $i, j \in \{0, n\}$ (Fig. 2.1.4) into a vector gives the edge vector \mathbf{x}^E of size n_p^E containing all the edge values of all the patches. The edge vector \mathbf{x}^E is computed by the patch coupling $\mathbf{x}^E(\mathbf{x}^I)$ of a particular patch scheme. The expressions (3.2.14) of §3.2.3 are some examples of the elements of the edge vector \mathbf{x}^E . For the

general linear wave with drag and viscous diffusion (i.e., with second-order spatial derivatives), a staggered patch grid needs two layers of edge nodes in the normal direction to the edges (§2.1.3) as in Fig. 2.1.5a. For the staggered patch grid in Fig. 2.1.5a, the total number of patch edge nodes, that is the size of the edge vector \mathbf{x}^E ,

$$n_p^E = (N^2/4)(18n - 16), \quad (2.1.8)$$

where N is the number of macro-grid intervals and n is the number of sub-patch micro-grid intervals. For example, for the staggered patch grid in Fig. 2.1.5a with $N = 6, 10, 14, 18, 22, 26$ and $n = 6$, $n_p^E = 828, 2300, 4508, 7452, 11132, 15548$ respectively.

In terms of the state vector \mathbf{x}^I and the edge vector \mathbf{x}^E , the staggered patch scheme (2.1.5) is represented as a dynamical system by the ODEs

$$\frac{d\mathbf{x}^I}{dt} = \mathbf{F}(\mathbf{x}^I; \mathbf{x}^E(\mathbf{x}^I)). \quad (2.1.9)$$

The $\mathbf{F}(\mathbf{x}^I; \mathbf{x}^E(\mathbf{x}^I))$ in the staggered patch scheme dynamical system (2.1.9) corresponds to the $\mathbf{f}(\mathbf{x})$ in the full-domain microscale model (2.1.4). The functions \mathbf{F} and \mathbf{f} encode the same microscale model for the generic wave-like system (2.1.1), except for the following difference:

- the only argument of \mathbf{f} is the nodal values \mathbf{x} in the full-domain microscale grid;
- the two arguments of \mathbf{F} are the patch interior values \mathbf{x}^I and the patch edge values \mathbf{x}^E in the staggered patch grid.

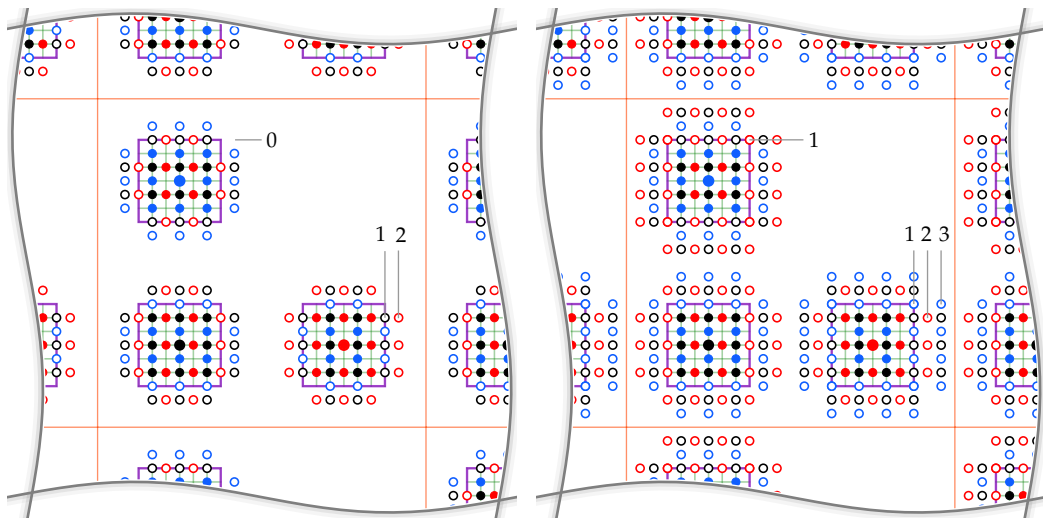
The ODEs (2.1.9) of the patch scheme represent a reduced-order approximation of the ODEs (2.1.4) of full domain microscale model. The expression (3.7.1) (p. 134 of §3.7.2) gives the ratio of the dimension of \mathbf{x}^I (2.1.9) to the dimension of \mathbf{x} (2.1.4).

Patch scheme simulation is performed by numerical time-integration of the ODEs (2.1.5) on the interior nodes of the patch grid (filled circles in Fig. 2.1.3b). Evaluating the time derivatives in the staggered patch scheme (2.1.5) is done in two steps:

1. Macroscale patch coupling (§2.2) to compute the patch edge nodes (unfilled circles in Fig. 2.1.5a);
2. Computing time derivative of the interior nodes (filled circles in Fig. 2.1.5a) for the microscale model (2.1.2) using both interior and edge values of the patches, which is expressed in complete detail by the staggered patch scheme (2.1.5).

Figure 2.1.5. Staggered patch grids with multi-layer edge nodes, for a given number of sub-patch micro-grid intervals ($n = 6$ here), contain the same number of interior nodes $\bullet h_{i,j}^{1,J}, \bullet u_{i,j}^{1,J}, \bullet v_{i,j}^{1,J}$ for $i, j \in \{1, \dots, n - 1\}$. But the number of edge values $\circ h_{i,j}^{1,J}, \circ u_{i,j}^{1,J},$ and $\circ v_{i,j}^{1,J}$ depend on the number of layers of edge nodes.

(a) Two layers of edge nodes in normal direction to the edges, no edge nodes in tangential direction to the edges (e.g., no \bullet node on corners of \bullet -centred patch). (b) Three layers of edge nodes in normal direction to the edges, one layer of edge nodes in tangential direction to the edges.



2.1.3 Multi-layer edge nodes for higher order spatial derivatives

Section 2.1.2 explains extending the staggered grid to multiscale modelling for systems with only first-order derivatives in their governing equations. This subsection explains extending the staggered grid to multiscale modelling for systems with higher order derivatives in their governing equations.

The patch grid in Fig. 2.1.3b is used for staggered patch scheme simulations of an ideal wave (PDEs (2.1.1) with only the terms that are explicitly written, that is, without the additional terms denoted by f_m) and other wave PDEs involving only first-order spatial derivatives. Finite difference discrete approximations for higher order spatial derivatives (such as second spatial derivative for viscous diffusion) use more surrounding nodes. More surrounding nodes participating in the calculation of higher order spatial derivatives is not an issue for most of the interior nodes, but the interior nodes closest to the edges of a patch need values of nodes that lie outside

the patches shown in Fig. 2.1.3b. We explored the following two cases of handling this situation.

- We first used the staggered patch grid Fig. 2.1.3b also for calculating higher order spatial derivatives (e.g., second order derivative for viscous diffusion); whenever the finite difference approximation involves nodes outside the patch edges, we extrapolated the required additional nodes using the nearest edge and interior nodes (we tried constant values, linear and quadratic extrapolation). But such extrapolations make many variants of the staggered patch schemes unstable (i.e., the solutions blow up in time).
- A second alternative is to append an additional layer of edge nodes to the staggered patch grid as in Figs. 2.1.5a and 2.1.5b and calculate their values at each iteration by macroscale patch coupling interpolation (similar to how the edge nodes in Fig. 2.1.3b are calculated). Because this way of calculating higher order spatial derivatives does not cause any instability for the staggered patch scheme, we use multi-layer edge nodes for the calculation of any higher order spatial derivatives (e.g., computing second spatial derivatives of viscous diffusion).

Figure 2.1.5 shows two examples of staggered patch grids with additional layers of edge nodes compared to Fig. 2.1.3b (which has one layer of edge nodes in the normal direction and no edge nodes in the tangential direction to the edges).

1. Irrespective of the number of layers of the edge nodes, the staggered patch grids contain the same number of interior nodes for a given number of sub-patch micro-grid intervals ($n = 6$ in Fig. 2.1.5). That is, the interior values are $\bullet h_{i,j}^{I,J}$, $\bullet u_{i,j}^{I,J}$, $\bullet v_{i,j}^{I,J}$ for $i, j \in \{1, \dots, n-1\}$.
2. Total number of edge nodes depends on the number of layers of the edge nodes. For Fig. 2.1.5a with two layers of edge nodes in normal direction to the edges and no edge nodes in tangential direction to the edges, the left and right edge values are $\circ h_{i,j}^{I,J}$, $\circ u_{i,j}^{I,J}$, $\circ v_{i,j}^{I,J}$, for $i \in \{-1, 0, n, n+1\}$ and $j \in \{1, 2, \dots, n-1\}$. Similarly the bottom and top edge value indices are $i \in \{1, 2, \dots, n-1\}$ and $j \in \{-1, 0, n, n+1\}$. For Fig. 2.1.5b with three layers of edge nodes in normal direction to the edges and one layer of edge nodes in tangential direction to the edges, the left and right edge values are $\circ h_{i,j}^{I,J}$, $\circ u_{i,j}^{I,J}$, $\circ v_{i,j}^{I,J}$, for $i \in \{-2, -1, 0, n, n+1, n+2\}$ and $j \in \{0, 1, 2, \dots, n-1, n\}$. Similarly the bottom and top edge value indices are $i \in \{0, 1, 2, \dots, n-1, n\}$ and $j \in \{-2, -1, 0, n, n+1, n+2\}$.

2.2 Patch coupling connects the scales

As explained in §2.1.2, a patch scheme simulation is performed in two steps:

1. Macroscale patch coupling to compute the patch edge nodes;
2. Computing time derivative of the interior nodes from the microscale model using both interior and edge values.

This section explains two kinds of patch coupling that lead to two families of staggered patch schemes: a spectral patch scheme, and four polynomial patch schemes. Section 2.2.1 details the method of patch coupling using the global spectral interpolation for the spectral patch scheme. Section 2.2.2 details four methods of patch coupling using local polynomial interpolations of different order for the polynomial patch schemes.

Computing patch edge values via patch coupling consists of two steps:

1. first, compute the *macroscale patch value* (a representative aggregate value, also called amplitude or order parameter) for each patch from their respective microscale interior values;
2. next, compute the *microscale* edge values of each patch by interpolating from the macroscale values of the neighbouring patches across the relatively large inter-patch distances.

Thus, patch coupling provides a two-way connection between the microscale and macroscale.

The staggered patch schemes that we design essentially provide a reduced order multiscale model of the given corresponding full-domain microscale model, where the macroscale (aggregate) values of patches are state variables in a slow manifold of reduced state space dimension (Roberts 2003, §5.3, p. 302; Kevrekidis et al. 2004, p.1349; Zagaris et al. 2009; Roberts 1988; Foias et al. 1988a; Lorenz 1986; Foias et al. 1988b; Temam 1990). The simple approach of taking the centre node value of a patch as the macroscale value of that patch is adopted in this work. Whereas many of the patch micro-grids in Fig. 2.1.3a do not have a node at their centre, all three types of patches in the chosen staggered patch grid in Fig. 2.1.3b each have one centre node— h , u or v node. So the simple approach of taking the centre node value of a patch as the macroscale value is particularly suitable for the chosen staggered patch grid (Fig. 2.1.3b). Hence we define the centre values H , U , V as the macroscale (aggregate) values of respectively the h -, u - and v -centred patches.

We have three macroscale values H , U - and V per macro-cell, corresponding to the h -, u - and v -centred patches within each macro-cell in the chosen staggered patch grid (orange square Fig. 2.1.3b). Hence with N macro-grid intervals in the domain, we have three $N/2 \times N/2$ arrays of h , u , and v macroscale values of all the patches in the staggered patch grid. Many choices of multivariate interpolations could be used for the patch coupling to compute the microscale patch edge values from the three $N/2 \times N/2$ arrays of h , u , and v macroscale values.

We use global spectral interpolation in §2.2.1 and local polynomial interpolations §2.2.2 for a family of staggered patch schemes.

2.2.1 Global spectral interpolation for patch coupling

For a staggered patch grid with N macro-grid intervals (N is even) across the square domain, we have three $N/2 \times N/2$ arrays of H , U and U macroscale values of all the patches, which are patch centre node values of h -, u - and v -centred patches. The inter-patch distance, between patches with the same centre nodes, is the same as the inter-cell distance 2Δ , that is h -centred patches are equally spaced among themselves and similarly the u - and v -centred patches. Hence, the *spectral patch scheme* we describe in this section uses the spectral interpolation to compute the microscale patch edge values h , u , and v from the equispaced patch macroscale values h , u , and v .

This subsection illustrates spectral interpolation patch coupling for calculating h edge values, the calculations of u and v edge values follow the same procedure. Consider the 2D discrete Fourier transform (DFT) of an $N/2 \times N/2$ array H containing h -patch aggregate values,

$$\tilde{H}_{k_x, k_y} = \text{DFT}(H) = \sum_{I, J=1}^{N/2} H_{I, J} \exp[-i(k_x x_I + k_y y_J)] \quad (2.2.1)$$

where the wavenumbers $k_x, k_y \in \{-(N/2 - 1)/2, \dots, (N/2 - 1)/2\}$.

The 2D inverse *semi*-discrete Fourier transform of the discrete Fourier transform \tilde{H} ($N/2 \times N/2$ array) gives a continuous function $\hat{H}(x, y)$, which is the macroscale field at any arbitrary position (x, y) . That is, the macroscale variation of the microscale field h is,

$$\hat{H}(x, y) = \text{ISDFT}(\tilde{H}) = \frac{1}{(N/2)^2} \sum_{k_x, k_y} \tilde{H}_{k_x, k_y} \exp[i(k_x x + k_y y)]. \quad (2.2.2)$$

When the size $N/2$ is even (e.g., the number of macro-grid intervals N is a multiple of four), special handling is required due to the presence of the

Algorithm 1 Patch coupling for •-nodes by global spectral interpolation

- 1: $H \leftarrow \text{GETALLAGGREGATESTATES}(\mathbf{h})$ “ $N/2 \times N/2$ array”
“Gets aggregate values of all the •-centred patches.”
 - 2: $\tilde{H} \leftarrow \text{FFT}(H)$
 - 3: **for all** offsets (ξ, η) (w.r.t centre node of left-bottom •-centred patch), of
all • edge nodes of left-bottom •-centred patch **do**
 - 4: $\tilde{H}_{m,n}^e = \tilde{H} \exp[i(k_{x,m}\xi + k_{y,n}\eta)]$ “ $N/2 \times N/2$ array”
“Fourier shift of patch centre node values of all •-centred patches,
by • edge node offset (ξ, η) .”
 - 5: $H^e = \text{IFFT}(\tilde{H}^e)$ “ $N/2 \times N/2$ array”
“Interpolated (ξ, η) -offset • edge value for all •-centred patches.”
 - 6: Assign H^e to (ξ, η) -offset • edge node of all •-centred patches
 - 7: **end for**
 - 8: **for all** offsets (ξ, η) (w.r.t centre node of left-bottom •-centred patch), of
all • edge nodes of left-bottom •-centred patch **do**
 - 9: $\tilde{H}_{m,n}^e = \tilde{H} \exp[i(k_{x,m}\xi + k_{y,n}\eta)]$
 - 10: $H^e = \text{IFFT}(\tilde{H}^e)$
 - 11: Assign H^e to (ξ, η) -offset • edge node of all •-centred patches
 - 12: **end for**
 - 13: **for all** offsets (ξ, η) (w.r.t centre node of left-bottom •-centred patch), of
all • edge nodes of left-bottom •-centred patch **do**
 - 14: $\tilde{H}_{m,n}^e = \tilde{H} \exp[i(k_{x,m}\xi + k_{y,n}\eta)]$
 - 15: $H^e = \text{IFFT}(\tilde{H}^e)$
 - 16: Assign H^e to (ξ, η) -offset • edge node of all •-centred patches
 - 17: **end for**
-

Nyquist frequency component—as we consider only even N where $N/2$ is odd, that is, $N \in \{6, 10, 14, 18, \dots\}$, this is not an issue here.

The Fast Fourier transform FFT provides efficient calculation of the transforms (2.2.1) and (2.2.2). Using FFT, one edge value of all the $h/u/v$ -centred patches (e.g., left-bottom h nodes of all u -centred patches in Fig. 2.1.3b), are calculated in one pass (one FFT, Fourier shift and one inverse fast Fourier transform IFFT) as in Algorithm 1. We use the left-bottom $h/u/v$ -centred patches as reference patches in Algorithm 1 for the edge node offsets (Fourier shifts); but any patch with the same type of centre node as the edge node being coupled could be used as the reference patch.

By capturing all the global information from wave components, spectral interpolation achieves high accuracy (Bunder et al. 2020); but the spectral

interpolation also imposes strict restrictions for its use such as equispaced patches and periodic macroscale boundary conditions. On the other hand, a local polynomial interpolation (§2.2.2) is more widely applicable for non-uniform complex geometries and boundary conditions.

2.2.2 A family of local polynomial interpolations for patch coupling

The requirements of spectral interpolation based patch coupling (namely, equispaced patches and periodic macroscale boundary conditions) pose restrictions for the practical use of patch schemes. Using 2D polynomial interpolation in the patch coupling to compute patch edge values avoids such restrictions. So, we developed four *polynomial staggered patch schemes*, namely Square-p2, Square-p4, Square-p6, and Square-p8, whose patch coupling is based on 2D Lagrangian polynomial interpolation over a near-square region where the parameter p in the name is the interpolation polynomial order. As opposed to the global spectral interpolation which uses the macroscale values of all patches to interpolate the edge values of a patch, local polynomial interpolation computes the edge values of a patch using macroscale values of only its near neighbouring patches.

The neighbourhood of a patch, characterised by the interpolation stencil, could be of different sizes leading to different order p of the interpolating polynomial. For example, Fig. 2.2.1 shows one individual interpolation stencil for each of the four polynomial staggered patch schemes, for interpolating v edge values of h -, u -, v -centred patches, using macroscale values of v -centred patches in the square stencil. Table 2.2.1 explains the meaning of the visual elements in the stencil plots. Figs. 2.2.2 to 2.2.5 show all the individual interpolation stencils (for coupling $h/u/v$ edge values of $h/u/v$ -centred patches) for each of the four polynomial schemes. Each of Figs. 2.2.2 to 2.2.5 shows the interpolation stencils for coupling h,u,v edge values on left-right and bottom-top edge nodes of h,u,v -centred patches in one cell.

- The square shape of the stencil is only in an approximate and qualitative sense. But depending upon the type of edge nodes ($h/u/v$) being interpolated and the type of the patch ($h/u/v$ -centred) for which edge nodes are interpolated, some of the individual stencils of a staggered patch scheme take rectangular shape. For example, for all the four polynomial staggered patch schemes in Fig. 2.2.1, all the left-most stencils for interpolating the v edge nodes of h -centred patches take a rectangular shape.

Figure 2.2.1. Example interpolation stencils of the four polynomial staggered patch schemes, for interpolating \bullet node values on edges of \bullet -, \bullet -, \bullet -centred patches (indicated respectively by \square , \square , and \square), using macroscale values of \bullet -centred patches (indicated by \square) in the stencil.

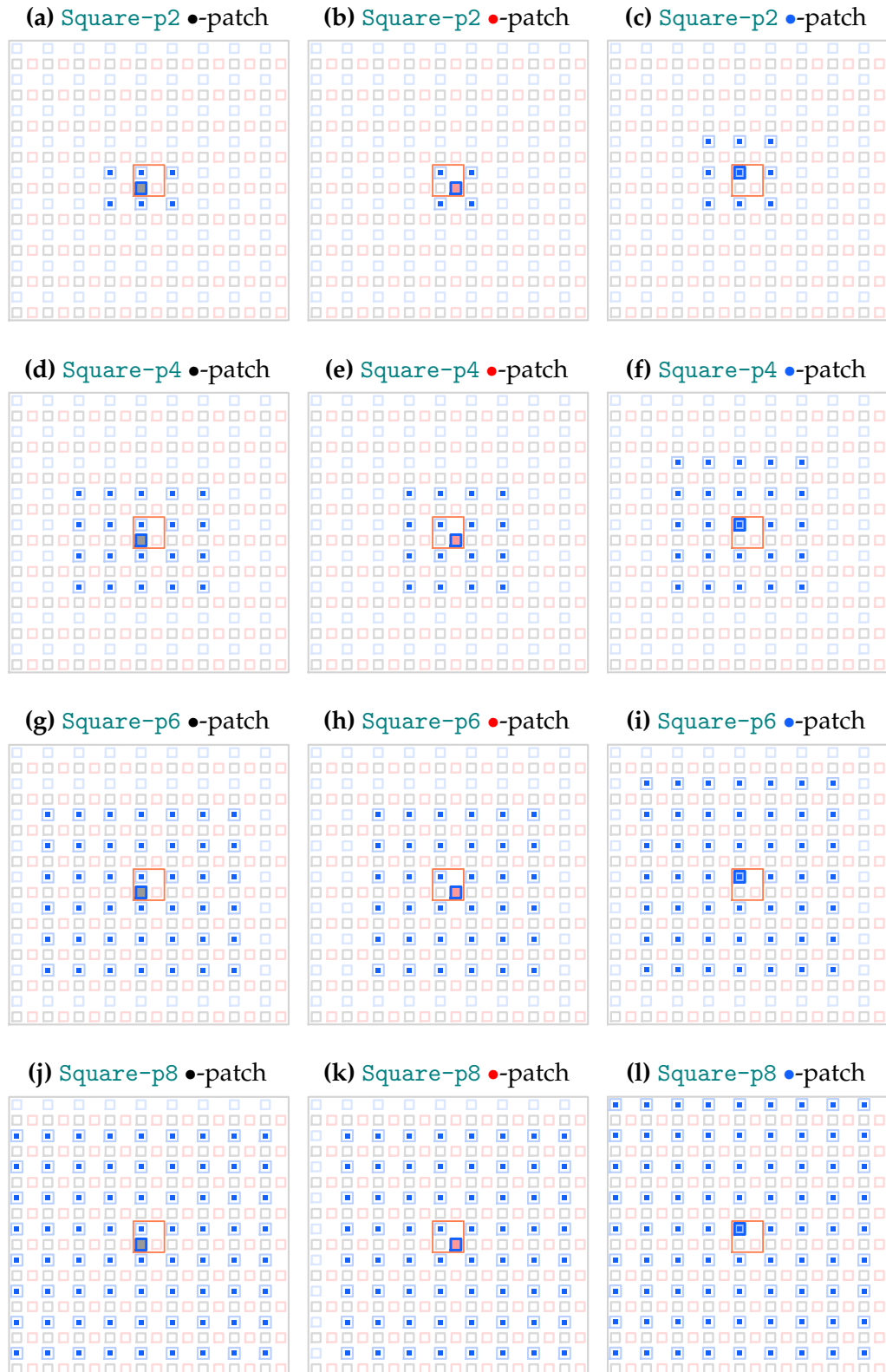



















Table 2.2.1. Meaning of visual elements of interpolation stencil plots. Figs. 2.2.2 to 2.2.5, each presents the interpolation stencils for computing the edge values of \bullet -, \bullet -, \bullet -centred patches in one macro-cell illustrated as . For example interpolating \bullet node values on edges of \bullet -, \bullet -, \bullet -centred patches (indicated respectively by , , and ) uses macroscale values of \bullet -centred patches (indicated by ) in the stencil.

	Edge node being interpolated		
	\bullet edge nodes	\bullet edge nodes	\bullet edge nodes
For \bullet -centred patch			
For \bullet -centred patch			
For \bullet -centred patch			

	Interpolating patches		
	\bullet -centred patch	\bullet -centred patch	\bullet -centred patch
For \bullet edge nodes			
For \bullet edge nodes			
For \bullet edge nodes			

- All the four polynomial staggered patch schemes have roughly the same square-shaped interpolation stencils, but differ in size and hence have different polynomial interpolation orders $p \in \{2, 4, 6, 8\}$, indicated respectively in their names by p2, p4, p6 and p8.

We define the polynomial interpolation order p as the maximum degree of the variables in the 2D Lagrangian basis polynomials of all the interpolation stencils of a staggered patch scheme. For example, for the Square-p2 staggered patch scheme the maximum degree of ξ, η in Tables 2.2.2 to 2.2.4 is two (Fig. 2.2.2 shows all the individual stencils), hence the polynomial interpolation order $p = 2$. But the maximum degree of ξ, η is one in Table 2.2.3 of the Square-p2 (for interpolating the \bullet edge values of \bullet -centred patch). Thus, not all the individual stencils of a staggered patch scheme have the same interpolation order. The maximum degree of ξ, η of individual stencils of a staggered patch scheme is either p or $p - 1$, hence the number of points in the interpolating stencils in ξ, η directions are either p or $p + 1$ as in Figs. 2.2.2 to 2.2.5.

In realistic uses of the patch schemes, the patch size l is much smaller than the inter-patch spacing Δ (patch scale ratio $r \ll 1$), hence we expect that the stencil points (centre nodes of the interpolating patches) that lie on the two coordinate lines passing through the current patch (whose edge nodes are interpolated) are the dominant influence on the patch coupling interpolation. In contrast to the square or rectangle stencils, using a few different shaped stencil shapes such as a plus and cruciform shape, we also found that patches that lie on a line perpendicular to the patch edge being interpolated have a stronger influence on the patch coupling than the patches that lie on a line parallel to the patch edge being interpolated. So interpolation stencils with fewer stencil points such as a plus or cruciform shape compared to the square or rectangle stencils could be a more efficient alternative and may be worth investigating in the future.

We perform the standard bivariate Lagrange interpolation (e.g., Gupta 2019, §10.10; Jain et al. 2004, §3.6; Fletcher 2020, §10.1) in patch local coordinate (ξ, η) , using following coordinate transformation from global coordinate (x, y) ,

$$\xi = (x - x^I)/\Delta, \quad (2.2.3a)$$

$$\eta = (y - y^J)/\Delta, \quad (2.2.3b)$$

where, Δ is inter-patch spacing and the patch local coordinate system origin (x^I, y^J) is the centre of the current patch (the patch whose edge values are being interpolated). For example, Tables 2.2.2 to 2.2.4 show the local coordinates of interpolation stencils of Square-p2 staggered patch scheme, for coupling \bullet edge nodes respectively for \bullet -, \bullet -, \bullet -centred patches.

Let's assign a *stencil index* $S \in \{0, 1, \dots, n_S - 1\}$ for each of the n_S patches in a polynomial patch coupling interpolation stencil (e.g., Tables 2.2.2 to 2.2.4). Let the stencil coordinate sets

$$\mathbb{X} = \{\xi_S : S = 0, 1, \dots, n_S - 1\}, \quad (2.2.4a)$$

$$\mathbb{Y} = \{\eta_S : S = 0, 1, \dots, n_S - 1\}, \quad (2.2.4b)$$

each contain the patch local coordinates ξ_S and η_S respectively of all the stencil points (i.e., interpolating patch centres shown by \blacksquare in Fig. 2.2.1). All the stencil points $\{(\xi_S, \eta_S) : S = 0, 1, \dots, n_S - 1\} = \mathbb{X} \times \mathbb{Y}$. The expressions we use for the 2D Lagrangian basis polynomials for every stencil index $S \in \{0, 1, \dots, n_S - 1\}$ are

$$\mathcal{B}_S(\xi, \eta) = \left(\prod_{\xi_k \in \mathbb{X} \setminus \{\xi_S\}} \frac{\xi - \xi_k}{\xi_S - \xi_k} \right) \left(\prod_{\eta_k \in \mathbb{Y} \setminus \{\eta_S\}} \frac{\eta - \eta_k}{\eta_S - \eta_k} \right). \quad (2.2.5)$$

Tables 2.2.2 to 2.2.4 illustrate the local coordinates, stencil indices and the corresponding 2D Lagrangian basis polynomials (2.2.5) of the interpolation stencils for Square-p2 staggered patch scheme, for coupling \bullet edge nodes respectively for \bullet -, \bullet -, \bullet -centred patches. The Lagrangian basis polynomials (2.2.5) are the standard 2D Lagrangian basis polynomials (Gupta 2019, §10.10; Jain et al. 2004, §3.6; Fletcher 2020, §10.1) but defined in terms of the stencil index S , for a regular grid of points with a spacing of 2Δ , over the square or rectangular stencil. Section 2.2.2.1 discusses these basis polynomials for the four polynomial staggered patch schemes.

In terms of the basis polynomials (2.2.5) and the known values f_s , the bivariate Lagrange interpolation polynomial, generic for the patch coupling of all the four polynomial staggered patch schemes is

$$\mathcal{L}(\xi, \eta) = \sum_{S=0}^{n_S-1} \mathcal{B}_S(\xi, \eta) f_S. \quad (2.2.6)$$

Algorithm 2 shows the key steps in coupling the patches using bivariate Lagrange interpolation polynomial (2.2.6).

Figure 2.2.2. Stencils of Square-p2 scheme (maximum order of basis polynomials $p = 2$), for interpolating h, u, v values on left-right and bottom-top edge nodes of $h-, u-, v$ -centred patches in one cell (orange square).

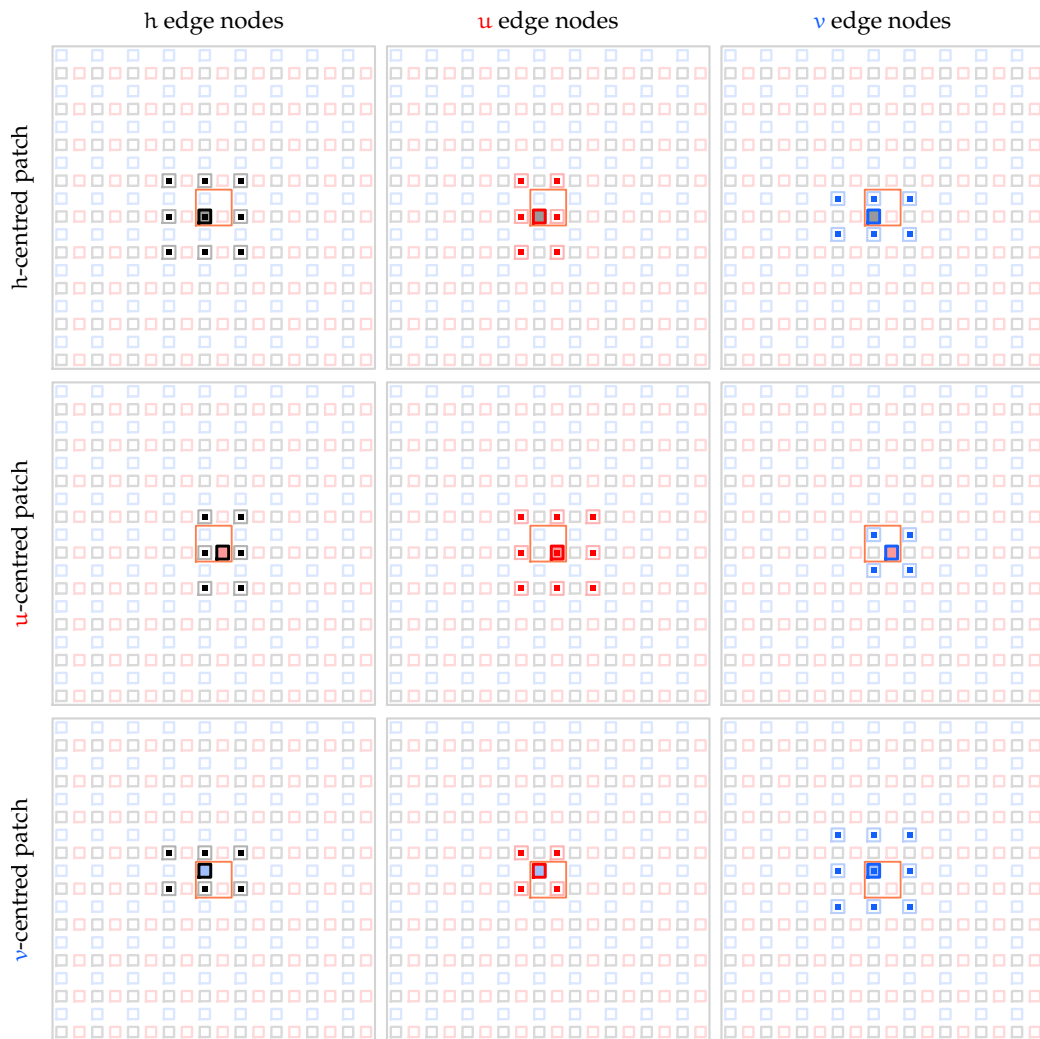


Figure 2.2.3. Stencils of Square-p4 scheme (maximum order of basis polynomials $p = 4$), for interpolating h, u, v values on left-right and bottom-top edge nodes of h, u, v -centred patches in one cell (orange square).

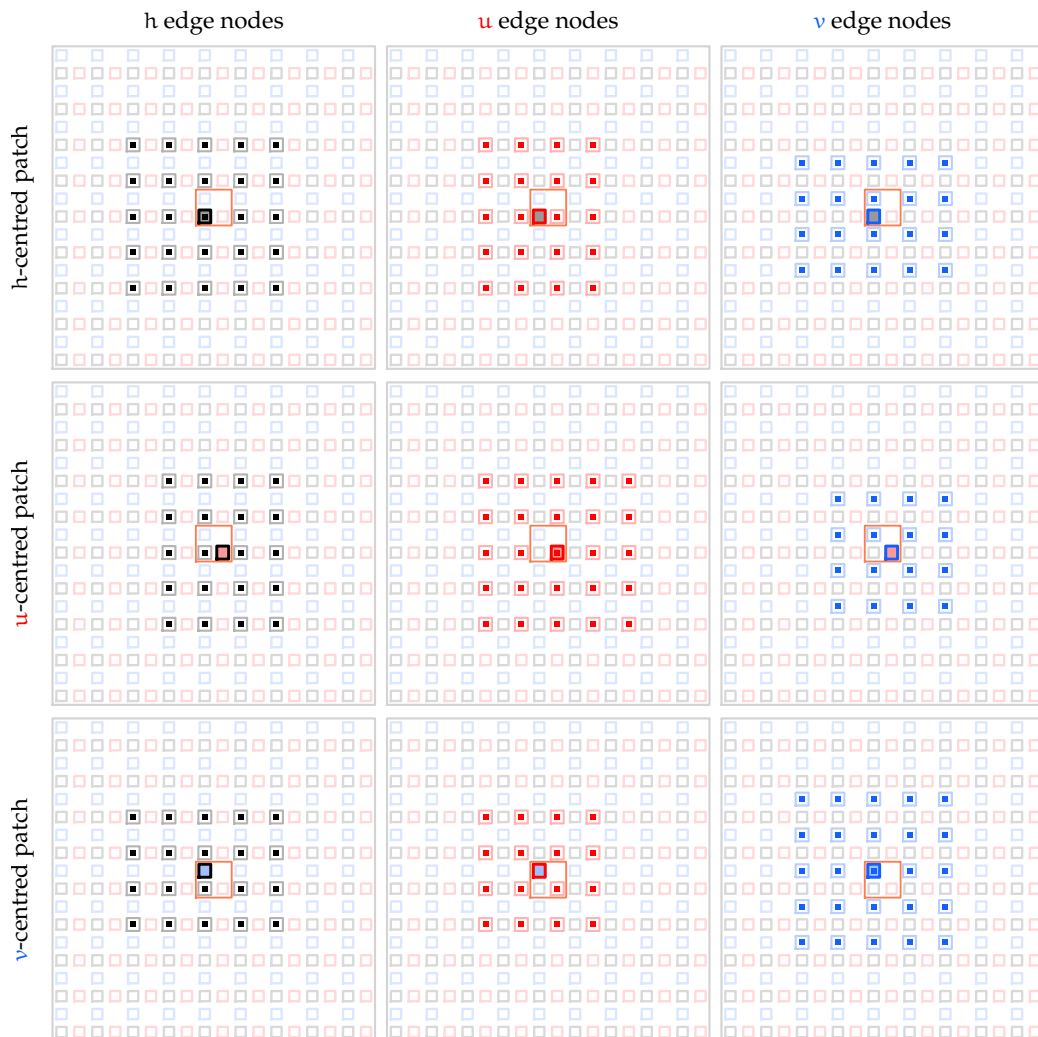


Figure 2.2.4. Stencils of Square-p6 scheme (maximum order of basis polynomials $p = 6$), for interpolating h, u, v values on left-right and bottom-top edge nodes of $h-, u-, v$ -centred patches in one cell (orange square).

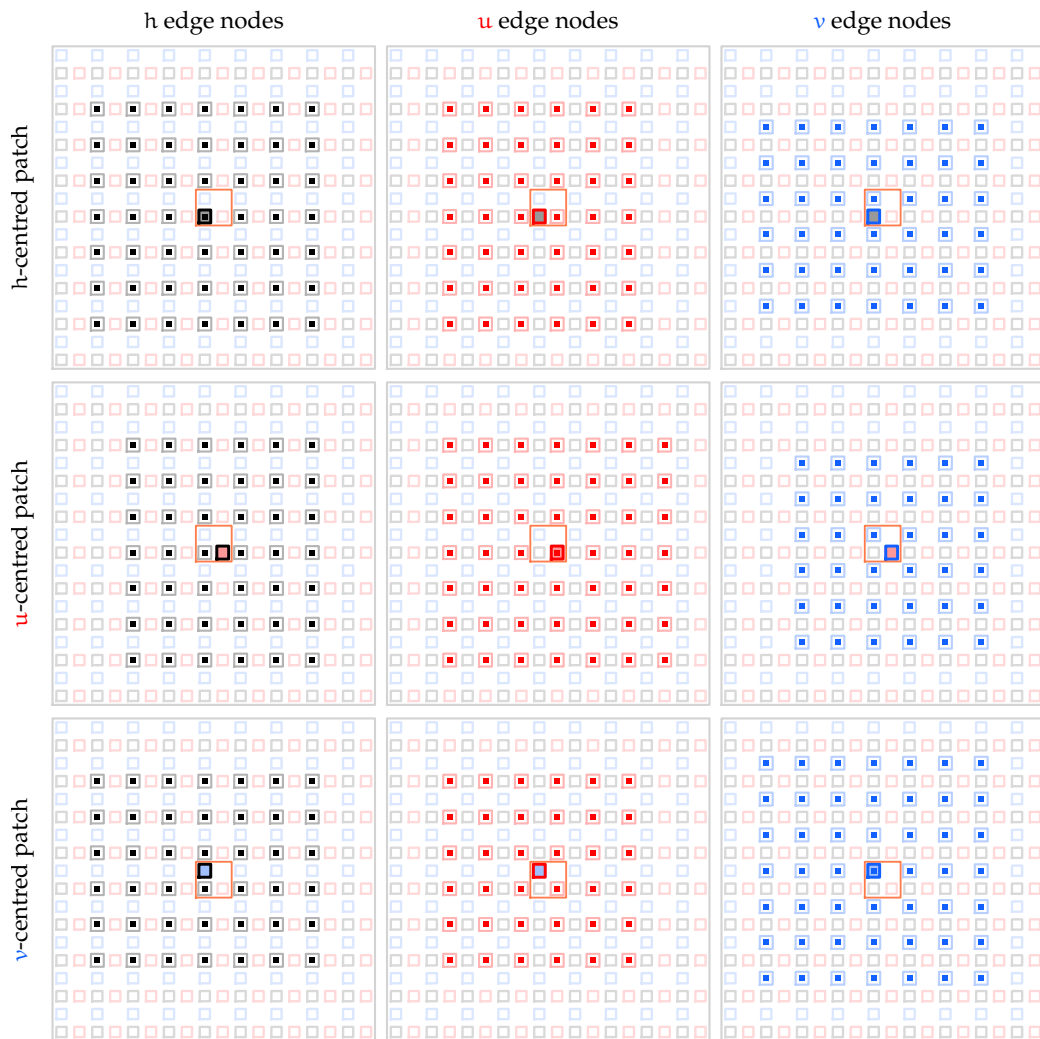
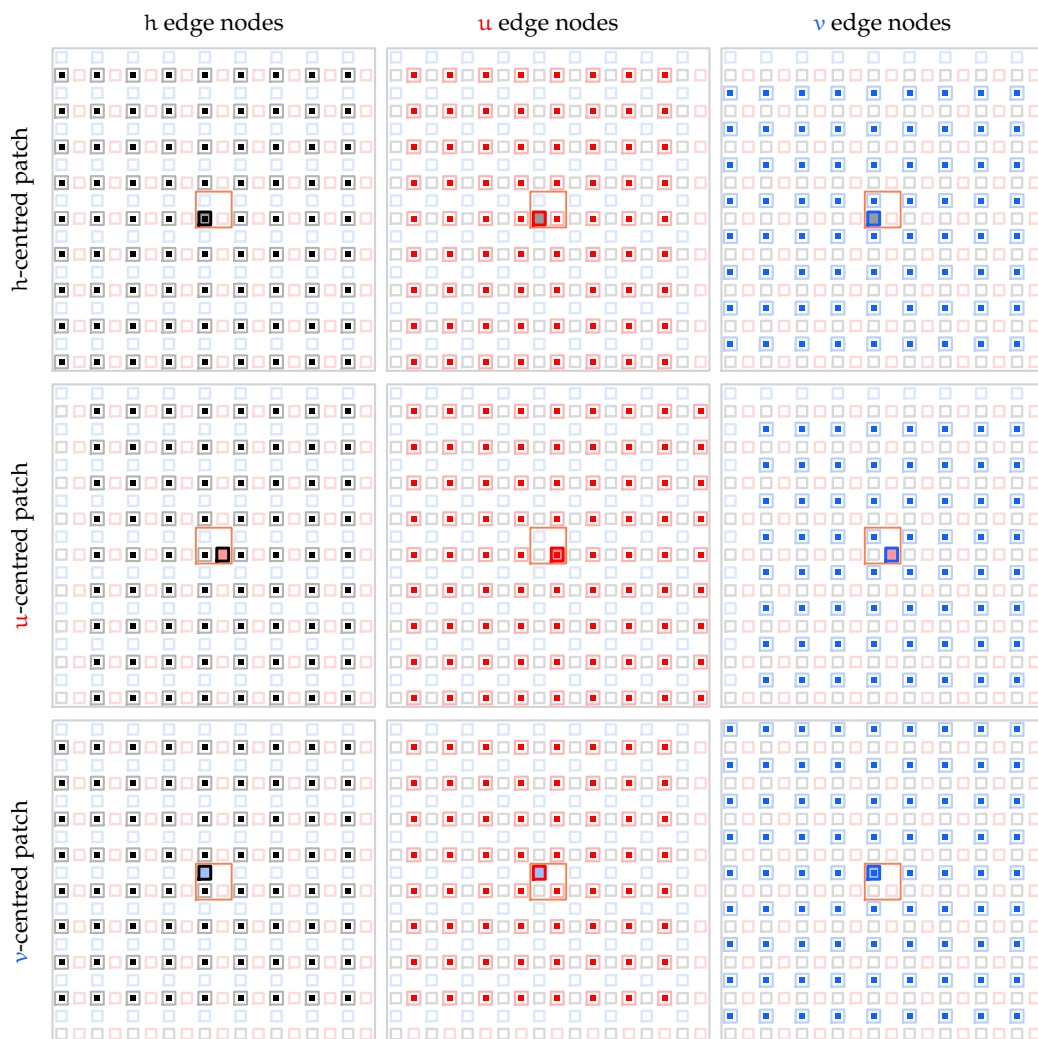


Figure 2.2.5. Stencils of Square-p8 scheme (maximum order of basis polynomials $p = 8$), for interpolating h, u, v values on left-right and bottom-top edge nodes of h, u, v -centred patches in one cell (orange square).



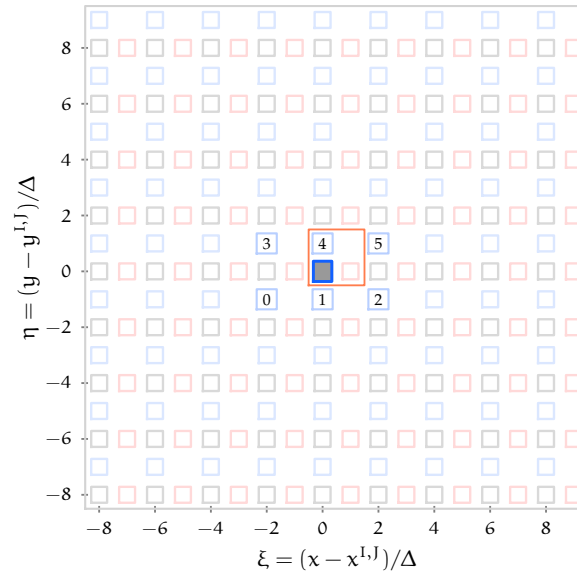
Algorithm 2 Patch coupling by 2D Lagrangian polynomial interpolation

```

1: stencil  $\leftarrow$  <stencilName> “for example Stencil  $\leftarrow$  ‘Cruciform2-p4’ ”
2: for all patch P in patch grid do
3:   for all node type T in [‘h’, ‘u’, ‘v’] do “to interpolate  $\bullet/\bullet/\bullet$  edge nodes”
4:     for all edge side S in [‘left-right’, ‘bottom-top’] do
5:       NbrsT,S  $\leftarrow$  GETNEIGHBOURPATCHES(P, stencil, T, S)
        “For patch P, gets neighbouring T-centred patches within the speci-
        fied stencil for interpolating S side edge nodes of type T.”
6:       MacrosT,S  $\leftarrow$  GETSTENCILMACROSCALEVALUES(NbrsT,S)
        “Gets macroscale values for all the patches in the set of neighbour-
        ing patches NbrsT,S.”
7:        $\mathcal{L}(\xi, \eta) \leftarrow$  MAKEINTERPFUNCTION(NbrsT,S, MacrosT,S)
        “Constructs 2D Lagrangian interpolating polynomial  $\mathcal{L}$  (2.2.6) in
        terms of the basis polynomials  $\mathcal{B}_S$  (2.2.5) for centre positions of the
        stencil patches NbrsT,S and their macroscale values MacrosT,S.”
        “ $\mathcal{L}(\xi, \eta)$  interpolates T-node values at any input position  $\xi, \eta$  rela-
        tive to the centre of patch P.”
8:       for all edge node E of type T on the S side of patch P do
9:         Compute position  $\xi_E, \eta_E$  of edge nodes
          “Patch local coordinate relative to the centre of patch P, using
          the coordinate transformation (2.2.3).”
10:        Assign edge node E of type T with a value  $\mathcal{L}(\xi_E, \eta_E)$ 
11:      end for
12:    end for
13:  end for
14: end for

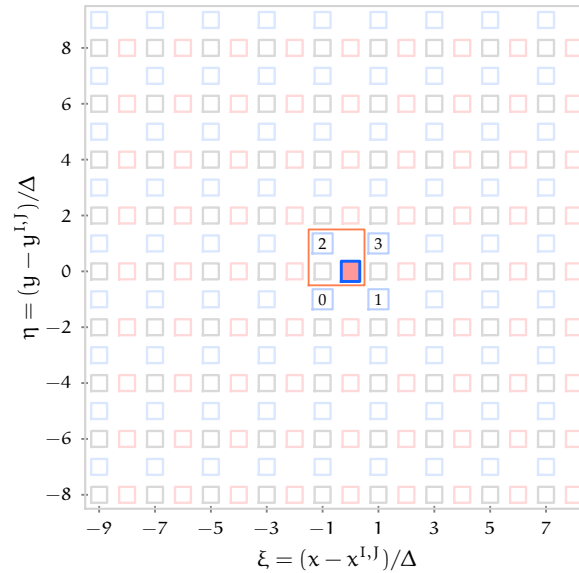
```

Table 2.2.2. 2D Lagrangian basis polynomials for Square-p2 patch coupling, for interpolating \bullet edge node values of \bullet -centred patch (indicated by \blacksquare). Stencil index $S \in \{0, 1, \dots, n_S - 1 = 5\}$. Global coordinate (x, y) corresponds to patch local coordinate (ξ, η) with origin (x^I, y^J)



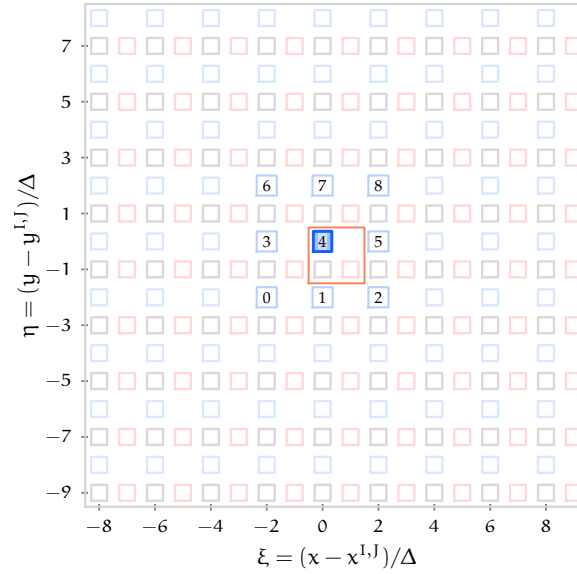
S	Basis polynomials $\mathcal{B}_S(\xi, \eta)$
0	$-\frac{\xi-2}{4} \cdot \frac{\xi}{2} \cdot \frac{\eta-1}{2}$
1	$\frac{\xi-2}{2} \cdot \frac{\xi+2}{2} \cdot \frac{\eta-1}{2}$
2	$-\frac{\xi}{2} \cdot \frac{\xi+2}{4} \cdot \frac{\eta-1}{2}$
3	$\frac{\xi-2}{4} \cdot \frac{\xi}{2} \cdot \frac{\eta+1}{2}$
4	$-\frac{\xi-2}{2} \cdot \frac{\xi+2}{2} \cdot \frac{\eta+1}{2}$
5	$\frac{\xi}{2} \cdot \frac{\xi+2}{4} \cdot \frac{\eta+1}{2}$
Sum:	1

Table 2.2.3. 2D Lagrangian basis polynomials for Square-p2 patch coupling, for interpolating \bullet edge node values of \bullet -centred patch (indicated by \square). Stencil index $S \in \{0, 1, \dots, n_S - 1 = 3\}$. Global coordinate (x, y) corresponds to patch local coordinate (ξ, η) with origin (x^I, y^J)



S	Basis polynomials $\mathcal{B}_S(\xi, \eta)$
0	$\frac{\xi-1}{2} \cdot \frac{\eta-1}{2}$
1	$-\frac{\xi+1}{2} \cdot \frac{\eta-1}{2}$
2	$-\frac{\xi-1}{2} \cdot \frac{\eta+1}{2}$
3	$\frac{\xi+1}{2} \cdot \frac{\eta+1}{2}$
Sum:	1

Table 2.2.4. 2D Lagrangian basis polynomials for Square-p2 patch coupling, for interpolating \bullet edge node values of \bullet -centred patch (indicated by \square). Stencil index $S \in \{0, 1, \dots, n_S - 1 = 8\}$. Global coordinate (x, y) corresponds to patch local coordinate (ξ, η) with origin (x^I, y^J)



S	Basis polynomials $\mathcal{B}_S(\xi, \eta)$
0	$\frac{\xi-2}{4} \cdot \frac{\xi}{2} \cdot \frac{\eta-2}{4} \cdot \frac{\eta}{2}$
1	$-\frac{\xi-2}{2} \cdot \frac{\xi+2}{2} \cdot \frac{\eta-2}{4} \cdot \frac{\eta}{2}$
2	$\frac{\xi}{2} \cdot \frac{\xi+2}{4} \cdot \frac{\eta-2}{4} \cdot \frac{\eta}{2}$
3	$-\frac{\xi-2}{4} \cdot \frac{\xi}{2} \cdot \frac{\eta-2}{2} \cdot \frac{\eta+2}{2}$
4	$\frac{\xi-2}{2} \cdot \frac{\xi+2}{2} \cdot \frac{\eta-2}{2} \cdot \frac{\eta+2}{2}$
5	$-\frac{\xi}{2} \cdot \frac{\xi+2}{4} \cdot \frac{\eta-2}{2} \cdot \frac{\eta+2}{2}$
6	$\frac{\xi-2}{4} \cdot \frac{\xi}{2} \cdot \frac{\eta}{2} \cdot \frac{\eta+2}{4}$
7	$-\frac{\xi-2}{2} \cdot \frac{\xi+2}{2} \cdot \frac{\eta}{2} \cdot \frac{\eta+2}{4}$
8	$\frac{\xi}{2} \cdot \frac{\xi+2}{4} \cdot \frac{\eta}{2} \cdot \frac{\eta+2}{4}$
Sum:	1

2.2.2.1 Comparison of patch coupling for the four polynomial staggered patch schemes

Tables 2.2.5 to 2.2.8 list the leading order terms of the interpolation errors $\mathcal{L}(\xi, \eta) - f(\xi, \eta)$ for a set of binomial terms as test function f respectively for the four polynomial staggered patch schemes. As our definition of the interpolation order p allows basis polynomials whose maximum degree is $p - 1$ (e.g., Square-p2 staggered patch scheme has linear basis polynomials in Table 2.2.3), hence a p th order staggered patch scheme has the interpolation error of $O(\xi^p + \eta^p)$, which is evident in the interpolation errors in Tables 2.2.5 to 2.2.8 for each of the four polynomial staggered patch schemes.

As the basis polynomials (2.2.5) are the standard 2D Lagrangian basis polynomials, the basis polynomials (2.2.5) possess all the properties of the standard Lagrangian basis polynomials (Gupta 2019, §10.10; Jain et al. 2004, §3.6; Fletcher 2020, §10.1). Following are some of the key properties of the Lagrangian basis polynomials (2.2.5) that are common to all the four polynomial staggered patch schemes, namely Square-p2, Square-p4, Square-p6, and Square-p8.

1. $\mathcal{B}_S(\xi_T, \eta_T) = 1$ at the stencil index $T = S$, as evident from the basis polynomials in Tables 2.2.2 to 2.2.4.
2. $\mathcal{B}_S(\xi_T, \eta_T) = 0$ at the stencil index $T \neq S$, also as evident from the basis polynomials in Tables 2.2.2 to 2.2.4.
3. Sum of all the basis polynomials of a stencil $\sum_{S=0}^{n_S-1} \mathcal{B}_S(\xi, \eta) = 1$, as listed Tables 2.2.2 to 2.2.4. This property ensures that constant functions are interpolated exactly, holds for all the four polynomial staggered patch schemes, for example the constant function c in Table 2.2.5 for Square-p2 staggered patch scheme.
4. $\sum_{S=0}^{n_S-1} \mathcal{B}_S(\xi, \eta) \cdot \xi_S = \xi$ and $\sum_{S=0}^{n_S-1} \mathcal{B}_S(\xi, \eta) \cdot \eta_S = \eta$. This property ensures that linear functions are interpolated exactly, holds for all the four polynomial staggered patch schemes, for example the linear functions ξ, η in Table 2.2.5 for Square-p2 staggered patch scheme.

Table 2.2.5. Leading order terms of interpolation errors $\mathcal{L}(\xi, \eta) - f(\xi, \eta)$, of Square-p2 patch scheme, for coupling $h/\mathbf{u}/\mathbf{v}$ edge nodes (each in two rows respectively for left-right and bottom-top edges) of $h/\mathbf{u}/\mathbf{v}$ -centred patches. Interpolation errors are $\mathcal{O}(\xi^2 + \eta^2)$.

	c	ξ	η	$\eta\xi$	ξ^2	η^2	$\eta^2\xi$	$\eta\xi^2$	ξ^3	η^3	$\eta^2\xi^2$	$\eta^3\xi$	$\eta\xi^3$	ξ^4	η^4	
h-centred patch	h-nodes	0	0	0	0	0	0	0	4 ξ	4 η	0	4 $\eta\xi$	4 $\eta\xi$	4 ξ^2	4 η^2	
		0	0	0	0	0	0	0	0	4 ξ	4 η	0	4 $\eta\xi$	4 $\eta\xi$	4 ξ^2	4 η^2
	u-nodes	0	0	0	0	1	0	0	$-\eta\xi^2 + \eta$	ξ	4 η	$-\eta^2\xi^2 + \eta^2$	4 $\eta\xi$	$\eta\xi$	1	4 η^2
		0	0	0	0	1	0	0	$-\eta\xi^2 + \eta$	ξ	4 η	$-\eta^2\xi^2 + \eta^2$	4 $\eta\xi$	$\eta\xi$	1	4 η^2
	v-nodes	0	0	0	0	0	1	$-\eta^2\xi + \xi$	0	4 ξ	η	$-\eta^2\xi^2 + \xi^2$	$\eta\xi$	4 $\eta\xi$	4 ξ^2	1
		0	0	0	0	0	1	$-\eta^2\xi + \xi$	0	4 ξ	η	$-\eta^2\xi^2 + \xi^2$	$\eta\xi$	4 $\eta\xi$	4 ξ^2	1
u-centred patch	h-nodes	0	0	0	0	1	0	0	$-\eta\xi^2 + \eta$	ξ	4 η	$-\eta^2\xi^2 + \eta^2$	4 $\eta\xi$	$\eta\xi$	1	4 η^2
		0	0	0	0	1	0	0	$-\eta\xi^2 + \eta$	ξ	4 η	$-\eta^2\xi^2 + \eta^2$	4 $\eta\xi$	$\eta\xi$	1	4 η^2
	u-nodes	0	0	0	0	0	0	0	0	4 ξ	4 η	0	4 $\eta\xi$	4 $\eta\xi$	4 ξ^2	4 η^2
		0	0	0	0	0	0	0	0	4 ξ	4 η	0	4 $\eta\xi$	4 $\eta\xi$	4 ξ^2	4 η^2
	v-nodes	0	0	0	0	1	1	$-\eta^2\xi + \xi$	$-\eta\xi^2 + \eta$	ξ	η	1	$\eta\xi$	$\eta\xi$	1	1
		0	0	0	0	1	1	$-\eta^2\xi + \xi$	$-\eta\xi^2 + \eta$	ξ	η	1	$\eta\xi$	$\eta\xi$	1	1
v-centred patch	h-nodes	0	0	0	0	1	$-\eta^2\xi + \xi$	0	4 ξ	η	$-\eta^2\xi^2 + \xi^2$	$\eta\xi$	4 $\eta\xi$	4 ξ^2	1	
		0	0	0	0	1	$-\eta^2\xi + \xi$	0	4 ξ	η	$-\eta^2\xi^2 + \xi^2$	$\eta\xi$	4 $\eta\xi$	4 ξ^2	1	
	u-nodes	0	0	0	0	1	1	$-\eta^2\xi + \xi$	$-\eta\xi^2 + \eta$	ξ	η	1	$\eta\xi$	$\eta\xi$	1	1
		0	0	0	0	1	1	$-\eta^2\xi + \xi$	$-\eta\xi^2 + \eta$	ξ	η	1	$\eta\xi$	$\eta\xi$	1	1
	v-nodes	0	0	0	0	0	0	0	0	4 ξ	4 η	0	4 $\eta\xi$	4 $\eta\xi$	4 ξ^2	4 η^2
		0	0	0	0	0	0	0	0	4 ξ	4 η	0	4 $\eta\xi$	4 $\eta\xi$	4 ξ^2	4 η^2

Table 2.2.6. Leading order terms of interpolation errors $\mathcal{L}(\xi, \eta) - f(\xi, \eta)$, of Square-p4 patch scheme, for coupling $h/\mathbf{u}/\mathbf{v}$ edge nodes (each in two rows respectively for left-right and bottom-top edges) of $h/\mathbf{u}/\mathbf{v}$ -centred patches. Interpolation errors are $\mathcal{O}(\xi^4 + \eta^4)$. Functions $f = \xi^a \cdot \eta^b$ with $a + b < 3$ are interpolated exactly.

	ξ^3	$\eta\xi^2$	$\eta^2\xi$	η^3	ξ^4	$\eta\xi^3$	$\eta^2\xi^2$	$\eta^3\xi$	η^4	ξ^5	$\eta\xi^4$	$\eta^2\xi^3$	$\eta^3\xi^2$	$\eta^4\xi$	
h-centred patch	h-nodes	0	0	0	0	0	0	0	0	0	-64ξ	0	0	0	
	h-nodes	0	0	0	0	0	0	0	0	0	-64ξ	0	0	0	
	u-nodes	0	0	0	0	-9	0	0	0	0	-9ξ	$10\eta\xi^2 - 9\eta$	0	0	
	u-nodes	0	0	0	0	-9	0	0	0	0	-9ξ	$10\eta\xi^2 - 9\eta$	0	0	
	v-nodes	0	0	0	0	0	0	0	0	-9	-64ξ	0	0	0	$10\eta^2\xi - 9\xi$
	v-nodes	0	0	0	0	0	0	0	0	-9	-64ξ	0	0	0	$10\eta^2\xi - 9\xi$
u-centred patch	h-nodes	0	0	0	0	-9	0	0	0	0	-9ξ	$10\eta\xi^2 - 9\eta$	0	0	
	h-nodes	0	0	0	0	-9	0	0	0	0	-9ξ	$10\eta\xi^2 - 9\eta$	0	0	
	u-nodes	0	0	0	0	0	0	0	0	0	-64ξ	0	0	0	
	u-nodes	0	0	0	0	0	0	0	0	0	-64ξ	0	0	0	
	v-nodes	0	0	0	0	-9	0	0	0	-9	-9ξ	$10\eta\xi^2 - 9\eta$	0	0	$10\eta^2\xi - 9\xi$
	v-nodes	0	0	0	0	-9	0	0	0	-9	-9ξ	$10\eta\xi^2 - 9\eta$	0	0	$10\eta^2\xi - 9\xi$
v-centred patch	h-nodes	0	0	0	0	0	0	0	0	-9	-64ξ	0	0	0	$10\eta^2\xi - 9\xi$
	h-nodes	0	0	0	0	0	0	0	0	-9	-64ξ	0	0	0	$10\eta^2\xi - 9\xi$
	u-nodes	0	0	0	0	-9	0	0	0	-9	-9ξ	$10\eta\xi^2 - 9\eta$	0	0	$10\eta^2\xi - 9\xi$
	u-nodes	0	0	0	0	-9	0	0	0	-9	-9ξ	$10\eta\xi^2 - 9\eta$	0	0	$10\eta^2\xi - 9\xi$
	v-nodes	0	0	0	0	0	0	0	0	0	-64ξ	0	0	0	
	v-nodes	0	0	0	0	0	0	0	0	0	-64ξ	0	0	0	

Table 2.2.7. Leading order terms of interpolation errors $\mathcal{L}(\xi, \eta) - f(\xi, \eta)$, of Square-p6 patch scheme, for coupling $h/\mathbf{u}/\mathbf{v}$ edge nodes (each in two rows respectively for left-right and bottom-top edges) of $h/\mathbf{u}/\mathbf{v}$ -centred patches. Interpolation errors are $\mathcal{O}(\xi^6 + \eta^6)$. Functions $f = \xi^a \cdot \eta^b$ with $a + b < 5$ are interpolated exactly.

	ξ^5	$\eta\xi^4$	$\eta^2\xi^3$	$\eta^3\xi^2$	$\eta^4\xi$	η^5	ξ^6	$\eta\xi^5$	$\eta^2\xi^4$	$\eta^3\xi^3$	$\eta^4\xi^2$	$\eta^5\xi$	η^6	ξ^7
h-centred patch	h-nodes	0	0	0	0	0	0	0	0	0	0	0	0	2304 ξ
	h-nodes	0	0	0	0	0	0	0	0	0	0	0	0	2304 ξ
	u-nodes	0	0	0	0	0	0	225	0	0	0	0	0	225 ξ
	u-nodes	0	0	0	0	0	0	225	0	0	0	0	0	225 ξ
	v-nodes	0	0	0	0	0	0	0	0	0	0	0	225	2304 ξ
	v-nodes	0	0	0	0	0	0	0	0	0	0	0	225	2304 ξ
u-centred patch	h-nodes	0	0	0	0	0	0	225	0	0	0	0	0	225 ξ
	h-nodes	0	0	0	0	0	0	225	0	0	0	0	0	225 ξ
	u-nodes	0	0	0	0	0	0	0	0	0	0	0	0	2304 ξ
	u-nodes	0	0	0	0	0	0	0	0	0	0	0	0	2304 ξ
	v-nodes	0	0	0	0	0	0	225	0	0	0	0	225	225 ξ
	v-nodes	0	0	0	0	0	0	225	0	0	0	0	225	225 ξ
v-centred patch	h-nodes	0	0	0	0	0	0	0	0	0	0	0	225	2304 ξ
	h-nodes	0	0	0	0	0	0	0	0	0	0	0	225	2304 ξ
	u-nodes	0	0	0	0	0	0	225	0	0	0	0	225	225 ξ
	u-nodes	0	0	0	0	0	0	225	0	0	0	0	225	225 ξ
	v-nodes	0	0	0	0	0	0	0	0	0	0	0	0	2304 ξ
	v-nodes	0	0	0	0	0	0	0	0	0	0	0	0	2304 ξ

Chapter 3

Staggered patch schemes accurately simulate general linear waves

This chapter shows that the staggered patch schemes accurately simulate the macroscale dynamics of the general linear wave PDEs as the microscale model within the patches. Specifically, this chapter focuses on the accurate macroscale simulation of the non-dimensional general dissipative linear wave PDE, with linear drag and viscous diffusion respectively characterised by the coefficients c_D, c_V ,

$$\frac{\partial h}{\partial t} = -\frac{\partial u}{\partial x} - \frac{\partial v}{\partial y}, \quad (3.0.1a)$$

$$\frac{\partial u}{\partial t} = -\frac{\partial h}{\partial x} - c_D u + c_V \frac{\partial^2 u}{\partial x^2} + c_V \frac{\partial^2 u}{\partial y^2}, \quad (3.0.1b)$$

$$\frac{\partial v}{\partial t} = -\frac{\partial h}{\partial y} - c_D v + c_V \frac{\partial^2 v}{\partial x^2} + c_V \frac{\partial^2 v}{\partial y^2}, \quad (3.0.1c)$$

with the boundary conditions that the three fields h , u , and v are L -periodic in both x and y , and an appropriate initial condition $h(x, y, 0)$, $u(x, y, 0)$, and $v(x, y, 0)$. The case $c_D = c_V = 0$ corresponds to the *ideal wave*, that is without any dissipation (Dean and Dalrymple 1991, pp. 136–137; Mehaute 1976, p. 260).

Section 3.1 derives a discrete full-domain microscale model and a generic staggered patch scheme corresponding to the general linear wave PDEs (3.0.1). Throughout this chapter, we use this full-domain microscale model as a reference to assess various characteristics (accuracy, stability, consistency, etc.) of the multiscale staggered patch schemes we develop.

Section 3.2 shows that the developed five staggered patch schemes are accurate for the general linear wave. Section 3.2 establishes the accuracy of the staggered patch schemes in general (as opposed to one specific initial condition) by comparing the eigenvalues of the staggered patch schemes with the eigenvalues of fine- and coarse-grid full-domain microscale model. Sections 3.2.1 to 3.2.5 derive the eigenvalues of the general linear wave PDEs, full-domain microscale model, and that of the staggered patch schemes. Section 3.2.6 illustrates the structure of the patch scheme eigenvalues in the complex plane and explains the corresponding dynamical modes via eigenvector plots. The eigenvalue analysis in §3.2.6 visually demonstrates the accuracy (in the complex plane eigenvalue plots) for a representative subset of the physical parameters and grid parameters. Section 3.6 on the consistency of the patch schemes establishes the accuracy over a wider range of parameters.

We quantitatively establish the consistency and stability of the patch schemes by comparing the specific macroscale eigenvalues (defined in p. 52 of §3.2) of the patch schemes with the corresponding eigenvalues of the full-domain microscale model. This comparison requires separating the microscale and macroscale patch scheme eigenvalues. Section 3.3 explains a method to perform wavenumber-wise classification and separation of microscale and macroscale patch scheme eigenvalues.

Despite the attractive characteristics, if the staggered patch schemes are very sensitive to numerical roundoff errors, then they would not be suitable for practical numerical simulations using finite precision floating-point representations. From both qualitative arguments and quantitative evidence, §3.4 shows that the staggered patch schemes are not sensitive to numerical roundoff errors for the general linear wave. The quantitative evidence in §3.4 comes from comparing the eigenvalues of analytic and numerical Jacobians of a patch scheme.

Section 3.5 demonstrates the stability of the staggered patch schemes and explores the dependence of the patch scheme stability on various aspects like grid symmetry, physical parameters, and grid parameters.

Section 3.6 shows that the staggered patch schemes are consistent with the given microscale model. Section 3.6 establishes the consistency of the patch schemes for the general linear wave by comparing the macroscale eigenvalues of the patch scheme with the corresponding eigenvalues of the full-domain microscale model for increasingly finer patch grids. Section 3.6.1 shows that the Spectral patch scheme is uniformly accurate with little dependence on the macro-grid interval Δ . Section 3.6.2 shows that the polynomial patch schemes are consistent to the order of the polynomial interpolation with decreasing macro-grid interval Δ .

[Section 3.7](#) quantifies and demonstrates the large computational savings of the staggered patch schemes for the general linear wave. [Section 3.7.1](#) shows the computational savings of the 2D staggered patch schemes theoretically in terms of the ratio of the space over which the patch schemes and the full-domain model computes. [Section 3.7.2](#) shows the computational savings of the patch schemes in terms of the ratio of the number of state variables for which the patch schemes and the full-domain model computes. [Section 3.7.4](#) demonstrates the computational savings of the 2D staggered patch schemes by measuring the elapsed time taken to compute the time derivative of the state vector (one time iteration) using a specific implementation.

[Section 3.7.5](#) demonstrates the accuracy and effectiveness of the patch schemes via time simulation of the general dissipative linear waves for two example cases. [Section 3.7.5](#), first compares the time simulation of a patch scheme with that of the fine-grid full-domain model for a simple progressive wave, second demonstrates the patch scheme time simulation for a moving Gaussian hump. Via random perturbation to the initial condition, [§3.7.5](#) also demonstrates the robustness of the patch schemes.

3.1 Full-domain microscale model and staggered patch schemes

This subsection derives a discrete full-domain microscale model corresponding to the general linear PDEs [\(3.0.1\)](#). Subsequently using the derived full-domain microscale model within the patches, this subsection also derives a generic staggered patch scheme. Throughout this chapter, we use this full-domain microscale model as a reference to assess various characteristics (accuracy, stability, consistency, etc.) of the multiscale staggered patch schemes we develop.

Approximating the spatial derivatives in the general dissipative linear wave PDEs [\(3.0.1\)](#) by central finite differences on the staggered grid nodes (filled circles in [Fig. 2.1.1](#) of [§2.1.1](#)), gives the *full-domain microscale model*

corresponding to the general dissipative linear wave PDEs (3.0.1) as

$$\bullet \frac{dh_{i,j}}{dt} = -\frac{u_{i+1,j} - u_{i-1,j}}{2\delta} - \frac{v_{i,j+1} - v_{i,j-1}}{2\delta} \quad (3.1.1a)$$

for $i, j \in \{0, 2, 4, \dots, n-2\}$;

$$\bullet \frac{du_{i,j}}{dt} = -\frac{h_{i+1,j} - h_{i-1,j}}{2\delta} - c_D u_{i,j} + c_V \frac{u_{i-2,j} - 2u_{i,j} + u_{i+2,j}}{4\delta^2} + c_V \frac{u_{i,j-2} - 2u_{i,j} + u_{i,j+2}}{4\delta^2} \quad (3.1.1b)$$

for $i \in \{1, 3, 5, \dots, n-1\}$, $j \in \{0, 2, 4, \dots, n-2\}$;

$$\bullet \frac{dv_{i,j}}{dt} = -\frac{h_{i,j+1} - h_{i,j-1}}{2\delta} - c_D v_{i,j} + c_V \frac{v_{i-2,j} - 2v_{i,j} + v_{i+2,j}}{4\delta^2} + c_V \frac{v_{i,j-2} - 2v_{i,j} + v_{i,j+2}}{4\delta^2} \quad (3.1.1c)$$

for $i \in \{0, 2, 4, \dots, n-2\}$, $j \in \{1, 3, 5, \dots, n-1\}$.

Analogous to the PDEs (3.0.1), the three fields h , u , v are n -periodic in both i and j where $n = L/\delta$, with an appropriate initial condition $h_{i,j}(0)$, $u_{i,j}(0)$, and $v_{i,j}(0)$. As a dynamical system, the full-domain microscale model (3.1.1) in vector notation, for the general dissipative linear wave (3.0.1) is

$$\frac{d\mathbf{x}}{dt} = \mathbf{f}(\mathbf{x}), \quad (3.1.2)$$

where \mathbf{x} is the same state vector (2.1.3) of the full-domain microscale model for generic wave-like system in §2.1.1.

A full-domain microscale simulation is performed by numerical time-integration of the ODEs (3.1.1) on the nodes of the microscale staggered grid (filled circles in Fig. 2.1.1), with the discrete macroscale n -periodic boundary conditions in i, j .

Now let's consider the patch scheme for the system (3.1.1), over a staggered patch grid with $N \times N$ macro-grid intervals and each patch containing $n \times n$ sub-patch micro-grid intervals. To use the finite difference equations (3.1.1) as the microscale model within the patches, a staggered patch grid with one layer of edge nodes, such as in Fig. 2.1.3b of §2.1.2, is not sufficient. For example, in equation (3.1.1b), to compute the time derivative $du_{i,j}/dt$ for the bottom left u node of the u -centred patch, the second spatial derivative in viscous diffusion term needs the value of $u_{i-2,j}$, which is outside to the left of the u -centred patch and not available in Fig. 2.1.3b. The additional layer of edge nodes in Fig. 2.1.5a of §2.1.3 provides the $u_{i-2,j}$ for the bottom left u node of the u -centred patch. Hence, a staggered

patch scheme with the 2D general dissipative linear wave (3.1.1) as the underlying microscale model within the patches, requires a patch grid with two layers of edge nodes as in Fig. 2.1.5a of §2.1.3.

Using the full-domain microscale model (3.1.1) within the patches of a suitable staggered patch grid (e.g., the patch grid of Fig. 2.1.5a with $n = 6$), gives the *staggered patch scheme*

$$\bullet \frac{d}{dt} h_{i,j}^{I,J}(t) = -\frac{u_{i+1,j}^{I,J} - u_{i-1,j}^{I,J}}{2\delta} - \frac{v_{i,j+1}^{I,J} - v_{i,j-1}^{I,J}}{2\delta}, \quad (3.1.3a)$$

$$\bullet \frac{d}{dt} u_{i,j}^{I,J}(t) = -\frac{h_{i+1,j}^{I,J} - h_{i-1,j}^{I,J}}{2\delta} - c_D u_{i,j}^{I,J} + c_V \frac{u_{i-2,j}^{I,J} - 2u_{i,j}^{I,J} + u_{i+2,j}^{I,J}}{4\delta^2} + c_V \frac{u_{i,j-2}^{I,J} - 2u_{i,j}^{I,J} + u_{i,j+2}^{I,J}}{4\delta^2}, \quad (3.1.3b)$$

$$\bullet \frac{d}{dt} v_{i,j}^{I,J}(t) = -\frac{h_{i,j+1}^{I,J} - h_{i,j-1}^{I,J}}{2\delta} - c_D v_{i,j}^{I,J} + c_V \frac{v_{i-2,j}^{I,J} - 2v_{i,j}^{I,J} + v_{i+2,j}^{I,J}}{4\delta^2} + c_V \frac{v_{i,j-2}^{I,J} - 2v_{i,j}^{I,J} + v_{i,j+2}^{I,J}}{4\delta^2}, \quad (3.1.3c)$$

and a patch coupling (e.g., Square-p4) to compute the edge values

$\circ h_{i,j}^{I,J}$, $\circ u_{i,j}^{I,J}$, $\circ v_{i,j}^{I,J}$ for

$i \in \{-1, 0, n, n+1\}$, $j \in \{1, 2, \dots, n-1\}$ for left and right edges and

$i \in \{1, 2, \dots, n-1\}$, $j \in \{-1, 0, n, n+1\}$ for bottom and top edges,

for the same interior indices i, j and patch indices I, J in (2.1.5) of §2.1.1,

separately for each equation.

Analogous to the full-domain microscale model (3.1.1), the three fields h , u , v in the patch scheme (3.1.3) are macroscale N -periodic in both I and J where $N = L/\Delta$, with an appropriate initial condition $h_{i,j}^{I,J}(0)$, $u_{i,j}^{I,J}(0)$, and $v_{i,j}^{I,J}(0)$. As a dynamical system, the staggered patch scheme (3.1.3) in vector notation, corresponding to the full-domain microscale model (3.1.1) of dissipative linear wave is

$$\frac{dx^I}{dt} = \mathbf{F}(x^I; x^E(x^I)). \quad (3.1.4)$$

with the same state vector x^I (2.1.6) and a similar edge vector x^E as those of the patch scheme in §2.1.2 for generic wave-like system. To distinguish from the analytic one-cell staggered patch scheme (3.2.15) (in p. 61 of §3.2.3), we call equation (3.1.4) as the *full-size* staggered patch scheme.

The $\mathbf{F}(\mathbf{x}^I; \mathbf{x}^E(\mathbf{x}^I))$ in the staggered patch scheme dynamical system (3.1.4) corresponds to the $\mathbf{f}(\mathbf{x})$ in the full-domain microscale model (3.1.2). The functions \mathbf{F} and \mathbf{f} encode the same microscale model for the general dissipative linear wave PDEs (3.0.1), except for the two differences that §2.1.2 of §2.1.2 explains for the generic wave-like system.

As in the patch scheme (2.1.5) of §2.1.2, a specific patch coupling (for example, Square-p2) computes patch edge values ($\circ h_{i,j}^{I,J}$, $\circ u_{i,j}^{I,J}$, $\circ v_{i,j}^{I,J}$ in Fig. 2.1.5a) from the centre values of neighbouring patches ($\bullet h_{i,j}^{I,J}$, $\bullet u_{i,j}^{I,J}$, $\bullet v_{i,j}^{I,J}$ with $i = j = n/2$ in Fig. 2.1.5a). The patch coupling provides a mechanism whereby patches influence each other, §2.2 gives various details of different patch couplings.

Patch scheme simulation is performed by numerical time-integration of the ODEs (3.1.3) on the interior nodes of the staggered patch grid (filled circles in Fig. 2.1.3b), with the discrete macroscale N -periodic boundary conditions in both I and J . As in §2.1.2, evaluating the time derivatives in the staggered patch scheme (3.1.3) is done in two steps: first, edge values $\mathbf{x}^E(\mathbf{x}^I)$ are computed via patch coupling; second, using both interior and edge values of each patch in the staggered patch grid, the time derivatives of \mathbf{x}^I are computed for the staggered patch scheme (3.1.3) of dissipative linear wave.

3.2 Staggered patch schemes are accurate

This section shows that the developed five staggered patch schemes are accurate for the general dissipative linear waves. We establish the accuracy of the staggered patch schemes in general (as opposed to just one initial condition) by comparing the eigenvalues of the staggered patch schemes with the eigenvalues of fine- and coarse-grid full-domain microscale model, and for completeness also compare with the eigenvalues of the general dissipative linear wave PDEs (3.0.1). But, for assessing the accuracy of the patch schemes, as p. 14 of §2.1.1 explains, the eigenvalues of the full domain *microscale model* are the reference eigenvalues, not that of the PDEs. The eigenvalue analysis for accuracy in this section is done for representative subsets of macro-grid intervals $N \in \{6, 10, 14\}$ and sub-patch micro-grid intervals $n \in \{6, 10\}$; Section 3.6 studies the consistency of the staggered patch schemes over various number of macro-grid intervals. The following paragraphs introduce the approach to studying the accuracy of the staggered patch schemes and discuss the conventions adopted.

Time-dependent solutions of linear/linearised ODEs are linear combinations of the spatial modes (i.e., eigenvectors) where the initial condition gives the amplitudes of the modes (Manneville 2004, p. 37–38; Cain and Reynolds 2010, Prop. 2.1.21, p. 28; Edwards et al. 2017, p.386; Maruskin 2018, general solution, p. 17). To characterise the patch scheme dynamics at micro- and macro-scales, we define the following patch scheme modes.

- *Macroscale modes* are those patch scheme modes (eigenvectors) that have pure macroscale structure (spatial variation) with negligible microscale structure. The eigenvalues corresponding to these macroscale modes are *macroscale eigenvalues*.
- *Microscale modes* are those patch schemes modes that have significant microscale structure irrespective of whether they also have macroscale structure. That is, a microscale mode can either be of pure microscale structure with negligible macroscale structure or can have a microscale structure modulated over the macroscale. The eigenvalues corresponding to these microscale modes are *microscale eigenvalues*.

Throughout this thesis, the phrase *microscale structure modulated over the macroscale* means that the microscale structure (spatial variation) is modulated over some nonnegligible macroscale structure.

Due to spatial homogeneity in the macroscale dynamics, the macroscale spatial structure of the full-domain model and the patch schemes are effectively the same. Hence, effectively there is no error in the macroscale modes (eigenvectors) of the patch schemes. The only error in the macroscale dynamics of the patch schemes is in the eigenvalues. Thus, when the macroscale eigenvalues of a patch scheme agree closely with the corresponding eigenvalues of the full-domain microscale model, the patch scheme simulation is *accurate in general for every initial condition* that only involves macroscale modes. We aim to design the multiscale staggered patch schemes to accurately simulate the large-scale waves that are characterised by the macroscale eigenvalues. A staggered patch scheme is accurate when the macroscale eigenvalues of that patch scheme agree closely with the corresponding macroscale eigenvalues of the full-domain microscale model. Thus, we aim to design the staggered patch schemes with the macroscale eigenvalues as close as possible to the corresponding macroscale eigenvalues of the full domain microscale model (3.1.1). Hence, the eigenvalue analysis for accuracy in this section compares the eigenvalues of the staggered patch schemes with the eigenvalues of the full-domain microscale model.

Sections 3.2.1 to 3.2.5 describe the methods of analytically deriving and numerically computing the eigenvalues for

1. the 2D general dissipative linear wave PDEs (3.0.1),
2. the full-domain microscale model (3.1.1), and
3. the staggered patch scheme (3.1.3).

Following a standard approach of substituting an arbitrary Fourier mode into the PDEs/ODEs, §§3.2.1 and 3.2.2 derive the analytic eigenvalues of general dissipative linear wave PDEs (3.0.1) and the corresponding discrete full-domain microscale model (3.1.1). Similarly §3.2.3 derives the analytic eigenvalues of a staggered patch scheme. To numerically compute the eigenvalues of the numerical staggered patch scheme, which includes any instabilities and inaccuracies due to the numerical roundoff errors, §§3.2.4 and 3.2.5 numerically computes the Jacobians of the evolution functions $f(\mathbf{x})$ in the full-domain model (3.1.2), and $\mathbf{F}(\mathbf{x}^I; \mathbf{x}^E(\mathbf{x}^I))$ in the patch scheme (3.1.4) respectively.

Section 3.2.6 compares and contrasts various eigenvalues (e.g., analytic and numerical eigenvalues of the PDEs, full-domain microscale model, and patch schemes). We use the following notational convention to identify the various eigenvalues.

- Eigenvalue *subscripts* in $\lambda_p^{()}, \lambda_{m\delta}^{()}, \lambda_{m\Delta}^{()}, \lambda_{\text{PDE}}^{()}$ denote the system.
 - $\lambda_p^{()}$ are for staggered patch schemes (e.g., λ_p^{NE1} of §3.2.3 and λ_p^{N} of §3.2.5).
 - $\lambda_{m\delta}^{()}$ are for fine-grid full domain microscale model with same grid-spacing as sub-patch micro-grid interval δ (e.g., $\lambda_{m\delta}^{\text{A}}$ of §3.2.2 and $\lambda_{m\delta}^{\text{N}}$ of §3.2.4).
 - $\lambda_{m\Delta}^{()}$ are for fine-grid full domain microscale model with same grid-spacing as the inter-patch distance Δ (e.g., $\lambda_{m\Delta}^{\text{A}}$ of §3.2.2 and $\lambda_{m\Delta}^{\text{N}}$ of §3.2.4).
 - $\lambda_{\text{PDE}}^{()}$ are for the general linear wave PDE (e.g., $\lambda_{\text{PDE}}^{\text{A}}$ of §3.2.1).
- Eigenvalue *superscripts* in $\lambda_{() }^{\text{N}}, \lambda_{() }^{\text{NE1}}, \lambda_{() }^{\text{A}}$ denote the method of computing numerical eigenvalues values.
 - $\lambda_{() }^{\text{N}}$ are computed from the numerical Jacobian of the system (e.g., $\lambda_{m\delta}^{\text{N}}, \lambda_{m\Delta}^{\text{N}}$ of §3.2.4 and λ_p^{N} of §3.2.5).

- λ_0^{NE1} are computed from numerically evaluated analytic one-cell Jacobian of the system (e.g., λ_p^{NE1} of §3.2.3).
- λ_0^{A} are computed from the closed-form analytic expressions for the eigenvalues (e.g., $\lambda_{\text{PDE}}^{\text{A}}$ of §3.2.1 and $\lambda_{m\delta}^{\text{A}}, \lambda_{m\Delta}^{\text{A}}$ of §3.2.2).

3.2.1 Eigenvalue analysis of the PDEs

This subsection derives the eigenvalues of the 2D general dissipative linear wave PDEs (3.0.1) to compare with the eigenvalues of the full-domain microscale model (3.1.1) and the various staggered patch schemes for a sanity check.

One of the standard analytic approaches to derive the eigenvalues of a linear PDE (e.g., Hinch 2020, pp. 138–139; G. W. Griffiths and Schiesser 2011) is to substitute an arbitrary Fourier mode into the PDE, derive an eigen-system in terms of a system matrix that characterises the time evolution, and subsequently compute the eigenvalues of the system matrix which characterises both the stability and accuracy of the system. Following this standard approach, consider an arbitrary Fourier mode of the general dissipative linear wave PDE (3.0.1), with real wavenumber (k_x, k_y) and complex growth rate λ ,

$$h(x, y, t) = H \exp[i(k_x x + k_y y) + \lambda t], \quad (3.2.1a)$$

$$u(x, y, t) = U \exp[i(k_x x + k_y y) + \lambda t], \quad (3.2.1b)$$

$$v(x, y, t) = V \exp[i(k_x x + k_y y) + \lambda t]. \quad (3.2.1c)$$

Substituting the Fourier mode (3.2.1) into the general dissipative linear wave PDEs (3.0.1) gives the eigensystem

$$\begin{bmatrix} 0 & -i k_x & -i k_y \\ -i k_x & -c_D - c_V (k_x^2 + k_y^2) & 0 \\ -i k_y & 0 & -c_D - c_V (k_x^2 + k_y^2) \end{bmatrix} \begin{bmatrix} H \\ U \\ V \end{bmatrix} = \lambda \begin{bmatrix} H \\ U \\ V \end{bmatrix}. \quad (3.2.2)$$

The three eigenvalues of the 3×3 Jacobian in eigensystem (3.2.2) are (one real and a complex conjugate pair),

$$\lambda_{\text{PDE}}^{\text{A}} = \begin{cases} -c_D - c_V (k_x^2 + k_y^2), \\ -\frac{c_D}{2} - \frac{c_V}{2} (k_x^2 + k_y^2) \pm \sqrt{\left[\frac{c_D}{2} + \frac{c_V}{2} (k_x^2 + k_y^2)\right]^2 - (k_x^2 + k_y^2)}. \end{cases} \quad (3.2.3)$$

With no dissipation, that is with $c_D = c_V = 0$ in expression (3.2.3), the three eigenvalues of the ideal wave are $(0, \pm i \omega_0)$, where the nonzero frequency of this ideal (undamped) wave $\omega_0 = \sqrt{k_x^2 + k_y^2}$.

Rewriting the eigenvalues (3.2.3) in terms of the ideal wave frequency ω_0 gives the alternative expression

$$\lambda_{\text{PDE}}^{\Lambda} = \begin{cases} -(c_D + c_V \omega_0^2), \\ -(c_D + c_V \omega_0^2)/2 \pm \sqrt{[(c_D + c_V \omega_0^2)/2]^2 - \omega_0^2}. \end{cases} \quad (3.2.4)$$

Expressions (3.2.3) and (3.2.4) give eigenvalues of the 2D general dissipative linear wave PDEs (3.0.1) with linear drag c_D and viscous diffusion c_V .

With dissipation, that is with $c_D, c_V > 0$, the real parts of all three eigenvalues (3.2.4) are negative, meaning that the wave solutions decay over time.

- For high dissipation (large positive values of c_D and/or c_V), the square root in expression (3.2.4) gives a real value, making all three eigenvalues real, which correspond to an overdamped system where any initial condition or disturbance will quickly decay to zero, which is not our interest.
- For low dissipation (small positive values of c_D and/or c_V), the square root in expression (3.2.4) gives an imaginary component, that is the damped frequency, so any initial wave will oscillate and decay slowly to zero.

We numerically evaluate eigenvalue expression (3.2.3) or (3.2.4) for various macroscale wavenumbers, and compare (for a sanity check) with the eigenvalues of the full-domain microscale model and the various staggered patch schemes in §3.2.6.

3.2.2 Eigenvalue analysis of staggered grid full-domain model

This subsection derives the eigenvalues of the staggered grid full-domain microscale model (3.1.1) for the general dissipative linear wave PDEs (3.0.1). Comparing these eigenvalues of the full-domain model with the eigenvalues of the staggered patch schemes, §3.2.6 studies the accuracy of the patch schemes and §3.5 studies stability of the patch schemes.

We follow the same standard analytic approach (e.g., Hinch 2020, pp. 138–139; G. W. Griffiths and Schiesser 2011), as done for the 2D general dissipative linear wave PDE in §3.2.1, but over a discrete infinite microscale staggered grid (number of grid intervals $n \rightarrow \infty$ in Fig. 2.1.1). Consider an

arbitrary Fourier mode of the full-domain microscale model (3.1.1), with real wavenumber (k_x, k_y) and complex growth rate λ ,

$$\bullet h_{i,j}(t) = H \exp[i(k_x i \delta + k_y j \delta) + \lambda t] \quad (3.2.5a)$$

for $i, j \in \{0, 2, 4, \dots, n-2\}$,

$$\bullet u_{i,j}(t) = U \exp[i(k_x i \delta + k_y j \delta) + \lambda t] \quad (3.2.5b)$$

for $i \in \{1, 3, 5, \dots, n-1\}$, $j \in \{0, 2, 4, \dots, n-2\}$,

$$\bullet v_{i,j}(t) = V \exp[i(k_x i \delta + k_y j \delta) + \lambda t] \quad (3.2.5c)$$

for $i \in \{0, 2, 4, \dots, n-2\}$, $j \in \{1, 3, 5, \dots, n-1\}$.

Throughout this thesis, i denotes the micro-grid index in x -direction (for both full-domain and sub-patch micro-grids), whereas $i = \sqrt{-1}$ is the imaginary unit. Substituting the Fourier mode (3.2.5) into the full-domain microscale model (3.1.1), some algebraic simplifications, and arranging in matrix form give the eigensystem

$$\mathbf{J} \begin{bmatrix} H \\ U \\ V \end{bmatrix} = \lambda \begin{bmatrix} H \\ U \\ V \end{bmatrix}, \quad (3.2.6)$$

where the Jacobian

$$\mathbf{J} = \begin{bmatrix} 0 & -\frac{i \sin(k_x \delta)}{\delta} & -\frac{i \sin(k_y \delta)}{\delta} \\ -\frac{i \sin(k_x \delta)}{\delta} & -c_D - c_V \left(\frac{\sin^2(k_x \delta)}{\delta^2} + \frac{\sin^2(k_y \delta)}{\delta^2} \right) & 0 \\ -\frac{i \sin(k_y \delta)}{\delta} & 0 & -c_D - c_V \left(\frac{\sin^2(k_x \delta)}{\delta^2} + \frac{\sin^2(k_y \delta)}{\delta^2} \right) \end{bmatrix}.$$

The three eigenvalues of the 3×3 Jacobian \mathbf{J} in the eigensystem (3.2.6) are (one real and a complex conjugate pair),

$$\lambda_m^\Lambda = \begin{cases} -(c_D + c_V \omega_{m,0}^2), \\ -(c_D + c_V \omega_{m,0}^2) / 2 \pm \sqrt{[(c_D + c_V \omega_{m,0}^2) / 2]^2 - \omega_{m,0}^2}, \end{cases} \quad (3.2.7)$$

where

$$\omega_{m,0} = \sqrt{\sin^2(k_x \delta) / \delta^2 + \sin^2(k_y \delta) / \delta^2} \quad (3.2.8)$$

is the frequency of the full-domain microscale model for ideal wave (i.e., undamped with $c_D = c_V = 0$). When we numerically evaluate these eigenvalues λ_m^Λ of the full-domain microscale model,

- for the same grid-spacing δ as the sub-patch micro-grid interval (also called δ), we call the eigenvalues $\lambda_{m\delta}^\Lambda$,

- for the same grid-spacing Δ as the inter-patch distance Δ , we call the eigenvalues $\lambda_{m\Delta}^\Delta$.

Comparing eigenvalue expression (3.2.7) with the eigenvalue expression (3.2.4) of the PDE, the full-domain microscale eigenvalues converge to the eigenvalues of the 2D general dissipative linear wave PDEs (3.0.1) when $\omega_{m,0}^2 \rightarrow \omega_0^2 = k_x^2 + k_y^2$. Expanding $\omega_{m,0}^2$ as power series in either (k_x, k_y) or δ we get,

$$\omega_{m,0}^2 = k_x^2 + k_y^2 - \frac{1}{3} (k_x^4 + k_y^4) \delta^2 + \frac{2}{45} (k_x^6 + k_y^6) \delta^4 - \frac{1}{315} (k_x^8 + k_y^8) \delta^6 + \mathcal{O}((k_x^{10} + k_y^{10})\delta^8). \quad (3.2.9)$$

The series expansion (3.2.9) shows that the eigenvalues of the full-domain microscale model converge to the analytic eigenvalues of the PDEs (3.0.1) as we decrease the grid interval δ and/or wavenumber (k_x, k_y) .

For assessing the accuracy and stability, §3.2.6 and §3.5 numerically evaluate the eigenvalue expression (3.2.7) for various macroscale wavenumbers and compare with the eigenvalues of the general linear wave PDEs and the patch schemes.

3.2.3 Analytic eigenvalue analysis of staggered patch schemes

This subsection explains a method of deriving analytic eigenvalues of a generic staggered patch scheme (3.1.3) over a staggered patch grid, for the 2D general dissipative linear wave PDEs (3.0.1). This subsection also gives example expressions for a specific patch coupling among the various staggered patch schemes. We use the patch scheme eigenvalues to assess accuracy (§3.2.6), stability (§3.5), and consistency (§3.6) of the staggered patch schemes.

We follow a similar analytic approach as in analytic eigenvalue analysis of the staggered grid full-domain microscale model in §3.2.2, but over an infinite *staggered patch grid* (number of macroscale grid intervals $N \rightarrow \infty$ in Fig. 2.1.5a). Section 2.1.3 explains why the staggered patch grid in Fig. 2.1.5a with such edge node arrangement is required for the current consideration of the 2D general dissipative linear wave.

Unlike the analysis of a staggered grid full-domain microscale model in §3.2.2, the dynamics of a staggered patch scheme that we aim to analyse via their eigenvalues has an emergent behaviour due to the coupled dynamics at two different length scales. One length scale is due to the microscale interactions within the patches, and another length scale is due

to the different macroscale patch coupling across the patches (Spectral, Square-p2, Square-p4, etc.). Hence, for eigenvalue analysis of a staggered patch scheme, our arbitrary Fourier mode needs to include spatial structures of the two scales: microscale within a patch and macroscale across the patches.

Our aim is to study the macroscale behaviour of the staggered patch scheme, which is manifested by the microscale behaviour within the patches.

1. To capture the macroscale behaviour the staggered patch scheme Fourier mode must include microscale spatial structure within the patches. Hence, in contrast to the full-domain microscale Fourier mode (3.2.5) with constant amplitudes H, U, V one each respectively for h, u, v , the staggered patch scheme Fourier mode must cater for a microscale spatial structure $h_{i,j}^{p,q}, u_{i,j}^{p,q}, v_{i,j}^{p,q}$ for the interior nodes of all three patches within a macro-cell (orange squares in Fig. 2.1.4b); here $p, q \in \{0, 1\}$ is the local sub-macro-cell patch index (Fig. 2.1.4b).
2. The microscale spatial structure $h_{i,j}^{p,q}, u_{i,j}^{p,q}, v_{i,j}^{p,q}$ within a macro-cell must be independent of the macroscale across the macro-cells. That is, the microscale structure in the staggered patch scheme mode must be invariant to translations in space by multiples of 2Δ . Hence, the staggered patch scheme Fourier mode must include the macroscale spatial structure as complex exponential factor $\exp[i(k_x I\Delta + k_y J\Delta)]$, where the indices I, J increment by two for each variable ($\bullet h_{i,j}^{I,J}$, $\bullet u_{i,j}^{I,J}$, and $\bullet v_{i,j}^{I,J}$ in Fig. 2.1.4b).

Thus, for the eigenvalue analysis of a staggered patch scheme, let us consider an arbitrary staggered patch scheme Fourier mode with the *macroscale* real wavenumber (k_x, k_y) , over an infinite staggered patch grid ($N \rightarrow \infty$ in Fig. 2.1.5a of §2.1.3),

$$\bullet h_{i,j}^{I,J}(t) = h_{i,j}^{p,q}(t) \exp[i(k_x I\Delta + k_y J\Delta)] , \quad (3.2.10a)$$

$$\bullet u_{i,j}^{I,J}(t) = u_{i,j}^{p,q}(t) \exp[i(k_x I\Delta + k_y J\Delta)] , \quad (3.2.10b)$$

$$\bullet v_{i,j}^{I,J}(t) = v_{i,j}^{p,q}(t) \exp[i(k_x I\Delta + k_y J\Delta)] , \quad (3.2.10c)$$

for the same interior indices i, j and global macroscale patch indices I, J in (2.1.5) of §2.1.1, separately for each equation. We define the indices $p, q \in \{0, 1\}$ as the local sub-macro-cell patch index with $p = I \bmod 2$ and $q = J \bmod 2$. Figure 2.1.4 of §2.1.2 illustrates these indices for the case of finite number of macro-grid intervals N where the global macroscale patch index $I, J \in \{0, 1, \dots, N-1\}$ as illustrated in Fig. 2.1.4 of §2.1.2. But for our

present case of $N \rightarrow \infty$ for analytic eigenvalue analysis, we use the global macroscale patch index $I, J \in \{\dots, -1, 0, 1, \dots\}$.

In the patch scheme Fourier mode (3.2.10), the time-dependent microscale structure $h_{i,j}^{p,q}(t), u_{i,j}^{p,q}(t), v_{i,j}^{p,q}(t)$ is *modulated* over the macroscale wave form $\exp[i(k_x I \Delta + k_y J \Delta)]$. So, the microscale structure $h_{i,j}^{p,q}(t), u_{i,j}^{p,q}(t), v_{i,j}^{p,q}(t)$ depends only on the sub-macro-cell patch index p, q and the sub-patch micro-grid node index i, j , but not on the global patch index I, J due to the 2Δ -translational symmetry in the Fourier shift. For example, substituting $I \rightarrow I + 2$ for the h -component in the arbitrary staggered patch scheme Fourier mode (3.2.10),

$$\begin{aligned} h_{i,j}^{I+2,J} &= h_{i,j}^{p,q}(t) \exp[i(k_x(I+2)\Delta + k_y J \Delta)] \\ &= h_{i,j}^{p,q}(t) \exp[i(k_x I \Delta + k_y J \Delta)] \exp[i(k_x 2\Delta)]. \end{aligned}$$

That is, the microscale structure within the patch $(I \pm 2, J)$ are 2Δ -Fourier shifts of the microscale structure within the patch (I, J) ; similarly the microscale structure within the patch $(I, J \pm 2)$ are also 2Δ -Fourier shifts of the microscale structure within the patch (I, J) .

In §3.2.2 for analytic eigenvalue analysis of the *full-domain microscale model*, the constant amplitudes (H, U, V) in the full-domain microscale Fourier mode (3.2.5) correspond to the three nodes (h, u, v) nodes of one micro-cell in the full-domain microscale grid (large filled circles in Fig. 2.1.1 of §2.1.1). Hence the eigensystem (3.2.6) has a state vector (H, U, V) of size three, leading to the 3×3 one-cell Jacobian of the full-domain microscale model. In analytic eigenvalue analysis of a *patch scheme*, the time-dependent microscale structure $h_{i,j}^{p,q}(t), u_{i,j}^{p,q}(t), v_{i,j}^{p,q}(t)$ in the staggered patch scheme Fourier mode (3.2.10) corresponds to the interior nodes of all three patches (h -, u -, v -centred patches) in any one macro-cell which we name the *centre macro-cell* illustrated by the orange square in Fig. 2.1.5a of §2.1.3. Collecting the interior values of all three patches in the centre macro-cell into a vector gives the *state vector* \mathbf{x}^i ; the superscript $(\cdot)^i$ is not an index or exponent, instead, a qualifier denoting the patch interior nodes for the *one-cell system* (we use $(\cdot)^I$ to denote the interior nodes of the full system (2.1.9)). The total number of patch interior nodes per macro-cell, that is the size of \mathbf{x}^i ,

$$n_p^i = 9n^2/4 - 4n + 2, \quad (3.2.11)$$

where n is the number of sub-patch grid intervals. For example, for the cases of $n = 6, 10, 14$ sub-patch micro-grid intervals, $n_p^i = 59, 187, 387$ respectively.

For example, for the staggered patch grid in Fig. 2.1.5a of §2.1.3, with $n = 6$ sub-patch grid intervals, the state vector containing 59 elements is

$$\begin{aligned}
 \mathbf{x}^i = & (h_{1,1}^{0,0}, h_{1,3}^{0,0}, h_{1,5}^{0,0}, h_{3,1}^{0,0}, h_{3,3}^{0,0}, h_{3,5}^{0,0}, h_{5,1}^{0,0}, h_{5,3}^{0,0}, h_{5,5}^{0,0}, \\
 & u_{2,1}^{0,0}, u_{2,3}^{0,0}, u_{2,5}^{0,0}, u_{4,1}^{0,0}, u_{4,3}^{0,0}, u_{4,5}^{0,0}, \\
 & v_{1,2}^{0,0}, v_{1,4}^{0,0}, v_{3,2}^{0,0}, v_{3,4}^{0,0}, v_{5,2}^{0,0}, v_{5,4}^{0,0}, \\
 & h_{1,2}^{0,1}, h_{1,4}^{0,1}, h_{3,2}^{0,1}, h_{3,4}^{0,1}, h_{5,2}^{0,1}, h_{5,4}^{0,1}, \\
 & u_{2,2}^{0,1}, u_{2,4}^{0,1}, u_{4,2}^{0,1}, u_{4,4}^{0,1}, \\
 & v_{1,1}^{0,1}, v_{1,3}^{0,1}, v_{1,5}^{0,1}, v_{3,1}^{0,1}, v_{3,3}^{0,1}, v_{3,5}^{0,1}, v_{5,1}^{0,1}, v_{5,3}^{0,1}, v_{5,5}^{0,1}, \\
 & h_{2,1}^{1,0}, h_{2,3}^{1,0}, h_{2,5}^{1,0}, h_{4,1}^{1,0}, h_{4,3}^{1,0}, h_{4,5}^{1,0}, \\
 & u_{1,1}^{1,0}, u_{1,3}^{1,0}, u_{1,5}^{1,0}, u_{3,1}^{1,0}, u_{3,3}^{1,0}, u_{3,5}^{1,0}, u_{5,1}^{1,0}, u_{5,3}^{1,0}, u_{5,5}^{1,0}, \\
 & v_{2,2}^{1,0}, v_{2,4}^{1,0}, v_{4,2}^{1,0}, v_{4,4}^{1,0}).
 \end{aligned} \tag{3.2.12}$$

Applying a specific patch coupling (Spectral, Square-p2, Square-p4, etc.) gives edge values of all the patches in a macro-cell, in terms of the substituted Fourier mode. That is, patch coupling gives the edge values of each patch in the centre macro-cell from the centre-node values of patches in other macro-cells, which are Fourier shifted centre-node values (by multiples of 2Δ) of the centre macro-cell. Collecting the edge values of all three patches in the centre macro-cell into a vector gives the *edge vector* \mathbf{x}^e ; the superscript $(\cdot)^e$ is not an index or exponent, instead, a qualifier denoting the edge nodes of the one-cell system (we use E to denote the edge nodes of the full system (2.1.9)). The total number of patch edge nodes per macro-cell for the compatible staggered patch grid (Fig. 2.1.5a) for general linear dissipative wave, that is the size of \mathbf{x}^e ,

$$n_p^e = 18n - 16, \tag{3.2.13}$$

where n is the number of sub-patch grid intervals. For example, for the cases of $n = 6, 10, 14$ sub-patch micro-grid intervals, $n_p^e = 92, 164, 236$ respectively.

For example, for the sub-cell patch index $(p, q) = (0, 0)$ (Fig. 2.1.4b), the simplest staggered patch scheme Square-p2 for $n = 6$, with the patch coupling stencil in Fig. 2.2.2, gives the edge values near the left-bottom of the h-centred patch,

$$\begin{aligned}
 h_{-1,1}^{0,0} = & h_{3,3}^{0,0}(t) \left[\frac{4r^4}{81} - \frac{5r^2}{9} + 1 \right. \\
 & \left. + \left(-\frac{2r^4}{81} + \frac{r^3}{27} + \frac{2r^2}{9} - \frac{r}{3} \right) e^{2ik_x\Delta} + \left(-\frac{2r^4}{81} - \frac{r^3}{27} + \frac{2r^2}{9} + \frac{r}{3} \right) e^{-2ik_x\Delta} \right]
 \end{aligned}$$

$$\begin{aligned}
& + \left(-\frac{2r^4}{81} + \frac{2r^3}{27} + \frac{r^2}{18} - \frac{r}{6} \right) e^{2ik_y\Delta} + \left(-\frac{2r^4}{81} - \frac{2r^3}{27} + \frac{r^2}{18} + \frac{r}{6} \right) e^{-2ik_y\Delta} \\
& + \left(\frac{r^4}{81} - \frac{r^3}{18} + \frac{r^2}{18} \right) e^{2i(k_x\Delta+k_y\Delta)} + \left(\frac{r^4}{81} + \frac{r^3}{18} + \frac{r^2}{18} \right) e^{-2i(k_x\Delta+k_y\Delta)} \\
& + \left(\frac{r^4}{81} + \frac{r^3}{54} - \frac{r^2}{18} \right) e^{2i(k_x\Delta-k_y\Delta)} + \left(\frac{r^4}{81} - \frac{r^3}{54} - \frac{r^2}{18} \right) e^{-2i(k_x\Delta-k_y\Delta)} \Big], \\
\end{aligned} \tag{3.2.14a}$$

$$\begin{aligned}
\mathbf{u}_{0,1}^{0,0} &= \mathbf{u}_{3,3}^{1,0}(t) \left[\frac{r^3}{18} - \frac{r^2}{18} - \frac{r}{2} + \frac{1}{2} + \left(-\frac{r^3}{18} - \frac{r^2}{18} + \frac{r}{2} + \frac{1}{2} \right) e^{-2ik_x\Delta} \right. \\
& + \left(-\frac{r^3}{36} + \frac{r^2}{9} - \frac{r}{12} \right) e^{2ik_y\Delta} + \left(-\frac{r^3}{36} - \frac{r^2}{18} + \frac{r}{12} \right) e^{-2ik_y\Delta} \\
& \left. + \left(\frac{r^3}{36} - \frac{r^2}{18} - \frac{r}{12} \right) e^{2i(-k_x\Delta+k_y\Delta)} + \left(\frac{r^3}{36} + \frac{r^2}{9} + \frac{r}{12} \right) e^{-2i(k_x\Delta+k_y\Delta)} \right], \\
\end{aligned} \tag{3.2.14b}$$

$$\begin{aligned}
\mathbf{v}_{1,0}^{0,0} &= \mathbf{v}_{3,3}^{0,1}(t) \left[\frac{r^3}{18} - \frac{r^2}{18} - \frac{r}{2} + \frac{1}{2} + \left(-\frac{r^3}{18} - \frac{r^2}{18} + \frac{r}{2} + \frac{1}{2} \right) e^{-2ik_y\Delta} \right. \\
& + \left(-\frac{r^3}{36} + \frac{r^2}{9} - \frac{r}{12} \right) e^{2ik_x\Delta} + \left(-\frac{r^3}{36} - \frac{r^2}{18} + \frac{r}{12} \right) e^{-2ik_x\Delta} \\
& \left. + \left(\frac{r^3}{36} - \frac{r^2}{18} - \frac{r}{12} \right) e^{2i(k_x\Delta-k_y\Delta)} + \left(\frac{r^3}{36} + \frac{r^2}{9} + \frac{r}{12} \right) e^{-2i(k_x\Delta+k_y\Delta)} \right]. \\
\end{aligned} \tag{3.2.14c}$$

For other staggered patch schemes such as Spectral, Square-p4, Square-p6, and Square-p8, the patch coupling expressions (3.2.14) are longer and more complicated.

For one macro-cell, substituting into the staggered patch scheme (3.1.3), the Fourier mode (3.2.10) and the coupled patch edge values (e.g., (3.2.14)) computed by a specific patch coupling, and cancelling the exponential factors on both sides, gives the time evolution of a staggered patch scheme as a dynamical system

$$\frac{d\mathbf{x}^i}{dt} = \mathbf{F}(\mathbf{x}^i; \mathbf{x}^e(\mathbf{x}^i)), \tag{3.2.15}$$

only for the specific modes of macroscale wavenumber (k_x, k_y) . The dynamical system (3.2.15) is in the same form as the full-size staggered patch scheme dynamical system (3.1.4) (in p. 50 of §3.1). The state vector \mathbf{x}^i of the full-size staggered patch scheme dynamical system (3.1.4) contain interior values of all the patches in a staggered patch grid, but the state vector \mathbf{x}^i of the staggered patch scheme dynamical system (3.2.15) for one macroscale

wavenumber (k_x, k_y) contain interior values of only one macro-cell. Hence, we call equation (3.2.15) as the *one-cell* staggered patch scheme dynamical system.

The one-cell staggered patch scheme dynamical system (3.2.15), written separately for h, u , and v is in the same form as the corresponding full-size staggered patch scheme (3.1.3) of §3.1 with one difference: state variables h, u , and v are only from one macro-cell expressed in sub-macro-cell patch index p, q as opposed to the state variables from all the macro-cells expressed in the global patch index I, J .

For the general dissipative linear waves, the one-cell staggered patch scheme dynamical system (3.2.15) is a linear system with the one-cell Jacobian $\mathbf{J} = \partial \mathbf{F} / \partial \mathbf{x}$. Hence the one-cell staggered patch scheme dynamical system (3.2.15) is written equivalently as

$$\frac{d\mathbf{x}^i}{dt} = \mathbf{J}\mathbf{x}^i. \quad (3.2.16)$$

The $n_p^i \times n_p^i$ one-cell Jacobian \mathbf{J} not only depends on the physical parameters c_D, c_V , discretisation parameters n, δ , but also on the macroscale wavenumber (k_x, k_y) . The one-cell Jacobian of the staggered patch schemes is useful in giving insights about the staggered patch schemes and for parametric studies, especially to compute eigenvalues corresponding to a macroscale wavenumber (k_x, k_y) for a patch grid of any size N . Via all macroscale wavenumbers, the one-cell Jacobian provides a complete solution for all initial conditions applied to the patch scheme.

For example, for $n = 6$ sub-patch grid intervals, the one-cell Jacobian \mathbf{J} is a 59×59 sparse matrix with at most only 318 of the 3481 elements are nonzero. This sparsity pattern holds irrespective of the particular patch coupling interpolation of the staggered patch schemes (i.e., same sparsity for both spectral scheme and polynomial patch schemes). For some particular combination of numerical values of the parameters, the sparsity could be higher. The 318 nonzero elements of the one-cell Jacobian of a staggered patch scheme (for $n = 6$) contain all the information about the underlying microscale model and the patch coupling for the macroscale waves of wavenumber (k_x, k_y) . A few elements of the one-cell Jacobian of

the simplest staggered patch scheme Square-p2 are,

$$\begin{aligned} \mathbf{J}_{1,1} &= 0, \quad \mathbf{J}_{1,16} = -\frac{1}{2\delta}, \quad \mathbf{J}_{4,10} = \frac{1}{2\delta}, \quad \mathbf{J}_{12,11} = \frac{c_V}{4\delta^2}, \\ \mathbf{J}_{16,16} &= -c_D - \frac{c_V}{\delta^2}, \quad \mathbf{J}_{18,36} = \left(\frac{c_V}{8\delta^2} + \frac{3c_V}{8\Delta\delta} \right) e^{-2\Delta i k_y} + \frac{c_V}{8\delta^2} - \frac{3c_V}{8\Delta\delta}, \\ \mathbf{J}_{46,36} &= \left(-\frac{1}{8\delta} - \frac{1}{2\Delta} - \frac{3\delta}{8\Delta^2} \right) e^{2\Delta i k_x} + \left(-\frac{1}{8\delta} + \frac{1}{2\Delta} - \frac{3\delta}{8\Delta^2} \right) e^{-2\Delta i k_y} \\ &\quad + \left(-\frac{1}{8\delta} + \frac{1}{4\Delta} + \frac{3\delta}{8\Delta^2} \right) e^{2\Delta i k_x - 2\Delta i k_y} - \frac{1}{8\delta} - \frac{1}{4\Delta} + \frac{3\delta}{8\Delta^2}, \\ \mathbf{J}_{50,51} &= \left(-\frac{c_V}{4\Delta\delta} + \frac{c_V}{2\Delta^2} \right) e^{2\Delta i k_y} + \left(\frac{c_V}{4\Delta\delta} + \frac{c_V}{2\Delta^2} \right) e^{-2\Delta i k_y} + \frac{c_V}{2\delta^2} - \frac{c_V}{\Delta^2}. \end{aligned}$$

The example expressions for $\mathbf{J}_{1,16}$, $\mathbf{J}_{4,10}$, $\mathbf{J}_{12,11}$ and $\mathbf{J}_{16,16}$ are independent of the macroscale wavenumber (k_x, k_y) and macro-grid interval Δ and hence characterise the microscale flow physics:

- $\mathbf{J}_{1,16}$, $\mathbf{J}_{4,10}$ characterise the microscale flow physics;
- c_V in $\mathbf{J}_{12,11}$ characterise the microscale viscous diffusion;
- c_D , c_V in $\mathbf{J}_{16,16}$ characterise the microscale drag and viscous diffusion.

All the Jacobian elements containing c_D are precisely the same and occur only as diagonal elements of the Jacobian. That is, all the nonzero diagonal elements

$$\begin{aligned} \mathbf{J}_{i,i} &= -c_D - c_V/\delta^2 \\ &\text{for } i \in \{10, 11, \dots, 21, \quad 28, 29, \dots, 40, \quad 47, 48, \dots, 59\}. \end{aligned} \quad (3.2.17)$$

The drag terms $-c_D u_{i,j}^{I,J}$ and $-c_D v_{i,j}^{I,J}$ in the patch scheme (3.1.3b) and (3.1.3c), involve only the drag coefficient and the respective velocities, leading to c_D appearing only in the diagonal of the Jacobian, without depending on macro-grid interval Δ , patch scale ratio r and the patch coupling.

The example expressions for $\mathbf{J}_{18,36}$, $\mathbf{J}_{46,36}$ and $\mathbf{J}_{50,51}$ depend on the macroscale wavenumber (k_x, k_y) and macro-grid interval Δ and hence characterise the macroscale flow physics:

- Expressions for $\mathbf{J}_{18,36}$ and $\mathbf{J}_{50,51}$ characterise macroscale wave with only viscous diffusion;
- $\mathbf{J}_{46,36}$ characterises a macroscale wave without any dissipation.

The 2Δ in the argument of the exponential factors in $\mathbf{J}_{18,36}$, $\mathbf{J}_{46,36}$, and $\mathbf{J}_{50,51}$ indicates the patch coupling influence by the patches in surrounding macro-cells which are 2Δ away from the centre macro-cell. Compared to the listed example Jacobian elements of the simple patch coupling Square-p2, more surrounding macro-cells influence the Jacobian elements for the cases of patch coupling with higher order interpolations (Square-p4, Square-p6, and Square-p8). Hence the corresponding expressions in the one-cell Jacobian elements are much longer than the listed example expressions.

We attempted to derive closed-form expressions for the eigenvalues of the one-cell Jacobian \mathbf{J} , through various algebraic simplification strategies, in various Computer Algebra Systems (CAS) such as SymPy, Reduce and Maple. Even for the simplest staggered patch scheme Square-p2, all the CAS packages we tried fail (no results in 48 hours) to compute the analytic eigenvalues of the 59×59 Jacobian ($n = 6$) for the general macroscale wavenumber (k_x, k_y) . For the special case of the undamped ideal wave ($c_D = c_V = 0$) with $k_x = k_y = 0$, which corresponds to a constant macroscale solution, SymPy derives the characteristic equation of the one-cell Jacobian \mathbf{J} as

$$\lambda^{19} (\lambda^2 + 1/\delta^2)^4 (\lambda^2 + 2/\delta^2)^3 (\lambda^2 + 3/\delta^2)^4 (\lambda^2 + 4/\delta^2)^6 (\lambda^2 + 6/\delta^2)^3 = 0. \quad (3.2.18)$$

The nineteen zero eigenvalues in the characteristic equation (3.2.18) are due to the microscale and macroscale vortex modes and a constant (flat, non-wave) macroscale mode. The forty pure imaginary eigenvalues $\lambda \in \{\pm i/\delta, \pm i\sqrt{2}/\delta, \pm i\sqrt{3}/\delta, \pm i\sqrt{4}/\delta, \pm i\sqrt{6}/\delta\}$ are due to pure sub-patch microscale wave modes (i.e., contained within the patches).

Our aim is to assess all the macroscale eigenvalues of the staggered patch schemes including those that correspond to nonzero wavenumbers (k_x, k_y) , so we numerically evaluate the one-cell Jacobian for numerical values of $\Delta, \delta, c_D, c_V, k_x, k_y$ and compute the eigenvalues λ_p^{NE1} . For example, for $n = 6$ sub-patch micro-grid intervals, such one-cell 59×59 Jacobian of a staggered patch scheme gives 59 eigenvalues λ_p^{NE1} . For each value of (k_x, k_y) , three among the 59 eigenvalues λ_p^{NE1} characterise macroscale modes (two wave modes and one vortex mode), and the remaining 56 eigenvalues characterise microscale modes corresponding to sub-patch microscale waves and sub-patch vortex modes.

Section 3.2.6 and §3.5 assess the accuracy and stability of the patch schemes, by comparing their eigenvalues λ_p^{NE1} of the numerically evaluated one-cell Jacobian, with the eigenvalues of the full domain microscale model and the eigenvalues of the general dissipative linear wave PDEs.

3.2.4 Compute numerical Jacobian of the full-domain model

This subsection explains the method of computing numerical eigenvalues of the full-domain microscale model (3.1.2) in p. 49 for all the resolved wavenumbers of the finite grid, as opposed to the analytic eigenvalues of one wavenumber for the full-domain model over an infinite grid.

The 3×3 analytic Jacobian (3.2.6) gives the closed form expression (3.2.7) for the eigenvalues λ_m^A of the full-domain microscale model, for one particular wavenumber (k_x, k_y) . A full-domain staggered grid (e.g., Fig. 2.1.1) with $n \times n$ grid intervals, has $n/2 \times n/2 = n^2/4$ cells, each containing three nodes. Hence the total number of nodes is $n_m = 3n^2/4$, which is the same as the number of dynamical variables, and hence the same as the number of eigenvalues. For example, the full-domain staggered grid in Fig. 2.1.1 with 6×6 grid intervals ($n = 6$), has $3n^2/4 = 27$ eigenvalues. To compute all the $3n^2/4$ eigenvalues λ_m^A of a full-domain grid with $n \times n$ grid intervals, we evaluate the analytic eigenvalue expression for all the $n^2/4$ wavenumbers corresponding to the $n^2/4$ cells (i.e., expression (3.2.7) gives three eigenvalues per wavenumber).

In practice, the full-domain microscale simulation is performed using the *full-size* numerical scheme, which is subject to the practical issue of numerical roundoff errors. The eigenvalues of the numerical full-size Jacobian \mathbf{J} characterise the accuracy and stability of the numerical staggered grid full-domain microscale model over a particular finite-sized domain (i.e., number of grid intervals n is finite as opposed to the case of 3×3 Jacobian for an infinite staggered grid). Hence we also compute the eigenvalues λ_m^N for a $n_m \times n_m$ numerical Jacobian of the full-domain microscale model as discussed in this subsection.

Consider the full-domain microscale model (3.1.2) in p. 49 of §3.1 (i.e., $dx/dt = f(x)$) where x is the state vector (2.1.3), for the general linear wave, over a full-domain staggered grid (e.g., Fig. 2.1.1) with $n \times n$ grid intervals. The linear system (3.1.2) is equivalent to $dx/dt = \mathbf{J}x$, where \mathbf{J} is a $n_m \times n_m$ *full-size* Jacobian, in contrast to the 3×3 Jacobian in the eigensystem (3.2.6), of the full-domain microscale model. The full-size Jacobian \mathbf{J} of the staggered grid full-domain microscale model, depends only on the physical parameters c_D, c_V and discretisation parameters n, δ, Δ , not on the wavenumber. That is the full-size numerical Jacobian \mathbf{J} encodes all the information about the time evolution, for all the wavenumbers.

As the physical parameters c_D, c_V and discretisation parameters n, δ are not varying with time, the system $dx/dt = \mathbf{J}x$ (and the corresponding full-domain dynamical system (3.1.2)) is a *linear time invariant* system. That is

the system \mathbf{f} in (3.1.2) is completely characterised by the full-size Jacobian \mathbf{J} whose columns are responses to unit impulses. Hence, we compute the i th column of the full-size Jacobian \mathbf{J} , by evaluating \mathbf{f} for a complete set of unit state vectors $\hat{\mathbf{x}}_i$ as

$$\mathbf{J} = [\mathbf{f}(\hat{\mathbf{x}}_1), \mathbf{f}(\hat{\mathbf{x}}_2), \dots, \mathbf{f}(\hat{\mathbf{x}}_{n_m})] \quad (3.2.19)$$

where the unit state vectors $\hat{\mathbf{x}}_i$ are vectors of size n_m whose i th element is one and all other elements are zero.

Section 3.2.6 uses the eigenvalues of the numerical Jacobian of the full-domain microscale model, for comparing with the eigenvalues of the patch scheme. For example, Figs. 3.2.1 and 3.2.2 of §3.2.6, show the trend of the eigenvalues of the full-domain model for all the resolved wavenumbers. We verified that the analytic eigenvalues $\lambda_{m\delta}^A$ of expression (3.2.7) and numerical eigenvalues $\lambda_{m\delta}^N$ of the full-domain microscale model agree within numerical roundoff errors. On the other hand, as p. 73 of §3.2.6 explains, the computational effort for computing the numerical eigenvalues is very large for fine-grid full-domain model (with grid interval same as sub-patch grid interval δ). Hence, to avoid large computational effort and as the primary focus is on the macroscale eigenvalues (not all wavenumbers), all other studies in this thesis use eigenvalues $\lambda_{m\delta}^A$ from the analytic expression (3.2.7) of the analytic Jacobian (§3.2.2).

3.2.5 Compute numerical Jacobian of the staggered patch schemes

The $n_p^i \times n_p^i$ one-cell Jacobian of the staggered patch scheme in §3.2.3, is useful in giving insights about the staggered patch schemes and to compute eigenvalues corresponding to a small macroscale wavenumber (k_x, k_y) for a patch grid of any size N . But, in practice, the staggered patch scheme numerical time simulation is performed using the *full-size* evolution equation (3.1.4) in p. 50 of §3.1. To confirm that the full-size staggered patch scheme (3.1.4) is stable, accurate, consistent, and not too sensitive to numerical roundoff errors, this subsection explains a method to compute the numerical eigenvalues λ_p^N of the staggered patch schemes.

Consider the full-size staggered patch scheme dynamical system (3.1.4) in p. 50 of §3.1 as a linear system

$$\frac{d\mathbf{x}^I}{dt} = \mathbf{J}\mathbf{x}^I \quad (3.2.20)$$

for general dissipative linear wave, similar to the one-cell patch scheme system (3.2.16). The $n_p^I \times n_p^I$ Jacobian \mathbf{J} is the full-size numerical Jacobian of

the staggered patch scheme (3.1.4). For the full-size patch scheme system, the number of state variables $n_p^I = (N^2/4)(9n^2/4 - 4n + 2)$ as in expression (2.1.7). In contrast to the one-cell Jacobian, the full-size Jacobian \mathbf{J} of the numerical staggered patch scheme depends only on the physical parameters c_D, c_V and discretisation parameters N, n, δ , not on a specific wavenumber (k_x, k_y) . The eigenvalues λ_p^N of the numerical staggered patch scheme Jacobian \mathbf{J} characterise the accuracy and stability of the numerical staggered patch schemes over a particular finite sized domain (i.e., N is finite as opposed to infinite staggered patch grid for the one-cell Jacobian).

As the physical parameters c_D, c_V and discretisation parameters N, n, δ are not varying with time, the system $dx^I/dt = \mathbf{J}x^I$ (and the corresponding staggered patch scheme dynamical system (3.1.4)) is a *linear time invariant* system. Hence, we compute the i th column of the staggered patch scheme Jacobian \mathbf{J} by evaluating \mathbf{F} for a complete set of unit state vectors \hat{x}_i^I as

$$\mathbf{J} = \left[\mathbf{F}(\hat{x}_1^I; \mathbf{x}^E(\hat{x}_1^I)), \mathbf{F}(\hat{x}_2^I; \mathbf{x}^E(\hat{x}_2^I)), \dots, \mathbf{F}(\hat{x}_{n_p^I}^I; \mathbf{x}^E(\hat{x}_{n_p^I}^I)) \right] \quad (3.2.21)$$

where the unit state vectors \hat{x}_i^I are vectors of size n_p^I whose i th element is one and all other elements are zero.

Sections 3.2.6, 3.5 and 3.4 assess the accuracy, stability, and consistency of the patch schemes, by comparing the eigenvalues λ_p^N of the staggered patch scheme numerical Jacobian with the eigenvalues of the full domain microscale model.

3.2.6 Staggered patch schemes are accurate for macroscale waves

This section explains the qualitative structure of the staggered patch scheme eigenvalues and eigenvectors, and qualitatively demonstrates the accuracy of the staggered patch schemes for the general linear wave for a few cases (e.g., $N \in \{6, 10\}$, $n = 6$, $r = 0.1$). Section 3.6 on the consistency of the staggered patch schemes, quantitatively establishes the patch scheme accuracy in more detail, over a much broader range of parameters.

This section demonstrates the accuracy of the developed five staggered patch schemes (Spectral, Square-p2, Square-p4, Square-p6, and Square-p8) by comparing the following eigenvalues in the complex plane plots.

1. Eigenvalues λ_p^N of the numerical Jacobian of a staggered patch scheme on a finite domain (§3.2.5).

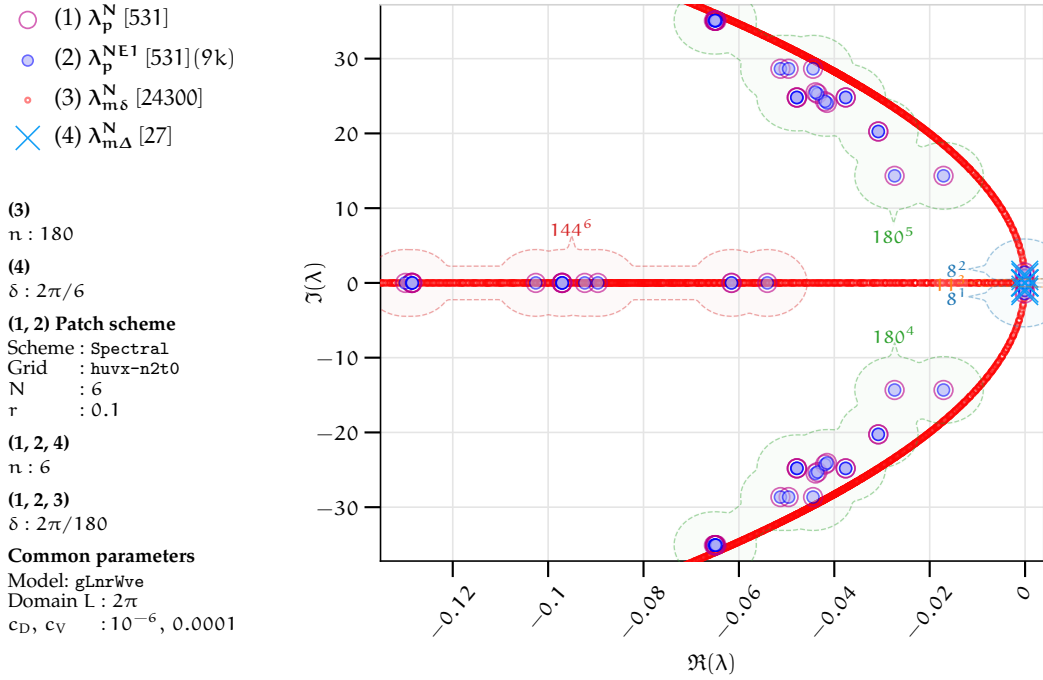
2. Eigenvalues λ_p^{NE1} of the numerically evaluated one-cell Jacobian in linear system (3.2.16) in §3.2.3, of a staggered patch scheme on an infinite domain.
3. Eigenvalues $\lambda_{m\delta}^A$ from the analytic expression (3.2.7) in §3.2.2, of fine-grid full-domain microscale model, with micro-grid interval equal to the sub-patch micro-grid interval δ . That is, $\delta_{m\delta} \equiv L/n_{m\delta} = \delta \equiv l/n \equiv 2Lr/(Nn)$ as $r = l/(2\Delta)$ and $\Delta = L/N$, where $n_{m\delta}$ is the number of full-domain microscale grid intervals and n is the number of sub-patch micro-grid intervals. When the context is clear we drop the subscript $m\delta$ in $n_{m\delta}$ and $\delta_{m\delta}$ for the fine-grid full-domain microscale model.
4. Eigenvalues $\lambda_{m\Delta}^A$ from the analytic expression (3.2.7) in §3.2.2 of coarse grid version of the full-domain microscale model, with $\delta = \Delta$. That is, $\delta_{m\Delta} \equiv L/n_{m\Delta} = \Delta \equiv L/N$, where $n_{m\Delta}$ is the number of full-domain microscale grid intervals and n is the number of sub-patch micro-grid intervals. When the context is clear we drop the subscript $m\Delta$ in $n_{m\delta}$ and $\delta_{m\Delta}$ for the coarse-grid full-domain microscale model.
5. Eigenvalues λ_{PDE}^A from the analytic expression (3.2.3) of the 2D general dissipative linear wave PDEs (3.0.1) (§3.2.1). Comparison with the eigenvalues λ_{PDE}^A is only for completeness.

All the analytic eigenvalues (λ_p^{NE1} , $\lambda_{m\delta}^A$, $\lambda_{m\Delta}^A$, λ_{PDE}^A) are numerically evaluated for all the $N^2/4$ *macroscale wavenumbers* (k_x, k_y) resolved on a corresponding finite staggered patch grid with $N \times N$ macro-grid intervals. To illustrate the complete structure of eigenvalues (i.e, for all wavenumbers) of the full-domain microscale model and to cross-verify analytic and numerical computation of the full-domain microscale model eigenvalues, we also compute the eigenvalues of the numerical Jacobian of the full-domain microscale model for few cases (e.g., Fig. 3.2.1).

The sets of eigenvalues (e.g., λ_p^N , λ_p^{NE1} , $\lambda_{m\delta}^N$, $\lambda_{m\Delta}^N$, λ_{PDE}^A), in all the complex plane plots, are numbered in the legend entries on the left. In all the complex plane plots, physical parameters for each of these eigenvalues are listed in groups *below the legend entries*. For example, the following listing explains the parameters specifically for Fig. 3.2.1 with $N = 6$, $n = 6$, and similarly for other plots.

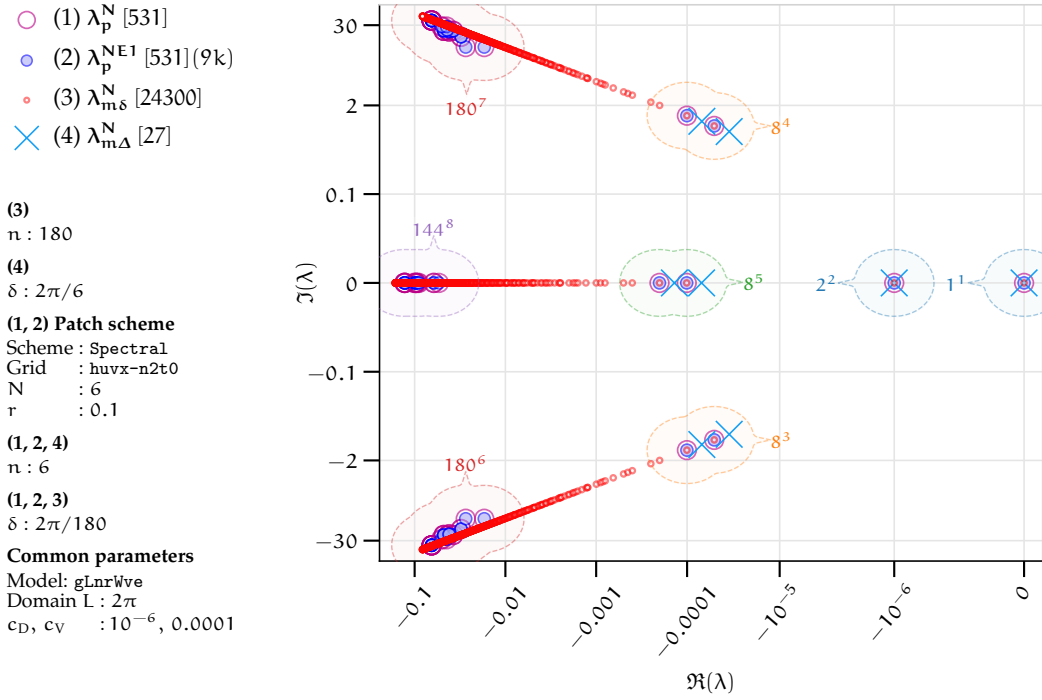
- The group labelled by (3) (in the left, below the legend entries) says that the third listed eigenvalues $\lambda_{m\delta}^N$ correspond to a fine full-domain micro-grid with 180×180 grid intervals ($n = 180$).

Figure 3.2.1. Spectral staggered patch scheme ($N = 6, n = 6$) eigenvalues ($\lambda_p^N, \lambda_p^{NE1}$) on complex plane (*linear scale*) for general linear wave. Due to large range of magnitudes of eigenvalues, details of eigenvalues for macroscale modes (mid-right clusters 1, 2, 3) are not discernable.



- The group labelled by (4) says that the fourth listed eigenvalues $\lambda_{m\Delta}^N$ correspond to a full-domain micro-grid with coarse grid interval $\delta = L/N = 2\pi/6 = \Delta$.
- The group labelled by (1, 2) lists all the parameters common to the first and second listed eigenvalues $\lambda_p^N, \lambda_p^{NE1}$ of the staggered patch scheme.
- The group labelled by (1, 2, 4) says that $n = 6$ for the first, second, and the fourth listed eigenvalues. We use the same symbol n for the number of grid intervals for both the full-domain micro-grid and the sub-patch micro-grid. That is, the eigenvalues $\lambda_p^N, \lambda_p^{NE1}$ correspond to a staggered patch grid where each patch contains 6×6 sub-patch micro-grid intervals ($n = 6$), and the eigenvalues $\lambda_{m\Delta}^N$ correspond to a coarse full-domain micro-grid with 6×6 grid intervals ($n = 6$).
- The group labelled by (1, 2, 3) says that $\delta = 2\pi/180$ for the first, second, and the third listed eigenvalues. We use the same symbol δ for

Figure 3.2.2. Spectral staggered patch scheme ($N = 6, n = 6$) eigenvalues ($\lambda_p^N, \lambda_p^{NE1}$) on complex plane (arcsinh *nonlinear* scale) for general linear wave. The arcsinh scaling zooms out the eigenvalues of macroscale modes (mid-right clusters 1, 2, 3 in Fig. 3.2.1 to clusters 1–5 here).



the grid interval for both the full-domain micro-grid and the sub-patch micro-grid. That is, the eigenvalues $\lambda_p^N, \lambda_p^{NE1}$ correspond to a staggered patch grid with sub-patch micro-grid interval $\delta = 2\pi/180$, and the eigenvalues $\lambda_{m\delta}^N$ correspond to a fine full-domain micro-grid interval $\delta = 2\pi/180$.

- The group *Common parameters* lists the parameters common to all the listed eigenvalues.

Figures 3.2.1 and 3.2.2 plot the eigenvalues ($\lambda_p^N, \lambda_p^{NE1}$) of the Spectral patch scheme on a staggered patch grid with 6×6 macro-grid intervals ($N = 6$) and each patch containing 6×6 sub-patch micro-grid intervals ($n = 6$). Also plotted are the eigenvalues $\lambda_{m\delta}^N, \lambda_{m\Delta}^N$ of respectively the fine- and coarse-grid versions of the full-domain microscale model (3.1.1) and the eigenvalues λ_{PDE}^A of the PDE (3.0.1). Similar to Figs. 3.2.1 and 3.2.2, in all the complex plane eigenvalue plots, eigenvalues are grouped within clusters based on eigenvalues λ_p^{NE1} of the staggered patch scheme Jacobian. Each cluster is annotated with the number of eigenvalues λ_p^{NE1} in the cluster

and the cluster number in the superscript.

Figure 3.2.1 presents the complex plane plot on a *linear scale*. Hence, due to the large range of magnitude of the eigenvalues, details of the eigenvalues for macroscale modes (mid-right clusters 1, 2, 3) are not discernable. The details of the eigenvalues for macroscale modes are of primary interest. On the other hand, the arcsinh scaling in Fig. 3.2.2 aptly zooms out the eigenvalues of macroscale modes (mid-right clusters 1, 2, 3 in Fig. 3.2.1 to clusters 1–5). That is, the nonlinear arcsinh scaling has a quasi-log nature, which empowers us to see very small (positive and negative) as well as large magnitude of eigenvalues, all together in the same plot. Hence, *most complex plane eigenvalue plots in this thesis are on arcsinh scaling*. Specifically, the complex plane plots on arcsinh scaling, plot an eigenvalue λ as a point on a 2D space with coordinates $(\text{arcsinh}\{S_h [\Re(\lambda) - O_h]\}/S_h + O_h, \text{arcsinh}[S_v \Im(\lambda)]/S_v)$, where S_h, S_v are the horizontal and vertical scale factors and $(O_h, 0)$ is the centre of zoom. In this chapter, most plots on arcsinh scaling use the scale factors $S_h = 5 \cdot 10^6$, $S_v = 100$ and the centre of zoom $(O_h, 0) = (-5 \cdot 10^{-7}, 0)$.

This paragraph explains the general qualitative structure of the patch scheme eigenvalues for the general linear wave, using as reference the complex plane plot of Fig. 3.2.2 for the Spectral staggered patch scheme. Figure 3.2.2 is for a staggered patch grid with 10×10 macro-grid intervals ($N = 10$) and each patch containing 6×6 sub-patch micro-grid intervals ($n = 6$). The following points are based on the Spectral patch scheme eigenvalues in Fig. 3.2.2 and the eigenvectors (the patch scheme modes) in Figs. 3.2.13 to 3.2.18. But these points hold in general for the eigenvalues of the PDE, full-domain microscale model, and all the five (Spectral and four polynomial) patch schemes. The number just next to each cluster is the number of eigenvalues in that cluster. The cluster numbers referred to below are indicated on the plots by the *superscript* of the number just next to each cluster. For the general linear wave, we find that the patch scheme eigenvalues typically form eight clusters as in Fig. 3.2.2 (clusters 1–8).

- Cluster 1 consisting of one zero eigenvalue corresponds to the macroscale mode of stagnant water (zero eigenvalue, hence temporally constant) with uniform height and no flow (i.e., $u = v = 0$) (e.g., eigenvector in Fig. 3.2.13). This mode is due to the conservation of mass/height of water with nonzero mean height (mean height is zero for the other modes).
- Cluster 2 consisting of two real eigenvalues $-c_D$, corresponds to the macroscale mode of *decelerating* (negative real part) *uniform mean flow* (e.g., eigenvector in Fig. 3.2.14) due to drag in two directions.

- Clusters 3, 4 together consisting of sixteen complex conjugate eigenvalues with small negative real parts, correspond to slowly decaying *macroscale wave modes* with small wavenumber (e.g., eigenvector in Fig. 3.2.15).
- Cluster 5 consisting of eight small real negative eigenvalues, corresponds to slowly decaying *macroscale vortex modes* (e.g., eigenvector in Fig. 3.2.16).
- Clusters 6, 7 together consisting of 360 complex conjugate eigenvalues with large negative real parts, correspond to fast decaying *sub-patch microscale wave modes* with large wavenumber (e.g., eigenvector in Fig. 3.2.17).
- Cluster 8 consisting of 144 large real negative eigenvalues, corresponds to fast decaying *sub-patch microscale vortex modes* (e.g., eigenvector in Fig. 3.2.18).
- As the clusters 1–5 correspond to macroscale modes, we call their eigenvalues *macroscale eigenvalues* (as defined in p. 52 of §3.2).
- As the clusters 6–8 correspond to microscale modes, we call their eigenvalues *microscale eigenvalues* (as defined in p. 52 of §3.2).

The previous paragraph shows that the clusters 1–5 (on the right) contain eigenvalues of the macroscale modes and the clusters 6–8 (on the left) contain eigenvalues of the microscale modes. As Figs. 3.2.1 and 3.2.2 show, a patch scheme contains only the small wavenumber macroscale modes (on the right) and large wavenumber microscale modes (on the left), not the modes of the intermediate scale. On the other hand, the eigenvalues $\lambda_{m\delta}^N$ of the full-domain microscale model, span the eigenvalue plot nearly uniformly from left to right, corresponding to all the wavenumbers resolved on the full-domain microscale staggered grid. Figures 3.2.1 and 3.2.2 show a *good qualitative agreement of the structure of microscale and macroscale patch scheme eigenvalues λ_p^N and the complete structure of the eigenvalues $\lambda_{m\delta}^N$ (i.e., for all wavenumbers) of the full-domain microscale model*. For the accurate multiscale modelling of the macroscale waves, the agreement between the macroscale eigenvalues of the patch scheme and those of the full-domain model is the primary focus. Figure 3.2.2 shows that, within the clusters 1–5, the numerical macroscale eigenvalues λ_p^N of the patch scheme (large magenta circles) and the numerical macroscale eigenvalues $\lambda_{m\delta}^N$ (small red circles) visually agree.

As Fig. 3.2.2 shows, for both microscale and macroscale modes, the patch scheme eigenvalues λ_p^{NE1} of the numerically evaluated one-cell analytic Jacobian (§3.2.3) and the patch scheme eigenvalues λ_p^N of the numerical Jacobian (§3.2.5), agree (i.e., the large magenta and blue circles). Hence, *all other complex plane plots in this subsection §3.2.6 use eigenvalues λ_p^{NE1} of the numerically evaluated one-cell analytic Jacobian (§3.2.3), as opposed to the numerical eigenvalues λ_p^N .*

For a staggered patch grid with 6×6 macro-grid intervals ($N = 6$) and each patch containing 6×6 sub-patch micro-grid intervals ($n = 6$), the total number of nodes and hence the total number of eigenvalues λ_p^N is $n_p^1 = 531$. The corresponding number of eigenvalues $\lambda_{m\delta}^N$ of the fine-grid full-domain microscale model (with patch scale ratio $r = 0.1$) is $(3/16)(Nn/r)^2 = 24300$, whose numerical Jacobian (§3.2.4) is of size 24300×24300 containing $5.9 \cdot 10^8$ elements. For patch grids with $N \geq 10$ and/or $r < 0.1$, the corresponding numerical Jacobians of the fine-grid full-domain microscale model, rapidly increase in size requiring substantially larger computational effort and memory (e.g., larger than 64 GB). For the accurate multiscale modelling of the macroscale waves, the agreement between the macroscale eigenvalues of the patch scheme and those of the full-domain model is the primary focus, not the eigenvalues corresponding to all the wavenumbers. That is, to assess the patch scheme accuracy, as in Fig. 3.2.3 it suffices to compare only the patch scheme macroscale eigenvalues with the macroscale eigenvalues $\lambda_{m\delta}^A$ of the full-domain microscale model (by evaluating the analytic expression (3.2.7) only for macroscale wavenumbers resolved on a staggered patch grid). Hence, to avoid large computational effort and as the primary focus is on the macroscale eigenvalues, *all other complex plane plots in this subsection §3.2.6 use eigenvalues $\lambda_{m\delta}^A$ from the analytic expression (3.2.7) of the analytic Jacobian (§3.2.2), as opposed to the numerical eigenvalues $\lambda_{m\delta}^N$.*

The specific location of eigenvalues on the complex plane plot of Fig. 3.2.2, for the Spectral staggered patch scheme, change with the physical parameters c_D , and c_V , but the above cluster structure is typical.

- When the drag tends to zero with nonzero viscous diffusion (i.e., $c_D \rightarrow 0$, $c_V \neq 0$), the two eigenvalues of the decelerating uniform mean flow mode (cluster 2) move to right in the complex plane and merge with cluster 1 of steady uniform mode as in Fig. 3.2.3.
- When the viscous diffusion tends to zero with nonzero drag (i.e., $c_V \rightarrow 0$, $c_D \neq 0$), two notable structural changes occur:
 1. the eigenvalues of the wave modes (clusters 3,4,7,8 in Fig. 3.2.2)

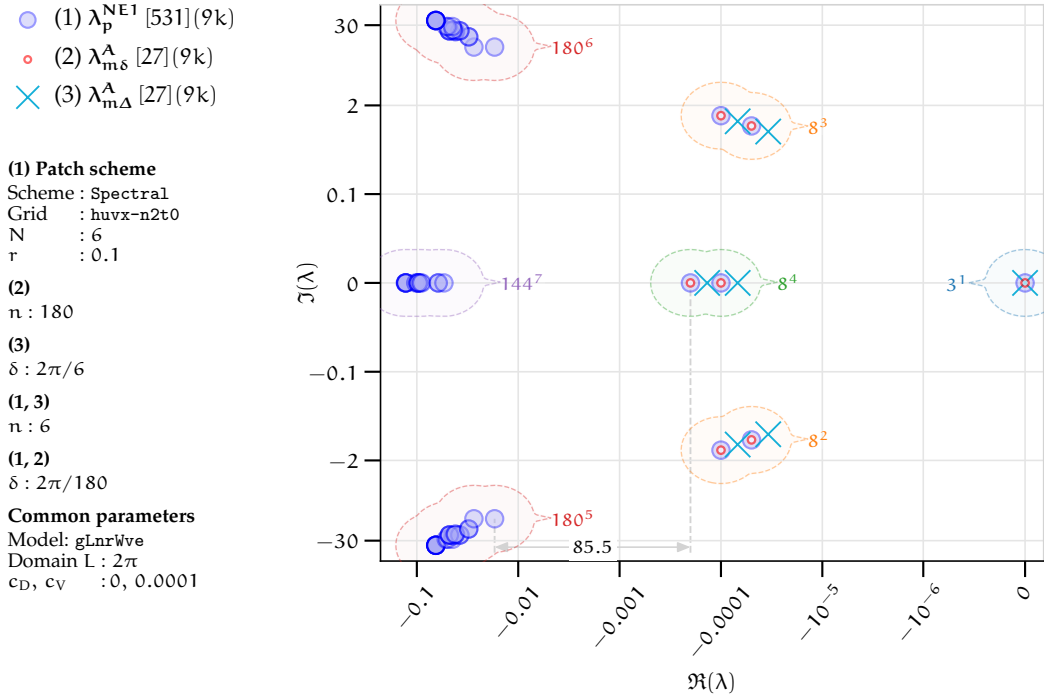
- move to the right to take constant real part value of $-c_D/2$ (clusters 2,3,4,5 in Fig. 3.2.4);
 - 2. the eigenvalues of the vortex modes (clusters 5,8 in Fig. 3.2.2) move to the right in the complex plane and merge with cluster 2 of the decelerating uniform mean flow mode, which is cluster 6 in Fig. 3.2.4.
- When both the drag and the viscous diffusion tend to zero, (i.e., $c_D, c_V \rightarrow 0$), two notable structural changes occur:
 1. the eigenvalues of the wave modes (clusters 3,4,7,8 in Fig. 3.2.2) move to the right to take zero real part (clusters 1,2,4,5 in Fig. 3.2.5);
 2. the eigenvalues of the vortex modes (clusters 5,8 in Fig. 3.2.2) and decelerating uniform mean flow modes (cluster 2 in Fig. 3.2.2) move to the right in the complex plane and merge with cluster 3 of the zero eigenvalues in Fig. 3.2.5.

The structure of eigenvalues and its qualitative dependence on the dissipation parameters (c_D, c_V) for the Spectral staggered patch scheme, explained in the preceding paragraph, also hold for all the four polynomial staggered patch schemes of the general linear wave (e.g., the eigenvalues of the polynomial staggered patch schemes in Figs. 3.2.9 to 3.2.12).

The number of wave modes (clusters 3, 4, 6, 7 in Fig. 3.2.2), and the number of vortex modes (clusters 5, 8 in Fig. 3.2.2), depend on N, n of a patch scheme for general linear wave (over a staggered patch grid containing $N \times N$ macro-grid intervals and each patch containing $n \times n$ sub-patch micro-grid intervals). The following listing explains the number of various modes (number of eigenvalues λ_p^N) of a staggered patch scheme for the general linear wave *with nonzero drag and the viscous diffusion*. For example, Figs. 3.2.2, 3.2.6 and 3.2.7 plot eigenvalues of the Spectral staggered patch scheme respectively for $(N, n) = (6, 6), (6, 10), (10, 6)$.

- There is one macroscale mode for the stagnant water (cluster 1) irrespective of N, n .
- There are two macroscale modes for the decelerating uniform mean flow (cluster 2) irrespective of N, n .
- The total number of macroscale wave modes (in clusters 3,4), is $2(N^2/4 - 1)$, which does not depend on the number of sub-patch micro-grid intervals n .

Figure 3.2.3. Spectral staggered patch scheme ($N = 6, n = 6$) eigenvalues for general linear wave with *no drag and nonzero viscous diffusion* ($c_D = 0, c_V \neq 0$). The macroscale eigenvalues λ_p^{NE1} agree with the macroscale eigenvalues $\lambda_{m\delta}^A$ of the fine-grid full-domain microscale model.



- The number of macroscale vortex modes (in cluster 5), is $N^2/4 - 1$, which does not depend on n .
- The total number of microscale sub-patch wave modes (in clusters 6, 7), is $(N^2/2)(3n^2/4 - n - 1)$.
- The number of microscale sub-patch vortex modes (in cluster 8), is $(N^2/4)(3n^2/4 - 2n + 1)$.
- The total number of macroscale modes is $3N^2/4$, which is the same as the number of patches in the staggered patch grid with $N \times N$ macro-grid intervals (each of the $(N/2)^2$ macro-cells contains three patches).
- The total number of microscale sub-patch modes is $(N^2/4)(9n^2/4 - 4n - 1)$.
- The total number of staggered patch scheme modes (number of eigenvalues λ_p^N) is $n_p^I = (N^2/4)(9n^2/4 - 4n + 2)$, which is same as the number

Figure 3.2.4. Spectral staggered patch scheme ($N = 6, n = 6$) eigenvalues for general linear wave with *nonzero drag and no viscous diffusion* ($c_D \neq 0, c_V = 0$). The macroscale eigenvalues λ_p^{NE1} agree with the macroscale eigenvalues $\lambda_{m\delta}^A$ of the fine-grid full-domain microscale model.

- (1) λ_p^{NE1} [531](9k)
- (2) $\lambda_{m\delta}^A$ [27](9k)
- × (3) $\lambda_{m\Delta}^A$ [27](9k)

(1) Patch scheme

Scheme : Spectral
Grid : huvx-n2t0
N : 6
r : 0.1

(2)

n : 180

(3)

$\delta : 2\pi/6$

(1, 3)

n : 6

(1, 2)

$\delta : 2\pi/180$

Common parameters

Model: gLnrWve
Domain L : 2π
 $c_D, c_V : 10^{-6}, 0$

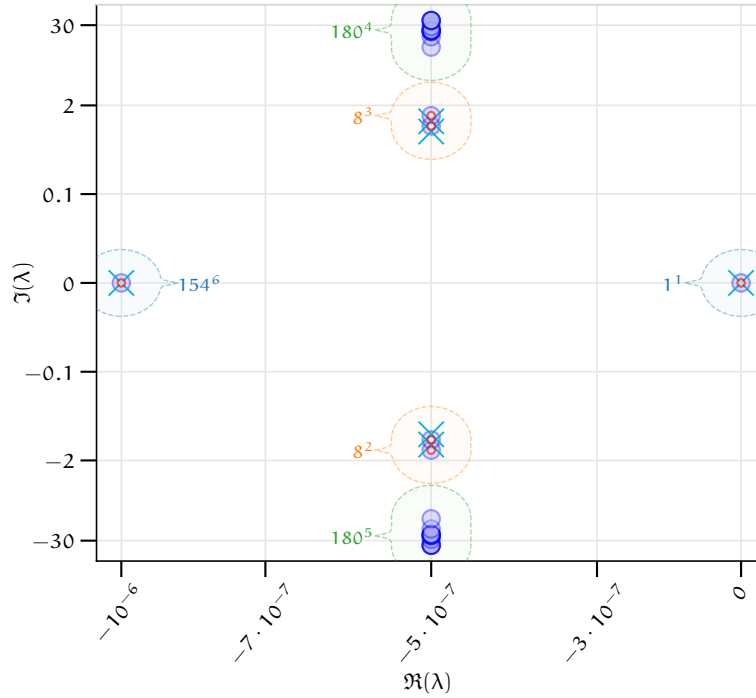


Figure 3.2.5. Spectral staggered patch scheme ($N = 6, n = 6$) eigenvalues for general linear wave with *no drag and no viscous diffusion* (ideal wave, $c_D = c_V = 0$). The macroscale eigenvalues λ_p^{NE1} agree with the macroscale eigenvalues $\lambda_{m\delta}^A$ of the fine-grid full-domain microscale model.

- (1) λ_p^{NE1} [531](9k)
- (2) $\lambda_{m\delta}^A$ [27](9k)
- × (3) $\lambda_{m\Delta}^A$ [27](9k)

(1) Patch scheme

Scheme : Spectral
Grid : huvx-n2t0
N : 6
r : 0.1

(2)

n : 180

(3)

$\delta : 2\pi/6$

(1, 3)

n : 6

(1, 2)

$\delta : 2\pi/180$

Common parameters

Model: gLnrWve
Domain L : 2π
 $c_D, c_V : 0, 0$

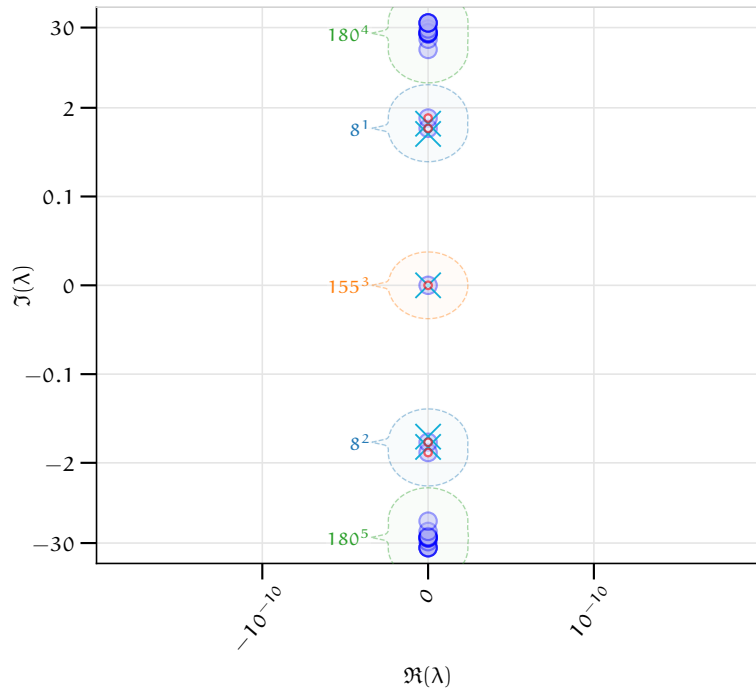


Figure 3.2.6. Spectral staggered patch scheme ($N = 6, n = 10$) eigenvalues for general linear wave with *drag and viscous diffusion*. The macroscale eigenvalues λ_p^{NE1} agree with the macroscale eigenvalues $\lambda_{m\delta}^A$ of the fine-grid full-domain microscale model.

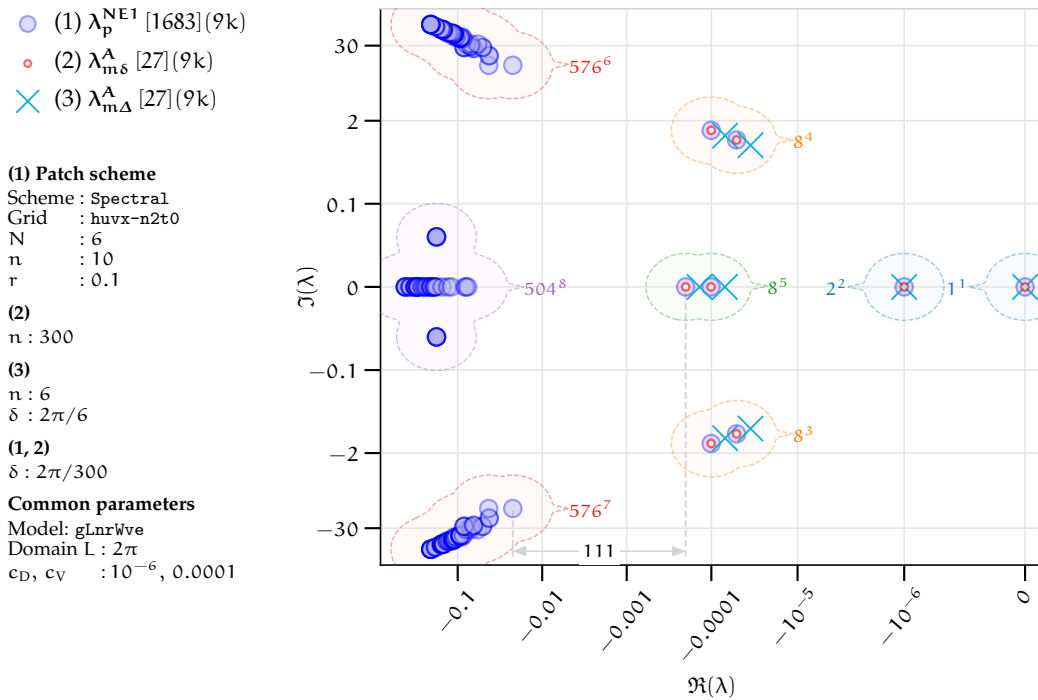
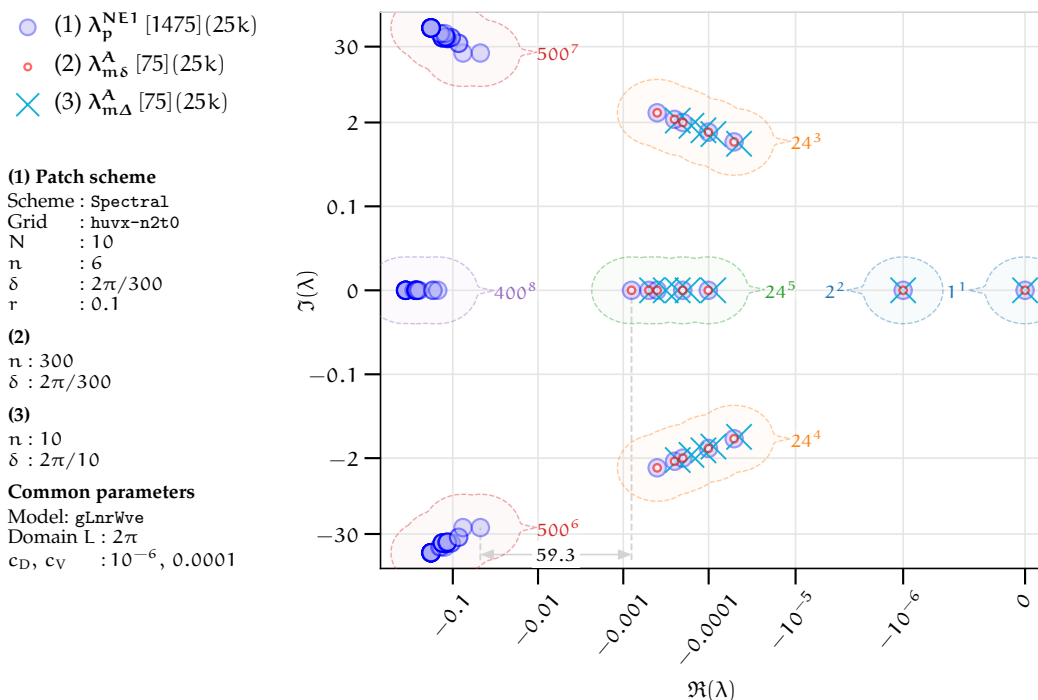


Figure 3.2.7. Spectral staggered patch scheme ($N = 10, n = 6$) eigenvalues for general linear wave with *drag and viscous diffusion*. The macroscale eigenvalues λ_p^{NE1} agree with the macroscale eigenvalues $\lambda_{m\delta}^A$ of the fine-grid full-domain microscale model.



of patch interior nodes (2.1.7) in p. 21 of §2.1.2.

The preceding paragraph explains the number of eigenvalues λ_p^N of the *full-size* numerical Jacobian of the staggered patch scheme (§3.2.5), this paragraph explains the number of eigenvalues λ_p^{NE1} of the *one-cell* analytic Jacobian of the staggered patch scheme (§3.2.3). The total number of eigenvalues λ_p^{NE1} of the numerically evaluated one-cell Jacobian of a staggered patch scheme for one wavenumber (k_x, k_y) , is $n_p^i = (9n^2/4 - 4n + 2)$. The number of eigenvalues n_p^i is same as the total number of state variables, and the number of patch interior nodes (3.2.11) in p. 59 of §3.2.3, for a one-cell analytic description of a staggered patch scheme for one macroscale wavenumber (k_x, k_y) . For example, as in p. 59 of §3.2.3, for $n = 6, 10, 14$ sub-patch micro-grid intervals, $n_p^i = 59, 187, 387$ respectively.

The numerical eigenvalues λ_p^N correspond to all the macroscale wavenumbers (k_x, k_y) resolved by a patch grid. But the analytic one-cell eigenvalues λ_p^{NE1} correspond to only one macroscale wavenumber. For how many macroscale wavenumbers, one must compute the one-cell eigenvalues λ_p^{NE1} towards one-to-one comparison with the full-size numerical eigenvalues λ_p^N ? A staggered patch grid with 6×6 macro-grid intervals $N = 6$ (with each of the $(N/2)^2$ macro-cells containing three patches), resolves a total of $(N/2)^2 = 9$ macroscale modes with macroscale wavenumbers $k_x, k_y \in \{-1, 0, 1\}$. To compare the one-cell eigenvalues λ_p^{NE1} with the eigenvalues λ_p^N of the numerical Jacobian for a staggered patch scheme on a patch grid with 6×6 macro-grid intervals, we numerically evaluate the one-cell Jacobian of a staggered patch scheme for all the nine macroscale wavenumbers. Hence the total number of one-cell eigenvalues λ_p^{NE1} is $59 \times 9 = 531$, matching the total number of numerical eigenvalues λ_p^N . The number of wavenumbers for which the one-cell eigenvalues λ_p^{NE1} are computed, is indicated in the eigenvalue plots next to the legend entry for λ_p^{NE1} . For example, the “(9k)” in Fig. 3.2.2 indicates the nine wavenumbers (k_x, k_y) (i.e., $k_x, k_y \in \{-1, 0, 1\}$) and the “(25k)” in Fig. 3.2.7 indicates the 25 wavenumbers (i.e., $k_x, k_y \in \{-2, -1, 0, 1, 2\}$).

Similar to the case of the λ_p^{NE1} in the preceding paragraph, in contrast to plotting all the eigenvalues of the coarse- and fine-grid full-domain microscale model, such as the numerical eigenvalues $\lambda_{m\Delta}^N, \lambda_{m\delta}^N$ in Figs. 3.2.1 and 3.2.2, all other eigenvalue plots plot the analytic full-domain eigenvalues $\lambda_{m\delta}^A, \lambda_{m\Delta}^A$ only for the macroscale wavenumbers. For example, for a patch grid with 6×6 macro-grid intervals, the analytic expression (3.2.7) is evaluated only for the $(N/2)^2 = 9$ macroscale wavenumbers (i.e., $k_x, k_y \in \{-1, 0, 1\}$). For each wavenumber (k_x, k_y) , expression (3.2.7) gives three eigenvalues, one real and a pair of complex conjugate eigenvalues. Hence

the total number of macroscale eigenvalues $\lambda_{m\delta}^A$ is $3 \times 9 = 27$, matching the total number of macroscale staggered patch scheme eigenvalues λ_p^N and λ_p^{NE1} in Fig. 3.2.6 (the “(9k)” next to the legend entry for $\lambda_{m\delta}^A$, $\lambda_{m\Delta}^A$ indicates the nine wavenumbers).

Comparing the number of eigenvalues in the complex plane plots of the Spectral staggered patch scheme for different sizes of the patch grid (e.g., Figs. 3.2.2, 3.2.6 and 3.2.7 respectively for $(N, n) = (6, 6), (6, 10), (10, 6)$), reveal the following.

1. Keeping the domain size L , patch scale ratio r , and the number of sub-patch micro-grid intervals n the same, *increasing the number of macro-grid intervals N of a patch grid increases both the macroscale modes and the microscale modes.* For example,
 - a patch grid with 6×6 macro-grid intervals, computes $3N^2/4 = 27$ macroscale modes and $(N^2/4)(9n^2/4 - 4n - 1) = 504$ microscale modes (clusters 1–5 and clusters 6–8 in Fig. 3.2.2), whereas
 - a patch grid with 10×10 macro-grid intervals, computes 75 macroscale modes and 1400 microscale modes (clusters 1–5 and clusters 6–8 in Fig. 3.2.7).
2. On the other hand, keeping L , r , and N the same, *increasing the number of sub-patch micro-grid intervals n of a patch grid increases only the microscale modes without any change in the number of macroscale modes.* For example,
 - a patch grid containing 6×6 sub-patch micro-grid intervals in each patch, computes 504 microscale modes (clusters 6–8 in Fig. 3.2.2), whereas
 - a patch grid containing 10×10 sub-patch micro-grid intervals in each patch, computes 1656 microscale modes (clusters 6–8 in Fig. 3.2.7), but
 - there are 27 macroscale modes in both cases.

As the comparison in Fig. 3.2.2 shows, the staggered patch scheme eigenvalues comprise the microscale eigenvalues on the left and the macroscale eigenvalues on the right but not the intermediate scales. To quantify this *spectral gap* in the scales, we define the *spectral gap factor* as the ratio of the maximum real part of the microscale eigenvalues (on the left) to the minimum real part of the macroscale eigenvalues (on the right). All the complex plane eigenvalue plots with arcsinh scaling indicate the spectral

gap by a grey arrow annotated with the spectral gap factor. When there is no gap, that is when the microscale eigenvalues and macroscale eigenvalues overlap, to quantify the overlap, we compute the spectral gap as negative of the ratio of the minimum real part of the macroscale eigenvalues to the maximum real part of the microscale eigenvalues.

Keeping the domain size L , patch scale ratio r , and number of sub-patch micro-grid intervals n the same, increasing the number of macro-grid intervals N resolves more macroscale modes with progressively higher wavenumbers (e.g., Figs. 3.2.2 and 3.2.7). Hence, *increasing N for the same patch scale ratio r , leads to decreasing spectral gap between the microscale and macroscale eigenvalues*, approaching the full-domain microscale model. On the other hand, keeping L , r , and N the same, increasing the number of sub-patch micro-grid intervals n increases the spectral gap (e.g., Figs. 3.2.2 and 3.2.6).

The clusters 4–6 in Fig. 3.2.1 and the clusters 6–8 in Fig. 3.2.2 correspond to sub-patch microscale modes (e.g., Figs. 3.2.17 and 3.2.18 show such modes). All the five staggered patch schemes have such sub-patch microscale modes. When the viscous diffusion is nonzero, the large negative real parts of these microscale modes mean that they decay rapidly and only the accurate macroscale modes dominate the long time solution, which are of primary interest for accurate macroscale modelling. The spectral gap (indicated by a grey arrow) in the eigenvalue plots, quantifies how rapidly the microscale modes are dissipated relative to macroscale dynamics. That is, *the spectral gap quantifies how rapidly the patch scheme macroscale solution emerges from the underlying microscale dynamics*.

Our objective is to design the staggered patch schemes to resolve the macroscale physics as accurately as possible compared to the corresponding fine-grid full-domain microscale model. Hence, we define a staggered patch scheme to be *accurate* when the macroscale eigenvalues (e.g., $\lambda_p^N, \lambda_p^{NE1}$) of the staggered patch schemes are close to the macroscale eigenvalues (e.g., $\lambda_{m\delta}^\Lambda$) of the corresponding fine-grid full-domain microscale model with the same grid interval as the sub-patch micro-grid interval.

Figures 3.2.2 to 3.2.7 present the eigenvalue plots for the Spectral staggered patch schemes, for different dissipation parameters ($c_D \in \{0, 10^{-6}\}$, $c_V \in \{0, 10^{-4}\}$), and for different sizes of the patch grid ($N \in \{6, 10\}$, $n \in \{6, 10\}$) with the patch scale ratio $r = 0.1$. The macroscale eigenvalues λ_p^{NE1} (large blue circles) of the Spectral staggered patch scheme agree exactly (within numerical roundoff errors) with the corresponding macroscale eigenvalues $\lambda_{m\delta}^\Lambda$ (small red circles) of the fine-grid full-domain microscale model. That is, *the Spectral staggered patch scheme accurately resolves the macroscale modes* of the general linear wave, for these combinations of the

parameters (§3.6 shows the accuracy for larger range of parameters).

Similar to the Spectral staggered patch scheme, the accuracy of the four polynomial patch schemes (Square-p2, Square-p4, Square-p6, and Square-p8) do not depend on the physical parameters ($c_D \in \{0, 10^{-6}\}$, $c_V \in \{0, 10^{-4}\}$) or the number of sub-patch micro-grid intervals n ; for brevity we omit the corresponding plots. However, unlike the Spectral staggered patch scheme which is exact, the polynomial patch schemes do have macroscale errors. Yet, the accuracy of the polynomial staggered patch schemes increases with increasing the macro-grid intervals N . For example, comparing Figs. 3.2.8 and 3.2.9 shows that for $N = 10$ (Fig. 3.2.9) the macroscale eigenvalues λ_p^{NE1} (large blue circles), with small real parts, agree more closely with the corresponding macroscale eigenvalues $\lambda_{m\delta}^A$ (small red circles), compared to the macroscale eigenvalues for $N = 6$ (Fig. 3.2.8). Section 3.6 on the consistency of the staggered patch schemes, quantifies how the errors decrease with increasing N .

Each patch is effectively one node in the macroscale grid. Hence, comparing the macroscale eigenvalues λ_p^{NE1} of the staggered patch scheme with the macroscale eigenvalues $\lambda_{m\Delta}^A$ of the coarse-grid full-domain microscale model (with same grid interval as the inter-patch spacing Δ) reveals how effective a staggered patch scheme is, as a multiscale scheme coupling across the scales. Figs. 3.2.9 to 3.2.12 plot the eigenvalues for the polynomial staggered patch schemes (§2.2.2) Square-p2, Square-p4, Square-p6, and Square-p8, on a patch grid with 10×10 macro-grid intervals ($N = 10$) and each patch containing 6×6 sub-patch micro-grid intervals ($n = 6$) and patch scale ratio $r = 0.1$. Figs. 3.2.9 to 3.2.12 show that increasing polynomial interpolation orders $p = 2, 4, 6, 8$ increases the accuracy of the polynomial staggered patch schemes due to the increasing interpolation accuracy. That is, the discrepancy, between the macroscale eigenvalues λ_p^{NE1} (large blue circles) of the patch schemes and the corresponding eigenvalues $\lambda_{m\delta}^A$ (small red circles) of the fine-grid full-domain microscale model, decreases with increasing interpolation order p . As the interpolation accuracy increases with increasing p , the macroscale eigenvalues λ_p^{NE1} of the patch scheme shift from being close to the macroscale eigenvalues $\lambda_{m\Delta}^A$ (coarse-grid) to being close to the macroscale eigenvalues $\lambda_{m\delta}^A$ (fine-grid) of the full-domain microscale model. Thus, depending upon the accuracy of the patch coupling interpolation, *the accuracy of the staggered patch schemes lies between the accuracy of the coarse- and fine-grid full-domain microscale model (two extremes).*

Figs. 3.2.13 to 3.2.18 plot one example eigenvector (mode shape) for each of eigenvalue clusters 1, 2, 3, 5, 6, 8 in Fig. 3.2.12 for the Square-p8 staggered patch scheme (with $N = 10$, $n = 6$, $r = 0.1$). These eigenvectors are computed for the numerical Jacobian (§3.2.5) of the Square-p8 staggered patch

Figure 3.2.8. Square-p2 staggered patch scheme ($N = 6, n = 6$) eigenvalues for general linear wave with *drag and viscous diffusion*. Low accuracy interpolation leads to poor patch scheme accuracy; that is, large discrepancy between λ_p^{NE1} (large blue circles) and $\lambda_{m\delta}^A$ (small red circles).

- (1) λ_p^{NE1} [531](9k)
- (2) $\lambda_{m\delta}^A$ [27](9k)
- × (3) $\lambda_{m\Delta}^A$ [27](9k)

(1) Patch scheme

Scheme : Square-p2
 Grid : huvx-n2t0
 N : 6
 r : 0.1

(2)
 n : 180

(3)
 $\delta : 2\pi/6$

(1, 3)
 n : 6

(1, 2)
 $\delta : 2\pi/180$

Common parameters

Model: gLnrWve
 Domain L : 2π
 $c_D, c_V : 10^{-6}, 0.0001$

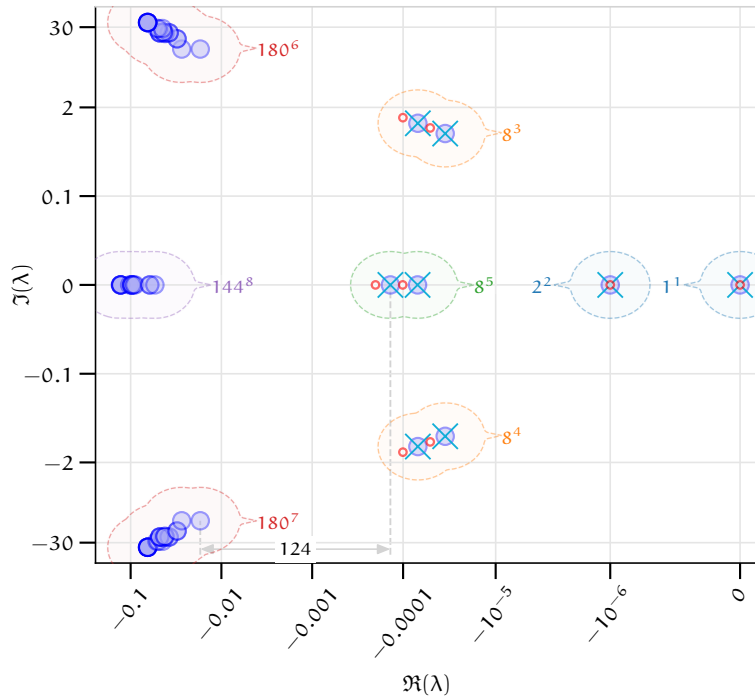


Figure 3.2.9. Square-p2 staggered patch scheme ($N = 10, n = 6$) eigenvalues for general linear wave with *drag and viscous diffusion*. The patch scheme accuracy with $N = 10$ is higher compared to Fig. 3.2.8 for $N = 6$; that is, smaller discrepancy between λ_p^{NE1} and $\lambda_{m\delta}^A$.

- (1) λ_p^{NE1} [1475](25k)
- (2) $\lambda_{m\delta}^A$ [75](25k)
- × (3) $\lambda_{m\Delta}^A$ [75](25k)

(1) Patch scheme

Scheme : Square-p2
 Grid : huvx-n2t0
 N : 10
 n : 6
 $\delta : 2\pi/300$
 r : 0.1

(2)
 n : 300

(3)
 $\delta : 2\pi/10$

(1, 3)
 n : 10

(1, 2)
 $\delta : 2\pi/10$

Common parameters

Model: gLnrWve
 Domain L : 2π
 $c_D, c_V : 10^{-6}, 0.0001$

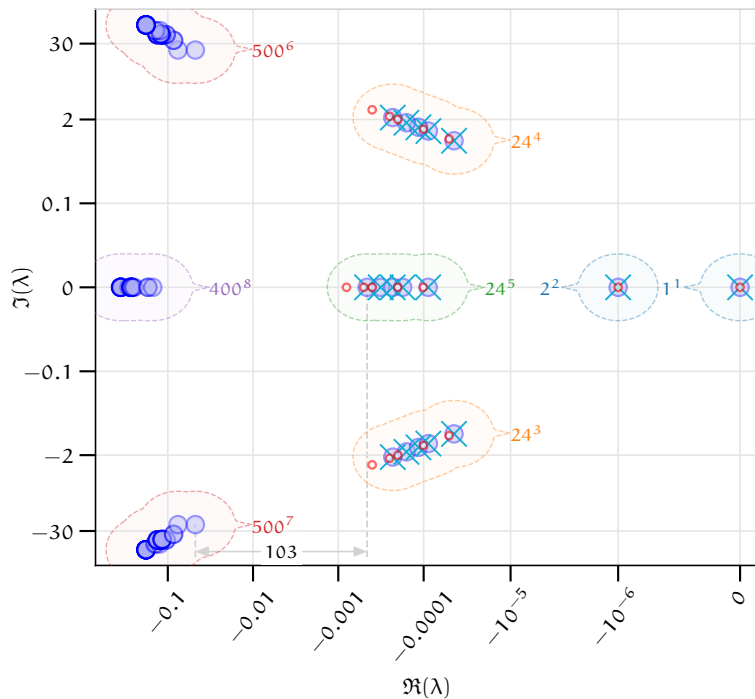


Figure 3.2.10. Square-p4 staggered patch scheme ($N = 10, n = 6$) eigenvalues for general linear wave with *drag and viscous diffusion*. The fourth order polynomial interpolation leads to higher patch scheme accuracy compared to Fig. 3.2.9 for Square-p2, smaller discrepancy between λ_p^{NE1} and $\lambda_{m\delta}^A$.

- (1) λ_p^{NE1} [1475](25k)
- (2) $\lambda_{m\delta}^A$ [75](25k)
- × (3) $\lambda_{m\Delta}^A$ [75](25k)

(1) Patch scheme

Scheme : Square-p4
 Grid : huvx-n2t0
 N : 10
 n : 6
 δ : $2\pi/300$
 r : 0.1

(2)
 n : 300
 δ : $2\pi/300$

(3)
 n : 10
 δ : $2\pi/10$

Common parameters

Model: gLnrWve
 Domain L : 2π
 c_D, c_V : $10^{-6}, 0.0001$

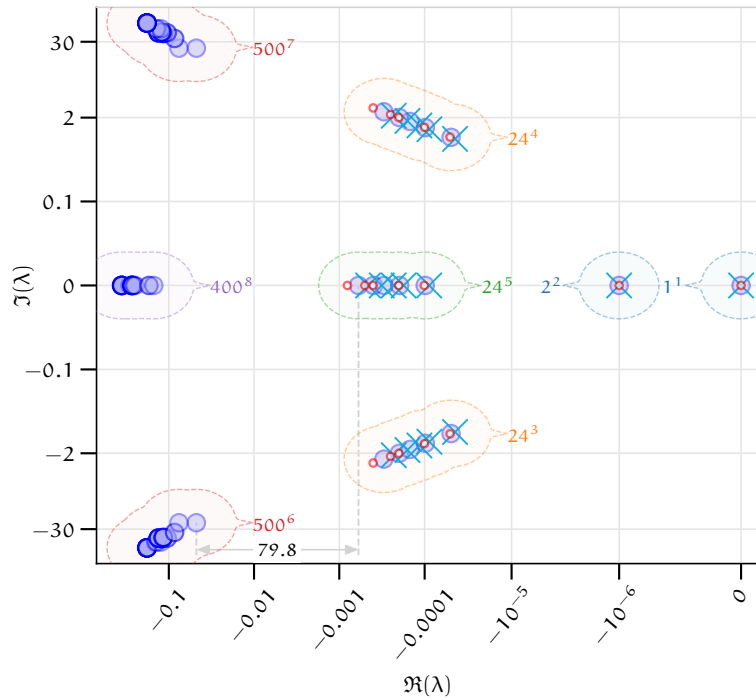


Figure 3.2.11. Square-p6 staggered patch scheme ($N = 10, n = 6$) eigenvalues for general linear wave with *drag and viscous diffusion*. The sixth order polynomial interpolation leads to higher patch scheme accuracy compared to Fig. 3.2.10 for Square-p4, smaller discrepancy between λ_p^{NE1} and $\lambda_{m\delta}^A$.

- (1) λ_p^{NE1} [1475](25k)
- (2) $\lambda_{m\delta}^A$ [75](25k)
- × (3) $\lambda_{m\Delta}^A$ [75](25k)

(1) Patch scheme

Scheme : Square-p6
 Grid : huvx-n2t0
 N : 10
 n : 6
 δ : $2\pi/300$
 r : 0.1

(2)
 n : 300
 δ : $2\pi/300$

(3)
 n : 10
 δ : $2\pi/10$

Common parameters

Model: gLnrWve
 Domain L : 2π
 c_D, c_V : $10^{-6}, 0.0001$

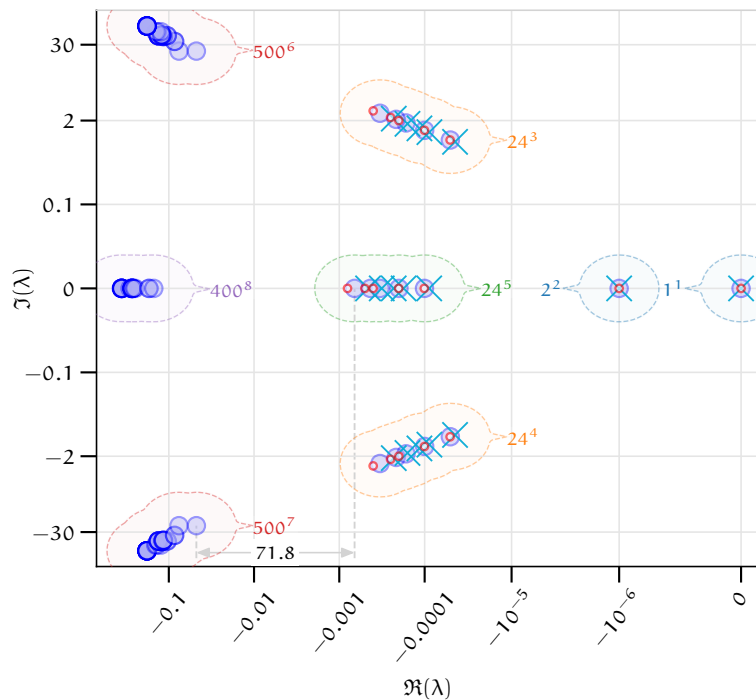


Figure 3.2.12. Square-p8 staggered patch scheme ($N = 10, n = 6$) eigenvalues for general linear wave with *drag and viscous diffusion*. The eighth order polynomial interpolation leads to higher patch scheme accuracy compared to Fig. 3.2.11 for Square-p6, smaller discrepancy between λ_p^{NE1} and $\lambda_{m\delta}^A$.

- (1) λ_p^{NE1} [1475](25k)
- (2) $\lambda_{m\delta}^A$ [75](25k)
- × (3) $\lambda_{m\Delta}^A$ [75](25k)

(1) Patch scheme

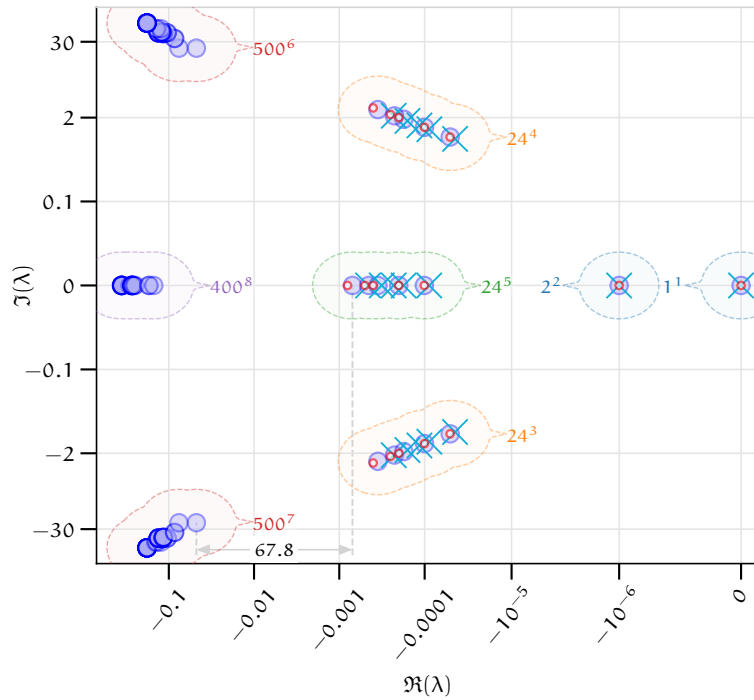
Scheme : Square-p8
 Grid : huvx-n2t0
 N : 10
 n : 6
 δ : $2\pi/300$
 r : 0.1

(2)
 n : 300
 δ : $2\pi/300$

(3)
 n : 10
 δ : $2\pi/10$

Common parameters

Model: gLnrWve
 Domain L : 2π
 c_D, c_V : $10^{-6}, 0.0001$



scheme. The qualitative shapes of the eigenvectors in Figs. 3.2.13 to 3.2.18 are the same for the Spectral (§2.2.1) and polynomial (§2.2.2) staggered patch schemes Square-p2, Square-p4, Square-p6, and Square-p8.

Figure 3.2.13. Eigenvector for eigenvalue $\lambda_p^N = 0+0i$ (cluster 1 in Fig. 3.2.12), for Square-p8 staggered patch scheme with $N = 10$, $n = 6$, $r = 0.1$. The macroscale mode of stagnant water with uniform height h and no flow (i.e., $\mathbf{u} = \mathbf{v} = 0$).

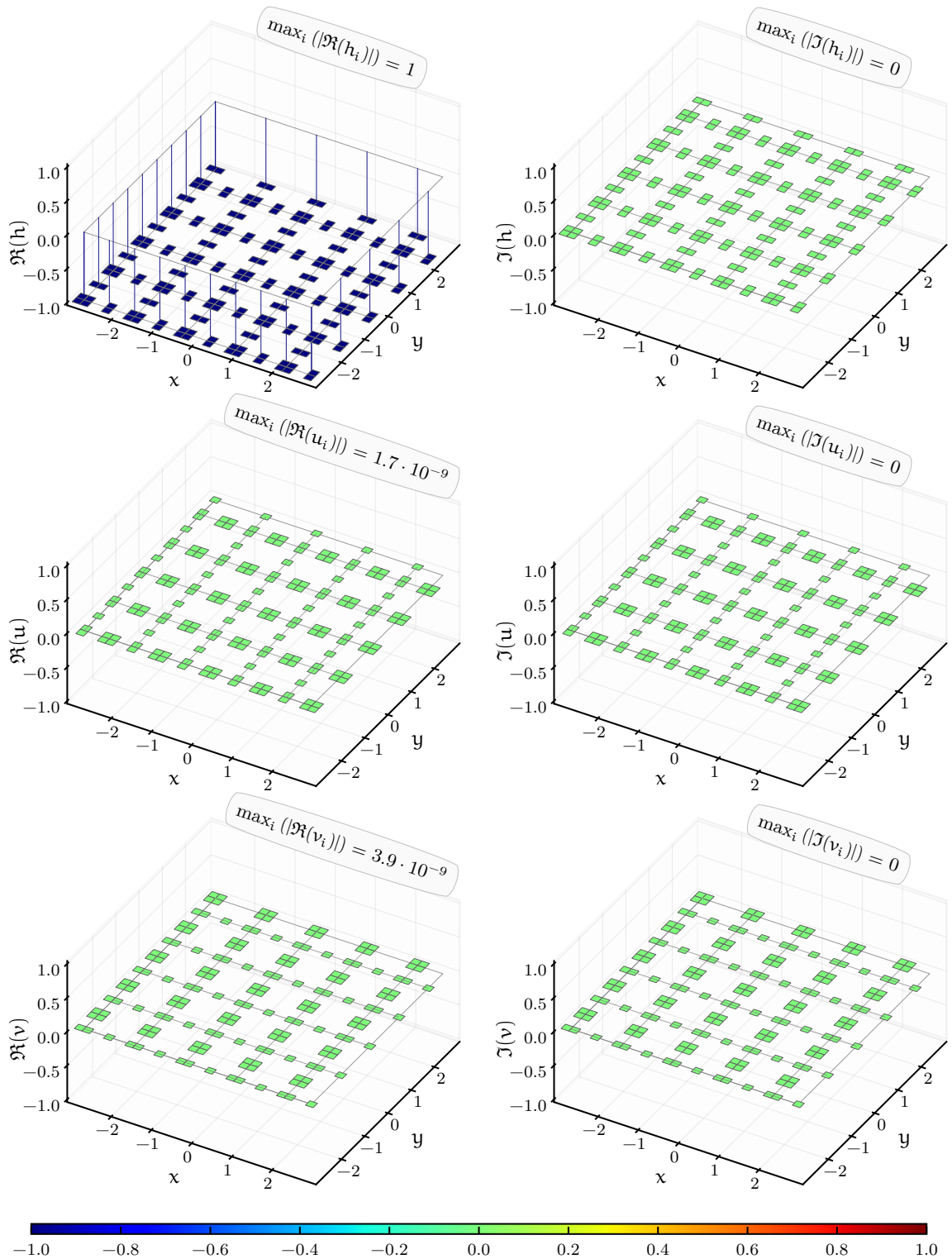


Figure 3.2.14. Eigenvector for eigenvalue $\lambda_p^N = -10^{-6} + 0i$ (cluster 2 in Fig. 3.2.12), for Square-p8 staggered patch scheme with $N = 10$, $n = 6$, $r = 0.1$. One of the two macroscale modes of *decelerating* (negative real part λ_p^N) *uniform mean flow* (spatially constant velocities u and v).

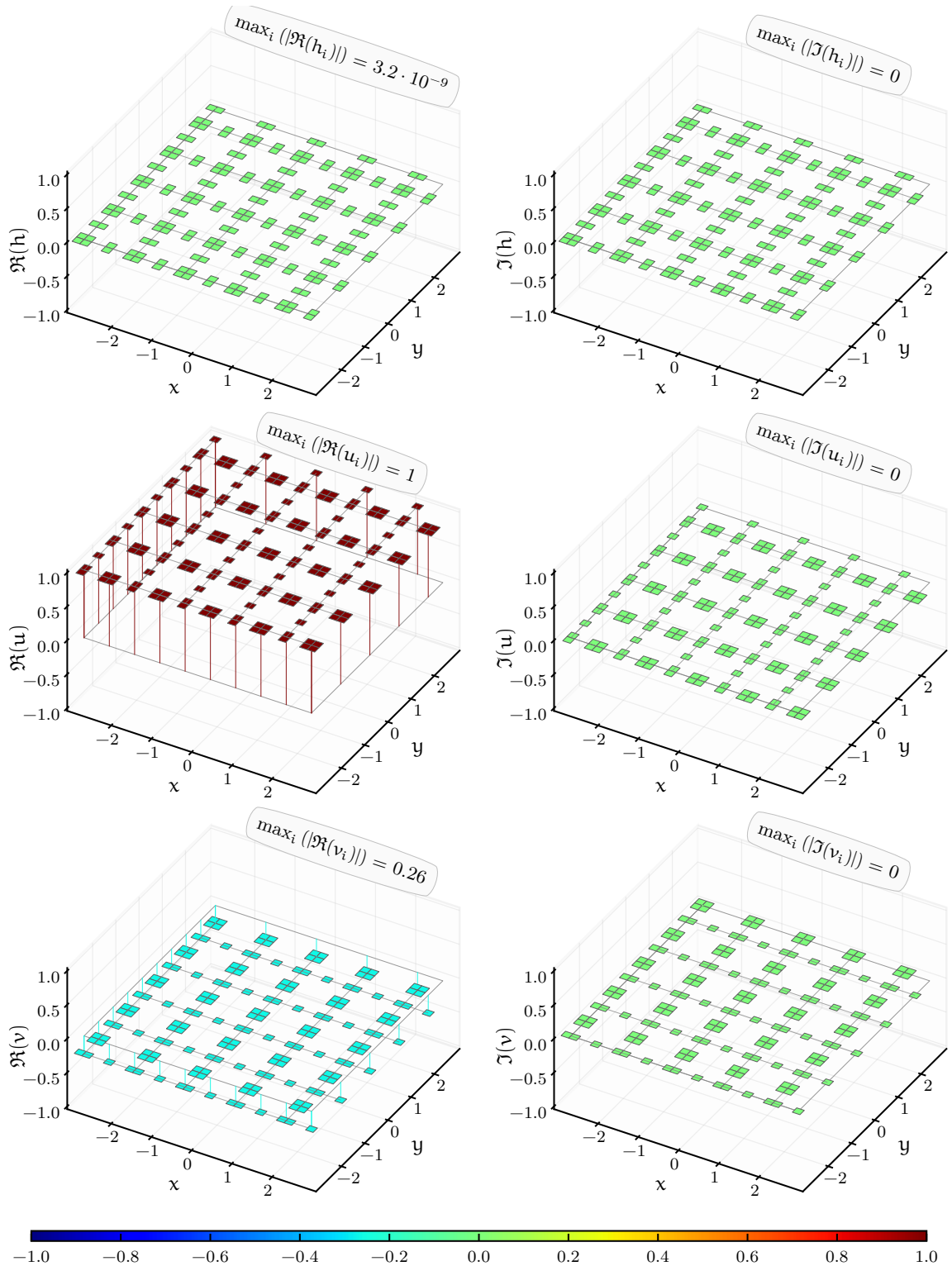


Figure 3.2.15. Eigenvector for eigenvalue $\lambda_p^N = -5 \cdot 10^{-5} + 1 i$ (cluster 3 in Fig. 3.2.12), for Square-p8 staggered patch scheme with $N = 10$, $n = 6$, $r = 0.1$. A macroscale wave mode (only h and u are of significant magnitude) with exchange of potential (h) and kinetic (u) energy.

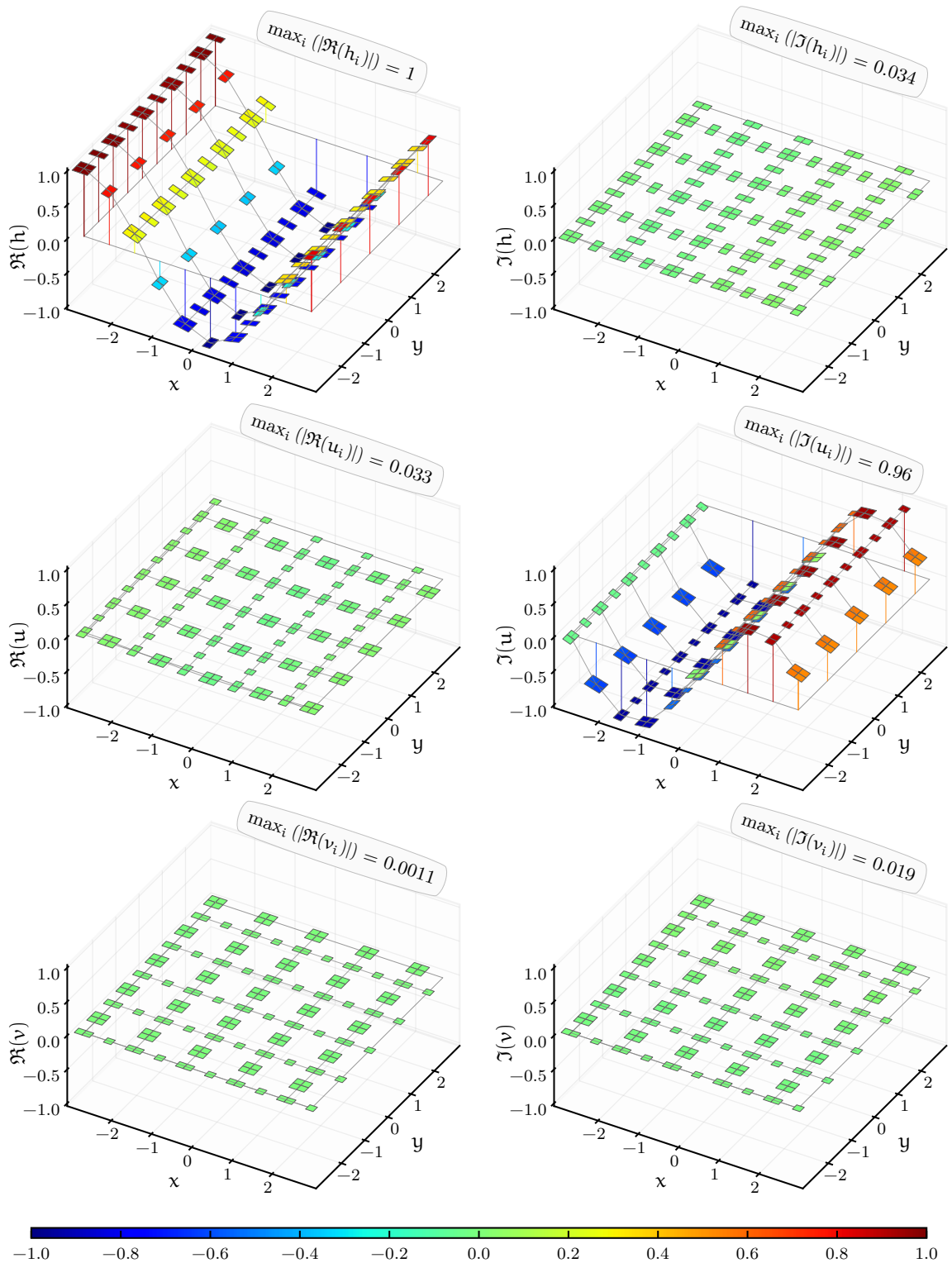


Figure 3.2.16. Eigenvector for eigenvalue $\lambda_p^N = -0.0001 + 0i$ (cluster 5 in Fig. 3.2.12), for Square-p8 staggered patch scheme with $N = 10$, $n = 6$, $r = 0.1$. A macroscale vortex mode (only u and v are of significant magnitude).

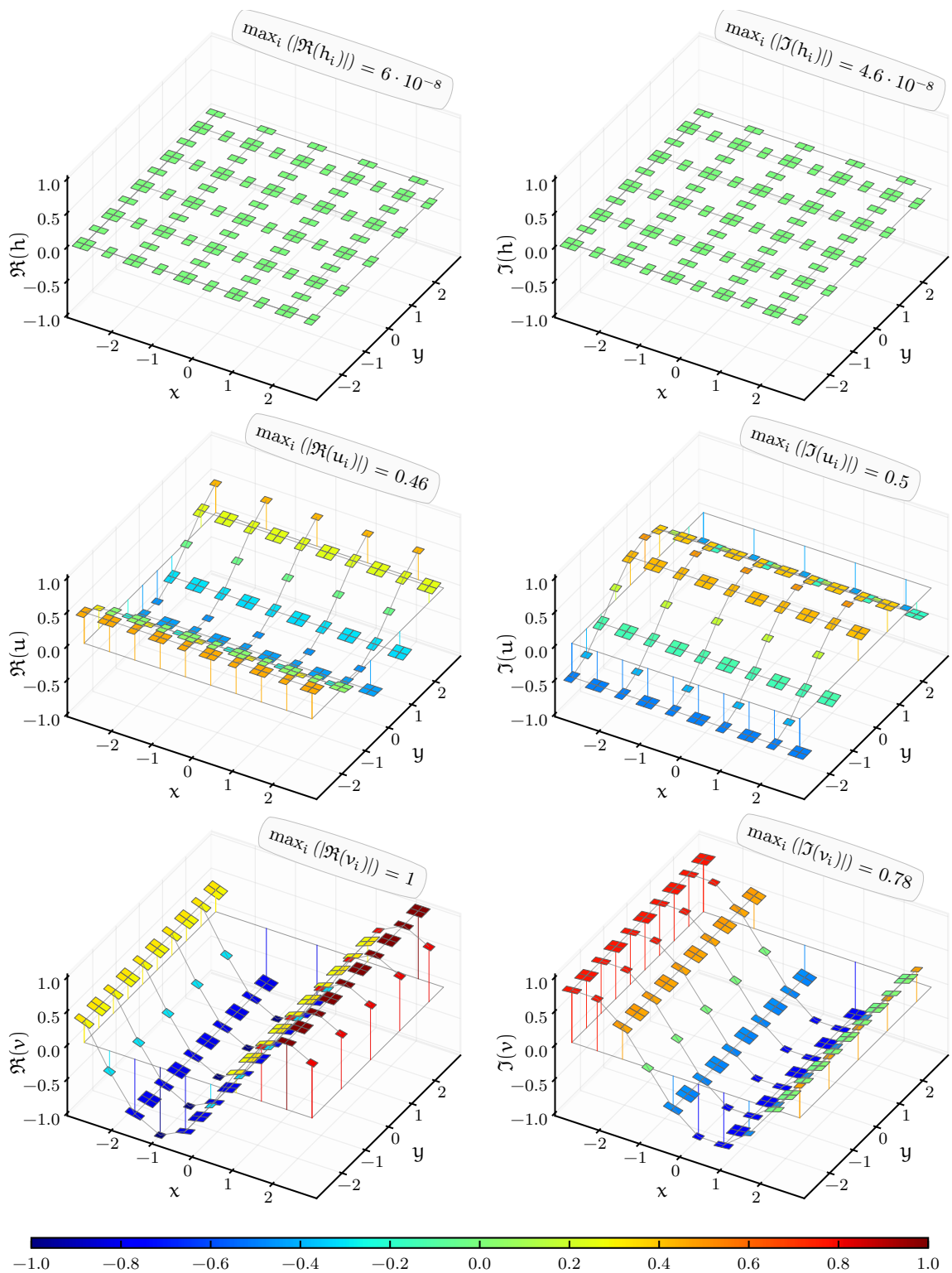


Figure 3.2.17. Eigenvector for eigenvalue $\lambda_p^N = -0.085 + 33.76i$ (cluster 6 in Fig. 3.2.12), for Square-p8 staggered patch scheme with $N = 10$, $n = 6$, $r = 0.1$. A sub-patch microscale wave mode (h , u , and v are of significant magnitude) with exchange of potential energy (h) and kinetic energy (u , v).

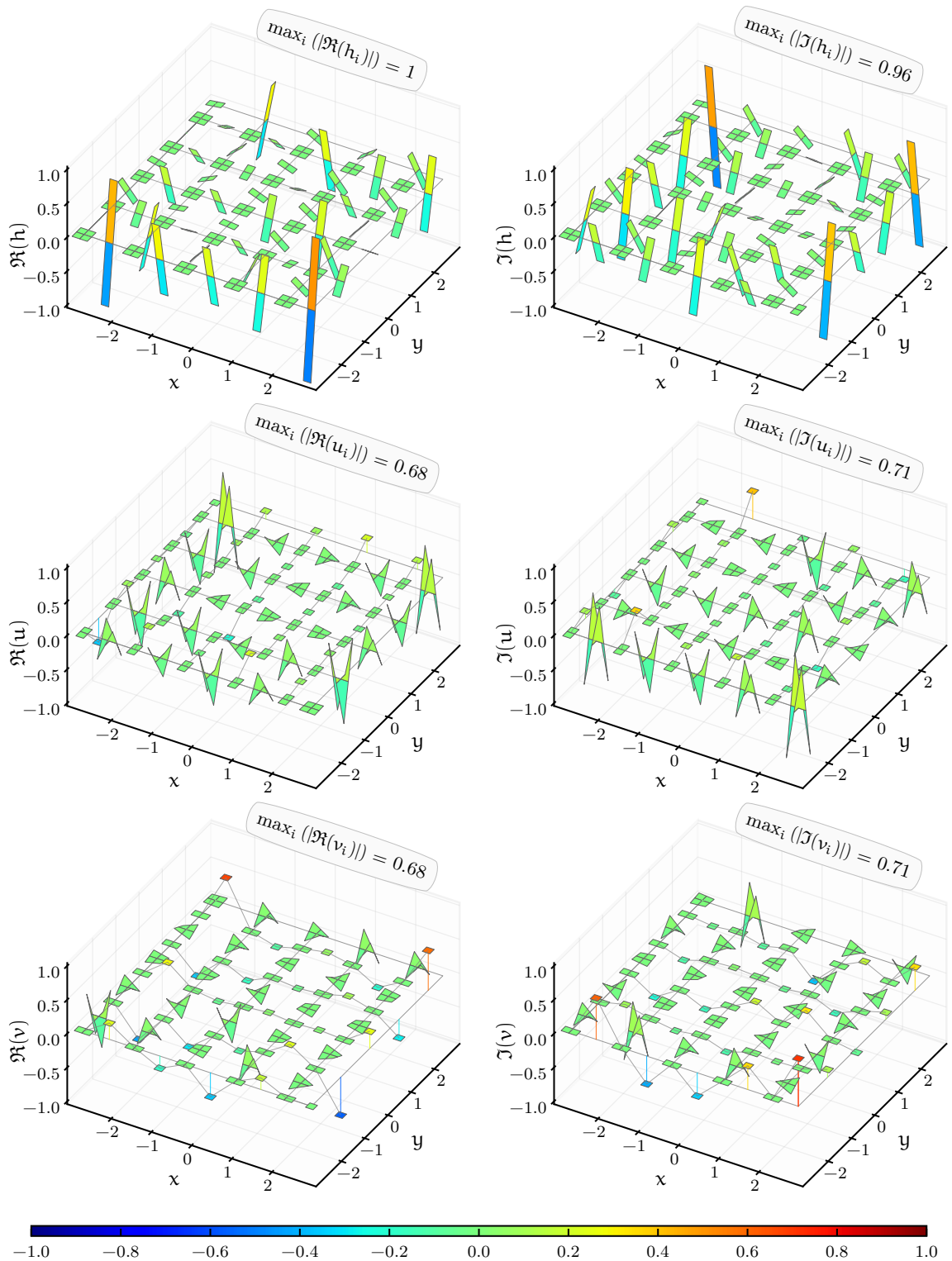
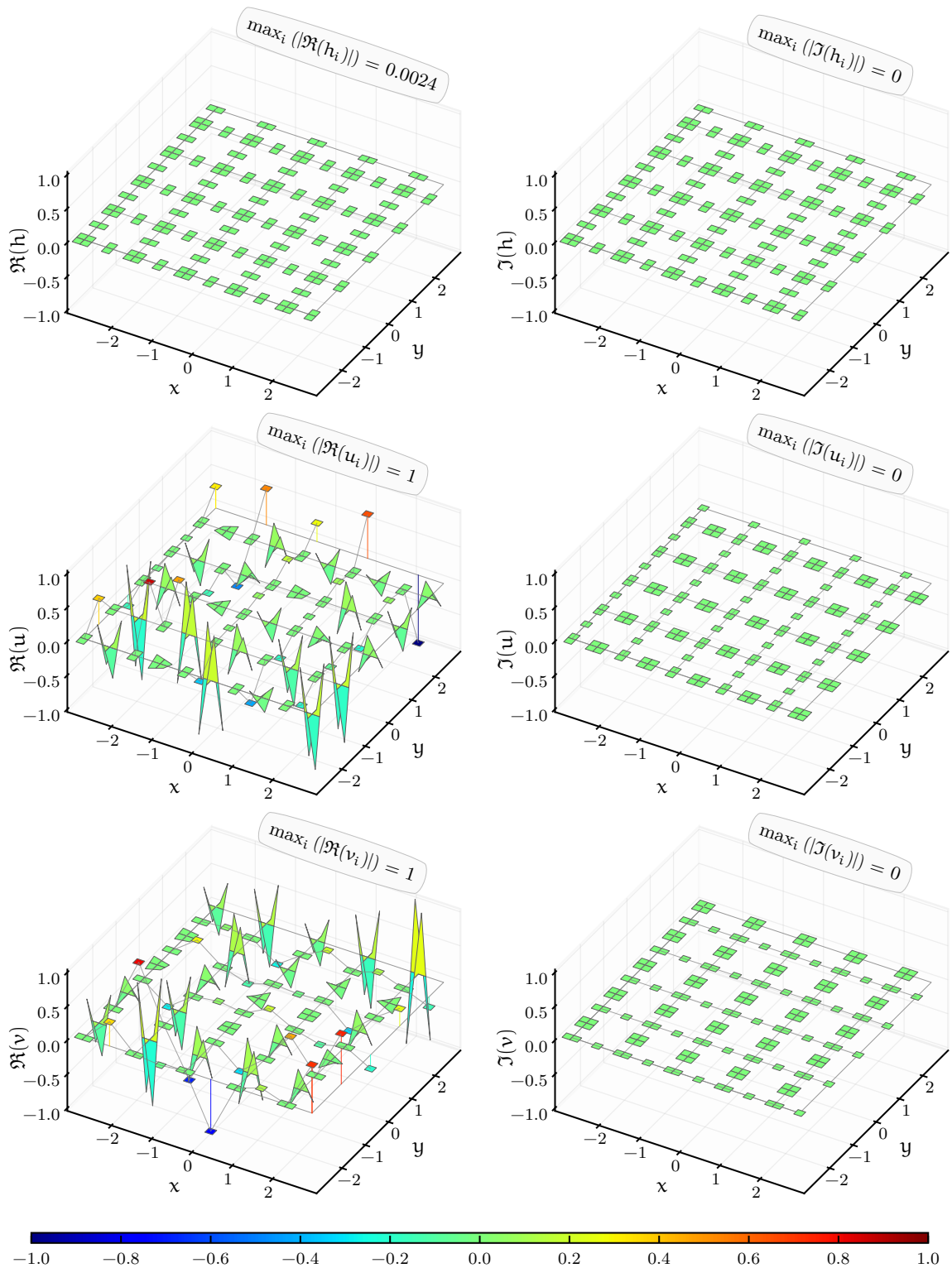


Figure 3.2.18. Eigenvector for eigenvalue $\lambda_p^N = -0.17 + 0i$ (cluster 8 in Fig. 3.2.12), for Square-p8 staggered patch scheme with $N = 10$, $n = 6$, $r = 0.1$. A sub-patch microscale vortex mode (only u and v are of significant magnitude).



3.3 A method of wavenumber-wise scale separation for patch scheme eigenvalues

[Section 3.6](#) quantitatively establishes the accuracy of the patch schemes by comparing the eigenvalues of the patch schemes and that of the full-domain microscale model corresponding to three specific macroscale wavenumbers $(k_x, k_y) \in \{(1, 0), (1, 1), (2, 1)\}$. [Section 3.6](#) shows that the staggered patch schemes are consistent with the given microscale model based on the eigenvalue error defined for these three wavenumbers. Similarly, quantitative study of the patch schemes, for the sensitivity to numerical roundoff errors ([§3.4](#)) and the stability ([§3.5](#)) requires separation of microscale and macroscale patch scheme eigenvalues for specific macroscale wavenumbers. This subsection explains a heuristic method we name as *method of wavenumber-wise scale separation*, that classifies the eigenvalues wavenumber-wise and separates into microscale and macroscale patch scheme eigenvalues. This method is robust without any assumption about eigenvalue structure or dispersion relation and is heuristic only in the sense that the wavenumber-eigenvalue association is established solely from the eigenvalues without using the information from the eigenvectors.

The symbols λ_{pM}^{NE1} and λ_{pM}^N denote the analytic and numerical macroscale eigenvalues of a patch scheme respectively. Similarly, the symbols $\lambda_{p\mu}^{NE1}$ and $\lambda_{p\mu}^N$ denote the analytic and numerical microscale eigenvalues of a patch scheme respectively. The required *method of wavenumber-wise scale separation* has three goals:

1. classify the analytic and numerical eigenvalues $(\lambda_p^{NE1}, \lambda_p^N)$ of a patch scheme based on all the $N^2/4$ macroscale wavenumbers (k_x, k_y) where $k_x, k_y \in \{\dots, -1, 0, 1, \dots\}$ resolved by a staggered patch grid;
2. separate the eigenvalues for each macroscale wavenumber (k_x, k_y) into *macroscale eigenvalues* $\lambda_{pM}^{NE1}, \lambda_{pM}^N$ (corresponding to pure macroscale modes defined in [p. 52](#) of [§3.2](#)) and *microscale eigenvalues* $\lambda_{p\mu}^{NE1}, \lambda_{p\mu}^N$ (corresponding to microscale modes with microscale structure modulated over the macroscale of wavenumber (k_x, k_y) , [p. 52](#));
3. for each wavenumber, associate each of the three macroscale eigenvalues $\lambda_{m\delta}^A, \lambda_{pM}^{NE1}, \lambda_{pM}^N$ and associate each of the several microscale eigenvalues $\lambda_{p\mu}^{NE1}, \lambda_{p\mu}^N$.

The method of wavenumber-wise scale separation identifies the correspondence of the patch scheme eigenvalues $(\lambda_p^{NE1}, \lambda_p^N)$ to each macroscale wavenumber resolved by a patch grid, and separates the eigenvalues into

microscale and macroscale eigenvalues, via the following steps. In all the following 3D arrays, the first two indices correspond to each macroscale wavenumber resolved by a patch grid.

1. Compute and save the analytic eigenvalues $\lambda_{m\delta}^A$ of full-domain microscale model (§3.2.2) as a 3D $N/2 \times N/2 \times 3$ array for each of the $N^2/4$ macroscale wavenumbers (k_x, k_y) resolved by a staggered patch grid. That is, three eigenvalues for each wavenumber.
2. Compute and save the analytic eigenvalues λ_p^{NE1} of a patch scheme (§3.2.3) as a 3D $N/2 \times N/2 \times n_p^i$ array for each of the $N^2/4$ macroscale wavenumbers (k_x, k_y) resolved by a patch grid. As in expression (3.2.11) (p. 59 of §3.2.3), there are $n_p^i = 9n^2/4 - 4n + 2$ eigenvalues λ_p^{NE1} for each wavenumber (e.g., 59 eigenvalues for $N = 10$). For Spectral patch scheme with $N > 14$, as the analytic expressions of the Jacobian elements become too long, we do not compute analytic eigenvalues λ_p^{NE1} ; hence this step does not apply. Among the total n_p^i eigenvalues of the patch scheme per wavenumber, $n_{pM}^i = 3$ eigenvalues (irrespective of N and n) correspond to the pure *macroscale modes*, and $n_{p\mu}^i = 9n^2/4 - 4n - 1$ eigenvalues correspond to artificial sub-patch *microscale modes* modulated over the macroscale.
3. Compute and save the numerical eigenvalues λ_p^N of a patch scheme (§3.2.5) as a 1D array of size n_p^I . As in expression (2.1.7) (p. 21 of §2.1.2), there are $n_p^I = (N^2/4)(9n^2/4 - 4n + 2)$ eigenvalues λ_p^N , which include $n_{pM}^I = 3N^2/4$ eigenvalues corresponding to the macroscale modes and $n_{p\mu}^I = (N^2/4)(9n^2/4 - 4n - 1)$ sub-patch microscale modes. Comparing with the number of patch scheme eigenvalues λ_p^{NE1} in step 2, $n_{pM}^I = n_{pM}^i(N^2/4)$, $n_{p\mu}^I = n_{p\mu}^i(N^2/4)$, $n_p^I = n_p^i(N^2/4)$. Thus, the 3D array of λ_p^{NE1} (with size $N/2 \times N/2 \times n_p^i$) in step 2 contain all the eigenvalues corresponding to the 1D array of λ_p^N with size n_p^I .
4. The task of this step is to split the $N/2 \times N/2 \times n_p^i$ array of analytic patch scheme eigenvalues λ_p^{NE1} in step 2 into $N/2 \times N/2 \times 3$ array of macroscale eigenvalues λ_{pM}^{NE1} (corresponding to the $N/2 \times N/2 \times 3$ array of $\lambda_{m\delta}^A$ in step 1) and $N/2 \times N/2 \times (n_p^i - 3)$ array of microscale eigenvalues $\lambda_{p\mu}^{NE1}$. For this task, loop over each of the $N^2/4$ macroscale wavenumbers (k_x, k_y) with index i, j and do the following sub-steps.
 - (a) To hold the microscale and macroscale analytic patch scheme eigenvalues $\lambda_{p\mu}^{NE1}$, λ_{pM}^{NE1} create two arrays of size $N/2 \times N/2 \times 3$ and $N/2 \times N/2 \times (n_p^i - 3)$ respectively.

- (b) Within the $N/2 \times N/2 \times n_p^i$ array of λ_p^{NE1} (in step 2), among the n_p^i eigenvalues with indices i, j and $k = 1, 2, \dots, n_p^i$, find three eigenvalues that are closest to the three eigenvalues $\lambda_{m\delta}^A$ (in step 1). These three among the n_p^i eigenvalues are macroscale eigenvalues λ_{pM}^{NE1} for this (k_x, k_y) , the remaining $n_p^i - 3$ eigenvalues are microscale eigenvalues $\lambda_{p\mu}^{NE1}$ for this (k_x, k_y) .
- (c) Assign the three macroscale eigenvalues λ_{pM}^{NE1} to the elements of $N/2 \times N/2 \times 3$ array of macroscale analytic patch scheme eigenvalues λ_{pM}^{NE1} (in step 4a) to indices i, j and $k = 1, 2, 3$. Assign the $n_p^i - 3$ microscale eigenvalues $\lambda_{p\mu}^{NE1}$ to the elements of $N/2 \times N/2 \times (n_p^i - 3)$ array of microscale analytic patch scheme eigenvalues $\lambda_{p\mu}^{NE1}$ (in step 4a) to indices i, j and $k = 1, 2, \dots, n_p^i - 3$.
5. The task of this step is to split the 1D array of numerical patch scheme eigenvalues λ_p^N (in step 3) with size $n_p^i = N/2 \cdot N/2 \cdot n_p^i$ into $N/2 \times N/2 \times 3$ array of macroscale eigenvalues λ_{pM}^N (corresponding to the $N/2 \times N/2 \times 3$ array of λ_{pM}^{NE1} in step 4) and $N/2 \times N/2 \times (n_p^i - 3)$ array of microscale eigenvalues $\lambda_{p\mu}^N$ (corresponding to the $N/2 \times N/2 \times (n_p^i - 3)$ array of $\lambda_{p\mu}^{NE1}$ in step 4). For this task, loop over each of the $N^2/4$ macroscale wavenumbers (k_x, k_y) with index i, j and do the following sub-steps.
- (a) To hold the microscale and macroscale numerical patch scheme eigenvalues $\lambda_{p\mu}^N, \lambda_{pM}^N$, create two arrays of size $N/2 \times N/2 \times 3$ and $N/2 \times N/2 \times (n_p^i - 3)$ respectively.
- (b) Among the 1D array of eigenvalues λ_p^N (in step 3), find three eigenvalues that are closest to the three analytic eigenvalues with indices i, j and $k = 1, 2, 3$ within the $N/2 \times N/2 \times 3$ array of λ_p^{NE1} (in step 4). These three eigenvalues are macroscale eigenvalues λ_{pM}^N for this (k_x, k_y) . Assign these three eigenvalues λ_{pM}^N to the elements of $N/2 \times N/2 \times 3$ array of macroscale numerical patch scheme eigenvalues λ_{pM}^N (in step 5a) for indices i, j and $k = 1, 2, 3$. Remove these three eigenvalues from the 1D array of eigenvalues λ_p^N .
- (c) Among the 1D array of remaining eigenvalues λ_p^N (in step 5b), find $n_p^i - 3$ eigenvalues that are closest to the $n_p^i - 3$ analytic eigenvalues within the $N/2 \times N/2 \times (n_p^i - 3)$ array of λ_p^{NE1} (in step 4) for indices i, j and $k = 1, 2, \dots, n_p^i - 3$. These $n_p^i - 3$ eigenvalues are microscale eigenvalues $\lambda_{p\mu}^N$ for this (k_x, k_y) . Assign these $n_p^i - 3$ eigenvalues $\lambda_{p\mu}^N$ to the elements of $N/2 \times N/2 \times (n_p^i - 3)$

array of microscale numerical patch scheme eigenvalues λ_{pM}^N (in step 5a) for indices i, j and $k = 1, 2, \dots, n_p^i - 3$. Remove these $n_p^i - 3$ eigenvalues from the 1D array of eigenvalues λ_p^N .

6. Do this step only when step 5 cannot be done due to unavailability of analytic patch scheme eigenvalues λ_p^{NE1} (in step 2) (e.g., for Spectral patch scheme with $N > 14$). The task of this step is to split the 1D array of numerical patch scheme eigenvalues λ_p^N (in step 3) with size $n_p^I = N/2 \cdot N/2 \cdot n_p^i$ into $N/2 \times N/2 \times 3$ array of macroscale eigenvalues λ_{pM}^N (corresponding to the $N/2 \times N/2 \times 3$ array of λ_p^{NE1} in step 4) and a 1D array with size $n_{p\mu}^I = n_{p\mu}^i (N^2/4)$ of microscale eigenvalues $\lambda_{p\mu}^N$ (corresponding to the $N/2 \times N/2 \times (n_p^i - 3)$ array of λ_p^{NE1} in step 4). As the analytic patch scheme eigenvalues λ_p^{NE1} are not available, in contrast to step 5, this step cannot compute an $N/2 \times N/2 \times (n_p^i - 3)$ array of microscale eigenvalues $\lambda_{p\mu}^N$. This step assumes that the patch scheme is highly accurate and so the macroscale patch scheme eigenvalues are very close to the eigenvalues $\lambda_{m\delta}^A$ of the full-domain microscale model. For this task, loop over each of the $N^2/4$ macroscale wavenumbers (k_x, k_y) with index i, j and do the following sub-steps.
 - (a) To hold the macroscale numerical patch scheme eigenvalues λ_{pM}^N , create an $N/2 \times N/2 \times 3$ array.
 - (b) Among the 1D array of eigenvalues λ_p^N (in step 3), find three eigenvalues that are closest to the three eigenvalues with indices i, j and $k = 1, 2, 3$ within the $N/2 \times N/2 \times 3$ array of eigenvalues $\lambda_{m\delta}^A$ of the full-domain microscale model (in step 1). These three eigenvalues are the macroscale eigenvalues λ_{pM}^N for this (k_x, k_y) . Assign these three eigenvalues λ_{pM}^N to the elements of $N/2 \times N/2 \times 3$ array of macroscale numerical patch scheme eigenvalues λ_{pM}^N (in step 6a) for indices i, j and $k = 1, 2, 3$. Remove these three eigenvalues from the 1D array of eigenvalues λ_p^N .

At the end of the loop over the macroscale wavenumbers (k_x, k_y) , having removed all the $3N^2/4$ macroscale eigenvalues λ_{pM}^N , the remaining $n_{p\mu}^I = n_p^I - n_{pM}^I$ eigenvalues are the sub-patch microscale eigenvalues.

After the preceding steps 1 to 6, the method of wavenumber-wise scale separation for the patch scheme eigenvalues gives the following arrays.

1. An $N/2 \times N/2 \times 3$ array of analytic eigenvalues $\lambda_{m\delta}^A$ of full-domain microscale model.
2. When the analytic patch scheme eigenvalues λ_p^{NE1} are available, both the macroscale eigenvalues and microscale eigenvalues are classified wavenumber-wise.
 - (a) An $N/2 \times N/2 \times 3$ array of macroscale *analytic* patch scheme eigenvalues λ_{pM}^{NE1} .
 - (b) An $N/2 \times N/2 \times 3$ array of macroscale *numerical* patch scheme eigenvalues λ_{pM}^N .
 - (c) An $N/2 \times N/2 \times (n_p^i - 3)$ array of microscale *analytic* patch scheme eigenvalues $\lambda_{p\mu}^{NE1}$.
 - (d) An $N/2 \times N/2 \times (n_p^i - 3)$ array of microscale *numerical* patch scheme eigenvalues $\lambda_{p\mu}^N$.
3. When the analytic patch scheme eigenvalues λ_p^{NE1} are not available (e.g., for Spectral patch scheme with $N > 14$), only the macroscale eigenvalues are classified wavenumber-wise.
 - (a) An $N/2 \times N/2 \times 3$ array of macroscale numerical patch scheme eigenvalues λ_{pM}^N .
 - (b) An 1D array with size $n_{p\mu}^I = n_p^I - n_{pM}^I$ of microscale numerical patch scheme eigenvalues $\lambda_{p\mu}^N$, without any association to the wavenumbers.

The association among each of the three macroscale eigenvalues $\lambda_{m\delta}^A$, λ_{pM}^{NE1} , λ_{pM}^N and association among each of the several microscale eigenvalues $\lambda_{p\mu}^{NE1}$, $\lambda_{p\mu}^N$ is established by for each wavenumber through the index order in the third dimension.

3.4 Staggered patch schemes are not sensitive to numerical roundoff errors

Despite the attractive characteristics, if the staggered patch schemes are very sensitive to numerical roundoff errors, then they will not be suitable for practical numerical simulations using finite precision floating-point

Table 3.4.1. Section 3.4 studies the sensitivity of the patch scheme eigenvalues to numerical roundoff errors for all the 1 944 combinations of the listed parameters.

Patch schemes	Spectral, Square-p2, Square-p4, Square-p6, and Square-p8
Drag coefficient	$c_D \in \{0, 10^{-6}, 0.001\}$
Viscous coefficient	$c_V \in \{0, 10^{-4}, 0.01\}$
Macro-grid intervals	$N \in \{6, 10, 14\}$ for Spectral scheme, $N \in \{6, 10, 14, 18, 22, 26\}$ for polynomial schemes.
Sub-patch micro-grid intervals	$n \in \{6, 10\}$
Patch scale ratio	$r \in \{0.0001, 0.001, 0.01, 0.1\}$

representations, for example, the common 64 bit format of IEEE754 (Goldberg 1991). From both qualitative and quantitative arguments, this section shows that the staggered patch schemes are not sensitive to numerical roundoff errors for the general linear wave.

The staggered patch scheme eigenvalues λ_p^{NE1} (for both the microscale and macroscale modes) of the numerically evaluated one-cell Jacobian (§3.2.3) and the staggered patch scheme eigenvalues λ_p^N of the numerical Jacobian (§3.2.5), *visually* agree in the complex plane eigenvalue plots of §3.2.6 (i.e., the large magenta and blue circles in Fig. 3.2.2). That the numerical and analytic eigenvalues ($\lambda_p^N, \lambda_p^{NE1}$) of a patch scheme visually agree indicates that the patch scheme is not sensitive to numerical roundoff errors. This subsection first *quantitatively* compares the numerical and analytic eigenvalues of the staggered patch schemes to show that the staggered patch schemes are not sensitive to numerical roundoff errors when the sub-patch micro-grid interval is not too small (i.e., $\delta \gtrsim 10^{-5}$). The later part of this subsection argues that even for very small sub-patch micro-grid interval $\delta \lesssim 10^{-5}$), the numerical roundoff errors are not due to the patch schemes.

For the time simulations, how sensitive are the patch scheme computations to numerical roundoff errors? This section answers this question in general for all the possible initial conditions by studying how sensitive the patch scheme eigenvalues are to the numerical roundoff errors. Hence we compare the eigenvalues λ_p^{NE1} of the analytically derived Jacobian (§3.2.3) with the eigenvalues λ_p^N of the numerically computed Jacobian (§3.2.5) for a total of 1 944 patch scheme cases as Table 3.4.1 lists.

To quantitatively assess the sensitivity of the staggered patch schemes to numerical roundoff errors, we show that the discrepancy $|\lambda_{p,i}^N - \lambda_{p,i}^{NE1}|$ is small separately for the microscale and macroscale eigenvalues. We define the *microscale and macroscale numerical roundoff errors* for the staggered patch scheme eigenvalues as

$$\epsilon_{\mu}^{\text{Num}} = \max_i |\lambda_{p,\mu,i}^N - \lambda_{p,\mu,i}^{NE1}| \quad (3.4.1a)$$

for indices i of the microscale eigenvalues,

$$\epsilon_M^{\text{Num}} = \max_i |\lambda_{pM,i}^N - \lambda_{pM,i}^{NE1}| \quad (3.4.1b)$$

for indices i of the macroscale eigenvalues.

If the errors $\epsilon_{\mu}^{\text{Num}}$ and ϵ_M^{Num} are negligibly small, that is, if the numerical and analytic macroscale eigenvalues $(\lambda_{pM}^N, \lambda_{pM}^{NE1})$ of a patch scheme agree very closely, then the patch scheme is not sensitive to the numerical roundoff errors.

The eigenvalues in the numerical roundoff errors (3.4.1a) and (3.4.1b) require separating the microscale and macroscale patch scheme eigenvalues and the association between the analytic and numerical eigenvalues. Section 3.3 computes the required eigenvalues as the following 3D arrays (analytic eigenvalues only for $N \leq 14$ for Spectral patch scheme)

1. An $N/2 \times N/2 \times 3$ array of macroscale *analytic* patch scheme eigenvalues λ_{pM}^{NE1} .
2. An $N/2 \times N/2 \times 3$ array of macroscale *numerical* patch scheme eigenvalues λ_{pM}^N .
3. An $N/2 \times N/2 \times (n_p^i - 3)$ array of microscale *analytic* patch scheme eigenvalues λ_p^{NE1} .
4. An $N/2 \times N/2 \times (n_p^i - 3)$ array of microscale *numerical* patch scheme eigenvalues λ_p^N .

The microscale and macroscale numerical roundoff errors in (3.4.1) are defined for the eigenvalues of a patch scheme for one specific set of parameters. We define the *peak microscale and macroscale numerical roundoff errors* as the maximum value of $\max_{c_D, c_V} \epsilon_{\mu}^{\text{Num}}$ and $\max_{c_D, c_V} \epsilon_M^{\text{Num}}$, over the nine combinations of the coefficients $c_D \in \{0, 10^{-6}, 0.001\}$ and $c_V \in \{0, 10^{-4}, 0.01\}$ as Table 3.4.1 lists.

Figure 3.4.1. Variation of the peak *microscale* numerical roundoff error with the number of macro-grid intervals N , patch scale ratio r and the number of sub-patch micro-grid intervals n . Each point is the peak $\epsilon_{\mu}^{\text{Num}}$ for the nine combinations of the coefficients c_D, c_V in Table 3.4.1, for a patch scheme with particular patch grid parameters (N, r, n) .

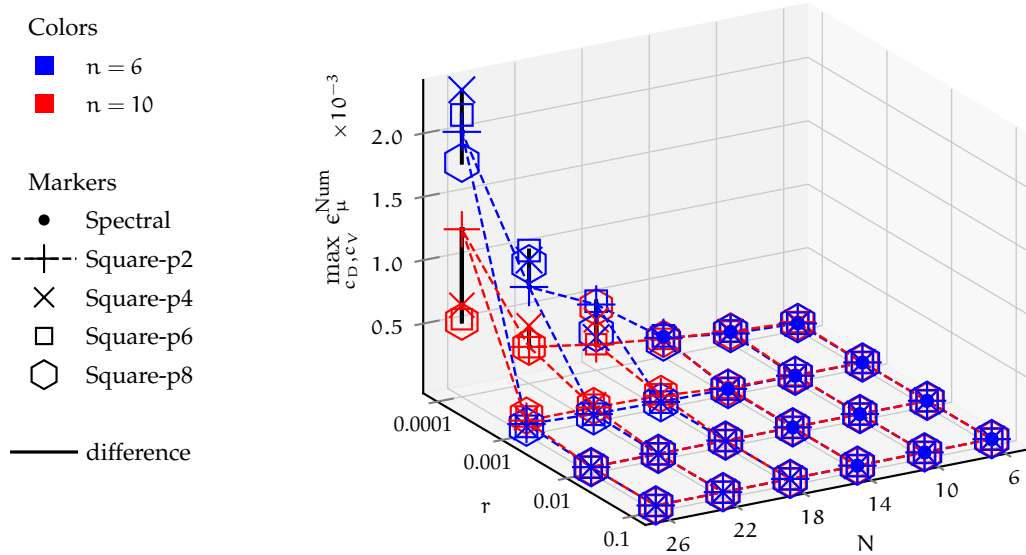


Figure 3.4.2. Variation of the peak *macroscale* numerical roundoff error with the number of macro-grid intervals N , patch scale ratio r and the number of sub-patch micro-grid intervals n . Each point is the peak ϵ_M^{Num} for the nine combinations of the coefficients c_D, c_V in Table 3.4.1, for a patch scheme with particular patch grid parameters (N, r, n) .

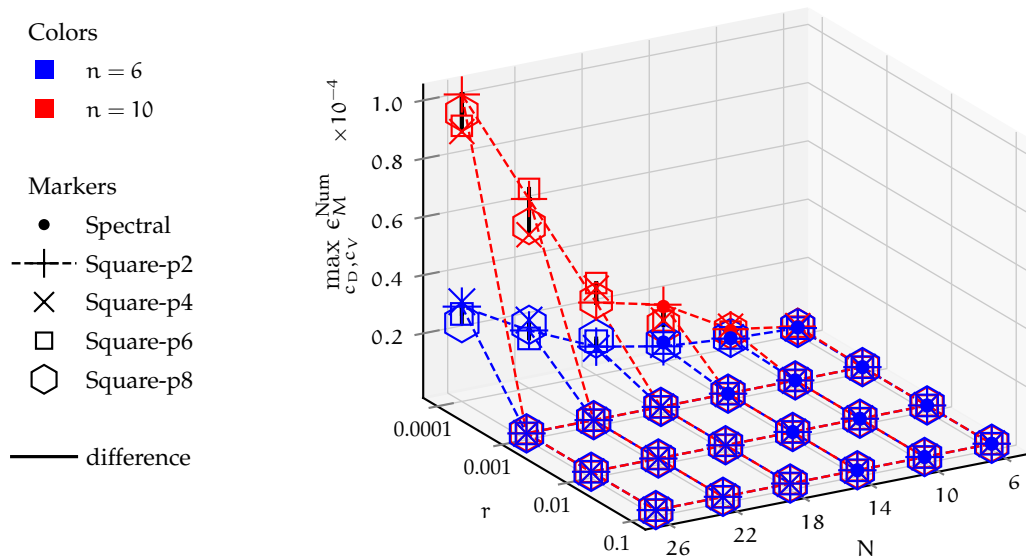


Table 3.4.2. Maximum numerical roundoff errors over all the combinations of the five patch schemes and c_D , c_V , and N in Table 3.4.1 for different patch scale ratio r and n . Red colour highlights the largest value in each column (based on full precision when values are same with two significant figures).

		Patch scale ratio r			
		0.0001	0.001	0.01	0.1
$\max e_{\mu}^{\text{Num}}$	$n = 6$	0.002	$4 \cdot 10^{-5}$	$3 \cdot 10^{-7}$	$6 \cdot 10^{-10}$
	$n = 10$	0.001	0.0001	$3 \cdot 10^{-7}$	$6 \cdot 10^{-9}$
$\max e_M^{\text{Num}}$	$n = 6$	$3 \cdot 10^{-5}$	$4 \cdot 10^{-8}$	10^{-10}	$2 \cdot 10^{-11}$
	$n = 10$	0.0001	10^{-7}	$5 \cdot 10^{-10}$	$2 \cdot 10^{-11}$

Nonnegligible numerical roundoff errors arise only for very small sub-patch micro-grid intervals $\delta \lesssim 10^{-5}$ (i.e., small r and large N , n). Figures 3.4.1 and 3.4.2 plot the peak microscale and macroscale numerical roundoff errors for the five patch schemes, for the 1 944 combinations of the parameters Table 3.4.1 lists. Table 3.4.2 presents the peak numerical roundoff errors for different patch scale ratios r (i.e peak value for each r -slice in Figs. 3.4.1 and 3.4.2). The largest microscale and macroscale numerical roundoff errors among the 1 944 cases are 0.0001 and 0.002 respectively, both corresponding to the smallest patch scale ratio $r = 0.0001$ and largest number of macro-grid intervals $N = 26$. The following are some key observations from Figs. 3.4.1 and 3.4.2 and Table 3.4.2.

1. For a given set of patch grid parameters N , n , r , the peak macroscale numerical roundoff errors $\max_{c_D, c_V} e_M^{\text{Num}}$ are about ten to thousand times smaller compared to the peak microscale numerical roundoff errors $\max_{c_D, c_V} e_{\mu}^{\text{Num}}$. That is, *the macroscale eigenvalues which are of primary interest are relatively less sensitive to numerical roundoff errors than the microscale eigenvalues.*
2. Both the microscale and macroscale peak numerical roundoff errors $\max_{c_D, c_V} e_{\mu}^{\text{Num}}$, $\max_{c_D, c_V} e_M^{\text{Num}}$, monotonically increase with increasing number of macro-grid intervals N and decreasing patch scale ratio r . The numerical roundoff errors also increase with increasing number of sub-patch micro-grid intervals n (blue and red colors in Figs. 3.4.1 and 3.4.2), except the off trend for $\max_{c_D, c_V} e_{\mu}^{\text{Num}}$ in Fig. 3.4.1 for $N \in \{22, 26\}$ and $r = 0.0001$. For a staggered patch grid, increasing N , decreasing r , and increasing n , all these lead to decreasing sub-patch micro-grid interval $\delta = 2Lr/(Nn)$. For example, for $r = 0.001$, $N = 26$, $n = 10$, sub-patch micro-grid interval $\delta \approx 5 \cdot 10^{-5}$. Thus, *nonnegligible*

numerical roundoff errors arise only for very small sub-patch micro-grid intervals $\delta \lesssim 10^{-5}$ (i.e., small r and large N, n).

3. In general, except $\epsilon_{\mu}^{\text{Num}}$ for $N \gtrsim 22$, $r = 0.0001$, the numerical roundoff errors of all the five patch schemes are roughly the same. That is, the numerical roundoff errors do not have a strong dependence on the specific patch scheme. If the numerical roundoff errors were due to the patch scheme, then the numerical roundoff errors must also depend on the specific patch scheme, showing a clear trend. The lack of such trends, among the patch schemes with different amounts of numerical computations, *indicates that the numerical roundoff errors are not due to the patch schemes.*

In Figs. 3.4.1 and 3.4.2 and Table 3.4.2, the large peak numerical roundoff errors for small sub-patch micro-grid intervals δ (i.e., small r and large N, n), have the following main sources.

1. The numerical roundoff errors due to the numerical computations in a patch scheme due to the patch coupling.
2. The numerical roundoff errors due to the numerical computations of the underlying microscale model (e.g., the finite difference computations).
3. The numerical roundoff errors in numerically computing the eigenvalues of the patch scheme numerical Jacobian.

We take the numerical roundoff errors in numerically computing the Jacobian (§3.2.5) of a patch scheme, to be small compared to the much higher number of numerical computations in the patch coupling, sub-patch microscale model and the eigenvalue computation.

The dependence of the numerical roundoff errors on the physical parameters (drag and viscous diffusion) and the lack of dependence on the specific patch schemes show that *the numerical roundoff errors are due to the underlying microscale model, not due to the staggered patch scheme.* Tables 3.4.3 and 3.4.4 present the microscale numerical roundoff errors $\epsilon_{\mu}^{\text{Num}}$, ϵ_M^{Num} for different coefficients of drag c_D and viscous diffusion c_V . Both the numerical roundoff errors strongly depend on the viscous diffusion; both $\epsilon_{\mu}^{\text{Num}}$ and ϵ_M^{Num} increase with increasing c_V , showing strong increase at small patch scale ratio r . The microscale numerical roundoff errors $\epsilon_{\mu}^{\text{Num}}$ in Table 3.4.3 do not have strong dependence on the drag coefficient c_D . But in Table 3.4.4, the values of maximum ϵ_M^{Num} for $c_D = 10^{-6}$ (for $c_V = 0.01$ and small patch scale ratios $r \in \{0.0001, 0.001\}$), indicate some dependence of the

Table 3.4.3. Maximum numerical roundoff errors $\epsilon_{\mu}^{\text{Num}}$ in microscale eigenvalues over the five patch schemes and all the combinations of N , n in Table 3.4.1, for different patch scale ratio r and coefficients of drag c_D and viscous diffusion c_V . Large $\epsilon_{\mu}^{\text{Num}}$ in each column corresponding to the largest $c_V = 0.01$ are red highlighted.

	Patch scale ratio r			
	0.0001	0.001	0.01	0.1
$c_D = 0, c_V = 0$	$7 \cdot 10^{-5}$	10^{-6}	$3 \cdot 10^{-7}$	$7 \cdot 10^{-10}$
$c_D = 0, c_V = 0.0001$	0.0001	$7 \cdot 10^{-7}$	$7 \cdot 10^{-9}$	$7 \cdot 10^{-10}$
$c_D = 0, c_V = 0.01$	0.002	0.0001	$9 \cdot 10^{-8}$	$6 \cdot 10^{-9}$
$c_D = 10^{-6}, c_V = 0$	$6 \cdot 10^{-5}$	10^{-6}	$3 \cdot 10^{-7}$	$7 \cdot 10^{-10}$
$c_D = 10^{-6}, c_V = 0.0001$	0.0001	$7 \cdot 10^{-7}$	$7 \cdot 10^{-9}$	$7 \cdot 10^{-10}$
$c_D = 10^{-6}, c_V = 0.01$	0.002	0.0001	$9 \cdot 10^{-8}$	$6 \cdot 10^{-9}$
$c_D = 0.001, c_V = 0$	0.0001	10^{-6}	$3 \cdot 10^{-7}$	$7 \cdot 10^{-10}$
$c_D = 0.001, c_V = 0.0001$	0.0001	$7 \cdot 10^{-7}$	$7 \cdot 10^{-9}$	$7 \cdot 10^{-10}$
$c_D = 0.001, c_V = 0.01$	0.002	0.0001	$9 \cdot 10^{-8}$	$6 \cdot 10^{-9}$

Table 3.4.4. Maximum numerical roundoff errors ϵ_M^{Num} in macroscale eigenvalues over the five patch schemes and all the combinations of N , n in Table 3.4.1, for different patch scale ratio r and coefficients of drag c_D and viscous diffusion c_V . Large ϵ_M^{Num} in each column corresponding to the largest $c_V = 0.01$ are red highlighted.

	Patch scale ratio r			
	0.0001	0.001	0.01	0.1
$c_D = 0, c_V = 0$	$2 \cdot 10^{-9}$	$2 \cdot 10^{-10}$	$3 \cdot 10^{-11}$	$2 \cdot 10^{-11}$
$c_D = 0, c_V = 0.0001$	$4 \cdot 10^{-8}$	$8 \cdot 10^{-10}$	$2 \cdot 10^{-11}$	$2 \cdot 10^{-11}$
$c_D = 0, c_V = 0.01$	$9 \cdot 10^{-5}$	$9 \cdot 10^{-8}$	$5 \cdot 10^{-10}$	$2 \cdot 10^{-11}$
$c_D = 10^{-6}, c_V = 0$	$2 \cdot 10^{-9}$	$2 \cdot 10^{-10}$	$3 \cdot 10^{-11}$	$2 \cdot 10^{-11}$
$c_D = 10^{-6}, c_V = 0.0001$	$4 \cdot 10^{-8}$	$7 \cdot 10^{-10}$	$2 \cdot 10^{-11}$	$2 \cdot 10^{-11}$
$c_D = 10^{-6}, c_V = 0.01$	0.0001	10^{-7}	$5 \cdot 10^{-10}$	$2 \cdot 10^{-11}$
$c_D = 0.001, c_V = 0$	$2 \cdot 10^{-9}$	$2 \cdot 10^{-10}$	$3 \cdot 10^{-11}$	$2 \cdot 10^{-11}$
$c_D = 0.001, c_V = 0.0001$	$4 \cdot 10^{-8}$	$7 \cdot 10^{-10}$	$2 \cdot 10^{-11}$	$2 \cdot 10^{-11}$
$c_D = 0.001, c_V = 0.01$	$9 \cdot 10^{-5}$	$9 \cdot 10^{-8}$	$5 \cdot 10^{-10}$	$2 \cdot 10^{-11}$

macroscale numerical roundoff errors on the drag coefficient c_D . In general, the staggered patch schemes are largely agnostic of the underlying microscale model. More specifically a discussion in §3.4 of this section, using Figs. 3.4.1 and 3.4.2 show that the numerical roundoff errors do not have strong dependence on the specific patch scheme. This lack of dependence on the specific patch schemes despite the different amounts of numerical computations indicates that the numerical roundoff errors are not due to the patch schemes. Moreover, if the patch schemes were sensitive to numerical roundoff errors, then the errors must have been large irrespective of the physical parameters (drag and viscous diffusion). For example, $\epsilon_\mu^{\text{Num}}$ and ϵ_M^{Num} must have been large also for small c_V , which is not the case in Tables 3.4.3 and 3.4.4. Thus, the dependence of the numerical roundoff errors on the physical parameters (c_D and c_V) and the lack of dependence of the specific patch schemes show that *the numerical roundoff errors are due to the underlying microscale model, not due to the staggered patch scheme*. The following two paragraphs detail the dependence of the numerical roundoff errors on c_V and c_D respectively.

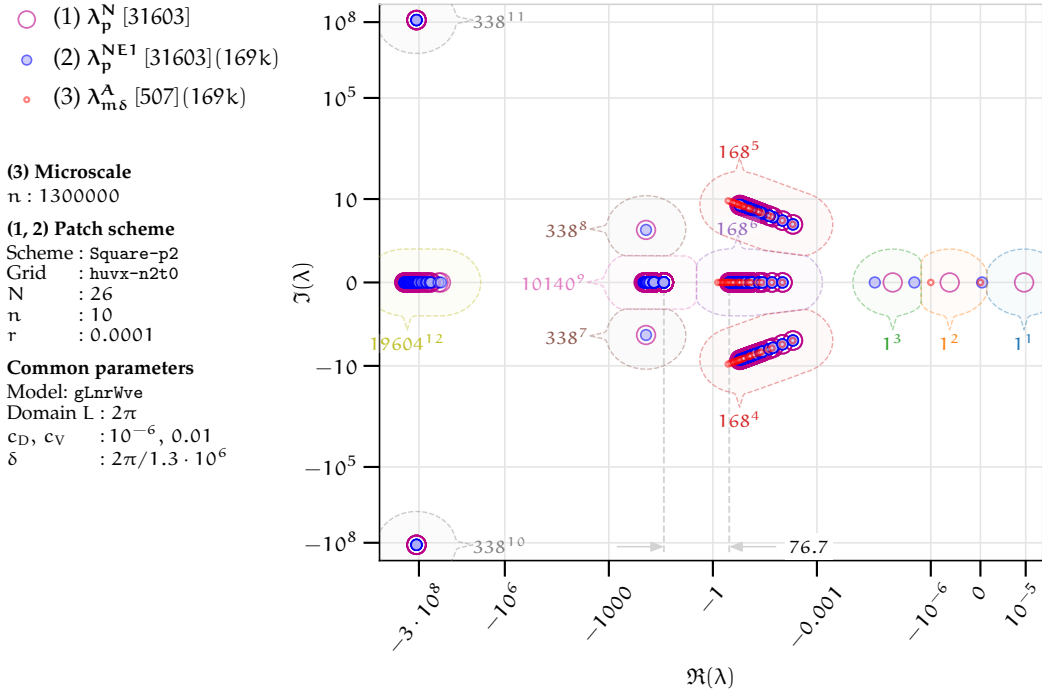
Scaling arguments on the general linear wave confirm the inherent sensitivity of the microscale model to numerical roundoff errors. terms scale with the grid interval δ . The wave term $\sim h/\delta$, the drag term $\sim c_D u$, and the viscous diffusion terms $\sim c_V u/\delta^2$. For example, for small $\delta = 10^{-5}$, the scales of the wave, drag, and viscous diffusion terms are about $10^5 h$, $c_D u$ and $10^{10} c_V u$ respectively. For small height h , when the viscous diffusion is not negligibly small (e.g., $c_V \sim 0.01$), irrespective of c_D , the addition (subtraction) of these small and large values leads to the loss of floating-point precision while lining up the decimal points in the finite precision arithmetic (Heister et al. 2019, p. 8; Goldberg 1991, pp. 16, 19). Hence, for nonnegligible viscous diffusion ($c_V \gtrsim 0.001$) both the full-domain microscale scheme and the sub-patch microscale model, are inherently sensitive to numerical roundoff errors, for small enough grid interval $\delta \lesssim 10^{-5}$. This inherent sensitivity of the microscale model to numerical roundoff errors is not severe for the time simulation (§3.7.5) but impacts the eigenvalue computation for both the full-domain microscale model and the patch scheme. Both the microscale and macroscale roundoff errors ($\epsilon_\mu^{\text{Num}}$ and ϵ_M^{Num}) are large for large c_V in Tables 3.4.3 and 3.4.4. Also, both $\epsilon_\mu^{\text{Num}}$ and ϵ_M^{Num} monotonically increase with decreasing r (and hence decreasing δ), at an increasing rate with increasing viscous diffusion c_V . Whereas this inherent sensitivity impacts both the microscale and macroscale eigenvalues, the macroscale numerical roundoff errors ϵ_M^{Num} are in general ten to thousand times smaller than the peak microscale numerical roundoff errors $\epsilon_\mu^{\text{Num}}$. We expect that this relatively smaller ϵ_M^{Num} is due to the macroscale interpolation in the

patch coupling, which acts as averaging/smoothing the inherent numerical roundoff errors of the computations within the patches. Thus, for very small grid interval $\delta \lesssim 10^{-5}$ and large viscous diffusion ($c_V \gtrsim 0.001$), the nonnegligible *numerical roundoff errors in both microscale and macroscale patch scheme eigenvalues are due to the inherent sensitivity of the microscale model to numerical roundoff errors.*

A part of the numerical roundoff errors are due to numerical computation of near-zero eigenvalues. The microscale numerical roundoff errors in [Table 3.4.3](#), in general remains independent of the drag coefficient c_D , except the change of about 10^{-5} for $c_D \in \{0, 10^{-6}, 0.0001\}$ with $c_V = 0$ and $r = 0.0001$. But in [Table 3.4.4](#), the maximum ϵ_M^{Num} for $c_D = 10^{-6}$ (for $c_V = 0.01$ and small patch scale ratios $r \in \{0.0001, 0.001\}$), suggest that the macroscale numerical roundoff errors also depend on the drag coefficient c_D . This paragraph explains the dependence of macroscale numerical roundoff error ϵ_M^{Num} on the drag coefficient c_D . For nonzero drag and viscous diffusion, patch schemes have one zero eigenvalue (cluster 1 in [Fig. 3.2.2](#)) corresponding to the macroscale mode of stagnant water ([Fig. 3.2.13](#)), and two eigenvalues (cluster 2 in [Fig. 3.2.2](#)) with $-c_D$ as their real part and zero imaginary part corresponding to the macroscale mode of decelerating uniform mean flow ([Fig. 3.2.14](#)). As $c_D \rightarrow 0$, the two eigenvalues $\lambda = -c_D + 0i$ corresponding to the decelerating uniform mean flow, tends to zero, merging with the zero eigenvalue as in [Fig. 3.2.3](#). Due to these near-zero repeated eigenvalues for small drag $c_D \lesssim 10^{-6}$, numerical computation of the eigenvalues is sensitive to the numerical roundoff errors, for both the patch scheme and the full-domain microscale model. As we compute the analytic eigenvalues λ_p^{NE1} after evaluating the analytic Jacobian, both the analytic and numeric eigenvalues $\lambda_p^{\text{NE1}}, \lambda_p^{\text{N}}$ are sensitive to numerical roundoff errors. Being random, the numerical roundoff errors in the eigenvalues λ_p^{NE1} and λ_p^{N} , do not cancel in computing the difference in our definition ([3.4.1](#)). Thus, for very small grid interval $\delta \lesssim 10^{-5}$ and very small drag $c_D \lesssim 10^{-6}$, the sensitivity of numerical eigenvalue computation also leads to large numerical roundoff errors in near-zero eigenvalues.

Numerical roundoff errors also arise due to near-zero repeated eigenvalues for small nonzero drag As discussed in the paragraph before the previous paragraph, the inherent sensitivity of the microscale model to numerical roundoff errors is large for large viscous diffusion, leading to an increase in both the microscale and macroscale numerical roundoff errors ($\epsilon_\mu^{\text{Num}}$ and ϵ_M^{Num}). But, as the repeated near-zero eigenvalues due to small drag correspond to the macroscale modes, the sensitivity of eigenvalue computation leads to an increase in the macroscale numerical roundoff errors ϵ_M^{Num} only. Hence, for small grid interval $\delta \lesssim 10^{-5}$, due to both the inherent sensitivity

Figure 3.4.3. Eigenvalues of Square-p2 staggered patch scheme ($N = 26$, $n = 10$, $r = 0.0001$) for general linear wave with large viscous diffusion $c_V = 0.01$ and a small drag $c_D = 10^{-6}$. Large numerical roundoff errors are evident from the large discrepancy among the near-zero eigenvalues λ_p^N , λ_p^{NE1} , and $\lambda_{m\delta}^A$ (clusters 1, 2, 3).



of the microscale model (for nonnegligible viscous diffusion $c_V \gtrsim 0.001$) and the sensitivity of eigenvalue computation of near-zero repeated eigenvalues (for small drag $c_D \lesssim 10^{-6}$), the macroscale numerical roundoff errors ϵ_M^{Num} are large. For example, the numerical roundoff errors in Table 3.4.4 for macroscale eigenvalues has maximum values of $\epsilon_M^{\text{Num}} = 10^{-7}, 0.0001$ for $r = 0.0001, 0.001$ for small nonzero drag $c_D = 10^{-6}$. Figure 3.4.3 shows the large numerical roundoff errors in the near-zero eigenvalues due to small drag. The numeric eigenvalues λ_p^N in clusters 1, 2, 3 have large numerical roundoff errors, due to the microscale model's inherent sensitivity (for large $c_V = 0.01$) and the sensitivity of eigenvalue computation of near-zero repeated eigenvalues (for small $c_D = 10^{-6}$). The analytic eigenvalues λ_p^{NE1} corresponding to λ_p^N in clusters 1, 2, 3, have relatively smaller numerical roundoff errors, as the computation of the underlying microscale model is derived analytically.

Thus, for a very small grid interval $\delta \lesssim 10^{-5}$, both the inherent sensitivity of the microscale model (for nonnegligible viscous diffusion $c_V \gtrsim 0.001$) and the sensitivity of eigenvalue computation of near-zero repeated eigenvalues (for very small drag $c_D \lesssim 10^{-6}$), are the characteristic of the microscale model. Hence, *for very small grid interval δ the numerical eigenvalues of the full-domain microscale model are also inaccurate*. But this inaccuracy in the eigenvalues of the full-domain microscale model system is not an issue for us in most cases, as we only evaluate the analytic expression (3.2.7), to compute the eigenvalues $\lambda_{m\delta}^\Lambda$ of the full-domain microscale model.

The following listing summarises the study of numerical sensitivity in this subsection.

1. For patch scale ratios $r \gtrsim 0.001$ the patch scheme eigenvalue are not sensitive to numerical roundoff errors (columns 2-4 in Table 3.4.2).
2. For smaller patch scale ratios $r \lesssim 0.001$ the patch scheme eigenvalues are a little sensitive to numerical roundoff errors (column 1 in Table 3.4.2). But this sensitivity to numerical roundoff errors for small grid interval $\delta \lesssim 10^{-5}$ is due to both the inherent sensitivity of the microscale model (for nonnegligible viscous diffusion $c_V \gtrsim 0.001$) and the sensitivity of eigenvalue computation of near-zero repeated eigenvalues (for small drag $c_D \lesssim 10^{-6}$). Hence, even for small patch scale ratios, the computations of staggered patch schemes are not sensitive to numerical roundoff errors.

3.5 Staggered patch schemes are stable

This section demonstrates the stability of the staggered patch schemes and explains the dependence of the patch scheme stability on various aspects like grid symmetry, physical parameters (c_d , c_V), and grid parameters such as the number of macro-grid intervals N , number of sub-patch micro-grid intervals n and patch scale ratio r .

A (linear or nonlinear) dynamical system is defined to be *stable* or Lyapunov stable, for both infinitesimally and finitely small perturbations about equilibrium, if all solutions that start nearby an equilibrium stay nearby over time (Chicone 2006, Dfn. 1.39, p. 21; Wiggins 2003, Dfn. 1.2.1, p.7; Hirsch et al. 2013, p. 174; Lynch 2018, Dfn. 5, p. 55; Edwards et al. 2017, p.507; Jordan and Smith 2007, Thm. 8.2, p. 268; Perko 2001, Dfn. 1, p. 129).

A linear or linearised dynamical system describes the time evolution of infinitesimal disturbances to an equilibrium solution (Marsden and Ratiu 1999, p. 32; D. F. Griffiths and Higham 2010, pp. 166-167). Hence, a Jacobian J of a linear or linearised dynamical system $dx/dt = Jx$ characterises the stability only for infinitesimally small perturbations to equilibrium solutions. Thus, a (linear or nonlinear) dynamical system is defined to be *linearly stable* if infinitesimally small perturbations to equilibrium solutions do not grow unbounded over time (Marsden and Ratiu 1999, p. 32; Mellodge 2016, p. 176, §3.4.1.2).

This section shows that the staggered patch schemes are linearly stable whenever the underlying full-domain microscale model is linearly stable. A dynamical system can be linearly stable (for infinitesimally small perturbations about equilibrium) and yet nonlinearly unstable, for finite perturbations about equilibrium. That is, *linear stability does not imply stability* (Wiggins 2003, pp. 11–12; Marsden and Ratiu 1999, pp. 32–33; Strogatz 2018, pp. 130–131). We have not noticed any such nonlinear instabilities in the staggered patch schemes from the time simulations for different initial conditions with random finite perturbations. Section 3.7.5 shows two examples of stable time simulations with initial random perturbation (Fig. 3.7.15). Hence, *this section focuses on the linear stability of the staggered patch schemes*.

A linear or linearised dynamical system $dx/dt = Jx$ is defined to be *spectrally stable* if all eigenvalues of the Jacobian J have nonpositive real part (Marsden and Ratiu 1999, p. 32; Mellodge 2016, p. 176; Meiss 2017, p. 53). A linear or linearised dynamical system with all eigenvalues having nonpositive real part can still be unstable, that is, *spectral stability does not imply stability* (Marsden and Ratiu 1999, pp. 32–34). For example, a free particle with neutral stability described by $dx/dt = Jx$ where the non-diagonalisable Jacobian $J = \begin{bmatrix} 0 & 1 \\ 0 & 0 \end{bmatrix}$, has *nonpositive eigenvalues yet is unstable over time*. Hence, for stability, it is also necessary that the Jacobian J is diagonalisable/semisimple (Bullo and Lewis 2019, Thm. 6.6, p. 317; Hirsch and Smale 1974, Prob. 4, p. 137, Prob. 3, p. 191; Perko 2001, Prob. 11, p. 50). Thus, to show that the system $dx/dt = Jx$ is linearly stable (for infinitesimally small perturbations about equilibrium), one must show that all eigenvalues of the Jacobian J have nonpositive real part and that the Jacobian J is diagonalisable.

Throughout this thesis, *by the term nonpositive real parts, we mean effectively nonpositive real parts within numerical roundoff errors*, for all the numerically computed eigenvalues, including the numerically evaluated analytic eigenvalues.

Practically, due to numerical round-off errors, almost all numerical matrices are diagonalisable, hence the condition of diagonalisability is not useful in assessing the stability. On the other hand, eigenvalues that are highly sensitive to numerical round-off errors indicate a non-diagonalisable Jacobian. That the patch scheme eigenvalues (in §3.4) are not sensitive to numerical round-off errors indicates that the patch schemes Jacobians are approximately diagonalisable. Hence, this *section establishes the linear stability of the staggered patch schemes via spectral stability* by showing that the patch schemes' eigenvalues have nonpositive real part.

For nonnegative dissipation coefficients c_D and c_V , the real parts of all three eigenvalues (3.2.7) of the full-domain microscale model are non-positive (§3.2.2). That is, the wave solutions either decay over time when $\Re(\lambda_m^A) < 0$ or retain the same amplitude over time when $\Re(\lambda_m^A) = 0$. Hence, as the solutions remain bounded over time, the staggered full-domain microscale model is stable. Similarly, we establish that the designed staggered patch schemes are stable by showing that the real parts of their eigenvalues are nonpositive. Hence, to assess the stability, we study the maximum real parts of the eigenvalues of the staggered patch schemes.

Section 3.5.1 explains the requirements of geometric symmetry for a staggered patch scheme to be stable and the constraints the symmetry imposes on the arrangement of sub-patch nodes, the number of sub-patch intervals, and the patch coupling.

Section 3.5.2 shows the trends of the maximum real parts of the Spectral patch scheme over a wide *range of physical parameters* (coefficients of drag c_D , and viscous diffusion c_V), for a fixed number of macro-grid intervals N , sub-patch micro-grid intervals n .

Section 3.5.3 shows the trends of the maximum real parts of all the five staggered patch schemes over a *range of grid parameters* (number of macro-grid intervals N , sub-patch micro-grid intervals n , and patch scale ratio r), for a fixed combinations of the physical parameters (c_D, c_V).

3.5.1 Patch scheme stability requires geometric symmetry

This subsection explains the requirements of geometric symmetry for a staggered patch scheme to be stable and the constraints the symmetry imposes on the arrangement of sub-patch nodes, the number of sub-patch intervals, and the patch coupling.

Section 2.1.2 shows the compatible staggered patch grids for wave-like systems. Our implementation generates all the possible 83 520 compatible staggered patch grids for the multiscale modelling of 2D wave-like systems.

We studied the dependence of the patch scheme stability on the patch grid geometry, the *geometry-stability study*, for about fifty patch grid patterns that are representative of sub-families of the 83 520 compatible 2D staggered patch grids for a given number of sub-patch micro-grid intervals n . We omit the details of this geometry-stability study for brevity, instead, we report the key outcomes of the study and focus on the patch grids that constitute stable patch schemes. Our recent article (Divahar et al. 2022, §4.2) gives more details. The geometry-stability study indicates that *a patch grid without a centre node does not constitute a stable staggered patch scheme*. That is, staggered patch grids containing micro-grids other than $uuvv$, $hhvv$ and $uuhh$ (green highlighted in Fig. 2.1.3a) even in any one of the patches, lead to unstable staggered patch schemes. For example, the patch grid in Fig. 3.5.1a does not contain a centre node in any of its sub-patch micro-grid. In our geometry-stability study, even when one patch in a macro-cell (orange squares in Fig. 3.5.1a) does not contain a centre node, the eigenvalues of the staggered patch schemes have large positive real parts. For patches without a centre node, we compute the macroscale patch value by averaging over the $h/u/v$ values of the nodes closest to the patch centre.

From the geometry-stability study, we also find that the higher the symmetry in the staggered patch grid, the better the accuracy and stability of the staggered patch schemes. Thus, the dominant role of a centre node in the patch scheme stability comes from the requirement of geometric symmetry in the patch grids for stability. Among those staggered patch grids that have a centre node in each of their patches, from the geometry-stability study, we find only two staggered patch grids, those depicted in Figs. 2.1.3b and 3.5.1b, over which stable patch schemes are possible.

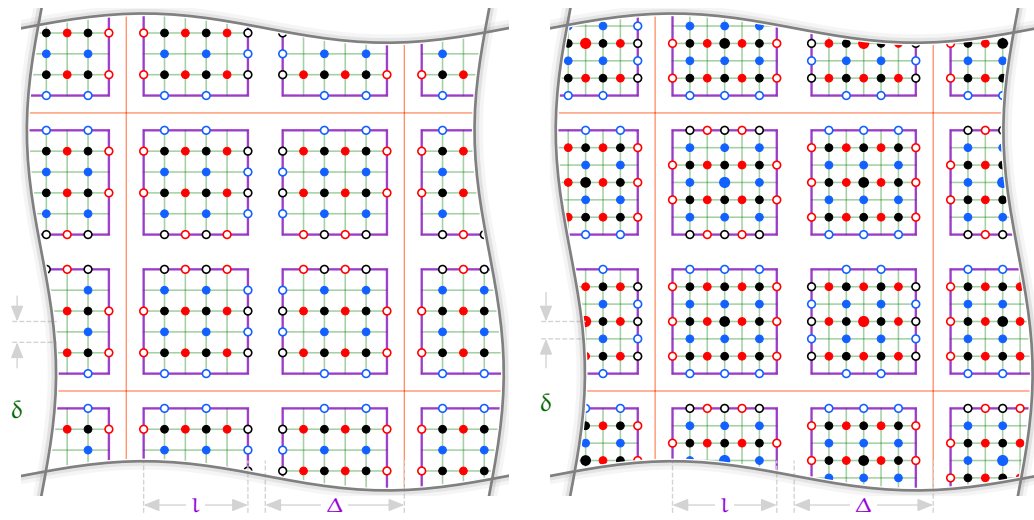
The sub-patch micro-grids in Fig. 3.5.1a do not have reflective symmetry about x and y axes (horizontal and vertical in Fig. 3.5.1a); for example the edge nodes on left and right edges are not the same for any of the sub-patch micro-grids. The geometry-stability shows that *lack of such sub-patch micro-grid reflective symmetry leads to unstable patch schemes*.

The sub-patch micro-grids each with a centre node in Fig. 3.5.1b have reflective symmetry about x and y axes; flipping any of the patches about x or y axes does not change the sub-patch nodes. The h -, u - and v -centred sub-patch micro-grids in Fig. 2.1.3b also have reflective symmetry about x and y axes. Stable patch schemes are possible on both the staggered patch grids in Figs. 3.5.1b and 2.1.3b. The patch grid Fig. 3.5.1b has three of the patches same as in Fig. 2.1.3b, along with an additional h -centred patch in place of the empty patch. The additional h -patch in Fig. 3.5.1b appears to provide slightly higher accuracy compared to the staggered patch grid with only three patches (Fig. 2.1.3b). But the staggered patch grid with

Figure 3.5.1. Two staggered patch grids with and without a centre node in each of the sub-patch micro-grids.

(a) A compatible but *unstable* staggered patch grid using micro-grids without a centre node (uhvh, huvh, uhhv, huvv in Fig. 2.1.3a) within each macro-cell.

(b) A *stable* staggered patch grid with three of the patches same as in Fig. 2.1.3b, and an additional h-centred patch in place of the empty patch.



only three patches (Fig. 2.1.3b) gives similar accuracy with roughly 25% reduction in computational cost by avoiding the one additional h-patch in Fig. 3.5.1b. Thus, among the two staggered patch grids (Figs. 3.5.1b and 2.1.3b) that constitute stable patch schemes, we choose the staggered patch grid depicted in Fig. 2.1.3b to be the best in terms of computational effort and accuracy. From here on, all the discussions in this thesis are based on the staggered patch grid in Fig. 2.1.3b, with one or more layers of edge nodes (§2.1.3). The chosen staggered patch grid in Fig. 2.1.3b, in addition to having the reflective symmetry, also has the *self-similarity* among the micro- and macro-scales, as discussed in p. 19 of §2.1.2.

The requirement of grid symmetry for the stability of staggered patch schemes, also constrain the number of sub-patch micro-grid intervals n (the number of green grid intervals within a patch in x - and y -directions in Fig. 3.5.1b), such that $n/2$ is an odd number greater than one (i.e., $n \in \{6, 10, 14, 18, \dots\}$).

On the chosen staggered patch grid shown in Fig. 2.1.3b, the macroscale coupling between the patches could be done in various possible ways. The geometry-stability study of §3.5.1 also shows that similar to the geometric asymmetry in patch grids causing the patch scheme instability, the asymmetry in the patch coupling also causes patch scheme instability. The five

staggered patch schemes we study in this thesis are a global spectral interpolation based patch coupling and four local polynomial interpolation based patch coupling (each with different order of interpolation) on a square stencil. The spectral patch scheme and the polynomial patch schemes (on square stencils) couple the patches symmetrically. Hence, the five staggered patch schemes have good stability characteristics as discussed in §§3.5.2 and 3.5.3.

3.5.2 Spectral patch scheme is stable for a range of physical parameters

This subsection shows that the Spectral staggered patch scheme is stable for different physical parameters. Specifically, this subsection shows that the Spectral staggered patch scheme is stable for different physical parameters c_D, c_V (dissipation coefficients), for four combinations of patch scale ratios r , keeping fixed the number of macro-grid intervals N , sub-patch micro-grid intervals n . We establish the patch scheme stability by showing that the maximum real part of the patch scheme eigenvalues is nonpositive, just as the maximum real part of the eigenvalues of the full-domain microscale model. Figure 3.5.2 plots the maximum real parts of versus dissipation coefficients (c_D, c_V) , for the following eigenvalues, for each of the 2646 combinations of the parameters listed in Table 3.5.1 (each subfigure is for one patch scale ratio r).

1. Eigenvalues λ_p^N of the Spectral patch scheme on a staggered patch grid with 10×10 macro-grid intervals ($N = 10$) and each patch containing 6×6 sub-patch micro-grid intervals ($n = 6$).
2. Eigenvalues $\lambda_{m\delta}^\Lambda$ of full-domain microscale model with same value of microscale grid interval $\delta_{m\delta}$ as the sub-patch micro-grid interval δ . That is, $\delta_{m\delta} \equiv L/n_{m\delta} = \delta \equiv l/n \equiv 2Lr/(Nn)$ as $r = l/(2\Delta)$ and $\Delta = L/N$, where $n_{m\delta}$ is the number of full-domain microscale grid intervals and n is the number of sub-patch micro-grid intervals. When the context is clear we drop the subscript $m\delta$ in $n_{m\delta}$ and $\delta_{m\delta}$ for the fine-grid full-domain microscale model.

Figures 3.5.2a and 3.5.2b show that, for non-small values of the patch scale ratios $r \in \{0.01, 0.1\}$, the Spectral patch scheme eigenvalues have the maximum real part $\max \Re(\lambda_p^N) \lesssim 10^{-11}$. Figures 3.5.2a and 3.5.2b also show that the $\max \Re(\lambda)$ is increasing in general for increasing viscous diffusion c_V for all values of drag c_D . The detailed discussion in p. 103 of §3.4, shows that for small grid interval δ the computations in the microscale model are

Table 3.5.1. Section 3.5.2 studies the stability of the Spectral staggered patch scheme using the eigenvalues for all the 1764 combinations of the listed parameters.

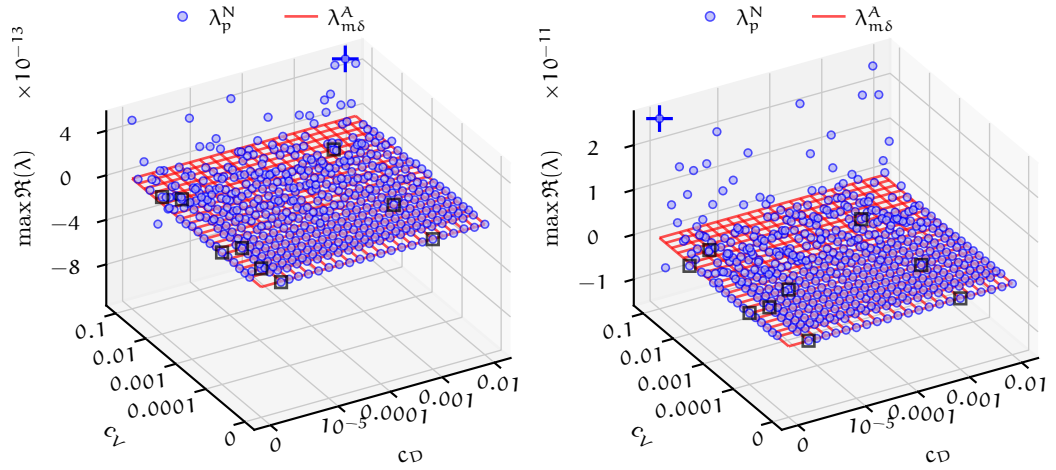
Drag coefficient	$c_D \in \{0\} \cup \{10^{-j} : j = 6, 5.8, 5.6, \dots, 2.2, 2\}$
Viscous coefficient	$c_V \in \{0\} \cup \{10^{-j} : j = 5, 4.8, 4.6, \dots, 1.2, 1\}$
Macro-grid intervals	$N = 10$
Sub-patch micro-grid intervals	$n = 6$
Patch scale ratio	$r \in \{0.0001, 0.001, 0.01, 0.1\}$

sensitive to numerical roundoff errors for large c_V , leading to inaccurate microscale and macroscale eigenvalues. Hence, the increase in $\max \Re(\lambda)$ for increasing c_V in Figs. 3.5.2a and 3.5.2b, is due to the inaccurate eigenvalue computation caused by the inherent sensitivity of the microscale model to numerical roundoff errors. But Figs. 3.5.2a and 3.5.2b show that such increase in $\max \Re(\lambda)$ for increasing c_V is not severe because of the non-small patch scale ratios $r \in \{0.01, 0.1\}$. Thus, Figs. 3.5.2a and 3.5.2b show that, for non-small patch scale ratios $r \gtrsim 0.01$, the maximum real parts of the Spectral patch scheme eigenvalues $\max \Re(\lambda_p^N) \lesssim 10^{-11}$. That is, for non-small patch scale ratios $r \gtrsim 0.01$, the Spectral patch scheme is stable for many combinations of the coefficients of drag c_D and viscous diffusion c_V as listed in Table 3.5.1.

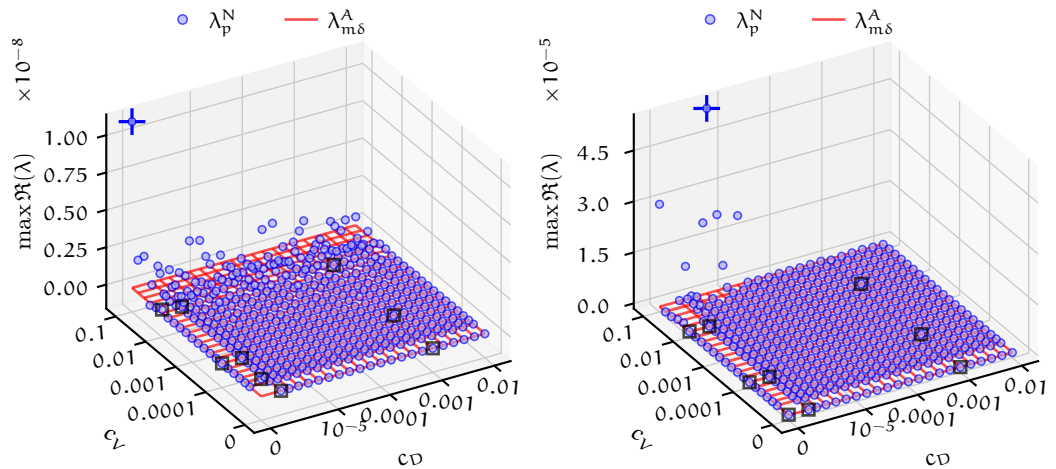
In this paragraph, we argue that the nonnegligible positive maximum real parts (e.g., $\max \Re(\lambda_p^N) \sim 10^{-5}$ in Fig. 3.5.2d) do not reflect an instability of the Spectral patch scheme. Figure 3.5.2d with nonnegligible positive maximum real parts is for small patch scale ratio $r = 0.0001$. When the patch scale ratio is small $r \sim 0.0001$ the sub-patch micro-grid interval $\delta = 2Lr/(Nn) \approx 0.0002Lr/(Nn)$. For example, for the domain size $L = 2\pi$, a patch grid with $N = 10$ macro-grid intervals, and $n = 6$ sub-patch micro-grid intervals, has $\delta \approx 0.0004\pi/60 \approx 2 \cdot 10^{-5}$. Figures 3.5.2d and 3.5.2c also show that the peak values of the maximum real parts (blue plusses) correspond to small c_D and large c_V . The discussion in p. 103 of §3.4, shows that, for small grid interval $\delta \lesssim 10^{-5}$, the combination of inherent sensitivity of the microscale model (for nonnegligible viscous diffusion $c_V \gtrsim 0.0001$) and the sensitivity of eigenvalue computation of near-zero repeated eigenvalues (for small $c_D \lesssim 10^{-6}$), leads to inaccurate near-zero macroscale eigenvalues. For example, Fig. 3.4.3 shows how the numerical roundoff errors in computing near-zero eigenvalues falsely give significantly positive real parts. Thus, the nonnegligible maximum real parts of about 10^{-5} in Figs. 3.5.2d and 3.5.2c are not a reflection of the patch scheme instability.

Figure 3.5.2. Maximum real parts of the eigenvalues for different coefficients of drag c_D and viscous diffusion c_V . The eigenvalues λ_p^N (blue circles) are for the Spectral patch scheme with $N = 10$, $n = 6$ for patch scale ratios $r \in \{0.0001, 0.001, 0.01, 0.1\}$ in each subfigure. The eigenvalues $\lambda_{m\delta}^A$ (red mesh, *all zeros*) are for the corresponding full-domain microscale model. Blue plusses mark the peak value for each subfigure. Black squares show the chosen nine combinations of $c_D \in \{0, 10^{-6}, 0.0001\}$, $c_V \in \{0, 10^{-4}, 0.001\}$ for studying stability for different grid parameters in §3.5.3.

(a) For $r = 0.1$, the peak value of $\max \Re(\lambda_p^N) \approx 5 \cdot 10^{-13}$ at $c_D \approx 0.0063$, $c_V = 0.1$. (b) For $r = 0.01$, the peak value of $\max \Re(\lambda_p^N) \approx 2 \cdot 10^{-11}$ at $c_D = 0$, $c_V = 0.1$.



(c) For $r = 0.001$, the peak value of $\max \Re(\lambda_p^N) \approx 10^{-8}$ at $c_D = 0$, $c_V = 0.1$. (d) For $r = 0.0001$, the peak value of $\max \Re(\lambda_p^N) \approx 5 \cdot 10^{-5}$ (marked by blue plus) at $c_D \approx 4 \cdot 10^{-6}$, $c_V = 0.1$.



As discussed in §3.4, for small grid intervals δ , the numerical eigenvalues of the full-domain microscale model are also sensitive to numerical roundoff errors. Hence, for the full-domain microscale model with the small grid interval δ (equal to the sub-patch grid interval), we expect that the numerical eigenvalues $\lambda_{m\delta}^N$ also have such nonzero maximum real parts. The computation of the numerical eigenvalues $\lambda_{m\delta}^N$ of the full-size numerical Jacobian (§3.2.4) for a full-domain microscale model requires huge computer memory. For example, on a $2\pi \times 2\pi$ domain, a patch grid, with 6×6 macro-grid intervals ($N = 6$) and each patch containing 6×6 sub-patch micro-grid intervals ($n = 6$) and patch scale ratio $r = 0.1$, has the sub-patch micro-grid interval $\delta = 2Lr/(Nn) = 2\pi/180$. The corresponding full-domain microscale model with the same grid interval has 180×180 grid intervals (like the 6×6 staggered grid in Fig. 2.1.1), leading to the 24300×24300 full-size numerical Jacobian (e.g., Fig. 3.2.1). For large N and small patch scale ratio r , the corresponding full-domain microscale model has a very large $(3/16)(Nn/r)^2 \times (3/16)(Nn/r)^2$ full-size numerical Jacobian. So we do not compute numerical eigenvalues $\lambda_{m\delta}^N$ corresponding to the same sub-patch micro-grid interval δ for the cases of large N and small r . We only evaluate the analytic expression (3.2.7) to compute the eigenvalues $\lambda_{m\delta}^A$ of the full-domain microscale model. As the analytic eigenvalues (3.2.7) are not sensitive to numerical roundoff errors, they do not have this nonzero maximum real parts (the red mesh in Fig. 3.5.2).

The nonnegligible positive maximum real parts in Figs. 3.5.2d and 3.5.2c appear nearly random without any trend with the c_D, c_V . There are also maximum real parts as small as 10^{-10} around the regions of c_D, c_V of the peak value of $\max \Re(\lambda)$ (blue plusses), which suggests that when the numerical roundoff errors are small, the maximum real parts of the Spectral patch scheme are as small as 10^{-10} . Hence we take that the eigenvalues of the Spectral patch scheme has negligibly small maximum positive real parts $\sim 10^{-10}$, also for the combination of large viscous diffusion, small drag, and small patch scale ratio. Thus, *the Spectral patch scheme is stable for a wide range of physical parameters (c_D, c_V) and for different patch scale ratios, that is for all the combinations of the parameters in Table 3.5.1.*

3.5.3 All five patch schemes are stable for a range of grid parameters

Section 3.5.2 shows that the Spectral patch scheme is stable for a wide range of physical parameters and patch scale ratios, for a staggered patch grid with $N = 10$ macro-grid intervals, and $n = 6$ sub-patch micro-grid inter-

Table 3.5.2. Section 3.5.3 studies the stability of the staggered patch schemes using the eigenvalues for all the 4 374 combinations of the listed parameters.

Patch schemes	Spectral, Square-p2, Square-p4, Square-p6, and Square-p8
Drag coefficient	$c_D \in \{0, 10^{-6}, 0.001\}$
Viscous coefficient	$c_V \in \{0, 10^{-4}, 0.01\}$
Macro-grid intervals	$N \in \{6, 10, 14\}$ for Spectral scheme, $N \in \{6, 10, 14, 18, 22, 26\}$ for polynomial schemes.
Sub-patch micro-grid intervals	$n \in \{6, 10\}$
Patch scale ratio	$r \in \{0.0001, 0.001, 0.01, 0.1\}$

vals. This subsection characterises the stability of all *the five staggered patch schemes* (Spectral, Square-p2, Square-p4, Square-p6, and Square-p8), for a *range of grid parameters*, macro-grid intervals N , sub-patch micro-grid intervals n , and patch scale ratio r , for nine combinations of the physical parameters c_D, c_V .

From the geometry-stability study (§3.5.1) we find the patch schemes on many asymmetric patch grids to be unstable, with large positive real parts in the order of tens and hundreds. Such instabilities may come from the eigenvalues of either the macroscale modes or the microscale modes. So, this subsection studies the maximum real parts of the numerical eigenvalues of the five staggered patch schemes, separately for the microscale and macroscale modes ($\max \Re(\lambda_{p\mu}^N)$ and $\max \Re(\lambda_{pM}^N)$), for the 4 374 combinations of the parameters listed in Table 3.5.2. The stability study in this subsection is for the nine combinations of $c_D \in \{0, 10^{-6}, 0.0001\}$, $c_V \in \{0, 10^{-4}, 0.001\}$ in Table 3.5.2, which we consider as a reasonable representative of the wide range of c_D and c_V from §3.5.2 for the Spectral patch scheme (black squares in Fig. 3.5.2).

Table 3.5.3 presents the peak maximum real parts of the patch scheme eigenvalues over all the combinations of c_D, c_V and N in Table 3.5.2, for different number of sub-patch intervals n and patch scale ratios r . Table 3.5.3 shows that, for non-small values of the patch scale ratios $r \in \{0.01, 0.1\}$, both the microscale and macroscale eigenvalues of all the five patch schemes have the maximum real parts less than about $6 \cdot 10^{-10}$. Thus, *for non-small patch scale ratios $r \gtrsim 0.01$, all the five patch schemes are stable* for all the combinations of the drag c_D , viscous diffusion c_V , number of macro-grid intervals N and the number of sub-patch micro-grid intervals n listed in Table 3.5.2.

For smaller patch scale ratios $r \in \{0.0001, 0.001\}$, some of the patch

Table 3.5.3. Overall maximum real parts of the microscale and macroscale eigenvalues ($\lambda_{p\mu}^N, \lambda_{pM}^N$) over the five patch schemes and all the combinations of c_D, c_V and N in Table 3.5.2, for different number of sub-patch intervals n and patch scale ratios r . Red colour highlights the largest value in each column separately for microscale and macroscale eigenvalues (based on full precision when the values are same with one significant figure).

		Patch scale ratio r			
		0.0001	0.001	0.01	0.1
Overall $\max \Re(\lambda_{p\mu}^N)$	$n = 6$	$2 \cdot 10^{-6}$	$2 \cdot 10^{-8}$	$2 \cdot 10^{-10}$	$2 \cdot 10^{-12}$
	$n = 10$	$5 \cdot 10^{-6}$	$7 \cdot 10^{-8}$	$6 \cdot 10^{-10}$	$7 \cdot 10^{-12}$
Overall $\max \Re(\lambda_{pM}^N)$	$n = 6$	$7 \cdot 10^{-6}$	$8 \cdot 10^{-9}$	$3 \cdot 10^{-11}$	10^{-12}
	$n = 10$	$3 \cdot 10^{-5}$	$2 \cdot 10^{-8}$	$2 \cdot 10^{-10}$	$3 \cdot 10^{-12}$

schemes have nonnegligible maximum real parts of the order of 10^{-5} for some combination of the physical parameters (c_D, c_V) and grid parameters N, n , which is investigated in following paragraphs in this subsection.

Figure 3.5.3 plots the maximum real parts of the microscale and macroscale eigenvalues ($\max \Re(\lambda_{p\mu}^N)$ and $\max \Re(\lambda_{pM}^N)$) for the combinations of the parameters in Table 3.5.2, with $c_D = 0$. A similar figure for $c_D = 10^{-6}$ is visually very similar to Fig. 3.5.3, hence we omit it here. Figure 3.5.4 plots the $\max \Re(\lambda_{p\mu}^N)$ and $\max \Re(\lambda_{pM}^N)$ for the combinations of the parameters in Table 3.5.2, with $c_D = 0.001$. Tables 3.5.4 and 3.5.5 separately present the overall maximum real parts of the microscale and macroscale eigenvalues over the five patch schemes and all the combinations of N and n in Table 3.5.2, for different patch scale ratios r .

Subfigures on the left of Figs. 3.5.3 and 3.5.4 and Table 3.5.4 show that only for the case of $c_D = c_V = 0$ (ideal wave), the maximum real part of the microscale eigenvalues are positive (all red highlighted values in Table 3.5.4). These maximum positive real parts increase with the increasing number of macro-grid intervals N and/or decreasing patch scale ratio r (i.e., decreasing sub-patch micro-grid interval δ). As in Fig. 3.2.5, among the eigenvalues for ideal there are $N^2(3n^2/16 - n/2 + 1/2) + 2$ zero eigenvalues (not just real part zero). For $N = 6, 10, 14, 18, 22, 26$ with $n = 6$, the number of zero eigenvalues are 155, 427, 835, 1379, 2059, 2875 respectively. The detailed discussions in p. 103 of §3.4, shows that, for small sub-patch grid interval $\delta \lesssim 10^{-5}$, the sensitivity of eigenvalue computation for near-zero repeated eigenvalues (for small $c_D \lesssim 10^{-6}$), leads to inaccurate eigenvalues. Hence, for ideal waves, the computation of very many repeated zero eigenvalues of the patch schemes, for small patch scale ratios is inaccurate lead-

Figure 3.5.3. The maximum real part of the microscale and macroscale eigenvalues ($\max \Re(\lambda_{p,\mu}^N)$ on left, $\max \Re(\lambda_{p,M}^N)$ on right) for the coefficients $c_D = 0$ and $c_V = 0, 0.0001, 0.01$ (each row). Markers indicate different patch schemes (Spectral, Square-p2, Square-p4, Square-p6, and Square-p8). Colours indicate the different number of sub-patch intervals n .

■ $n=6$ ■ $n=10$ • Spectral -+ p2 × p4 □ p6 ○ p8 — difference

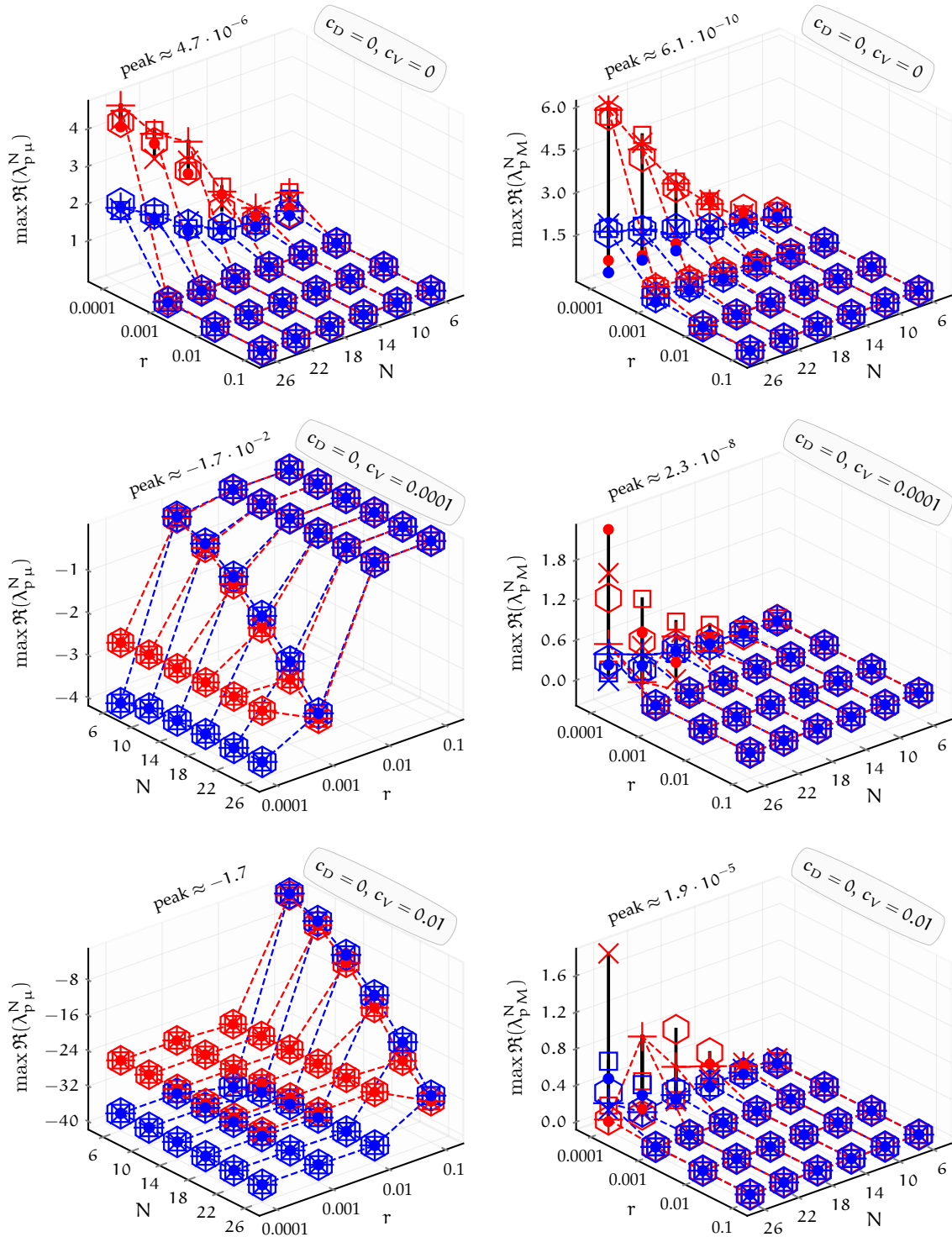


Figure 3.5.4. The maximum real part of the microscale and macroscale eigenvalues ($\max \Re(\lambda_{p,\mu}^N)$ on left, $\max \Re(\lambda_{p,M}^N)$ on right) for the coefficients $c_D = 0.001$ and $c_V = 0, 0.0001, 0.01$ (each row). Markers indicate different patch schemes (Spectral, Square-p2, Square-p4, Square-p6, and Square-p8). Colours indicate the different number of sub-patch intervals n .

■ $n=6$ ■ $n=10$ • Spectral -+ p2 × p4 □ p6 ○ p8 — difference

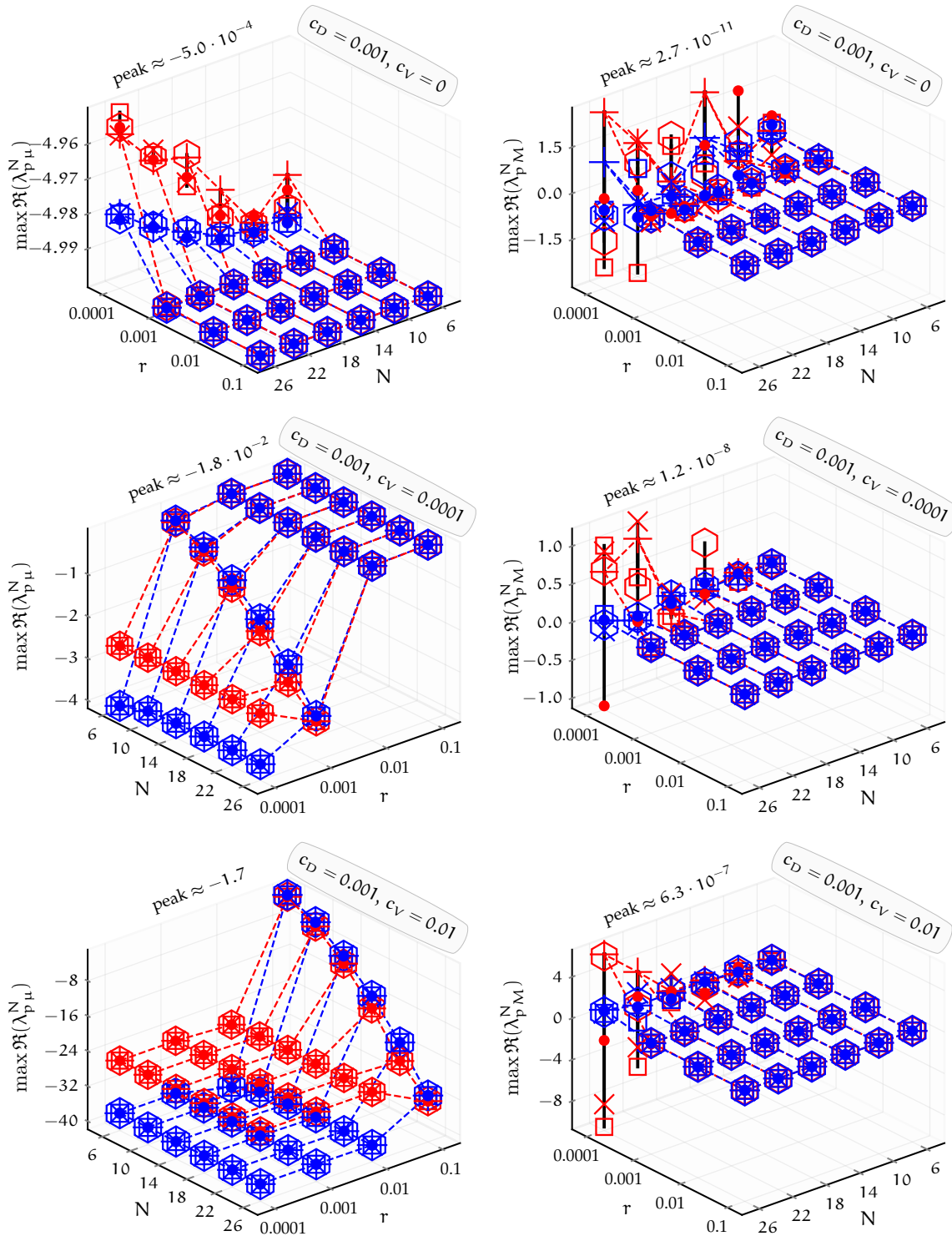


Table 3.5.4. Overall maximum real parts of the microscale eigenvalues $\lambda_{p\mu}^N$ over the five patch schemes and all the combinations of N and n in [Table 3.5.2](#), for different patch scale ratios r . Red colour highlights the largest value in each column (based on full precision when the values are same with one significant figure).

	Patch scale ratio r			
	0.0001	0.001	0.01	0.1
$c_D = 0, c_V = 0$	$5 \cdot 10^{-6}$	$7 \cdot 10^{-8}$	$6 \cdot 10^{-10}$	$7 \cdot 10^{-12}$
$c_D = 0, c_V = 0.0001$	-3000	-200	-2	-0.02
$c_D = 0, c_V = 0.01$	-3	-3	-3	-2
$c_D = 10^{-6}, c_V = 0$	$4 \cdot 10^{-6}$	$4 \cdot 10^{-7}$	$5 \cdot 10^{-7}$	$5 \cdot 10^{-7}$
$c_D = 10^{-6}, c_V = 0.0001$	-3000	-200	-2	-0.02
$c_D = 10^{-6}, c_V = 0.01$	-3	-3	-3	-2
$c_D = 0.001, c_V = 0$	-0.0005	-0.0005	-0.0005	-0.0005
$c_D = 0.001, c_V = 0.0001$	-3000	-200	-2	-0.02
$c_D = 0.001, c_V = 0.01$	-3	-3	-3	-2

ing to nonnegligible positive real parts. So, we take that the nonnegligible positive real parts of $5 \cdot 10^{-6}$, $4 \cdot 10^{-6}$ and $7 \cdot 10^{-8}$ in [Table 3.5.4](#), are due to the inaccurate eigenvalue computation of near-zero repeated eigenvalues for small drag $c_D \lesssim 10^{-6}$ and zero viscous diffusion. Thus, *the microscale modes of the five staggered patch schemes are stable* for all the combinations of the drag c_D , viscous diffusion c_V , number of macro-grid intervals N , number of sub-patch micro-grid intervals n and the patch scale ratios r listed in [Table 3.5.2](#).

The following are key additional points from the subfigures on the left of [Figs. 3.5.3](#) and [3.5.4](#) and [Table 3.5.4](#) for the microscale eigenvalues.

- Maximum positive real parts of the microscale eigenvalues $\lambda_{p\mu}^N$ of all five patch schemes are approximately the same (all within the same order of magnitude). For each combination of the parameters N, r, c_D, c_V , we computed the standard deviation of maximum positive real parts $\lambda_{p\mu}^N$ over the five patch schemes (i.e. vertical deviation of the points in [Figs. 3.5.3](#) and [3.5.4](#) and [Table 3.5.4](#)). The overall maximum standard deviation (i.e., variation among the patch schemes) over all the parameter combinations in [Table 3.5.2](#) is $3 \cdot 10^{-7}$. This maximum standard deviation corresponds to the largest $N = 26$ and the smallest $r = 0.0001$ in [Table 3.5.2](#). As [§3.4](#) shows, these varia-

Table 3.5.5. Overall maximum real parts of the macroscale eigenvalues λ_{pM}^N over the five patch schemes and all the combinations of N and n in [Table 3.5.2](#), for different patch scale ratios r . Red colour highlights the largest value in each column (based on full precision when the values are same with one significant figure).

	Patch scale ratio r			
	0.0001	0.001	0.01	0.1
$c_D = 0, c_V = 0$	$6 \cdot 10^{-10}$	$6 \cdot 10^{-11}$	$6 \cdot 10^{-12}$	$6 \cdot 10^{-13}$
$c_D = 0, c_V = 0.0001$	$2 \cdot 10^{-8}$	$2 \cdot 10^{-10}$	$5 \cdot 10^{-12}$	$3 \cdot 10^{-13}$
$c_D = 0, c_V = 0.01$	$2 \cdot 10^{-5}$	$2 \cdot 10^{-8}$	$2 \cdot 10^{-10}$	$3 \cdot 10^{-12}$
$c_D = 10^{-6}, c_V = 0$	$3 \cdot 10^{-11}$	$2 \cdot 10^{-12}$	$2 \cdot 10^{-13}$	$4 \cdot 10^{-14}$
$c_D = 10^{-6}, c_V = 0.0001$	10^{-8}	$2 \cdot 10^{-10}$	$2 \cdot 10^{-12}$	$4 \cdot 10^{-13}$
$c_D = 10^{-6}, c_V = 0.01$	$3 \cdot 10^{-5}$	$4 \cdot 10^{-9}$	$9 \cdot 10^{-11}$	$2 \cdot 10^{-12}$
$c_D = 0.001, c_V = 0$	$3 \cdot 10^{-11}$	$3 \cdot 10^{-12}$	$3 \cdot 10^{-13}$	$4 \cdot 10^{-14}$
$c_D = 0.001, c_V = 0.0001$	10^{-8}	10^{-10}	$2 \cdot 10^{-12}$	$7 \cdot 10^{-13}$
$c_D = 0.001, c_V = 0.01$	$6 \cdot 10^{-7}$	$6 \cdot 10^{-9}$	$2 \cdot 10^{-10}$	10^{-12}

tions are due to eigenvalue computation being affected by numerical roundoff errors.

- For the same c_D , increasing the viscous diffusion c_V pushes real parts of the microscale eigenvalues to larger negative values, increasing the spectral gap. The increasingly large negative values of $\max \Re(\lambda_{p\mu}^N)$ with increasing c_V is also evident in the complex plane eigenvalue plots. For example the microscale eigenvalues in the clusters 4, 5 in the complex plane plot of [Fig. 3.2.4](#) for $c_D = 10^{-6}$, $c_V = 0$ move to the left and become the clusters 6, 7 in [Fig. 3.2.2](#) for $c_D = 10^{-6}$, $c_V = 0.0001$.
- Decreasing the patch scale ratio r also leads to large negative values of $\max \Re(\lambda_{p\mu}^N)$, leading to a large spectral gap.

Subfigures on the right of [Figs. 3.5.3](#) and [3.5.4](#) and [Table 3.5.5](#) show that the macroscale eigenvalues have large $\max \Re(\lambda_{p\mu}^N \gtrsim 10^{-8})$, only for the combinations of $c_V \gtrsim 0.0001$, the small patch scale ratio $r \lesssim 0.001$, and large number of macroscale intervals N (i.e., for small sub-patch micro-grid interval δ). For the same c_D , increasing the viscous diffusion c_V slightly increases the maximum positive real parts of the macroscale eigenvalues. The discussion in [p. 103](#) of [§3.4](#), shows that, for small grid interval $\delta \lesssim 10^{-5}$,

the combination of inherent sensitivity of the microscale model (for non-negligible viscous diffusion $c_V \gtrsim 0.0001$) and the sensitivity of eigenvalue computation of near-zero repeated eigenvalues (for small $c_D \lesssim 10^{-6}$), leads to inaccurate near-zero macroscale eigenvalues. For example, Fig. 3.4.3 shows how the numerical roundoff errors in computing near-zero eigenvalues falsely give positive real parts. So, we take that the maximum real parts of $5 \cdot 10^{-6}$, $4 \cdot 10^{-6}$ and $7 \cdot 10^{-8}$ in Table 3.5.5 for small patch scale ratios $r \in \{0.0001, 0.001\}$, are due to the inaccurate eigenvalue computation due to the inherent sensitivity of the microscale model (for nonnegligible viscous diffusion $c_V \gtrsim 0.0001$) and the sensitivity of eigenvalue computation of near-zero repeated eigenvalues (for small $c_D \lesssim 10^{-6}$). Thus, *the macroscale modes of the five staggered patch schemes are stable* for all the combinations of the drag c_D , viscous diffusion c_V , number of macro-grid intervals N , number of sub-patch macro-grid intervals n and the patch scale ratios r listed in Table 3.5.2.

The following are key additional points from the subfigures on the right of Figs. 3.5.3 and 3.5.4 and Table 3.5.5 for the microscale eigenvalues.

- Maximum positive real parts of the macroscale eigenvalues λ_{pM}^N of all five patch schemes are approximately the same (all within the same order of magnitude). An analysis similar to that (in p. 118 of this subsection) for the microscale eigenvalues $\lambda_{p\mu}^N$, based on the overall maximum standard deviation (i.e., variation among the patch schemes) confirms this trend. As discussed in §3.4 these discrepancies are due to eigenvalue computation being affected by numerical roundoff errors.
- For the same c_D , increasing the viscous diffusion c_V leads to large maximum real parts of the macroscale eigenvalues. Decreasing the patch scale ratio also leads to increasing maximum real parts. As discussed in p. 103 of §3.4 these increasing maximum real parts are due to inherent sensitivity of the microscale model to numerical roundoff errors, for nonnegligible viscous diffusion $c_V \gtrsim 0.0001$ and for small grid interval δ .

The previous paragraphs establish the stability of the five chosen staggered patch schemes separately for the microscale and macroscale eigenvalues. Those detailed arguments show that the observed maximum real parts of the eigenvalues are due numerical round-off errors in the eigenvalue computations; that is, due to either the inherent sensitivity of the microscale model, or the sensitivity of eigenvalue computation for near-zero repeated eigenvalues, or both. Despite the different amount of patch

coupling computations, all the five (Spectral and four polynomial) patch schemes agree within the same order of magnitude. This agreement among the patch schemes also shows that the maximum positive real parts do not reflect any patch scheme instability. The insensitivity of the patch schemes to numerical roundoff errors is also shown separately in §3.4. In addition, the patch schemes are stable in our time simulations (§3.7.5) even for large number macro-grid intervals N and small patch scale ratios r , and for finite initial perturbations. Thus, *all the five staggered patch schemes (Spectral, Square-p2, Square-p4, Square-p6, and Square-p8) are stable.*

3.6 Staggered patch schemes are consistent

This section shows that the staggered patch schemes are consistent with the given microscale model. Subsections of this section establish the consistency of the patch schemes by comparing the macroscale eigenvalues of the patch scheme with the corresponding eigenvalues of the full-domain microscale model for increasingly finer patch grids. Section 3.6.1 shows that the Spectral patch scheme is uniformly accurate with little dependence on the macro-grid interval Δ . Section 3.6.2 shows that the polynomial patch schemes are consistent to the order of the polynomial interpolation with decreasing macro-grid interval Δ .

The full-domain microscale model (3.1.1) is consistent, when the discretized equations (3.1.1) approach to the corresponding PDEs (3.0.1), as the grid interval $\delta \rightarrow 0$ (on the full-domain grid Fig. 2.1.1). Such standard definition of consistency (e.g., Ferziger et al. 2020, p. 34) is useful for analysing the full-domain discrete systems whose goal is to accurately represent the corresponding PDEs. But the goal of our multiscale staggered patch scheme (3.1.3) is to accurately represent the *macroscale* waves of the corresponding *discrete* full-domain microscale model (§3.2.2). Hence we define a staggered patch scheme to be consistent, when the macroscale characteristics of the patch scheme (e.g., (3.1.3)) approach to the corresponding macroscale characteristics of the full-domain microscale model (e.g., (3.1.1)), as the macro-grid interval $\Delta \rightarrow 0$ (on the patch grid Fig. 2.1.3b).

We show the consistency of the staggered patch schemes by demonstrating that the macroscale eigenvalues λ_{pM}^N of the patch schemes *converge* to the macroscale eigenvalues of the corresponding full-domain microscale model as $\Delta \rightarrow 0$. The eigenvalue spectra in Figs. 3.2.2 to 3.2.7, show that the staggered patch scheme macroscale eigenvalues λ_{pM}^{NE1} (e.g., clusters 1, 2, 3, 4, 5 in Fig. 3.2.9) are qualitatively similar, and visually close, to the corresponding macroscale eigenvalues $\lambda_{m\delta}^\Delta$ of the fine-grid full-domain

Table 3.6.1. Section 3.6 studies the consistency of the patch schemes using eigenvalues for all the 2 160 combinations of the listed parameters.

Patch schemes	Spectral, Square-p2, Square-p4, Square-p6, and Square-p8
Drag coefficient	$c_D \in \{0, 10^{-6}, 0.001\}$
Viscous coefficient	$c_V \in \{0, 10^{-4}, 0.01\}$
Macro-grid intervals	$N \in \{6, 10, 14, 18, 22, 26\}$
Sub-patch micro-grid intervals	$n \in \{6, 10\}$
Patch scale ratio	$r \in \{0.0001, 0.001, 0.01, 0.1\}$

microscale model (by varying degrees depending upon the specific staggered patch scheme, N , n , and r). To numerically quantify the discrepancy between the macroscale eigenvalues λ_{pM}^N of staggered patch scheme and the corresponding macroscale eigenvalues $\lambda_{m\delta}^A$ of fine grid full domain microscale model, we define the *eigenvalue error* for the *macroscale* wavenumber (k_x, k_y) as

$$\epsilon^{k_x, k_y} = \|\lambda_{pM}^N(k_x, k_y) - \lambda_{m\delta}^A(k_x, k_y)\| / \|\lambda_{m\delta}^A(k_x, k_y)\|, \quad (3.6.1)$$

where $\|\cdot\|$ is the Euclidean norm of the three element complex vectors of eigenvalues λ_{pM}^N and $\lambda_{m\delta}^A$ (three macroscale eigenvalues for each macroscale wavenumber).

To assess the patch scheme consistency in this section (i.e., eigenvalue convergence), we compute the three eigenvalue errors $\epsilon^{1,0}$, $\epsilon^{1,1}$ and $\epsilon^{2,1}$, for the patch schemes on different staggered patch grids, corresponding to the three macroscale (angular) wavenumbers $(k_x, k_y) \in \{(1, 0), (1, 1), (2, 1)\}$ over the $2\pi \times 2\pi$ non-dimensional domain. The smallest wavenumber $(1, 0)$ corresponds to the largest wavelength of $(2\pi, 0)$ over the chosen $2\pi \times 2\pi$ domain. Specifically, to show the consistency of the staggered patch schemes, this section computes the three macroscale eigenvalue errors $\epsilon^{1,0}$, $\epsilon^{1,1}$ and $\epsilon^{2,1}$ for the 2 160 combinations of the parameters listed in Table 3.6.1.

Computing the three element vector of eigenvalues $\lambda_{m\delta}^A(k_x, k_y)$ in the eigenvalue error (3.6.1), is straightforward, we evaluate the analytic expression (3.2.7) to get three eigenvalues for each macroscale wavenumber $(k_x, k_y) \in \{(1, 0), (1, 1), (2, 1)\}$. Among the numerical eigenvalues λ_p^N , finding which three eigenvalues correspond to the three eigenvalues in $\lambda_{m\delta}^A(k_x, k_y)$ (for the same macroscale wavenumber), is not straightforward. The *method of wavenumber-wise scale separation* in §3.3 classifies the eigenvalues wavenumber-wise and separates as microscale and macroscale patch scheme eigenvalues. The method of wavenumber-wise scale separation in §3.3 gives the re-

quired eigenvalues as the following 3D arrays (analytic eigenvalues only for $N \leq 14$ for Spectral patch scheme)

1. An $N/2 \times N/2 \times 3$ array of *analytic* eigenvalues $\lambda_{m\delta}^A$ of the full-domain microscale model.
2. An $N/2 \times N/2 \times 3$ array of macroscale *analytic* patch scheme eigenvalues λ_{pM}^{NE1} .
3. An $N/2 \times N/2 \times 3$ array of macroscale *numerical* patch scheme eigenvalues λ_{pM}^N .

The third dimension of these three arrays establishes the wavenumber-wise correspondence among the three eigenvalues $\lambda_{m\delta}^A$, λ_{pM}^{NE1} and λ_{pM}^N . For any macroscale wavenumber (k_x, k_y) resolved on a patch grid, each of the three elements along the third dimension of the eigenvalues $\lambda_{m\delta}^A$ and λ_{pM}^N gives the required three element vectors $\underline{\lambda}_{m\delta}^A$ and $\underline{\lambda}_{pM}^N$ in the patch scheme eigenvalue error (3.6.1).

A staggered patch grid with $N \times N$ macro-grid intervals, irrespective of which patch scheme, resolves $3N^2/4$ macroscale modes (p. 74 of §3.2.6). That is, with increasing macro-grid intervals N , all the patch schemes resolve an increasing number of macroscale modes of increasing wavenumbers. A patch grid with $N = 6$ macro-grid intervals resolves nine macroscale wavenumbers such that $k_x, k_y \in \{-1, 0, 1\}$. For $N = 6$, there are no macroscale eigenvalues corresponding to wavenumber $(k_x, k_y) = (2, 1)$, and so the eigenvalue error $\epsilon^{2,1}$ is computed only for $N \geq 10$.

3.6.1 Spectral patch scheme is uniformly accurate

With the highly accurate global spectral interpolation (§2.2.1), we expect the *Spectral patch scheme to resolve the macroscale modes exactly* (within numerical roundoff errors), irrespective of the number of macro-grid intervals N (e.g., the complex plane eigenvalue plot in Figs. 3.2.6 and 3.2.7). That is, the Spectral patch scheme is uniformly accurate without any dependence on the macro-grid interval Δ . To confirm this exactness, this subsection shows that the accuracy of the macroscale modes indeed does not deteriorate with decreasing macro-grid interval Δ (increasing N). Specifically, this subsection studies this exactness via the eigenvalue errors $\epsilon^{1,0}$, $\epsilon^{1,1}$ and $\epsilon^{2,1}$ of the Spectral patch scheme for all the 432 combinations of the parameters c_D, c_V, N, n, r listed in Table 3.6.1.

Tables 3.6.2 to 3.6.4 shows the maximum eigenvalue errors $\epsilon^{1,0}$, $\epsilon^{1,1}$ and $\epsilon^{2,1}$ respectively, over six different number of macro-grid intervals N

Table 3.6.2. Maximum logarithmic eigenvalue error $\max_N \log_{10}(\epsilon^{1,0})$ for the Spectral staggered patch scheme over six different number of macro-grid intervals N in Table 3.6.1. Red colour highlights $\epsilon^{1,0} > 10^{-8}$. Overall maximum $\epsilon^{1,0} = 10^{-5.1}$.

c_D, c_V	Patch scale ratio r							
	0.0001		0.001		0.01		0.1	
	$n = 6$	$n = 10$	$n = 6$	$n = 10$	$n = 6$	$n = 10$	$n = 6$	$n = 10$
0, 0	-10	-9.3	-12	-11	-12	-12	-12	-12
0, 0.0001	-9.4	-8.4	-11	-10	-12	-12	-12	-12
0, 0.01	-5.7	-5.3	-8.5	-8	-11	-10	-12	-12
$10^{-6}, 0$	-9.9	-9.1	-11	-10	-12	-12	-12	-12
$10^{-6}, 0.0001$	-9	-8.3	-11	-10	-12	-12	-12	-12
$10^{-6}, 0.01$	-5.9	-5.2	-8.7	-8.2	-11	-10	-12	-12
0.001, 0	-10	-9.2	-11	-11	-12	-11	-12	-12
0.001, 0.0001	-9	-8.2	-11	-10	-12	-12	-12	-12
0.001, 0.01	-5.7	-5.1	-8.4	-8	-11	-10	-12	-12

Figure 3.6.1. Worst case eigenvalue errors $\epsilon^{1,0}$ (log scale) of the Spectral staggered patch scheme ($\max \log_{10}(\epsilon^{1,0}) \approx -5.1$ in Table 3.6.2), for $c_D = 0.001$, $c_V = 0.01$, $n = 10$, for different macro-grid intervals Δ and patch scale ratio r .

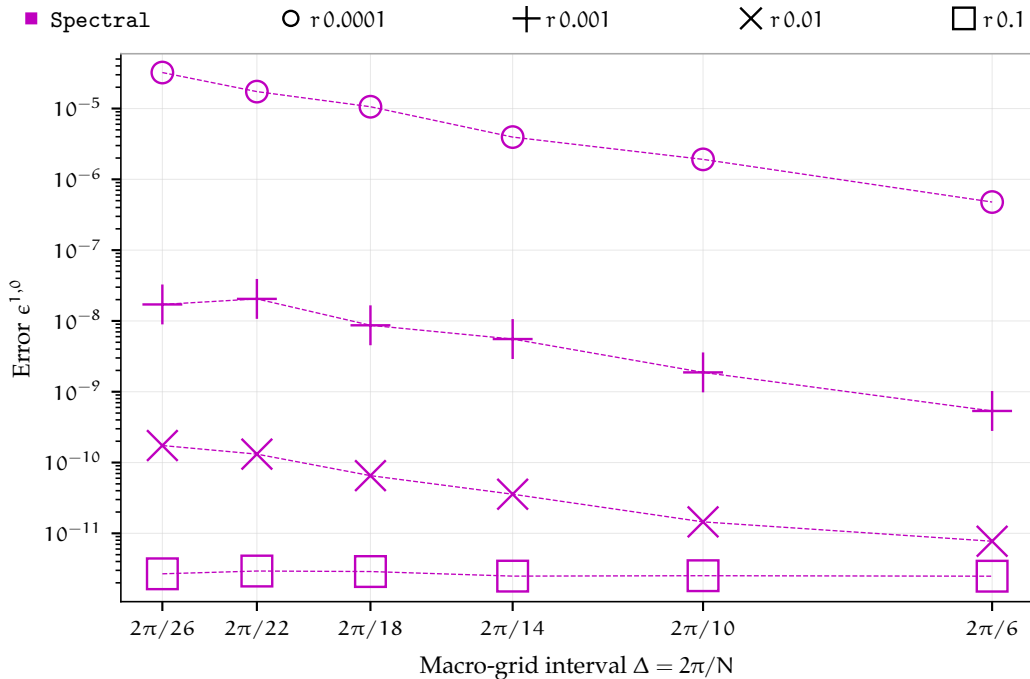


Table 3.6.3. Maximum logarithmic eigenvalue error $\max_N \log_{10}(\epsilon^{1,1})$ for the Spectral staggered patch scheme over six different number of macro-grid intervals N in Table 3.6.1. Red colour highlights $\epsilon^{1,1} > 10^{-8}$. Overall maximum $\epsilon^{1,1} = 10^{-4.9}$.

c_D, c_V	Patch scale ratio r							
	0.0001		0.001		0.01		0.1	
	$n = 6$	$n = 10$	$n = 6$	$n = 10$	$n = 6$	$n = 10$	$n = 6$	$n = 10$
0, 0	-10	-9.6	-12	-11	-12	-12	-12	-12
0, 0.0001	-9.4	-8.2	-11	-10	-12	-11	-12	-12
0, 0.01	-5.6	-5.5	-8.7	-8.5	-11	-10	-12	-12
$10^{-6}, 0$	-11	-9.7	-12	-11	-12	-12	-12	-12
$10^{-6}, 0.0001$	-9.2	-8.5	-11	-10	-12	-12	-12	-12
$10^{-6}, 0.01$	-5.5	-5.1	-8.6	-7.9	-11	-10	-12	-12
0.001, 0	-10	-9.6	-12	-11	-12	-12	-12	-12
0.001, 0.0001	-9.2	-8.2	-11	-11	-12	-12	-12	-12
0.001, 0.01	-5.8	-4.9	-8.6	-8.2	-11	-11	-12	-12

Figure 3.6.2. Worst case eigenvalue errors $\epsilon^{1,1}$ (log scale) of the Spectral staggered patch scheme ($\max \log_{10}(\epsilon^{1,1}) \approx -4.9$ in Table 3.6.3), for $c_D = 0.001$, $c_V = 0.01$, $n = 10$, for different macro-grid intervals Δ and patch scale ratio r .

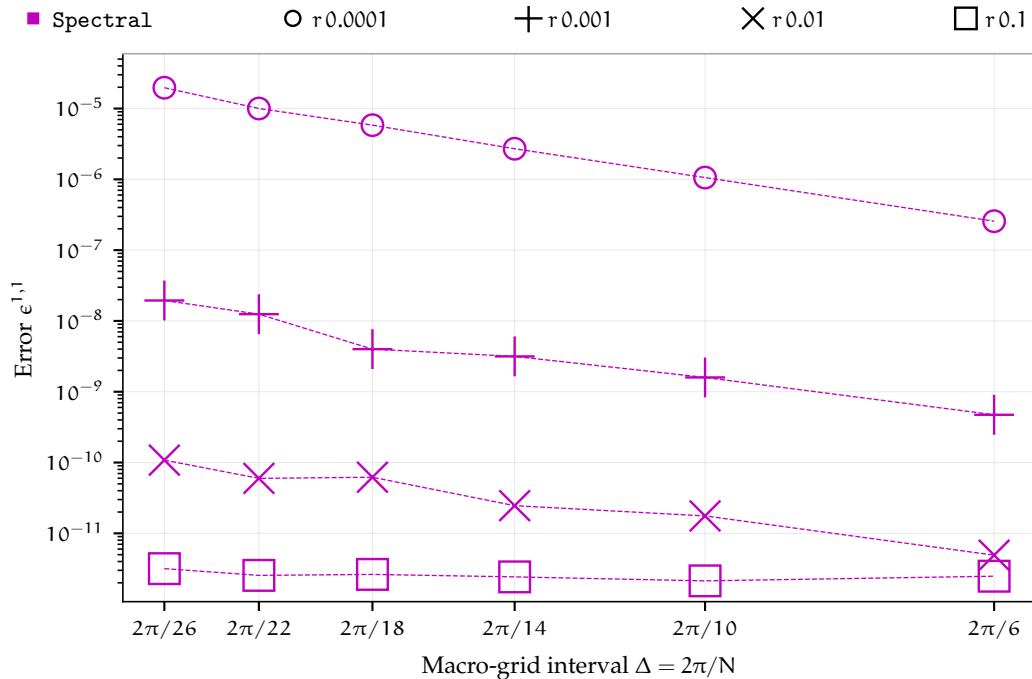
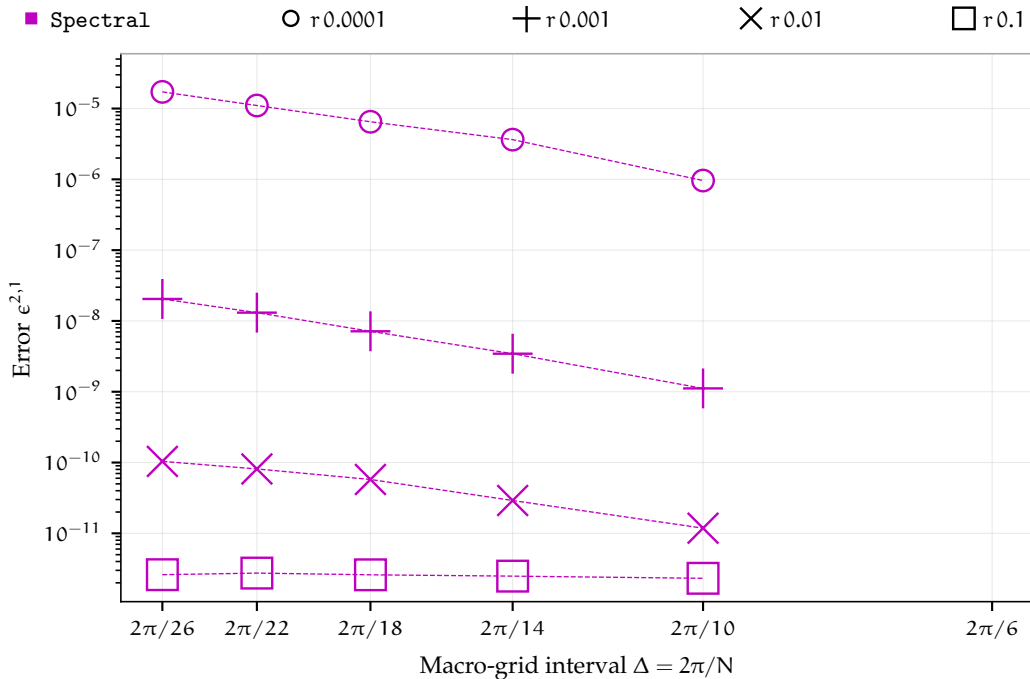


Table 3.6.4. Maximum logarithmic eigenvalue error $\max_N \log_{10}(\epsilon^{2,1})$ for the Spectral staggered patch scheme over six different number of macro-grid intervals N in Table 3.6.1. Red colour highlights $\epsilon^{2,1} > 10^{-8}$. Overall maximum $\epsilon^{2,1} = 10^{-5.1}$.

c_D, c_V	Patch scale ratio r							
	0.0001		0.001		0.01		0.1	
	$n = 6$	$n = 10$	$n = 6$	$n = 10$	$n = 6$	$n = 10$	$n = 6$	$n = 10$
0, 0	-11	-11	-12	-12	-12	-12	-12	-12
0, 0.0001	-9.2	-8.9	-11	-11	-12	-12	-12	-12
0, 0.01	-5.8	-5.3	-8.8	-8.3	-11	-11	-12	-12
$10^{-6}, 0$	-11	-10	-12	-12	-12	-12	-12	-12
$10^{-6}, 0.0001$	-9.6	-9	-11	-11	-12	-12	-12	-12
$10^{-6}, 0.01$	-5.9	-5.1	-9	-8.4	-11	-11	-12	-12
0.001, 0	-11	-11	-12	-12	-12	-12	-12	-12
0.001, 0.0001	-9.4	-8.8	-11	-10	-12	-12	-12	-12
0.001, 0.01	-6	-5.3	-8.9	-8.4	-11	-11	-12	-12

Figure 3.6.3. Worst case eigenvalue errors $\epsilon^{2,1}$ (log scale) of the Spectral staggered patch scheme ($\max \log_{10}(\epsilon^{2,1}) \approx -5.1$ in Table 3.6.4), for $c_D = 10^{-6}$, $c_V = 0.01$, $n = 10$, for different macro-grid intervals Δ and patch scale ratio r . No eigenvalue errors $\epsilon^{2,1}$ for $N = 6$ (p. 123 of §3.6).



in Table 3.6.1. For the cases of the largest eigenvalue error in each table, Figures 3.6.1 to 3.6.3 plot the variation of the eigenvalue errors $\epsilon^{1,0}$, $\epsilon^{1,1}$ and $\epsilon^{2,1}$ respectively, with the number of macro-grid intervals N . Tables 3.6.2 to 3.6.4 show that, except the red highlighted values for the combination of the small patch scale ratio $r \sim 0.0001$, and large viscous diffusion $c_V = 0.01$, all the three eigenvalue errors are about 10^{-8} or smaller. Figures 3.6.1 to 3.6.3 show that the eigenvalue errors of about 10^{-8} corresponding to the small patch scale ratios $r \lesssim 0.01$ increase with increasing number of macro-grid intervals N . Thus, Tables 3.6.2 to 3.6.4 and Figures 3.6.1 to 3.6.3 show that the eigenvalue errors of the Spectral patch scheme are small (about 10^{-8} or smaller), except for the combination of the small patch scale ratio r , large number of macro-grid intervals N and large viscous diffusion c_V . Both small patch scale ratio r and a large number of macro-grid intervals N lead to small sub-patch micro-grid interval δ . Hence, these eigenvalue errors (about 10^{-8} or larger) are due to numerical roundoff errors inherent to the microscale model, for nonnegligible viscous diffusion $c_V \gtrsim 0.0001$ and for small grid interval δ (p. 103 of §3.4 discuss this sensitivity in more detail). So we take that the high accuracy of the Spectral patch scheme eigenvalues do not deteriorate with decreasing macro-grid interval Δ (increasing N). That is, *the Spectral patch scheme itself is uniformly accurate without any dependence on the macro-grid interval Δ .*

3.6.2 The four polynomial patch schemes are consistent

Figures 3.2.8 and 3.2.9 of §3.2.6 present the eigenvalue spectra for the Square-p2 patch scheme with $N = 6, 10$ respectively, keeping all other parameters n, r, c_D, c_V the same. Comparing Figs. 3.2.8 and 3.2.9 suggest that, keeping L, r , and n the same, increasing the number of macro-grid intervals N (decreasing the macro-grid interval Δ) makes the macroscale eigenvalues λ_p^{NE1} of the patch scheme become increasingly close to the corresponding macroscale eigenvalues $\lambda_{m\delta}^A$ of the full-domain microscale model. For the four polynomial patch schemes (Square-p2, Square-p4, Square-p4, Square-p6, and Square-p8), to confirm that the accuracy of the macroscale modes indeed increases with decreasing macro-grid interval Δ (increasing N), we study the eigenvalue errors $\epsilon^{1,0}$, $\epsilon^{1,1}$ and $\epsilon^{2,1}$ of the polynomial patch schemes for all the 1728 combinations of the parameters listed in Table 3.6.1.

As §2.2.2 describes, using interpolating polynomials of order $p = 2, 4, 6, 8$ for the patch coupling gives the four polynomial staggered patch schemes Square-p2, Square-p4, Square-p4, Square-p6, and Square-p8 respectively

In our implementation, the patch coupling for these four patch schemes is based on 2D Lagrangian polynomial interpolation over a near-square region (i.e., square stencil), hence the names of polynomial patch schemes contain “Square” in them.

The macroscale eigenvalues λ_p^N for the wavenumber $(k_x, k_y) = (1, 0)$ converge to the macroscale eigenvalues $\lambda_{m\delta}^A$ of the full-domain microscale model. Figures 3.6.4 and 3.6.5 show the best and the worst convergence plots for the eigenvalue error $\epsilon^{1,0}$. Except for a few specific cases, in general, the eigenvalues errors $\epsilon^{1,0}$ of all the four polynomial patch schemes, converge to zero, closely following the power law curve fit $\tilde{\epsilon}^{1,0} = 0.3333 \cdot (0.7 \cdot \Delta)^p$ (solid lines). The worst case convergence in Fig. 3.6.5 shows a slight deterioration of the eigenvalue convergence for the combination of the small patch scale ratio $r = 0.0001$, large interpolation order $p = 8$, large number of macro-grid intervals $N > 14$ and large viscous diffusion $c_V = 0.01$. That is, for all the four polynomial patch schemes, except for the combination of parameters (the small r and large N, p, c_V), the macroscale eigenvalues λ_p^N for the wavenumber $(k_x, k_y) = (1, 0)$ converge to the corresponding macroscale eigenvalues $\lambda_{m\delta}^A$ of the full-domain microscale model. Moreover, the exponent p in the power law fit shows that this convergence of patch scheme eigenvalues λ_p^N for the wavenumber $(k_x, k_y) = (1, 0)$ with decreasing macro-grid interval Δ is to the same order of the polynomial interpolation p .

The macroscale eigenvalues λ_p^N for the wavenumber $(k_x, k_y) = (1, 1)$ converge to the macroscale eigenvalues $\lambda_{m\delta}^A$ of the full-domain microscale model. The eigenvalue errors $\epsilon^{1,1}$ converge to zero following the same power law curve fit for the eigenvalue errors $\epsilon^{1,0}$ in the previous paragraph. That is, $\tilde{\epsilon}^{1,1} = \tilde{\epsilon}^{1,0} = 0.3333 \cdot (0.7 \cdot \Delta)^p$ (solid lines in Figs. 3.6.6 and 3.6.7). The best-case convergence plot for the eigenvalue errors $\epsilon^{1,1}$ are visually identical to Fig. 3.6.4. So, Figs. 3.6.6 and 3.6.7 show the moderately worse and the worst convergence plots for the eigenvalue error $\epsilon^{1,1}$ respectively. Similar to the case of the wave number $(k_x, k_y) = (1, 0)$, for all the four polynomial patch schemes, except for the combination of parameters (the small r and large N, p, c_V), the macroscale eigenvalues λ_p^N for the wavenumber $(k_x, k_y) = (1, 1)$ converge to the corresponding macroscale eigenvalues $\lambda_{m\delta}^A$ of the full-domain microscale model. As for the case of the wave number $(k_x, k_y) = (1, 0)$, this convergence of patch scheme eigenvalues λ_p^N for the wavenumber $(k_x, k_y) = (1, 1)$ with decreasing macro-grid interval Δ is to the same order of the polynomial interpolation p .

The macroscale eigenvalues λ_p^N for the wavenumber $(k_x, k_y) = (2, 1)$ converge to the macroscale eigenvalues $\lambda_{m\delta}^A$ of the full-domain microscale model. Figures 3.6.8 and 3.6.9 show the best and the worst convergence plots for the eigenvalue error $\epsilon^{2,1}$. As discussed in p. 123 of §3.6, a patch grid with $N = 6$

macro-grid intervals do not resolve the macroscale mode with wavenumber $(k_x, k_y) = (2, 1)$. Hence the convergence plots of the eigenvalue error $\epsilon^{2,1}$ do not have a data point corresponding to $N = 6$. The eigenvalue errors $\epsilon^{2,1}$ converge to zero following the power law curve fit $\tilde{\epsilon}^{2,1} = 0.3333 \cdot (1.333 \cdot \Delta)^p$ (solid lines in Figs. 3.6.8 and 3.6.9). Figures 3.6.8 and 3.6.9 of the best and worst convergence plots for the eigenvalue error $\epsilon^{2,1}$, are nearly the same except for the largest polynomial order $p = 8$ with $N = 22$, $r = 0.0001$. Unlike the case of the eigenvalue errors $\epsilon^{1,0}$ and $\epsilon^{1,1}$, the macroscale eigenvalues corresponding to the wavenumber $(k_x, k_y) = (2, 1)$ converge to the corresponding macroscale eigenvalues of the full-domain microscale model, without any exception for r, N, p, c_v . As for the case of the wave number $(k_x, k_y) = (1, 0), (1, 1)$, this convergence of patch scheme eigenvalues λ_p^N for the wavenumber $(k_x, k_y) = (2, 1)$ with decreasing macro-grid interval Δ is to the same order of the polynomial interpolation p .

All four polynomial staggered patch schemes are consistent with the corresponding full-domain microscale model. In the eigenvalue convergence plots of Figs. 3.6.4 to 3.6.9, all the nonnegligible deviations from the respective power law fit (discrepancy between the solid and dashed lines) correspond to the combination of the small r and large N, p, c_v . Both small patch scale ratio r and a large number of macro-grid intervals N lead to small sub-patch micro-grid interval δ . Hence, as discussed in p. 103 of §3.4 the deviations from the eigenvalue convergence are due to inherent sensitivity of the microscale model to numerical roundoff errors, for nonnegligible viscous diffusion $c_v \gtrsim 0.0001$ and for small grid interval δ . So we take that the eigenvalue convergence for the macroscale wavenumbers does not deteriorate with decreasing macro-grid interval Δ (increasing N), due to any deficiency of the four polynomial patch schemes. That is, *all four polynomial staggered patch schemes are consistent with the corresponding full-domain microscale model with decreasing macro-grid interval Δ to the same order of the polynomial interpolation p .*

Figure 3.6.4. Best case convergence of $\epsilon^{1,0}$ (log scale) with macro-grid interval Δ , for $c_D = 10^{-6}$, $c_V = 10^{-4}$, $n = 6$, for the four polynomial patch schemes with interpolation orders $p \in \{2, 4, 6, 8\}$ and patch scale ratio r . Solid lines are the power law curve fit $\tilde{\epsilon}^{1,0} = 0.3333 \cdot (0.7 \cdot \Delta)^p$.

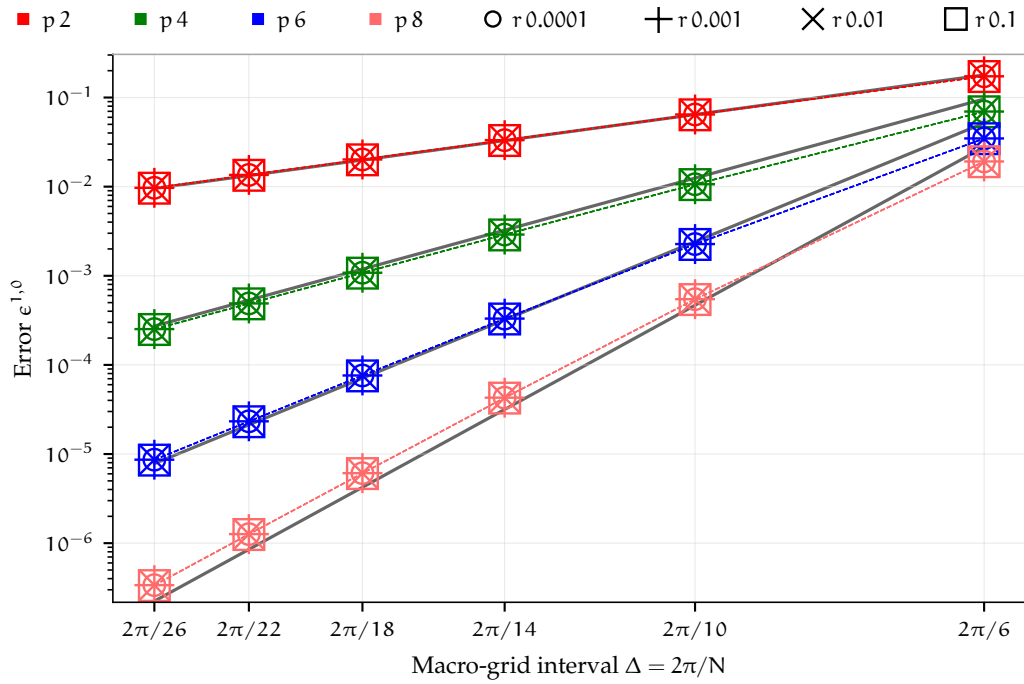


Figure 3.6.5. Worst case convergence of $\epsilon^{1,0}$ (log scale) with macro-grid interval Δ , for $c_D = 0.001$, $c_V = 0.01$, $n = 10$, for the four polynomial patch schemes with interpolation orders $p \in \{2, 4, 6, 8\}$ and patch scale ratio r . Solid lines are the power law curve fit $\tilde{\epsilon}^{1,0} = 0.3333 \cdot (0.7 \cdot \Delta)^p$.

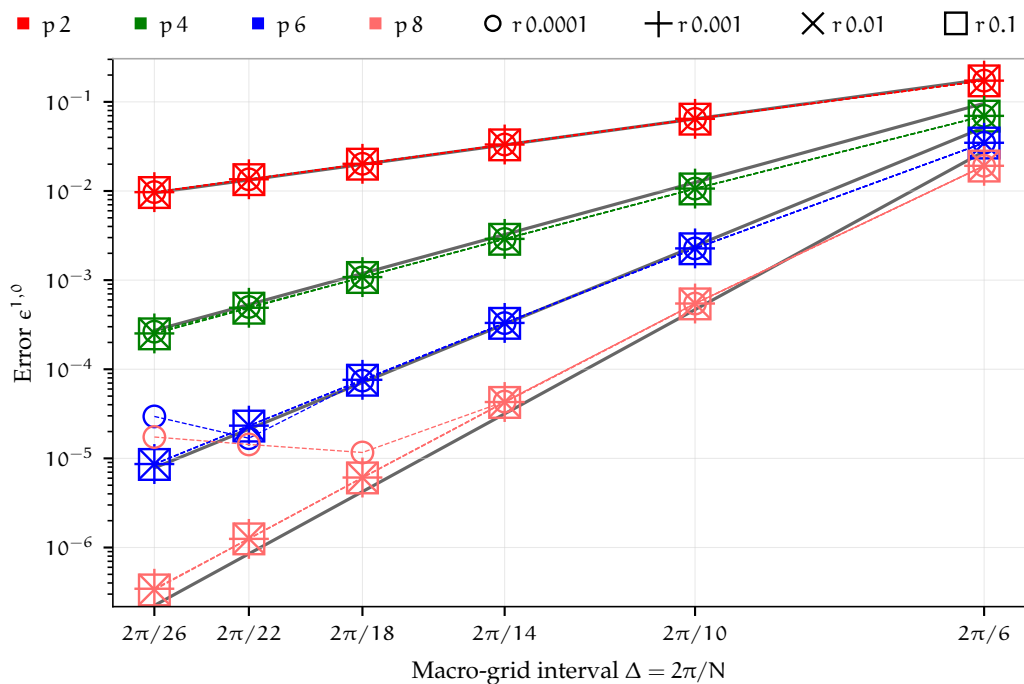


Figure 3.6.6. Moderately worse case convergence of $\epsilon^{1,1}$ (log scale) with macro-grid interval Δ , or $c_D = 0.001$, $c_V = 0.01$, $n = 10$, for the four polynomial patch schemes with interpolation orders $p \in \{2, 4, 6, 8\}$ and patch scale ratio r . Solid lines are the power law curve fit $\tilde{\epsilon}^{1,1} = 0.3333 \cdot (0.7 \cdot \Delta)^p$.

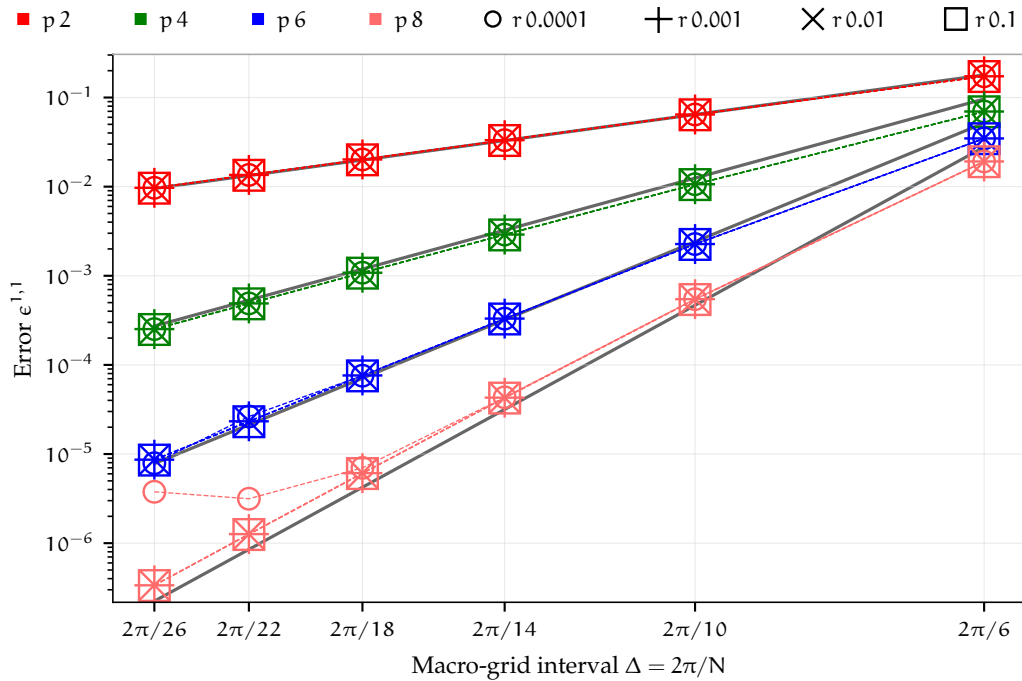


Figure 3.6.7. Worst case convergence of $\epsilon^{1,1}$ (log scale) with macro-grid interval Δ , for $c_D = 0.001$, $c_V = 0.01$, $n = 10$, for the four polynomial patch schemes with interpolation orders $p \in \{2, 4, 6, 8\}$ and patch scale ratio r . Solid lines are the power law curve fit $\tilde{\epsilon}^{1,1} = 0.3333 \cdot (0.7 \cdot \Delta)^p$.

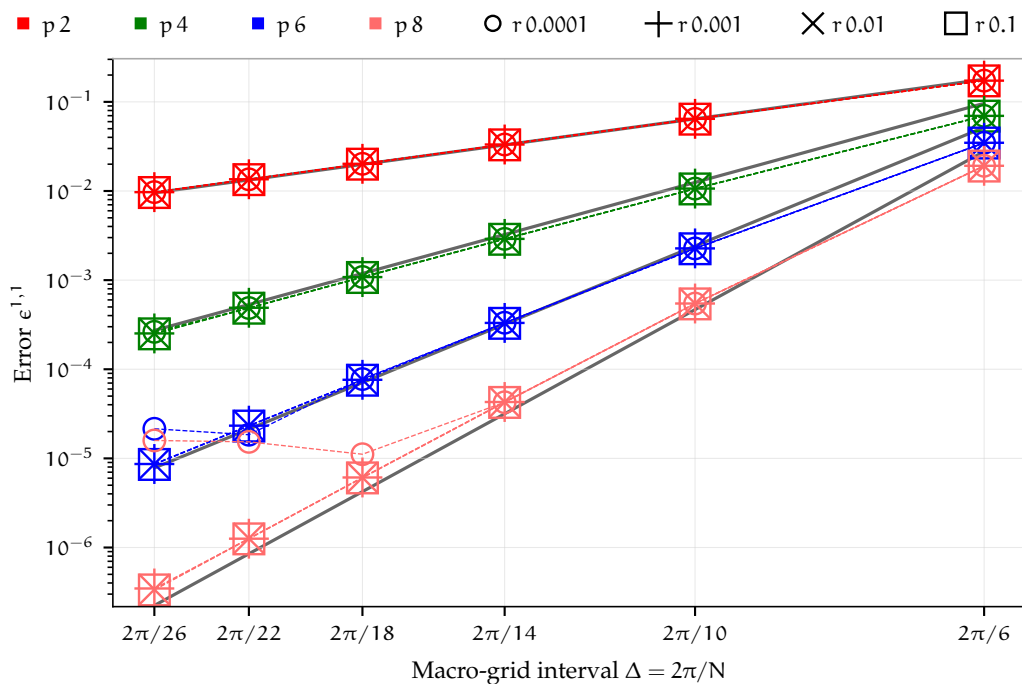


Figure 3.6.8. Best case convergence of $\epsilon^{2,1}$ (log scale) with macro-grid interval Δ , for $c_D = 10^{-6}$, $c_V = 10^{-4}$, $n = 10$, for the four polynomial patch schemes with interpolation orders $p \in \{2, 4, 6, 8\}$ and patch scale ratio r . Solid lines are the power law curve fit $\tilde{\epsilon}^{2,1} = 0.3333 \cdot (1.333 \cdot \Delta)^p$.

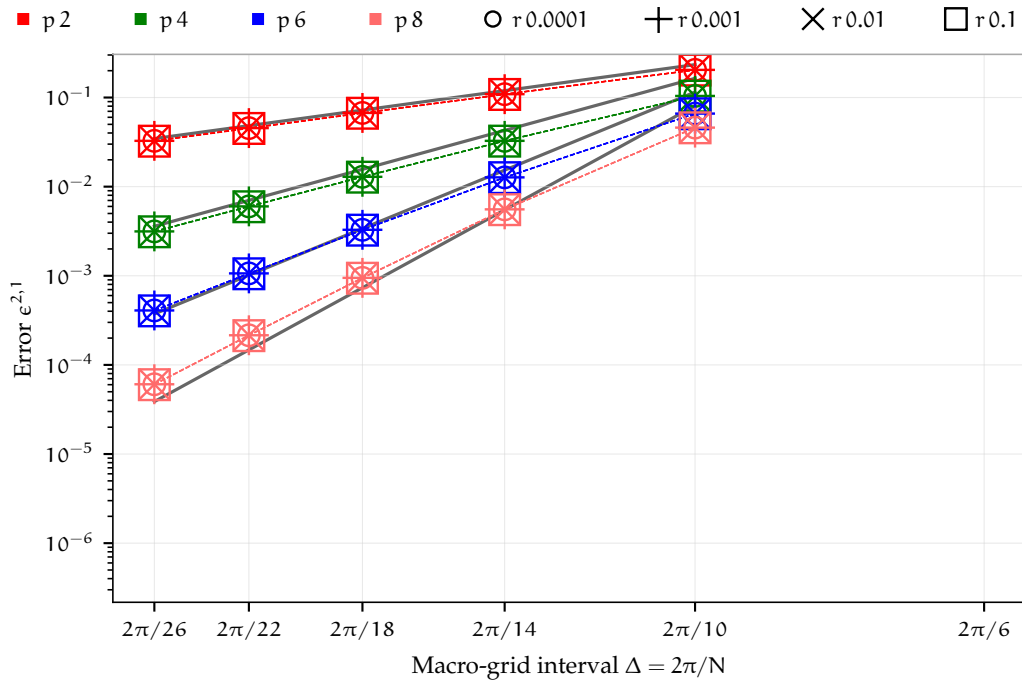
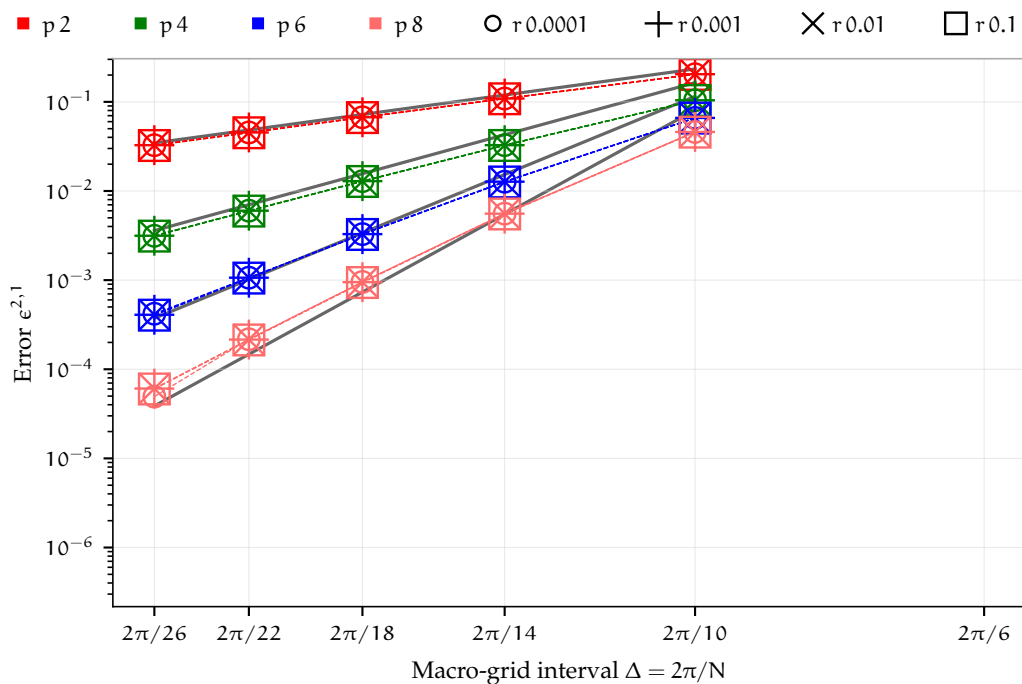


Figure 3.6.9. Worst case convergence of $\epsilon^{2,1}$ (log scale) with macro-grid interval Δ , for $c_D = 0.001$, $c_V = 0.01$, $n = 10$, for the four polynomial patch schemes with interpolation orders $p \in \{2, 4, 6, 8\}$ and patch scale ratio r . Solid lines are the power law curve fit $\tilde{\epsilon}^{2,1} = 0.3333 \cdot (1.333 \cdot \Delta)^p$.



3.7 Large computational savings in staggered patch scheme time simulation

This section quantifies and demonstrates the potentially large computational savings of the staggered patch schemes for the general linear wave. [Section 3.7.1](#) shows the computational savings of the 2D staggered patch schemes theoretically in terms of the ratio of the space over which the patch schemes and the full-domain model computes. [Section 3.7.2](#) shows the computational savings of the patch schemes in terms of the ratio of the number of state variables for which the patch schemes and the full-domain model computes. [Section 3.7.3](#) quantifies the computational complexity of the staggered patch schemes and compares the compute times of the staggered patch schemes to that of the full-domain microscale model. [Section 3.7.4](#) demonstrates the computational savings of the 2D staggered patch schemes by measuring the elapsed time taken to compute the time derivative of the state vector (one time iteration) using a specific implementation. [Section 3.7.5](#) demonstrates the accuracy and the effectiveness of the staggered patch schemes by numerically simulating the general dissipative linear waves for two example cases: a simple progressive wave; and a moving Gaussian hump.

3.7.1 Patch schemes compute only within a small fraction of space

For large-scale problems, the primary interest is only the large-scale waves, not the smallest details. To simulate such large-scale waves accurately, a fine-grid full-domain microscale model (e.g., [\(3.1.1\)](#) for the general linear wave) computes on the whole $L \times L$ domain. But the staggered patch schemes compute only within small patches sparsely located within the domain, occupying a much smaller fraction of the space in the full domain. For example, [Fig. 2.1.3b](#) of [§2.1.2](#) shows a staggered patch grid, where the patches are enlarged for visual clarity.

Consider the staggered patch grid in [Fig. 2.1.3b](#) with macro-grid interval Δ and patch size l . In terms of the patch scale ratio $r = l/(2\Delta)$, the area of one patch is $l^2 = 4r^2\Delta^2$. When a macro-cell contains three patches in a patch grid (as in the chosen patch grid [Fig. 2.1.3b](#)), with $N \times N$ macro-grid intervals, there are a total of $3N^2/4$ patches. Hence the total area occupied by the patches is $3N^2l^2/4 = 3r^2N^2\Delta^2 = 3r^2L^2$ as the macro-grid interval $\Delta = L/N$. That is, the total area of the simulated space in a patch scheme is $3r^2L^2$ whereas the corresponding total area of the simulated space in a fine-grid

full-domain microscale model is L^2 . For a small patch scale ratio r , the 2D staggered patch schemes compute only within a small fraction $3r^2$ of the area of the full domain. For example, for $r = 0.1, 0.01, 0.001, 0.0001$, the staggered patch schemes compute over the fraction of area $0.03, 3 \cdot 10^{-4}, 3 \cdot 10^{-6}, 3 \cdot 10^{-8}$ respectively. Similar 3D staggered patch schemes compute only within a small fraction $4r^3$ of the volume in the full domain, where the computational saving is much more. Thus, the staggered patch schemes compute only within a small fraction of the space in the full domain.

3.7.2 Patch schemes compute for a small number of state variables

Section 3.7.1 shows that 2D staggered patch schemes compute only within a small fraction $3r^2$ of the space in the full domain, which is a rough indication of the computational savings of the staggered patch schemes. This section quantifies the computational savings of the staggered patch schemes, more concretely in terms of the number of the dynamical state variables of the 2D staggered patch schemes and that of the corresponding fine-grid full-domain microscale model.

For a staggered patch grid in Fig. 2.1.5a with $N \times N$ macro-grid intervals and each patch containing $n \times n$ sub-patch micro-grid intervals, the total number of patch interior nodes is $n_p^I = (N^2/4)(9n^2/4 - 4n + 2)$, which is same as the number of state variables (p. 21 of §2.1.2). For a staggered grid in Fig. 2.1.1 corresponding to a fine-grid full-domain model, with the same grid interval as the sub-patch micro-grid interval δ , the total number of interior nodes is $n_{m\delta}^I = 3N^2n^2/(16r^2)$. The ratio of the number of state variables of the staggered patch scheme to that of the fine-grid full-domain microscale model,

$$n_p^I/n_{m\delta}^I = 3r^2 \left(1 - \frac{16}{9n} + \frac{8}{9n^2} \right). \quad (3.7.1)$$

With increasing n , the ratio $n_p^I/n_{m\delta}^I$ tends to $3r^2$, which is the same fraction of the space derived in §3.7.1 over which the patch schemes compute. For example, for $n = 6, 10, 14$ sub-patch micro-grid intervals with a fixed patch scale ratio $r = 0.1$, the ratio $n_p^I/n_{m\delta}^I = 0.022, 0.025, 0.026$ respectively. For $r = 0.1, 0.01, 0.001, 0.0001$ with a fixed $n = 6$, the ratio of number of nodes $n_p^I/n_{m\delta}^I = 0.022, 2.2 \cdot 10^{-4}, 2.2 \cdot 10^{-6}, 2.2 \cdot 10^{-8}$ respectively. Thus, the staggered patch schemes compute only for a small number of dynamical state variables compared to the corresponding fine-grid full-domain microscale model with the same grid interval as the sub-patch micro-grid interval δ .

3.7.3 Computational complexity of the staggered patch schemes

This subsection quantifies the computational complexity of the staggered patch schemes and compares the compute times of the staggered patch schemes to that of the full-domain microscale model. To simplify and keep the smaller uncertainties aside, for the patch schemes and the full-domain microscale model this subsection assumes a similar level of vectorisation and a similar pattern of cache and memory access.

Let the average compute time for computing the time derivative of one state variable is T_M for the fine-grid full-domain microscale model. We call T_M , the *model compute time* per interior node. There are $n_{m\delta}^I = 3N^2n^2/(16r^2)$ state variables in the fine-grid full-domain microscale model. Hence, the total compute time for computing the time derivative of the state vector (i.e., the compute time for one iteration in time simulation),

$$T_{m\delta} = n_{m\delta}^I T_M = 3N^2n^2 T_M/(16r^2). \quad (3.7.2)$$

The compute time T_p for computing the time derivative of the state vector dx^I/dt in the patch system (2.1.9) has two components: time for computing the patch coupling; and time for computing the node values using the microscale model.

- Let the average compute time for computing one patch edge node from the patch coupling is T_C . We call T_C , the *coupling compute time* per edge node. There are $n_p^E = (N^2/4)(18n - 16)$ edge nodes (expression (2.1.8) in p. 22 of §2.1.2) in the staggered patch grid of Fig. 2.1.5a for the general linear wave with drag and viscous diffusion. Hence, the total compute time for computing the patch edge vector x^E in the patch system (2.1.9) (i.e., the patch coupling compute time for one iteration in time simulation) is $n_p^E T_C = (N^2/4)(18n - 16) T_C$.
- Using the same microscale model within the patches as that of the full-domain microscale model costs the same average compute time T_M for computing the time derivative of one state variable of a patch scheme. There are $n_p^I = (N^2/4)(9n^2/4 - 4n + 2)$ state variables in the staggered patch scheme (p. 21 of §2.1.2). Hence, using the known values of the patch edge nodes x^E and the patch interior nodes x^I , the compute time for computing the time derivative of the state vector dx^I/dt in the patch system (2.1.9) is $n_p^I T_M = (N^2/4)(9n^2/4 - 4n + 2) T_M$.

Thus, the total compute time for computing the time derivative of the state

vector dx^I/dt in the patch system (2.1.9),

$$T_p = n_p^E T_C + n_p^I T_M = (N^2/4)(18n - 16) T_C + (N^2/4)(9n^2/4 - 4n + 2) T_M. \quad (3.7.3)$$

The ratio of the compute time (3.7.3) for computing the time derivative of the state vector of a patch scheme to the compute time (3.7.2) of the fine-grid full-domain microscale model,

$$T_p/T_{m\delta} = (n_p^E T_C + n_p^I T_M)/(n_{m\delta}^I T_M) = (n_p^E/n_{m\delta}^I) (T_C/T_M) + n_p^I/n_{m\delta}^I. \quad (3.7.4)$$

From the expressions for the number of state variables in a fine-grid full-domain microscale model $n_{m\delta}^I = 3N^2n^2/(16r^2)$ and the number of patch edge nodes $n_p^E = (N^2/4)(18n - 16)$, the ratio

$$n_p^E/n_{m\delta}^I = 24r^2/n - 64r^2/(3n^2). \quad (3.7.5)$$

Using the expressions (3.7.1) and (3.7.5), the ratio of compute time for computing the time derivative of the state vector of a patch scheme to that of the fine-grid full-domain microscale model (i.e., the compute time ratio for one iteration in time simulation) is

$$T_p/T_{m\delta} = (T_C/T_M) \left(\frac{24r^2}{n} - \frac{64r^2}{3n^2} \right) + 3r^2 \left(1 - \frac{16}{9n} + \frac{8}{9n^2} \right). \quad (3.7.6)$$

The compute time ratio (3.7.6) for one iteration in time simulation, describes the computational cost savings of the staggered patch schemes. The ratio T_C/T_M of coupling compute time to model compute time, in the compute time ratio (3.7.6), encapsulates the following:

1. the details of the specific patch scheme (Spectral or polynomial patch scheme, interpolation order p of the polynomial patch scheme, etc.);
2. the details of the specific implementation (specific algorithmic choices, data structures, serial or parallel computations, etc.).

In general, for modelling any reasonably complex physical process (e.g., non-hydrostatic nonlinear waves, sediment transport, etc), the model compute time per interior node T_M is greater than the coupling compute time per edge node T_C , with $T_C/T_M \lesssim 1$. Hence, substituting $T_C/T_M = 1$ into the compute time ratio (3.7.6) gives a rough indication of the possible computational cost savings of the staggered patch schemes as

$$T_p/T_{m\delta} \lesssim 3r^2 + \frac{56r^2}{3n} - \frac{56r^2}{3n^2}. \quad (3.7.7)$$

3.7.4 Staggered patch schemes simulate with small compute time

Sections 3.7.1 and 3.7.2 show the computational savings of the 2D staggered patch schemes theoretically in terms of the ratio of the space and the ratio of the number of state variables respectively. This section shows the computational savings of the 2D staggered patch schemes by measuring the elapsed time taken to compute the time derivative of the state vector (one time iteration) using a specific implementation in the Julia programming language.

This subsection measures the compute time ratio $T_p/T_{m\delta}$ for a specific implementation and compares with expression (3.7.6) by empirically estimating the model compute time per interior node T_M and the coupling compute time per edge node T_C . The compute times in this subsection are measured on a custom assembled liquid-cooled workstation with Intel i7-6900k processor and 64GB DDR4 RAM. Both the full-domain microscale model and the patch schemes are implemented as serial programs.

Figure 3.7.1 plots the measured compute time $T_{m\delta}$ of the fine-grid full-domain microscale model (3.1.1) (p. 49 of §3.1), for computing the time derivative of the state vector (i.e., the compute time for one iteration in time simulation) for the initial condition (3.7.8) of the simple progressive wave (p. 146 of §3.7.5). Figure 3.7.1 plots the compute time $T_{m\delta}$ of the fine-grid full-domain model with the same grid interval as the sub-patch micro-grid interval δ of a staggered patch grid with different number of macro-grid intervals N , sub-patch micro-grid intervals n , and patch scale ratio r . We measured one hundred samples of compute times $T_{m\delta}$ for each of the nine combinations of $c_D \in \{0, 10^{-6}, 0.0001\}$, $c_V \in \{0, 10^{-4}, 0.001\}$. Each point in Fig. 3.7.1 is the mean over the nine combinations of c_D , c_V . For the measured compute times $T_{m\delta}$, fitting one common power law curve (solid lines in Fig. 3.7.1) using expression (3.7.2), we estimate the model compute time per interior node $T_M = 0.062 \mu\text{s}$ (same value for all n , r). The measured compute times $T_{m\delta}$ reasonably closely follow the trend of expression (3.7.2) (solid lines).

Figure 3.7.2 plots the measured compute time T_p of the five staggered patch schemes for computing the time derivative of the state vector (i.e., the compute time for one iteration in time simulation), for different macro-grid intervals N and sub-patch micro-grid intervals n . We measured one hundred samples of compute times T_p for each of the nine combinations of $c_D \in \{0, 10^{-6}, 0.0001\}$, $c_V \in \{0, 10^{-4}, 0.001\}$. Each point in Fig. 3.7.2 is the mean over the nine combinations of c_D , c_V . For the measured compute times T_p , fitting a power law curve for each patch scheme (solid

Figure 3.7.1. Measured compute times $T_{m\delta}$ of the fine-grid full-domain model (general linear wave) with the same grid interval as the sub-patch micro-grid interval δ of a staggered patch grid with different N , n , and patch scale ratio r . Solid lines represent expression (3.7.2) using the estimated model compute time $T_M = 0.062 \mu\text{s}$.

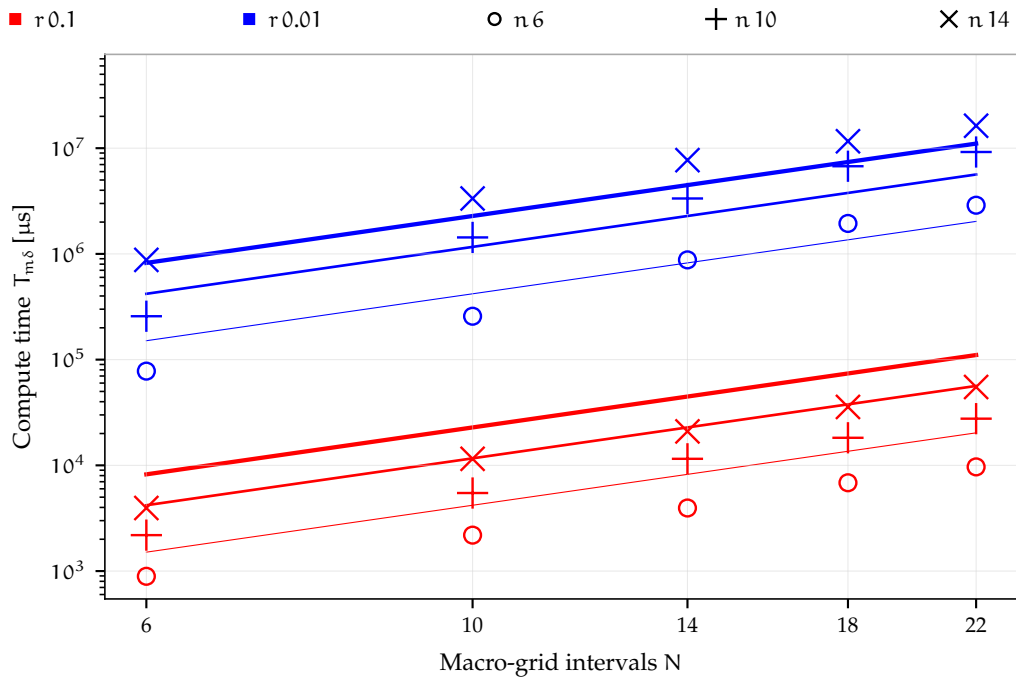
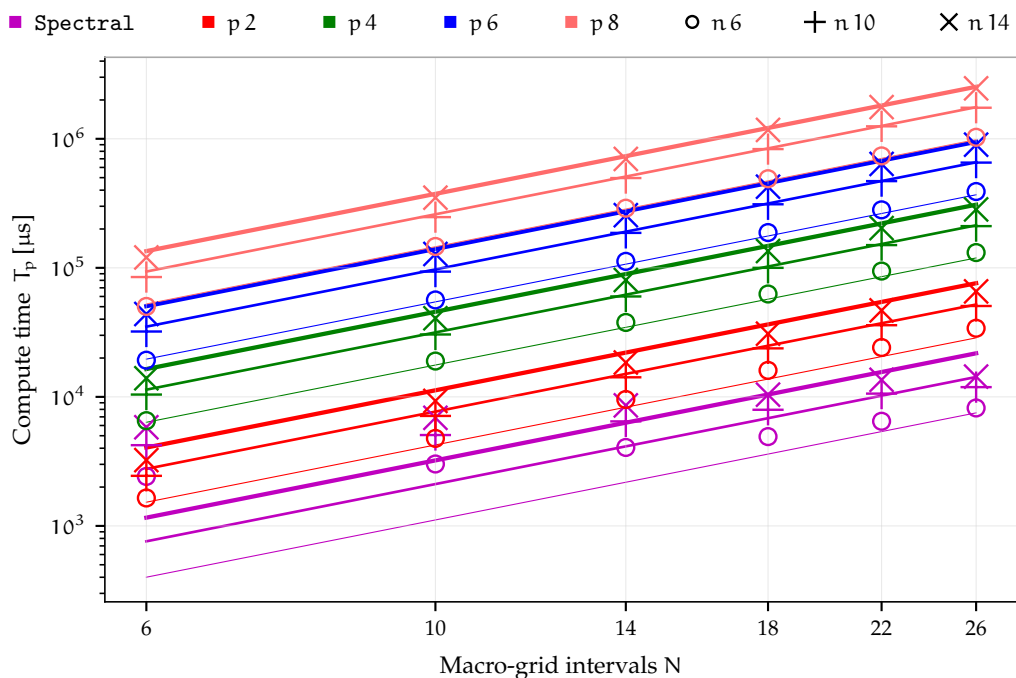


Figure 3.7.2. Measured compute times T_p of the five staggered patch schemes (general linear wave) with different N and n . Solid lines represent expression (3.7.3) using the estimated model compute time $T_M = 0.062 \mu\text{s}$ and the respective estimated coupling compute times T_C for the five patch schemes.



lines in Fig. 3.7.2) using the model compute time $T_M = 0.062 \mu\text{s}$ in expression (3.7.3), we estimate the approximate coupling compute times per edge node $T_C = 0.44, 1.8, 7.6, 24, 63 \mu\text{s}$ for the five staggered patch schemes Spectral, Square-p2, Square-p4, Square-p6, and Square-p8 respectively.

The measured compute times T_p of all the five staggered patch schemes reasonably closely follow the trend of expression (3.7.3) (solid lines).

The smallest coupling compute time $T_C = 0.44 \mu\text{s}$ for the spectral patch scheme is because Algorithm 1 efficiently calculates the edge values for all the $h/u/v$ -centred patches in one shot using the fast Fourier transform via the Fourier shift property. But for the polynomial patch schemes, Algorithm 2 calculates looping over each of the $h/u/v$ -centred patches individually. For the polynomial patch schemes, the coupling compute time per edge node T_C increases monotonically from $1.8 \mu\text{s}$ to $63 \mu\text{s}$ with the increase in the order p of interpolation from two to eight. This increasing T_C with increasing p is expected as there are more computations involved in higher order interpolation.

The relatively simple microscale model of the general linear wave with drag and viscous diffusion has small model compute time per interior node $T_M = 0.062 \mu\text{s}$ from Fig. 3.7.1. The focus of the current patch scheme implementation is on the flexibility to explore a large number of possible designs of the patch grid and a large number of possible patch schemes. So, the current patch scheme implementation, being not computationally efficient, leads to large coupling compute times per edge node T_C from Fig. 3.7.2. Hence, the ratios of the coupling compute times to the model compute times are $T_C/T_M = 7, 29, 123, 381, 1020$, for the five staggered patch schemes Spectral, Square-p2, Square-p4, Square-p6, and Square-p8 respectively.

Figure 3.7.3 plots the ratio $T_p/T_{m\delta}$ of the measured compute time of the fine-grid full-domain model to that of the staggered patch schemes, for different number of sub-patch micro-grid intervals n and patch scale ratio r . Solid lines represent expression (3.7.6) for $T_p/T_{m\delta}$ using the estimated model compute time $T_M = 0.062 \mu\text{s}$ and the respective estimated coupling compute times T_C for each patch scheme. A fine-grid for full-domain model (with the same grid interval δ as the sub-patch micro-grid interval), has very large number of interior nodes $n_{m\delta}^1 = 3N^2n^2/(16r^2)$ corresponding to a small patch scale ratio, requiring memory larger than 64 GB. Hence, for $r = 0.001$ we compute $T_p/T_{m\delta}$ (plusses in Fig. 3.7.3) using the measured T_p of the patch schemes and the estimated $T_{m\delta}$ of the full-domain model using expression (3.7.6). The measured compute time ratio $T_p/T_{m\delta}$ reasonably closely follow the trend of expression (3.7.6) (solid lines) for the five staggered patch schemes (with the respective T_C).

Figure 3.7.3. Ratio $T_p/T_{m\delta}$ of the measured compute time of the staggered patch schemes (general linear wave) to that of the fine-grid full-domain model, for different n , r . Solid lines represent expression (3.7.6) for $T_p/T_{m\delta}$ using the estimated model compute time $T_M = 0.062 \mu\text{s}$ and the respective estimated coupling compute times T_C for each patch scheme.

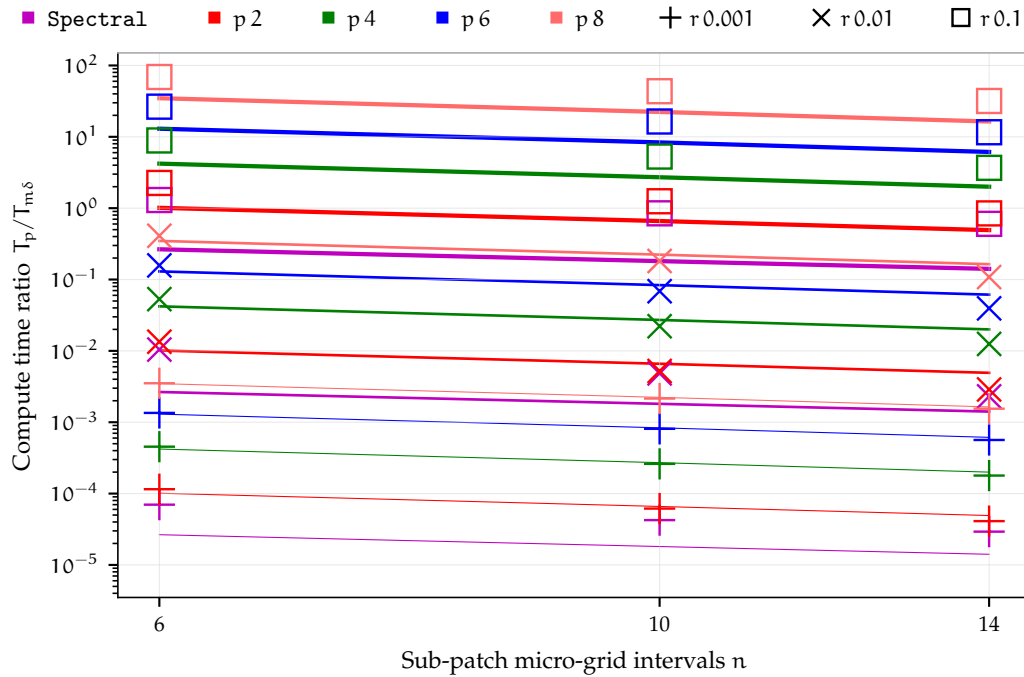


Figure 3.7.3 shows that despite the estimated large T_C/T_M (between 13 and 1031), for sufficiently small patch scale ratio $r = 0.01, 0.001$ the compute time ratios $T_p/T_{m\delta}$ are about $10^{-2}, 10^{-4}$. That is, despite the large T_C/T_M , for small patch scale ratios, the compute times of the multiscale staggered patch schemes are about 100 to 10 000 times smaller than the corresponding fine-grid full-domain microscale model. A reduction of 10 000 times is equivalent to reducing the computation time from one week to one minute.

For patch scheme simulations with fixed grid geometry, the patch coupling coefficients can be precomputed as a sparse matrix, which gives the patch edge values when multiplied by the patch centre values at each instant in time. Such patch coupling via sparse matrix multiplication instead of direct patch coupling reduces the coupling compute time T_C , leading to smaller T_C/T_M in (3.7.6), and hence larger computational savings of the staggered patch schemes via smaller $T_p/T_{m\delta}$. Using the sparse matrix multiplication for the patch coupling of the five staggered patch schemes, Fig. 3.7.4 plots the measured compute time T_p for computing the time derivative of the state vector (i.e., the compute time for one iteration in

Figure 3.7.4. Measured compute times T_p , with *patch coupling via sparse matrix multiplication*, for the five staggered patch schemes with different N and n . Solid lines represent expression (3.7.3) using the estimated model compute time $T_M = 0.062 \mu\text{s}$ and the respective estimated coupling compute times T_C for the five patch schemes.

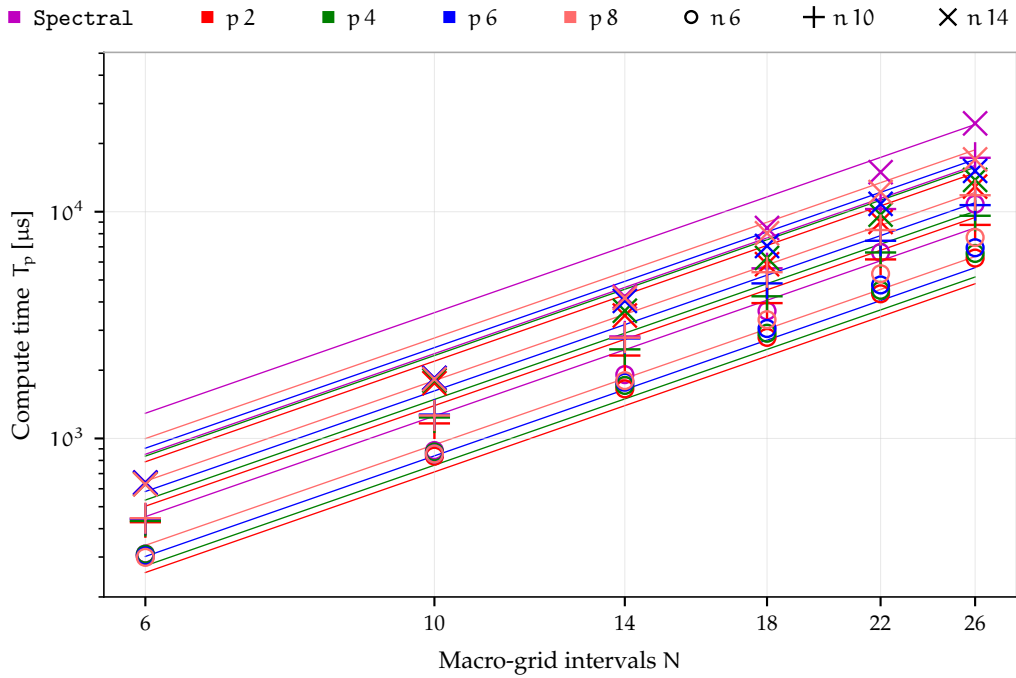
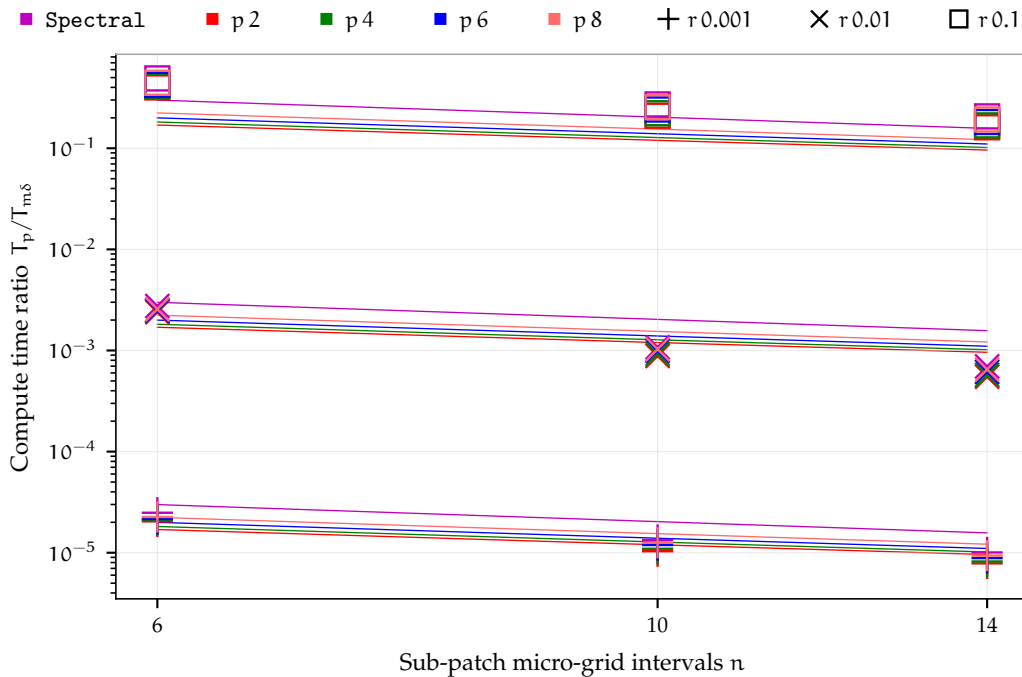


Figure 3.7.5. Ratio $T_p/T_{m\delta}$ of the measured compute time of the staggered patch schemes with *patch coupling via sparse matrix multiplication* to that of the fine-grid full-domain model, for different n , r . Solid lines represent expression (3.7.6) for $T_p/T_{m\delta}$ using the estimated $T_M = 0.062 \mu\text{s}$ and the respective estimated coupling compute times T_C for each patch scheme.



time simulation), for different N and n . We measured 10 000 samples of compute times T_p for each of the nine combinations of $c_D \in \{0, 10^{-6}, 0.0001\}$, $c_V \in \{0, 10^{-4}, 0.001\}$. Each point in Fig. 3.7.4 is the mean over the nine combinations of c_D, c_V .

For the measured compute times T_p in Fig. 3.7.4, fitting a power law curve (solid lines in Fig. 3.7.4) using the model compute time $T_M = 0.062 \mu\text{s}$ in expression (3.7.3), we estimate the approximate coupling compute times per edge node $T_C = 0.51, 0.27, 0.29, 0.32, 0.37 \mu\text{s}$ for the five staggered patch schemes Spectral, Square-p2, Square-p4, Square-p6, and Square-p8 respectively. The patch coupling via sparse matrix multiplication reduces the coupling compute time T_C by as large as 170 times compared to the direct coupling compute times ($T_C = 0.44, 1.8, 7.6, 24, 63 \mu\text{s}$ computed from Fig. 3.7.2). In contrast to the direct patch coupling, via sparse matrix multiplication, the coupling compute time $T_C = 0.51 \mu\text{s}$ for the Spectral patch scheme is not the smallest among the five patch schemes. The large $T_C = 0.51 \mu\text{s}$ for the Spectral patch scheme, compared to $T_C = 0.27 \mu\text{s}$ for the Square-p2 patch scheme, comes from the smaller sparsity of the coupling matrix due to the global spectral interpolation, compared to the larger sparsity of the quadratic interpolation of Square-p2 patch scheme. Compared to the patch scheme compute times T_p in Fig. 3.7.2 via direct coupling, the patch scheme compute times T_p in Fig. 3.7.4 with patch coupling via sparse matrix multiplication, do not have strong dependence on the specific patch schemes nor the number of sub-patch intervals n .

Compared to the direct patch coupling, the smaller coupling compute time T_C for the patch coupling via sparse matrix multiplication leads to a smaller ratio of the coupling compute time to the model compute time. Using $T_M = 0.062 \mu\text{s}$, the ratio $T_C/T_M = 8.1, 4.3, 4.7, 5.2, 5.9$ for the patch coupling via sparse matrix multiplication, is much smaller compared to the ratio $T_C/T_M = 7, 29, 123, 381, 1020$ of the direct coupling, for the five staggered patch schemes Spectral, Square-p2, Square-p4, Square-p6, and Square-p8 respectively. As per expression (3.7.6), this smaller T_C/T_M also results in smaller ratio $T_p/T_{m\delta}$ of the measured compute time of the staggered patch schemes to that of the fine-grid full-domain model.

Figure 3.7.5 plots the ratio $T_p/T_{m\delta}$ of the measured compute time of the staggered patch schemes with *patch coupling via sparse matrix multiplication* to that of the fine-grid full-domain model, for different number of sub-patch micro-grid intervals n and patch scale ratio r . Solid lines represent expression (3.7.6) for $T_p/T_{m\delta}$ using the estimated $T_M = 0.062 \mu\text{s}$ and the respective estimated coupling compute times T_C for each patch scheme. As discussed in the paragraph before (for direct coupling), the computation for the fine-grid full-domain model corresponding to a patch grid with a small

patch scale ratio, requires large memory. Hence, for $r = 0.001$ we compute $T_p/T_{m\delta}$ (plusses in Fig. 3.7.5) using the measured T_p of the patch schemes and the estimated $T_{m\delta}$ of the full-domain model using expression (3.7.6). The measured compute time ratio $T_p/T_{m\delta}$ reasonably closely follow the trend of expression (3.7.6) (solid lines) for the five staggered patch schemes (through the respective T_C). Compared to the compute time ratios $T_p/T_{m\delta}$ in Fig. 3.7.3 via direct coupling, the compute time ratios $T_p/T_{m\delta}$ in Fig. 3.7.5 with patch coupling via sparse matrix multiplication, do not have strong dependence on the specific patch schemes nor the patch scale ratio r . Compared to the compute time ratios $T_p/T_{m\delta}$ in Fig. 3.7.3 via direct coupling, the *patch coupling via sparse matrix multiplication (for fixed grid) reduces the compute time ratios $T_p/T_{m\delta}$ by about ten times* as in Fig. 3.7.5, especially for higher order patch schemes.

Figure 3.7.5 shows that despite $T_C/T_M > 1$ (between five and eight), for sufficiently small patch scale ratio $r = 0.01, 0.001$ the compute time ratios $T_p/T_{m\delta}$ are about $10^{-3}, 10^{-5}$. That is, for small patch scale ratios, *the compute times of the multiscale patch schemes are about 1000 to 10^5 times smaller than the corresponding fine-grid full-domain microscale model*. A reduction of 10^5 times is equivalent to reducing the computation time from one week to six seconds.

The demonstrated large computational savings of the patch schemes via compute time ratio $T_p/T_{m\delta}$ in Figs. 3.7.3 and 3.7.5 are for the case of large ratio of coupling compute time to model compute time, $T_C/T_M > 1$. Even larger computational savings of the patch schemes are possible with smaller ratio T_C/T_M in (3.7.6) in the following cases.

1. Compared to the current simple general linear wave, modelling more complex physical processes (e.g., non-hydrostatic nonlinear waves, sediment transport, etc) with a larger model compute time T_M , leads to smaller T_C/T_M in (3.7.6), and hence smaller $T_p/T_{m\delta}$, that is larger computational savings of the staggered patch schemes.
2. Compared to the current computationally not efficient implementation (with a focus on exploratory studies), a more efficient implementation (via code specialisation, code optimisation, parallelisation, etc) with a smaller coupling compute time T_C , leads to smaller T_C/T_M in (3.7.6), and larger computational savings of the staggered patch schemes. As discussed in the article by Bunder et al. (2020, p. 962), in a parallel implementation, patch schemes require lesser communication across the compute nodes compared to the fine-grid full-domain model, due shorter messages across the patches in different compute nodes. This lesser communication across the compute nodes, leads

to additional computational savings of the parallel implementation of the staggered patch schemes compared to the current serial implementation.

3.7.5 Staggered patch scheme time simulations of general linear waves

This subsection demonstrates the accuracy and the effectiveness of the staggered patch schemes by numerically simulating the general dissipative linear waves for two example cases: a simple progressive wave; and a moving Gaussian hump. This subsection, first compares the time simulation of a patch scheme with that of the fine-grid full-domain model for a simple progressive wave, and second demonstrates the patch scheme time simulation for a moving Gaussian hump. Via random perturbation to the initial condition, this section also demonstrates the robustness of the patch schemes.

For the patch scheme time simulations, first we need to choose a suitable ODE integrator and an appropriate error tolerance. We use the package `DifferentialEquations.jl` by Rackauckas and Nie (2017), a suite of various ODE integrators in Julia programming language, to study various ODE integrators suitable for the staggered patch scheme. Specifically, we study nine ODE integrators for the suitability for the patch schemes, namely `BS3`, `DP5`, `Tsit5`, `Vern7`, `sp.RK45`, `sp.RK23`, `sp.Radau`, `sp.BDF` and `sp.LSODA` as detailed in `DifferentialEquations.jl` (2021). Equations (3.7.9) define the relative simulation errors ϵ_t^h , ϵ_t^u , ϵ_t^v to quantify the discrepancy between the solutions of the patch scheme and the full-domain model at patch centres. We compute the maximum of the mean of Spectral patch scheme simulation errors ϵ_t^h , ϵ_t^u , ϵ_t^v over the time $t \in (2\pi, 14\pi)$ for a simple progressive wave (3.7.8) using the nine ODE integrators. Figures 3.7.6 to 3.7.8 plot the mean simulation error, compute time for the ODE integration for $t = 0$ to 14π , and the memory used in the ODE integration, respectively, for the nine ODE integrators and for different relative and absolute error tolerances. The compute times in this subsection are measured on a custom assembled liquid-cooled workstation with Intel i7-6900k processor and 64GB DDR4 RAM. The compute time typically increases with decreasing tolerance, due to more time steps and function calls, as is the case for `BS3`, and `sp.RK23` in Fig. 3.7.7. But due to adaptations and variations of specific algorithms and their implementation, several other ODE integrators do not follow such monotonic trends. Detailed characterisation of such trends is not the current focus. Hence, considering the simulation error, compute time and

Figure 3.7.6. Mean error ϵ_t^h (3.7.9) over time $t \in (2\pi, 14\pi)$ for Spectral patch scheme simulation of a simple progressive wave (3.7.8).

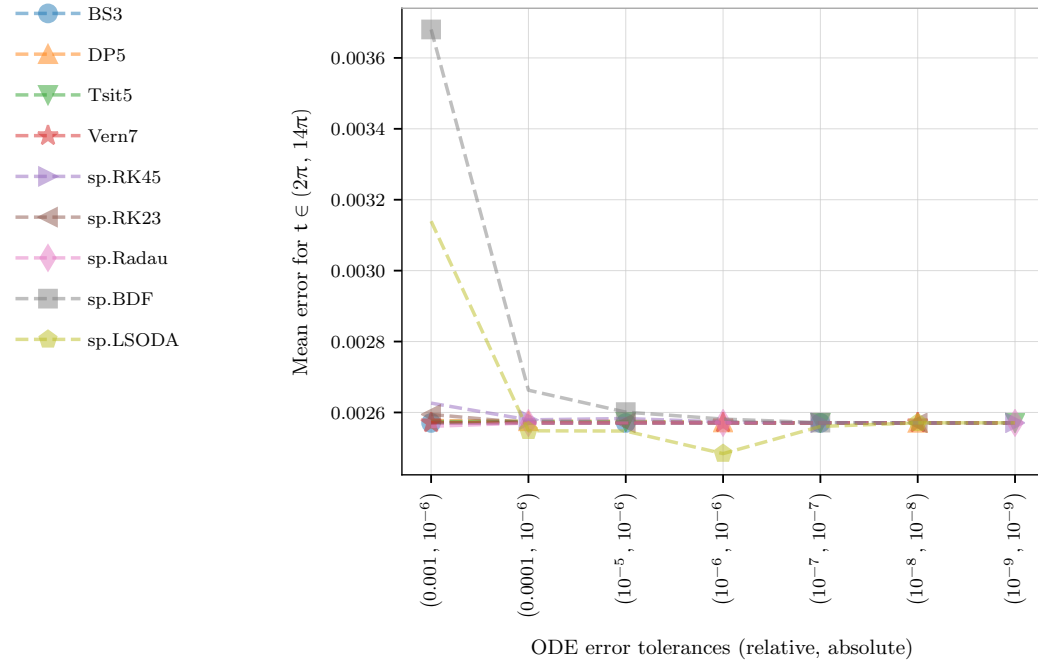


Figure 3.7.7. Compute time for the Spectral patch scheme simulation for time $t = 0$ to 14π for a simple progressive wave (3.7.8), for the nine ODE integrators and for different relative and absolute error tolerances.

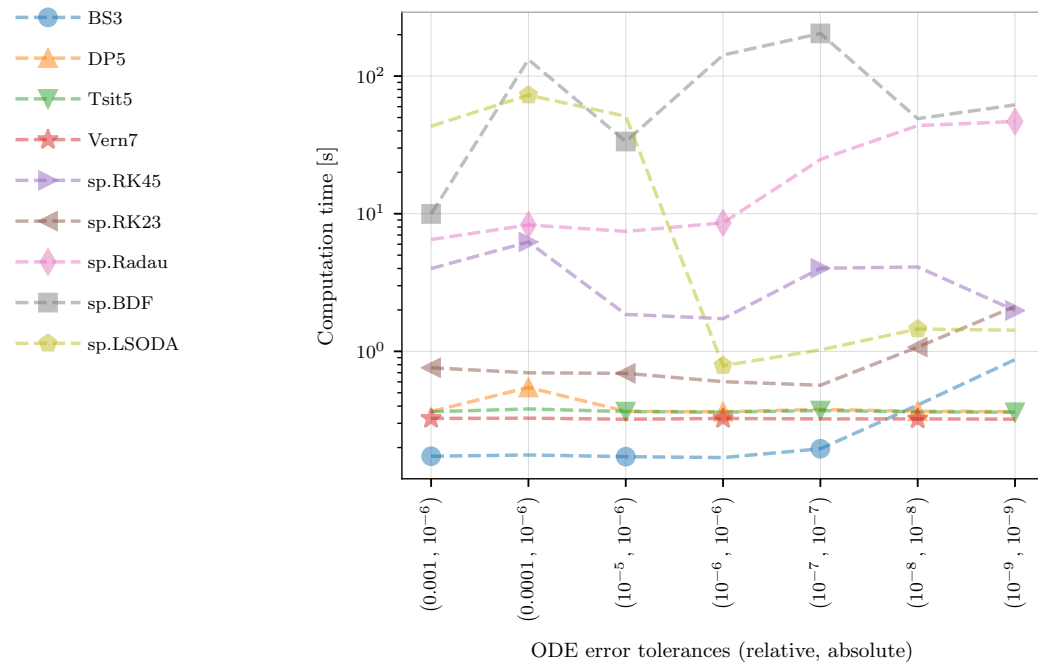
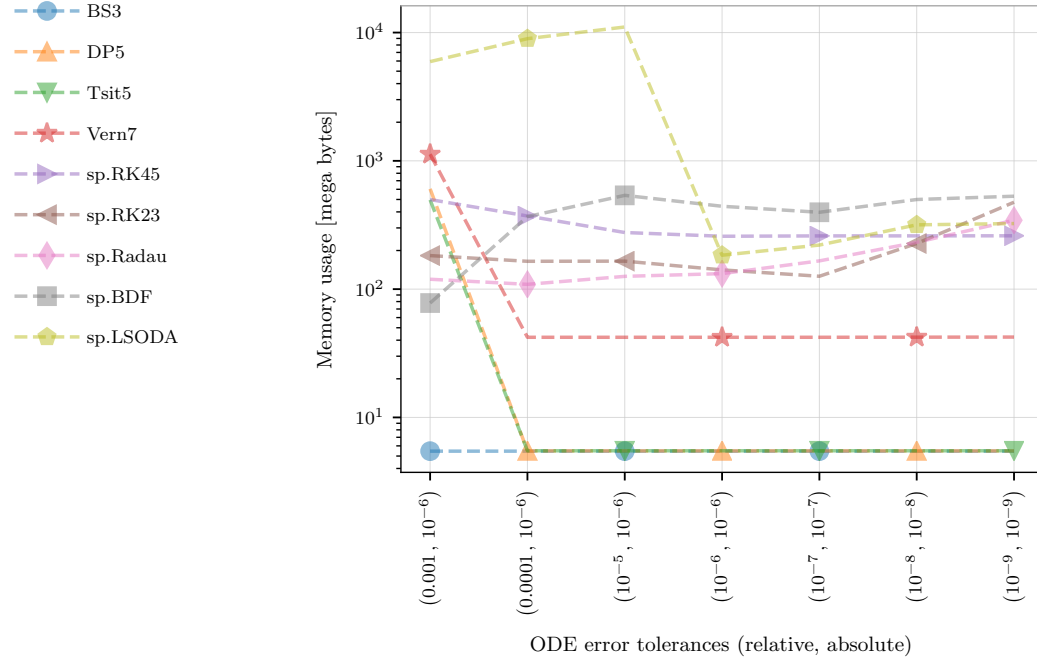


Figure 3.7.8. Memory usage of the Spectral patch scheme simulation for time $t = 0$ to 14π for a simple progressive wave (3.7.8), for the nine ODE integrators and for different relative and absolute error tolerances.



the memory usage in Figs. 3.7.6 to 3.7.8, we choose the *BS3* ODE integrator and the relative and absolute error tolerances of 10^{-3} and 10^{-6} respectively, for all the time simulations in this thesis. The *BS3* is a lower order Bogacki–Shampine 3/2 method (Bogacki and L. Shampine 1989; L. F. Shampine and Reichelt 1997), similar to the *ode23* of MATLAB (DifferentialEquations.jl 2021).

Figures 3.7.9 to 3.7.11 compare the time evolution of the general linear progressive wave with the coefficients $c_D = 10^{-6}$ and $c_V = 10^{-4}$, using the Square-p4 staggered patch scheme (3.1.3) (colour-coded ribbons) with that using the fine-grid full-domain model (3.7.2) (grey mesh), for height h , velocities u , v respectively. The time simulation of both the patch scheme and the fine-grid full-domain model are for the initial condition (plotted in top left of Figs. 3.7.9 to 3.7.11) of the simple progressive wave

$$h_0(x, y) = 0.2 + 0.1 \sin(x + y), \quad (3.7.8a)$$

$$u_0(x, y) = 0.3 + (0.1/\sqrt{2}) \sin(x + y), \quad (3.7.8b)$$

$$v_0(x, y) = 0. \quad (3.7.8c)$$

The Square-p4 patch scheme (fourth order polynomial interpolation patch coupling) in Figs. 3.7.9 to 3.7.11 use $N = 14$ macro-grid intervals, $n = 6$

Figure 3.7.9. Height h for time evolution of the progressive wave with initial condition (3.7.8), using Square-p4 patch scheme (3.1.3) (colour-coded ribbons, with $N = 14$, $n = 6$, and $r = 0.01$) agrees closely with that of the fine-grid full-domain model (grey mesh). Black circles on h -centred patches show small discrepancies. *The patch scheme compute time is 1300 times smaller.*

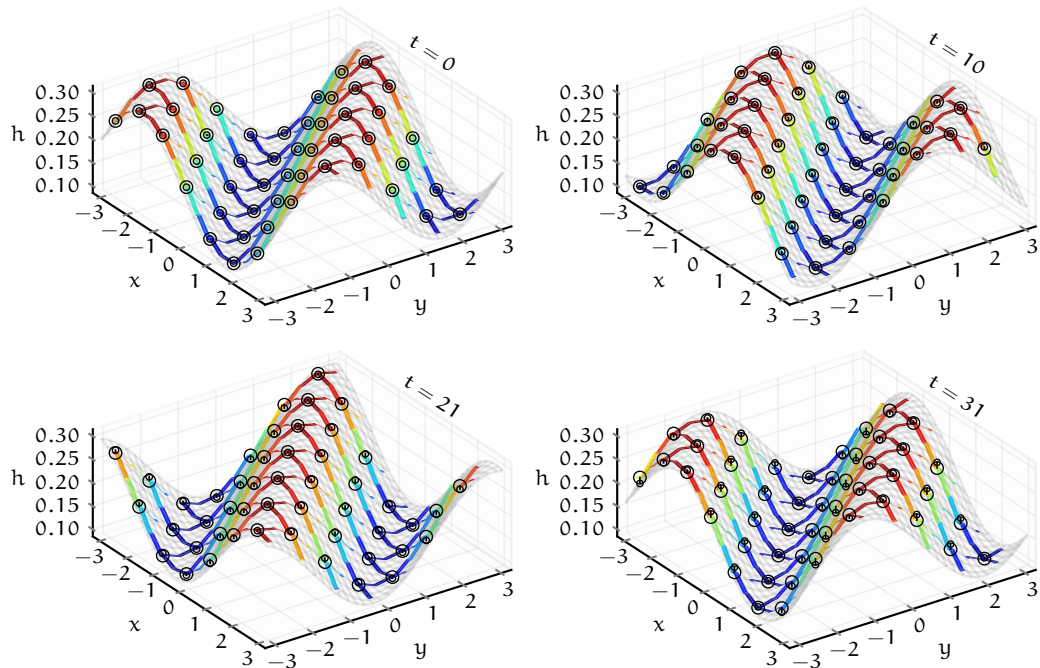


Figure 3.7.10. Velocity u for time evolution of the progressive wave, for the same patch scheme simulation detailed in Fig. 3.7.9 (colour-coded ribbons) agrees closely with that of the fine-grid full-domain model (grey mesh). Black circles on u -centred patches show that the discrepancy is small.

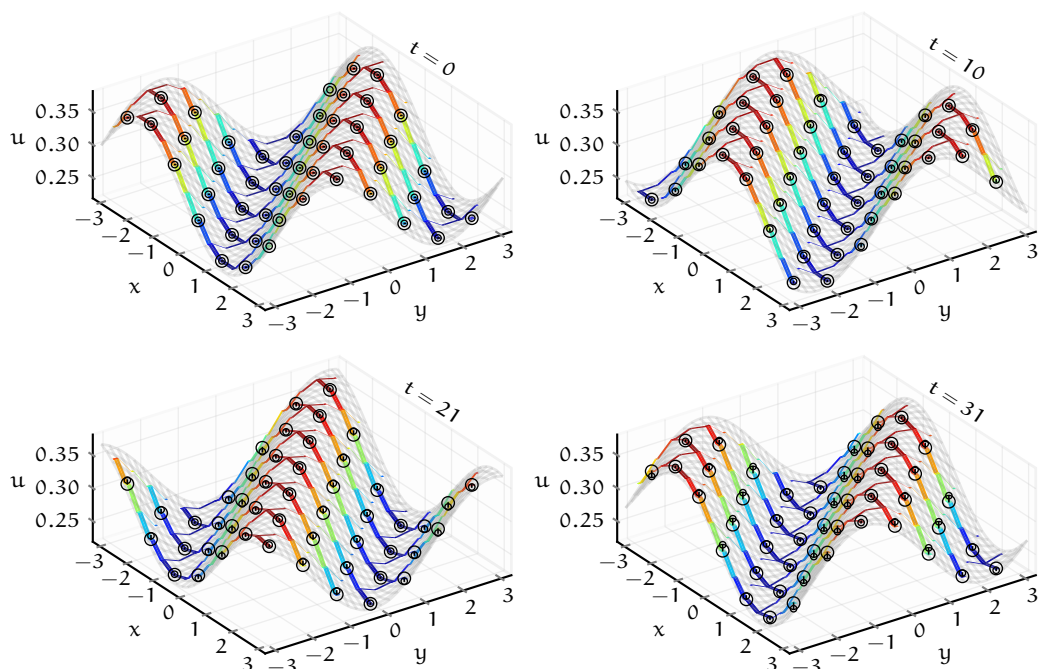
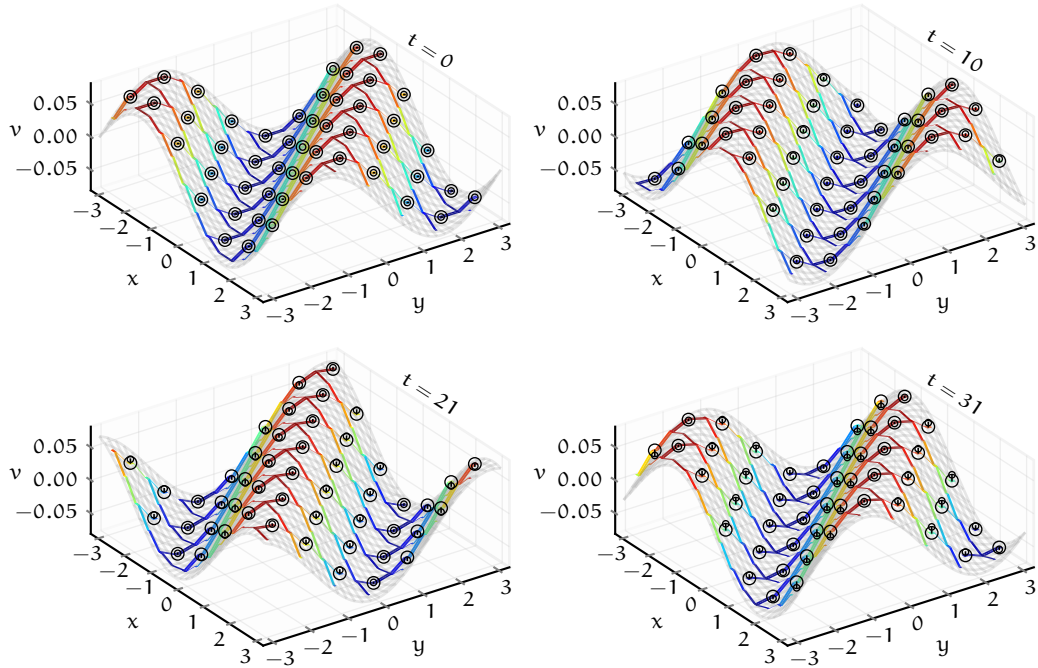


Figure 3.7.11. Velocity v for time evolution of the progressive wave, for the same patch scheme simulation detailed in Fig. 3.7.9 (colour-coded ribbons) agrees closely with that of the fine-grid full-domain model (grey mesh). Black circles on v -centred patches show that the discrepancy is small.



sub-patch micro-grid intervals, and the patch scale ratio $r = 0.01$. The fine-grid full-domain microscale model (3.7.2) (grey mesh) uses the same micro-grid interval as the sub-patch micro-grid interval $\delta = 2Lr/(Nn) = 2\pi/4200 \approx 0.0015$. But the grey mesh of the full-domain model plots only 29×29 grid instead of all the 4201×4201 grid lines, skipping many lines for visual clarity. The colour-coded ribbons of the patch scheme in Fig. 3.7.9 consist of all the lines (along the coordinate axes x and y) passing through all the h nodes within all the patches; similarly Figs. 3.7.10 and 3.7.11 for u , v nodes within all the patches respectively. The color ribbons in y direction for u in Fig. 3.7.10 are narrower due to the smaller number of u nodes in x direction in the h - and v -centred patches (e.g., Fig. 2.1.5a). Similarly the color ribbons in x direction for v in Fig. 3.7.11 are narrower due to the smaller number of v nodes in y direction in the h - and u -centred patches (e.g., Fig. 2.1.5a). Although the patch scale ratio is $r = 0.01$, the patches are enlarged here for visual clarity so that the ribbons appear wider.

Figures 3.7.9 to 3.7.11, plot time evolution of h , u , v from $t = 0$ to 10π (five full cycles). In Figs. 3.7.9 to 3.7.11, the solutions $h/u/v$ of fine-grid full-domain microscale model are linearly interpolated using nearest four

values to the centres of the respective $h/u/v$ -centred patches, illustrated by small black circles. The large circles are the patch scheme solution $h/u/v$. [Figures 3.7.9 to 3.7.11](#) visually show that the discrepancy between the patch scheme and fine-grid full-domain model is small, non concentric black circles are offset only slightly. Despite being small, the increasing error (distance between centres of non-concentric black circles) with increasing time is due to the accumulation of the ODE integrator error.

[Figures 3.7.9 to 3.7.11](#) qualitatively show that the progressive wave time simulation using Square-p4 patch scheme [\(3.1.3\)](#) (colour-coded ribbons) with $N = 14$, $n = 6$, and $r = 0.01$, agrees closely with that of the fine-grid full-domain model [\(3.7.2\)](#) (grey mesh). Next, we aim to numerically assess how well the time simulations of the full-domain model compare with that of the patch schemes for a different number of macro-grid intervals N and patch scale ratio r . To numerically quantify the discrepancy, we compute the solutions $h_{m\delta}^c, u_{m\delta}^c, v_{m\delta}^c$ of the fine-grid full-domain microscale model, at the positions of the respective $h/u/v$ -centred patches, by a bilinear interpolation using the four nearest full-domain node values. For example, [Figs. 3.7.9 to 3.7.11](#) indicate the full-domain solutions at the respective patch centres as small black circles. In terms of the full-domain solutions $h_{m\delta}^c, u_{m\delta}^c, v_{m\delta}^c$ and the patch centre values h_p^c, u_p^c, v_p^c of a patch scheme (large black circles [Figs. 3.7.9 to 3.7.11](#)), we define the relative *simulation errors* at time t as

$$\epsilon_t^h = \|h_{m\delta}^c - h_p^c\| / \|h_{m\delta}^c\|, \quad (3.7.9a)$$

$$\epsilon_t^u = \|u_{m\delta}^c - u_p^c\| / \|u_{m\delta}^c\|, \quad (3.7.9b)$$

$$\epsilon_t^v = \|v_{m\delta}^c - v_p^c\| / \|v_{m\delta}^c\|. \quad (3.7.9c)$$

The norm in the simulation errors [\(3.7.9\)](#) is the Euclidean norm over all the patch centres of the same node type. For example, for a patch grid with 14×14 macro-grid intervals ($N = 14$), there are $7 \times 7 = 49$ macro-cells with each cell containing three patches namely h -, u - and v -centred patches. Thus, for $N = 14$, there are 49 values of the full-domain solutions $h_{m\delta}^c, u_{m\delta}^c, v_{m\delta}^c$ and the patch centre values h_p^c, u_p^c, v_p^c ; hence the norm in [\(3.7.9\)](#) is the Euclidean norm of the 49-element vectors.

[Figures 3.7.12 to 3.7.14](#), the *solution convergence plots*, plot the simulation errors $\epsilon_{2\pi}^h, \epsilon_{2\pi}^u, \epsilon_{2\pi}^v$ at $t = 2\pi$ for progressive wave time evolution with initial condition [\(3.7.8\)](#), for the general linear wave with the coefficients $c_D = 10^{-6}$ and $c_V = 10^{-4}$. [Figures 3.7.12 to 3.7.14](#) show that the simulation errors are small, about 10^{-3} for the Spectral patch scheme, without any dependence on the macro-grid interval Δ . That is, the Spectral patch scheme macroscale solutions agree closely with the macroscale solutions of the fine-grid

Figure 3.7.12. Convergence of patch scheme time solution h in terms of simulation error $\epsilon_{2\pi}^h$ of (3.7.9a) for progressive wave time evolution with initial condition (3.7.8). Solid lines are the power law curve fit given by $\tilde{\epsilon}_{2\pi}^h = 0.83 \cdot (0.71 \cdot \Delta)^p$.

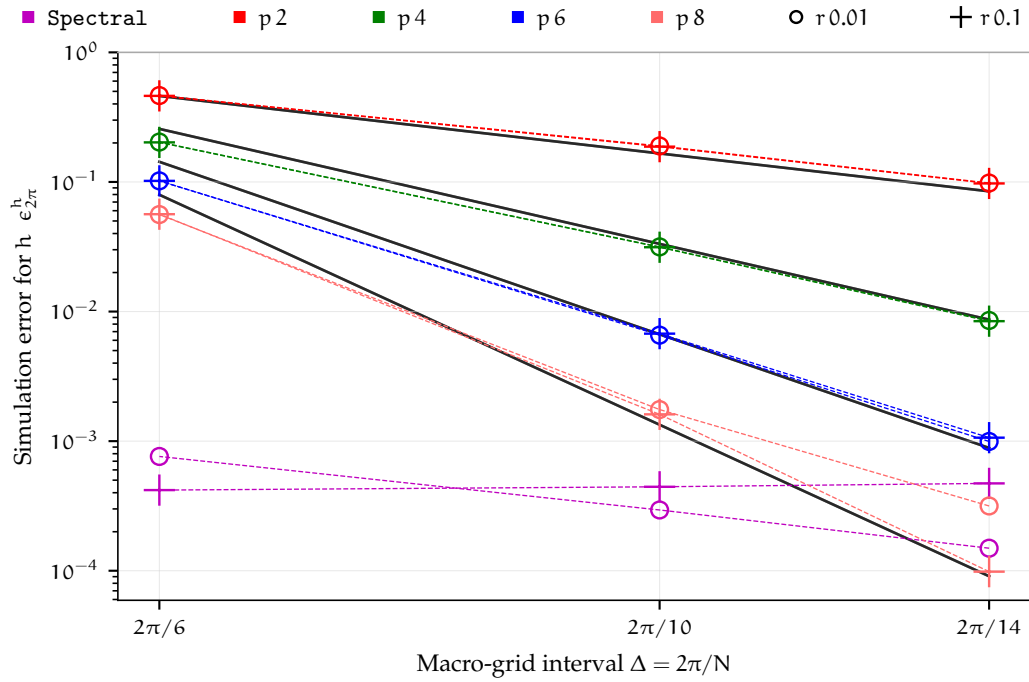


Figure 3.7.13. Convergence of patch scheme time solution u in terms of simulation error $\epsilon_{2\pi}^u$ of (3.7.9b) for progressive wave time evolution with initial condition (3.7.8). Solid lines are the power law curve fit given by $\tilde{\epsilon}_{2\pi}^u = 0.65 \cdot (0.65 \cdot \Delta)^p$.

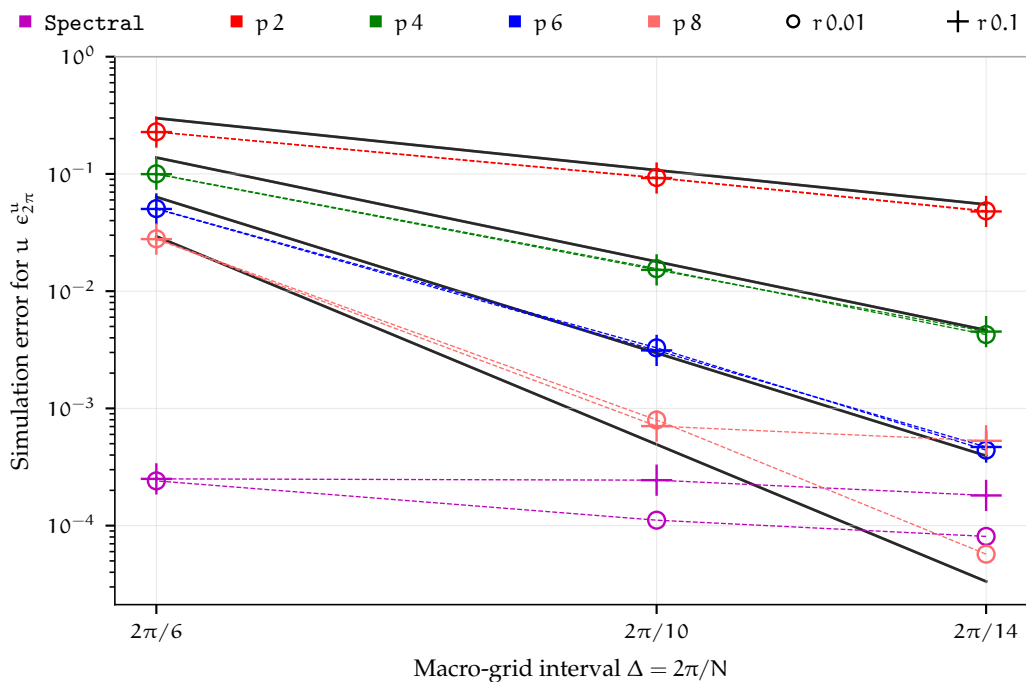
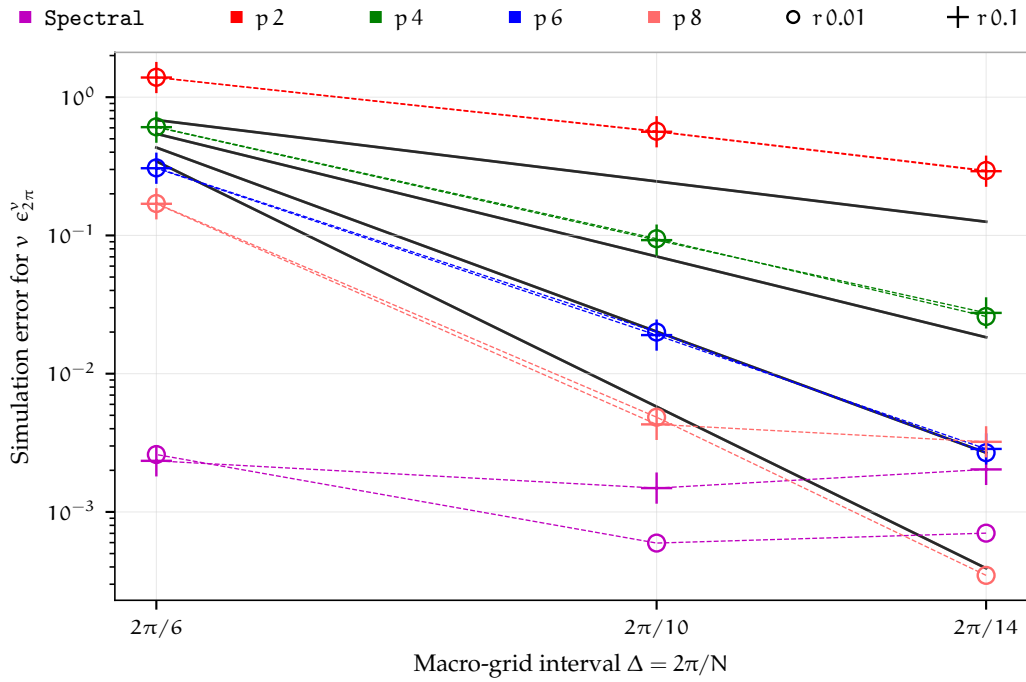


Figure 3.7.14. Convergence of patch scheme time solution v in terms of simulation error $\epsilon_{2\pi}^v$ of (3.7.9c) for progressive wave time evolution with initial condition (3.7.8). Solid lines are the power law curve fit given by $\tilde{\epsilon}_{2\pi}^v = 0.86 \cdot (0.85 \cdot \Delta)^p$.



full-domain model, without any dependence on the macro-grid interval Δ , just as the eigenvalue convergence in §3.6.1. The solution convergence plots Figs. 3.7.12 to 3.7.14 also show that the simulation errors converge to zero for the polynomial patch schemes (Square-p2, Square-p4, Square-p6, Square-p8) with decreasing macro-grid interval Δ (increasing N). That is, the polynomial patch scheme macroscale solutions converge to the macroscale solutions of the fine-grid full-domain model with decreasing macro-grid intervals Δ (increasing N), just as the eigenvalue convergence in §3.6.2. Thus, the staggered patch schemes accurately simulate the macroscale general linear waves.

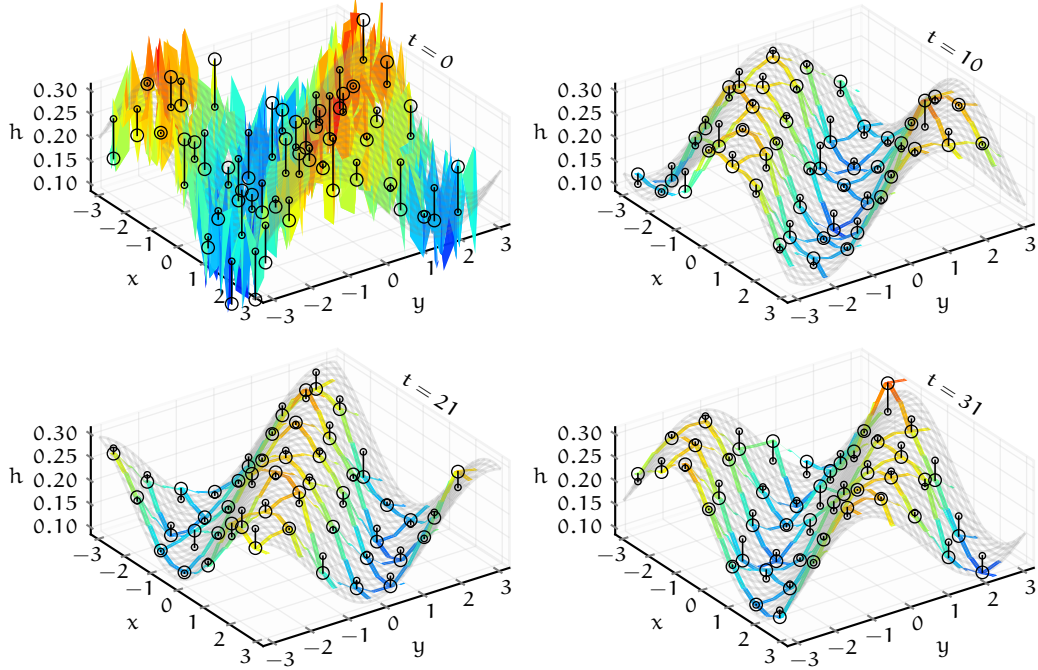
Figure 3.7.15 plots the Square-p4 patch scheme simulation of height h (colour-coded ribbons, with $N = 14$, $n = 6$, and $r = 0.01$) of the progressive wave for the initial condition with uniform random perturbation

$$h_0(x, y) = 0.2 + 0.1 [\sin(x + y) + 1.2 \text{rand}(-1, 1)], \tag{3.7.10a}$$

$$u_0(x, y) = 0.3 + (0.1/\sqrt{2})[\sin(x + y) + 1.2 \text{rand}(-1, 1)], \tag{3.7.10b}$$

$$v_0(x, y) = 0, \tag{3.7.10c}$$

Figure 3.7.15. Height h for Square-p4 patch scheme simulation (colour-coded ribbons, with $N = 14$, $n = 6$, and $r = 0.01$) of the progressive wave with initial uniform random perturbation (3.7.10) (compare with Fig. 3.7.9 without the perturbation). The patch scheme robustly simulates the emergent macroscale solution by rapidly dissipating the random perturbation.



where $\text{rand}(-1, 1)$ generates a pseudo random number within $[-1, 1)$ via Mersenne Twister algorithm. The initial condition (3.7.10) is same as the initial condition (3.7.8) except the added uniform random perturbation for h_0 and u_0 . Figure 3.7.9 plots the corresponding patch scheme simulation without the random perturbation. Figure 3.7.15 shows that the *patch scheme robustly simulates the emergent macroscale solution* where the viscous diffusion rapidly dissipates the random perturbation (microscale waves). That is, the slow manifold of the patch scheme solution space is exponentially attracting.

For the time simulation in Figs. 3.7.9 to 3.7.11 from $t = 0$ to 10π , Table 3.7.1 lists the total compute times of the fine-grid full-domain model and that of the five staggered patch schemes. The compute times in this subsection are measured on a custom assembled liquid-cooled workstation with Intel i7-6900k processor and 64GB DDR4 RAM. The total function calls by the BS3 ODE integrator to evaluate the derivative of the state vector for the fine-grid full-domain model and that of the patch schemes are similar (i.e., within 10%). But the ratio of the total compute time of the full-domain

Table 3.7.1. Total compute times in minutes for the progressive wave time simulation from $t = 0$ to 10π (e.g., Figs. 3.7.9 to 3.7.11) with initial condition (3.7.8). Patch schemes use $N = 14$, $n = 6$, and $r = 0.01$. The fine-grid full-domain model has the same grid interval as the sub-patch micro-grid interval δ . The ratio of total compute time of the full-domain model to that of the patch schemes, *compute time gain*, is on average about 1300.

	Full-domain	Spectral	p2	p4	p6	p8
Total compute time [m]	2925 (48.75 h)	2.10	1.82	2.22	2.18	2.24
Total function calls	45261	39432	40599	40503	40482	40437
Compute time gain (full-domain / patch)	–	1390	1610	1316	1343	1305

model to that of a patch schemes, *compute time gain*, in Table 3.7.1 shows that on average the *patch scheme compute time is 1300 times smaller*. This computational savings by three orders of magnitude based on the total compute time also agree with the computational savings in terms of the compute time per iteration for $r = 0.01$ in Fig. 3.7.5 (crosses).

As another example, we demonstrate a higher order polynomial patch scheme simulation on a finer patch grid for a moving Gaussian hump in x direction with the initial condition

$$h_0(x, y) = 0.2 + 0.4 \exp[-(x + 1.5)^2 - y^2/2.2^2], \quad (3.7.11a)$$

$$u_0(x, y) = 0.3 + 0.5 \exp[-(x + 1.5)^2 - y^2/2.2^2], \quad (3.7.11b)$$

$$v_0(x, y) = 0. \quad (3.7.11c)$$

For the general linear wave with coefficients $c_D = 10^{-6}$ and $c_V = 10^{-4}$, Figs. 3.7.16 to 3.7.18 show the time simulation of a moving Gaussian hump in x direction with the initial condition (3.7.11), using Square-p8 patch scheme with $N = 22$, $n = 6$, and $r = 0.001$. For the patch scheme simulation in Figs. 3.7.16 to 3.7.18 from $t = 0$ to 10π , the total compute time is 85 min. For the corresponding fine-grid full-domain model (i.e., with the same grid interval as the sub-patch micro-grid interval δ) the compute time is about 10^5 times larger than the patch scheme (the plus marker in Fig. 3.7.5 for $n = 6$ and $r = 0.001$). That is, for the similar grid resolution and accuracy as in Figs. 3.7.16 to 3.7.18, the estimated compute time of a full-domain simulation is about 16 years, but the measured patch scheme compute time is only 85 min.

Figure 3.7.19 plots the Square-p8 patch scheme simulation of height h (with $N = 14$, $n = 6$, and $r = 0.01$) of a moving Gaussian hump in x direction

Figure 3.7.16. Height h for time simulation of a moving Gaussian hump in x direction with initial condition (3.7.11), using Square-p8 patch scheme with $N = 22$, $n = 6$, and $r = 0.001$. Patch scheme compute time is 85 min; for the full-domain simulation with the same grid resolution the estimated compute time is about 16 years (i.e., 10^5 times larger, from Fig. 3.7.5).

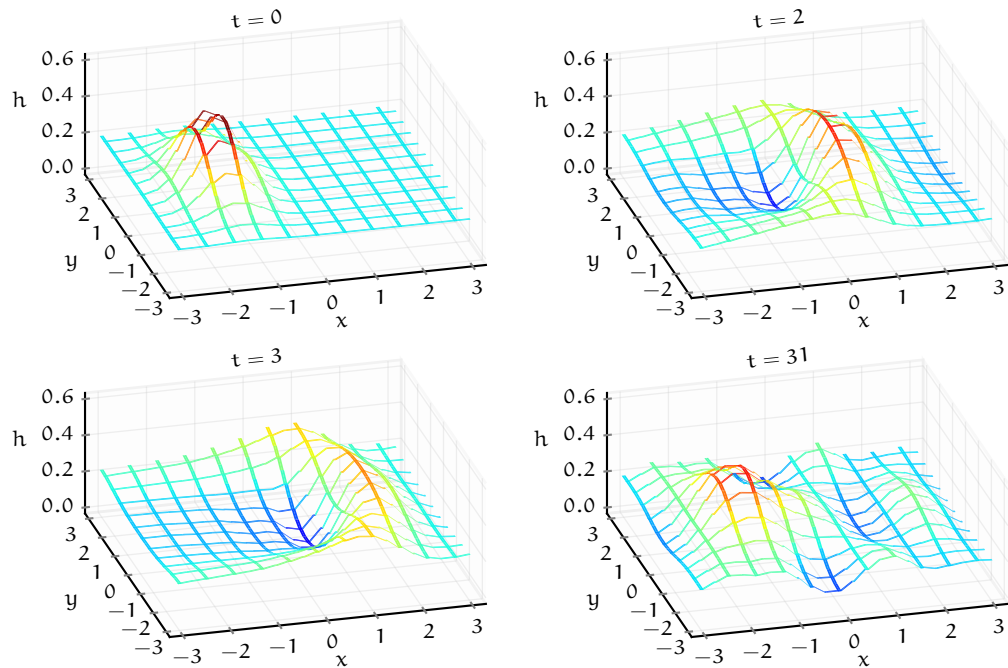


Figure 3.7.17. Velocity u for time simulation of a moving Gaussian hump, for the same patch scheme simulation detailed in Fig. 3.7.16.

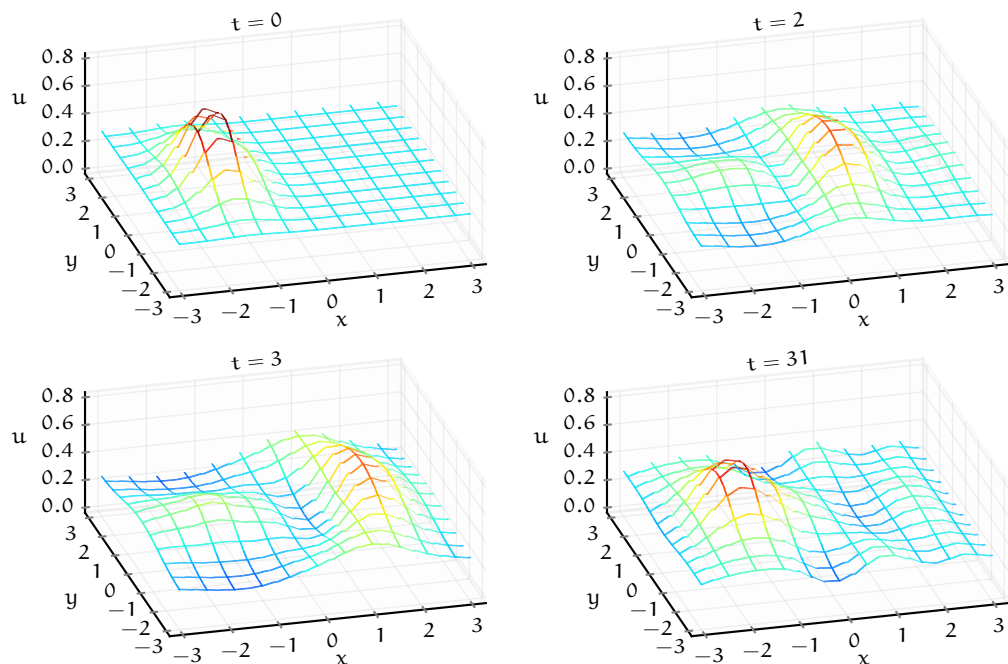


Figure 3.7.18. Velocity v for time simulation of a moving Gaussian hump, for the same patch scheme simulation detailed in Fig. 3.7.16.

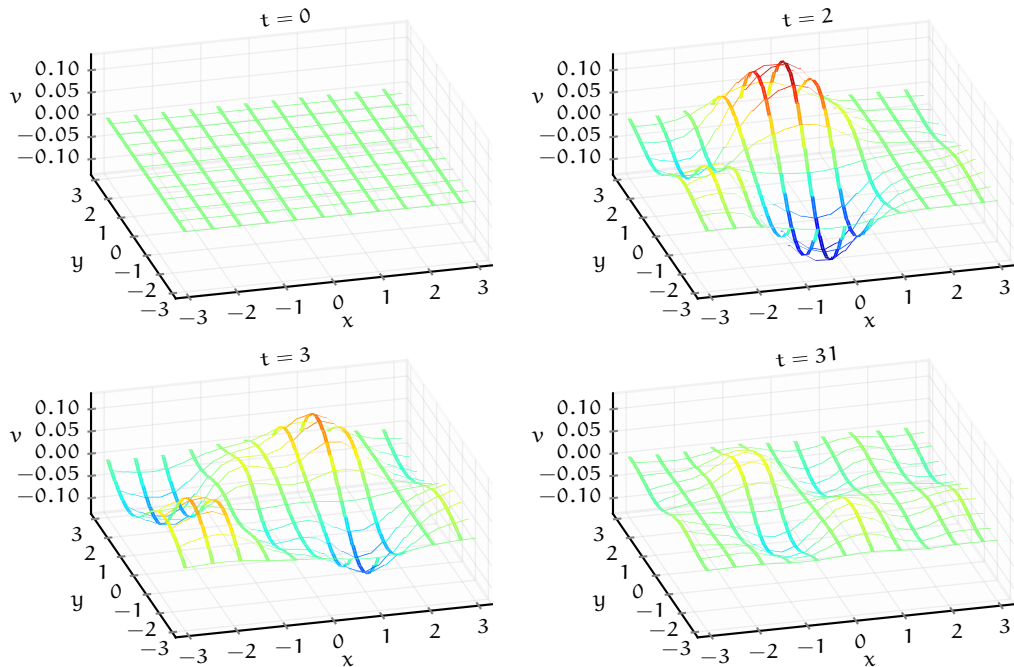
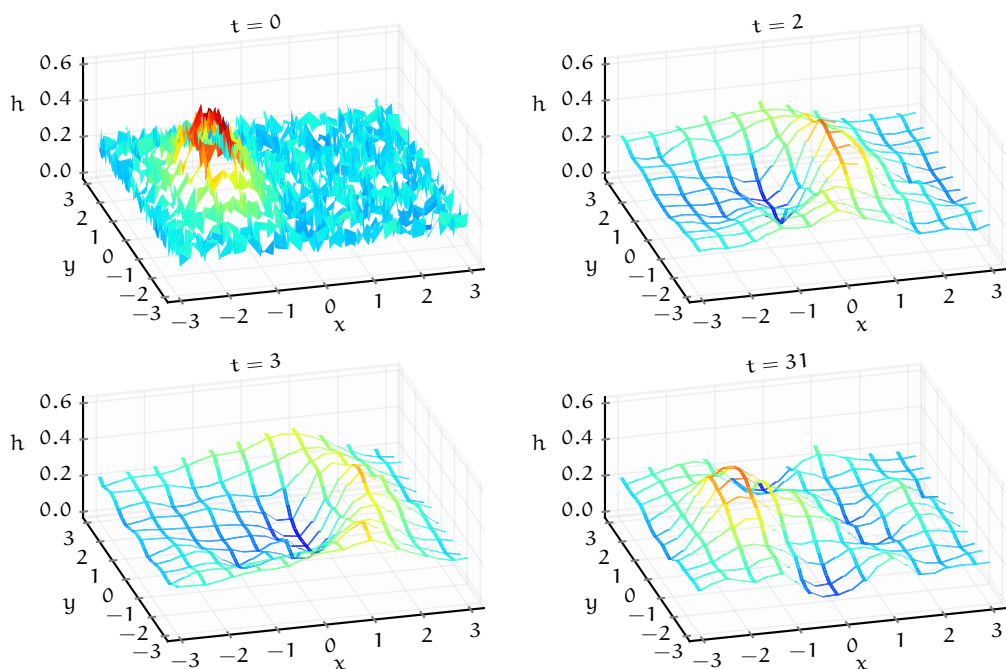


Figure 3.7.19. Height h for time simulation of a moving Gaussian hump in x direction *with initial uniform random perturbation* (3.7.12), using Square-p8 patch scheme with $N = 22$, $n = 6$, and $r = 0.001$ (compare with Fig. 3.7.16 without the perturbation). The patch scheme robustly simulates the emergent macroscale solution.



with uniform random perturbation

$$h_0(x, y) = 0.2 + 0.4 \exp[-(x + 1.5)^2 - y^2/2.2^2] + 0.08 \operatorname{rand}(-1, 1), \quad (3.7.12a)$$

$$u_0(x, y) = 0.3 + 0.5 \exp[-(x + 1.5)^2 - y^2/2.2^2] + 0.1 \operatorname{rand}(-1, 1), \quad (3.7.12b)$$

$$v_0(x, y) = 0. \quad (3.7.12c)$$

where $\operatorname{rand}(-1, 1)$ generates a pseudo random number within $[-1, 1)$ via Mersenne Twister algorithm. The initial condition (3.7.12) is same as the initial condition (3.7.11) except the added uniform random perturbation for h_0 and u_0 . Figure 3.7.16 plots the corresponding patch scheme simulation without the random perturbation. Figure 3.7.19 shows that the patch scheme robustly simulate the emergent the macroscale solution for a moving Gaussian hump.

Thus, the staggered patch schemes accurately simulate the macroscale general linear waves, with large computational savings such as 10^5 times smaller compute times compared to the fine-grid full-domain model.

Chapter 4

Patch schemes accurately simulate viscous shallow water flows

This chapter shows that the staggered patch schemes of [Chapter 2](#) accurately simulate the macroscale dynamics of viscous shallow water flows, using the PDEs derived by Roberts and Li (2006) as the microscale model within the patches. Roberts and Li (2006) derived comprehensive viscous shallow water PDEs in terms of the depth-averaged variables, but without depth-averaging the PDEs. Instead, from the full incompressible 3D Navier–Stokes equation, they derive the 2D viscous shallow water PDEs using centre manifold theory, in terms of the depth-averaged variables. The article by Roberts and Li (2006) demonstrates the utility of the viscous shallow water PDEs by simulating various thin-fluid flows such as drop formation on cylindrical fibres, wave transitions, three-dimensional instabilities, Faraday waves, viscous hydraulic jumps, flow vortices in a compound channel and flow down and up a step.

[Section 4.1](#) first non-dimensionalises the viscous shallow water PDEs of Roberts and Li (2006) slightly differently to facilitate extensive analysis of the staggered patch schemes. Subsequently, [§4.1](#) derives a discrete full-domain microscale model and a generic staggered patch scheme corresponding to the viscous shallow water flows. Throughout this chapter, we use this full-domain microscale model as the reference to assess various characteristics (accuracy, stability, consistency, etc.) of the multiscale staggered patch schemes we develop. [Section 4.1.4](#) chooses a set of values for the non-dimensional parameters towards exploration of patch schemes for viscous shallow water PDEs.

[Section 4.2](#) shows that the developed five staggered patch schemes are accurate for viscous shallow water flows by comparing the eigenvalues of the staggered patch schemes with the eigenvalues of the full-domain micro-

scale model. [Section 4.2](#) establishes the accuracy of the staggered patch schemes in general (as opposed to one specific initial condition) by comparing the eigenvalues of the staggered patch schemes with the eigenvalues of fine- and coarse-grid full-domain microscale model. [Sections 4.2.1 to 4.2.5](#) derives the eigenvalues of the viscous shallow water PDEs, full-domain microscale model, and that of the staggered patch schemes. [Section 4.2.6](#) illustrates the structure of the patch scheme eigenvalues in the complex plane and explains the corresponding dynamical modes via eigenvector plots. The eigenvalue analysis in [§4.2.6](#) visually demonstrates the accuracy (in the complex plane eigenvalue plots) for a representative subset of the physical parameters and grid parameters. [Section 4.5](#) on the consistency of the patch schemes establishes the accuracy over a wider range of parameters.

Despite the attractive characteristics, if the staggered patch schemes are very sensitive to numerical roundoff errors, then they would not be suitable for practical numerical simulations using finite precision floating-point arithmetic. For viscous shallow water flows, from both qualitative arguments and quantitative evidence, [§4.3](#) shows that the staggered patch schemes are not sensitive to numerical roundoff errors, except when the patches are too small relative to inter-patch distance, and/or when the underlying microscale model is sensitive to numerical roundoff errors. The quantitative evidence in [§4.3](#) comes from comparing the eigenvalues of analytic Jacobian and numerical Jacobians of a patch scheme. Even for very small patches, [p. 250 of §4.5.1](#) confirms the consistency of the patch schemes via arbitrary-precision floating-point implementation.

In contrast to the general linear wave in [Chapter 3](#), the viscous shallow water flows over a sloping bed have a physical instability of roll waves. Hence, a good patch scheme must reflect this physical instability depending upon the physical parameters (Reynolds number Re , mean flow h_M, u_M, v_M), but *without any additional/artificial instability*. So, [§4.4](#) shows that with an appropriate patch grid the staggered patch schemes are not artificially unstable for a wide range of physical parameters by comparing the eigenvalues of the patch schemes with those of the full-domain microscale model and the PDEs.

[Section 4.5](#) shows that the staggered patch schemes are consistent with the given microscale model. [Section 4.5](#) establishes the consistency of the patch schemes for the viscous shallow water flows by comparing the macro-scale eigenvalues (defined in [p. 52 of §3.2](#)) of the patch scheme with the corresponding eigenvalues of the full-domain microscale model for increasingly finer patch grids. [Section 4.5.1](#) shows that the Spectral patch scheme is uniformly accurate with little dependence on the macro-grid interval Δ . [Section 4.5.2](#) shows that the polynomial patch schemes are consistent to

the same order of the polynomial interpolation with decreasing macro-grid interval Δ .

Almost all the key studies in this chapter are performed for a range of parameters but keeping the horizontal mean velocity $v_M = 0$. That is, most results in this chapter correspond to flow angle $\alpha = \arctan(v_M/u_M) = 0$, where the velocities are $u_M = q \cos(\alpha)$ and $v_M = q \sin(\alpha)$. [Section 4.6](#) validates that assumption, by showing that the variation of the patch scheme eigenvalue errors (discrepancy between the patch scheme and full-domain model) are negligible with varying flow angles α . That is, [§4.6](#) shows that staggered patch schemes are invariant to flow direction.

[Section 4.7](#) quantifies and demonstrates the large computational savings of the staggered patch schemes for the viscous shallow water flows. [Section 4.7.1](#) shows the computational savings of the 2D staggered patch schemes theoretically in terms of the ratio of the space over which the patch schemes and the full-domain model computes. [Section 4.7.1](#) shows the computational savings of the patch schemes in terms of the ratio of the number of state variables for which the patch schemes and the full-domain model computes. [Section 4.7.3](#) demonstrates the computational savings of the 2D staggered patch schemes by measuring the elapsed time taken to compute the time derivative of the state vector (one time iteration) using a specific implementation. [Section 4.7.5](#) demonstrates the accuracy and the effectiveness of the staggered patch schemes by numerically simulating a localised nearly discontinuous macroscale viscous roll waves (e.g., Balmforth and Mandre 2004) emerging from the initial condition of a simple progressive wave within the small sparsely located patches. [Section 4.7.6](#) establishes the accuracy of the staggered patch scheme simulations more quantitatively and explains some subtle details of the practical issues in the patch scheme simulations.

4.1 PDEs, full-domain microscale model, and staggered patch schemes

This section first non-dimensionalises the viscous shallow water PDEs of Roberts and Li (2006) slightly differently to facilitate extensive analysis of the staggered patch schemes. Subsequently, this section derives a discrete full-domain microscale model and a generic staggered patch scheme corresponding to the viscous shallow water flows.

[Section 4.1.1](#) non-dimensionalises the viscous shallow water PDEs and the boundary conditions derived by Roberts and Li (2006) using a refer-

ence length in terms of domain size as opposed to the characteristic height used by Roberts and Li (2006). Sections 4.1.2 and 4.1.3 derives a discrete full-domain microscale model and a generic staggered patch scheme, corresponding to the viscous shallow water PDEs of §4.1.1. Throughout this chapter, we use this full-domain microscale model as a reference to assess various characteristics (accuracy, stability, consistency, etc.) of the multi-scale staggered patch schemes we develop. Section 4.1.4 chooses a set of values for the non-dimensional parameters towards exploration of patch schemes for viscous shallow water PDEs.

4.1.1 Non-dimensionalise the PDEs to keep same domain size

In deriving the viscous shallow water PDEs which we use as the microscale model for patch scheme, Roberts and Li (2006) non-dimensionalise the space by characteristic water height H . Such non-dimensionalisation by characteristic water height H leads to different non-dimensional domain sizes for different non-dimensional heights. We want to explore patch schemes *keeping the non-dimensional domain size the same, to reuse some of the patch scheme computations*. Hence, this subsection non-dimensionalises the 2D space by a reference length $L/(2\pi)$; that is, $x' = 2\pi x/L$, $y' = 2\pi y/L$ so that the dimensional square domain $[0, L] \times [0, L]$ corresponds to the non-dimensional square domain $[0, 2\pi] \times [0, 2\pi]$ irrespective of the characteristic (dimensional) water height H .

The non-dimensional *comprehensive* viscous shallow water PDEs (64)–(66) in the article by Roberts and Li (2006, pp.56–57) are, omitting the over bar for dependent variables and using daggers for the non-dimensional

dependent and independent variables $h^\dagger, u^\dagger, v^\dagger, x^\dagger, y^\dagger, t^\dagger$,

$$\frac{\partial h^\dagger}{\partial t^\dagger} \approx -\frac{\partial h^\dagger u^\dagger}{\partial x^\dagger} - \frac{\partial h^\dagger v^\dagger}{\partial y^\dagger}, \quad (4.1.1a)$$

$$\begin{aligned} \text{Re} \frac{\partial u^\dagger}{\partial t^\dagger} \approx & -\frac{\pi^2}{4} \frac{u^\dagger}{h^{\dagger 2}} + \frac{\pi^2}{12} \left[\text{Gr} \left(g_x + g_n \frac{\partial h^\dagger}{\partial x^\dagger} \right) + \text{We} \left(\frac{\partial^3 h^\dagger}{\partial x^{\dagger 3}} + \frac{\partial^3 h^\dagger}{\partial x^\dagger \partial y^{\dagger 2}} \right) \right] \\ & - \text{Re} \left[1.5041 u^\dagger \frac{\partial u^\dagger}{\partial x^\dagger} + 1.3464 v^\dagger \frac{\partial u^\dagger}{\partial y^\dagger} + 0.1577 u^\dagger \frac{\partial v^\dagger}{\partial y^\dagger} \right. \\ & \quad \left. + 0.1483 \frac{u^\dagger}{h^\dagger} \left(u^\dagger \frac{\partial h^\dagger}{\partial x^\dagger} + v^\dagger \frac{\partial h^\dagger}{\partial y^\dagger} \right) \right] \\ & + 4.0930 \frac{\partial^2 u^\dagger}{\partial x^{\dagger 2}} + \frac{\partial^2 u^\dagger}{\partial y^{\dagger 2}} + 3.0930 \frac{\partial^2 v^\dagger}{\partial x^\dagger \partial y^\dagger} + 4.8333 \frac{1}{h^\dagger} \frac{\partial h^\dagger}{\partial x^\dagger} \frac{\partial u^\dagger}{\partial x^\dagger} + \frac{1}{h^\dagger} \frac{\partial h^\dagger}{\partial y^\dagger} \frac{\partial u^\dagger}{\partial y^\dagger} \\ & + 1.9167 \frac{1}{h^\dagger} \frac{\partial h^\dagger}{\partial x^\dagger} \frac{\partial v^\dagger}{\partial y^\dagger} + 1.9167 \frac{1}{h^\dagger} \frac{\partial h^\dagger}{\partial y^\dagger} \frac{\partial v^\dagger}{\partial x^\dagger} \\ & - \left[0.5033 \frac{1}{h^{\dagger 2}} \left(\frac{\partial h^\dagger}{\partial y^\dagger} \right)^2 + \frac{1}{2h^\dagger} \frac{\partial^2 h^\dagger}{\partial y^{\dagger 2}} - 0.1061 \frac{1}{h^{\dagger 2}} \left(\frac{\partial h^\dagger}{\partial x^\dagger} \right)^2 + 0.5834 \frac{1}{h^\dagger} \frac{\partial^2 h^\dagger}{\partial x^{\dagger 2}} \right] u^\dagger \\ & + \left[0.6094 \frac{1}{h^{\dagger 2}} \frac{\partial h^\dagger}{\partial x^\dagger} \frac{\partial h^\dagger}{\partial y^\dagger} - 0.0833 \frac{1}{h^\dagger} \frac{\partial^2 h^\dagger}{\partial x^\dagger \partial y^\dagger} \right] v^\dagger, \quad (4.1.1b) \end{aligned}$$

$$\begin{aligned} \text{Re} \frac{\partial v^\dagger}{\partial t^\dagger} \approx & -\frac{\pi^2}{4} \frac{v^\dagger}{h^{\dagger 2}} + \frac{\pi^2}{12} \left[\text{Gr} \left(g_y + g_n \frac{\partial h^\dagger}{\partial y^\dagger} \right) + \text{We} \left(\frac{\partial^3 h^\dagger}{\partial y^{\dagger 3}} + \frac{\partial^3 h^\dagger}{\partial y^\dagger \partial x^{\dagger 2}} \right) \right] \\ & - \text{Re} \left[1.5041 v^\dagger \frac{\partial v^\dagger}{\partial y^\dagger} + 1.3464 u^\dagger \frac{\partial v^\dagger}{\partial x^\dagger} + 0.1577 v^\dagger \frac{\partial u^\dagger}{\partial x^\dagger} \right. \\ & \quad \left. + 0.1483 \frac{v^\dagger}{h^\dagger} \left(u^\dagger \frac{\partial h^\dagger}{\partial x^\dagger} + v^\dagger \frac{\partial h^\dagger}{\partial y^\dagger} \right) \right] \\ & + 4.0930 \frac{\partial^2 v^\dagger}{\partial y^{\dagger 2}} + \frac{\partial^2 v^\dagger}{\partial x^{\dagger 2}} + 3.0930 \frac{\partial^2 u^\dagger}{\partial x^\dagger \partial y^\dagger} + 4.8333 \frac{1}{h^\dagger} \frac{\partial h^\dagger}{\partial y^\dagger} \frac{\partial v^\dagger}{\partial y^\dagger} + \frac{1}{h^\dagger} \frac{\partial h^\dagger}{\partial x^\dagger} \frac{\partial v^\dagger}{\partial x^\dagger} \\ & + 1.9167 \frac{1}{h^\dagger} \frac{\partial h^\dagger}{\partial x^\dagger} \frac{\partial u^\dagger}{\partial y^\dagger} + 1.9167 \frac{1}{h^\dagger} \frac{\partial h^\dagger}{\partial y^\dagger} \frac{\partial u^\dagger}{\partial x^\dagger} \\ & - \left[0.5033 \frac{1}{h^{\dagger 2}} \left(\frac{\partial h^\dagger}{\partial x^\dagger} \right)^2 + \frac{1}{2h^\dagger} \frac{\partial^2 h^\dagger}{\partial x^{\dagger 2}} - 0.1061 \frac{1}{h^{\dagger 2}} \left(\frac{\partial h^\dagger}{\partial y^\dagger} \right)^2 + 0.5834 \frac{1}{h^\dagger} \frac{\partial^2 h^\dagger}{\partial y^{\dagger 2}} \right] v^\dagger \\ & + \left[0.6094 \frac{1}{h^{\dagger 2}} \frac{\partial h^\dagger}{\partial x^\dagger} \frac{\partial h^\dagger}{\partial y^\dagger} - 0.0833 \frac{1}{h^\dagger} \frac{\partial^2 h^\dagger}{\partial x^\dagger \partial y^\dagger} \right] u^\dagger. \quad (4.1.1c) \end{aligned}$$

In *comprehensive* viscous shallow water PDEs (4.1.1), the non-dimensional parameters *Reynolds number* $\text{Re} = \rho U H / \mu$, *Gravity number* $\text{Gr} = g \rho H^2 / (\mu U)$ and *Weber number* $\text{We} = \sigma / (\mu U)$ are in terms of the following dimensional

quantities: gravitational acceleration g ; density of water ρ ; characteristic mean velocity U ; characteristic mean height H ; kinematic viscosity ν ; surface tension σ . The grey-coloured terms in (4.1.1) are less significant compared to the other terms.

The viscous shallow water PDEs (4.1.1) are written in the bed-attached local coordinate system with the bed in xy -plane and height h perpendicular to the bed. The constants $g_x = \sin(\theta)$, $g_n = -\cos(\theta)$ are components of the unit vector of gravitational acceleration, where θ is the bed inclination angle relative to the local horizontal plane of earth (positive for downward slopping bed along x axis). For example, for the horizontal flat bed, $\theta = 0$, hence $g_x = 0$ and $g_n = -1$.

The only difference between the non-dimensionalisation of Roberts and Li (2006) in the non-dimensional comprehensive viscous shallow water PDEs (4.1.1) and the non-dimensionalisation we aim to, is that their non-dimensionalisation of lengths are

$$x = x^\dagger H, \quad y = y^\dagger H, \quad h = h^\dagger H, \quad (4.1.2a)$$

$$\Rightarrow \frac{\partial^n}{\partial x^n} = (1/H)^n \frac{\partial^n}{\partial x^{\dagger n}}, \quad \frac{\partial^n}{\partial y^n} = (1/H)^n \frac{\partial^n}{\partial y^{\dagger n}}, \quad (4.1.2b)$$

using daggers for non-dimensional parameters, which is different from our non-dimensionalisation of lengths, using primes for non-dimensional parameters

$$x = x' L / (2\pi), \quad y = y' L / (2\pi), \quad h = h' L / (2\pi), \quad (4.1.3a)$$

$$\Rightarrow \frac{\partial^n}{\partial x^n} = (2\pi/L)^n \frac{\partial^n}{\partial x'^n}, \quad \frac{\partial^n}{\partial y^n} = (2\pi/L)^n \frac{\partial^n}{\partial y'^n}. \quad (4.1.3b)$$

So, for converting the non-dimensional comprehensive viscous shallow water PDEs (4.1.1) to use our non-dimensionalisation, we substitute the following relations into the PDEs (4.1.1)

$$x^\dagger = x' L / (2\pi H), \quad y^\dagger = y' L / (2\pi H), \quad h^\dagger = h' L / (2\pi H)$$

$$\Rightarrow \frac{\partial^n}{\partial x^{\dagger n}} = (2\pi H/L)^n \frac{\partial^n}{\partial x'^n}, \quad \frac{\partial^n}{\partial y^{\dagger n}} = (2\pi H/L)^n \frac{\partial^n}{\partial y'^n},$$

which we get by equating the dimensional quantities in the two different non-dimensionalisations (4.1.2) and (4.1.3). Using the definition of the characteristic mean non-dimensional height $h_M = 2\pi H/L$, the substitutions become

$$x^\dagger = x' / h_M, \quad y^\dagger = y' / h_M, \quad h^\dagger = h' / h_M, \quad (4.1.4a)$$

$$\Rightarrow \frac{\partial^n}{\partial x^{\dagger n}} = h_M^n \frac{\partial^n}{\partial x'^n}, \quad \frac{\partial^n}{\partial y^{\dagger n}} = h_M^n \frac{\partial^n}{\partial y'^n}. \quad (4.1.4b)$$

After substituting (4.1.4) into the non-dimensional comprehensive viscous shallow water PDEs (4.1.1), we get the non-dimensional *comprehensive viscous shallow water* PDEs with our non-dimensionalisation of space by the reference length $L/(2\pi)$ as

$$\frac{1}{h_M} \frac{\partial h'}{\partial t'} \approx -\frac{\partial h' u'}{\partial x'} - \frac{\partial h' v'}{\partial y'}, \quad (4.1.5a)$$

$$\begin{aligned} \text{Re} \frac{\partial u'}{\partial t'} \approx & -\frac{\pi^2 h_M^2}{4} \frac{u'}{h'^2} + \frac{\pi^2}{12} \left[\text{Gr} \left(g_x + g_n \frac{\partial h'}{\partial x'} \right) + \text{We} h_M^2 \left(\frac{\partial^3 h'}{\partial x'^3} + \frac{\partial^3 h'}{\partial x' \partial y'^2} \right) \right] \\ & - \text{Re} h_M \left[1.5041 u' \frac{\partial u'}{\partial x'} + 1.3464 v' \frac{\partial u'}{\partial y'} + 0.1577 u' \frac{\partial v'}{\partial y'} \right. \\ & \quad \left. + 0.1483 \frac{u'}{h'} \left(u' \frac{\partial h'}{\partial x'} + v' \frac{\partial h'}{\partial y'} \right) \right] \\ & + h_M^2 \left[4.0930 \frac{\partial^2 u'}{\partial x'^2} + \frac{\partial^2 u'}{\partial y'^2} + 3.0930 \frac{\partial^2 v'}{\partial x' \partial y'} + 4.8333 \frac{1}{h'} \frac{\partial h'}{\partial x'} \frac{\partial u'}{\partial x'} + \frac{1}{h'} \frac{\partial h'}{\partial y'} \frac{\partial u'}{\partial y'} \right] \\ & + h_M^2 \left[1.9167 \frac{1}{h'} \frac{\partial h'}{\partial x'} \frac{\partial v'}{\partial y'} + 1.9167 \frac{1}{h'} \frac{\partial h'}{\partial y'} \frac{\partial v'}{\partial x'} \right] \\ & - h_M^2 \left[0.5033 \frac{1}{h'^2} \left(\frac{\partial h'}{\partial y'} \right)^2 + \frac{1}{2h'} \frac{\partial^2 h'}{\partial y'^2} - 0.1061 \frac{1}{h'^2} \left(\frac{\partial h'}{\partial x'} \right)^2 + 0.5834 \frac{1}{h'} \frac{\partial^2 h'}{\partial x'^2} \right] u' \\ & + h_M^2 \left[0.6094 \frac{1}{h'^2} \frac{\partial h'}{\partial x'} \frac{\partial h'}{\partial y'} - 0.0833 \frac{1}{h'} \frac{\partial^2 h'}{\partial x' \partial y'} \right] v', \quad (4.1.5b) \end{aligned}$$

$$\begin{aligned} \text{Re} \frac{\partial v'}{\partial t'} \approx & -\frac{\pi^2 h_M^2}{4} \frac{v'}{h'^2} + \frac{\pi^2}{12} \left[\text{Gr} \left(g_y + g_n \frac{\partial h'}{\partial y'} \right) + \text{We} h_M^2 \left(\frac{\partial^3 h'}{\partial y'^3} + \frac{\partial^3 h'}{\partial y' \partial x'^2} \right) \right] \\ & - \text{Re} h_M \left[1.5041 v' \frac{\partial v'}{\partial y'} + 1.3464 u' \frac{\partial v'}{\partial x'} + 0.1577 v' \frac{\partial u'}{\partial x'} \right. \\ & \quad \left. + 0.1483 \frac{v'}{h'} \left(u' \frac{\partial h'}{\partial x'} + v' \frac{\partial h'}{\partial y'} \right) \right] \\ & + h_M^2 \left[4.0930 \frac{\partial^2 v'}{\partial y'^2} + \frac{\partial^2 v'}{\partial x'^2} + 3.0930 \frac{\partial^2 u'}{\partial x' \partial y'} + 4.8333 \frac{1}{h'} \frac{\partial h'}{\partial y'} \frac{\partial v'}{\partial y'} + \frac{1}{h'} \frac{\partial h'}{\partial x'} \frac{\partial v'}{\partial x'} \right] \\ & + h_M^2 \left[1.9167 \frac{1}{h'} \frac{\partial h'}{\partial x'} \frac{\partial u'}{\partial y'} + 1.9167 \frac{1}{h'} \frac{\partial h'}{\partial y'} \frac{\partial u'}{\partial x'} \right] \\ & - h_M^2 \left[0.5033 \frac{1}{h'^2} \left(\frac{\partial h'}{\partial x'} \right)^2 + \frac{1}{2h'} \frac{\partial^2 h'}{\partial x'^2} - 0.1061 \frac{1}{h'^2} \left(\frac{\partial h'}{\partial y'} \right)^2 + 0.5834 \frac{1}{h'} \frac{\partial^2 h'}{\partial y'^2} \right] v' \\ & + h_M^2 \left[0.6094 \frac{1}{h'^2} \frac{\partial h'}{\partial x'} \frac{\partial h'}{\partial y'} - 0.0833 \frac{1}{h'} \frac{\partial^2 h'}{\partial x' \partial y'} \right] u'. \quad (4.1.5c) \end{aligned}$$

In comprehensive viscous shallow water PDEs (4.1.5), neglecting the grey coloured terms, that are less significant compared to the other terms, gives the *simplified* viscous shallow water PDEs. Dropping grey coloured terms and the primes, using “=” instead of “≈”, in the PDEs (4.1.5) and dividing both sides of the momentum equations (4.1.5b) and (4.1.5c) by h_M^2 , we get the non-dimensional *simplified viscous shallow water* PDEs, with our non-dimensionalisation of space by the reference length $L/(2\pi)$ as

$$\frac{1}{h_M} \frac{\partial h}{\partial t} = -\frac{\partial hu}{\partial x} - \frac{\partial hv}{\partial y}, \quad (4.1.6a)$$

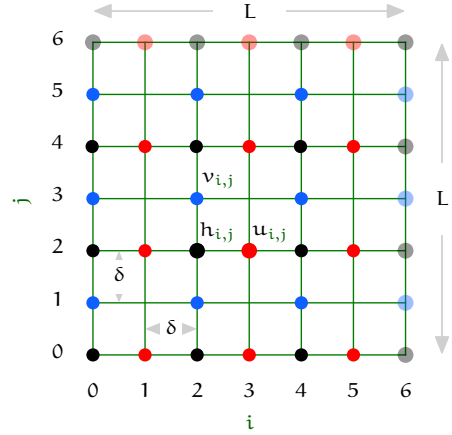
$$\begin{aligned} \frac{\text{Re}}{h_M^2} \frac{\partial u}{\partial t} = & -\frac{\pi^2}{4} \frac{u}{h^2} + \frac{\pi^2}{12} \frac{\text{Re}}{h_M^2} \left[g_x + g_n \frac{\partial h}{\partial x} \right] \\ & - \frac{\text{Re}}{h_M} \left[1.5041u \frac{\partial u}{\partial x} + 1.3464v \frac{\partial u}{\partial y} + 0.1577u \frac{\partial v}{\partial y} \right] \\ & + 4.0930 \frac{\partial^2 u}{\partial x^2} + \frac{\partial^2 u}{\partial y^2} + 3.0930 \frac{\partial^2 v}{\partial x \partial y}, \end{aligned} \quad (4.1.6b)$$

$$\begin{aligned} \frac{\text{Re}}{h_M^2} \frac{\partial v}{\partial t} = & -\frac{\pi^2}{4} \frac{v}{h^2} + \frac{\pi^2}{12} \frac{\text{Re}}{h_M^2} \left[g_y + g_n \frac{\partial h}{\partial y} \right] \\ & - \frac{\text{Re}}{h_M} \left[1.5041v \frac{\partial v}{\partial y} + 1.3464u \frac{\partial v}{\partial x} + 0.1577v \frac{\partial u}{\partial x} \right] \\ & + 4.0930 \frac{\partial^2 v}{\partial y^2} + \frac{\partial^2 v}{\partial x^2} + 3.0930 \frac{\partial^2 u}{\partial x \partial y}, \end{aligned} \quad (4.1.6c)$$

where dividing the dimensional velocities by the characteristic inviscid wave velocity $U = \sqrt{gH}$ gives the non-dimensional velocities u, v , and dividing the dimensional spatial variables by reference length $L/(2\pi)$ gives the non-dimensional spatial variables x, y, h . The PDE (4.1.6a) represents mass conservation, and the PDEs (4.1.6b) and (4.1.6c) represent momentum balance in the x and y directions respectively.

We use the simplified viscous shallow water PDEs (4.1.6) as the micro-scale model within the patches in our study of the staggered patch schemes. In all our further use “viscous shallow water PDEs” means these *simplified* viscous shallow water PDEs (4.1.6). For the viscous shallow water PDEs (4.1.6), throughout this chapter, we consider the boundary conditions that the three fields h, u , and v are 2π -periodic in both x and y (for the non-dimensional domain size 2π), and an appropriate initial condition $h(x, y, 0)$, $u(x, y, 0)$, and $v(x, y, 0)$.

Figure 4.1.1. Same as Fig. 2.1.1 of §2.1.1 for general linear waves. Schematic of the full-domain microscale *staggered grid* where variables are simulated only on staggered/alternating discrete points, *nodes*, \bullet h for height, \bullet u , \bullet v for horizontal velocities along x and y directions respectively. Here we draw $n = 6$ grid intervals in the green grid, both in x and y directions. Transparent filled circles on the boundaries indicate the discrete n -periodic boundary conditions in i, j .



4.1.2 Full-domain microscale model for viscous shallow water flows

This subsection derives a discrete full-domain microscale model for viscous shallow water flows corresponding to the viscous shallow water PDEs (4.1.6). Throughout this chapter, we use this full-domain microscale model as the reference to assess various characteristics (accuracy, stability, consistency, etc.) of the multiscale staggered patch schemes we develop.

Approximating the spatial derivatives in the viscous shallow water PDEs (4.1.6) by central finite differences on the nodes of the full-domain staggered grid (filled circles in Fig. 4.1.1) with the micro-grid interval δ gives the *full-domain microscale model* (4.1.11) corresponding to the PDEs (4.1.6). To compute the “missing” values on the staggered grid (e.g., $h_{3,1}$, $v_{3,1}$, and $v_{3,3}$ are missing in Fig. 4.1.1), the full-domain microscale model (4.1.11) averages the nearest values. The following listing gives some examples.

- For computing $[\mathrm{d}h/\mathrm{d}t]_{i,j}$ at the locations of $h_{i,j}$, the discretisation in conservative form in (4.1.11a),

$$\begin{aligned} [\partial(hu)/\partial x]_{i,j} &\approx [h_{i+1,j}u_{i+1,j} - h_{i-1,j}u_{i-1,j}]/(2\delta) \\ &= [(h_{i,j} + h_{i+2,j})u_{i+1,j} - (h_{i-2,j} + h_{i,j})u_{i-1,j}]/(4\delta), \end{aligned} \quad (4.1.7)$$

computes the missing h values at the locations of the u nodes on the staggered grid (e.g., missing $h_{3,2}$, $h_{1,2}$ in Fig. 4.1.1), by averaging over the two neighbouring values $h_{i+1,j} = (h_{i,j} + h_{i+2,j})/2$, and $h_{i-1,j} = (h_{i-2,j} + h_{i,j})/2$.

- For computing $[du/dt]_{i,j}$ at the locations of $u_{i,j}$, the discretisation in (4.1.11b),

$$\begin{aligned} [v\partial u/\partial y]_{i,j} &\approx v_{i,j} \frac{u_{i,j+2} - u_{i,j-2}}{4\delta} \\ &= \frac{(v_{i-1,j-1} + v_{i+1,j-1} + v_{i-1,j+1} + v_{i+1,j+1})}{4} \frac{u_{i,j+2} - u_{i,j-2}}{4\delta}, \end{aligned} \quad (4.1.8)$$

computes the missing v values at the locations of the u nodes on the staggered grid (e.g., missing $v_{3,2}$ in Fig. 4.1.1) by averaging over the four neighbouring v values.

- For computing $[du/dt]_{i,j}$ at the locations of $u_{i,j}$, the discretisation in (4.1.11b),

$$\begin{aligned} u\partial v/\partial y &\approx u_{i,j} (v_{i,j+1} - v_{i,j-1})/(2\delta) \\ &= u_{i,j} \frac{(v_{i-1,j+1} + v_{i+1,j+1})/2 - (v_{i-1,j-1} + v_{i+1,j-1})/2}{2\delta}, \end{aligned} \quad (4.1.9)$$

computes the missing v values at the locations of the empty node on the staggered grid (e.g., missing $v_{3,3}$, $v_{3,1}$ in Fig. 4.1.1) by averaging.

- For computing $[dv/dt]_{i,j}$ at the locations of $v_{i,j}$, the discretisation in (4.1.11c),

$$\begin{aligned} \left[\frac{\partial^2 u}{\partial x \partial y} \right]_{i,j} &\approx \frac{(\partial u/\partial x)_{i,j+1} - (\partial u/\partial x)_{i,j-1}}{2\delta} \\ &= \frac{(u_{i+1,j+1} - u_{i-1,j+1})/(2\delta) - (u_{i+1,j-1} - u_{i-1,j-1})/(2\delta)}{2\delta}, \end{aligned} \quad (4.1.10)$$

computes the missing u values at the locations of h nodes on the staggered grid (e.g., missing $u_{2,4}$, $u_{2,2}$ in Fig. 4.1.1).

Thus, corresponding to the viscous shallow water PDEs (4.1.6), the full-domain microscale model is

$$\begin{aligned} \bullet \frac{1}{h_M} \frac{dh_{i,j}}{dt} &= - \frac{(h_{i,j} + h_{i+2,j}) u_{i+1,j} - (h_{i-2,j} + h_{i,j}) u_{i-1,j}}{4\delta} \\ &\quad - \frac{(h_{i,j} + h_{i,j+2}) v_{i,j+1} - (h_{i,j-2} + h_{i,j}) v_{i,j-1}}{4\delta} \end{aligned} \quad (4.1.11a)$$

$$\text{for } i, j \in \{0, 2, 4, \dots, n-2\},$$

$$\begin{aligned}
\bullet \frac{\text{Re}}{h_M^2} \frac{du_{i,j}}{dt} = & -\frac{\pi^2}{4} \frac{u_{i,j}}{[(h_{i-1,j} + h_{i+1,j})/2]^2} + \frac{\pi^2}{12} \frac{\text{Re}}{h_M^2} \left[g_x + g_n \frac{h_{i+1,j} - h_{i-1,j}}{2\delta} \right] \\
& - \frac{\text{Re}}{h_M} \left[1.5041 u_{i,j} \frac{u_{i+2,j} - u_{i-2,j}}{4\delta} \right. \\
& \quad + 1.3464 \frac{(v_{i-1,j-1} + v_{i+1,j-1} + v_{i-1,j+1} + v_{i+1,j+1})}{4} \frac{u_{i,j+2} - u_{i,j-2}}{4\delta} \\
& \quad \left. + 0.1577 u_{i,j} \frac{(v_{i-1,j+1} + v_{i+1,j+1})/2 - (v_{i-1,j-1} + v_{i+1,j-1})/2}{2\delta} \right] \\
& + 4.093 \frac{u_{i-2,j} - 2u_{i,j} + u_{i+2,j}}{4\delta^2} + \frac{u_{i,j-2} - 2u_{i,j} + u_{i,j+2}}{4\delta^2} \\
& + 3.093 \frac{(v_{i+1,j+1} - v_{i+1,j-1})/(2\delta) - (v_{i-1,j+1} - v_{i-1,j-1})/(2\delta)}{2\delta}
\end{aligned} \tag{4.1.11b}$$

for $i \in \{1, 3, 5, \dots, n-1\}$, $j \in \{0, 2, 4, \dots, n-2\}$,

$$\begin{aligned}
\bullet \frac{\text{Re}}{h_M^2} \frac{dv_{i,j}}{dt} = & -\frac{\pi^2}{4} \frac{v_{i,j}}{[(h_{i,j-1} + h_{i,j+1})/2]^2} + \frac{\pi^2}{12} \frac{\text{Re}}{h_M^2} \left[g_y + g_n \frac{h_{i,j+1} - h_{i,j-1}}{2\delta} \right] \\
& - \frac{\text{Re}}{h_M} \left[1.5041 v_{i,j} \frac{v_{i,j+2} - v_{i,j-2}}{4\delta} \right. \\
& \quad + 1.3464 \frac{(u_{i-1,j-1} + u_{i+1,j-1} + u_{i-1,j+1} + u_{i+1,j+1})}{4} \frac{v_{i+2,j} - v_{i-2,j}}{4\delta} \\
& \quad \left. + 0.1577 v_{i,j} \frac{(u_{i+1,j-1} + u_{i+1,j+1})/2 - (u_{i-1,j-1} + u_{i-1,j+1})/2}{2\delta} \right] \\
& + 4.093 \frac{v_{i,j-2} - 2v_{i,j} + v_{i,j+2}}{4\delta^2} + \frac{v_{i-2,j} - 2v_{i,j} + v_{i+2,j}}{4\delta^2} \\
& + 3.093 \frac{(u_{i+1,j+1} - u_{i-1,j+1})/(2\delta) - (u_{i+1,j-1} - u_{i-1,j-1})/(2\delta)}{2\delta}
\end{aligned} \tag{4.1.11c}$$

for $i \in \{0, 2, 4, \dots, n-2\}$, $j \in \{1, 3, 5, \dots, n-1\}$.

Analogous to the PDEs (4.1.6), the three fields h , u , v are n -periodic in both i and j where $n = 2\pi/\delta$ (for the non-dimensional domain size 2π), with an appropriate initial condition $h_{i,j}(0)$, $u_{i,j}(0)$, and $v_{i,j}(0)$.

Substituting the solution of a steady uniform flow $h = h_M$, $u = u_M$, $v = v_M$ with mean height h_M and horizontal mean velocity u_M , v_M into the full-domain microscale model (4.1.11) and setting the time derivatives to zero gives the fixed points or the *equilibrium solution*

$$h = h_M, \quad u = \text{Re } g_x/3, \quad v = \text{Re } g_y/3, \tag{4.1.12}$$

for the full-domain microscale model (4.1.11). The equilibrium solution (4.1.12) is also the equilibrium solution for the viscous shallow water PDEs (4.1.6).

For a bed with a positive slope (downward inclination along x), the viscous shallow water flows reach the equilibrium velocity of the fixed point (4.1.12) when the bed drag and gravitational force are in balance. That is, larger the downward inclination, larger the components g_x, g_y and hence larger the equilibrium velocity is; for a horizontal bed, the fixed point is stagnant water with $u = 0, v = 0$.

As a dynamical system, the full-domain microscale model (4.1.11) in vector notation, for the viscous shallow water PDEs (4.1.6) is of the autonomous form

$$\frac{d\mathbf{x}}{dt} = \mathbf{f}(\mathbf{x}), \quad (4.1.13)$$

where the state vector of the system

$$\mathbf{x} = (\quad h_{0,0}, h_{0,2}, h_{0,4}, \dots, h_{2,0}, h_{2,2}, h_{2,4}, \dots, \\ \dots, u_{1,0}, u_{1,2}, u_{1,4}, \dots, u_{3,0}, u_{3,2}, u_{3,4}, \dots, \\ \dots, v_{0,1}, v_{0,3}, v_{0,5}, \dots, v_{2,1}, v_{2,3}, v_{2,5}, \dots), \quad (4.1.14)$$

is the same as the state vector (2.1.3) of the full-domain model for generic wave-like system in §2.1.1

A full-domain microscale simulation is performed by numerical time-integration of the ODEs (4.1.11) on the nodes of the microscale staggered grid (filled circles in Fig. 4.1.1), with the discrete macroscale n -periodic boundary conditions in i, j .

4.1.3 Staggered patch scheme for viscous shallow water flows

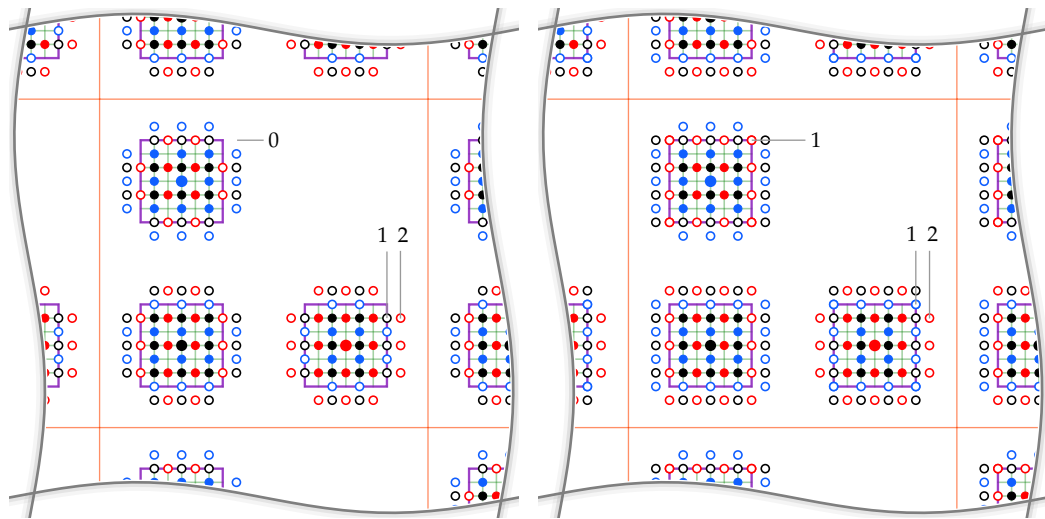
This subsection derives a generic staggered patch scheme for viscous shallow water flows, using the derived full-domain microscale model (4.1.11) within the patches.

Fig. 4.1.2 shows two staggered patch grids with different number of layers of edge nodes. The patch grid in Fig. 4.1.2a (with two layers of edge nodes in the normal direction to the edges and no edge nodes in the tangential direction to the edges), is sufficient for the general linear wave with viscous diffusion in Chapters 2 and 3. But, to use the finite difference equations (4.1.11) of the viscous shallow water flows as the microscale model within the patches, a staggered patch grid requires two layers of edge nodes in the normal direction to the edges, and one layer of edge nodes in the tangential direction to the edges, as in Fig. 4.1.2b.

1. A discussion in p. 49 of §3.1 shows that for computing the second spatial derivative of velocities (e.g., $\partial^2 u / \partial x^2$ in the viscous diffusion)

Figure 4.1.2. For viscous shallow water flows microscale model (4.1.15), a staggered patch grid requires two layers of edge nodes in the normal direction to edges, and one layer of edge nodes in the tangential direction to edges, as in Fig. 4.1.2b.

- (a) Same as Fig. 2.1.5a for general linear wave. Two layers of edge nodes in normal direction to edges, no edge nodes in tangential direction to edges.
- (b) Two layers of edge nodes in normal direction to the edges, one layer of edge nodes in tangential direction to the edges.



within the patches requires a staggered patch grid with two layers of edge nodes in normal direction to the edges as in both Figs. 4.1.2a and 4.1.2b.

- Computing the term (4.1.9) at the top-right interior u node (solid red filled circle) of the u -centred patch in Fig. 4.1.2b, requires the v edge value at the right-top patch corner, which does not exist in Fig. 4.1.2a. Similarly, computing the term (4.1.10) at the top-right interior v node (solid blue filled circle) of the v -centred patch in Fig. 4.1.2b, requires the u edge value at the right-top patch corner, which does not exist in Fig. 4.1.2a. Hence, a staggered patch scheme with the 2D viscous shallow water PDEs (4.1.11) as the underlying microscale model within the patches, requires a patch grid with one layer of edge nodes in the tangential direction to the edges as in Fig. 4.1.2b.

Throughout this chapter, for the viscous shallow water flows, the staggered patch schemes use the patch grid in Fig. 4.1.2b, with two layers of edge nodes in the normal direction to the edges, and one layer of edge nodes in the tangential direction to the edges. For the staggered patch grid in Fig. 4.1.2b,

the left and right edge values are $\circ h_{i,j}^{I,J}$, $\circ u_{i,j}^{I,J}$, $\circ v_{i,j}^{I,J}$, for $i \in \{-1, 0, n, n+1\}$ and $j \in \{0, 1, 2, \dots, n-1, n\}$. Similarly the bottom and top edge value indices are $i \in \{0, 1, 2, \dots, n-1, n\}$ and $j \in \{-1, 0, n, n+1\}$.

Using the full-domain microscale model (4.1.11) within the patches of a suitable staggered patch grid (e.g., Fig. 4.1.2b with $n = 6$), gives the *staggered patch scheme* (notationally same as the full-domain microscale model (4.1.11) with patch index I, J in the superscript)

$$\bullet \frac{1}{h_M} \frac{dh_{i,j}^{I,J}}{dt} = - \frac{(h_{i,j}^{I,J} + h_{i+2,j}^{I,J}) u_{i+1,j}^{I,J} - (h_{i-2,j}^{I,J} + h_{i,j}^{I,J}) u_{i-1,j}^{I,J}}{4\delta} - \frac{(h_{i,j}^{I,J} + h_{i,j+2}^{I,J}) v_{i,j+1}^{I,J} - (h_{i,j-2}^{I,J} + h_{i,j}^{I,J}) v_{i,j-1}^{I,J}}{4\delta}, \quad (4.1.15a)$$

$$\bullet \frac{\text{Re}}{h_M^2} \frac{du_{i,j}^{I,J}}{dt} = - \frac{\pi^2}{4} \frac{u_{i,j}^{I,J}}{[(h_{i-1,j}^{I,J} + h_{i+1,j}^{I,J})/2]^2} + \frac{\pi^2}{12} \frac{\text{Re}}{h_M^2} \left[g_x + g_n \frac{h_{i+1,j}^{I,J} - h_{i-1,j}^{I,J}}{2\delta} \right] - \frac{\text{Re}}{h_M} \left[1.5041 u_{i,j}^{I,J} \frac{u_{i+2,j}^{I,J} - u_{i-2,j}^{I,J}}{4\delta} + 1.3464 \frac{(v_{i-1,j-1}^{I,J} + v_{i+1,j-1}^{I,J} + v_{i-1,j+1}^{I,J} + v_{i+1,j+1}^{I,J})}{4} \frac{u_{i,j+2}^{I,J} - u_{i,j-2}^{I,J}}{4\delta} + 0.1577 u_{i,j}^{I,J} \frac{(v_{i-1,j+1}^{I,J} + v_{i+1,j+1}^{I,J})/2 - (v_{i-1,j-1}^{I,J} + v_{i+1,j-1}^{I,J})/2}{2\delta} \right] + 4.093 \frac{u_{i-2,j}^{I,J} - 2u_{i,j}^{I,J} + u_{i+2,j}^{I,J}}{4\delta^2} + \frac{u_{i,j-2}^{I,J} - 2u_{i,j}^{I,J} + u_{i,j+2}^{I,J}}{4\delta^2} + 3.093 \frac{(v_{i+1,j+1}^{I,J} - v_{i+1,j-1}^{I,J})/(2\delta) - (v_{i-1,j+1}^{I,J} - v_{i-1,j-1}^{I,J})/(2\delta)}{2\delta}, \quad (4.1.15b)$$

$$\bullet \frac{\text{Re}}{h_M^2} \frac{dv_{i,j}^{I,J}}{dt} = - \frac{\pi^2}{4} \frac{v_{i,j}^{I,J}}{[(h_{i,j-1}^{I,J} + h_{i,j+1}^{I,J})/2]^2} + \frac{\pi^2}{12} \frac{\text{Re}}{h_M^2} \left[g_y + g_n \frac{h_{i,j+1}^{I,J} - h_{i,j-1}^{I,J}}{2\delta} \right] - \frac{\text{Re}}{h_M} \left[1.5041 v_{i,j}^{I,J} \frac{v_{i,j+2}^{I,J} - v_{i,j-2}^{I,J}}{4\delta} + 1.3464 \frac{(u_{i-1,j-1}^{I,J} + u_{i+1,j-1}^{I,J} + u_{i-1,j+1}^{I,J} + u_{i+1,j+1}^{I,J})}{4} \frac{v_{i+2,j}^{I,J} - v_{i-2,j}^{I,J}}{4\delta} + 0.1577 v_{i,j}^{I,J} \frac{(u_{i+1,j-1}^{I,J} + u_{i+1,j+1}^{I,J})/2 - (u_{i-1,j-1}^{I,J} + u_{i-1,j+1}^{I,J})/2}{2\delta} \right] + 4.093 \frac{v_{i,j-2}^{I,J} - 2v_{i,j}^{I,J} + v_{i,j+2}^{I,J}}{4\delta^2} + \frac{v_{i-2,j}^{I,J} - 2v_{i,j}^{I,J} + v_{i+2,j}^{I,J}}{4\delta^2}$$

$$+ 3.093 \frac{(u_{i+1,j+1}^{I,J} - u_{i-1,j+1}^{I,J})/(2\delta) - (u_{i+1,j-1}^{I,J} - u_{i-1,j-1}^{I,J})/(2\delta)}{2\delta}, \quad (4.1.15c)$$

and a patch coupling (e.g., Square-p6) to compute the edge values

$\circ h_{i,j}^{I,J}, \circ u_{i,j}^{I,J}, \circ v_{i,j}^{I,J}$ for

$i \in \{-1, 0, n, n+1\}, j \in \{0, 1, \dots, n\}$ for left and right edges and

$i \in \{0, 1, \dots, n\}, j \in \{-1, 0, n, n+1\}$ for bottom and top edges,

for the same interior indices i, j and patch indices I, J in (2.1.5) of §2.1.1,

separately for each equation.

Analogous to the full-domain microscale model (4.1.11), the three fields h, u, v in the patch scheme (4.1.15) are macroscale N -periodic in both I and J where $N = 2\pi/\Delta$ (for the non-dimensional domain size 2π), with an appropriate initial condition $h_{i,j}^{I,J}(0), u_{i,j}^{I,J}(0),$ and $v_{i,j}^{I,J}(0)$. A specific patch coupling (e.g., Square-p6) computes patch edge values ($\circ h_{i,j}^{I,J}, \circ u_{i,j}^{I,J}, \circ v_{i,j}^{I,J}$ in Fig. 2.1.5a) from the centre values of neighbouring patches ($\bullet h_{i,j}^{I,J}, \bullet u_{i,j}^{I,J}, \bullet v_{i,j}^{I,J}$ with $i = j = n/2$ in Fig. 2.1.5a). The patch coupling provides a mechanism whereby patches influence each other, §2.2 discusses various details of different patch couplings.

Arranging the patch interior values of (4.1.15), (with the same index convention as in Fig. 2.1.4 of §2.1.2), into a vector gives the state vector \mathbf{x}^I of the staggered patch scheme, which is a dynamic state variable evolving in time. As in §2.1.2, the superscript $(\cdot)^I$ is not an index or exponent, instead, a qualifier denoting the patch interior nodes. For the viscous shallow water flows, the general form of a staggered patch scheme state vector \mathbf{x}^I of size n_p^I containing all the interior values of all the patches is same as the state vector (2.1.6) of §2.1.2 for the general linear wave. That is, the number of patch interior nodes which is also the size of the state vector \mathbf{x}^I is (same as expression (2.1.7) of §2.1.2),

$$n_p^I = (N^2/4)(9n^2/4 - 4n + 2), \quad (4.1.16)$$

where N is the number of macro-grid intervals and n is the number of sub-patch micro-grid intervals. For example, for $N = 6, 10, 14, 18, 22, 26$ macro-grid intervals with $n = 6$ sub-patch micro-grid intervals, size of the state vector $n_p^I = 531, 1475, 2891, 4779, 7139, 9971$ respectively.

For the staggered patch grid in Fig. 4.1.2b, the left and right edge values are $\circ h_{i,j}^{I,J}, \circ u_{i,j}^{I,J}, \circ v_{i,j}^{I,J}$, for $i \in \{-1, 0, n, n+1\}$ and $j \in \{0, 1, 2, \dots, n-1, n\}$. Similarly the bottom and top edge value indices are $i \in \{0, 1, 2, \dots, n-1, n\}$ and $j \in \{-1, 0, n, n+1\}$. Arranging these patch edge values of all the

patches into a vector gives the edge vector \mathbf{x}^E of size n_p^E . The edge vector \mathbf{x}^E is computed by the patch coupling function $\mathbf{x}^E(\mathbf{x}^I)$ that encodes a particular patch scheme. For the staggered patch grid in Fig. 4.1.2b, the total number of patch edge nodes, that is the size of the edge vector \mathbf{x}^E ,

$$n_p^E = (N^2/4)(18n + 16), \quad (4.1.17)$$

where N is the number of macro-grid intervals and n is the number of sub-patch micro-grid intervals. Compared to expression (2.1.8) (p. 22 of §2.1.2) for the general linear wave, expression (4.1.17) for the viscous shallow water flows has 32 more edge nodes per macro-cell. For example, for the staggered patch grid in Fig. 4.1.2b with $N = 6, 10, 14, 18, 22, 26$ and $n = 6$, $n_p^E = 1116, 3100, 6076, 10044, 15004, 20956$ respectively.

As a dynamical system, the staggered patch scheme (4.1.15) in vector notation, corresponding to the full-domain microscale model (4.1.11) of viscous shallow water flows is

$$\frac{d\mathbf{x}^I}{dt} = \mathbf{F}(\mathbf{x}^I; \mathbf{x}^E(\mathbf{x}^I)), \quad (4.1.18)$$

with the same state vector \mathbf{x}^I (2.1.6) and a similar edge vector \mathbf{x}^E as those of the patch scheme for generic wave-like system in §2.1.2. The $\mathbf{F}(\mathbf{x}^I; \mathbf{x}^E(\mathbf{x}^I))$ in the staggered patch scheme dynamical system (4.1.18) corresponds to the $\mathbf{f}(\mathbf{x})$ in the full-domain microscale model (4.1.13). The functions \mathbf{F} and \mathbf{f} encode the same full-domain microscale model for the viscous shallow water PDEs (4.1.6); Section 2.1.2 explains this difference for the generic wave-like system.

Patch scheme simulation is performed by numerical time-integration of the ODEs (4.1.15) on the interior nodes of the staggered patch grid (filled circles in Fig. 4.1.2b), with the discrete macroscale N -periodic boundary conditions in both I and J . As in §2.1.2, evaluating the time derivatives in the staggered patch scheme (4.1.15) is done in two steps: first, edge values $\mathbf{x}^E(\mathbf{x}^I)$ are computed via patch coupling; second, using both interior and edge values of each patch in the staggered patch grid, the time derivatives of \mathbf{x}^I are computed for the full-domain microscale model (4.1.11) of viscous shallow water flows.

Table 4.1.1. Dimensional parameter ranges relevant for the exploration of viscous shallow water PDEs. Height H is within the shallow water regime such that ($H/L \in [1/100, 1/20]$). Range of density ρ and dynamic viscosity μ are from Haynes et al. (2016, p.6-7–6-8, p.6-247).

Parameter	Range of values
domain size L	0.5 to 100 cm
wavelength λ	0.5 to 100 cm
characteristic mean water height H	0.005 to 5 cm ($H/L \in [1/100, 1/20]$)
inviscid wave velocity $U = \sqrt{gH}$	10 to 70 cm/s
density ρ	992 to 1000 kg/m ³
dynamic viscosity μ	0.65 to 1.8 m Pa s
kinematic viscosity $\nu = \mu/\rho$	0.0066 to 0.018 cm ² /s
bed inclination angle θ	-10° to 10°

4.1.4 Selection of parameter regime for patch scheme exploration

Table 4.1.1 lists the dimensional parameter ranges we choose in order to explore the patch schemes for viscous shallow water flows:

- Height H is within the shallow water regime such that $H/L \in [1/100, 1/20]$;
- Range of density ρ and dynamic viscosity μ are from Haynes et al. (2016, p.6-7–6-8, p.6-247) for the temperature range from 0°C to 40°C at standard atmospheric pressure.

The non-dimensional parameter ranges within the dimensional parameters in Table 4.1.1 are listed in Table 4.1.2:

- Characteristic mean non-dimensional mean height $h_M = 2\pi H/L$ for the H and L values listed in Table 4.1.2;
- We heuristically choose $u_M = u/U$ around the midpoint of the range of U in Table 4.1.2;
- Reynolds number Re is limited to be within the regime of laminar flow.

Based on the eigenvalues of Spectral patch scheme (§4.4.1) for different combinations of the parameter values in Table 4.1.2, we select the sets of parameters listed in Table 4.1.3 for exploring the patch schemes for the simplified viscous shallow water flows. The key reasons for this choice are the following.

Table 4.1.2. Non-dimensional parameter ranges for viscous shallow water PDEs corresponding to the dimensional parameters in Table 4.1.1.

Parameter	Range of values
Mean height $h_M = 2\pi H/L$	0.025 to 0.4
Mean velocity $u_M = u/U$	0 to 1
Reynolds number Re	5 to 2000

Table 4.1.3. Chosen parameters for patch scheme convergence study using viscous shallow water PDEs.

Parameter	Values
Linearisation points (Non-dimensional)	$\{(h_M, u_M, v_M)\}$ where $h_M \in \{0.025, 0.05, \dots, 0.035, 0.4\}$, $u_M \in \{0, 0.05, \dots, 0.95, 1\}$, $v_M = 0$
Reynolds number	$Re \in \{10, 50, 250, 1250\}$
Bed inclination angle	$\theta = 0$, i.e., $g_x = 0, g_y = 1$

- Extent and spacing of the parameters are such that they cover significant variations in the structure of patch scheme eigenvalues.
- For $Re \lesssim 10$ there are no wave modes in the patch scheme as viscosity dominates the physical system.

4.2 Staggered patch schemes are accurate

This section shows that the developed five staggered patch schemes are accurate for the viscous shallow water flows. We establish the accuracy of the staggered patch schemes in general (as opposed to just one initial condition) by comparing the eigenvalues of the staggered patch schemes with the eigenvalues of fine- and coarse-grid full-domain microscale model, and for completeness also compare with the eigenvalues of the viscous shallow water PDEs (4.1.6). The objective of the staggered patch scheme is to perform reduced order multiscale modelling of the underlying microscale model. Hence, as p. 14 of §2.1.1 explains, the reference eigenvalues for us are the eigenvalues of the full domain microscale model, not that of the PDEs. The eigenvalue analysis for accuracy in this section is done for a representative subset of the physical parameters (Reynolds number Re and mean flow h_M, u_M, v_M) and the grid parameters (macro-grid intervals N , sub-patch micro-grid intervals n , patch scale ratio r). Section 4.5 on the

consistency of the patch schemes establishes the accuracy over a wider range of parameters. The following paragraphs introduce the approach to studying the accuracy of the staggered patch schemes and discuss the conventions adopted.

Time-dependent solutions of linear/linearised ODEs are linear combinations of the spatial modes (i.e., eigenvectors) where the initial condition gives the amplitudes of the modes (Manneville 2004, p. 37–38; Cain and Reynolds 2010, Prop. 2.1.21, p. 28; Edwards et al. 2017, p.386; Maruskin 2018, general solution, p. 17). Due to spatial homogeneity in the macroscale dynamics, the macroscale spatial structure of the full-domain model and the patch schemes are effectively the same. Hence, effectively there is no error in the macroscale modes (defined in p. 52 of §3.2) of the patch schemes. The only error in the macroscale dynamics of the patch schemes is in the eigenvalues. Thus, when the macroscale eigenvalues (defined in p. 52 of §3.2) of a patch scheme agree closely with the corresponding eigenvalues of the full-domain microscale model, the patch scheme simulation is *accurate in general for every initial condition* that only involves macroscale modes, provided it is near enough to the reference equilibrium for the linearisation to be valid. We aim to design the multiscale staggered patch schemes to accurately simulate the large-scale waves that are characterised by the macroscale eigenvalues. Thus, we aim to design the staggered patch schemes with the macroscale eigenvalues as close as possible to the corresponding macroscale eigenvalues of the full domain microscale model (4.1.11). Hence, in the eigenvalue analysis for accuracy in this section, we compare in the complex plane the eigenvalues of the staggered patch schemes with the eigenvalues of the full-domain microscale model.

Sections 4.2.1 to 4.2.5 describe the methods of analytically deriving and numerically computing the eigenvalues for

1. the 2D viscous shallow water PDEs (4.1.6),
2. the full-domain microscale model (4.1.11), and
3. the staggered patch scheme (4.1.15).

Following a standard approach of substituting an arbitrary Fourier mode into the PDEs/ODEs, §§4.2.1 and 4.2.2 derive the analytic eigenvalues of the viscous shallow water PDEs (4.1.6) and the corresponding discrete full-domain microscale model (4.1.11). Similarly, §4.2.3 derives the analytic eigenvalues of a staggered patch scheme. To numerically compute the eigenvalues of the numerical staggered patch scheme, which includes any instabilities and inaccuracies due to the numerical roundoff errors,

§§4.2.4 and 4.2.5 numerically differentiate the evolution functions $f(\mathbf{x})$ in the full-domain model (4.1.13), and $\mathbf{F}(\mathbf{x}^I; \mathbf{x}^E(\mathbf{x}^I))$ in the patch scheme (4.1.18) respectively.

Section 4.2.6 compares and contrasts various eigenvalues (e.g., analytic and numerical eigenvalues of the PDEs, full-domain microscale model, and patch schemes). We use the following notational convention to identify the various eigenvalues.

- Eigenvalue *subscripts* in $\lambda_p^{()}, \lambda_{m\delta}^{()}, \lambda_{m\Delta}^{()}, \lambda_{PDE}^{()}$ denote the system.
 - Eigenvalues $\lambda_p^{()}$ are for staggered patch schemes (e.g., λ_p^{NE1} of §4.2.3 and λ_p^N of §4.2.5).
 - Eigenvalues $\lambda_{m\delta}^{()}$ are for fine-grid full domain microscale model with same grid-spacing as sub-patch micro-grid interval δ (e.g., $\lambda_{m\delta}^A$ of §4.2.2 and $\lambda_{m\delta}^N$ of §4.2.4).
 - Eigenvalues $\lambda_{m\Delta}^{()}$ are for fine-grid full domain microscale model with same grid-spacing as the inter-patch distance Δ (e.g., $\lambda_{m\Delta}^A$ of §4.2.2 and $\lambda_{m\Delta}^N$ of §4.2.4).
 - Eigenvalues $\lambda_{PDE}^{()}$ are for the viscous shallow water PDE (e.g., λ_{PDE}^A of §4.2.1).
- Eigenvalue *superscripts* in $\lambda_{() }^N, \lambda_{() }^{NE1}, \lambda_{() }^A$ denote the method of computing numerical eigenvalues values.
 - Eigenvalues $\lambda_{() }^N$ are computed from the numerical Jacobian of the system (e.g., $\lambda_{m\delta}^N, \lambda_{m\Delta}^N$ of §4.2.4 and λ_p^N of §4.2.5).
 - Eigenvalues $\lambda_{() }^{NE1}$ are computed from numerically evaluated analytic one-cell Jacobian of the system (e.g., λ_p^{NE1} of §4.2.3).
 - Eigenvalues $\lambda_{() }^A$ are computed from the closed-form analytic expressions for the eigenvalues (e.g., λ_{PDE}^A of §4.2.1 and $\lambda_{m\delta}^A, \lambda_{m\Delta}^A$ of §4.2.2).

4.2.1 Eigenvalue analysis of the PDEs

This subsection discusses a method of computing the eigenvalues of the 2D viscous shallow water PDEs (4.1.6). For a sanity check, we compare the eigenvalues of the PDEs (4.1.6) with the eigenvalues of the full-domain microscale model (4.1.11) and the various staggered patch schemes.

We want to characterise the accuracy and stability of the patch schemes for the non-trivial nonlinear evolution of the viscous shallow water flows,

apart from the mean flow and any constant drift over time in the solution h, u, v . Hence, in contrast to the arbitrary Fourier mode for the *solution* of general linear wave in §3.2.1, we consider an arbitrary Fourier mode for *linear perturbation* about $h_M, u_M + a_1 t$ and $v_M + a_2 t$ of the *nonlinear* viscous shallow water PDE (4.1.6), where h_M is the mean height, u_M, v_M are the mean velocities, and a_1, a_2 are the constant mean accelerations. That is, for the viscous shallow water PDE (4.1.6), we consider an arbitrary Fourier mode for linear perturbation about the mean accelerating flow, with real wavenumber (k_x, k_y) and complex growth rate λ ,

$$h(x, y, t) = h_M + H \exp[i(k_x x + k_y y) + \lambda t], \quad (4.2.1a)$$

$$u(x, y, t) = u_M + a_1 t + U \exp[i(k_x x + k_y y) + \lambda t], \quad (4.2.1b)$$

$$v(x, y, t) = v_M + a_2 t + V \exp[i(k_x x + k_y y) + \lambda t], \quad (4.2.1c)$$

where H, U, V are small enough so the linearisation is valid.

With zero perturbation $H = U = V = 0$, taking time derivative of the Fourier mode (4.2.1b) and (4.2.1c) about the mean flow state $\mathbf{x}_M = (h_M, u_M, v_M)$,

$$\left[\frac{\partial u}{\partial t} \right]_{\mathbf{x}_M} = a_1; \quad \left[\frac{\partial v}{\partial t} \right]_{\mathbf{x}_M} = a_2. \quad (4.2.2)$$

Substituting $h(x, y, t) = h_M, u(x, y, t) = u_M$, and $v(x, y, t) = v_M$, into the momentum equations (4.1.6b) and (4.1.6c) and comparing with the equation (4.2.2) gives the constant mean accelerations for the viscous shallow water PDE (4.1.6)

$$\left[\frac{\partial u}{\partial t} \right]_{\mathbf{x}_M} = a_1 = \frac{\pi^2 g_x}{12} - \frac{\pi^2 u_M}{4 \text{Re}}, \quad (4.2.3a)$$

$$\left[\frac{\partial v}{\partial t} \right]_{\mathbf{x}_M} = a_2 = \frac{\pi^2 g_y}{12} - \frac{\pi^2 v_M}{4 \text{Re}}. \quad (4.2.3b)$$

Substituting the Fourier mode (4.2.1) into the viscous shallow water PDE (4.1.6), neglecting the terms that are nonlinear in H, U, V gives the eigensystem

$$\mathbf{J}(\mathbf{x}_M) \begin{bmatrix} H \\ U \\ V \end{bmatrix} = \lambda \begin{bmatrix} H \\ U \\ V \end{bmatrix}, \quad (4.2.4)$$

where the nine elements of the 3×3 Jacobian $\mathbf{J}(\mathbf{x}_M)$ are

$$\mathbf{J}_{1,1} = -i h_M u_M k_x - i h_M v_M k_y, \quad (4.2.5a)$$

$$\mathbf{J}_{1,2} = -i h_M^2 k_x, \quad (4.2.5b)$$

$$\mathbf{J}_{1,3} = -i h_M^2 k_y, \quad (4.2.5c)$$

$$\mathbf{J}_{2,1} = i \frac{\pi^2 g_n}{12} k_x + \frac{\pi^2 u_M}{2 \operatorname{Re} h_M}, \quad (4.2.5d)$$

$$\begin{aligned} \mathbf{J}_{2,2} = & -1.5041 i h_M u_M k_x - 1.3464 i h_M v_M k_y \\ & - \frac{4.093 h_M^2}{\operatorname{Re}} k_x^2 - \frac{h_M^2}{\operatorname{Re}} k_y^2 - \frac{\pi^2}{4 \operatorname{Re}}, \end{aligned} \quad (4.2.5e)$$

$$\mathbf{J}_{2,3} = -0.1577 i h_M u_M k_y - \frac{3.093 h_M^2}{\operatorname{Re}} k_x k_y, \quad (4.2.5f)$$

$$\mathbf{J}_{3,1} = i \frac{\pi^2 g_n}{12} k_y + \frac{\pi^2 v_M}{2 \operatorname{Re} h_M}, \quad (4.2.5g)$$

$$\mathbf{J}_{3,2} = -0.1577 i h_M v_M k_x - \frac{3.093 h_M^2}{\operatorname{Re}} k_x k_y, \quad (4.2.5h)$$

$$\mathbf{J}_{3,3} = -1.3464 i h_M u_M k_x - 1.5041 i h_M v_M k_y \quad (4.2.5i)$$

$$- \frac{h_M^2}{\operatorname{Re}} k_x^2 - \frac{4.093 h_M^2}{\operatorname{Re}} k_y^2 - \frac{\pi^2}{4 \operatorname{Re}}. \quad (4.2.5j)$$

In contrast to the Jacobian of the general linear wave PDEs which depends only on the physical parameters and the wavenumber (k_x, k_y) , this Jacobian $\mathbf{J}(\mathbf{x}_M)$ for the nonlinear viscous shallow water flows depends on

1. the physical parameters Re, g_n ,
2. the wavenumber (k_x, k_y) ,
3. and *also on the linearisation point* $\mathbf{x}_M = (h_M, u_M, v_M)$, which is the mean flow state.

Section 3.2.2 derives analytic expression (3.2.3) for the eigenvalues of the general linear wave. Similarly, using SymPy CAS, we derived the analytic expression for the eigenvalues of the Jacobian $\mathbf{J}(\mathbf{x}_M)$ in the eigensystem (3.2.2), for the viscous shallow water PDEs (4.1.6). The analytic expression for the eigenvalues of the viscous shallow water flows is too long to be useful. Hence, we compute the eigenvalues $\lambda_{\text{PDE}}^{\text{NE1}}$ of the numerically evaluated Jacobian $\mathbf{J}(\mathbf{x}_M)$ in the eigensystem (3.2.2) for specific physical parameters, wavenumber and the linearisation point \mathbf{x}_M .

We compare (for a sanity check) the eigenvalues $\lambda_{\text{PDE}}^{\text{NE1}}$ with the eigenvalues of the full domain microscale model and the various staggered patch schemes in §4.2.6.

4.2.2 Eigenvalue analysis of staggered grid full-domain model

This subsection discusses a method of computing the eigenvalues of the staggered grid full-domain microscale model (4.1.11) for the 2D viscous shallow water PDEs (4.1.6). Comparing these eigenvalues of the full-domain model with the eigenvalues of the staggered patch schemes, §4.2.6 studies the accuracy of the patch schemes and §4.4 studies stability of the patch schemes.

We follow the same analytic approach in §4.2.1 for the 2D viscous shallow water PDEs in §4.2.1, but over a discrete infinite staggered grid (number of grid intervals $n \rightarrow \infty$ in Fig. 4.1.1). We consider an arbitrary Fourier mode for the perturbation about h_M , $u_M + a_1 t$ and $v_M + a_2 t$ of the full-domain microscale model (4.1.11) for the viscous shallow water flows. That is, for the full-domain microscale model (4.1.11), we consider an arbitrary Fourier mode of the perturbation about the mean accelerating flow, with real wavenumber (k_x, k_y) and complex growth rate λ ,

$$\bullet h_{i,j}(t) = h_M + H \exp[i(k_x i \delta + k_y j \delta) + \lambda t] \quad (4.2.6a)$$

for $i, j \in \{0, 2, 4, \dots, n-2\}$,

$$\bullet u_{i,j}(t) = u_M + a_1 t + U \exp[i(k_x i \delta + k_y j \delta) + \lambda t] \quad (4.2.6b)$$

for $i \in \{1, 3, 5, \dots, n-1\}$, $j \in \{0, 2, 4, \dots, n-2\}$,

$$\bullet v_{i,j}(t) = v_M + a_2 t + V \exp[i(k_x i \delta + k_y j \delta) + \lambda t] \quad (4.2.6c)$$

for $i \in \{0, 2, 4, \dots, n-2\}$, $j \in \{1, 3, 5, \dots, n-1\}$.

Throughout this thesis, i denotes the micro-grid index in x -direction (for both full-domain and sub-patch micro-grids), whereas $i = \sqrt{-1}$ is the imaginary unit.

Substituting the Fourier mode (4.2.1) into the full-domain microscale model (4.1.11), and neglecting the terms that are nonlinear in H , U , V gives the eigensystem

$$\mathbf{J}(\mathbf{x}_M) \begin{bmatrix} H \\ U \\ V \end{bmatrix} = \lambda \begin{bmatrix} H \\ U \\ V \end{bmatrix}, \quad (4.2.7)$$

where the elements of the 3×3 Jacobian $\mathbf{J}(\mathbf{x}_M)$ are

$$\mathbf{J}_{1,1} = -i h_M u_M \frac{\sin(2\delta k_x)}{2\delta} - i h_M v_M \frac{\sin(2\delta k_y)}{2\delta}, \quad (4.2.8a)$$

$$\mathbf{J}_{1,2} = -i h_M^2 \frac{\sin(\delta k_x)}{\delta}, \quad (4.2.8b)$$

$$\mathbf{J}_{1,3} = -i h_M^2 \frac{\sin(\delta k_y)}{\delta}, \quad (4.2.8c)$$

$$\mathbf{J}_{2,1} = i \frac{\pi^2 g_n \sin(\delta k_x)}{12 \delta} + \frac{\pi^2 u_M}{2 \operatorname{Re} h_M} \cos(\delta k_x), \quad (4.2.8d)$$

$$\begin{aligned} \mathbf{J}_{2,2} = & -1.5041 i h_M u_M \frac{\sin(2\delta k_x)}{2\delta} - 1.3464 i h_M v_M \frac{\sin(2\delta k_y)}{2\delta} \\ & - \frac{4.0930 h_M^2}{\operatorname{Re}} \left[\frac{\sin(\delta k_x)}{\delta} \right]^2 - \frac{h_M^2}{\operatorname{Re}} \left[\frac{\sin(\delta k_y)}{\delta} \right]^2 - \frac{\pi^2}{4 \operatorname{Re}}, \end{aligned} \quad (4.2.8e)$$

$$\mathbf{J}_{2,3} = -0.1577 i h_M u_M \frac{\sin(\delta k_y)}{\delta} \cos(\delta k_x) - \frac{3.0930 h_M^2 \sin(\delta k_x) \sin(\delta k_y)}{\operatorname{Re} \delta \delta}, \quad (4.2.8f)$$

$$\mathbf{J}_{3,1} = i \frac{\pi^2 g_n \sin(\delta k_y)}{12 \delta} + \frac{\pi^2 v_M}{2 \operatorname{Re} h_M} \cos(\delta k_y), \quad (4.2.8g)$$

$$\mathbf{J}_{3,2} = -0.1577 i h_M v_M \frac{\sin(\delta k_x)}{\delta} \cos(\delta k_y) - \frac{3.0930 h_M^2 \sin(\delta k_x) \sin(\delta k_y)}{\operatorname{Re} \delta \delta}, \quad (4.2.8h)$$

$$\begin{aligned} \mathbf{J}_{3,3} = & -1.3464 i h_M u_M \frac{\sin(2\delta k_x)}{2\delta} - 1.5041 i h_M v_M \frac{\sin(2\delta k_y)}{2\delta} \\ & - \frac{h_M^2}{\operatorname{Re}} \left[\frac{\sin(\delta k_x)}{\delta} \right]^2 - \frac{4.0930 h_M^2}{\operatorname{Re}} \left[\frac{\sin(\delta k_y)}{\delta} \right]^2 - \frac{\pi^2}{4 \operatorname{Re}}. \end{aligned} \quad (4.2.8i)$$

As the grid interval $\delta \rightarrow 0$ and/or the wavenumber $(k_x, k_y) \rightarrow (0, 0)$, we get following limits for the terms in the Jacobian elements (4.2.8)

$$\begin{aligned} \frac{\sin(\delta k_x)}{\delta} &\rightarrow k_x, & \frac{\sin(\delta k_y)}{\delta} &\rightarrow k_y, \\ \frac{\sin(2\delta k_x)}{2\delta} &\rightarrow k_x, & \frac{\sin(2\delta k_y)}{2\delta} &\rightarrow k_y, \\ \cos(\delta k_x) &\rightarrow 1, & \cos(\delta k_y) &\rightarrow 1. \end{aligned} \quad (4.2.9)$$

In the limits (4.2.9), the Jacobian elements (4.2.8) of the full-domain microscale model converge to the Jacobian elements (4.2.5) of the viscous shallow water PDEs. Hence, the eigenvalues of the full-domain microscale model (4.1.11) converge to the analytic eigenvalues of the PDEs (4.1.6) as we decrease the grid interval δ and/or wavenumber (k_x, k_y) .

We compute the eigenvalues λ_m^{NE1} of the numerically evaluated Jacobian $\mathbf{J}(\mathbf{x}_M)$ in the eigensystem (4.2.7) for specific physical parameters, wavenumber and the linearisation point \mathbf{x}_M . When we compute the eigenvalues λ_m^{NE1} of the full-domain microscale model,

- for the same grid-spacing δ as the sub-patch micro-grid interval (also called δ), we call the eigenvalues $\lambda_{m\delta}^{\text{NE1}}$,

- for the same grid-spacing Δ as the inter-patch distance Δ , we call the eigenvalues $\lambda_{m\Delta}^{\text{NE1}}$.

For various macroscale wavenumbers, we compute the eigenvalues of the numerically evaluated Jacobian $\mathbf{J}(\mathbf{x}_M)$, and compare with the eigenvalues of the viscous shallow water PDEs and the patch schemes for assessing the accuracy (§4.2.6) and stability (§4.4) of the patch schemes.

4.2.3 Analytic eigenvalue analysis of staggered patch schemes

This subsection discusses a method of deriving analytic eigenvalues of a generic staggered patch scheme (4.1.15) over a staggered patch grid, for the 2D viscous shallow water PDEs (4.1.6). Section 4.3 uses the analytic patch scheme eigenvalues to assess the numerical roundoff errors in the patch schemes. Section 3.3 uses the analytic patch scheme eigenvalues to separate the microscale and macroscale eigenvalues and in establishing the wavenumber-wise association of eigenvalues with the full-domain model, the numerical eigenvalue error computations passively use analytic eigenvalues to establish this association. Hence, the analytic patch scheme eigenvalues are used to assess accuracy (§4.2.6), stability (§4.4), and consistency (§4.5) of the staggered patch schemes.

To derive the analytic one-cell Jacobian for the patch scheme (4.1.15), we follow the same approach in §3.2.3 for the general linear wave, except for the following two differences.

1. For viscous shallow water flows, we use a patch grid in Fig. 4.1.2b with two layers of edge nodes in the normal direction to the edges, one layer of edge nodes in the tangential direction to the edges. Page 168 of §4.1.3 discusses why the staggered patch grid in Fig. 4.1.2b with such edge node arrangement is required for the viscous shallow water flows.
2. We adapt the analytic approach in §4.2.1 for the staggered grid full-domain microscale model (4.1.11), to an infinite *staggered patch grid* (number of macroscale grid intervals $N \rightarrow \infty$ in Fig. 4.1.2b). That is, we use an arbitrary Fourier mode for the perturbation about h_M , $u_M + a_1 t$ and $v_M + a_2 t$ of the patch scheme (4.1.15). Thus, for the patch scheme (4.1.15), we use an arbitrary Fourier mode of the perturbation about the mean accelerating flow, with real wavenumber (k_x, k_y) and

complex growth rate λ ,

$$\bullet h_{i,j}^{I,J}(t) = h_M + h_{i,j}^{p,q}(t) \exp[i(k_x I \Delta + k_y J \Delta)] , \quad (4.2.10a)$$

$$\bullet u_{i,j}^{I,J}(t) = u_M + a_1 t + u_{i,j}^{p,q}(t) \exp[i(k_x I \Delta + k_y J \Delta)] , \quad (4.2.10b)$$

$$\bullet v_{i,j}^{I,J}(t) = v_M + a_2 t + v_{i,j}^{p,q}(t) \exp[i(k_x I \Delta + k_y J \Delta)] , \quad (4.2.10c)$$

for the same interior indices i, j and global macroscale patch indices I, J in (2.1.5) of §2.1.1, separately for each equation. As defined in p. 58 of §3.2.3, the indices $p, q \in \{0, 1\}$ are local sub-macro-cell patch index with $p = I \bmod 2$ and $q = J \bmod 2$. Figure 2.1.4 of §2.1.2 illustrates these indices, for our present case of $N \rightarrow \infty$ for analytic eigenvalue analysis, we use the global macroscale patch index $I, J \in \{\dots, -1, 0, 1, \dots\}$.

In contrast to the Fourier mode (3.2.10) for the state variables of the general linear wave, the Fourier mode (4.2.10) are for perturbations of the state variables of the viscous shallow water flows. As explained in §3.2.3, in the patch scheme Fourier mode (4.2.10), the time-dependent microscale structure $h_{i,j}^{p,q}(t)$, $u_{i,j}^{p,q}(t)$, $v_{i,j}^{p,q}(t)$ is modulated over the macroscale wave form $\exp[i(k_x I \Delta + k_y J \Delta)]$. So, the microscale structure $h_{i,j}^{p,q}(t)$, $u_{i,j}^{p,q}(t)$, $v_{i,j}^{p,q}(t)$ depends only on the sub-macro-cell patch index p, q and the sub-patch micro-grid node index i, j , but not on the global patch index I, J due to the 2Δ -translational symmetry in the Fourier shift.

As in §3.2.3, collecting the interior values of all three patches in the centre macro-cell into a vector gives the *state vector* \mathbf{x}^i . For a given number of macro-grid intervals N and sub-patch micro-grid intervals n , the number of patch interior nodes n_p^i per macro-cell, that is the size of \mathbf{x}^i , is same for the different number of layers of the edge nodes. Hence, the n_p^i for the viscous shallow water flows is same as expression (3.2.11) of §3.2.3 for the general linear wave. That is, the total number of patch interior nodes per macro-cell

$$n_p^i = 9n^2/4 - 4n + 2, \quad (4.2.11)$$

where n is the number of sub-patch grid intervals. For example, for $n = 6, 10, 14$ sub-patch micro-grid intervals, $n_p^i = 59, 187, 387$ respectively. The state vector for the staggered patch grid in Fig. 4.1.2b for the viscous shallow water flows, is the same as the state vector (3.2.12) for the general linear wave.

Applying a specific patch coupling (Spectral1, Square-p2, Square-p4, etc.) gives edge values of all the patches in centre macro-cell, in terms of the substituted Fourier mode. That is, patch coupling gives the edge values of each patch in the centre macro-cell from the centre-node values of

patches in other macro-cells, which are Fourier shifted centre-node values (by multiples of 2Δ) of the centre macro-cell. Collecting the edge values of all three patches in the centre macro-cell into a vector gives the *edge vector* \mathbf{x}^e . The total number of patch edge nodes per macro-cell for the compatible staggered patch grid (Fig. 4.1.2b) for viscous shallow water flows, that is the size of \mathbf{x}^e ,

$$n_p^e = 18n + 8, \quad (4.2.12)$$

where n is the number of sub-patch grid intervals. For example, for the cases of $n = 6, 10, 14$ sub-patch micro-grid intervals, $n_p^e = 116, 188, 260$ respectively. The expression (4.2.12) shows that the patch grid in Fig. 4.1.2b for the viscous shallow water flows, has a larger number of edge nodes compared to expression (3.2.13) of §3.2.3 for the staggered patch grid in Fig. 4.1.2a for the general linear wave. Page 60 of §3.2.3 presents some example coupling expressions (3.2.14) for the edge nodes using the simplest staggered patch scheme Square-p2.

For one macro-cell, substituting into the staggered patch scheme (4.1.15), the Fourier mode (4.2.10) and the coupled patch edge values (e.g., expressions (3.2.14) in p. 60 of §3.2.3) computed by a specific patch coupling, and cancelling the exponential factors on both sides, gives the time evolution of a macroscale Fourier component of a staggered patch scheme, as a dynamical system

$$\frac{d\mathbf{x}^i}{dt} = \mathbf{F}(\mathbf{x}^i; \mathbf{x}^e(\mathbf{x}^i)), \quad (4.2.13)$$

only for the specific modes of macroscale wavenumber (k_x, k_y) . The dynamical system (4.2.13) is in the same form as the full-size staggered patch scheme dynamical system (4.1.18). The state vector \mathbf{x}^I of the full-size staggered patch scheme dynamical system (4.1.18) contain interior values of all the patches in a staggered patch grid, but the state vector \mathbf{x}^i of the staggered patch scheme dynamical system (4.2.13) for one macroscale wavenumber (k_x, k_y) contain interior values of only one macro-cell. Hence, similar to the general linear wave, we call equation (4.2.13) as the one-cell staggered patch scheme dynamical system for viscous shallow water flows. Unlike the full-size staggered patch scheme dynamical system (4.1.18), *the one-cell staggered patch scheme dynamical system (4.2.13) is the evolution about the mean accelerating flow.*

The one-cell staggered patch scheme dynamical system (4.2.13), written separately for h, u , and v is similar to the corresponding full-size staggered patch scheme (4.1.15) of §4.1.3 with the following two differences.

1. The state variables $h_{i,j}^{I,J}, u_{i,j}^{I,J}, v_{i,j}^{I,J}$ in \mathbf{x}^I of the full-size system (4.1.15) are from all the macro-cells expressed in the global patch index $I, J \in \{\dots, -1, 0, 1, \dots\}$. But the state variables $h_{i,j}^{p,q}, u_{i,j}^{p,q}, v_{i,j}^{p,q}$ in \mathbf{x}^i of the one-cell system (4.2.13) are node values only from one macro-cell, expressed in sub-macro-cell patch index $p, q \in \{0, 1\}$.
2. The state variables $h_{i,j}^{I,J}, u_{i,j}^{I,J}, v_{i,j}^{I,J}$ in \mathbf{x}^I of the full-size system (4.1.15) are the values of $h, u,$ and v . But the state variables $h_{i,j}^{p,q}, u_{i,j}^{p,q}, v_{i,j}^{p,q}$ in \mathbf{x}^i of the one-cell system (4.2.13) are only perturbations about the mean accelerating flow.

From the one-cell patch system (4.2.13), we aim to derive an eigensystem, following an approach similar to deriving the eigensystem (4.2.7) of §4.2.2 for the full-domain model. The one-cell patch system (4.2.13) for the viscous shallow water flows are nonlinear in the state variables $h_{i,j}^{p,q}, u_{i,j}^{p,q}, v_{i,j}^{p,q}$. Linearising the one-cell patch system (4.2.13) by neglecting the terms that are nonlinear in the state variables $h_{i,j}^{p,q}, u_{i,j}^{p,q}, v_{i,j}^{p,q}$ gives the eigensystem

$$\mathbf{J}(\mathbf{x}_M) \mathbf{x}^i = \lambda \mathbf{x}^i, \quad (4.2.14)$$

where $\mathbf{J}(\mathbf{x}_M) = [\partial \mathbf{F} / \partial \mathbf{x}^i]_{\mathbf{x}_M}$ is the $n_p^i \times n_p^i$ one-cell Jacobian of the staggered patch scheme. The number of state variables $n_p^i = 9n^2/4 - 4n + 2$ for the one-cell patch scheme system, as in expression (4.2.11).

Similar to the Jacobian of the viscous shallow water PDEs (p. 178 of §4.2.1), the patch scheme one-cell Jacobian $\mathbf{J}(\mathbf{x}_M)$ in the eigensystem (4.2.14) depends on the physical parameters $Re, g_x, g_n, (k_x, k_y), \mathbf{x}_M = (h_M, u_M, v_M)$. In addition, the patch scheme Jacobian $\mathbf{J}(\mathbf{x}_M)$ also depends upon the patch design parameters: total number of patch interior nodes n_p^i , sub-patch micro-grid interval δ , macro-grid interval Δ , and the specific patch coupling.

For example, similar to the case of general linear wave, for $n = 6$ sub-patch grid intervals, the one-cell Jacobian $\mathbf{J}(\mathbf{x}_M)$ for the viscous shallow water flows, is a 59×59 sparse matrix generally with only 318 of the 3481 elements being nonzero irrespective of the particular patch coupling interpolation of the staggered patch schemes, even among the global Spectral patch coupling and the local polynomial patch coupling. For some particular combinations of numerical values of the parameters, the sparsity is higher. The 318 nonzero elements of the one-cell Jacobian of a staggered patch scheme (for $n = 6$) contain all the information about the underlying microscale model and the patch coupling, for the macroscale waves of wavenumber (k_x, k_y) . For example, a few elements of the one-cell Jacobian

of the simplest staggered patch scheme Square-p2 are,

$$\begin{aligned}
\mathbf{J}_{1,1} &= 0, \quad \mathbf{J}_{1,16} = -\frac{h_M^2}{2\delta}, \quad \mathbf{J}_{4,10} = \frac{h_M^2}{2\delta}, \\
\mathbf{J}_{12,11} &= \frac{0.3366h_M v_M}{\delta} + \frac{h_M^2}{4\text{Re}\delta^2}, \quad \mathbf{J}_{16,16} = -\frac{2.4674}{\text{Re}} - \frac{2.5465h_M^2}{\text{Re}\delta^2}, \\
\mathbf{J}_{18,36} &= \left(\frac{0.188h_M v_M}{\delta} + \frac{0.5116h_M^2}{\text{Re}\delta^2} + \frac{0.564h_M v_M}{\Delta} + \frac{1.5349h_M^2}{\Delta\text{Re}\delta} \right) e^{-2\Delta i k_y} \\
&\quad + \frac{0.188h_M v_M}{\delta} + \frac{0.5116h_M^2}{\text{Re}\delta^2} - \frac{0.564h_M v_M}{\Delta} - \frac{1.5349h_M^2}{\Delta\text{Re}\delta}, \\
\mathbf{J}_{46,36} &= \left(-\frac{h_M^2}{8\delta} - \frac{h_M^2}{2\Delta} - \frac{3\delta h_M^2}{8\Delta^2} \right) e^{2\Delta i k_x} + \left(-\frac{h_M^2}{8\delta} + \frac{h_M^2}{2\Delta} - \frac{3\delta h_M^2}{8\Delta^2} \right) e^{-2\Delta i k_y} \\
&\quad + \left(-\frac{h_M^2}{8\delta} + \frac{h_M^2}{4\Delta} + \frac{3\delta h_M^2}{8\Delta^2} \right) e^{2\Delta i k_x - 2\Delta i k_y} - \frac{h_M^2}{8\delta} - \frac{h_M^2}{4\Delta} + \frac{3\delta h_M^2}{8\Delta^2}, \\
\mathbf{J}_{50,51} &= \left(-\frac{0.3366h_M v_M}{\Delta} - \frac{h_M^2}{4\Delta\text{Re}\delta} + \frac{0.6732\delta h_M v_M}{\Delta^2} + \frac{h_M^2}{2\Delta^2\text{Re}} \right) e^{2\Delta i k_y} \\
&\quad + \left(\frac{0.3366h_M v_M}{\Delta} + \frac{h_M^2}{4\Delta\text{Re}\delta} + \frac{0.6732\delta h_M v_M}{\Delta^2} + \frac{h_M^2}{2\Delta^2\text{Re}} \right) e^{-2\Delta i k_y} \\
&\quad + \frac{h_M^2}{2\text{Re}\delta^2} - \frac{1.3464\delta h_M v_M}{\Delta^2} - \frac{h_M^2}{\Delta^2\text{Re}}.
\end{aligned}$$

Compared to the above listed example Jacobian elements of the simple patch coupling Square-p2, more surrounding macro-cells influence the Jacobian elements for the cases of patch coupling with higher order interpolations (Square-p4, Square-p6, and Square-p8). Hence the expressions for the one-cell Jacobian elements are much longer than the listed example expressions.

Due to the large Jacobian size (e.g., 59×59 for $n = 6$) and the long expressions in their elements, all the CAS packages we tried (SymPy, Reduce and Maple) fail to compute the analytic eigenvalues of the one-cell Jacobian, even for the simplest staggered patch scheme Square-p2 with $n = 6$ sub-patch micro-grid intervals. So we numerically evaluate the one-cell Jacobian for numerical values of Δ , δ , Re , g_x , g_n , h_M , u_M , v_M , k_x , k_y and compute the eigenvalues λ_p^{NE1} . We compare with the eigenvalues λ_p^{NE1} of the numerically evaluated one-cell Jacobian of the patch schemes, with the eigenvalues of the full domain microscale model and the eigenvalues of the general linear wave PDEs, for assessing the accuracy (§4.2.6) and stability (§4.4) of the patch schemes.

4.2.4 Compute numerical Jacobian of the full-domain model

This subsection discusses a method to compute the numerical *full-size* Jacobian of the staggered grid *full-domain microscale model* (4.1.15) in contrast to the corresponding analytic 3×3 Jacobian in §4.2.2. Section 4.2.6 uses the eigenvalues of the numerical Jacobian of the full-domain microscale model, for comparing the eigenvalues of the staggered grid full-domain model with the eigenvalues of the patch scheme for the viscous shallow water flows.

Section 3.2.4 for the general linear wave, discusses some key differences between the 3×3 analytic Jacobian and the corresponding full-size numerical Jacobian for the full-domain model. In practice, the full-domain microscale simulation is subject to the practical issue of numerical roundoff errors. Hence we also compute the eigenvalues λ_m^N of the full-size numerical Jacobian of the full-domain microscale model as discussed in this subsection.

Consider the full-domain microscale model (4.1.13), $\mathbf{dx}/dt = \mathbf{f}(\mathbf{x})$, where \mathbf{x} is the state vector (4.1.14), for the viscous shallow water flows, over a full-domain staggered grid (e.g., Fig. 4.1.1) with $n \times n$ grid intervals. We want to characterise the accuracy and stability of the staggered grid full-domain model for the non-trivial nonlinear evolution of the viscous shallow water flows, apart from the mean flow and any constant drift with time in the solution \mathbf{x} . Hence, consider the solution $\mathbf{x}(t)$ as a small perturbation $\boldsymbol{\epsilon}(t)$ for small t , about the mean accelerating flow, that is,

$$\mathbf{x}(t) = \mathbf{x}_M + \mathbf{a}_M t + \boldsymbol{\epsilon}(t), \quad (4.2.15)$$

where the mean flow state $\mathbf{x}_M = (h_M, u_M, v_M)$ and the mean acceleration $\mathbf{a}_M = (0, a_1, a_2)$ as in equations (4.2.3). Substituting the solution form (4.2.15) into the full-domain microscale model (4.1.13) (i.e., $\mathbf{dx}/dt = \mathbf{f}(\mathbf{x})$) gives

$$\mathbf{a}_M + \frac{d\boldsymbol{\epsilon}}{dt} = \mathbf{f}(\mathbf{x}_M + \mathbf{a}_M t + \boldsymbol{\epsilon}(t)). \quad (4.2.16)$$

The time derivative of the state vector \mathbf{dx}/dt at the constant mean flow state $\mathbf{x}_M = (h_M, u_M, v_M)$ is

$$\left[\frac{d\mathbf{x}}{dt} \right]_{\mathbf{x}_M} = \mathbf{a}_M = \mathbf{f}(\mathbf{x}_M). \quad (4.2.17)$$

Expanding the RHS of equation (4.2.16) as Taylor series about \mathbf{x}_M gives

$$\begin{aligned} \mathbf{a}_M + \frac{d\boldsymbol{\epsilon}}{dt} &= \mathbf{f}(\mathbf{x}_M) + \left[\frac{\partial \mathbf{f}}{\partial \mathbf{x}} \right]_{\mathbf{x}_M} \cdot (\mathbf{a}_M \mathbf{t} + \boldsymbol{\epsilon}) + \mathcal{O}(\|\mathbf{a}_M \mathbf{t} + \boldsymbol{\epsilon}\|^2), \quad \text{as } \mathbf{t}, \|\boldsymbol{\epsilon}\| \rightarrow 0 \\ &= \mathbf{a}_M + \mathbf{J}(\mathbf{x}_M) \cdot (\mathbf{a}_M \mathbf{t} + \boldsymbol{\epsilon}) + \mathcal{O}(\|\mathbf{a}_M \mathbf{t} + \boldsymbol{\epsilon}\|^2), \quad \text{as } \mathbf{t}, \|\boldsymbol{\epsilon}\| \rightarrow 0 \\ \Rightarrow \frac{d\boldsymbol{\epsilon}}{dt} &= \mathbf{J}(\mathbf{x}_M) \cdot (\mathbf{a}_M \mathbf{t} + \boldsymbol{\epsilon}) + \mathcal{O}(\|\mathbf{a}_M \mathbf{t} + \boldsymbol{\epsilon}\|^2), \quad \text{as } \mathbf{t}, \|\boldsymbol{\epsilon}\| \rightarrow 0. \end{aligned}$$

Thus, for sufficiently small time \mathbf{t} , we get the eigensystem

$$\frac{d\boldsymbol{\epsilon}}{dt} \approx \mathbf{J}(\mathbf{x}_M) \cdot \boldsymbol{\epsilon} = \left[\frac{\partial \mathbf{f}}{\partial \mathbf{x}} \right]_{\mathbf{x}_M} \cdot \boldsymbol{\epsilon}, \quad (4.2.18)$$

in terms of the perturbation $\boldsymbol{\epsilon}(\mathbf{t})$ about the mean accelerating flow. In the eigensystem (4.2.18), $\mathbf{J}(\mathbf{x}_M)$ is the numerical *full-size* Jacobian of the staggered grid full-domain microscale model (4.2.15), in contrast to the analytic 3×3 Jacobian in the eigensystem (4.2.7) of §4.2.2. We calculate the j th column of the Jacobian $\mathbf{J}(\mathbf{x}_M)$ by numerical differentiation to second order approximation (error $\sim \mathcal{O}(\varepsilon^2)$) as,

$$\mathbf{J}_j(\mathbf{x}_M) = \frac{\mathbf{f}(\mathbf{x}_M + \varepsilon \mathbf{e}_j) - \mathbf{f}(\mathbf{x}_M - \varepsilon \mathbf{e}_j)}{2\varepsilon}, \quad (4.2.19)$$

where \mathbf{e}_j is the j th canonical Euclidean basis vector of size n_m whose j th element is one and all other elements are zero. We use $\varepsilon = 5 \cdot 10^{-6}$ to balance discretisation and roundoff errors in the calculation of numerical Jacobian. For example, with $\varepsilon = 5 \cdot 10^{-6}$, the discretisation error in Jacobian calculation is roughly about $\varepsilon^2 = 2.5 \cdot 10^{-11}$ and the numerical roundoff error is roughly about $10^{-16}/(2\varepsilon) = 10^{-11}$ for 64 bit floating-point representation.

The full-size numerical Jacobian $\mathbf{J}(\mathbf{x}_M)$ of the staggered grid full-domain microscale model, depends only on the physical parameters Re, g_x, g_y , and discretisation parameters n, δ , and the mean state \mathbf{x}_M , not on the wavenumber. That is the full-size numerical Jacobian $\mathbf{J}(\mathbf{x}_M)$ encodes the information for all the wavenumbers for the time evolution about the mean accelerating flow.

Section 4.2.6 uses the eigenvalues of the numerical Jacobian of the full-domain microscale model, for comparing the eigenvalues of the staggered grid full-domain model with the eigenvalues of the patch scheme for the viscous shallow water flows. For example, Figs. 4.2.1 and 4.2.2 of §4.2.6, compares the eigenvalues $\lambda_{m\delta}^N, \lambda_{m\Delta}^N$ of the numerical Jacobian of the full-domain microscale model, with grid interval δ and Δ respectively, of a staggered patch grid.

4.2.5 Compute numerical Jacobian of the staggered patch schemes

The one-cell Jacobian of the staggered patch schemes in §4.2.3, is useful in giving insights about the staggered patch schemes and to compute eigenvalues corresponding to every small macroscale wavenumber (k_x, k_y) for a patch grid of any size N . But, in practice, the staggered patch scheme numerical time simulation is performed using the *full-size* evolution equation (4.1.15). To confirm that full-size staggered patch scheme (4.1.18) is stable, accurate, consistent, and not too sensitive to numerical round-off errors, this subsection discusses a method to compute the numerical eigenvalues λ_p^N of the staggered patch schemes for the full evolution equations (4.1.15).

The $\mathbf{F}(\mathbf{x}^I; \mathbf{x}^E(\mathbf{x}^I))$ in the patch scheme dynamical system (4.1.18) corresponds to the $\mathbf{f}(\mathbf{x})$ in the full-domain microscale model (4.1.13). The functions \mathbf{F} and \mathbf{f} encode the same full-domain microscale model for the viscous shallow water PDES (4.1.6); Section 2.1.2 explains this difference for the generic wave-like system. Consider the full-size staggered patch scheme dynamical system (4.1.18), $d\mathbf{x}^I/dt = \mathbf{F}(\mathbf{x}^I; \mathbf{x}^E(\mathbf{x}^I))$ for viscous shallow water flows, with the same state vector \mathbf{x}^I (2.1.6) and a similar edge vector \mathbf{x}^E as those of the patch scheme for generic wave-like system in §2.1.2. We want to characterise the accuracy and stability of the patch schemes for the non-trivial nonlinear evolution of the viscous shallow water flows, apart from the mean flow and any constant drift with time in the solution \mathbf{x}^I . Hence, consider the solution $\mathbf{x}^I(t)$ as a small perturbation $\boldsymbol{\epsilon}(t)$ for small t , about the mean accelerating flow, that is,

$$\mathbf{x}^I(t) = \mathbf{x}_M + \mathbf{a}_M t + \boldsymbol{\epsilon}(t), \quad (4.2.20)$$

where the mean flow state $\mathbf{x}_M = (h_M, u_M, v_M)$ and the mean acceleration $\mathbf{a}_M = (0, a_1, a_2)$ as in equations (4.2.3). Substituting the solution form (4.2.20) into the staggered patch scheme dynamical system (4.1.18), $d\mathbf{x}^I/dt = \mathbf{F}(\mathbf{x}^I; \mathbf{x}^E(\mathbf{x}^I))$, and following the same steps described in §4.2.4 gives the eigensystem

$$\frac{d\boldsymbol{\epsilon}}{dt} \approx \mathbf{J}(\mathbf{x}_M) \cdot \boldsymbol{\epsilon} = \left[\frac{\partial \mathbf{F}}{\partial \mathbf{x}^I} \right]_{\mathbf{x}_M} \cdot \boldsymbol{\epsilon}, \quad (4.2.21)$$

in terms of the perturbation $\boldsymbol{\epsilon}(t)$ about the mean accelerating flow. In the eigensystem (4.2.21), $\mathbf{J}(\mathbf{x}_M)$ is the numerical *full-size* $n_p^I \times n_p^I$ Jacobian of the staggered patch scheme (4.1.15), in contrast to the analytic one-cell Jacobian in the eigensystem (4.2.14) of §4.2.3. The number of state

variables $n_p^I = (N^2/4)(9n^2/4 - 4n + 2)$ for the full-size patch scheme system, as in expression (2.1.7). We calculate the columns of the numerical full-size Jacobian $\mathbf{J}(\mathbf{x}_M)$ by numerical differentiation to second order approximation (error is $\mathcal{O}(|\epsilon|^2)$) as described in §4.2.4,

The full-size numerical Jacobian $\mathbf{J}(\mathbf{x}_M)$ of the staggered patch scheme, depends on the physical parameters Re , g_x , g_n , patch discretisation parameters N , n , r , δ , Δ , and the mean state \mathbf{x}_M , but not on the wavenumber. That is the full-size numerical Jacobian $\mathbf{J}(\mathbf{x}_M)$ encodes the information for all wavenumbers in the finite domain for the time evolution about the mean accelerating flow.

The eigenvalues λ_p^N of the numerical staggered patch scheme Jacobian $\mathbf{J}(\mathbf{x}_M)$ characterises the accuracy and stability of the numerical staggered patch schemes over a particular finite sized domain (i.e., N is finite as opposed to infinite staggered patch grid for the one-cell Jacobian). Sections 4.2.6 and 4.4 compare the eigenvalues λ_p^N of the staggered patch scheme numerical Jacobian, with the eigenvalues of the full domain micro-scale model and the eigenvalues of the viscous shallow water PDEs, for assessing the accuracy and stability of the patch schemes respectively.

4.2.6 Staggered patch schemes are accurate for macroscale waves

Similar to §3.2.6 for the general linear wave, this section explains the qualitative structure of the staggered patch scheme eigenvalues and eigenvectors, and qualitatively demonstrates the accuracy of the staggered patch schemes for the *viscous shallow water flows* for few representative cases. Section 4.5 on the consistency of the staggered patch schemes, quantitatively establishes the patch scheme accuracy in more detail, over a much broader range of parameters.

Similar to §3.2.6, this section demonstrates the accuracy of the developed five staggered patch schemes (Spectral, Square-p2, Square-p4, Square-p6, and Square-p8) by comparing the following eigenvalues in the complex plane plots.

1. Eigenvalues λ_p^N of the numerical Jacobian of a staggered patch scheme on a finite domain (§4.2.5).
2. Eigenvalues λ_p^{NE1} of the numerically evaluated one-cell Jacobian in eigensystem (4.2.14) in §4.2.3, of a staggered patch scheme on an infinite domain.

3. Eigenvalues $\lambda_{m\delta}^{\text{NE1}}$ of the numerically evaluated analytic Jacobian in eigensystem (4.2.7) in §4.2.2, of fine-grid full-domain microscale model, with micro-grid interval equal to the sub-patch micro-grid interval δ . We use the same symbol δ for the grid interval for both the full-domain micro-grid and the sub-patch micro-grid.
4. Eigenvalues $\lambda_{m\Delta}^{\text{NE1}}$ of the numerically evaluated analytic Jacobian in eigensystem (4.2.7), of coarse grid version of the full-domain microscale model, with $\delta = \Delta$.
5. Eigenvalues $\lambda_{\text{PDE}}^{\text{NE1}}$ of the numerically evaluated analytic Jacobian in eigensystem (4.2.4) in §4.2.1, of viscous shallow water PDEs (4.1.6). Comparison with the eigenvalues $\lambda_{\text{PDE}}^{\text{NE1}}$ is only for completeness.

All the analytic eigenvalues ($\lambda_p^{\text{NE1}}, \lambda_{m\delta}^{\text{NE1}}, \lambda_{m\Delta}^{\text{NE1}}, \lambda_{\text{PDE}}^{\text{NE1}}$) are numerically evaluated for all *macroscale wavenumbers* resolved on a corresponding finite staggered patch grid. To illustrate the complete structure of eigenvalues (i.e, for all wavenumbers) of the full-domain microscale model and to cross-verify analytic and numerical computation of the full-domain microscale model eigenvalues, we also compute the eigenvalues of the numerical Jacobian of the full-domain microscale model for few cases (e.g., Figs. 4.2.1 and 4.2.2).

The sets of eigenvalues (e.g., $\lambda_p^{\text{N}}, \lambda_p^{\text{NE1}}, \lambda_{m\delta}^{\text{N}}, \lambda_{m\Delta}^{\text{N}}, \lambda_{\text{PDE}}^{\text{NE1}}$), in all the complex plane plots, are numbered in the legend entries on the left. In all the complex plane plots, physical parameters for each of these eigenvalues are listed in groups *below the legend entries*. Page 68 of §3.2.6 explains with an example, the conventions of this parameter listing.

Figures 4.2.1 and 4.2.2 plot the eigenvalues ($\lambda_p^{\text{N}}, \lambda_p^{\text{NE1}}$) of the Spectral patch scheme on a staggered patch grid with 6×6 macro-grid intervals ($N = 6$) and each patch containing 6×6 sub-patch micro-grid intervals ($n = 6$). Also plotted are the eigenvalues $\lambda_{m\delta}^{\text{N}}, \lambda_{m\Delta}^{\text{N}}$ of respectively the fine- and coarse-grid versions of the full-domain microscale model (4.1.11) and the eigenvalues $\lambda_{\text{PDE}}^{\text{NE1}}$ of the PDE (4.1.6). Similar to Figs. 4.2.1 and 4.2.2, in all the complex plane eigenvalue plots, eigenvalues are grouped within clusters based on eigenvalues λ_p^{NE1} of the staggered patch scheme Jacobian. Each cluster is annotated with the number of eigenvalues λ_p^{NE1} in the cluster and the cluster number in the superscript.

Page 71 of §3.2.6 explains the rationale and utility of the arcsinh scaling. For example, the clusters of macroscale eigenvalues on arcsinh scaling (i.e., clusters 1–6 in Fig. 4.2.2) reveal more details, compared to the clusters of macroscale eigenvalues on linear scaling (i.e., cluster 1 in Fig. 4.2.1). Hence,

Figure 4.2.1. Spectral staggered patch scheme ($N = 6, n = 6$) eigenvalues ($\lambda_p^N, \lambda_p^{NE1}$) on complex plane (*linear scale*) for viscous shallow water flows. Due to the large range of magnitudes of eigenvalues, details of eigenvalues for macroscale modes (mid-right cluster 1) are not discernible.

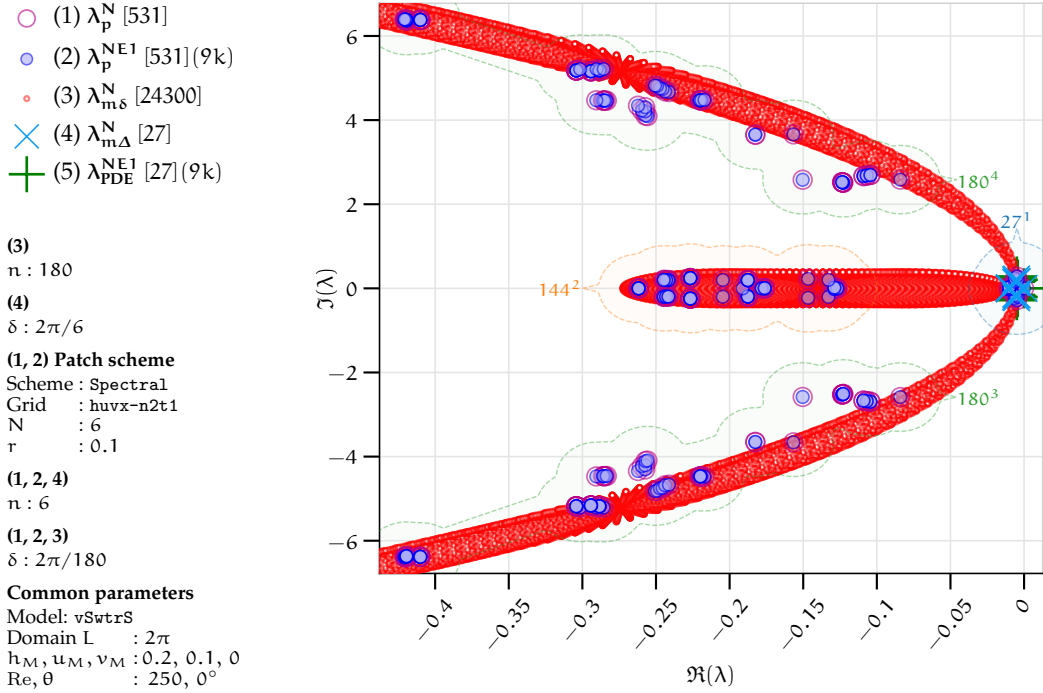
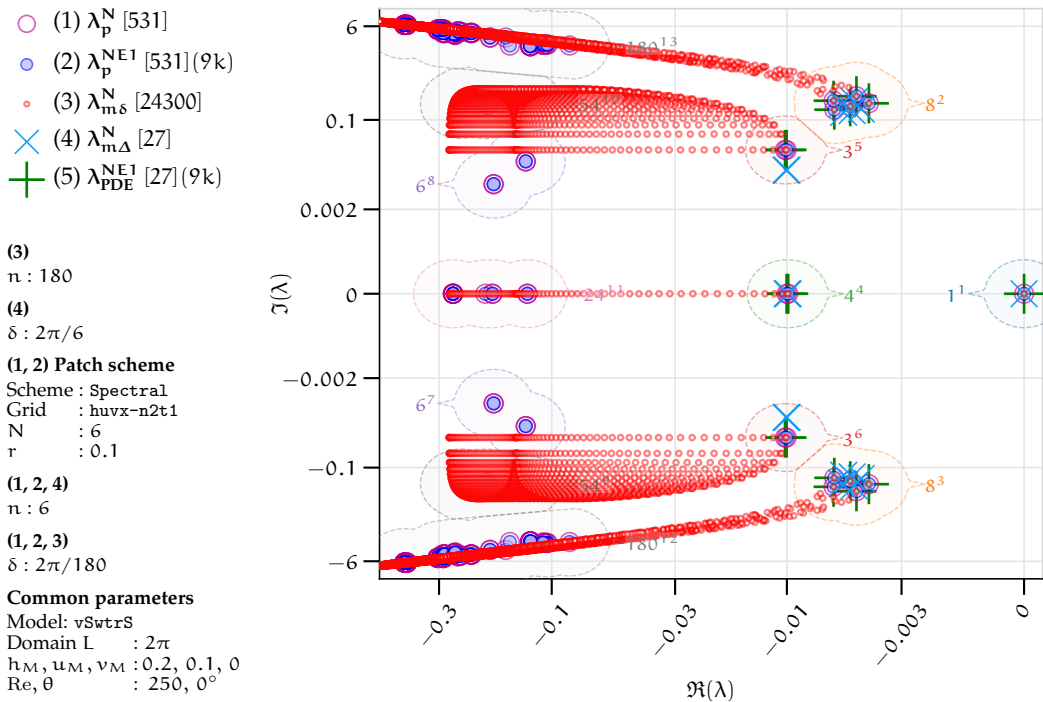


Figure 4.2.2. Spectral staggered patch scheme ($N = 6, n = 6$) eigenvalues ($\lambda_p^N, \lambda_p^{NE1}$) on complex plane (*arcsinh nonlinear scale*) for viscous shallow water flows. The arcsinh scaling zooms out the eigenvalues of macroscale modes (mid-right cluster 1 in Fig. 4.2.1 to clusters 1–6 here).



most complex plane eigenvalue plots in this thesis are on arcsinh scaling. Specifically, the complex plane plots on arcsinh scaling, plot an eigenvalue λ as 2D points with coordinates $(\text{arcsinh}[S_h \Re(\lambda)]/S_h, \text{arcsinh}[S_v \Im(\lambda)]/S_v)$, where S_h, S_v are the horizontal and vertical scale factors and $(0, 0)$ is the centre of zoom. In this chapter, most plots on arcsinh scaling use the scale factors $S_h = 500, S_v = 10^4$ (different from those in §3.2.6 for general linear wave).

As Figs. 4.2.1 and 4.2.2 show, a patch scheme contains only the small wavenumber macroscale modes on the right (clusters 1–6 in Fig. 4.2.2) and large wavenumber microscale modes on the left (clusters 7, 8, 9 in Fig. 4.2.2), not the modes of the intermediate scale. On the other hand, the eigenvalues $\lambda_{m\delta}^N$ of the full-domain microscale model, span the eigenvalue plot nearly uniformly from left to right, corresponding to all the wavenumbers resolved on the full-domain microscale staggered grid. Figures 4.2.1 and 4.2.2 show a good qualitative agreement of the structure of microscale and macroscale patch scheme eigenvalues λ_p^N and the complete structure of the eigenvalues $\lambda_{m\delta}^N$ (i.e., for all wavenumbers) of the full-domain microscale model. For the accurate multiscale modelling of the macroscale waves, the agreement between the macroscale eigenvalues of the patch scheme and those of the full-domain model is the primary focus. Figure 4.2.2 shows that, within the clusters 1–6, the numerical macroscale eigenvalues λ_p^N of the patch scheme (large magenta circles) and the numerical macroscale eigenvalues $\lambda_{m\delta}^N$ (small red circles) visually agree.

As Fig. 4.2.2 shows, for both microscale and macroscale modes, the patch scheme eigenvalues λ_p^{NE1} of the numerically evaluated one-cell analytic Jacobian (§4.2.3) and the patch scheme eigenvalues λ_p^N of the numerical Jacobian (§4.2.5), agree (i.e., the large magenta and blue circles). Hence, all other complex plane plots in this subsection §4.2.6 use eigenvalues λ_p^{NE1} of the numerically evaluated one-cell analytic Jacobian (§4.2.3), as opposed to the numerical eigenvalues λ_p^N .

Figures 4.2.1 and 4.2.2 show the complete structure of eigenvalues $\lambda_{m\delta}^N$ (i.e., for all wavenumbers) of the full-domain microscale model, for a full-domain staggered grid with the same grid interval δ as the sub-patch micro-grid interval of a patch grid with $N = 6$ and patch scale ratio $r = 0.1$. As p. 71 of §3.2.6 explains, for patch grids with $N \geq 10$ and/or $r < 0.1$, the corresponding full-size Jacobians of the fine-grid full-domain microscale model, rapidly increase in size, requiring substantially larger computational effort and memory. For the accurate multiscale modelling of the macroscale waves, the agreement between the macroscale eigenvalues of the patch scheme and those of the full-domain model is the primary focus, not the eigenvalues corresponding to all the wavenumbers. That is, to assess the patch scheme accuracy, as in Fig. 4.2.4 it suffices to compare only the patch

scheme macroscale eigenvalues with the macroscale eigenvalues $\lambda_{m\delta}^{NE1}$ of the full-domain microscale model (by numerically evaluating the analytic Jacobian (§4.2.2) only for macroscale wavenumbers resolved on a staggered patch grid). Hence, to avoid large computational effort and as the primary focus is on the macroscale eigenvalues, *all other complex plane plots in this subsection §4.2.6 use eigenvalues $\lambda_{m\delta}^{NE1}$ of the numerically evaluated analytic Jacobian (§4.2.2), as opposed to the numerical eigenvalues $\lambda_{m\delta}^N$.*

Figures 4.2.3 to 4.2.12 present the eigenvalue spectra for various parameter combinations. Figures 4.2.3 to 4.2.12 plot the Spectral patch scheme eigenvalues, over a staggered patch grid with 10×10 macro-grid intervals ($N = 10$) and each patch containing 6×6 sub-patch micro-grid intervals ($n = 6$). Figures 4.2.3 to 4.2.6 plot the eigenvalues for different linearisation point (h_M, u_M, v_M) , where h_M is the mean height and u_M, v_M are the mean horizontal velocities. Figures 4.2.9 to 4.2.10 plot the eigenvalues for different Reynolds numbers Re . Figures 4.2.11 and 4.2.12 plot the eigenvalues for different patch scale ratios r . The number just next to each cluster is the number of eigenvalues in that cluster. The cluster numbers referred to below are indicated on the plots by the *superscript* of the number just next to each cluster.

This paragraph explains the general qualitative structure of the patch scheme eigenvalues for the viscous shallow water flows. The following points are mainly based on the Spectral patch scheme eigenvalues in Figs. 4.2.3 to 4.2.6 and the corresponding eigenvectors (the patch scheme modes in Figs. 3.2.13 to 3.2.18 and Figs. 4.2.13 and 4.2.14). But *these points hold in general for the eigenvalues of, the PDE, full-domain microscale model, and all the five (Spectral and four polynomial) patch schemes, for the viscous shallow water flows.*

- The *macroscale clusters* (containing macroscale eigenvalues) are identified in the caption for each of Figures 4.2.3 to 4.2.12. The eigenvalues within all *other* clusters correspond to sub-patch *microscale modes*. There are $3N^2/4$ macroscale modes and $(N^2/4)(9n^2/4 - 4n - 1)$ microscale modes, same as those of the general linear wave in p. 75 of §3.2.6. All the following points in this listing are about the patch scheme macroscale modes for the viscous shallow water flows.
- As comparing Figs. 4.2.2 and 4.2.4 for $N = 6, 10$ shows, increasing N computes more macroscale modes for larger wavenumbers. For example, the clusters 2–6 in Fig. 4.2.2 extend to the left along the eigenvalues of the full-domain model (small red circles).
- *Steady uniform flow mode.* There is precisely one zero eigenvalue in

Figure 4.2.3. Spectral staggered patch scheme ($N = 10, n = 6$) eigenvalues for viscous shallow water flows for $(h_M, u_M, v_M) = (0.2, 0, 0)$. The macroscale eigenvalues λ_p^{NE1} in clusters 1–4 agree with the macroscale eigenvalues $\lambda_{m\delta}^{NE1}$ of the fine-grid full-domain microscale model.

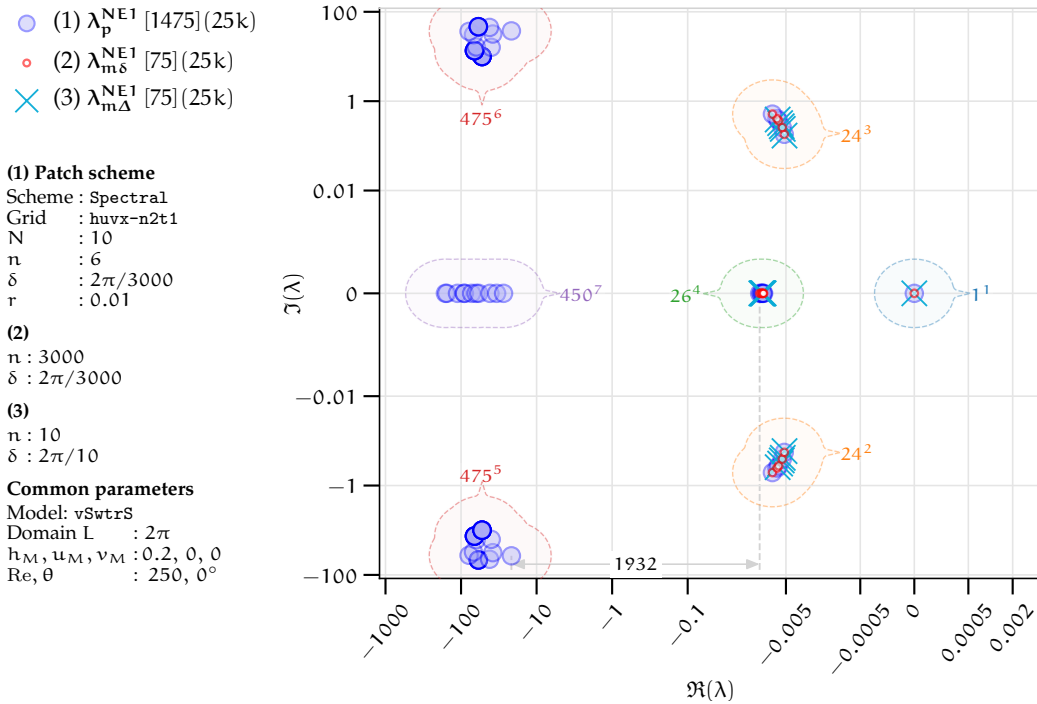


Figure 4.2.4. Spectral staggered patch scheme ($N = 10, n = 6$) eigenvalues for viscous shallow water flows for $(h_M, u_M, v_M) = (0.2, 0.1, 0)$. The macroscale eigenvalues λ_p^{NE1} in clusters 1–6 agree with the macroscale eigenvalues $\lambda_{m\delta}^{NE1}$ of the fine-grid full-domain microscale model.

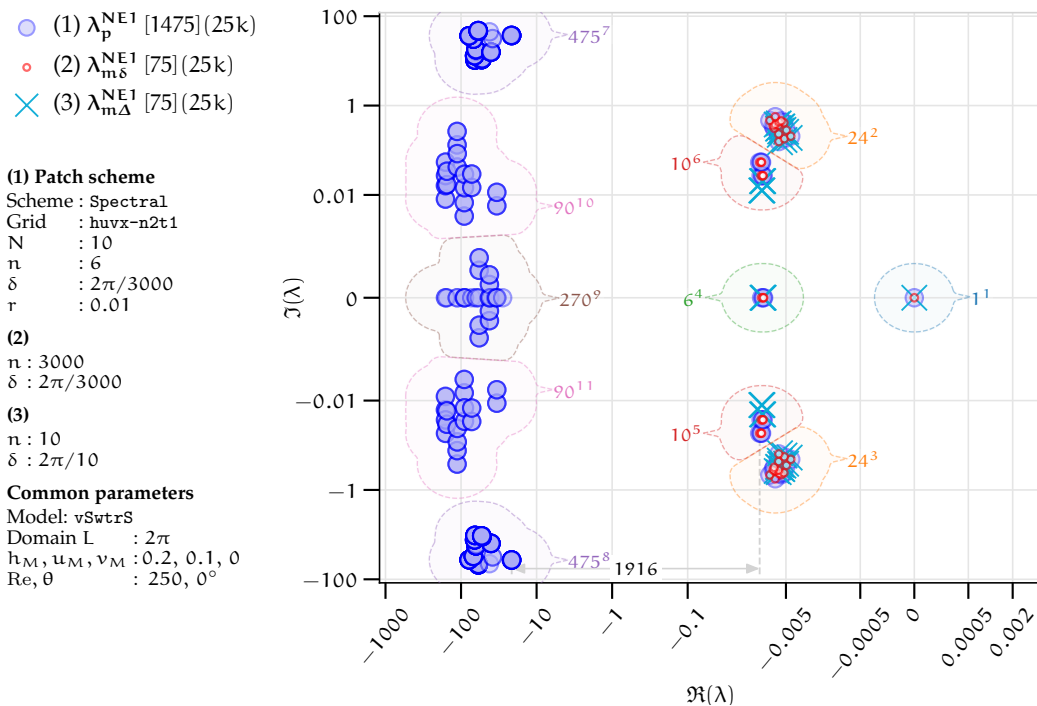


Figure 4.2.5. Spectral patch scheme ($N = 10, n = 6$) eigenvalues for viscous shallow water flows for $(h_M, u_M, v_M) = (0.2, 0.4, 0)$. Eigenvalues λ_p^{NE1} and $\lambda_{m\delta}^{NE1}$ agree for macroscale modes in clusters 1–6. Minimum real parts $\min \Re(\lambda_p^{NE1}) = -156$ (microscale), $\min \Re(\lambda_p^{NE1}) = -0.011$ (macroscale).

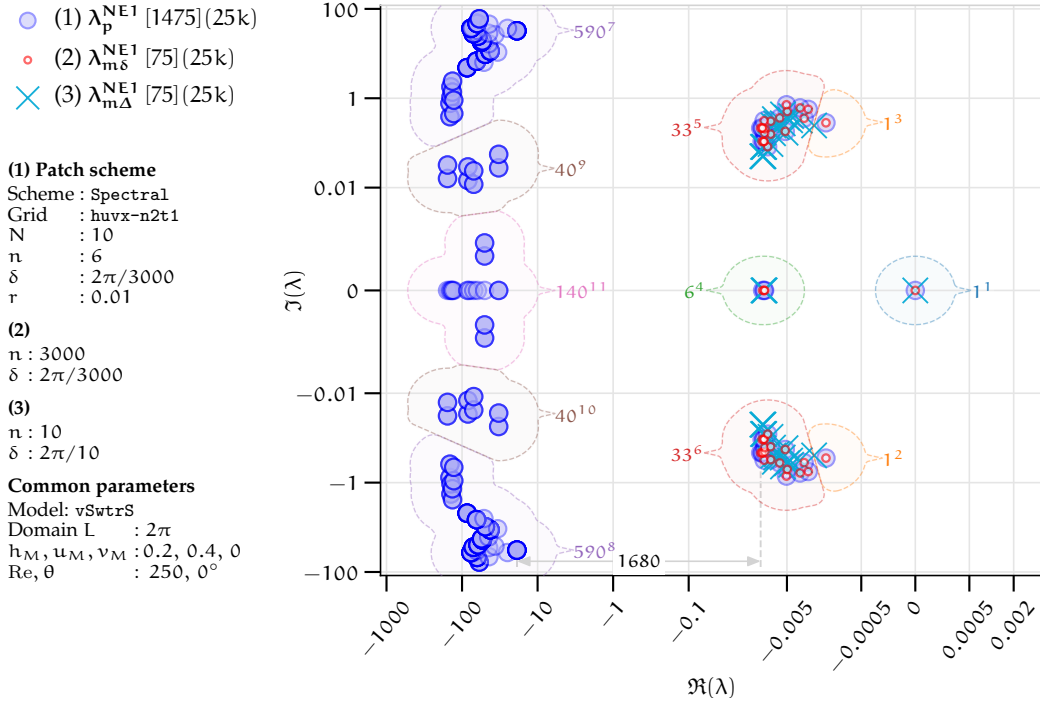
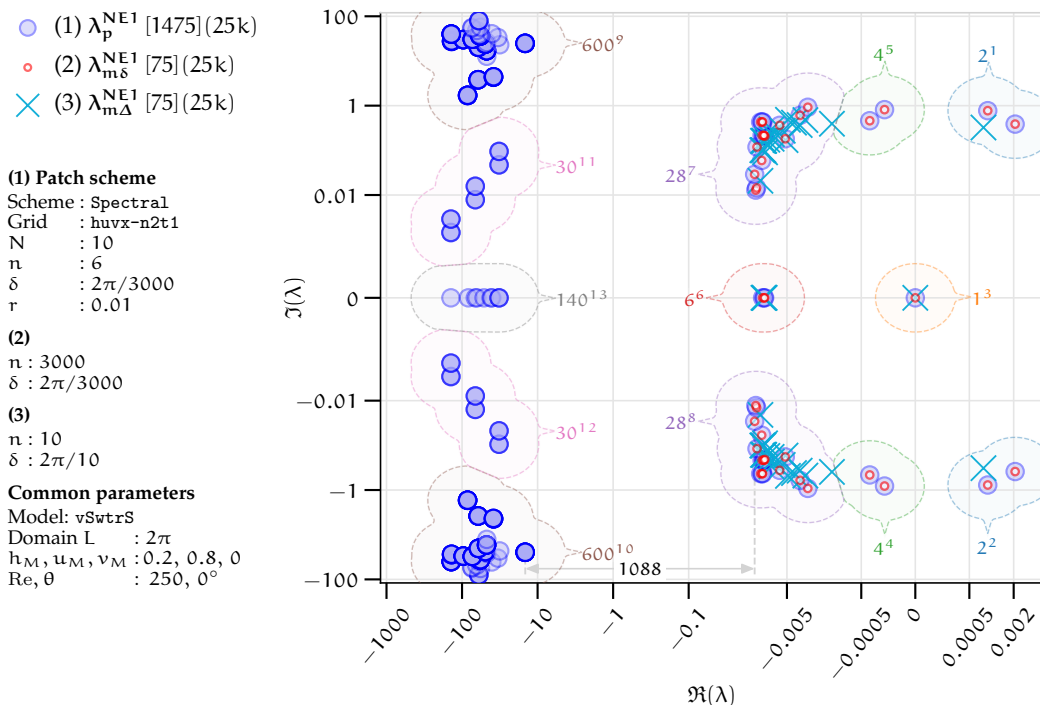


Figure 4.2.6. Spectral staggered patch scheme ($N = 10, n = 6$) eigenvalues for viscous shallow water flows for $(h_M, u_M, v_M) = (0.2, 0.8, 0)$. Eigenvalues λ_p^{NE1} and $\lambda_{m\delta}^{NE1}$ agree for macroscale modes in clusters 1–8. Maximum real parts $\max \Re(\lambda_{m\delta}^{NE1}) = \max \Re(\lambda_p^{NE1}) = 0.0021$ indicate *physical instability*.



the cluster 1 in all of [Figures 4.2.3 to 4.2.12](#), that corresponds to the *macroscale mode of steady* (zero eigenvalue, hence temporally constant) *uniform flow* (spatially constant h, u, v). For example, the eigenvector in [Fig. 4.2.14](#) shows the macroscale mode of steady uniform flow corresponding to the cluster 1 of [Fig. 4.2.4](#). When the mean velocity is zero $u_M = v_M = 0$, (e.g., cluster 1 of [Fig. 4.2.3](#)) this mode corresponds to stagnant water of uniform height, which is qualitatively same as the macroscale mode of the general linear wave (e.g., eigenvector in [Fig. 3.2.13](#)).

- *Decelerating uniform mean flow modes.* Same as for the general linear wave, *two* of the small real negative eigenvalues correspond to the *macroscale mode of decelerating uniform mean flow* irrespective of N, n . For example, two eigenvalues, among the 26 eigenvalues within the cluster 4 of [Fig. 4.2.3](#), and among the 6 eigenvalues within the cluster 4 of [Fig. 4.2.4](#), are of the macroscale modes of decelerating uniform mean flow. These modes of decelerating uniform mean flow are qualitatively same as the modes of the general linear wave (e.g., the eigenvector in [Fig. 3.2.14](#) of [§3.2.6](#)).
- *Macroscale wave modes.* Some of the complex conjugate eigenvalues with small negative real parts, correspond to slowly decaying *macroscale wave modes* with small wavenumber. These macroscale wave modes are qualitatively same as the macroscale wave modes of the general linear wave (e.g., the eigenvector in [Fig. 3.2.15](#) of [§3.2.6](#)). Such eigenvalues of macroscale wave modes are present in all of [Figures 4.2.3 to 4.2.12](#). For example, all the 24 eigenvalues in each of the clusters 2, 3 in [Figs. 4.2.3 and 4.2.4](#) are of macroscale wave modes. There are $2(N^2/4 - 1)$ macroscale wave modes, same as those of general linear wave in [p. 74](#) of [§3.2.6](#).
- *Macroscale vortex modes.* For zero mean velocities $u_M = v_M = 0$, as for the general linear wave in [p. 75](#) of [§3.2.6](#), there are $N^2/4 - 1$ the small real negative eigenvalues that correspond to slowly decaying *macroscale vortex modes* with small wavenumber. For example, for $N = 10$, the 24 among the 26 eigenvalues within the cluster 4 of [Fig. 4.2.3](#) correspond to such macroscale vortex modes. These macroscale vortex modes are qualitatively same as the macroscale vortex modes of the general linear wave (e.g., the eigenvector in [Fig. 3.2.16](#) of [§3.2.6](#)).

- *Advecting shear flow modes.* When mean velocity is increased from zero, $u_M > 0$ or $v_M > 0$, the $N^2/4 - 1$ macroscale vortex modes (e.g., the 24 among the 26 eigenvalues within the cluster 4 of Fig. 4.2.3) split into $N/2 - 1$ macroscale vortex modes with real negative eigenvalues and $N^2/4 - N/2$ decaying macroscale *advecting shear flow modes* with $N^2/8 - N/4$ pairs of complex conjugate eigenvalues. For example, for $N = 10$, the four among the six eigenvalues in the cluster 4 of Fig. 4.2.4 are of the macroscale vortex modes, the ten eigenvalues in each of the clusters 5, 6 are of the macroscale advecting shear flow modes. For example, Fig. 4.2.13 shows the eigenvector of a macroscale advecting shear flow mode corresponding to an eigenvalue in cluster 6 in Fig. 4.2.4. In Fig. 4.2.13, only v is nonzero, which indicates that the wavy spatial v -profile is static (i.e., non-oscillatory), unlike the wave modes with the dynamic energy exchange between the potential (height h) and kinetic energy (velocity u, v). Specifically, the eigenvector in Fig. 4.2.13 corresponds to a shear flow in y -direction that is being advected along in the x -direction by the mean flow $u_M = 0.1$. These advecting shear flow modes are *not present in general linear wave*.
- For small nonzero mean velocity $u_M \lesssim 0.1$, the eigenvalues of macroscale advecting shear flow modes form clearly distinguishable clusters, as the clusters 5, 6 in Fig. 4.2.4. For larger mean velocity $u_M \gtrsim 0.4$, the eigenvalue clusters of the macroscale wave modes and clusters of the macroscale advecting shear flow modes distort and overlap, as in Figs. 4.2.5 to 4.2.10.

As Page 80 of §3.2.6 defines, a *staggered patch scheme is accurate* when the macroscale eigenvalues (e.g., $\lambda_p^N, \lambda_p^{NE1}$) of the staggered patch schemes are close to the macroscale eigenvalues (e.g., $\lambda_{m\delta}^{NE1}$) of the corresponding fine-grid full-domain microscale model with the same grid interval as the sub-patch micro-grid interval. Comparing macroscale eigenvalues $\lambda_p^{NE1}, \lambda_{m\delta}^{NE1}$ the following paragraphs show that the staggered patch schemes are accurate for macroscale viscous shallow water flows for different linearisation point h_M, u_M, v_M and Reynolds number Re .

The *staggered patch schemes are accurate for macroscale viscous shallow water flows for different mean velocity u_M, v_M* . In contrast to the eigenvalues of the general linear wave in §3.2.6, due to the nonlinearity, the *eigenvalues of the viscous shallow water flows depend on the mean height h_M and the mean velocity h_M, v_M* . That is, the eigenvalues of the viscous shallow water flows depend on the linearisation point (h_M, u_M, v_M) . Figures 4.2.3 to 4.2.6 plot the Spectral patch scheme ($N = 10, n = 6$) eigenvalues for different mean velocity $u_M = 0, 0.1, 0.4, 0.8$ respectively, keeping $h_M = 0.2$ and $v_M = 0$.

The following points summarise the key dependence of the patch scheme eigenvalues on increasing mean velocity u_M . As §4.6 establishes, the patch schemes are invariant (within discretisation errors) with different flow angle α for macroscale waves, where $q = \sqrt{u_M^2 + v_M^2}$, $u_M = q \cos(\alpha)$ and $v_M = q \sin(\alpha)$. Hence, whereas the following points are based on increasing u_M keeping $v_M = 0$, they hold in general for increasing u_M and/or v_M . All the characteristics in the following listing also hold for the four polynomial patch schemes (§2.2.2).

- Figures 4.2.3 to 4.2.6 show that for the different mean velocity of $u_M = 0, 0.1, 0.4, 0.8$, the macroscale eigenvalues λ_p^{NE1} of the Spectral patch scheme (large blue circles within macroscale clusters identified in figure caption), agree with the macroscale eigenvalues $\lambda_{m\delta}^{NE1}$ (small red circles) of the fine-grid full-domain microscale model. This macroscale agreement of eigenvalues $\lambda_p^{NE1}, \lambda_{m\delta}^{NE1}$ indicates that the *patch schemes are accurate for macroscale viscous shallow water flows of different mean velocity*.
- While increasing u_M from zero to 0.8, as the previous paragraph explains, first the vortex modes (cluster 4 in Fig. 4.2.3) split into vortex modes and advecting shear flow modes (clusters 4 and clusters 5, 6 respectively in Fig. 4.2.4), next the clusters of advecting shear flow modes distort and overlap with the clusters of the (dynamical/oscillatory) wave mode (clusters 5, 6 in Fig. 4.2.5 and clusters 7, 8 in Fig. 4.2.6).
- The *spectral gap* (between the microscale and macroscale patch scheme eigenvalues) *decreases with increasing mean velocity* u_M . For example, in Figs. 4.2.3 to 4.2.6 for $u_M = 0, 0.1, 0.4, 0.8$, the corresponding spectral gaps are 1932, 1916, 1680, 1088. Physically, increasing u_M , increases the bed drag (macroscale eigenvalues move to the left), on the hand, the viscous diffusion (microscale eigenvalues) remains roughly the same, leading to decreasing spectral gap. This decreasing spectral gap with increasing u_M is the most prevalent trend among the various combinations of u_M , Reynolds number Re , mean height h_M , and patch scale ratio r . But, for some combinations of the grid parameters (N, n, r) and physical parameters (Re, h_M, u_M), increasing u_M decreases spectral gap due to artificial sub-patch microscale modes. In such cases, a small subset of the microscale eigenvalues in the complex plane move to the right with increasing u_M , leading to decreasing the spectral gap. For example, the clusters 5–7 in Fig. 4.2.10 contain such eigenvalues of sub-patch microscale modes.

- For large mean velocity $u_M \gtrsim 0.5$, the viscous shallow water flows have inherent *physical instability*, that is, the full-domain microscale model itself is unstable. Such physical instability is evident from the positive real part eigenvalues of the full-domain microscale model in Fig. 4.2.6 (clusters 1, 2). Section 4.4.1 shows the detailed trends of such physical instabilities as captured by the patch scheme for a wide range of parameters h_M, u_M, Re, N, r, n .

The *staggered patch schemes are accurate for macroscale viscous shallow water flows for different mean height h_M* . Figures 4.2.7, 4.2.4 and 4.2.8 plot the Spectral patch scheme ($N = 10, n = 6$) eigenvalues for different mean heights $h_M = 0.1, 0.2, 0.3$ respectively, keeping $u_M = 0.1$ and $v_M = 0$. The following points summarise the key dependence of the patch scheme eigenvalues on increasing mean height h_M . All the characteristics in the following listing also hold for the four polynomial patch schemes (§2.2.2).

- Figures 4.2.7, 4.2.4 and 4.2.8 show that for the different mean heights of $h_M = 0.1, 0.2, 0.3$, the macroscale eigenvalues λ_p^{NE1} of the Spectral patch scheme (large blue circles within macroscale clusters identified in figure caption), agree with the macroscale eigenvalues $\lambda_{m\delta}^{NE1}$ (small red circles) of the fine-grid full-domain microscale model. This macroscale agreement of eigenvalues $\lambda_p^{NE1}, \lambda_{m\delta}^{NE1}$ indicates that the *patch schemes are accurate for macroscale viscous shallow water flows for different mean heights*.
- While increasing h_M from 0.1 to 0.3, both the microscale and macroscale eigenvalues move to the left, taking larger negative real parts. That is, increasing h_M increases both the microscale and macroscale dissipation.
- Whereas both the microscale and macroscale dissipation increases with increasing h_M , the microscale dissipation increases at a larger rate. That is, increasing h_M decreases the real parts of microscale eigenvalues (e.g., on the left most clusters in Figs. 4.2.7, 4.2.4 and 4.2.8) at larger rate than increasing the real parts of macroscale eigenvalues, resulting in increasing spectral gap. Hence, the spectral gap increases with increasing mean height h_M . For example, in Figs. 4.2.7, 4.2.4 and 4.2.8 for mean heights $h_M = 0.1, 0.2, 0.3$, the corresponding spectral gaps are 383, 1916, 2162. Similar to the deviation in the trend of spectral gap with u_M explained in p. 198, for some combinations of the grid parameters (N, n, r) and physical parameters (Re, h_M, u_M), increasing h_M decreases spectral gap due to artificial sub-patch

Figure 4.2.7. Spectral staggered patch scheme ($N = 10, n = 6$) eigenvalues for viscous shallow water flows for $(h_M, u_M, v_M) = (0.1, 0.4, 0)$. Eigenvalues λ_p^{NE1} and $\lambda_{m\delta}^{NE1}$ agree for macroscale modes in clusters 1–6. Increasing mean height h_M increases spectral gap (Figs. 4.2.7, 4.2.4 and 4.2.8).

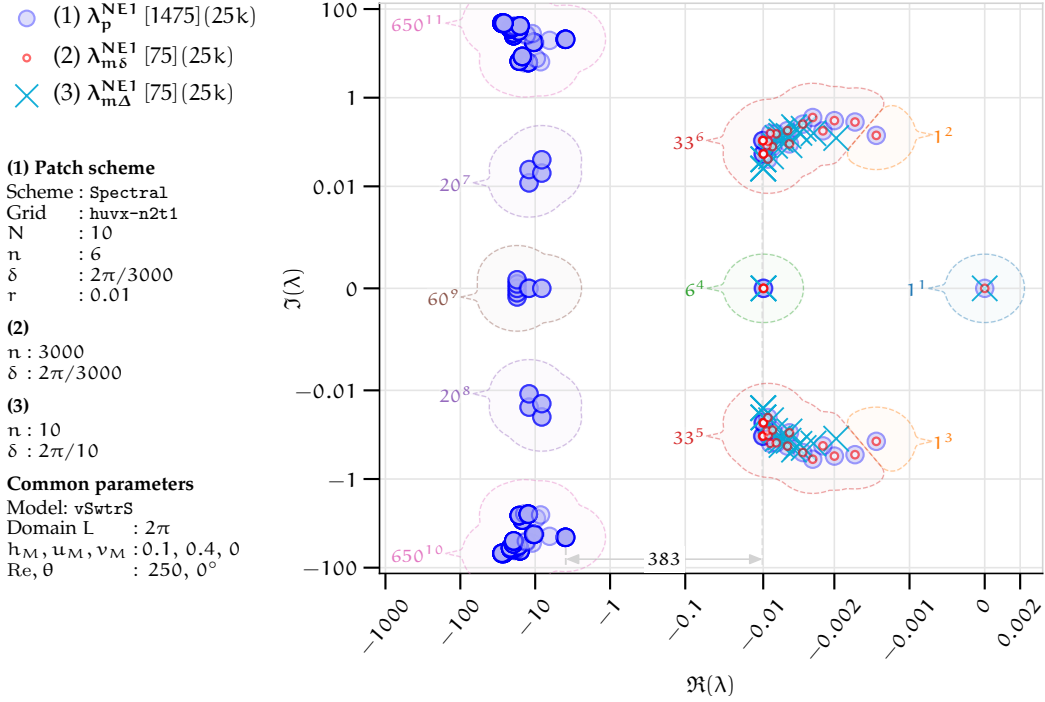
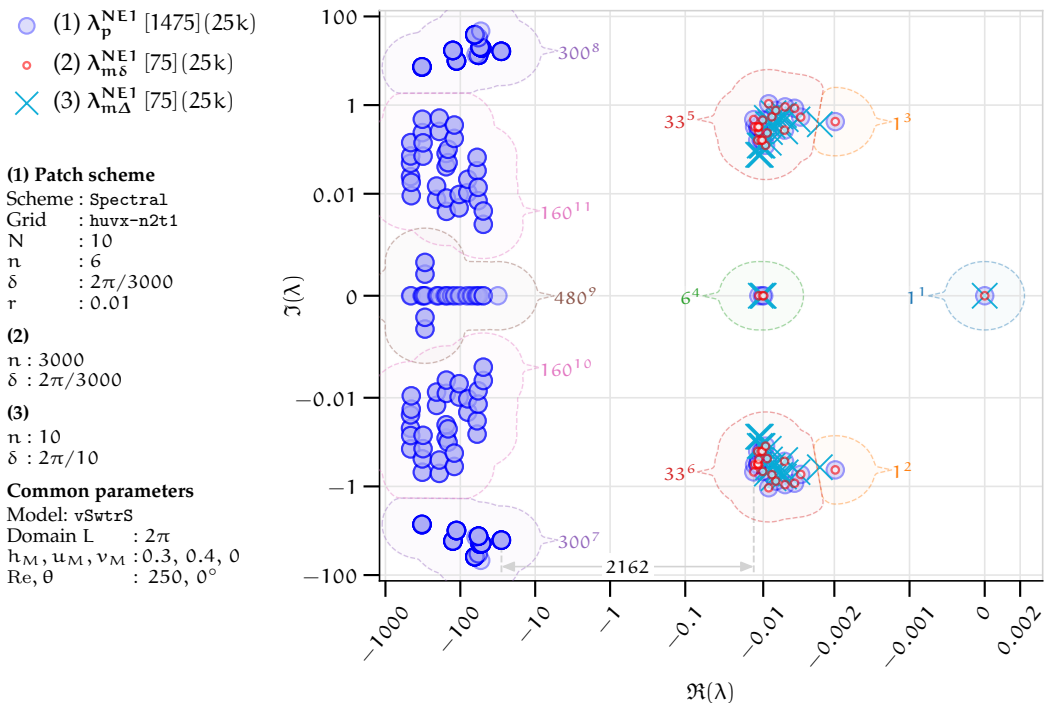


Figure 4.2.8. Spectral staggered patch scheme ($N = 10, n = 6$) eigenvalues for viscous shallow water flows for $(h_M, u_M, v_M) = (0.3, 0.4, 0)$. Eigenvalues λ_p^{NE1} and $\lambda_{m\delta}^{NE1}$ agree for macroscale modes in clusters 1–6. Increasing mean height h_M increases spectral gap (Figs. 4.2.7, 4.2.4 and 4.2.8).



microscale modes. *In general increasing h_M increases or decreases spectral gap depending upon the combinations of the grid parameters (N, n, r) and physical parameters (Re, h_M, u_M) .*

The staggered patch schemes are accurate for macroscale viscous shallow water flows for different Reynolds number Re . Figures 4.2.9, 4.2.10 and 4.2.5 plot the Spectral patch scheme ($N = 10, n = 6$) eigenvalues for different Reynolds numbers $Re = 10, 50, 250$ respectively. The following points summarise the key dependence of the patch scheme eigenvalues on increasing Reynolds numbers Re . All the characteristics in the following listing also hold for the four polynomial patch schemes (§2.2.2).

- Figures 4.2.9, 4.2.10 and 4.2.5 show that for the different Reynolds numbers of $Re = 10, 50, 250$, the macroscale eigenvalues λ_p^{NE1} of the Spectral patch scheme (large blue circles within macroscale clusters identified in figure caption), agree with the macroscale eigenvalues $\lambda_{m\delta}^{NE1}$ (small red circles) of the fine-grid full-domain microscale model. This macroscale agreement of eigenvalues $\lambda_p^{NE1}, \lambda_{m\delta}^{NE1}$ indicates that the patch schemes are accurate for macroscale viscous shallow water flows of different Reynolds numbers.
- Increasing Reynolds number Re decreases the dissipation for both macroscale and sub-patch microscale modes of the patch schemes. Decreasing dissipation increases the real parts of the microscale and macroscale patch scheme eigenvalues, moving to the right in the complex plane plots. For example, in Figs. 4.2.9, 4.2.10 and 4.2.5 for $Re = 10, 50, 250$, the minimum real parts of the patch scheme for microscale eigenvalues are $\min \Re(\lambda_{p\mu}^{NE1}) = -5785, -1147, -156$, and for macroscale eigenvalues are $\min \Re(\lambda_{pM}^{NE1}) = -0.28, -0.056, -0.011$ respectively.
- In general, for both zero and nonzero mean velocities u_M, v_M , the spectral gap (between the microscale and macroscale patch scheme eigenvalues) increases with increasing Reynolds number Re . The Reynolds number Re in the viscous shallow water PDEs (4.1.6) is defined based on inviscid wave velocity $U = \sqrt{gH}$, not the flow velocity. Hence, the Reynolds number Re is not necessarily zero when the mean velocity is zero. For example, in Figs. 4.2.9, 4.2.10 and 4.2.5 for $Re = 10, 50, 250$, the corresponding spectral gaps are 3.1, 65, and 1680. Except for some combinations of the grid parameters (N, n, r) , this increasing spectral gap with increasing Re is the most prevalent trend among the various combinations of mean height h_M , mean velocity u_M , Reynolds number Re , and patch scale ratio r .

Figure 4.2.9. Spectral staggered patch scheme ($N = 10, n = 6$) eigenvalues for viscous shallow water flows for $Re = 10$. Eigenvalues λ_p^{NE1} and $\lambda_{m\delta}^{NE1}$ agree for macroscale modes in clusters 1–4. Minimum real parts $\min \Re(\lambda_p^{NE1}) = -5785$ (microscale), $\min \Re(\lambda_{pM}^{NE1}) = -0.28$ (macroscale).

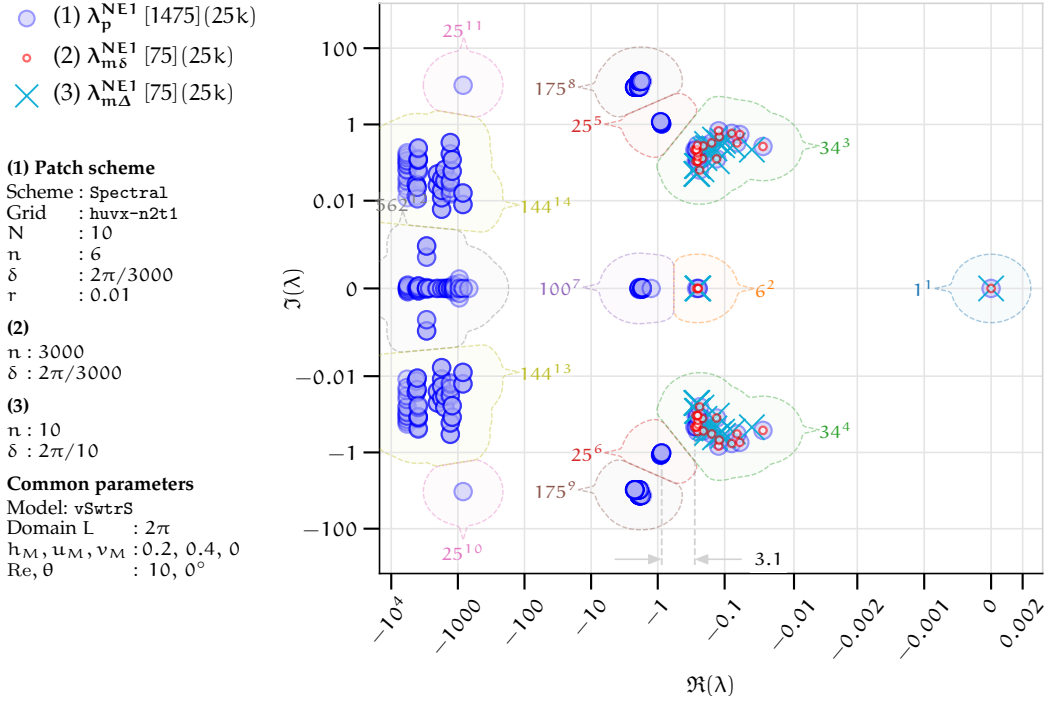
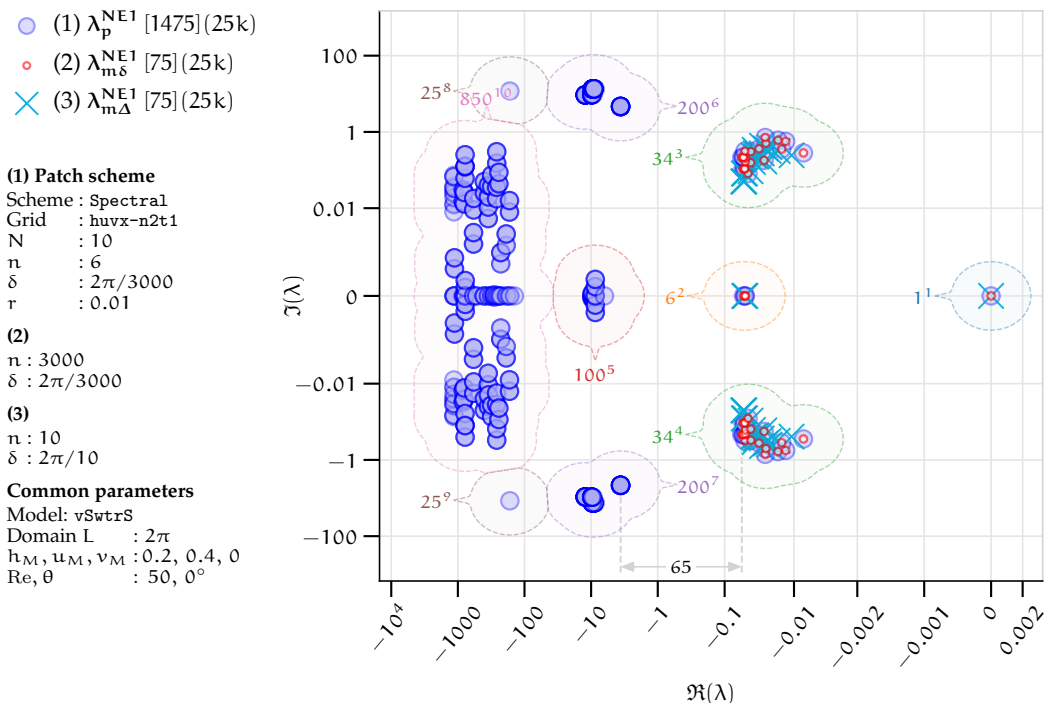


Figure 4.2.10. Spectral staggered patch scheme ($N = 10, n = 6$) eigenvalues for viscous shallow water flows for $Re = 50$. Eigenvalues λ_p^{NE1} and $\lambda_{m\delta}^{NE1}$ agree for macroscale modes in clusters 1–4. Minimum real parts $\min \Re(\lambda_p^{NE1}) = -1147$ (microscale), $\min \Re(\lambda_{pM}^{NE1}) = -0.056$ (macroscale).



The *staggered patch schemes are accurate for macroscale viscous shallow water flows for different patch scale ratio r* . [Figures 4.2.11](#) and [4.2.12](#) plot the Spectral patch scheme ($N = 10, n = 6$) eigenvalues for patch scale ratio $r = 0.1, 0.001$ respectively. The following points summarise the key dependence of the patch scheme eigenvalues on decreasing patch scale ratio r . All the characteristics in the following listing also hold for the four polynomial patch schemes ([§2.2.2](#)).

- [Figures 4.2.11](#) and [4.2.12](#) indicate that for the different patch scale ratio $r = 0.1, 0.001$, the macroscale eigenvalues λ_p^{NE1} of the Spectral patch scheme (large blue circles within macroscale clusters identified in figure caption), agree with the macroscale eigenvalues $\lambda_{m\delta}^{NE1}$ (small red circles) of the fine-grid full-domain microscale model. This macroscale agreement of eigenvalues $\lambda_p^{NE1}, \lambda_{m\delta}^{NE1}$ indicates that the *patch schemes are accurate for macroscale viscous shallow water flows for different patch scale ratio r* .
- As [Figs. 4.2.11](#) and [4.2.12](#) show, decreasing the patch scale ratio r dissipates the sub-patch microscale modes at a larger rate than, as evident from the increasingly large negative real parts (the blue circles move to the left); but the eigenvalues of the macroscale modes (small red circles on the right) remains unchanged.
- In general, the *spectral gap* (between the microscale and macroscale patch scheme eigenvalues) *increases with decreasing patch scale ratio r* . For example, decreasing the patch scale ratio of $r = 0.1, 0.001$ in [Figs. 4.2.11](#) and [4.2.12](#) leads to increasing spectral gap from 5.88 to 2370. Except for some combinations of the grid parameters (N, n, r), this increasing spectral gap with decreasing r is the most prevalent trend among the various combinations of mean height h_M , mean velocity u_M , Reynolds number Re , and patch scale ratio r .

The staggered patch schemes are accurate for different parameters. In [Figs. 4.2.3](#) to [4.2.8](#) for different linearisation point h_M, u_M, v_M , and in [Figs. 4.2.9, 4.2.10](#) and [4.2.5](#) for different Reynolds number Re , the macroscale eigenvalues λ_p^{NE1} of the Spectral patch scheme (large blue circles within macroscale clusters identified in figure caption), agree with the macroscale eigenvalues $\lambda_{m\delta}^{NE1}$ (small red circles) of the fine-grid full-domain microscale model. This agreement of the Spectral patch scheme macroscale eigenvalues with those of the fine-grid full-domain model, is exact (within numerical round-off errors). The polynomial patch scheme macroscale eigenvalues also agree with those of the fine-grid full-domain model. Unlike the exact accuracy of the Spectral patch scheme, the polynomial patch scheme error

Figure 4.2.11. Spectral staggered patch scheme ($N = 10, n = 6, r = 0.1$) eigenvalues for viscous shallow water flows for $(h_M, u_M, v_M) = (0.1, 0.1, 0)$. Eigenvalues λ_p^{NE1} and $\lambda_{m\delta}^{NE1}$ agree for macroscale modes in clusters 1–6. Decreasing r increases spectral gap (Figs. 4.2.11 and 4.2.12).

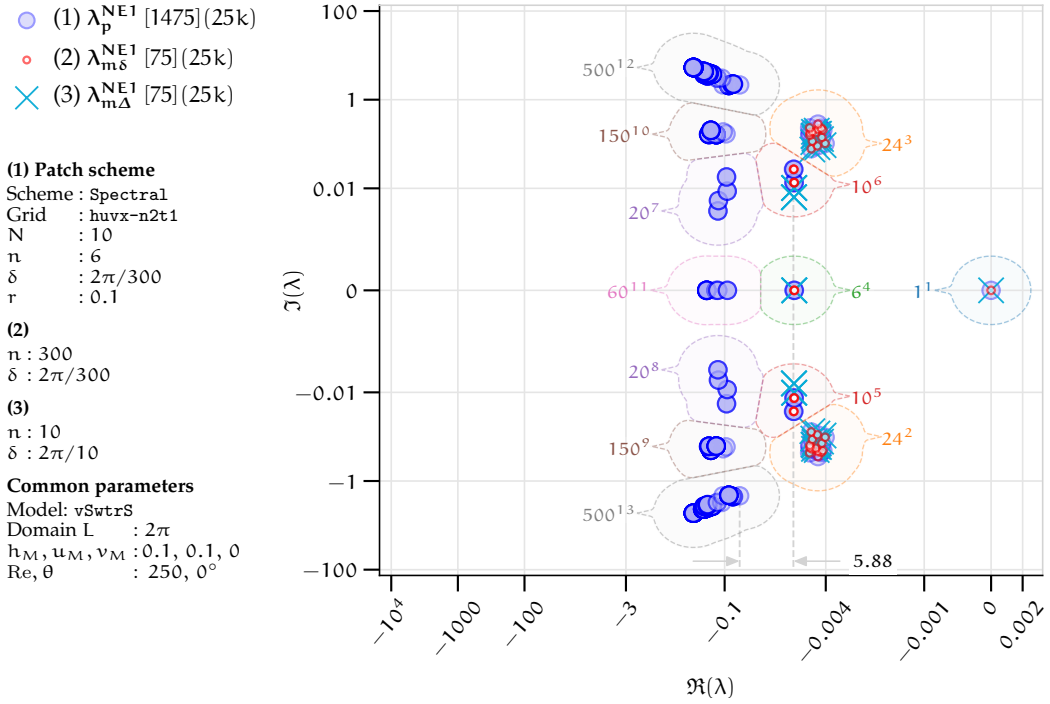
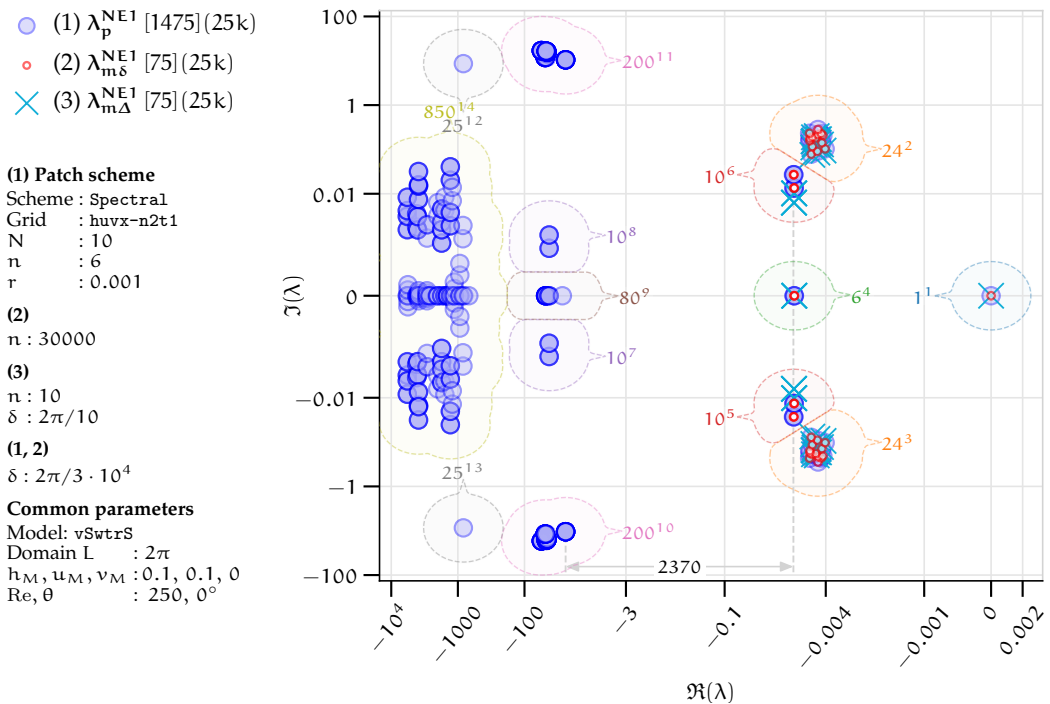


Figure 4.2.12. Spectral staggered patch scheme ($N = 10, n = 6, r = 0.001$) eigenvalues for viscous shallow water flows for $(h_M, u_M, v_M) = (0.1, 0.1, 0)$. Eigenvalues λ_p^{NE1} and $\lambda_{m\delta}^{NE1}$ agree for macroscale modes in clusters 1–6. Decreasing r increases spectral gap (Figs. 4.2.11 and 4.2.12).



decreases with increasing polynomial interpolation order p and decreasing macro-grid interval Δ (§4.5 shows such parametric dependence of the accuracy). Thus, from Figs. 4.2.3 to 4.2.12 and the discussions in the previous paragraphs for a representative set of parameters, the *staggered patch schemes are accurate for macroscale viscous shallow water flows, about different linearisation points, for different Reynolds numbers, and for different patch scale ratios*. Section 4.5 on the consistency of the staggered patch schemes, quantitatively demonstrates the accuracy for a wider range of parameters h_M, u_M, Re, N, r, n .

Figures 4.2.13 and 4.2.14 plot two patch scheme eigenvectors (modes) for the viscous shallow water flows, that are qualitatively different from the patch scheme modes of the general linear wave in Figs. 3.2.13 to 3.2.18. These eigenvectors are computed for the numerical Jacobian (§3.2.5) of the Spectral staggered patch scheme. The qualitative shapes of the eigenvectors in Figs. 4.2.13 and 4.2.14 are the same for the Spectral (§2.2.1) and polynomial (§2.2.2) staggered patch schemes Square-p2, Square-p4, Square-p6, and Square-p8. As p. 197 of this §4.2.6 explains, Fig. 4.2.13 plots the macroscale advecting shear flow mode corresponding to an eigenvalue in cluster 6 of Fig. 4.2.4. As p. 196 of this §4.2.6 explains, Fig. 4.2.14 plots the steady uniform flow mode corresponding to the zero eigenvalues in cluster 1 of Fig. 4.2.4.

Figure 4.2.13. Eigenvector for eigenvalue $\lambda_p^N = 0.0100 + 0.0269i$ (cluster 6 in Fig. 4.2.4), for Spectral staggered patch scheme with $N = 10$, $n = 6$, $r = 0.01$. Only v is nonzero, indicating *advecting shear flow mode* (static spatial v -profile) without any dynamic energy exchange with height ($h = 0$).

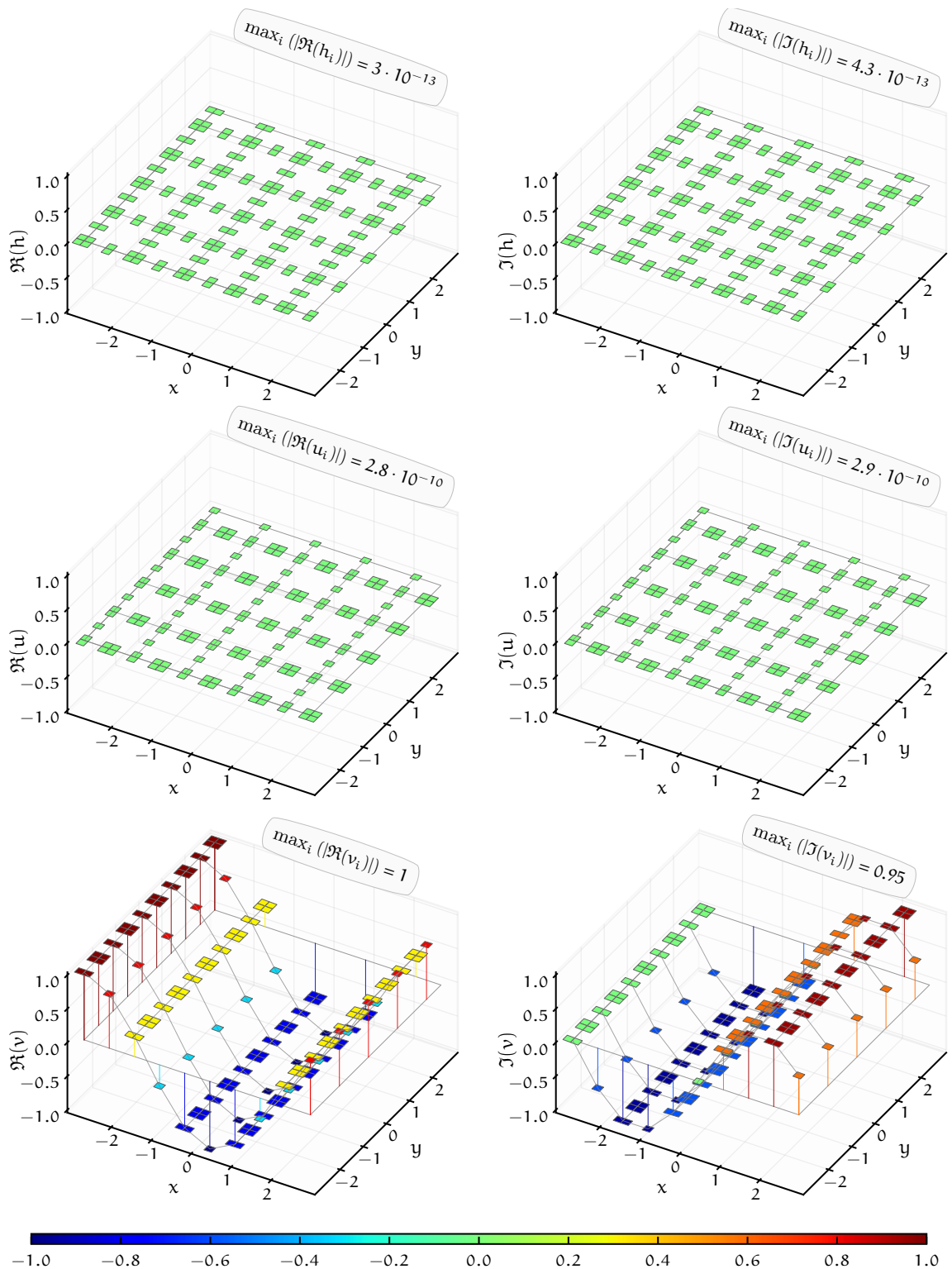
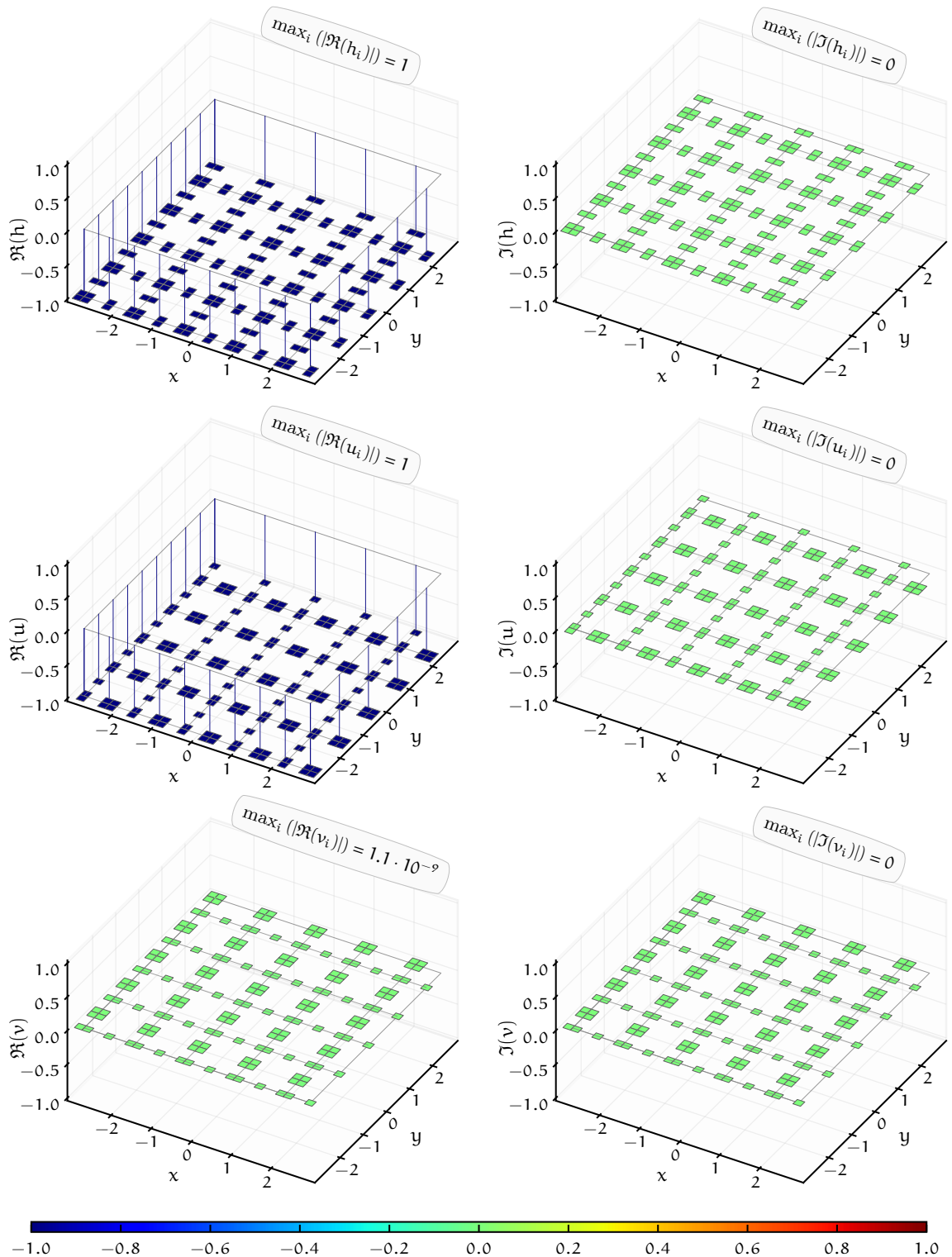


Figure 4.2.14. Eigenvector for eigenvalue $\lambda_p^N = 0 + 0i$ (cluster 1 in Fig. 4.2.4), for Spectral staggered patch scheme with $N = 10$, $n = 6$, $r = 0.01$. For $u_M = 0.1$, the macroscale mode of steady (zero eigenvalue, hence temporally constant) uniform flow (spatially constant height h and velocity u).



4.3 Staggered patch schemes are not sensitive to numerical roundoff errors

Despite the attractive characteristics, if the staggered patch schemes are very sensitive to numerical roundoff errors, then they would not be suitable for practical numerical simulations using finite precision floating-point arithmetic (Goldberg 1991). From both qualitative arguments and quantitative evidence, this section shows that the staggered patch schemes are not sensitive to numerical roundoff errors for the viscous shallow water flows, except when the patches are too small relative to inter-patch distance, and/or when the underlying microscale model is sensitive to numerical roundoff errors. The quantitative evidence comes from comparing the eigenvalues of analytic Jacobian and numerical Jacobians of a patch scheme.

The staggered patch scheme eigenvalues λ_p^{NE1} (for both the microscale and macroscale mdoes) of the numerically evaluated one-cell Jacobian (§4.2.3) and the staggered patch scheme eigenvalues λ_p^N of the numerical Jacobian (§4.2.5), *visually* agree in the complex plane eigenvalue plots of §4.2.6 (i.e., the large magenta and blue circles in Fig. 4.2.2). That the numerical and analytic eigenvalues ($\lambda_p^N, \lambda_p^{NE1}$) of a patch scheme visually agree indicates that the patch scheme is not sensitive to numerical roundoff errors. This subsection first *quantitatively* compares the numerical and analytic eigenvalues of the staggered patch schemes to show that the staggered patch schemes are not sensitive to numerical roundoff errors when the sub-patch micro-grid interval is not too small (i.e., $\delta \gtrsim 10^{-5}$). The later part of this subsection argues that even for very small sub-patch micro-grid interval $\delta \lesssim 10^{-5}$), the numerical roundoff errors are not due to the patch schemes.

As in §3.4 for the general linear wave, this section for the viscous shallow water flows assesses the sensitivity of the staggered patch scheme time simulations to numerical roundoff errors, in general for all the possible initial conditions by studying *how sensitive the patch scheme eigenvalues are to the numerical roundoff errors*. Hence we compare the eigenvalues λ_p^{NE1} of the analytically derived Jacobian (§4.2.3) with the eigenvalues λ_p^N of the numerically computed Jacobian (§4.2.5) for a total of 7776 patch scheme cases as Table 4.3.1 lists.

This subsection uses the same definition (3.4.1) in p. 97 of §3.4 for the *microscale and macroscale numerical roundoff errors* of the staggered patch scheme eigenvalues. If the errors $\epsilon_\mu^{\text{Num}}$ and ϵ_M^{Num} in (3.4.1) are negligibly small, that is, if the numerical and analytic macroscale eigenvalues ($\lambda_{pM}^N,$

Table 4.3.1. Section 4.3 studies the sensitivity of the patch scheme eigenvalues to numerical roundoff errors for all the 7776 combinations of the listed parameters.

Patch schemes	Spectral, Square-p2, Square-p4, Square-p6, and Square-p8
Mean height	$h_M \in \{0.1, 0.2, 0.3\}$
Mean velocity	$u_M \in \{0, 0.4, 0.8\}$, $v_M = 0$ (§4.6 shows that the staggered patch schemes are invariant to flow direction)
Reynold number	$Re \in \{10, 50, 250, 1250\}$
Macro-grid intervals	$N \in \{6, 10, 14\}$ for Spectral scheme, $N \in \{6, 10, 14, 18, 22, 26\}$ for polynomial schemes.
Sub-patch micro-grid intervals	$n \in \{6, 10\}$
Patch scale ratio	$r \in \{0.0001, 0.001, 0.01, 0.1\}$

λ_{pM}^{NE1}) of a patch scheme agree very closely, then the patch scheme is not sensitive to the numerical roundoff errors.

The eigenvalues in the numerical roundoff errors (3.4.1a) and (3.4.1b) require separating the microscale and macroscale patch scheme eigenvalues and the association between the analytic and numerical eigenvalues. In the method of wavenumber-wise scale separation in §3.3, using the full-domain microscale eigenvalues $\lambda_{m\delta}^{NE1}$ in place of the eigenvalues $\lambda_{m\delta}^A$ gives the required eigenvalues as the following 3D arrays (analytic eigenvalues only for $N \leq 14$ for Spectral patch scheme)

1. An $N/2 \times N/2 \times 3$ array of macroscale *analytic* patch scheme eigenvalues λ_{pM}^{NE1} .
2. An $N/2 \times N/2 \times 3$ array of macroscale *numerical* patch scheme eigenvalues λ_{pM}^N .
3. An $N/2 \times N/2 \times (n_p^i - 3)$ array of microscale *analytic* patch scheme eigenvalues λ_{pM}^{NE1} .
4. An $N/2 \times N/2 \times (n_p^i - 3)$ array of microscale *numerical* patch scheme eigenvalues λ_{pM}^N .

The microscale and macroscale numerical roundoff errors in (3.4.1) are defined for the eigenvalues of a patch scheme for one specific set of parameters. We define the *peak microscale and macroscale numerical roundoff*

Table 4.3.2. Maximum numerical roundoff errors over all the combinations of the five patch schemes and h_M, u_M, Re and N in Table 4.3.1 for different patch scale ratio r and n . The red colour highlights the largest value in each column (based on full precision).

		Patch scale ratio r			
		0.0001	0.001	0.01	0.1
$\max e_\mu^{\text{Num}}$	$n = 6$	0.02	$9 \cdot 10^{-5}$	10^{-5}	$4 \cdot 10^{-9}$
	$n = 10$	0.07	0.0002	$2 \cdot 10^{-5}$	$7 \cdot 10^{-8}$
$\max e_M^{\text{Num}}$	$n = 6$	0.01	$2 \cdot 10^{-5}$	$2 \cdot 10^{-7}$	$2 \cdot 10^{-9}$
	$n = 10$	0.01	$2 \cdot 10^{-5}$	10^{-8}	$2 \cdot 10^{-10}$

errors as the maximum value of $\max_{h_M, u_M} e_\mu^{\text{Num}}$ and $\max_{h_M, u_M} e_M^{\text{Num}}$, over the nine combinations of the mean flows $h_M \in \{0.1, 0.2, 0.3\}$ and $u_M \in \{0, 0.4, 0.8\}$ as Table 3.4.1 lists.

Nonnegligible numerical roundoff errors arise only for very small sub-patch micro-grid intervals $\delta \lesssim 10^{-5}$ (i.e., small r and large N, n). For each Reynolds number $Re \in \{10, 50, 250, 1250\}$, 3D plots of peak numerical roundoff errors $\max_{h_M, u_M} e_\mu^{\text{Num}}$ and $\max_{h_M, u_M} e_M^{\text{Num}}$ versus (N, r) , are qualitatively same as Figs. 3.4.1 and 3.4.2 for general linear wave. Table 4.3.2 lists the maximum peak numerical roundoff errors for different patch scale ratios r (i.e., peak value for each r -slice in 3D plots similar to Figs. 3.4.1 and 3.4.2). The largest microscale and macroscale numerical roundoff errors among the 7776 cases are 0.07 and 0.01 respectively, both corresponding to the smallest patch scale ratio $r = 0.0001$. The trend in Table 4.3.2 and the omitted 3D plots qualitatively agree with Table 3.4.2 and Figs. 3.4.1 and 3.4.2 of general linear wave in that the combination of large N , large n and small r leads to large numerical roundoff errors. For the viscous shallow water waves, the largest numerical roundoff error for the macroscale eigenvalues is about 100 times larger than that of the general linear wave in Table 3.4.2. The following are some key observations from Table 3.4.2 and 3D plots of peak numerical roundoff errors versus (N, r) (omitted here as qualitatively same as Figs. 3.4.1 and 3.4.2).

1. Both the microscale and macroscale peak numerical roundoff errors $\max_{h_M, u_M} e_\mu^{\text{Num}}$, $\max_{h_M, u_M} e_M^{\text{Num}}$, monotonically increase with increasing number of macro-grid intervals N and decreasing patch scale ratio r . For a staggered patch grid, increasing N , decreasing r , and increasing n , all these lead to decreasing sub-patch micro-grid interval $\delta = 2(2\pi)r/(Nn)$ (for the non-dimensional domain size 2π).

Table 4.3.3. Maximum numerical roundoff errors over all the combinations of the five patch schemes and h_M, u_M, N and r in Table 4.3.1 for different Reynolds number Re and n . The red colour highlights the largest value in each column.

		Patch scale ratio r			
		0.0001	0.001	0.01	0.1
$\max \epsilon_\mu^{\text{Num}}$	$Re = 10$	0.07	0.0002	$2 \cdot 10^{-5}$	$7 \cdot 10^{-8}$
	$Re = 50$	0.01	$8 \cdot 10^{-5}$	$9 \cdot 10^{-6}$	$4 \cdot 10^{-9}$
	$Re = 250$	0.006	$3 \cdot 10^{-5}$	10^{-7}	$3 \cdot 10^{-10}$
	$Re = 1250$	0.001	$5 \cdot 10^{-6}$	$2 \cdot 10^{-7}$	$4 \cdot 10^{-10}$
$\max \epsilon_M^{\text{Num}}$	$Re = 10$	0.01	$2 \cdot 10^{-5}$	$2 \cdot 10^{-7}$	$2 \cdot 10^{-9}$
	$Re = 50$	0.0003	10^{-6}	$2 \cdot 10^{-8}$	$2 \cdot 10^{-10}$
	$Re = 250$	$9 \cdot 10^{-6}$	$5 \cdot 10^{-8}$	10^{-9}	$3 \cdot 10^{-11}$
	$Re = 1250$	$9 \cdot 10^{-6}$	$5 \cdot 10^{-8}$	10^{-9}	$3 \cdot 10^{-11}$

For example, for $r = 0.001, N = 26, n = 10$, sub-patch micro-grid interval $\delta \approx 5 \cdot 10^{-5}$. Thus, as for the general linear wave, also for the viscous shallow water flows, the *nonnegligible numerical roundoff errors arise only for very small sub-patch micro-grid intervals $\delta \lesssim 10^{-5}$ (i.e., small r and large N, n).*

- In general, except $\epsilon_\mu^{\text{Num}}$ for $N \gtrsim 22, r = 0.0001$, the numerical roundoff errors of all the five patch schemes are roughly the same, similar to Figs. 3.4.1 and 3.4.2 for general linear wave. That is, the numerical roundoff errors do not have a strong dependence on the specific patch scheme. If the numerical roundoff errors were due to the patch scheme, then the numerical roundoff errors must also depend on the specific patch scheme, showing a clear trend. The lack of such trends, among the patch schemes with different amounts of numerical computations, *indicates that the numerical roundoff errors are not due to the patch schemes.*

The numerical roundoff errors in the patch scheme eigenvalues decrease with increasing Reynolds number. Table 4.3.3 lists the maximum numerical roundoff errors ($\max \epsilon_\mu^{\text{Num}}, \max \epsilon_M^{\text{Num}}$) for microscale and macroscale eigenvalues over all the combinations of the five patch schemes and h_M, u_M, Re, N, n and r that are listed in Table 4.3.1. In the columns of Table 4.3.3, the decreasing numerical roundoff errors from top to bottom shows that the numerical roundoff errors decrease with increasing Reynolds number Re .

The numerical roundoff errors decrease roughly as $\epsilon_{\mu}^{\text{Num}}, \epsilon_{\mu}^{\text{Num}} \propto 1/\text{Re}$. In the rows of [Table 4.3.3](#), the decreasing numerical roundoff errors from left to right show that the numerical roundoff errors decrease with increasing patch scale ratio r . The numerical roundoff errors decrease roughly as $\epsilon_{\mu}^{\text{Num}}, \epsilon_{\mu}^{\text{Num}} \propto 1/r^2$. That is, the numerical roundoff errors decrease more rapidly with increasing patch scale ratio than with increasing Reynolds number. As [Table 4.3.3](#) lists the maximum numerical roundoff errors for all the combinations of the parameters in [Table 4.3.3](#), even for large $N \sim 26$ and $n = 10$, *using appropriately large patch scale ratio removes the nonnegligible numerical roundoff errors for small Reynolds number $\text{Re} \lesssim 10$.*

The *patch scheme macroscale eigenvalues, which are of primary interest are less sensitive to numerical roundoff errors than the corresponding microscale eigenvalues.* Based on [Table 4.3.2](#), a preceding paragraph states that the peak macroscale numerical roundoff errors $\max_{h_M, u_M} \epsilon_M^{\text{Num}}$ are about the same as the peak microscale numerical roundoff errors $\max_{h_M, u_M} \epsilon_{\mu}^{\text{Num}}$ (i.e., within the same order of magnitude). [Table 4.3.3](#) shows that the maximum numerical roundoff errors (over h_M, u_M, N) of microscale and macroscale eigenvalues are about the same only for small Reynolds number $\text{Re} \lesssim 10$. Even for small Reynolds numbers, the numerical roundoff errors for macroscale eigenvalues are less than that of the microscale eigenvalues. [Table 4.3.3](#) also shows that for large Reynolds number $\text{Re} \gtrsim 250$, the numerical roundoff errors for macroscale eigenvalues are ten to one hundred times smaller than that of the microscale eigenvalues. Thus, the patch scheme macroscale eigenvalues for viscous shallow water flows, despite being more sensitive compared to the general linear wave, are less sensitive to numerical roundoff errors than the corresponding microscale eigenvalues.

For shallow and/or slow viscous shallow water flows, patch scheme eigenvalues are less sensitive to numerical roundoff errors, than deep or fast flows. [Tables 4.3.4](#) and [4.3.5](#) lists the maximum numerical roundoff errors ($\max \epsilon_{\mu}^{\text{Num}}, \max \epsilon_M^{\text{Num}}$) for microscale and macroscale eigenvalues respectively over all the combinations of the five patch schemes and $h_M, u_M, \text{Re}, N, n$ and r that are listed in [Table 4.3.1](#). [Tables 4.3.4](#) and [4.3.5](#) show that the maximum numerical roundoff errors for both microscale and macroscale eigenvalues are the smallest for smallest mean height h_M , for any Reynolds number Re and mean velocity u_M . Due to the dominance of nonlinearity, shallow water flows are more challenging to simulate accurately. *Being least sensitive to numerical roundoff errors for shallow water flows, the staggered patch schemes enable accurate multiscale simulation of the viscous shallow water flows.* [Tables 4.3.4](#) and [4.3.5](#) show that for the smallest mean velocity $u_M \sim 0$, the maximum numerical roundoff errors are the smallest for all large Reynolds number $\text{Re} \in \{10, 50, 250, 1250\}$ (except for $h_M = 0.1, u_M = 0$

Table 4.3.4. Maximum numerical roundoff errors $\max e_{\mu}^{\text{Num}}$ in microscale eigenvalues over the five patch schemes and all the combinations of N , n , r in Table 3.4.1, for different mean flow (h_M, u_M) and Reynolds number Re . Red colour highlights the largest $\max e_{\mu}^{\text{Num}}$ in each column for each mean height h_M (based on full precision)

	Reynolds number Re			
	10	50	250	1250
$h_M = 0.1, u_M = 0$	0.0007	0.0001	$2 \cdot 10^{-5}$	$2 \cdot 10^{-5}$
$h_M = 0.1, u_M = 0.4$	0.003	0.0005	0.0003	$4 \cdot 10^{-5}$
$h_M = 0.1, u_M = 0.8$	0.01	0.003	0.0006	0.0001
$h_M = 0.2, u_M = 0$	0.01	0.0005	10^{-5}	$2 \cdot 10^{-5}$
$h_M = 0.2, u_M = 0.4$	0.02	0.006	0.0006	0.0001
$h_M = 0.2, u_M = 0.8$	0.02	0.005	0.002	0.0005
$h_M = 0.3, u_M = 0$	0.04	0.0008	0.0002	0.0002
$h_M = 0.3, u_M = 0.4$	0.07	0.01	0.001	0.0009
$h_M = 0.3, u_M = 0.8$	0.05	0.009	0.006	0.001

Table 4.3.5. Maximum numerical roundoff errors $\max e_M^{\text{Num}}$ in macroscale eigenvalues over the five patch schemes and all the combinations of N , n , r in Table 3.4.1, for different mean flow (h_M, u_M) and Reynolds number Re . Red colour highlights the largest $\max e_M^{\text{Num}}$ in each column for each mean height h_M (based on full precision)

	Reynolds number Re			
	10	50	250	1250
$h_M = 0.1, u_M = 0$	0.0003	$4 \cdot 10^{-6}$	$2 \cdot 10^{-7}$	10^{-8}
$h_M = 0.1, u_M = 0.4$	0.0001	$3 \cdot 10^{-6}$	$3 \cdot 10^{-7}$	$5 \cdot 10^{-8}$
$h_M = 0.1, u_M = 0.8$	0.0002	$2 \cdot 10^{-5}$	$5 \cdot 10^{-6}$	$9 \cdot 10^{-7}$
$h_M = 0.2, u_M = 0$	0.001	$4 \cdot 10^{-5}$	10^{-6}	$5 \cdot 10^{-8}$
$h_M = 0.2, u_M = 0.4$	0.0007	$5 \cdot 10^{-5}$	10^{-5}	10^{-6}
$h_M = 0.2, u_M = 0.8$	0.002	0.0001	$3 \cdot 10^{-5}$	$6 \cdot 10^{-6}$
$h_M = 0.3, u_M = 0$	0.01	$7 \cdot 10^{-5}$	$3 \cdot 10^{-6}$	10^{-7}
$h_M = 0.3, u_M = 0.4$	0.01	$7 \cdot 10^{-5}$	$9 \cdot 10^{-6}$	$2 \cdot 10^{-6}$
$h_M = 0.3, u_M = 0.8$	0.009	0.0003	$5 \cdot 10^{-5}$	$9 \cdot 10^{-6}$

in Table 4.3.5). Thus, for shallow and/or slow viscous shallow water flows (mean height $h_M \lesssim 0.1$ and/or mean velocity $u_M \lesssim 0.4$), patch schemes are less sensitive to numerical roundoff errors than the deep or fast waves.

Similar to p. 100 of §3.4 for the general linear wave, the dependence of the numerical roundoff errors on the physical parameters (Reynolds number Re and mean flow h_M, u_M) and the lack of dependence of the specific patch schemes show that *the numerical roundoff errors are due to the underlying microscale model, not due to the staggered patch scheme*. Page 100 of §3.4 for general linear wave shows the strong dependence of numerical roundoff errors in the patch scheme eigenvalues on the viscous diffusion via the coefficient c_V . The preceding paragraph in p. 211 using Tables 4.3.3, 4.3.4 and 4.3.5 shows that the numerical roundoff errors strongly depend on the Reynolds number especially for $Re \lesssim 10$ where viscous diffusion is large. That is, similar to the general linear wave, *the numerical roundoff errors for the viscous shallow water strongly depends on the viscous diffusion*. Scaling arguments on the viscous shallow water flows confirm the inherent sensitivity of the microscale model to numerical roundoff errors. For example, the largest roundoff error is in the second derivative term containing $h_M^2/(Re \delta^2)$. Thus, for small grid interval $\delta \lesssim 10^{-5}$, large mean height $h_M \gtrsim 0.2$, and small Reynolds number $Re \lesssim 10$, the nonnegligible numerical roundoff errors in both microscale and macroscale patch scheme eigenvalues are due to the inherent sensitivity of the microscale model to numerical roundoff errors. As in the discussion for the general linear wave in §3.4 of §3.4, for viscous shallow water flows too a part of the numerical roundoff errors are due to numerical computation of near-zero repeated eigenvalues. The numerical roundoff errors in the numerical computation of near-zero repeated eigenvalues are amplified by the microscale model's sensitivity to numerical roundoff errors.

As in §3.4 for the general linear wave, the numerical roundoff errors in the patch scheme eigenvalues have the following main sources.

1. The numerical roundoff errors due to the numerical computations in a patch scheme due to the patch coupling.
2. The numerical roundoff errors due to the numerical computations of the underlying microscale model (e.g., the finite difference computations).
3. The numerical roundoff errors in numerically computing the eigenvalues of the patch scheme numerical Jacobian.

We take the numerical roundoff errors in numerically computing the Jacobian (§3.2.5) of a patch scheme, to be small compared to the much higher

number of numerical computations in the patch coupling, sub-patch micro-scale model and the eigenvalue computation. The preceding paragraphs establish the contribution of the following extreme parameters to the non-negligible numerical roundoff errors (e.g., $\epsilon_{\mu}^{\text{Num}}, \epsilon_M^{\text{Num}} > 10^{-5}$) in the patch scheme eigenvalues (in the order of roughly decreasing dominance):

1. very small sub-patch micro-grid intervals $\delta \lesssim 10^{-5}$, due to combination of small patch scale ratio $r \lesssim 0.0001$, many macroscale intervals $N \gtrsim 26$, and many sub-patch micro-grid intervals $n \gtrsim 10$;
2. small Reynolds number $\text{Re} \lesssim 10$;
3. large mean height $h_M \gtrsim 0.2$.

The following listing summarises the study of numerical sensitivity in this subsection.

1. For patch scale ratios $r \gtrsim 0.001$ the patch scheme eigenvalue are not sensitive to numerical roundoff errors (columns 2-4 in [Table 4.3.3](#)). Hence for large r the staggered patch schemes are not sensitive to numerical roundoff errors.
2. For small patch scale ratios $r \lesssim 0.001$ the patch scheme eigenvalues are sensitive to numerical roundoff errors (column 1 in [Table 4.3.3](#)). But this sensitivity to numerical roundoff errors for small sub-patch micro-grid interval $\delta \lesssim 10^{-5}$ is due to both the inherent sensitivity of the microscale model (due to viscous diffusion $\text{Re} \lesssim 10$) and the sensitivity of eigenvalue computation of near-zero repeated eigenvalues. Hence, even for small patch scale ratios, *the computations of staggered patch schemes are not sensitive to numerical roundoff errors.*

4.4 Staggered patch schemes are not artificially unstable for appropriate patch grids

In contrast to the general linear wave, the viscous shallow water flows have *physical instability*, that is, the stability of the full-domain microscale model depends upon the physical parameters (Reynolds number Re , mean flow h_M, u_M, v_M). Such physical instability is evident from the positive real part eigenvalues of the full-domain microscale model in [Fig. 4.2.6](#) (clusters 1, 2) of [§4.2.6](#). Thus, for viscous shallow water flows, a positive real part of the patch scheme eigenvalue does not necessarily mean that the patch scheme computations are erroneous or unphysical. That is, a good patch

scheme must reflect the stability/instability of the underlying microscale model depending upon the physical parameters (Re, h_M, u_M, v_M) , but *without any additional/artificial instability*. Hence, we define *artificial instability* as a characteristic of a patch scheme to be *more unstable* than the corresponding full-domain microscale model. That is, *a patch scheme is artificially unstable when the maximum real part of the patch scheme eigenvalues is both positive and larger than the maximum real part of the corresponding full-domain microscale model*. To quantitatively study the patch scheme artificial instability, we define the *condition of no artificial instability* as

$$\max \Re(\lambda_p^N) \leq \max \Re(\lambda_{m\delta}^{NE1}), \quad (4.4.1)$$

within a tolerance of 10^{-5} .

As p. 197 of §4.2.6 states, in contrast to the eigenvalues of the general linear wave in §3.2.6, due to the nonlinearity, the *eigenvalues of the viscous shallow water flows depend on the mean height h_M and the mean velocity h_M, v_M* . That is, the eigenvalues and hence the stability of the viscous shallow water flows depend on the linearisation point (h_M, u_M, v_M) . So, §4.4.1 shows that for an appropriate patch grid the Spectral patch scheme is not artificially unstable, for a wide range of physical parameters (Reynolds number Re , mean height h_M , and horizontal mean velocity (u_m, v_M)) for a representative set of patch grid parameters (number of macro-grid intervals N , number of sub-patch micro-grid intervals n , patch scale ratio r).

Page 217 of §4.4.1 establishes that the patch scheme artificial instability arises only for the sub-patch microscale modes. That is, the patch scheme macroscale modes which are of primary interest, do not have artificial instability. Section 4.4.2 more specifically shows that artificial instabilities of the patch schemes are due to sub-patch microscale modes with microscale structure modulated over the macroscale of large wavenumbers.

Section 4.4.3 shows that the five staggered patch schemes are not artificially unstable, for a wide range of patch grid parameters (macro-grid intervals N , sub-patch micro-grid intervals n , and patch scale ratio r), for a representative set of physical parameters (Reynolds number Re , mean height h_M , and horizontal mean velocity (u_m, v_M) indicated by nine black squares in Figs. 4.4.5 to 4.4.7 of §4.4.1). Section 4.4.3 also gives a heuristic general rule to get rid of artificial instability, when a patch scheme has artificial instability for some combinations of system and patch grid parameters.

4.4.1 Spectral staggered patch scheme is not artificially unstable for a range of physical parameters

This subsection shows that for an appropriate patch grid the Spectral staggered patch scheme is not artificially unstable for a wide range of physical parameters (Reynolds number Re , mean height h_M , horizontal mean velocity u_M) for a representative set of patch grid parameters (number of macro-grid intervals $N \in \{10, 14\}$, number of sub-patch micro-grid intervals $n \in \{6, 10\}$, patch scale ratio ($r \in \{0.0001, 0.001\}$). That is, this subsection shows that for a wide range of physical parameters and a representative set of patch grid parameters, the condition of no artificial instability (4.4.1) holds (within a tolerance of 10^{-5}).

This subsection studies the presence or absence of artificial instability via the Spectral patch scheme eigenvalues for a total of 21 504 cases consisting of all the combinations of the physical parameters

1. mean height $h_M \in \{0.025, 0.05, \dots, 0.035, 0.4\}$,
2. mean velocity $u_M \in \{0, 0.05, \dots, 0.95, 1\}$, $v_M = 0$ (§4.6 shows that the staggered patch schemes are invariant to flow direction),
3. Reynold number $Re \in \{10, 50, 250, 1250\}$,

and the patch grid parameters

- number of macroscale intervals $N \in \{10, 14\}$,
- number of sub-patch micro-grid intervals $n \in \{6, 10\}$,
- patch scale ratio $r \in \{0.0001, 0.001, 0.01, 0.1\}$.

For some combinations of the physical parameters (Re , h_M , (u_m , v_M)) and the patch grid parameters (N , n , r), some patch scheme modes are *artificially unstable*. That is, some patch scheme modes are unstable (positive real part eigenvalues) while the corresponding modes of the full-domain micro-scale model are stable (no positive real part eigenvalues). For example, in Figs. 4.4.1 and 4.4.2, the clusters 1, 2 and the clusters 1–4 (blue and magenta circles on the right) respectively, contain the eigenvalues of artificial instability as for these clusters $[\Re(\lambda_p^{NE1}) = \Re(\lambda_p^N)] > [\max \Re(\lambda_{m\delta}^{NE1}) = 0]$; that is, the condition of no artificial instability (4.4.1) does not hold. *Decreasing the patch scale ratio r removes such artificial instability of the staggered patch schemes*, as evident from the nonpositive real part patch scheme eigenvalues in Fig. 4.2.6 of §4.2.6 for $r = 0.01$, compared to those in Fig. 4.4.2 for $r = 0.1$, keeping all other parameters the same.

Figure 4.4.1. Spectral patch scheme ($N = 10, n = 6, r = 0.1$) has artificial instability for viscous shallow water flows for $(h_M, u_M, v_M) = (0.2, 0.3, 0)$, in contrast to Fig. 4.2.5 for same parameters except $r = 0.01$. Maximum real parts $\max \Re(\lambda_{m\delta}^{NE1}) = 0, \max \Re(\lambda_p^{NE1}) = 0.062$.

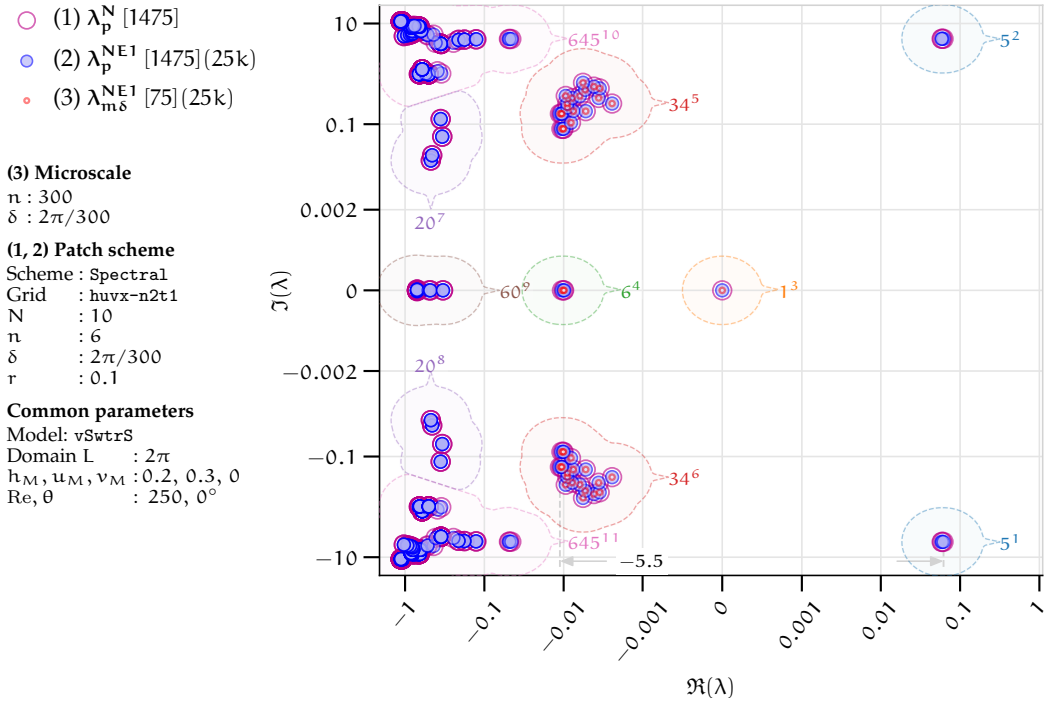
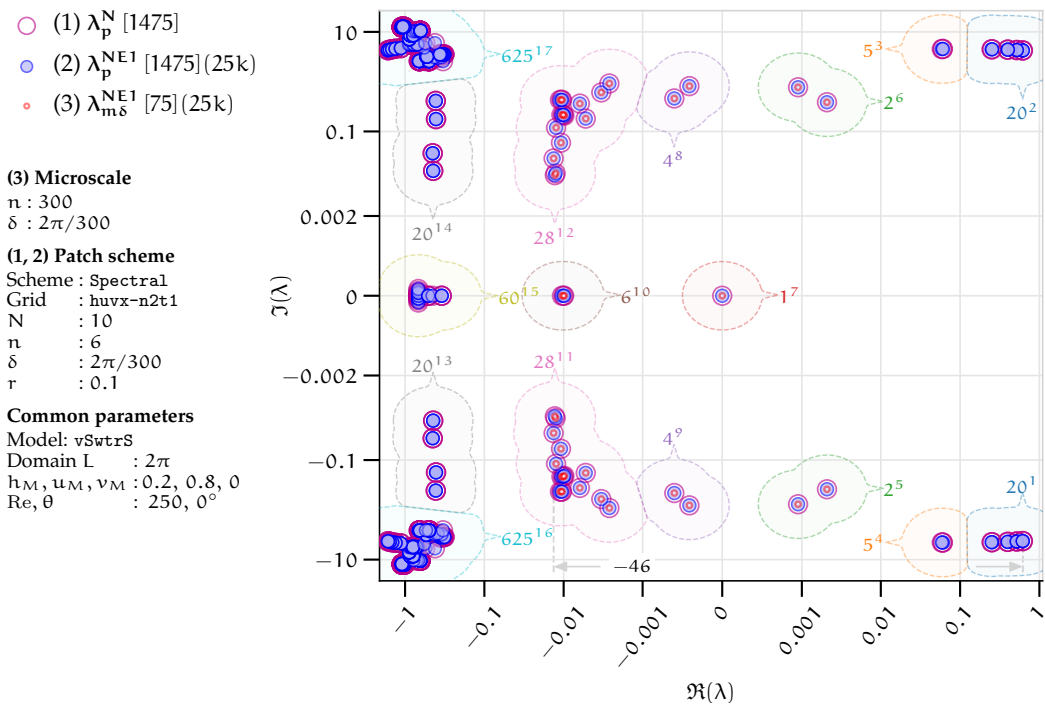


Figure 4.4.2. Spectral patch scheme ($N = 10, n = 6, r = 0.1$) has artificial instability for viscous shallow water flows for $(h_M, u_M, v_M) = (0.2, 0.8, 0)$, in contrast to Fig. 4.2.6 for same parameters except $r = 0.01$. Maximum real parts $\max \Re(\lambda_{m\delta}^{NE1}) = 0.0021, \max \Re(\lambda_p^{NE1}) = 0.62$ (point d in Fig. 4.4.7c).



The artificial instability of the patch schemes arises only for the sub-patch microscale modes. That is, the patch scheme macroscale modes which are of primary interest, do not have artificial instability. For example, consider the patch scheme eigenvalues in Figs. 4.4.1 and 4.4.2. In Figs. 4.4.1 and 4.4.2, the clusters 1, 2 and the clusters 1–4 respectively, contain the eigenvalues of artificial instability. That is, for these clusters, the condition of no artificial instability (4.4.1) does not hold as $[\Re(\lambda_p^{NE1}) = \Re(\lambda_p^N)] > [\max \Re(\lambda_{m\delta}^{NE1}) = 0]$. In Figs. 4.4.1 and 4.4.2, each of the patch scheme eigenvalues λ_p^{NE1} in clusters 3–6 and clusters 5–12 respectively, agree with the corresponding eigenvalues $\lambda_{m\delta}^{NE1}$ of the full-domain model that are evaluated for all the $N^2/4 = 25$ macroscale wavenumbers (k_x, k_y) where $k_x, k_y \in \{0, \pm 1, \pm 2\}$ resolved by a patch grid. That is, in Figs. 4.4.1 and 4.4.2, the clusters 3–6 and clusters 5–12 respectively, contain the eigenvalues of all the $n_p^I = 75$ macroscale modes ($n_p^I = 3N^2/4$ as in p. 193 of §4.2.6). Figure 4.4.1 shows that the macroscale modes are not artificially unstable as for the eigenvalues in the clusters 3–6, $\max \Re(\lambda_p^{NE1}) = \max \Re(\lambda_{m\delta}^{NE1}) = 0$. Figure 4.4.2 shows that the macroscale modes are not artificially unstable as for the eigenvalues in the clusters 5–12, $\max \Re(\lambda_p^{NE1}) = \max \Re(\lambda_{m\delta}^{NE1}) = 0.0021$. The large imaginary parts of the artificially unstable modes, in clusters 1, 2 and clusters 1–4 in Figs. 4.4.1 and 4.4.2 respectively, compared to the imaginary parts of the corresponding macroscale eigenvalues in the clusters 3–6 and clusters 5–12 respectively, also indicate that artificially unstable modes must be microscale modes. The eigenvector plots in Figs. 4.4.3 and 4.4.4 show the artificially unstable sub-patch microscale modes with microscale structure modulated over the macroscale of wavenumbers $(k_x, k_y) = (1, 0), (2, 0)$ respectively, for the Spectral staggered patch scheme. In the eigenvector plot of Figs. 4.4.3 and 4.4.4, the grey curves connecting the patch centre values (patch mean) indicate the unmodulated macroscale wave. The eigenvector plots in Figs. 4.4.3 and 4.4.4 corresponding to the eigenvalues of the artificially unstable modes in cluster 2 of Fig. 4.4.2 definitively confirm that *the patch scheme artificially unstable modes are due to sub-patch microscale modes with microscale structure modulated over the macroscale.* More specifically, §4.4.2 shows that artificial instabilities of the patch schemes are due to sub-patch microscale modes with microscale structure modulated over the macroscale of large wavenumbers.

Figure 4.4.3. Eigenvector for eigenvalue $\lambda_p^{NE1} = \lambda_p^N = 0.52 - 4.3237i$ (cluster 1 in Fig. 4.4.2) corresponding to artificial instability of Spectral staggered patch scheme ($N = 10, n = 6, r = 0.1$) with $(k_x, k_y) = (1, 0)$ for viscous shallow water flows with $Re = 250, (h_M, u_M, v_M) = (0.2, 0.8, 0)$.

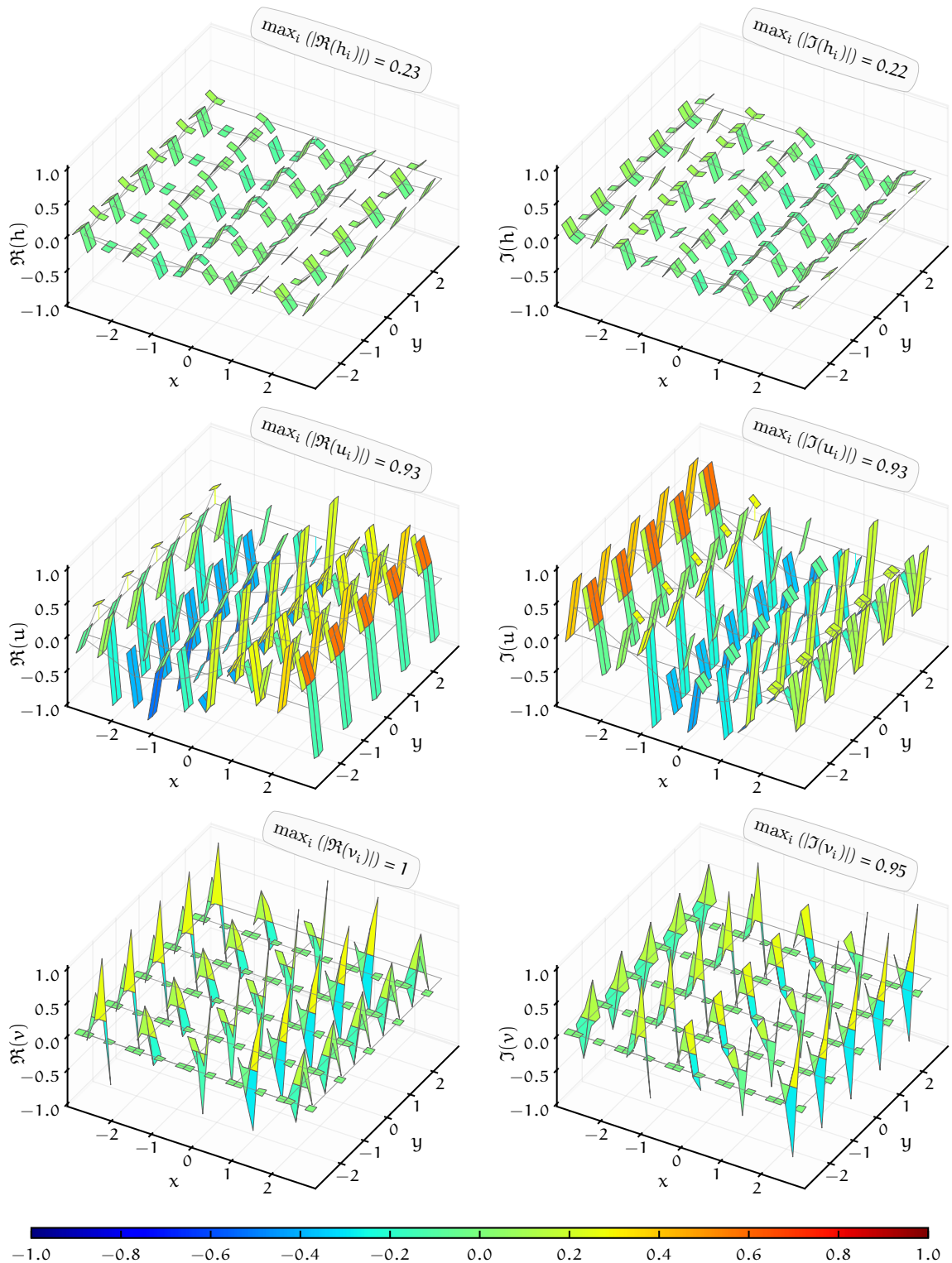


Figure 4.4.4. Eigenvector for eigenvalue $\lambda_p^{NE1} = \lambda_p^N = 0.62 - 4.2439i$ (cluster 1 in Fig. 4.4.2) corresponding to maximum artificial instability of Spectral patch scheme ($N = 10, n = 6, r = 0.1$) with $(k_x, k_y) = (2, 0)$ for viscous shallow water flows with $Re = 250, (h_M, u_M, v_M) = (0.2, 0.8, 0)$.

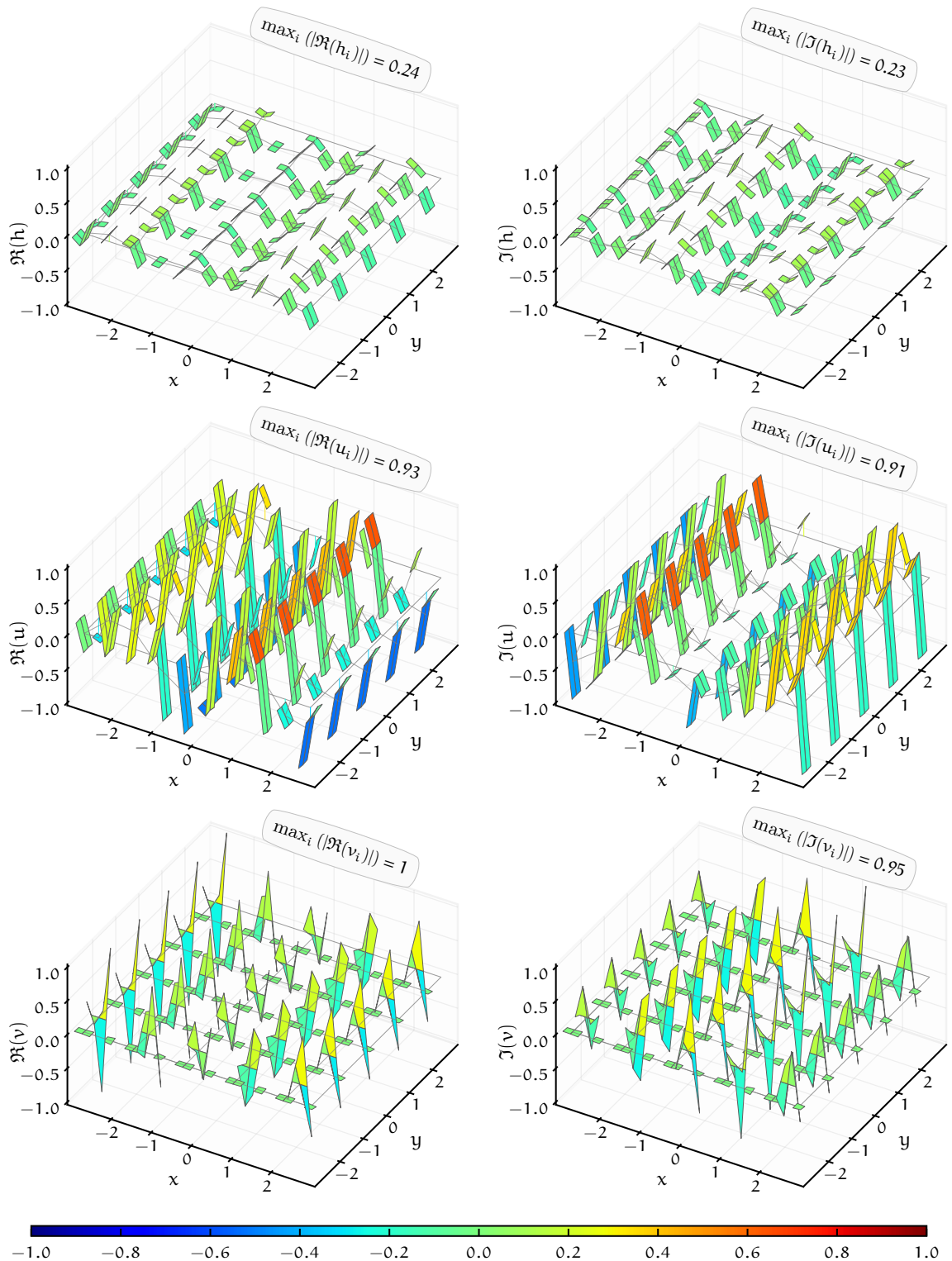
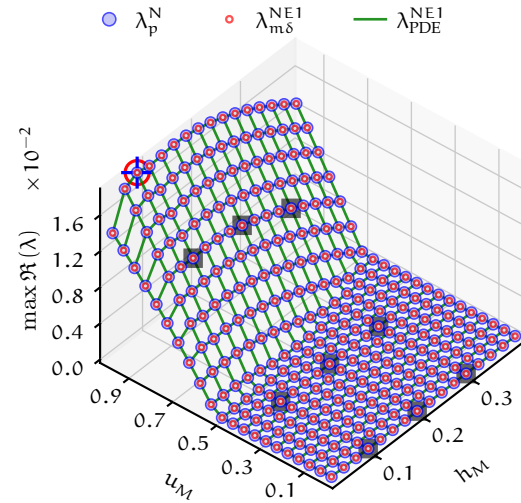
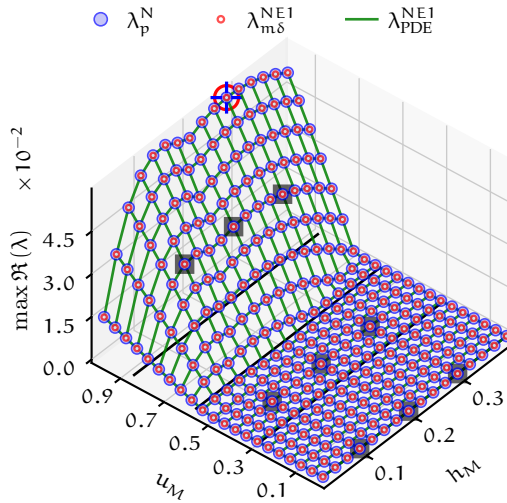


Figure 4.4.5. Maximum real part of the eigenvalues for, λ_p^N of Spectral patch scheme ($N = 10$, $n = 6$, $r = 0.001$), $\lambda_{m\delta}^{NE1}$ of full-domain microscale model, and λ_{PDE}^{NE1} of the viscous shallow water PDE, about different mean flow (h_M, u_M) with $v_M = 0$ and bed inclination $\theta = 0^\circ$. Increasing Re decreases physical instability. *No artificial instability* for wide range of mean flow $\{(h_M, u_M) : h_M \in [0.025, 0.4], u_M \in [0, 1]\}$ and $Re \in \{10, 50, 250, 1250\}$.

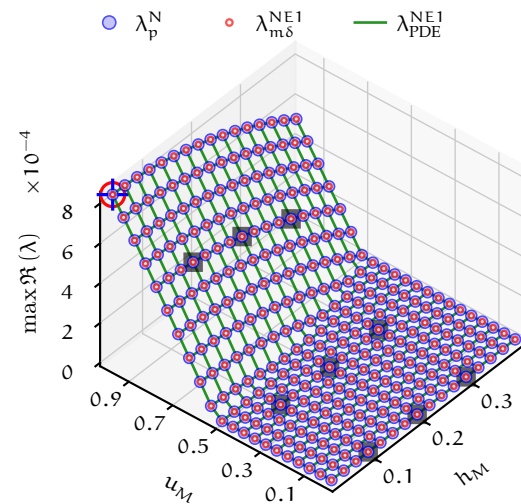
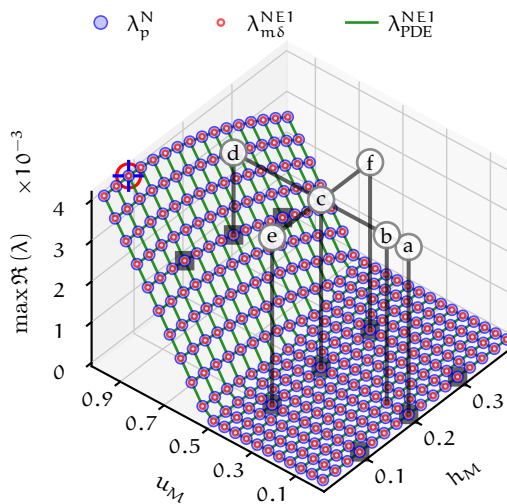
(a) Reynolds number $Re = 10$. *No artificial instability*, as $\max \Re(\lambda_p^N) = 0$ or $\max \Re(\lambda_p^N) = \max \Re(\lambda_{m\delta}^{NE1}) > 0$. Peak values (blue plus and red circle) are $\max \Re(\lambda_p^N) = 0.059 = \max \Re(\lambda_{m\delta}^{NE1})$.

(b) Reynolds number $Re = 50$. *No artificial instability*. Peak values are $\max \Re(\lambda_p^N) = 0.019 = \max \Re(\lambda_{m\delta}^{NE1})$.



(c) Reynolds number $Re = 250$. *No artificial instability*. Peak values are $\max \Re(\lambda_p^N) = 0.0041 = \max \Re(\lambda_{m\delta}^{NE1})$. Points a–d $h_M = 0.2$, $u_M = 0, 0.1, 0.4, 0.8$. Points e–f $h_M = 0.1, 0.2, 0.3$, $u_M = 0.1$.

(d) Reynolds number $Re = 1250$. *No artificial instability*. Peak values are $\max \Re(\lambda_p^N) = 0.00084 = \max \Re(\lambda_{m\delta}^{NE1})$.



Each subplot in Figs. 4.4.5 to 4.4.7 plot the maximum real part of the following eigenvalues for viscous shallow water flows, linearising about 336 cases of mean flow (h_M, u_M, v_M) , for 16 mean heights $h_M \in \{0.025, 0.05, \dots, 0.035, 0.4\}$, and 21 mean velocities $u_M \in \{0, 0.05, \dots, 0.95, 1\}$ with $v_M = 0$ and bed inclination $\theta = 0^\circ$.

1. Eigenvalues λ_p^N of the Spectral patch scheme.
2. Eigenvalues $\lambda_{m\delta}^{NE1}$ of full-domain microscale model with same value of microscale grid interval $\delta_{m\delta}$ as the sub-patch micro-grid interval δ . That is, for the non-dimensional domain size 2π , the full-domain micro-grid interval $\delta_{m\delta} \equiv 2\pi/n_{m\delta} = \delta \equiv l/n \equiv 2(2\pi)r/(Nn)$ as $r = l/(2\Delta)$ and $\Delta = 2\pi/N$, where $n_{m\delta}$ is the number of full-domain microscale grid intervals and n is the number of sub-patch micro-grid intervals. When the context is clear we drop the subscript $m\delta$ in $n_{m\delta}$ and $\delta_{m\delta}$ for the case of full-domain microscale model.
3. Eigenvalues λ_{PDE}^{NE1} of the viscous shallow water PDE.

The analytic eigenvalues $\lambda_{m\delta}^{NE1}$ and λ_{PDE}^{NE1} are numerically evaluated for all the $N^2/4$ macroscale wavenumbers (k_x, k_y) resolved on a corresponding finite staggered patch grid with $N \times N$ macro-grid intervals. The following listing explains the various visual elements in Figs. 4.4.5 to 4.4.7.

- For each of the subplot, the blue plus shows the maximum value of $\max \Re(\lambda_p^N)$ and the red circle shows the maximum value of $\max \Re(\lambda_{m\delta}^{NE1})$.
- The nine black squares show the chosen subset of the mean flow $\{(h_M, u_M) : h_M \in \{0.1, 0.2, 0.3\}, u_M \in \{0.0, 0.4, 0.8\}\}$ for further study of stability (§4.4.1) and consistency (§4.5).
- The annotated points a–d in the subplots for $Re = 250$, correspond to increasing mean velocity $u_M = 0, 0.1, 0.4, 0.8$ keeping $h_M = 0.2$, $v_M = 0$. For patch scale ratio $r = 0.01$, the complex plane eigenvalue plots in Figs. 4.2.3 to 4.2.6 of §4.2.6 correspond to these four points a–d. The annotated points e, c, f in the subplots for $Re = 250$, correspond to increasing mean height $h_M = 0.1, 0.2, 0.3$ keeping $u_M = 0.1$, $v_M = 0$. For $r = 0.01$, the complex plane eigenvalue plots in Figs. 4.2.7, 4.2.4 and 4.2.8 of §4.2.6 correspond to these three points e, c, f.
- The four black lines at the bottom of the subplots for $Re = 10$, are the set of equilibrium points (h_M, u_M) of the viscous shallow water flows. For Reynolds number $Re = 10$ with $v = v_M = 0$ and the bed

inclination angles $\theta = 0, 5, 10, 15$, the equilibrium solution (4.1.12) gives the equilibrium velocity $u = u_M = \text{Re } g_x/3 \equiv \text{Re } \sin(\theta)/3 = 0, 0.29, 0.58, 0.86$ respectively. The four lines in the subplots for $\text{Re} = 10$ correspond to these four equilibrium velocities. In the subplots for Reynolds number $\text{Re} \in \{50, 250, 1250\}$ there are no black lines of equilibrium points (h_M, u_M) , because equilibrium velocities are larger than one and outside the plot limits $u_M \in [0, 1]$.

For small patch scale ratio $r \lesssim 0.001$, the staggered patch schemes do not have any artificial instability over a wide range of mean flow and Reynolds numbers. Figure 4.4.5 plot the maximum real part of the eigenvalues versus (h_M, u_M) , for the Spectral staggered patch scheme with a small patch scale ratio $r = 0.001$. The maximum real part of the eigenvalues in Fig. 4.4.5 corresponds to a staggered patch grid with 10×10 macro-grid intervals ($N = 10$) and each patch containing 6×6 sub-patch micro-grid intervals ($n = 6$). Figure 4.4.5 shows that either $\max \Re(\lambda_p^N) = 0$ or $\max \Re(\lambda_p^N) = \max \Re(\lambda_{m\delta}^{NE1}) > 0$ (within a tolerance of 10^{-5}), over the chosen wide range of mean flows ($h_M \in [0.025, 0.4]$, $u_M \in [0, 1]$) and Reynolds numbers ($\text{Re} \in \{10, 50, 250, 1250\}$). That is, the condition of no artificial instability (4.4.1) holds. All the plots of the maximum real parts of the Spectral patch scheme eigenvalues versus (h_M, u_M) are identical to Figure 4.4.5 number of macro-grid intervals $N \in \{10, 14\}$, number of sub-patch micro-grid intervals $n \in \{6, 10\}$, patch scale ratio ($r \in \{0.0001, 0.001\}$). Thus, for small patch scale ratio $r \lesssim 0.001$, the Spectral staggered patch scheme does not have any artificial instability over a wide range of mean flows and Reynolds numbers. As §4.4.3 shows, this characteristic of no artificial instability for small patch scale ratio holds also for the polynomial patch schemes.

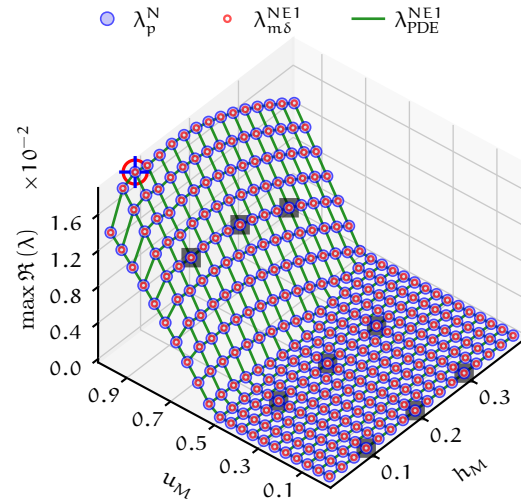
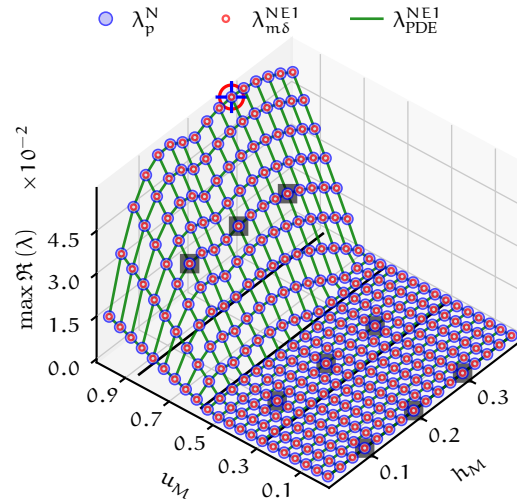
To quantify the physical and artificial instability, we define the following two terms over 336 cases of mean flow (h_M, u_M, v_M) , for 16 mean heights $h_M \in \{0.025, 0.05, \dots, 0.035, 0.4\}$, and 21 horizontal mean velocities $u_M \in \{0, 0.05, \dots, 0.95, 1\}$.

1. The *peak physical instability* is $\max_{h_M, u_M} [\max \Re(\lambda_{m\delta}^{NE1})]$, that is, the peak value of $\max \Re(\lambda_{m\delta}^{NE1})$ (red circle) for each of the subplots.
2. The *peak artificial instability* is $\max_{h_M, u_M} [\max \Re(\lambda_p^N) - \max \Re(\lambda_{m\delta}^{NE1})]$, that is, the difference between the peak value of $\max \Re(\lambda_p^N)$ (blue plus) and the peak value of $\max \Re(\lambda_{m\delta}^{NE1})$ (red circle) for each of the subplots.

Figure 4.4.6. Maximum real part of the eigenvalues for, λ_p^N of Spectral patch scheme ($N = 10, n = 6, r = 0.01$), $\lambda_{m\delta}^{NE1}$ and λ_{PDE}^{NE1} of the viscous shallow water flows, about different mean flow (h_M, u_M) with $v_M = 0$ and $\theta = 0^\circ$. No artificial instability for Reynolds number $Re \in \{10, 50\}$. Increasing Re increases the (h_M, u_M) -region of artificial instability for $Re \in \{250, 1250\}$.

(a) Reynolds number $Re = 10$. Identical to Fig. 4.4.5a of $r = 0.001$ and Spectral patch scheme has no artificial instability. Peak values (blue plus and red circle) are $\max \Re(\lambda_p^N) = 0.059 = \max \Re(\lambda_{m\delta}^{NE1})$.

(b) Reynolds number $Re = 50$. Identical to Fig. 4.4.5b of $r = 0.001$ and Spectral patch scheme has no artificial instability. Peak values (blue plus and red circle) are $\max \Re(\lambda_p^N) = 0.019 = \max \Re(\lambda_{m\delta}^{NE1})$.



(c) $Re = 250$. Artificial instability (i.e., $\max \Re(\lambda_p^N) > \max \Re(\lambda_{m\delta}^{NE1}) \geq 0$) for very shallow mean flow $h_M \lesssim 0.05$ and large $u_M \gtrsim 0.3$; $\max \Re(\lambda_p^N) = 0.52$, $\max \Re(\lambda_{m\delta}^{NE1}) = 0.0041$.

(d) $Re = 1250$. Artificial instability (i.e., $\max \Re(\lambda_p^N) > \max \Re(\lambda_{m\delta}^{NE1}) \geq 0$) for moderately shallow mean flow $h_M \lesssim 0.25$ and large $u_M \gtrsim 0.3$; $\max \Re(\lambda_p^N) = 2.66$, $\max \Re(\lambda_{m\delta}^{NE1}) = 0.00084$.

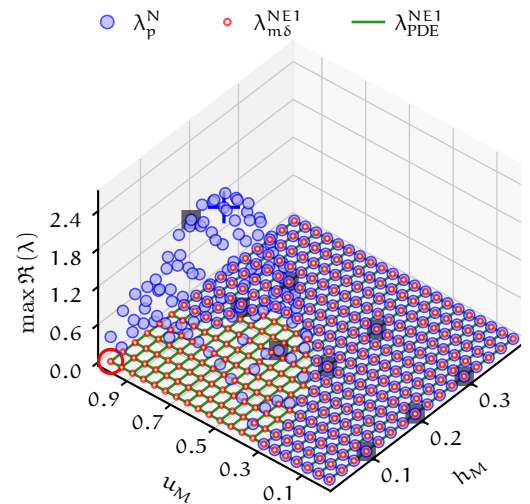
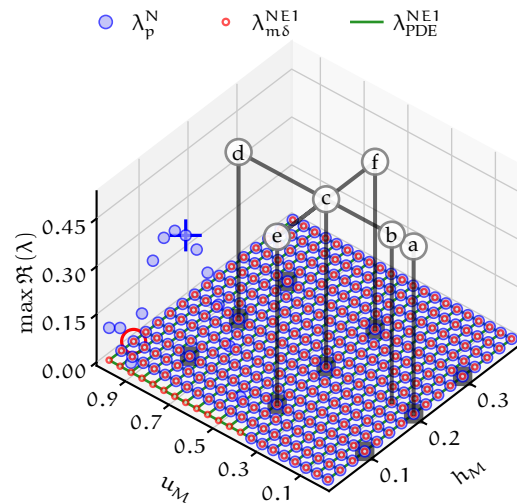
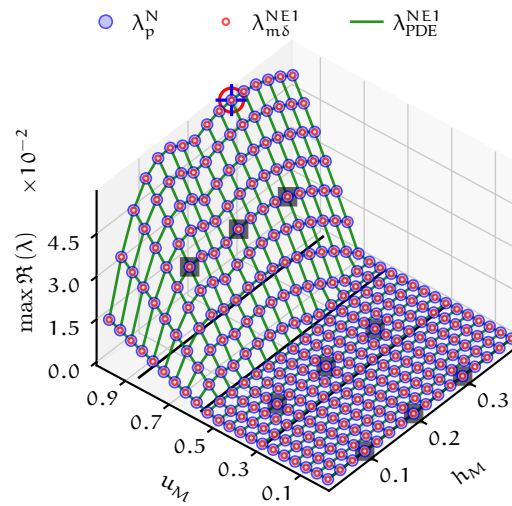
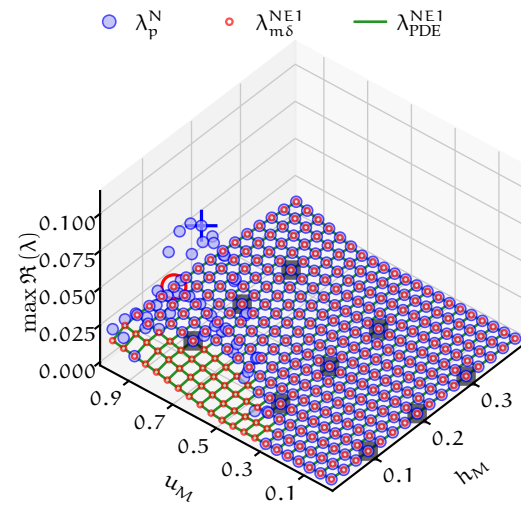


Figure 4.4.7. Maximum real part of the eigenvalues for, λ_p^N of Spectral patch scheme ($N = 10$, $n = 6$, $r = 0.1$), $\lambda_{m\delta}^{NE1}$ and λ_{PDE}^{NE1} of the viscous shallow water flows, about different mean flow (h_M, u_M) with $v_M = 0$ and $\theta = 0^\circ$. No artificial instability only for $Re = 10$. Artificial instability spreads to smaller Re with increasing r , Figs. 4.4.5 to 4.4.7 for $r = 0.001, 0.01, 0.1$.

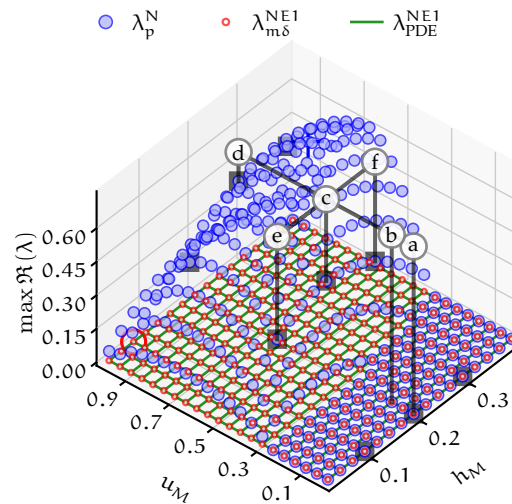
(a) Reynolds number $Re = 10$. Identical to Fig. 4.4.5a of $r = 0.001$ and Fig. 4.4.6a of $r = 0.01$; no artificial instability. Peak values (blue plus and red circle) are $\max \Re(\lambda_p^N) = 0.059 = \max \Re(\lambda_{m\delta}^{NE1})$.



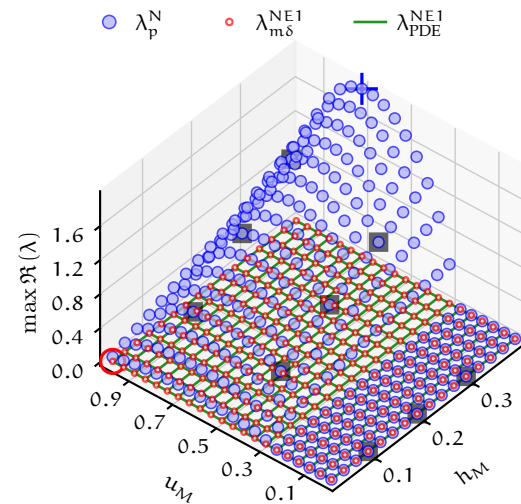
(b) $Re = 50$. Artificial instability (i.e., $\max \Re(\lambda_p^N) > \max \Re(\lambda_{m\delta}^{NE1}) \geq 0$) for very shallow mean flow $h_M \lesssim 0.1$ and large $u_M \gtrsim 0.3$; $\max \Re(\lambda_p^N) = 0.11$, $\max \Re(\lambda_{m\delta}^{NE1}) = 0.019$.



(c) $Re = 250$. Artificial instability (i.e., $\max \Re(\lambda_p^N) > \max \Re(\lambda_{m\delta}^{NE1}) \geq 0$) for nearly all mean height $h_M \in [0.025, 0.4]$ and large $u_M \gtrsim 0.3$; $\max \Re(\lambda_p^N) = 0.75$, $\max \Re(\lambda_{m\delta}^{NE1}) = 0.0041$.



(d) $Re = 1250$. Artificial instability (i.e., $\max \Re(\lambda_p^N) > \max \Re(\lambda_{m\delta}^{NE1}) \geq 0$) for all mean height $h_M \in [0.025, 0.4]$ and large $u_M \gtrsim 0.3$; $\max \Re(\lambda_p^N) = 2$, $\max \Re(\lambda_{m\delta}^{NE1}) = 0.00084$.



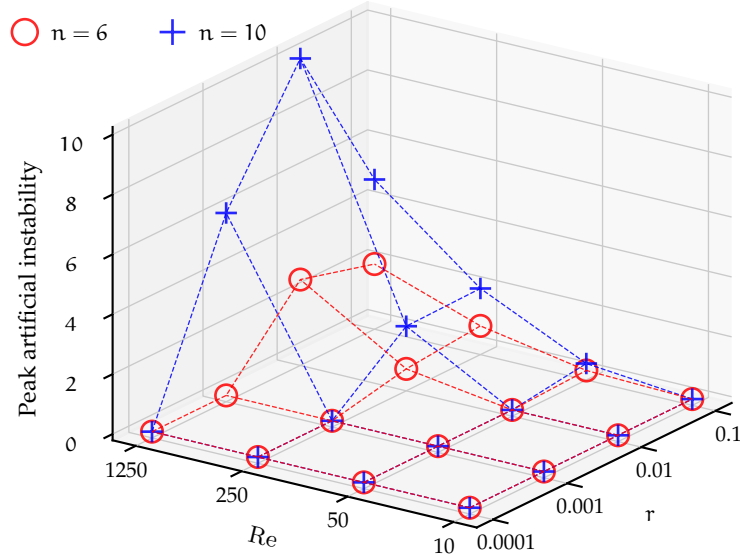
For patch scale ratio $r \sim 0.1$, the staggered patch schemes are stable for small mean velocity $u_M \lesssim 0.3$ where the underlying full-domain microscale model is stable. Figures 4.4.6 and 4.4.7 plot the maximum real part of the eigenvalues versus (h_M, u_M) , for the Spectral staggered patch scheme ($N = 10, n = 6$) with patch scale ratios $r = 0.01, 0.1$ respectively. Figures 4.4.6 and 4.4.7 show that the Spectral patch scheme is stable ($\max \Re(\lambda_p^{NE1}) \not\approx 0$) even for non-small patch scale ratio $r = 0.01, 0.1$, for small mean velocity $u_M \lesssim 0.3$ where the underlying full-domain microscale model is stable ($\max \Re(\lambda_{m\delta}^{NE1}) \not\approx 0$). Similarly, for small mean velocity $u_M \lesssim 0.3$, all the four polynomial staggered patch schemes are also stable for patch scale ratio $r \in \{0.0001, 0.001, 0.01, 0.1\}$ for $h_M \in [0.025, 4]$.

For patch scale ratio $r \gtrsim 0.01$, the staggered patch schemes have artificial instability for some mean flows (h_M, u_M) for the combination of large mean velocity u_M and large Reynolds number Re . Figures 4.4.6 and 4.4.7 show that the Spectral patch scheme ($N = 10, n = 6, r = 0.01, 0.1$) has artificial instability $\max \Re(\lambda_p^{NE1}) > \max \Re(\lambda_{m\delta}^{NE1})$ (condition (4.4.1) does not hold) for the combination of large mean velocity $u_M \gtrsim 0.3$ and large Reynolds number $Re \gtrsim 10$. For example, Figs. 4.4.1 and 4.4.2 show the artificial instability in the complex plane plots for $(h_m, u_M) = (0.2, 0.3)$ and $(h_m, u_M) = (0.2, 0.8)$ (the point d in Fig. 4.4.7c) respectively, with Reynolds number $Re = 250$ for the Spectral patch scheme ($N = 10, n = 6, r = 0.1$). The patch scheme artificial instability in Fig. 4.4.1 arises as $\max \Re(\lambda_p^N) = \max \Re(\lambda_p^{NE1}) = 0.062 > \max \Re(\lambda_{m\delta}^{NE1}) = 0$. Figure 4.4.2 for $r = 0.1$ shows patch scheme artificial instability, in contrast to Fig. 4.2.6 for the same parameters except $r = 0.01$. Compared to the $\max \Re(\lambda_p^{NE1}) = 0.0021$ (physical instability) in Fig. 4.2.6 for $r = 0.01$, Fig. 4.4.2 for $r = 0.1$ has $\max \Re(\lambda_p^{NE1}) = 0.62 > \max \Re(\lambda_{m\delta}^{NE1}) = 0.0021$ (artificial instability).

Figures 4.4.6 and 4.4.7 illustrate the following key trends about the patch scheme stability. All the trends in the following listing also hold for the four polynomial patch schemes (§2.2.2), we omit the corresponding figures for brevity.

- For small Reynolds numbers $Re \sim 10$, the Spectral patch scheme does not have any artificial instability (condition (4.4.1) holds) for $h_M \in [0.025, 0.4]$, $u_M \in [0, 1]$, and patch scale ratio $r \in \{0.001, 0.01, 0.1\}$.
- Increasing Reynolds number Re increases the peak artificial instability. For example, Figs. 4.4.7a to 4.4.7d for patch scale ratio $r = 0.1$ show that for Reynolds number $Re = 10, 50, 250, 1250$ the peak artificial instability, $\max_{h_M, u_M} [\max \Re(\lambda_p^N) - \max \Re(\lambda_{m\delta}^{NE1})] = 0, 0.11, 0.75, 2$ respectively.

Figure 4.4.8. Variation of Spectral patch scheme peak artificial instability $\max_{h_M, u_M} [\max \Re(\lambda_p^N) - \max \Re(\lambda_{m\delta}^{NE1})]$ (over $h_M \in [0.025, 0.4]$, $u_M \in [0, 1]$), with the Reynolds number Re and the patch scale ratio r . Artificial instability increases with increasing sub-patch micro-grid intervals n for large r and Re . Artificial instability decreases, with decreasing Reynolds number Re , and with decreasing patch scale ratio r .



- Increasing Re from $Re \approx 10$ causes a small region of artificial instability to develop for the Spectral patch scheme for the very shallow flow (small h_M) with large mean velocity u_M (Figs. 4.4.6c and 4.4.7b). Increasing Re further from $Re \approx 50$ causes the region of artificial instability to grow large towards larger values of mean height h_M and smaller values of mean velocity u_M (Figs. 4.4.6d and 4.4.7d).
- Increasing Re also causes the h_M for peak instability of the Spectral patch scheme $\max_{h_M} (\max \Re(\lambda_p^N))$ to move towards larger values of h_M ; but the u_M for peak instability $\max_{u_M} (\max \Re(\lambda_p^N))$ remains the same at $u_M \approx 0.7$ and unaffected by the Reynolds number.

The patch scheme artificial instability for large Reynolds numbers is removed by appropriately decreasing the patch scale ratio r . Figures 4.4.6 and 4.4.7 show that the Spectral patch scheme ($N = 10$, $n = 6$, $r = 0.01, 0.1$) has artificial instability. Figures 4.4.5 to 4.4.7 show how the variation of maximum real part of eigenvalues with h_M , u_M depend on Reynolds number $Re \in \{10, 50, 250, 1250\}$ and patch scale ratio $r \in \{0.001, 0.01, 0.1\}$, for the Spectral patch scheme ($N = 10$, $n = 6$). Figures 4.4.5 to 4.4.7 shows the following

key trends about the stability of the Spectral patch scheme, all of which also hold for the four polynomial patch schemes (§2.2.2).

- For small mean velocity $u_M \in [0, 0.3]$ where the underlying full-domain microscale model is stable ($\max \Re(\lambda_{m\delta}^{NE1}) \not\approx 0$), the Spectral patch scheme is also stable for $h_M \in [0.025, 0.4]$, Reynolds number $Re \in \{10, 50, 250, 1250\}$ and patch scale ratio $r \in \{0.001, 0.01, 0.1\}$.
- Similar to the trend with increasing Re , increasing patch scale ratio r increases the peak artificial instability. For example, Figs. 4.4.5c, 4.4.6c and 4.4.7c for Reynolds number $Re = 250$ show that for increasing patch scale ratio $r = 0.001, 0.01, 0.1$ the peak artificial instability, $\max_{h_M, u_M} [\max \Re(\lambda_p^N) - \max \Re(\lambda_{m\delta}^{NE1})] = 0, 0.52, 0.75$ respectively.
- Similar to the trend with increasing Re , increasing r from $r \approx 0.001$ causes a small region of artificial instability to develop for the Spectral patch scheme for the very shallow flow (small h_M) with large mean velocity u_M . Increasing r further from $r \approx 0.01$ causes the region of artificial instability to grow large for the Spectral patch scheme towards larger values of mean height h_M and smaller values of mean velocity u_M .
- Similar to the trend with increasing Re , increasing r also causes the h_M for peak instability of the Spectral patch scheme $\max_{h_M} (\max \Re(\lambda_p^N))$ to move towards larger values of h_M ; but the u_M for peak instability $\max_{u_M} (\max \Re(\lambda_p^N))$ remains the same at $u_M \approx 0.7$ and unaffected by the Reynolds number.

In summary, both increasing Reynolds number Re and increasing patch scale ratio r cause the patch scheme artificial instability to develop and spread to larger regions of mean flow (h_M, u_M). In other words, increasing Re causes artificial instability to develop and grow, but decreasing r causes the artificial instability to shrink and disappear. Figure 4.4.8 also shows this trend of artificial instability by plotting the peak artificial instability $\max_{h_M, u_M} [\max \Re(\lambda_p^N) - \max \Re(\lambda_{m\delta}^{NE1})]$ (over $h_M \in [0.025, 0.4]$, $u_M \in [0, 1]$), versus Reynolds number $Re \in \{10, 50, 250, 1250\}$ and the patch scale ratio $r \in \{0.0001, 0.001, 0.01, 0.01, 0.1\}$. Thus, the *patch scheme artificial instability for large Reynolds numbers is removed by appropriately decreasing the patch scale ratio r .*

Keeping the domain size 2π , patch scale ratio r , and the number of macro-grid intervals N , *increasing the number of sub-patch micro-grid intervals n increases the artificial instability of the Spectral patch scheme for non-*

small patch scale ratio. The preceding two paragraphs show that both increasing Reynolds number Re and increasing patch scale ratio r cause the patch scheme artificial instability to develop and spread to larger regions of mean flow (h_M, u_M) . [Figure 4.4.8](#) shows the same trend by plotting peak artificial instability $\max_{h_M, u_M} [\max \Re(\lambda_p^N) - \max \Re(\lambda_{m\delta}^{NE1})]$ (over $h_M \in [0.025, 0.4]$, $u_M \in [0, 1]$), with the Reynolds number $Re \in \{10, 50, 250, 1250\}$ and the patch scale ratio $r \in \{0.0001, 0.001, 0.01, 0.01, 0.1\}$ for different number of sub-patch micro-grid intervals $n \in \{6, 10\}$. [Figure 4.4.8](#) shows that for patch scale ratio $r \gtrsim 0.01$, increasing n increases the peak artificial instability of the Spectral patch scheme. This trend of increasing peak artificial instability with increasing n , is large for large Reynolds numbers $Re \gtrsim 250$. But [p. 239](#) of [§4.4.3](#) shows that increasing the number of sub-patch micro-grid intervals to $n = 10$ removes the artificial instability of the polynomial patch schemes due to small patch scale ratio r and/or large number macro-grid intervals N .

Overall the following listing summarises the stability characteristics of the Spectral patch scheme for viscous shallow water flows. All the following characteristics also hold for all the four polynomial patch schemes ([§2.2.2](#)).

1. For small mean velocity $u_M \in [0, 0.2]$ where the underlying full-domain microscale model is stable ($\max \Re(\lambda_{m\delta}^{NE1}) \leq 0$), the Spectral patch scheme is stable for a wide range of patch scale ratio $r \in [0.001, 0.1]$ and Reynolds number $Re \in [10, 1250]$.
2. For large mean velocity $u_M \gtrsim 0.2$ and large Reynolds number $Re > 10$, the Spectral patch scheme with patch scale ratio $r \gtrsim 0.01$ has artificial instability for both when the underlying full-domain microscale model is stable and physically unstable.
3. For large mean velocity $u_M \gtrsim 0.2$, the Spectral patch scheme with patch scale ratio $r \gtrsim 0.01$ has artificial instability for when the underlying full-domain microscale model is both stable and physically unstable. Increasing the Reynolds number $Re \gtrsim 10$ causes artificial instability to develop and spread to larger regions of mean flow (h_M, u_M) . But decreasing patch scale ratio $r \lesssim 0.01$ causes the artificial instability to shrink and disappear.
4. The artificial instability of the patch schemes arises only for the sub-patch microscale modes.
5. Keeping the domain size 2π , patch scale ratio r , and the number of macro-grid intervals N , increasing the number of sub-patch micro-

grid intervals n increases the patch scheme artificial instability for non-small patch scale ratio.

As §4.6 establishes, the patch schemes are invariant (within discretisation errors) with different flow angle α for macroscale waves, where $q = \sqrt{u_M^2 + v_M^2}$, $u_M = q \cos(\alpha)$ and $v_M = q \sin(\alpha)$. Hence, whereas all the points in the preceding summary are based on the Spectral patch scheme over a wide range of mean height h_M and the mean velocity u_M keeping $v_M = 0$, they also hold for the resultant mean velocity $q = \sqrt{u_M^2 + v_M^2}$ (u_M, v_M) along any orientation. Thus, for an appropriate patch grid the Spectral patch scheme is not artificially unstable, for a wide range of physical parameters (Reynolds number Re , mean height h_M , and horizontal mean velocity (u_M, v_M)).

4.4.2 Dominant artificial instabilities are due to sub-patch microscale structure modulated over non-small macroscale wavenumbers

Page 217 of §4.4.1 establishes that an instability arises only for the sub-patch microscale modes. This subsection shows the dependence of physical and artificial instability on the macroscale wavenumbers and shows that dominant artificial instabilities of the patch schemes are due to sub-patch microscale whose microscale structure is modulated over non-small macroscale wavenumbers. The analysis in this subsection uses Spectral patch scheme, but all qualitative characteristics in this subsection also hold for other patch grid parameters (N, n, r) and for the four polynomial patch schemes (§2.2.2).

Increasing the mean velocity u_M increases monotonically the physical instability of the viscous shallow water. Figure 4.4.9a plot wavenumber-wise contribution to the physical instability $\max \Re(\lambda_{m\delta}^{NE1})$ for the full-microscale domain system, for the macroscale wavenumbers resolved by a patch scheme with $N = 10$ macro-grid intervals and each patch containing $n = 6$ sub-patch intervals. Figure 4.4.9a shows that increasing mean velocity u_M increases physical instability monotonically, with two peaks at $(k_x, k_y) = (\pm 1, 0)$ to each side of a valley at $k_x = 0$ (for $v_M = 0$). For nonzero v_M , the valley is along the line $k_x = -(v_M/u_M)k_y$. That is, the maximum physical instability is due to large waves corresponding to two small macroscale wavenumbers (k_x, k_y) on the domain moving along the mean velocity (u_M, v_M) , with smallest two macroscale wavenumber (k_x, k_y) on each side of the valley in Fig. 4.4.9a.

The physical instability monotonically increases with increasing mean velocity u_M . But, with increasing mean velocity u_M , the patch scheme

artificial instability first increases, then decreases, and then again increases. **Figure 4.4.9c** plots wavenumber-wise variation of the artificial instability $\max \Re(\lambda_p^{NE1}) - \max \Re(\lambda_{m\delta}^{NE1})$ of the Spectral patch scheme with $N = 10$, $n = 6$, $r = 0.1$, for all the $N^2/4 = 25$ macroscale wavenumbers (k_x, k_y) where $k_x, k_y \in \{0, \pm 1, \pm 2\}$. **Figure 4.4.9c** shows that increasing mean velocity u_M increases the patch scheme artificial instability for $u_M \lesssim 0.6$ (light red small discs near top region) after which the artificial instability decreases (light green and light blue small discs). But the artificial instability does not disappear with a further increase, instead, the artificial instability increases again with increasing mean velocity for $u_M \gtrsim 2$. This increasing, decreasing and then again increasing patch scheme artificial instability with increasing u_M , is also evident in the same trend along the line a-d in **Fig. 4.4.7c**.

Increasing the mean velocity u_M increases monotonically the number of physically unstable modes of the viscous shallow water. **Figure 4.4.9b** plot wavenumber-wise contribution to the number of physically unstable modes for the full-microscale domain system, for all the macroscale wavenumbers resolved by a patch grid with $N = 10$ macro-grid intervals. **Figure 4.4.9b** shows that increasing mean velocity u_M increases the number of physically unstable modes for the full-domain microscale model, symmetrically to each side of a valley at $k_x = 0$ (for $v_M = 0$). For nonzero v_M , the valley is along line $k_x = -(v_M/u_M)k_y$. The small circles of dark red, dark green and dark blue colours at the bottom of **Fig. 4.4.9b** shows that for mean velocity up to $u_M = 0.4$, there are no unstable modes. Two light red inner circles in central region of **Fig. 4.4.9b** show that increasing the mean velocity to $u_M = 0.6$ leads to physical instability in two smallest wavenumber $(k_x, k_y) = (\pm 1, 0)$ on each side of the valley. With further increase in $u_M = 0.8, 1$, the initially developed physical instability for two small wavenumbers spread to larger wavenumbers, and increase to four and twelve artificially unstable microscale modes respectively. For example, for $u_M = 0.8$, the top four light green inner circles in **Fig. 4.4.9b** show that the wavenumbers $(k_x, k_y) \in \{(-2, 0), (-1, 0), (1, 0), (2, 0)\}$ each has one artificially unstable mode, corresponding to the four physically unstable modes in clusters 5, 6 of **Fig. 4.4.2**.

Increasing the mean velocity u_M increases the number of artificially unstable microscale modes for the patch schemes. **Figures 4.4.1** and **4.4.2** for $u_M = 0.3, 0.8$ with ten and fifty artificially unstable microscale modes, suggest that the number of artificially unstable microscale modes increases with mean velocity u_M . This increasing number of artificially unstable microscale modes is due to two sources:

1. increasing mean velocity u_M increases the number of wavenumbers

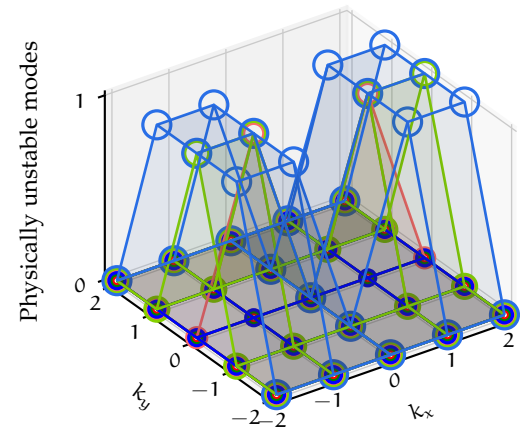
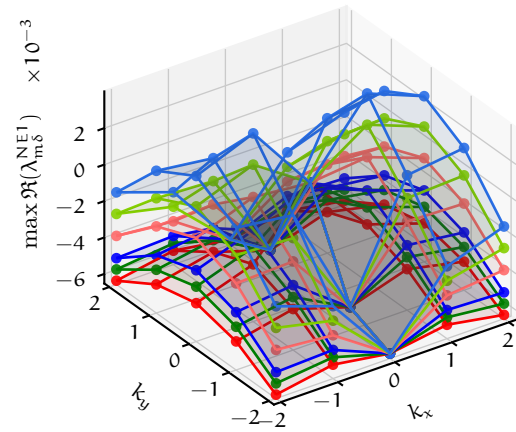
Figure 4.4.9. Wavenumber-wise contribution to viscous shallow water flows instability for different mean velocity u_M ($h_M = 0.2, v_M = 0, Re = 250$): (a) and (b) plot physical instability and the number of unstable modes of *full-domain model*; (c) and (d) plot artificial instability and number of unstable modes of *Spectral patch scheme* ($N = 10, n = 6, r = 0.1$).

(a) Increasing u_M increases physical instability monotonically, with two peaks at $(k_x, k_y) = (\pm 1, 0)$ to each side of a valley at $k_x = 0$. The valley is along the line $k_x = -(v_M/u_M)k_y$.

(b) Increasing u_M increases the number of physically unstable modes monotonically, symmetrically to each side of a valley at $k_x = 0$. The valley is along the line $k_x = -(v_M/u_M)k_y$.

● $u_M = 0.2$ ● $u_M = 0.3$ ● $u_M = 0.4$
● $u_M = 0.6$ ● $u_M = 0.8$ ● $u_M = 1$

○ $u_M = 0.2$ ○ $u_M = 0.3$ ○ $u_M = 0.4$
○ $u_M = 0.6$ ○ $u_M = 0.8$ ○ $u_M = 1$

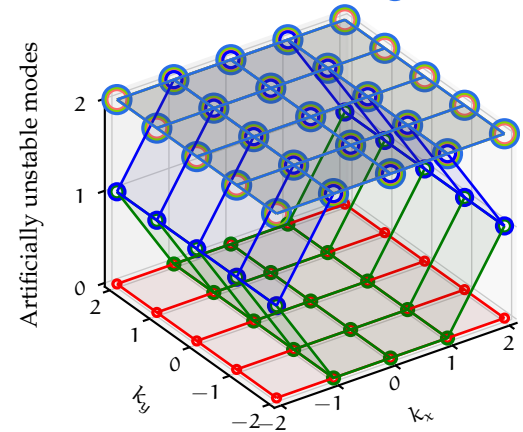
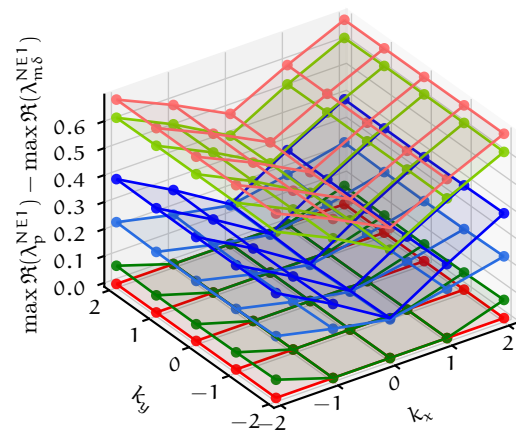


(c) Increasing u_M increases artificial instability for $u_M \lesssim 0.6$, then decreases. Artificial instability increase with $|k_x|$. The valley is along the line $k_x = -(v_M/u_M)k_y$.

(d) Increasing $u_M \in [0, 1]$ increases number of artificially unstable microscale modes, symmetrically on both sides of the ridge/valley that is along the line $k_x = -(v_M/u_M)k_y$.

● $u_M = 0.2$ ● $u_M = 0.3$ ● $u_M = 0.4$
● $u_M = 0.6$ ● $u_M = 0.8$ ● $u_M = 1$

○ $u_M = 0.2$ ○ $u_M = 0.3$ ○ $u_M = 0.4$
○ $u_M = 0.6$ ○ $u_M = 0.8$ ○ $u_M = 1$



for which at least one mode is unstable;

2. increasing mean velocity u_M also increases the number of artificially unstable microscale modes of a particular macroscale wavenumber over which the microscale structure is modulated.

Figure 4.4.9d plot wavenumber-wise contribution to the number of artificially unstable microscale modes of the Spectral patch scheme with $N = 10$, $n = 6$, $r = 0.1$, for all the $N^2/4 = 25$ macroscale wavenumbers (k_x, k_y) where $k_x, k_y \in \{0, \pm 1, \pm 2\}$. **Figure 4.4.9d** shows that for increasing mean velocity $u_M = 0.2, 0.3, 0.4, 0.6, 0.8, 1$ (along the line a-d in **Fig. 4.4.7c**) the number of artificially unstable microscale modes increases, symmetrically to each side of a valley/ridge along k_y -axis (for $v_M = 0$). For nonzero v_M , the valley/ridge is along line $k_x = -(v_M/u_M)k_y$. Increasing the mean velocity u_M increases the number of wavenumbers for which a patch scheme is unstable, for $u_M \lesssim 0.4$ after which a patch scheme is unstable for all the 25 wavenumbers. For example, for $u_M = 0.2, 0.3, 0.4$, **Figure 4.4.9d** (dark red, dark green and dark blue circles near the bottom) shows that the *number of wavenumbers* for which the Spectral patch scheme is unstable are 0, 10, 25 respectively. The corresponding total *number of artificially unstable microscale modes* for $u_M = 0.2, 0.3, 0.4, 0.6, 0.8, 1$ are 0, 10, 40, 50, 50, 50 respectively.

- The small dark red circles at the bottom of **Fig. 4.4.9d** show that for mean velocity $u_M = 0.2$, there are no artificially unstable microscale modes.
- The small dark green circles near the bottom of **Fig. 4.4.9d** show that increasing to $u_M = 0.3$ triggers the patch scheme artificial instability, but only for $k_x = \pm 2$. That is the sub-patch microscale modes are artificially unstable corresponding to the largest ten macroscale wave modes moving along the mean velocity (u_M, v_M) (five on each side of the green valley in **Fig. 4.4.9d**).
- The dark blue circles near the middle and top region of **Fig. 4.4.9d** show that increasing to $u_M = 0.4$ makes the patch scheme artificially unstable for all 25 wavenumbers. There is one unstable microscale mode for each of ten wavenumbers with $k_x = \pm 2$ (corresponding to the ten largest macroscale wave modes) and there are two unstable microscale modes for each of fifteen wavenumbers with $k_x \in \{0, \pm 1\}$ (corresponding to thirty macroscale wave modes).

- All the large circles of light red, light green, and light blue circles at the of Fig. 4.4.9d show that for $u_M \gtrsim 0.6$ the patch scheme is artificially unstable for all 25 wavenumbers. There are two unstable microscale modes for each of 25 wavenumbers with $k_x \in \{0, \pm 1\}$ (corresponding to all fifty macroscale wave modes). For example, Fig. 4.4.2 for $u_M = 0.8$ shows the fifty artificially unstable microscale modes contained within the clusters 1–4.

From Fig. 4.4.2, the total number of maximum artificially unstable microscale modes remain the same as fifty for $u_M = 0.6, 0.8, 1$ (two unstable modes for each of 25 wavenumbers). But this total number of maximum artificially unstable microscale modes is not an upper bound. With a further increase in mean velocity $u_M > 1$, the total number of artificially unstable microscale modes increases larger than fifty.

For moderate mean velocities $u_M, v_M \lesssim 0.3$, *only those sub-patch microscale modes whose microscale structure is modulated over non-small macroscale wavenumber are artificially unstable.* Figures 4.4.10 and 4.4.11 show the same complex plane plot as Fig. 4.4.1 of §4.4.1 (with artificial instability of Spectral patch scheme for $N = 10$, $n = 6$, $r = 0.1$, and $u_M = 0.3$) except one difference:

- analytic eigenvalues λ_p^{NE1} and $\lambda_{m\delta}^{NE1}$ in Fig. 4.4.1 are evaluated for all the $N^2/4 = 25$ macroscale wavenumbers (k_x, k_y) resolved by a patch grid where $k_x, k_y \in \{0, \pm 1, \pm 2\}$;
- analytic eigenvalues λ_p^{NE1} and $\lambda_{m\delta}^{NE1}$ in Figs. 4.4.10 and 4.4.11 are evaluated for only one macroscale wavenumber $(k_x, k_y) = (1, 0), (2, 0)$ respectively.

In Fig. 4.4.10, the nonpositive real parts of the eigenvalues λ_p^{NE1} for wavenumber $(k_x, k_y) = (1, 0)$ (blue circles) show that, the patch scheme does not have artificial instability for this wavenumber. On the other hand, in Fig. 4.4.11, the positive real part of the eigenvalue λ_p^{NE1} in cluster 1 for wavenumber $(k_x, k_y) = (2, 0)$ (blue circle) shows that, the patch scheme has artificial instability for this wavenumber. Similarly, for the parameters in Figs. 4.4.10 and 4.4.11, for all the resolved $k_y \in \{0, \pm 1, \pm 2\}$, the patch schemes modes for wavenumber $k_x = \pm 2$ have artificial instability, but the modes for wavenumber $k_x = 0, \pm 1$ do not have any have artificial instability. That is, for moderate mean velocities $u_M, v_M \lesssim 0.3$, *only those sub-patch microscale modes whose microscale structure is modulated over non-small macroscale wavenumber are artificially unstable.* But as the previous paragraph shows, increasing the mean velocity u_M increases the number of artificially

unstable microscale modes for the patch schemes. So, for a sufficiently large mean velocity u_M , all the modes become artificially unstable. For example, in Fig. 4.4.9d, for $u_M \geq 0.4$ the number of artificially unstable modes is at least one for all the resolved wavenumbers. The wavenumber-wise variation of the artificial instability in Fig. 4.4.9c confirms that only non-small wavenumber modes are artificially unstable for $u_M \leq 0.3$.

Dominant artificial instabilities are due to those sub-patch microscale modes whose microscale structure is modulated over non-small macroscale wavenumber. Figure 4.4.9c plots wavenumber-wise variation of the artificial instability $\max \Re(\lambda_p^{NE1}) - \max \Re(\lambda_{m\delta}^{NE1})$ of the Spectral patch scheme with $N = 10$, $n = 6$, $r = 0.1$, for all the $N^2/4 = 25$ macroscale wavenumbers (k_x, k_y) where $k_x, k_y \in \{0, \pm 1, \pm 2\}$. Figure 4.4.9c (for $v_M = 0$) shows that for all mean velocity $u_M \in \{0.2, 0.3, 0.4, 0.6, 0.8, 1\}$, the artificial instability is large for large magnitudes of macroscale wavenumber $|k_x|$, on both sides of the valley at $k_x = 0$. More generally, the artificial instability is large for those sub-patch microscale modes whose microscale structure is modulated over large macroscale waves moving along the mean velocity (u_M, v_M) . Thus, irrespective of the mean velocities u_M, v_M , dominant artificial instabilities of the patch schemes are due to sub-patch microscale modes whose microscale structure is modulated over non-small macroscale wavenumber.

Overall the following listing summarises the characteristics of physically unstable modes of the full-domain model and the artificially unstable modes of the Spectral patch scheme for viscous shallow water flows. Whereas all the following points are based on the Spectral patch scheme with $N = 10$, $n = 6$, $r = 0.1$, they also hold for other patch grid parameters (N, n, r) and for all the four polynomial patch schemes (§2.2.2).

- Increasing the mean velocity u_M increases monotonically the physical instability and the number of physically unstable modes of the viscous shallow water.
- Increasing mean velocity u_M, v_M increases both the artificial instability $\max \Re(\lambda_p^{NE1}) - \max \Re(\lambda_{m\delta}^{NE1})$ and the number of artificially unstable microscale modes per wavenumber.
- The maximum physical instability is due to large waves corresponding to two small macroscale wavenumbers (k_x, k_y) on the domain moving along the mean velocity (u_M, v_M) .
- The artificial instability of the sub-patch microscale modes depends on the specific macroscale wavenumber (k_x, k_y) over which the microscale structure is modulated. For moderate mean velocities $u_M, v_M \lesssim$

0.3, only those sub-patch microscale modes whose microscale structure is modulated over non-small macroscale wavenumber are artificially unstable. Irrespective of the mean velocities u_M, v_M , dominant artificial instabilities of the patch schemes are due to those sub-patch microscale modes whose microscale structure is modulated over non-small macroscale wavenumber.

4.4.3 No artificial instability among the five staggered patch schemes for a range of grid parameters

Section 4.4.1 shows that for an appropriate patch grid the Spectral patch scheme is not artificially unstable, for a wide range of physical parameters for a representative set of patch grid parameters. This subsection shows that the five staggered patch schemes are not artificially unstable, for a wide range of patch grid parameters (macro-grid intervals N , sub-patch micro-grid intervals n , and patch scale ratio r), for a representative set of physical parameters (Reynolds number Re , mean height h_M , and horizontal mean velocity (u_m, v_M) indicated by nine black squares in Figs. 4.4.5 to 4.4.7 of §4.4.1). That is, this subsection shows that for a wide range of parameters, the maximum real part of the patch scheme eigenvalues (analytic λ_p^{NE1} , numerical λ_p^N) is not both positive and larger than the maximum real part of the eigenvalues $\lambda_{m\delta}^{NE1}$ of the corresponding full-domain microscale model (the condition of no artificial instability (4.4.1)). This subsection also gives a general rule to get rid of artificial instability.

We expect the polynomial patch schemes to follow similar stability trend with different mean flow (h_M, u_M) as the Spectral patch scheme for which §4.4.1 studies in detail for 336 combinations of the mean flow (h_M, u_M) . So, as opposed to the many combinations (336) of linearisation points $\{(h_M, u_M, v_M)\}$ in §4.4.1, this subsection limits the study of artificial stability of patch schemes to the nine linearisation points $\{(h_M, u_M, v_M)\}$ where $h_M \in \{0.1, 0.2, 0.3\}$, $u_M \in \{0, 0.4, 0.8\}$, $v_M = 0$ (the black squares in Figs. 4.4.5 to 4.4.7 of §4.4.1). Thus, this subsection studies the artificial instability via the patch scheme eigenvalues for a total of 7776 cases consisting of all the combinations of the Spectral and polynomial patch schemes (Square-p2, Square-p4, Square-p6, and Square-p8) for the patch grid parameters

- number of macroscale intervals $N \in \{6, 10, 14, 18, 22, 26\}$,
- number of sub-patch micro-grid intervals $n \in \{6, 10\}$,
- patch scale ratio $r \in \{0.0001, 0.001, 0.01, 0.1\}$,

and the physical parameters

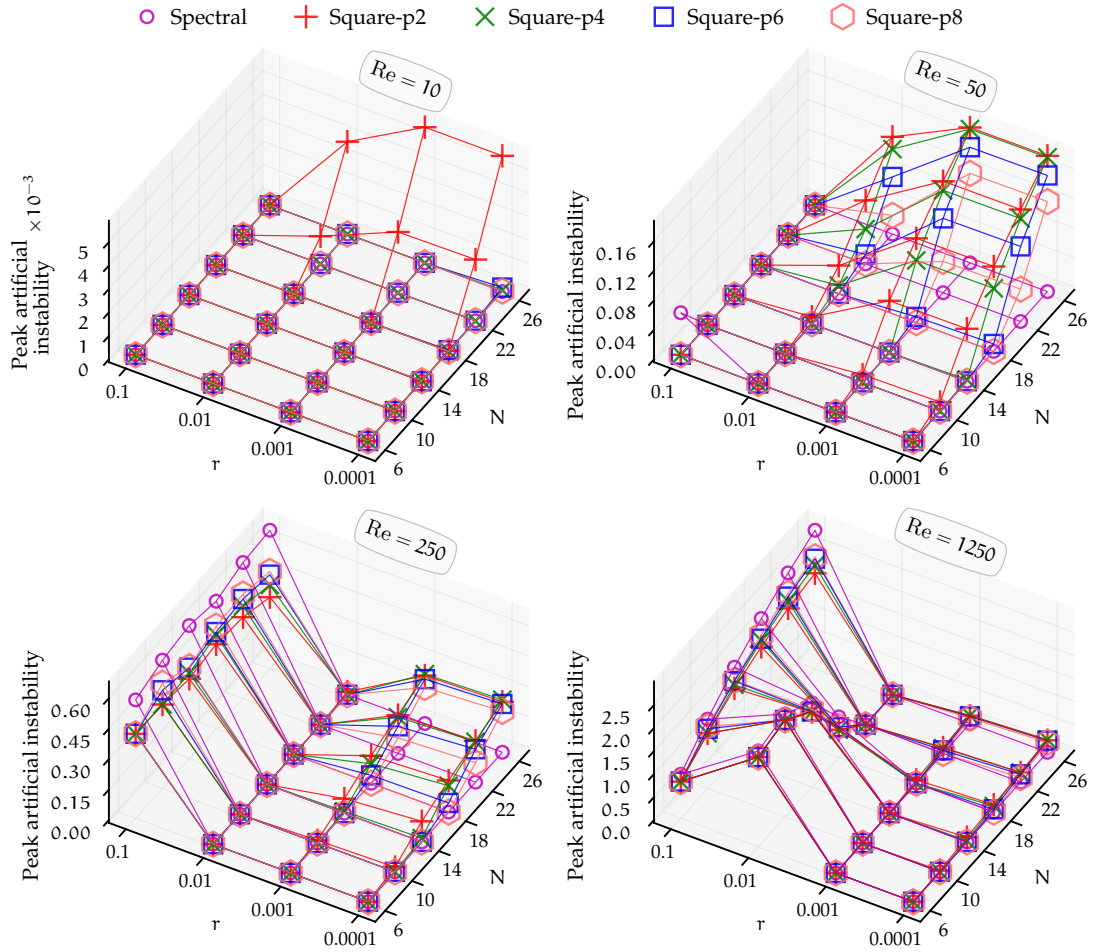
1. mean height $h_M \in \{0.1, 0.2, 0.3\}$,
2. mean velocity $u_M \in \{0, 0.4, 0.8\}$, $v_M = 0$ (§4.6 shows that the staggered patch schemes are invariant to flow direction),
3. Reynold number $Re \in \{10, 50, 250, 1250\}$.

As opposed to the definition of peak artificial instability in p. 224 of §4.4.1 over 336 cases, the term *peak artificial instability* throughout this subsection refers to $\max_{h_M, u_M} [\max \Re(\lambda_p^N) - \max \Re(\lambda_{m\delta}^{NE1})]$ or using analytic eigenvalues $\max_{h_M, u_M} [\max \Re(\lambda_p^{NE1}) - \max \Re(\lambda_{m\delta}^{NE1})]$, over the nine cases of the mean height $h_M \in \{0.1, 0.2, 0.3\}$ and the mean velocity $u_M \in \{0.0, 0.4, 0.8\}$.

For the small number of sub-patch micro-grid intervals $n = 6$, *accurate patch coupling interpolation removes the artificial instability for small patch scale ratio r* . For small number of sub-patch micro-grid intervals (Fig. 4.4.12 for $n = 6$), the artificial instability increases with increasing N . For patch scale ratio $r \gtrsim 0.1$, increasing patch coupling error decreases the artificial instability for large Reynolds number $Re \gtrsim 250$. For example, in the bottom two subplots of Fig. 4.4.12 for Reynolds number $Re = 250, 1250$, for patch scale ratio $r = 0.1$, going from Square-p2 to Spectral patch scheme the increasing patch coupling error decreases the peak artificial instability (red plus to magenta circle). *The only way to remove artificial instability due to the non-small patch scale ratio is to reduce the patch scale ratio to $r \lesssim 0.01$* . But for small patch scale ratio $r \lesssim 0.01$, the trend is the opposite, increasing patch coupling accuracy decreases the artificial instability. For example, in the subplots of Fig. 4.4.12 for Reynolds number $Re = 50, 250, 1250$, for small patch scale ratio $r \lesssim 0.01$, going from Square-p2 to Spectral patch scheme the increasing patch coupling accuracy decreases the peak artificial instability (red plus to magenta circle). For the highly accurate Spectral staggered patch scheme there is no artificial instability for small patch scale ratio $r \lesssim 0.01$ in Fig. 4.4.12 for all Reynolds numbers $Re \in \{10, 50, 250, 1250\}$. This effect of decreasing artificial instability with increasing patch coupling accuracy decreases with increasing Reynolds number Re .

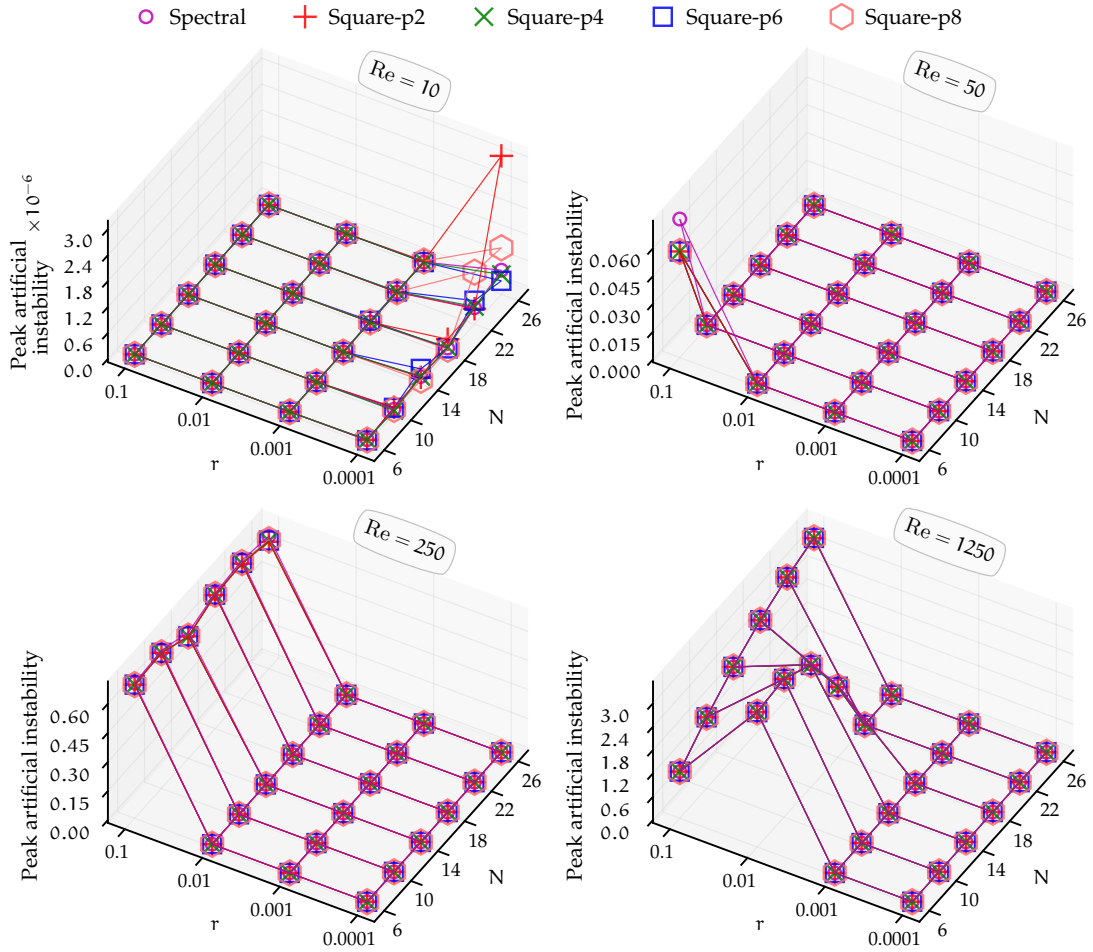
Sufficient number of sub-patch micro-grid intervals n remove the artificial instability of the polynomial patch schemes for small patch scale ratio r and/or large number macro-grid intervals N . For small number of sub-patch micro-grid intervals (Fig. 4.4.12 for $n = 6$), all the polynomial staggered patch schemes have varying degree of artificial instability which increases with increasing N . A sufficient number of sub-patch micro-grid intervals, which is $n = 10$ for viscous shallow water flows, removes such artificial

Figure 4.4.12. Variation of the patch scheme peak ($n = 6$) artificial instability $\max_{h_M, u_M} [\max \Re(\lambda_p^N) - \max \Re(\lambda_{m\delta}^{NE1})]$ (over $h_M \in \{0.1, 0.2, 0.3\}$, $u_M \in \{0.0, 0.4, 0.8\}$), with patch scale ratio r and macro-grid intervals N , for different Reynolds number $Re \in \{10, 50, 250, 1250\}$. *Artificial instability increases with increasing N for $n = 6$. Large artificial instability decreases, with increasing accuracy of patch coupling interpolation, and decreasing r .*



instabilities of the polynomial patch schemes. For example, comparing Figs. 4.4.12 and 4.4.13 shows that the sufficient number of sub-patch micro-grid intervals $n = 10$ remove the artificial instability for small patch scale ratio $r \lesssim 0.001$ for all the Reynolds numbers $Re \in \{10, 50, 250, 1250\}$ and macro-grid intervals $N \in \{6, 10, 14, 18, 22, 26\}$ for all the polynomial staggered patch schemes. The maximum peak artificial instabilities in Fig. 4.4.13 for $r \in \{0.0001, 0.001\}$ are $3.1 \cdot 10^{-6}$, $3.9 \cdot 10^{-7}$, $9.8 \cdot 10^{-8}$, $1.5 \cdot 10^{-8}$ corresponding to the Reynolds numbers $Re \in \{10, 50, 250, 1250\}$ respectively, all of which satisfy the condition of no artificial instability (4.4.1) (within a tolerance

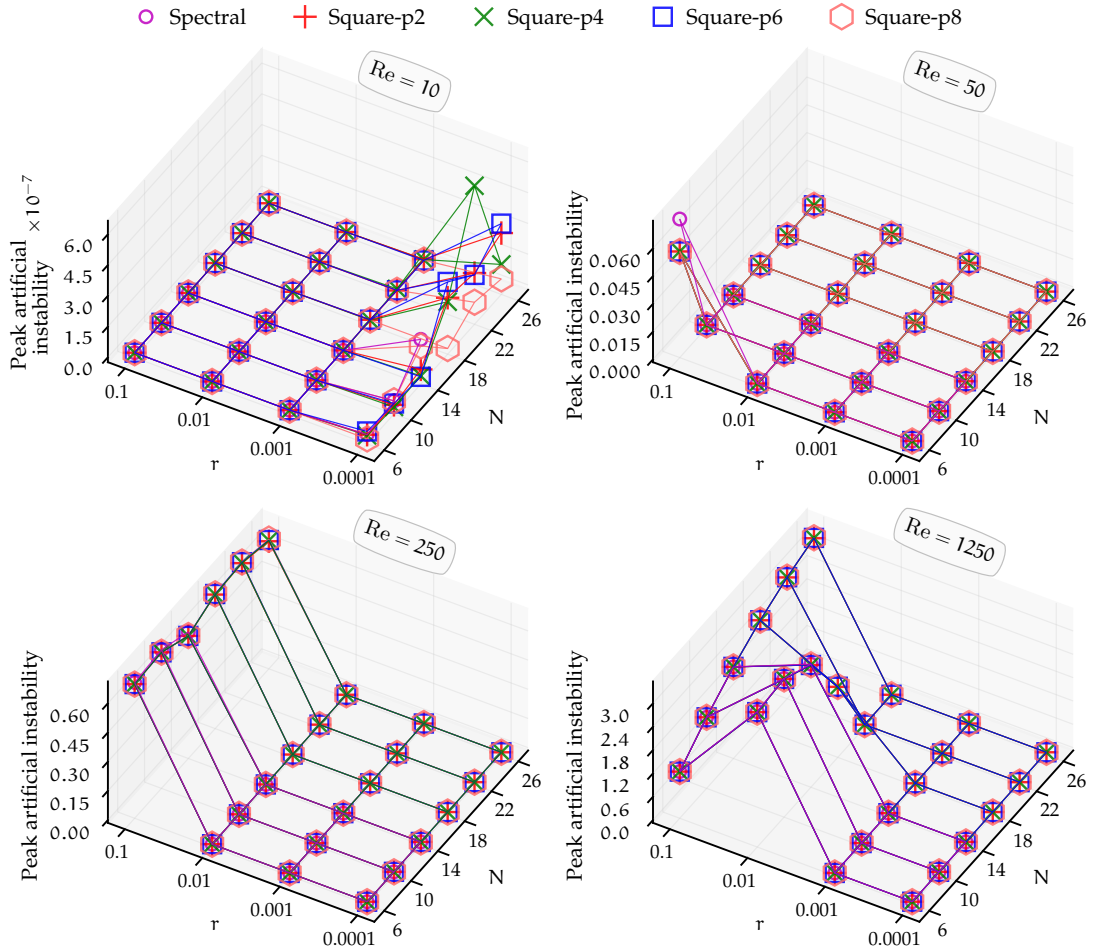
Figure 4.4.13. Variation of the patch scheme ($n = 10$) peak artificial instability $\max_{h_M, u_M} [\max \Re(\lambda_p^N) - \max \Re(\lambda_{m\delta}^{NE1})]$ (over $h_M \in \{0.1, 0.2, 0.3\}$, $u_M \in \{0.0, 0.4, 0.8\}$), with patch scale ratio r and macro-grid intervals N , for different Reynolds number Re . For $r \lesssim 0.01$, except roundoff errors (e.g., $Re = 10$) artificial instability does not significantly increase with N compared to $n = 6$ in Fig. 4.4.12. No artificial instability for $r \in \{0.001, 0.0001\}$.



of 10^{-5}). Thus, sufficient number of sub-patch micro-grid intervals n remove the artificial instability of the polynomial patch schemes for small patch scale ratio $r \lesssim 0.001$ and/or large number macro-grid intervals $N \gtrsim 10$. On the other hand, p. 229 of §4.4.1 shows that increasing the number of sub-patch micro-grid intervals n increases the artificial instability of the Spectral patch scheme for non-small patch scale ratio.

The preceding paragraph shows that increasing the number of sub-patch micro-grid intervals from $n = 6$ to $n = 10$ removes the artificial instability for small patch scale ratio $r \lesssim 0.001$ and/or large number macro-

Figure 4.4.14. Variation of the patch scheme ($n = 10$) peak artificial instability $\max_{r_M, u_M} [\max \Re(\lambda_p^{NE1}) - \max \Re(\lambda_{m\delta}^{NE1})]$, with patch scale ratio r and macro-grid intervals N , for the same parameters in Fig. 4.4.13 but using analytic eigenvalues λ_p^{NE1} of the patch schemes. Numerical roundoff errors cause the off-trend in artificial instability for small $Re \lesssim 10$ for the combination of small $r \lesssim 0.001$ and a large number of macro-grid intervals $N \gtrsim 14$.



grid intervals $N \gtrsim 10$. But any further increase in the number of sub-patch micro-grid intervals $n > 10$ does not remove the remaining artificial instability for patch scale ratio $r \gtrsim 0.01$ (e.g., the bottom-right subplot in Fig. 4.4.13 for $Re = 1250$). On the other hand, expression (3.7.3) (in p. 136 of §3.7.3) for patch scheme compute time shows that increasing the number of sub-patch micro-grid intervals n quadratically increases the patch scheme compute time.

In the left-top subplot of Fig. 4.4.13 for $Re = 10$, the seemingly large and off-trend artificial instability for small patch scale ratio $r \lesssim 0.001$ (i.e., increasing artificial instability with increasing N and increasing patch coupling accuracy) is due to floating-point numerical roundoff errors. Figure 4.4.14 shows a plot of variation of the patch scheme ($n = 10$) peak artificial instability $\max_{h_M, u_M} [\max \Re(\lambda_p^{NE1}) - \max \Re(\lambda_{m\delta}^{NE1})]$, with patch scale ratio r and macro-grid intervals N , for the same parameters in Fig. 4.4.13 but using analytic eigenvalues λ_p^{NE1} of the patch schemes. For the Spectral patch scheme, Fig. 4.4.14 includes the analytic eigenvalues λ_p^{NE1} (magenta circles) only for macro-grid intervals $N \in \{6, 10, 14\}$ to avoid numerically evaluating very long analytic expressions. Figure 4.4.14 shows that for small Reynolds number $Re = 10$ (top-left subplot) the peak artificial instability of analytic eigenvalues λ_p^{NE1} are different from the corresponding artificial instability of numerical eigenvalues λ_p^N .

In many numerical simulations, the divergence of a numerical scheme is a common issue for some combinations of the physical parameters and discretisation/grid parameters. The patch scheme artificial instability leads to such diverging time solution during ODE integration for numerical simulation. Based on the discussions in the preceding paragraphs, when a patch scheme has artificial instability for some combinations of system and patch grid parameters, a general rule to get rid of artificial instability is to take the following steps (in the order of large to small impact).

1. Decrease patch scale ratio r .
2. Increase the sub-patch micro-grid intervals n to a sufficient value (e.g., $n = 10$). Further increase in n is not beneficial.
3. Increase patch coupling interpolation accuracy, for example, choose a higher order polynomial patch scheme.
4. Decrease the macro-grid interval Δ .

As §4.6 establishes, the patch schemes are invariant (within discretisation errors) with different flow angle α where $u_M = q \cos(\alpha)$ and $v_M = q \sin(\alpha)$. Hence, whereas all preceding discussions in this subsection §4.4.3 are based on the five patch schemes over a range of mean height h_M and the mean velocity u_M keeping $v_m = 0$, they also hold for the resultant mean velocity $q = \sqrt{u_M^2 + v_M^2}$ along any orientation. Thus, *the five staggered patch schemes are not artificially unstable, for a wide range of patch grid parameters* (macro-grid intervals N , sub-patch micro-grid intervals n , and patch scale ratio r).

4.5 Staggered patch schemes are consistent

This section shows that the staggered patch schemes are consistent with the full-domain microscale model of viscous shallow water flows, with decreasing macro-grid interval Δ , via the convergence of the patch scheme eigenvalues. Similar to §3.6 for the general linear wave, subsections of this section establish the consistency of the patch schemes for the viscous shallow water flows by comparing the macroscale eigenvalues of the patch scheme with the corresponding eigenvalues of the full-domain microscale model. This eigenvalue comparison is done for increasingly finer patch grids. Section 4.5.1 shows that the Spectral patch scheme is uniformly accurate with little dependence on the macro-grid interval Δ . Section 4.5.2 shows that the polynomial patch schemes are consistent to the order of the polynomial interpolation with decreasing macro-grid interval Δ .

The full-domain microscale model (4.1.11) is consistent, when the discretized equations (4.1.11) approach to the corresponding PDEs (4.1.6), as the micro-grid interval $\delta \rightarrow 0$ (on the grid in Fig. 4.1.1). Such standard definition of consistency (e.g., Ferziger et al. 2020, p. 34) is useful for analysing the full-domain discrete systems whose goal is to accurately represent the corresponding PDEs. But the goal of our multiscale staggered patch scheme (4.1.15) is to accurately represent the *macroscale* waves of the corresponding *discrete* full-domain microscale model (§4.2.2). As defined in §3.6, a staggered patch scheme is consistent, when the macroscale characteristics of the patch scheme (e.g., (4.1.15)) approach to the corresponding macroscale characteristics of the given full-domain microscale model (e.g., (4.1.11)), as the macro-grid interval $\Delta \rightarrow 0$ (on the patch grid Fig. 2.1.3b).

As in §3.6 for the general linear wave, for viscous shallow water we show the consistency of the staggered patch schemes by demonstrating that the macroscale eigenvalues λ_{pM}^N of the patch schemes *converge* to the macroscale eigenvalues of the corresponding full-domain microscale model as $\Delta \rightarrow 0$, *to the same order p as the patch coupling interpolation*. The eigenvalue spectra in Figs. 4.2.2 to 4.2.10, show that the staggered patch scheme macroscale eigenvalues λ_{pM}^{NE1} (e.g., clusters 1, 2, 3, 4, 5 in Fig. 4.2.6) are qualitatively similar, and visually close, to the corresponding macroscale eigenvalues $\lambda_{m\delta}^A$ of the fine-grid full-domain microscale model (by varying degrees depending upon the specific staggered patch scheme, N , n , and r). To numerically quantify the discrepancy between the macroscale eigenvalues λ_{pM}^N of staggered patch scheme and the corresponding macroscale eigenvalues $\lambda_{m\delta}^A$ of fine grid full domain microscale model, we use the *eigenvalue error* defined in §3.6 for the *macroscale* wavenumber (k_x, k_y)

Table 4.5.1. Section 4.5 studies the consistency of the patch schemes using eigenvalues for all the 8 640 combinations of the listed parameters.

Patch schemes	Spectral, Square-p2, Square-p4, Square-p6, and Square-p8
Mean height	$h_M \in \{0.1, 0.2, 0.3\}$
Mean velocity	$u_M \in \{0, 0.4, 0.8\}$, $v_M = 0$ (§4.6 shows that the staggered patch schemes are invariant to flow direction)
Reynold number	$Re \in \{10, 50, 250, 1250\}$
Macro-grid intervals	$N \in \{6, 10, 14, 18, 22, 26\}$
Sub-patch micro-grid intervals	$n \in \{6, 10\}$
Patch scale ratio	$r \in \{0.0001, 0.001, 0.01, 0.1\}$

which is

$$\epsilon^{k_x, k_y} = \|\lambda_{pM}^N(k_x, k_y) - \lambda_{m\delta}^A(k_x, k_y)\| / \|\lambda_{m\delta}^A(k_x, k_y)\|, \quad (4.5.1)$$

where $\|\cdot\|$ is the Euclidean norm of the three element complex vectors of eigenvalues λ_{pM}^N and $\lambda_{m\delta}^A$ (three macroscale eigenvalues for each macroscale wavenumber).

As in §3.6 for the general linear wave, to assess the patch scheme consistency in this section (i.e., eigenvalue convergence) for the viscous shallow water flows, we compute the three eigenvalue errors $\epsilon^{1,0}$, $\epsilon^{1,1}$ and $\epsilon^{2,1}$, for the patch schemes on different staggered patch grids, corresponding to the three macroscale (angular) wavenumbers $(k_x, k_y) \in \{(1, 0), (1, 1), (2, 1)\}$ over the $2\pi \times 2\pi$ non-dimensional domain. The smallest wavenumber $(1, 0)$ corresponds to the largest wavelength of $(2\pi, 0)$ over the chosen $2\pi \times 2\pi$ non-dimensional domain. Specifically, to show the consistency of the staggered patch schemes, this section computes the three macroscale eigenvalue errors $\epsilon^{1,0}$, $\epsilon^{1,1}$ and $\epsilon^{2,1}$ for the 8 640 combinations of the parameters listed in Table 3.6.1.

Computing the three element vector of eigenvalues $\lambda_{m\delta}^A(k_x, k_y)$ in the eigenvalue error (4.5.1), is straightforward. As explained in p. 180 of §4.2.2, we numerically evaluate the Jacobian $\mathbf{J}(\mathbf{x}_M)$ in the eigensystem (4.2.7) and then compute the three eigenvalues for each of the three macroscale wavenumbers $(k_x, k_y) \in \{(1, 0), (1, 1), (2, 1)\}$. Among the numerical eigenvalues λ_p^N , finding which three eigenvalues correspond to the three eigenvalues in $\lambda_{m\delta}^A(k_x, k_y)$ (for the same macroscale wavenumber), is not straightforward. The *method of wavenumber-wise scale separation* in §3.3 classifies the

eigenvalues wavenumber-wise and separates as microscale and macroscale patch scheme eigenvalues. In the method of wavenumber-wise scale separation in §3.3, using the full-domain microscale eigenvalues $\lambda_{m\delta}^{NE1}$ in place of the eigenvalues $\lambda_{m\delta}^A$ gives the required eigenvalues as the following 3D arrays (analytic eigenvalues only for $N \leq 14$ for Spectral patch scheme)

1. An $N/2 \times N/2 \times 3$ array of *analytic* eigenvalues $\lambda_{m\delta}^{NE1}$ of the full-domain microscale model.
2. An $N/2 \times N/2 \times 3$ array of macroscale *analytic* patch scheme eigenvalues λ_{pM}^{NE1} .
3. An $N/2 \times N/2 \times 3$ array of macroscale *numerical* patch scheme eigenvalues λ_{pM}^N .

The third dimension of these three arrays establishes the wavenumber-wise correspondence among the three eigenvalues $\lambda_{m\delta}^{NE1}$, λ_{pM}^{NE1} and λ_{pM}^N . For any macroscale wavenumber (k_x, k_y) resolved on a patch grid, each of the three elements along the third dimension of the eigenvalues $\lambda_{m\delta}^{NE1}$ and λ_{pM}^N gives the required three element vectors $\underline{\lambda}_{m\delta}^A$ and $\underline{\lambda}_{pM}^N$ in the patch scheme eigenvalue error (4.5.1). As explained in p. 123 of §3.6, for $N = 6$, there are no macroscale eigenvalues corresponding to wavenumber $(k_x, k_y) = (2, 1)$, and so the eigenvalue error $\epsilon^{2,1}$ is computed only for $N \geq 10$.

4.5.1 Spectral patch scheme is uniformly accurate

With the highly accurate global spectral interpolation (§2.2.1), as in §3.6.1 for the general linear wave, we expect the *Spectral patch scheme to resolve the macroscale modes exactly* (within numerical roundoff errors), irrespective of the number of macro-grid intervals N (e.g., the spectra in Figs. 4.2.5 and 4.2.6). That is, the Spectral patch scheme is uniformly accurate with the full-domain microscale model without any dependence on the macro-grid interval Δ . To confirm this exactness, this subsection shows that the accuracy of the macroscale modes indeed does not deteriorate with decreasing macro-grid interval Δ (increasing N). Specifically, this subsection studies this exactness via the eigenvalue errors $\epsilon^{1,0}$, $\epsilon^{1,1}$ and $\epsilon^{2,1}$ of the Spectral patch scheme for all the 1728 combinations of the parameters h_M, u_M, Re, N, n, r listed in Table 4.5.1.

For large Reynolds number $Re \gtrsim 250$, *Spectral patch scheme is uniformly accurate*. Figure 4.5.1 plots the eigenvalue errors $\epsilon^{1,0}$ versus macro-grid intervals Δ for the best case (with smallest errors) of large Reynolds number $Re = 1250$, and mean flow $(h_M, u_M) = (0.1, 0)$ for different patch scale

Figure 4.5.1. Reynolds number $Re = 1250$, $(h_M, u_M) = (0.1, 0)$. Best case eigenvalue errors $\epsilon^{1,0}$ (log scale) of the Spectral staggered patch scheme for different macro-grid intervals Δ and patch scale ratio r (as in Table 4.5.2, for $r = 0.1$, $n = 6$, $\min(\max_N \epsilon^{1,0}) = 10^{-12.3} = 4.6 \cdot 10^{-13}$).

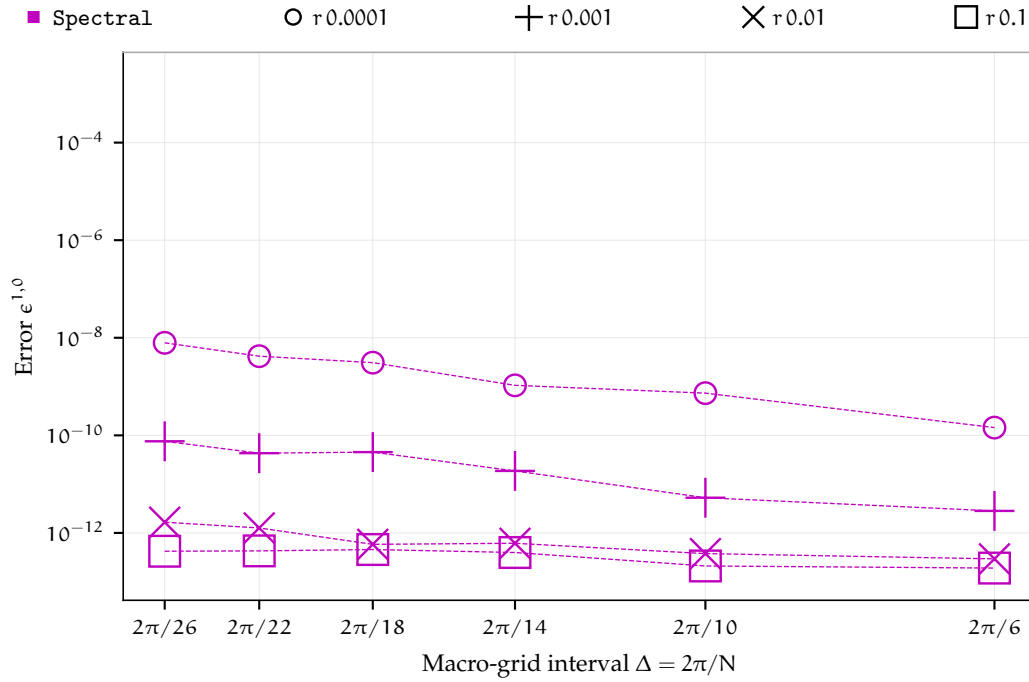


Table 4.5.2. Reynolds number $Re = 1250$. Maximum logarithmic eigenvalue error $\max_N \log_{10}(\epsilon^{1,0})$ of the Spectral staggered patch scheme over the number of macro-grid intervals N in Table 4.5.1. The grey box highlights the largest error in each column. Eigenvalue errors $\epsilon^{1,0} \leq 10^{-5}$. Overall $\min(\max_N \epsilon^{1,0}) = 10^{-12.3}$ for $(h_M, u_M) = (0.1, 0)$, $r = 0.1$, $n = 6$.

h_M, u_M	Patch scale ratio r							
	0.0001		0.001		0.01		0.1	
	$n = 6$	$n = 10$	$n = 6$	$n = 10$	$n = 6$	$n = 10$	$n = 6$	$n = 10$
0.1, 0	-8.1	-7.5	-10	-9.3	-12	-11	-12	-12
0.1, 0.4	-6.6	-8.3	-8.6	-8.9	-11	-10	-11	-11
0.1, 0.8	-5.5	-7.9	-7.5	-8.5	-9.4	-9.1	-11	-11
0.2, 0	-7.6	-6.9	-9.7	-8.9	-11	-11	-12	-12
0.2, 0.4	-5.7	-7.8	-7.6	-8.3	-9.6	-9.4	-11	-11
0.2, 0.8	-5	-7.8	-7	-8.4	-9	-8.9	-11	-11
0.3, 0	-7.3	-6.7	-9.4	-8.9	-11	-11	-12	-12
0.3, 0.4	-6.2	-7.1	-8.2	-9.2	-10	-10	-12	-12
0.3, 0.8	-5.1	-7.8	-7.2	-8.7	-9.2	-9.2	-11	-11

ratio r . [Figure 4.5.1](#) shows that maximum eigenvalue error $\epsilon^{1,0} \approx 8 \cdot 10^{-9}$ for smallest patch scale ratio $r = 0.0001$ and smallest macro-grid interval $\Delta = 2\pi/26$ (for the non-dimensional domain size 2π). For larger patch scale ratio $r > 0.0001$, the eigenvalue errors are smaller. That is, for large Reynolds number $Re \gtrsim 250$, Spectral patch scheme is uniformly accurate without any dependence on the macro-grid interval Δ .

For large Reynolds number $Re \gtrsim 250$, Spectral patch scheme is uniformly accurate over a wide range of the mean flow (h_m, u_M) . For a large Reynolds number $Re = 1250$, for various mean flow (h_M, u_M) , patch scale ratio r , and the number of sub-patch micro-grid intervals n , [Table 4.5.2](#) shows the maximum eigenvalue errors $\epsilon^{1,0}$ of the Spectral patch scheme over six different number of macro-grid intervals N in [Table 4.5.1](#). [Table 4.5.2](#) shows that for a large Reynolds number $Re = 1250$, the maximum eigenvalue error $\max_{N, h_M, u_M} \epsilon^{1,0} = 10^{-5}$ over the six different number of macro-grid intervals N and nine different mean flows (h_M, u_M) in [Table 4.5.1](#). This small maximum eigenvalue error $\max_{N, h_M, u_M} \epsilon^{1,0}$ shows that for large Reynolds number $Re \gtrsim 250$, Spectral patch scheme is uniformly accurate over a wide range of the mean flow (h_m, u_M) , without any dependence on the macro-grid interval Δ .

For small Reynolds number $Re \lesssim 250$ the seemingly large eigenvalue errors of the Spectral patch scheme is due to numerical roundoff error. [Page 214 of §4.3](#) shows that for small grid interval $\delta \lesssim 10^{-5}$ (i.e., small r and/or small Δ), large mean height $h_M \gtrsim 0.2$ and small Reynolds number $Re \lesssim 10$, the numerically computed patch scheme eigenvalues have nonnegligible numerical roundoff errors. Both from the parametric trends of the numerical roundoff errors and from using scaling arguments on the viscous shallow water flows, [§4.3](#) shows that the nonnegligible numerical roundoff errors in the patch scheme eigenvalues are due to the inherent sensitivity of the underlying microscale model and the numerical computation of near-zero repeated eigenvalues. As [§4.3](#) shows, the numerical roundoff errors in the patch scheme eigenvalues are nonnegligible only for small Reynolds Re . Yet the onset of the effect of numerical roundoff errors is seen even for large Reynolds number $Re \sim 1250$. For example, in [Fig. 4.5.1](#), for small patch scale ratio $r = 0.0001$ the monotonically increasing eigenvalue error $\epsilon^{1,0}$ (magenta circles) with decreasing macro-grid intervals Δ is due to the numerical roundoff errors. Except fluctuating small deviations, [Table 4.5.2](#) shows that in general the maximum eigenvalue error $\max_N \epsilon^{1,0}$ increases with decreasing patch scale ratio r and increasing mean height h_M , which is also due to numerical roundoff error. For small Reynolds number $Re \lesssim 250$ the patch scheme eigenvalues have large numerical roundoff errors. For example, for a small Reynolds number $Re = 10$, [Fig. 4.5.2](#) shows large eigenvalue

Figure 4.5.2. Reynolds number $Re = 10$, $(h_M, u_M) = (0.3, 0)$. Worst case eigenvalue errors $\epsilon^{1,0}$ (log scale) of the Spectral staggered patch scheme for different macro-grid intervals Δ and patch scale ratio r (as in Table 4.5.3, for $r = 0.0001$, $n = 10$, $\max(\max_N \epsilon^{1,0}) = 10^{-2.5} = 0.0034$).

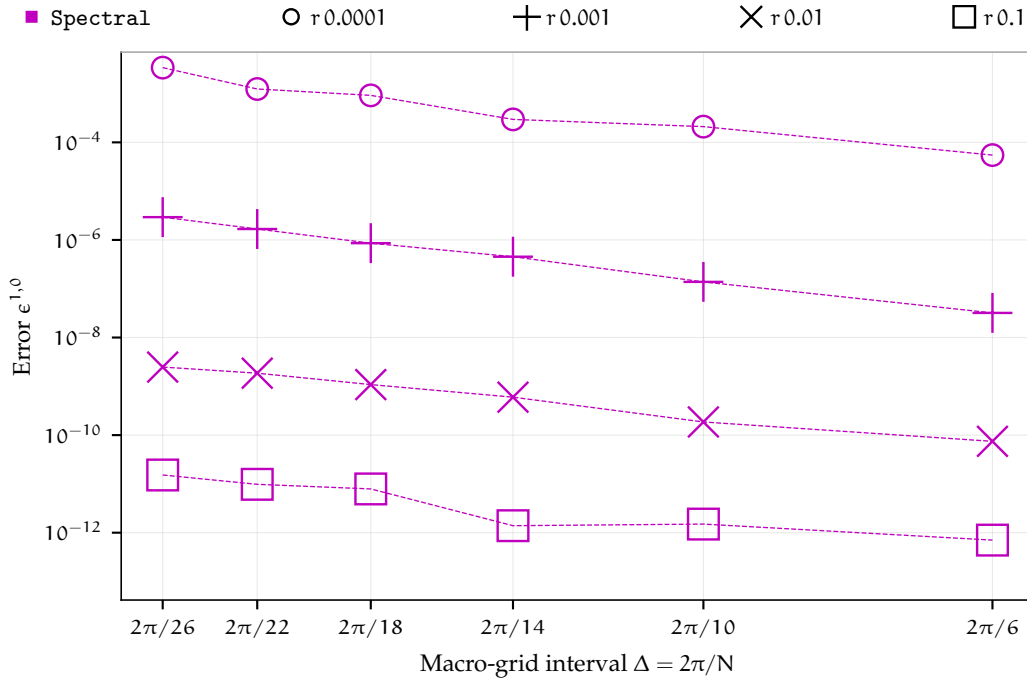


Table 4.5.3. Reynolds number $Re = 10$. Maximum logarithmic eigenvalue error $\max_N \log_{10}(\epsilon^{1,0})$ for Spectral patch scheme over six different number of macro-grid intervals N in Table 4.5.1. Grey box highlights largest error in each column, red colour highlights $\epsilon^{1,0} > 10^{-5}$.

h_M, u_M	Patch scale ratio r							
	0.0001		0.001		0.01		0.1	
	$n = 6$	$n = 10$	$n = 6$	$n = 10$	$n = 6$	$n = 10$	$n = 6$	$n = 10$
0.1, 0	-4.4	-3.6	-7.4	-6.7	-10	-9.6	-12	-11
0.1, 0.4	-4.7	-4.4	-7.1	-7.4	-9.1	-9.5	-9.5	-9.5
0.1, 0.8	-3.5	-4.7	-5.6	-7.8	-7.6	-9.3	-9.4	-9.4
0.2, 0	-3.5	-2.9	-6.6	-5.8	-9.5	-8.8	-11	-11
0.2, 0.4	-3.7	-4.1	-5.6	-6.9	-7.7	-9.7	-9.8	-10
0.2, 0.8	-2.9	-3.9	-4.8	-6.8	-6.9	-9.6	-8.9	-10
0.3, 0	-3	-2.5	-6.3	-5.5	-9.2	-8.6	-11	-11
0.3, 0.4	-3.8	-3.4	-6	-6	-8.3	-9.2	-10	-10
0.3, 0.8	-3	-3	-5	-6.5	-7	-9.4	-9	-10

error $\epsilon^{1,0} = 0.0034$. [Figure 4.5.2](#) and [Table 4.5.3](#) also show that the large eigenvalues errors $\max_N \epsilon^{1,0}$ correspond to small grid interval $\delta \lesssim 10^{-5}$ (i.e., small r and/or small Δ) and large mean height $h_M \gtrsim 0.2$, for which the numerically computed patch scheme eigenvalues have nonnegligible numerical roundoff errors ([p. 214](#) of [§4.3](#)). That is, for small Reynolds $Re \lesssim 250$ the seemingly large eigenvalue error $\epsilon^{1,0}$ for the Spectral patch scheme does not reflect the characteristic of the patch scheme, but an artifact due to numerical roundoff errors in numerically computing the patch scheme eigenvalues.

The preceding paragraph shows the evidence that the seemingly large Spectral patch scheme eigenvalue errors $\epsilon^{1,0}$ for small Reynolds numbers are due to numerical roundoff errors. The *arbitrary-precision floating-point arithmetic definitively confirms that the seemingly large eigenvalue errors $\epsilon^{1,0}$ for small Reynolds number are indeed due to numerical roundoff errors* in numerical eigenvalue computation. Using the analytic patch scheme eigenvalues λ_{pM}^{NE1} of the numerically evaluated analytic one-cell Jacobian ([§4.2.3](#)) in place of the numerical eigenvalues λ_{pM}^N in the eigenvalue error ([4.5.1](#)), gives about five times smaller eigenvalue error $\epsilon^{1,0}$ compared to the eigenvalue error $\epsilon^{1,0}$ of the numerical patch scheme eigenvalues. For example, in [Fig. 4.5.2](#) for Reynolds number $Re = 10$, mean flow $(h_M, u_M) = (0.3, 0)$ on a patch grid with $N = 10$ macro-grid intervals, $n = 6$ sub-patch micro-grid intervals and patch scale ratio $r = 0.0001$, the error $\epsilon^{1,0} = 7.5 \cdot 10^{-5}$ for numerical eigenvalue λ_{pM}^N , but the error $\epsilon^{1,0} = 1.5 \cdot 10^{-5}$ for the analytic patch scheme eigenvalues λ_{pM}^{NE1} . The analytic eigenvalues λ_p^{NE1} are still computed numerically after evaluating the one-cell Jacobian for specific numeric values of the wavenumber (k_x, k_y) and physical parameters Re, h_M, u_M . So, the analytic eigenvalues λ_p^{NE1} also have numerical roundoff errors due to the numerical eigenvalue computation. As a further step to confirm that the seemingly large eigenvalue errors of the Spectral patch scheme is indeed due to numerical roundoff error, we resort to `mpmath`, a Python library for arbitrary-precision floating-point arithmetic ([Johansson et al. 2018](#)). Specifically, we evaluate the one-cell analytic Jacobian ([§4.2.3](#)) using the higher precision `mpmath` floating-point number format and compute the eigenvalues using `mpmath`'s arbitrary-precision eigenvalue function. For the case of $N = 10$, $r = 0.0001$ in [Fig. 4.5.2](#) with $Re = 10$, $(h_M, u_M) = (0.3, 0)$, analytic eigenvalues λ_p^{NE1} evaluated using `mpmath` with the precision of 80 decimal places gives the eigenvalue error $\epsilon^{1,0} = 6.8 \cdot 10^{-8}$, compared to the large $\epsilon^{1,0} = 7.5 \cdot 10^{-5}$ of the numerical eigenvalues λ_p^{NE1} (four orders of magnitude less error). This small eigenvalue error $\epsilon^{1,0}$ of the arbitrary-precision floating-point arithmetic definitively confirms that the seemingly large eigenvalue errors $\epsilon^{1,0}$ for small Reynolds number are indeed due to

numerical roundoff errors in numerical eigenvalue computation. That is, the accuracy of the Spectral patch scheme eigenvalues do not deteriorate with decreasing macro-grid interval Δ (increasing N).

The preceding paragraphs explore the eigenvalue errors $\max_N \epsilon^{1,0}$ for small and large Reynolds numbers $Re \in \{10, 1250\}$ (i.e., the worst and best-case errors). For various Reynolds number Re , patch scale ratio r , and number of sub-patch micro-grid intervals n , Table 4.5.4 shows the maximum eigenvalue error $\max_{N, h_M, u_M} \epsilon^{1,0}$ of the Spectral patch scheme over six different number of macro-grid intervals N and nine different mean flows (h_M, u_M) in Table 4.5.1. Table 4.5.4 shows the progressively decreasing maximum eigenvalue error $\max_{N, h_M, u_M} \epsilon^{1,0}$ with increasing Reynolds number Re for both $n = 6$ and $n = 10$. Similarly, Tables 4.5.5 and 4.5.6 show

Table 4.5.4. Maximum logarithmic eigenvalue error $\max_{N, h_M, u_M} \log_{10}(\epsilon^{1,0})$ of the Spectral patch scheme over the number of macro-grid intervals N and mean flows (h_M, u_M) in Table 4.5.1. Grey box highlights largest error in each column, red colour highlights large $\epsilon^{1,0} > 10^{-5}$.

Re	Patch scale ratio r							
	0.0001		0.001		0.01		0.1	
	$n = 6$	$n = 10$	$n = 6$	$n = 10$	$n = 6$	$n = 10$	$n = 6$	$n = 10$
10	-2.9	-2.5	-4.8	-5.5	-6.9	-8.6	-8.9	-9.4
50	-3.6	-4.1	-5.6	-7	-7.6	-9.5	-9.5	-9.6
250	-4.3	-5.4	-6.3	-8.4	-8.3	-9.1	-10	-10
1250	-5	-6.7	-7	-8.3	-9	-8.9	-11	-11

Table 4.5.5. Maximum logarithmic eigenvalue error $\max_{N, h_M, u_M} \log_{10}(\epsilon^{1,1})$ of the Spectral patch scheme over the number of macro-grid intervals N and mean flows (h_M, u_M) in Table 4.5.1. Grey box highlights largest error in each column, red colour highlights large $\epsilon^{1,1} > 10^{-5}$.

Re	Patch scale ratio r							
	0.0001		0.001		0.01		0.1	
	$n = 6$	$n = 10$	$n = 6$	$n = 10$	$n = 6$	$n = 10$	$n = 6$	$n = 10$
10	-2.8	-2.8	-4.8	-5.7	-6.9	-8.5	-8.9	-9.4
50	-3.7	-4.1	-5.7	-7.2	-7.8	-9.4	-9.7	-9.7
250	-4.5	-5.5	-6.4	-8	-8.5	-9.3	-10	-10
1250	-5.2	-6.9	-7.1	-8.5	-9.2	-9	-11	-11

Table 4.5.6. Maximum logarithmic eigenvalue error $\max_{N, h_M, u_M} \log_{10}(\epsilon^{2,1})$ of the Spectral patch scheme over the number of macro-grid intervals N and mean flows (h_M, u_M) in Table 4.5.1. Grey box highlights largest error in each column, red colour highlights large $\epsilon^{2,1} > 10^{-5}$.

Re	Patch scale ratio r							
	0.0001		0.001		0.01		0.1	
	$n = 6$	$n = 10$	$n = 6$	$n = 10$	$n = 6$	$n = 10$	$n = 6$	$n = 10$
10	-3.1	-2.7	-5	-5.7	-7.1	-8.7	-9.1	-9.4
50	-3.9	-4.2	-5.9	-7.1	-7.9	-9.8	-9.8	-9.9
250	-4.6	-5.5	-6.6	-8.4	-8.7	-9.5	-10	-10
1250	-5.3	-7	-7.3	-8.7	-9.4	-9.2	-11	-11

the progressively decreasing maximum eigenvalue errors $\max_{N, h_M, u_M} \epsilon^{1,1}$ and $\max_{N, h_M, u_M} \epsilon^{2,1}$ (for wavenumbers $(k_x, k_y) = (1, 1), (2, 1)$) with increasing Reynolds number Re for both $n = 6$ and $n = 10$. Both the magnitudes and the trends of the eigenvalue errors $\epsilon^{1,1}$ and $\epsilon^{2,1}$ are similar to that of the eigenvalue errors $\epsilon^{1,0}$ in Figs. 4.5.1 and 4.5.2 and Tables 4.5.2 and 4.5.3. As the previous paragraphs show, the seemingly large eigenvalue errors $\epsilon^{1,0}, \epsilon^{1,1}, \epsilon^{2,1}$ for small Reynolds number $Re \lesssim 250$ are due to numerical roundoff errors in numerical eigenvalue computation, not due to any inaccuracy/deficiency in the Spectral patch scheme. That is, for all the explored Reynolds numbers $Re \in \{10, 50, 250, 1250\}$, the accuracy of the Spectral patch scheme eigenvalues do not deteriorate with decreasing macro-grid interval Δ (increasing N). Hence, *the Spectral patch scheme itself is uniformly accurate with the full-domain microscale model without any dependence on the macro-grid interval Δ .*

4.5.2 The four polynomial patch schemes are consistent

As §3.6.2 for the general linear wave shows, also for the viscous shallow water flows, the accuracy of the polynomial patch schemes (Square-p2, Square-p4, Square-p6, Square-p8) increases with decreasing macro-grid interval Δ to the same order p as the patch coupling interpolation. This subsection shows this consistency of the polynomial patch schemes through the converging eigenvalue errors $\epsilon^{1,0}, \epsilon^{1,1}$ and $\epsilon^{2,1}$ (corresponding to macro-scale wavenumbers $(k_x, k_y) = (1, 0), (1, 1), (2, 1)$), for all the 6912 combinations of the parameters h_M, u_M, Re, N, n, r listed in Table 4.5.1.

To establish the consistency of the polynomial patch schemes, this subsection studies the convergence of patch scheme eigenvalue errors with decreasing macro-grid Δ , via convergence plots such as Figs. 4.5.4 and 4.5.3. All the convergence plots also contain a power law curve fit (grey solid lines) for the eigenvalue error of the form $\tilde{\epsilon}^{k_x, k_y} = a(b\Delta)^p$. Each convergence plot, contains an eigenvalue error (e.g., $\epsilon^{1,0}$ in Fig. 4.5.4) for a total of 96 cases among the 6912 cases listed in Table 4.5.1: four polynomial patch schemes, one specific number of sub-patch micro-grid intervals n , six macro-grid intervals Δ , four patch scale ratios r , for one set of physical parameters (e.g., Re, h_M, u_M). Hence for each eigenvalue error (e.g., $\epsilon^{1,0}$), the total of 6912 cases listed in Table 4.5.1 lead to 72 convergence plots such as Fig. 4.5.4; the three eigenvalue errors $\epsilon^{1,0}, \epsilon^{1,1}, \epsilon^{2,1}$ lead to a total of 216 convergence plots. This subsection explicitly presents four such convergence plots (Figs. 4.5.3 to 4.5.6) that are representative of the best and worst eigenvalue convergence.

For large Reynolds number $Re \gtrsim 250$ the macroscale eigenvalues of all the polynomial patch schemes converge as Δ decreases to the same order p as the interpolation for the patch coupling. For the eigenvalue error $\epsilon^{1,0}$ of the macroscale wavenumber $(k_x, k_y) = (1, 0)$, many among the 72 convergence plots (each for different n, Re, h_M, u_M in Table 4.5.1) show good convergence, where the eigenvalue error $\epsilon^{1,0}$ closely follows the power law curve fit (grey solid lines). That is, the eigenvalue errors $\epsilon^{1,0} \approx a(b\Delta)^p$, where p is the interpolation order of the polynomial patch scheme (e.g., $p = 4$ for the patch scheme Square-p4). For example, for the best-case convergence of the eigenvalue error $\epsilon^{1,0}$, for Reynolds number $Re = 1250$, mean flow $(h_M, u_M) = (0.2, 0)$ over a patch grid with $n = 6$ sub-patch micro-grid intervals, the convergence plot (not included) is visually identical to Fig. 3.6.4 of §3.6.2 for the general linear wave; but with different coefficients $a = 0.66, b = 0.66$ in the power law curve fit (i.e., $\epsilon^{1,0} \approx 0.66 \cdot (0.66 \cdot \Delta)^p$). Hence, for brevity, we omit such best-case convergence plots throughout this subsection. As with the general linear wave, also for the viscous shallow water flows, the best-case convergence plots of the eigenvalue error $\epsilon^{1,1}$ are identical to the best-case convergence plots of the eigenvalue errors $\epsilon^{1,0}$ both visually and quantitatively. The best-case convergence plots of the eigenvalue error $\epsilon^{2,1}$ for the viscous shallow water flows, are visually identical to Fig. 3.6.8 of §3.6.2 for the general linear wave, but with different coefficients in the power law curve fit. For the general linear wave in §3.6.2 the coefficients a, b in the power law curve fit are the same for different physical parameters c_D, c_V . But for the nonlinear viscous shallow water flows, the coefficients a, b in the power law curve fit are different for different physical parameters Re, h_M, u_M .

Figure 4.5.3. Reynolds number $Re = 10$, $(h_M, u_M) = (0.3, 0)$, $n = 10$. Worst case convergence of $\epsilon^{1,0}$ (log scale) with macro-grid interval Δ , for polynomial patch schemes with interpolation orders $p \in \{2, 4, 6, 8\}$ and different patch scale ratio r . Except numerical roundoff errors for $p \geq 4, r \leq 0.001$, $\epsilon^{1,0}$ converge with power law curve fit $\tilde{\epsilon}^{1,0} = 0.66 \cdot (0.66 \cdot \Delta)^p$ (grey solid lines).

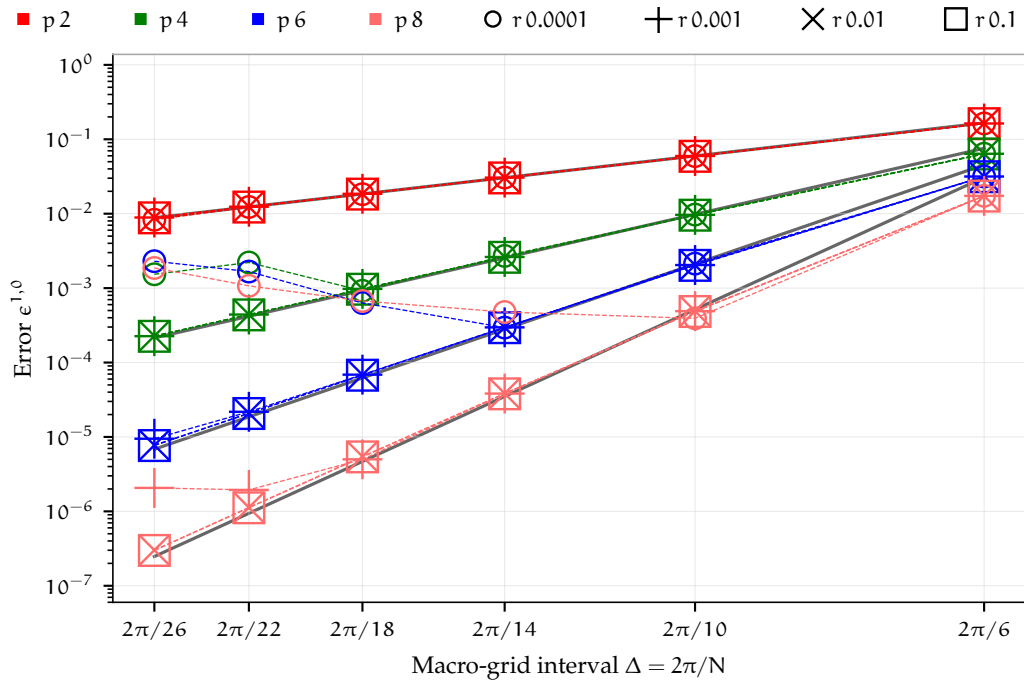
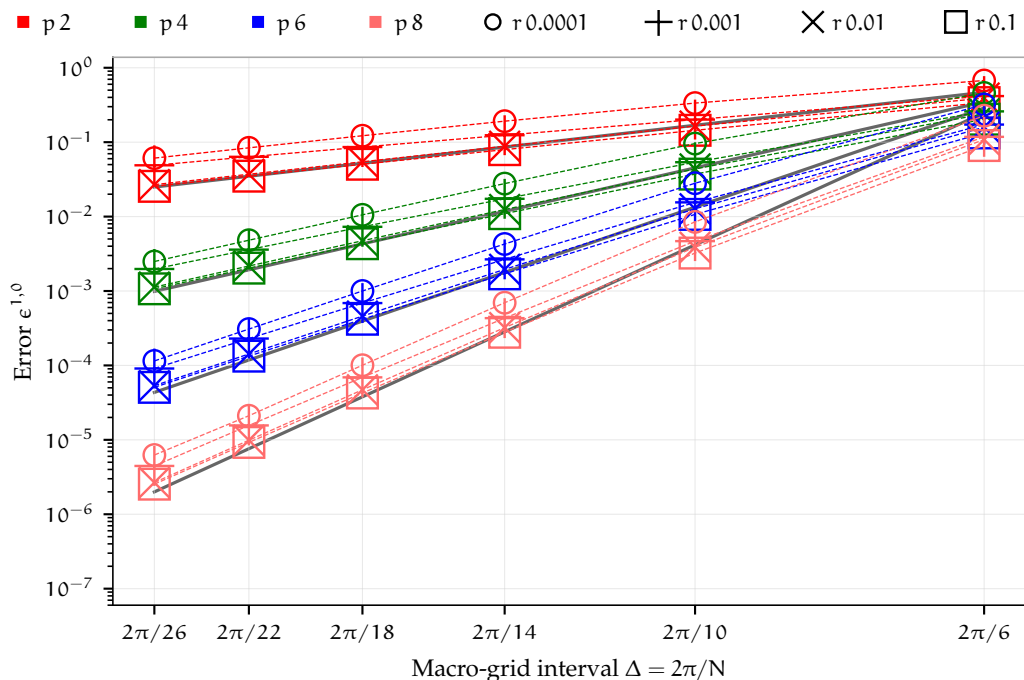


Figure 4.5.4. Reynolds number $Re = 1250$, $(h_M, u_M) = (0.2, 0.4)$, $n = 6$. For small $r \lesssim 0.001$, convergence of $\epsilon^{1,0}$ deteriorates for all macro-grid interval Δ due to numerical roundoff error, for all polynomial patch schemes with interpolation orders $p \in \{2, 4, 6, 8\}$. Convergence deterioration is only via coefficients in the power law $\epsilon^{1,0} \approx 0.83 \cdot (0.82 \cdot \Delta)^p$, not in the order p .



The previous paragraph shows the eigenvalue convergence for large Reynolds number $Re \gtrsim 250$. Also for small Reynolds number $Re \lesssim 250$ the macroscale eigenvalues of all the polynomial patch schemes converge as Δ decreases to the same order p as the interpolation for the patch coupling (except the numerical roundoff errors for small patch scale ratio). Figure 4.5.3 shows the worst case convergence of the eigenvalue error $\epsilon^{1,0}$ among the 72 convergence plots (each for different n , Re , h_M , u_M in Table 4.5.1), for the small Reynolds number $Re = 10$, mean flow $(h_M, u_M) = (0.3, 0)$ over a patch grid with $n = 10$ sub-patch micro-grid intervals. In Fig. 4.5.3, except the numerical roundoff errors for higher order patch schemes with $p \geq 4$ and small patch scale ratio $r \leq 0.01$ (green, blue and light red circles), the eigenvalue error $\epsilon^{1,0}$ of all the polynomial patch schemes converge to the same order p as the patch coupling interpolation. That is, except for $p \geq 4, r \leq 0.01$, eigenvalues converge as $\epsilon^{1,0} \approx 0.66 \cdot (0.66 \cdot \Delta)^p$. As in §4.5.1 for the Spectral patch scheme, the seemingly large deterioration of the eigenvalue convergence in Fig. 4.5.3, for higher order patch schemes with $p \geq 4$ and small patch scale ratio $r \leq 0.01$ is due to numerical roundoff errors for the small Reynolds number $Re = 10$; §4.3 shows the detailed trends of the numerical roundoff errors in the patch scheme eigenvalues. Hence, for all Reynolds numbers $Re \in \{10, 50, 250, 1250\}$, the macroscale eigenvalues of all the polynomial patch schemes converge to the same order p as the patch coupling interpolation.

For large Reynolds number $Re \gtrsim 250$, the numerical roundoff errors for small patch scale ratio $r \lesssim 0.001$ do not affect the order of convergence. Figure 4.5.3 shows that for small Reynolds number $Re = 10$, for higher order patch schemes with $p \geq 4$ and small patch scale ratio $r \leq 0.01$, the eigenvalue convergence deteriorates only for small $\Delta \lesssim 2\pi/14$ due to numerical roundoff error. On the other hand, Fig. 4.5.4 shows that for large Reynolds number $Re = 1250$, and $u_M = 0.2$, for all the polynomial patch schemes with small patch scale ratio $r \leq 0.01$, the eigenvalue convergence deteriorates for all macro-grid interval Δ , which is also due to numerical roundoff error. But, unlike for the small Reynolds number $Re = 10$ in Fig. 4.5.3, Fig. 4.5.4 shows that for large Reynolds number $Re = 1250$ the eigenvalue convergence deterioration is only via the coefficients a, b in the power law $\epsilon^{1,0} \approx a(b\Delta)^p$. This trend of eigenvalue convergence deterioration via coefficients a, b in the power law due to numerical roundoff errors, also extends to other large Reynolds numbers $Re \gtrsim 250$. That is, for large Reynolds number $Re \gtrsim 250$, the numerical roundoff errors for small patch scale ratio $r \lesssim 0.01$ do not affect the order of convergence.

Figure 4.5.5. Reynolds number $Re = 10$, $(h_M, u_M) = (0.3, 0)$, $n = 10$. *Worst case convergence* of $\epsilon^{1,1}$ (log scale) with macro-grid interval Δ , for polynomial patch schemes with interpolation orders $p \in \{2, 4, 6, 8\}$ and different patch scale ratio r . Except numerical roundoff errors for $p \geq 4, r \leq 0.001$, $\epsilon^{1,1}$ converge with power law curve fit $\tilde{\epsilon}^{1,1} = 0.65 \cdot (0.65 \cdot \Delta)^p$ (grey solid lines).

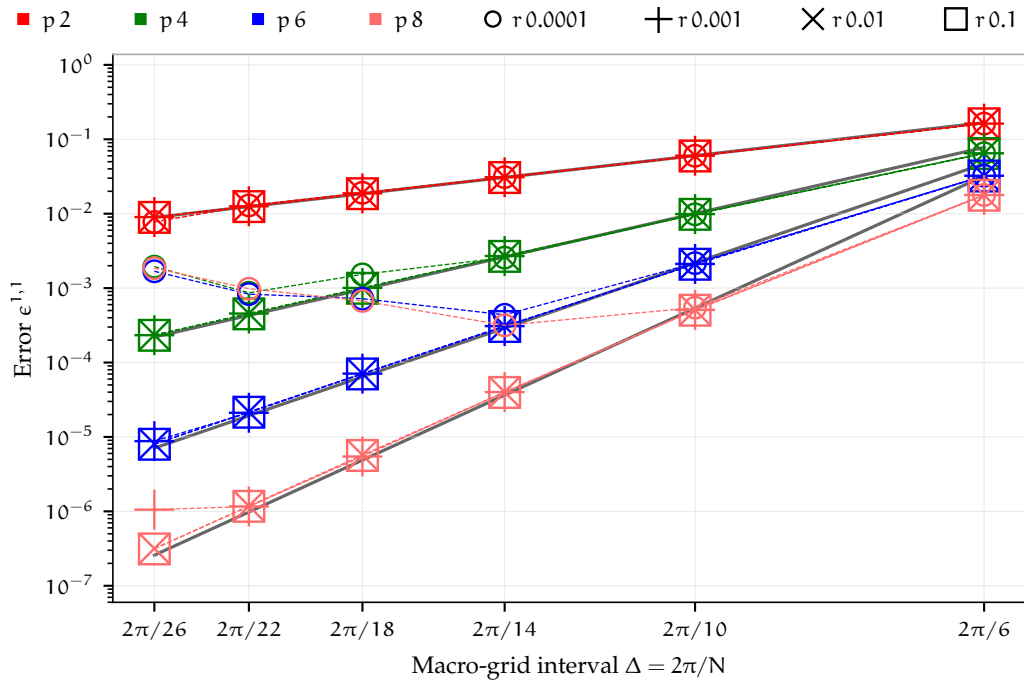
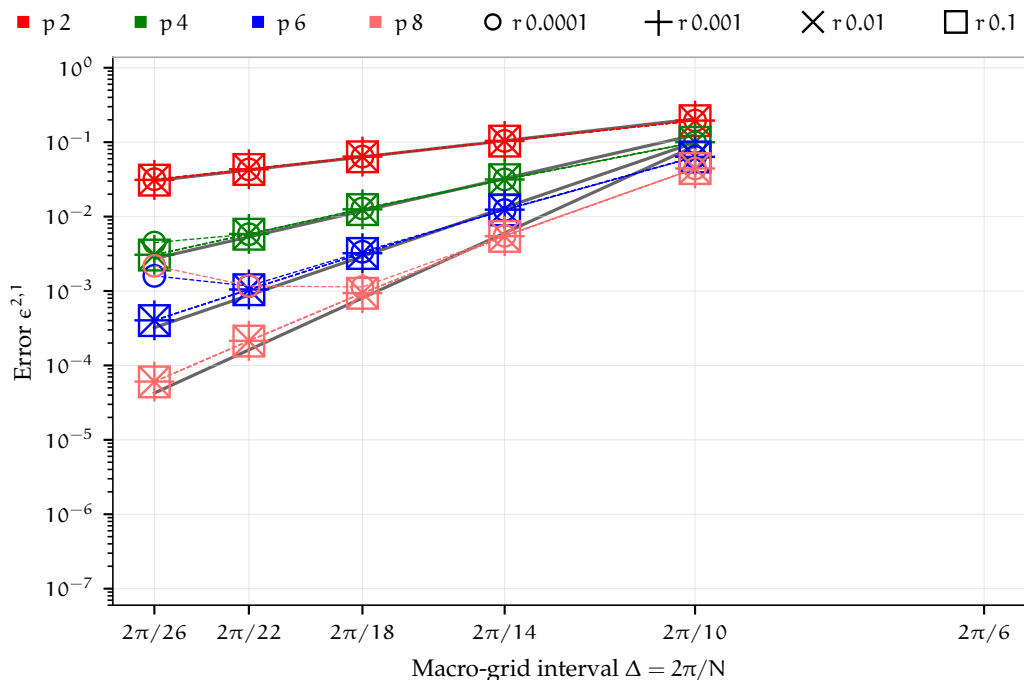


Figure 4.5.6. Reynolds number $Re = 10$, $(h_M, u_M) = (0.3, 0)$, $n = 10$. *Worst case convergence* of $\epsilon^{2,1}$ (log scale) with macro-grid interval Δ , for polynomial patch schemes with interpolation orders $p \in \{2, 4, 6, 8\}$ and different patch scale ratio r . Except numerical roundoff errors for $p \geq 4, r \leq 0.001$, $\epsilon^{2,1}$ converge with power law curve fit $\tilde{\epsilon}^{2,1} = 0.64 \cdot (1.2 \cdot \Delta)^p$ (grey solid lines).



All the qualitative characteristics of the preceding paragraphs in this subsection about the convergence of eigenvalue error $\epsilon^{1,0}$ and the numerical roundoff errors, also hold for the eigenvalue errors $\epsilon^{1,1}$ and $\epsilon^{2,1}$. For example, Figs. 4.5.5 and 4.5.6 show the worst case convergence of the eigenvalue errors $\epsilon^{1,1}$ and $\epsilon^{2,1}$ respectively. A patch grid with 6×6 macro-grid intervals resolves only the nine macroscale wavenumber $(k_x, k_y) : k_x, k_y = 0, \pm 1$, hence there are no data points of $\epsilon^{2,1}$ for $\Delta = 2\pi/6$ in Fig. 4.5.6. As in Fig. 4.5.3 for the eigenvalue error $\epsilon^{1,0}$, the deterioration of the eigenvalue convergence of $\epsilon^{1,1}$ and $\epsilon^{2,1}$ in Figs. 4.5.5 and 4.5.6, for higher order patch schemes with $p \geq 4$ and small patch scale ratio $r \leq 0.01$ is due to numerical roundoff errors for the small Reynolds number $Re = 10$; §4.3 shows the detailed trends of the numerical roundoff errors in the patch scheme eigenvalues. Hence, as the macroscale eigenvalue of wavenumber $(k_x, k_y) = (1, 0)$, also the macroscale eigenvalues of macroscale wavenumbers $(k_x, k_y) = (1, 1), (2, 1)$ of all the polynomial patch schemes converge to the same order p as the patch coupling interpolation.

Except the numerical roundoff errors, the following listing gives two global trends about the dependence of the eigenvalue errors $\epsilon^{1,0}$, $\epsilon^{1,1}$ and $\epsilon^{2,1}$ on the mean height h_M and mean velocity u_M . The following points hold for all the macro-grid interval Δ , for all the patch scale ratio r and for the patch schemes of all interpolation order p .

1. For any fixed Reynolds number Re and any fixed mean height h_M , increasing the mean velocity u_M increases the eigenvalue errors monotonically. These increasing errors are still within worst convergence shown in Figs. 4.5.3, 4.5.5 and 4.5.6 for the eigenvalue errors $\epsilon^{1,0}$, $\epsilon^{1,1}$ and $\epsilon^{2,1}$ respectively. This dependence of eigenvalue errors on mean velocity u_M remains the same for all mean height $h_M \in \{0.1, 0.2, 0.3\}$, and all Reynolds numbers $Re \in \{10, 50, 250, 1250\}$.
2. For a fixed small Reynolds number $Re \lesssim 250$ and any fixed mean velocity u_M , increasing the mean height h_M increases the eigenvalue errors up to about $h_M = 0.4$ and then decreases. These increasing errors are still within worst convergence shown in Figs. 4.5.3, 4.5.5 and 4.5.6 for the eigenvalue errors $\epsilon^{1,0}$, $\epsilon^{1,1}$ and $\epsilon^{2,1}$ respectively. This dependence of eigenvalue errors on mean height h_M decreases with increasing mean velocity $u_M \in \{0, 0.4, 0.8\}$, and is negligible for large Reynolds number $Re \gtrsim 250$.

As the preceding listing explains, the change in the eigenvalue errors with increasing h_M , u_M retains the same order of convergence p with macro-grid interval Δ as the order p of the patch coupling interpolation. Thus,

for the viscous shallow water flows all the *four polynomial patch schemes are consistent with the full-domain microscale model to the same order p as the patch coupling interpolation, and with the same order of convergence p for all the physical parameters Re, h_M, u_M .*

4.6 Staggered patch schemes are invariant to flow direction

Almost all the key studies in this chapter are performed for a wide range of parameters but keeping the horizontal mean velocity $v_M = 0$. That is, most results in this chapter correspond to flow angle $\alpha = \arctan(v_M/u_M) = 0$, where the velocities are $u_M = q \cos(\alpha)$ and $v_M = q \sin(\alpha)$.

- [Section 4.2.6](#) shows that the staggered patch schemes are accurate showing the results for $\alpha = 0$.
- [Section 4.3](#) shows that the patch schemes are not sensitive to numerical roundoff errors based on a study over a range of velocities, but all with $v_M = 0$, that is with $\alpha = 0$.
- [Section 4.4](#) establishes that the staggered patch schemes are not artificially unstable showing the results over a range of velocities all with $\alpha = 0$.
- [Section 4.5](#) establishes the consistency of the staggered patch scheme showing the results for different velocities all with $\alpha = 0$.

This section validates that assumption, by showing that the variation of the patch scheme eigenvalue errors is negligible with varying flow angles α , or equivalently for varying coordinate frame orientation.

To establish that the patch schemes are invariant (within discretisation errors) with flow angle $\alpha = \arctan(v_M/u_M)$, this subsection shows that the eigenvalue errors $\epsilon^{1,0}$, $\epsilon^{1,1}$, and $\epsilon^{2,1}$ are small for all the flow angles $\alpha \in \{0^\circ, 10^\circ, 20^\circ, \dots, 360^\circ\}$.

Patch scheme eigenvalue errors are small irrespective of the flow angles α and the magnitude of velocity q . For Spectral and Square-p8 patch schemes, [Figs. 4.6.1](#) and [4.6.2](#) plot the variation of the eigenvalue error $\epsilon^{1,0}$ with the flow angle α , for different magnitudes $q = \sqrt{u_M^2 + v_M^2}$ of mean velocity. In [Figs. 4.6.1](#) and [4.6.2](#), the patch schemes use $N = 22$ macro-grid intervals, $n = 6$ sub-patch micro-grid intervals, and the patch scale ratio $r = 0.001$, for Reynolds number $Re = 250$ and mean height $h_M = 0.2$. [Figures 4.6.1](#)

Figure 4.6.1. Variation of Spectral patch scheme eigenvalue error $\epsilon^{1,0}$ with flow angle α for different magnitudes $q = \sqrt{u_M^2 + v_M^2}$ of mean velocity. Grid parameters are $N = 22$ macro-grid intervals, $n = 6$ sub-patch micro-grid intervals, patch scale ratio $r = 0.001$. physical parameters are Reynolds number $Re = 250$, mean height $h_M = 0.2$.

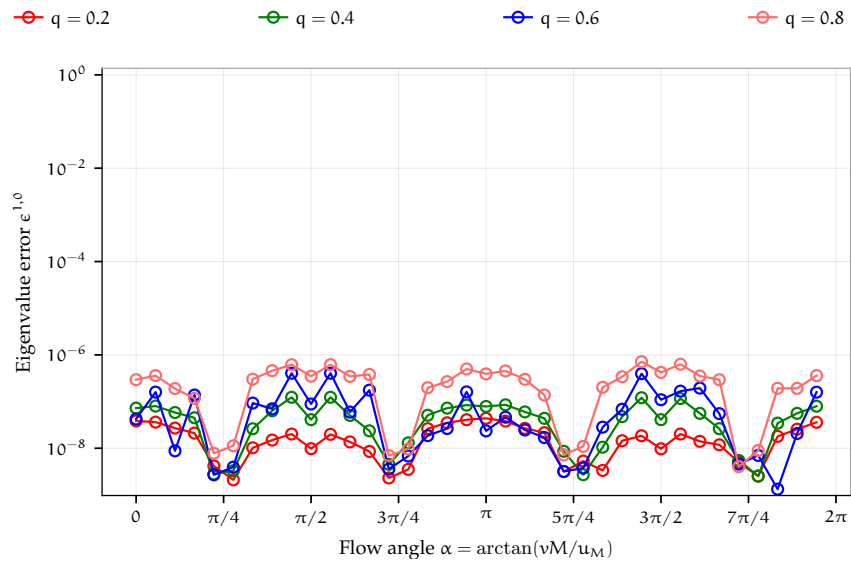
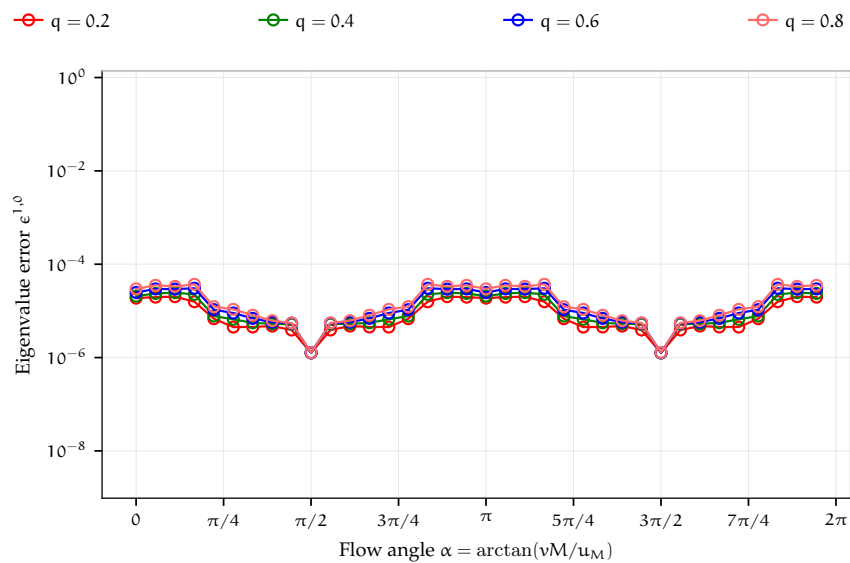


Figure 4.6.2. Variation of Square-p8 patch scheme eigenvalue error $\epsilon^{1,0}$ with flow angle α for different magnitudes $q = \sqrt{u_M^2 + v_M^2}$ of mean velocity for the same grid and physical parameters in Fig. 4.6.1.



and 4.6.2 show that the eigenvalue error $\epsilon^{1,0}$ are small irrespective of the flow angles $\alpha \in \{0^\circ, 10^\circ, 20^\circ, \dots, 360^\circ\}$ and the magnitude of horizontal velocity $q \in \{0.2, 0.4, 0.6, 0.8\}$; specifically, $\epsilon^{1,0} < 8 \cdot 10^{-7}$ for the Spectral and $\epsilon^{1,0} < 4 \cdot 10^{-5}$ for the Square-p8 patch schemes.

Variation of the patch scheme eigenvalue errors with the flow angle α is negligibly small. As Figs. 4.6.1 and 4.6.2 show, the variation of the eigenvalue error $\epsilon^{1,0}$ is small; specifically the eigenvalue error $\epsilon^{1,0}$ is within the same order of magnitude. As the previous paragraph explains, the magnitude of the error itself is small, so this small variation of the eigenvalue errors with the flow angle is negligible. This trend of negligibly small variation of the patch scheme eigenvalue error also holds for the eigenvalue errors $\epsilon^{1,1}$ and $\epsilon^{2,1}$, and also for other patch grid parameters (N, n, r). In general, depending upon the specific patch scheme and the grid parameters, the patch scheme eigenvalue errors vary. Yet, this trend of negligible variation of the patch scheme eigenvalue errors hold for all the five staggered patch schemes (Spectral, Square-p2, Square-p4, Square-p6, Square-p8) irrespective of the patch grid parameters.

The small variation of the patch scheme eigenvalue errors with the flow angle α is due to discretisation error, not a deficiency of the patch schemes. Any discrete grid including that of the full-domain model and a patch scheme, introduces non-isotropy for any discrete numerical simulations. This non-isotropy due to discretisation error leads to small changes in the solution with a change in orientation of flow features (e.g., a wave in some direction), or equivalently the orientation of the coordinate frame. Thus, the small variation of the patch scheme eigenvalue errors with the flow angle α (e.g., in Figs. 4.6.1 and 4.6.2), is mainly due to the microscale and macroscale discretisation error, not a deficiency of the patch schemes.

The previous three paragraphs in this section establish the following three points respectively.

1. Patch scheme eigenvalue errors are small irrespective of the flow angles α and the magnitude of velocity q .
2. Variation of the patch scheme eigenvalue errors with the flow angle α is negligibly small.
3. The small variation of the patch scheme eigenvalue errors with the flow angle α is due to discretisation error, not a deficiency of the patch schemes.

These points together establish that any change in the patch scheme solution with a change in orientation of flow features (e.g., a wave in some direction),

or equivalently any change in the orientation of the coordinate frame, is not due to the patch scheme, *except the small discretisation errors*. Thus, *the staggered patch schemes are invariant to flow direction*.

4.7 Large computational savings via staggered patch schemes

Following very closely §3.7 for the general linear wave, this section quantifies and demonstrates the large computational savings of the staggered patch schemes for the viscous shallow water flows. Section 4.7.1 shows the computational savings of the 2D staggered patch schemes theoretically in terms of the ratio of the space over which the patch schemes and the full-domain model computes. Section 4.7.2 shows the computational savings of the patch schemes in terms of the ratio of the number of state variables for which the patch schemes and the full-domain model computes. Section 4.7.3 quantifies the computational complexity of the staggered patch schemes and compares the compute times of the staggered patch schemes to that of the full-domain microscale model. Section 4.7.4 demonstrates the computational savings of the 2D staggered patch schemes by measuring the elapsed time taken to compute the time derivative of the state vector (one time iteration) using a specific implementation. Section 4.7.5 demonstrates the accuracy and the effectiveness of the staggered patch schemes by numerically simulating a localised nearly discontinuous macroscale viscous roll waves (e.g., Balmforth and Mandre 2004) emerging from the initial condition of a simple progressive wave within the small sparsely located patches. Section 4.7.6 establishes the accuracy of the staggered patch scheme simulations more quantitatively and explains some subtle details of the practical issues in the patch scheme simulations.

4.7.1 Patch schemes compute only within a small fraction of space

As for the general linear wave, also for the viscous shallow water flows, *the staggered patch schemes compute only within a small fraction of the space in the full domain*. Section 3.7.1 for the general linear wave shows that for a small patch scale ratio $r = l/(2\Delta)$, the 2D staggered patch schemes compute only within a small fraction $3r^2$ of the area in the full domain. As all the discussions in §3.7.1 are based on only the area over which computations are performed (i.e., disregarding the specific number of discrete nodes), all

the discussions in §3.7.1 also hold for the viscous shallow water flows. That is, the total area of the simulated space in a patch scheme is $3r^2L^2$ whereas the corresponding total area of the simulated space in a fine-grid full-domain microscale model is L^2 . Thus, for the viscous shallow water flows, the 2D staggered patch schemes compute only within a small fraction $3r^2$ of the space in the full domain.

4.7.2 Patch schemes compute for a small number of state variables

The *staggered patch schemes compute only for a small number of dynamical state variables* compared to the corresponding fine-grid full-domain microscale model with the same grid interval as the sub-patch micro-grid interval δ . Section 4.7.1 gives a rough indication of the computational savings of the staggered patch schemes in terms of the space over which computation happens. This subsection shows the computational savings of the staggered patch schemes more concretely in terms of the number of the dynamical state variables of the 2D staggered patch schemes and that of the corresponding fine-grid full-domain microscale model. As in §4.1.3, for viscous shallow water flows, a staggered patch grid requires two layers of edge nodes in the normal direction to the edges, and one layer of edge nodes in the tangential direction to the edges, as in Fig. 4.1.2b. Yet the patch grid in Fig. 4.1.2a for the general linear wave and the patch grid in Fig. 4.1.2b for the viscous shallow water flows have the same number of patch interior nodes (the filled circles), $n_p^I = (N^2/4)(9n^2/4 - 4n + 2)$, which is same as the number of state variables (p. 21 of §2.1.2). Similarly, for a staggered grid in Fig. 4.1.1 corresponding to a fine-grid full-domain model, with the same grid interval as the sub-patch micro-grid interval δ , the total number of interior nodes is $n_{m\delta}^I = 3N^2n^2/(16r^2)$, same as that of the general linear wave. Hence, all the discussions in §3.7.2 for the general linear wave also hold for the viscous shallow water flows. Specifically, the ratio $n_p^I/n_{m\delta}^I$ of the number of state variables of the staggered patch scheme to that of the fine-grid full-domain microscale model for viscous shallow water flows is same as the expression (3.7.1) of §3.7.2 for general linear wave.

4.7.3 Computational complexity of the staggered patch schemes

As §3.7.3 for the general linear wave, for viscous shallow water flows this subsection quantifies the computational complexity of the staggered patch

schemes and compares the compute times of the staggered patch schemes to that of the full-domain microscale model. As in §3.7.3, to simplify and keep the smaller uncertainties aside, for the patch schemes and the full-domain microscale model this subsection assumes a similar level of vectorisation, and a similar pattern of cache and memory access.

As §4.7.2 details, the total number of state variables n_p^I of a patch scheme, and the total number of state variables $n_{m\delta}^I$ of a fine-grid full-domain model for viscous shallow water flows are respectively the same as those of the general linear wave. Hence, for patch scheme simulation of viscous shallow water flows, the ratio $n_p^I/n_{m\delta}^I$ is same as expression (3.7.1) of §3.7.2 for the general linear wave.

A patch grid for simulating viscous shallow water flows requires a larger number of edge nodes (Fig. 4.1.2b) compared to that of the general linear wave (Fig. 4.1.2a). Hence, for patch scheme simulation of viscous shallow water flows, with $n_{m\delta}^I = 3N^2n^2/(16r^2)$ as in §3.7.3, using expression (4.1.17) for n_p^E ,

$$n_p^E/n_{m\delta}^I = 24r^2/n + 64r^2/(3n^2). \quad (4.7.1)$$

Due to the larger number of edge nodes in the patch grid for the viscous shallow water flows compared to the general linear wave, expression (4.7.1) has $+64r^2/(3n^2)$ as opposed to $-64r^2/(3n^2)$ in the corresponding expression (3.7.5) of $n_p^E/n_{m\delta}^I$ for the general linear wave (p. 136 of §3.7.3).

Using expression (3.7.1) of §3.7.2 for $n_p^I/n_{m\delta}^I$ and expression (4.7.1) for $n_p^E/n_{m\delta}^I$, the ratio of compute time for computing the time derivative of the state vector of a patch scheme to that of the fine-grid full-domain microscale model (i.e., the compute time ratio for one iteration in time simulation) is

$$\begin{aligned} T_p/T_{m\delta} &= (n_p^E T_C + n_p^I T_M)/(n_{m\delta}^I T_M) = (n_p^E/n_{m\delta}^I) (T_C/T_M) + n_p^I/n_{m\delta}^I \\ \Rightarrow T_p/T_{m\delta} &= (T_C/T_M) \left(\frac{24r^2}{n} + \frac{64r^2}{3n^2} \right) + 3r^2 \left(1 - \frac{16}{9n} + \frac{8}{9n^2} \right). \end{aligned} \quad (4.7.2)$$

Due to the larger number of edge nodes in the patch grid for the viscous shallow water flows compared to the general linear wave, expression (4.7.2) has $+64r^2/(3n^2)$ as opposed to $-64r^2/(3n^2)$ in the corresponding expression (3.7.6) of $T_p/T_{m\delta}$ for the general linear wave (p. 136 of §3.7.3).

Substituting $T_C/T_M = 1$ into the compute time ratio (4.7.2) gives a rough indication of the possible computational cost savings of the staggered patch schemes as

$$T_p/T_{m\delta} \lesssim 3r^2 + \frac{56r^2}{3n} + \frac{24r^2}{n^2}. \quad (4.7.3)$$

The expression (4.7.3) has $+24r^2/(n^2)$ as opposed to $-36r^2/(3n^2)$ in the corresponding expression (3.7.7) for the general linear wave (p. 136 of §3.7.3).

4.7.4 Staggered patch schemes simulate with small compute time

Section 4.7.1 shows the computational savings of the 2D staggered patch schemes theoretically in terms of the ratio of the space and the ratio of the number of state variables respectively. As in §3.7.4 for the general linear wave, this section shows the computational savings of the 2D staggered patch schemes by measuring the elapsed time taken to compute the time derivative of the state vector (one time iteration) using a specific implementation in Julia programming language.

As in §3.7.4, this subsection measures the compute time ratio $T_p/T_{m\delta}$ for a specific implementation and compares with expression (4.7.2) by empirically estimating the model compute time per interior node T_M and the coupling compute time per edge node T_C . As in §3.7.4, the compute times in this subsection are measured on a custom assembled liquid-cooled workstation with Intel i7-6900k processor and 64GB DDR4 RAM. Both the full-domain microscale model and the patch schemes are implemented as serial programs.

Figure 4.7.1 plots the measured compute time $T_{m\delta}$ of the fine-grid full-domain microscale model (4.1.11) (p. 166 of §4.1.2), for computing the time derivative of the state vector for the initial condition (3.7.8) of the simple progressive wave (p. 146 of §3.7.5). Figure 4.7.1 plots the compute time $T_{m\delta}$ of the fine-grid full-domain model with the same grid interval as the sub-patch micro-grid interval δ of a staggered patch grid with different number of macro-grid intervals N , sub-patch micro-grid intervals n , and patch scale ratio r . We measured one hundred samples of compute times $T_{m\delta}$ for each of the four Reynolds numbers $Re \in \{10, 50, 250, 1250\}$. Each point in Fig. 4.7.1 is the mean over the four Reynolds numbers Re . For the measured compute times $T_{m\delta}$, fitting one common power law curve (solid lines in Fig. 4.7.1) using expression (3.7.2) (in p. 135 of §3.7.3), we estimate the model compute time per interior node $T_M = 0.19 \mu\text{s}$ (same value for all n , r). The measured compute times $T_{m\delta}$ reasonably closely follow the trend of expression (3.7.2) of §3.7.3 (solid lines). For the viscous shallow water flows, the model compute time $T_M = 0.19 \mu\text{s}$ is about three times larger than the model compute time $T_M = 0.062 \mu\text{s}$ of the general linear wave (p. 137 of §3.7.4). This larger model compute time T_M is due to the relatively larger complexity

Figure 4.7.1. Measured compute times $T_{m\delta}$ of the fine-grid full-domain model (viscous shallow water flows) with the same grid interval as the sub-patch micro-grid interval δ of a staggered patch grid with different N , n , and patch scale ratio r . Solid lines represent expression (3.7.2) (in p. 135 of §3.7.3) with the estimated model compute time $T_M = 0.19 \mu\text{s}$.

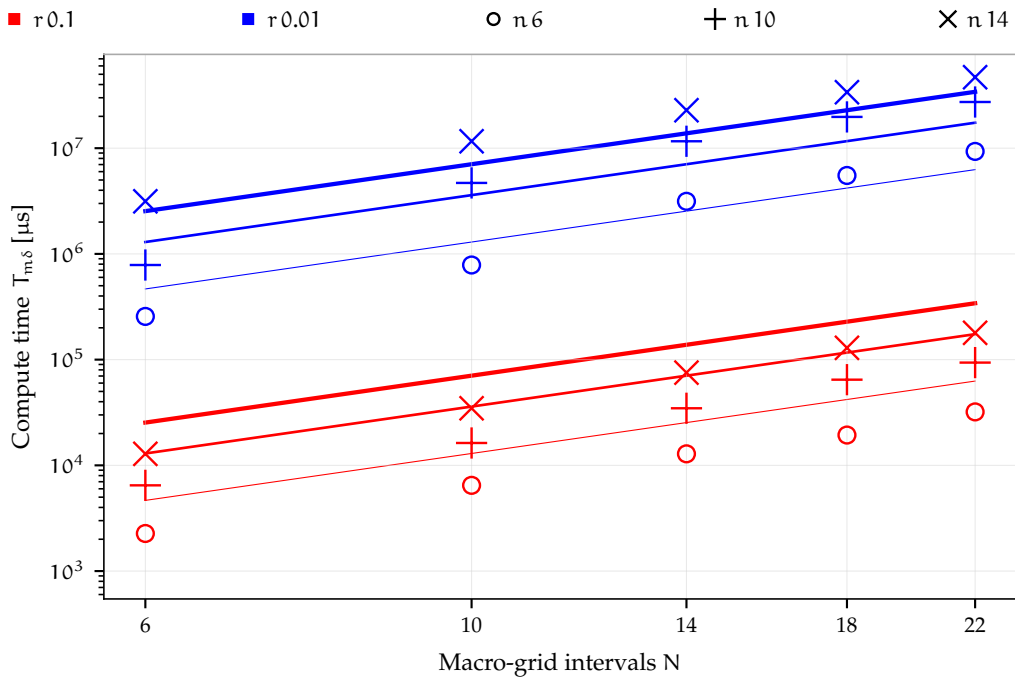
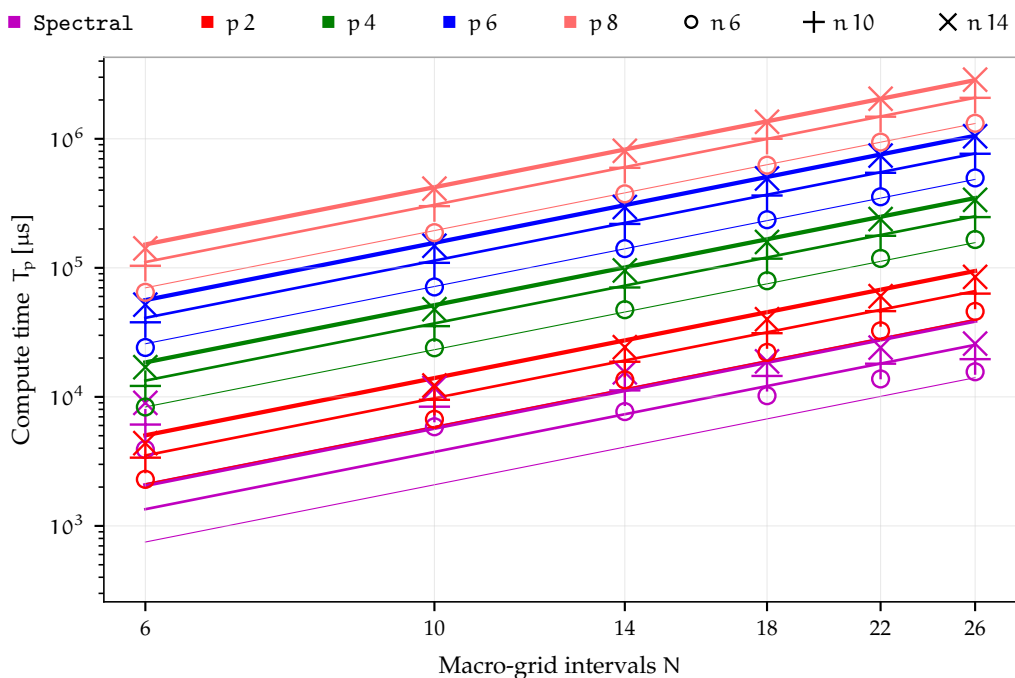


Figure 4.7.2. Measured compute times T_p of the five staggered patch schemes (viscous shallow water flows) with different N and n . Solid lines represent expression (3.7.3) (in p. 136 of §3.7.3) using the estimated model compute time $T_M = 0.19 \mu\text{s}$ and the respective estimated coupling compute times T_C for the five patch schemes.



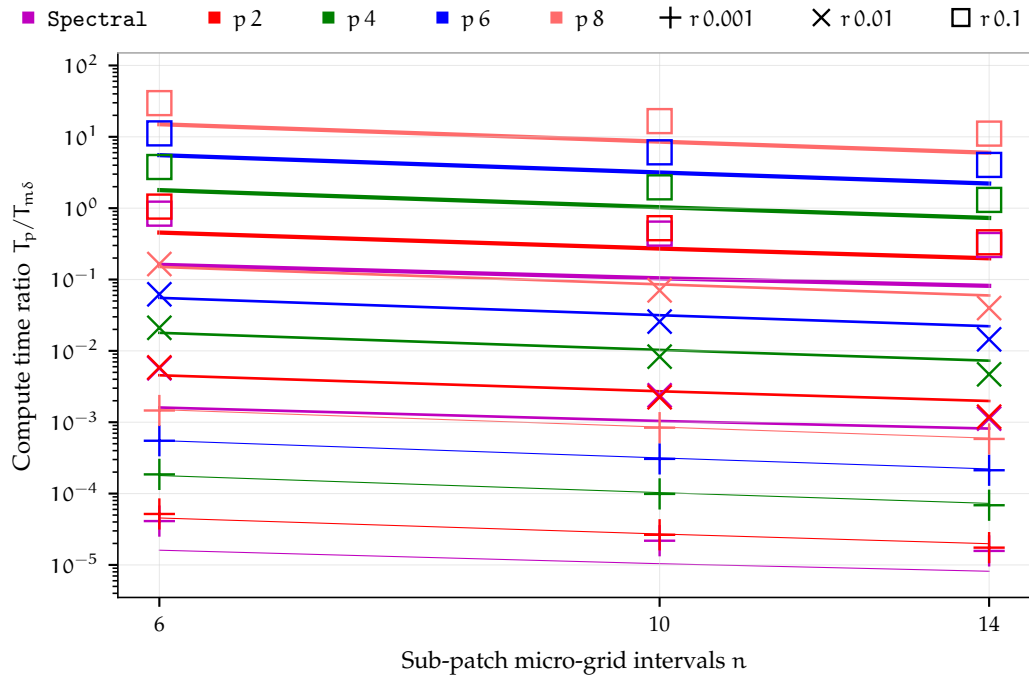
and computations of the microscale model (4.1.11) for the viscous shallow water flows (p. 166 of §4.1.2) compared to the microscale model (3.1.1) for the general linear wave (p. 49 of §3.1).

Figure 4.7.2 plots the measured compute time T_p of the five staggered patch schemes for computing the time derivative of the state vector (i.e., the compute time for one iteration in time simulation), for different macro-grid intervals N and sub-patch micro-grid intervals n . We measured one hundred samples of compute times T_p for each of the four Reynolds numbers $Re \in \{10, 50, 250, 1250\}$. Each point in Fig. 4.7.2 is the mean over the four Reynolds numbers Re . For the measured compute times T_p , fitting a power law curve for each patch scheme (solid lines in Fig. 4.7.2) using the model compute time $T_M = 0.19 \mu\text{s}$ in expression (3.7.3) (in p. 136 of §3.7.3), we estimate the approximate coupling compute times per edge node $T_C = 0.58, 1.8, 7.4, 23, 63 \mu\text{s}$ for the five staggered patch schemes Spectral, Square-p2, Square-p4, Square-p6, and Square-p8 respectively. The measured compute times T_p of all the five staggered patch schemes reasonably closely follow the trend of expression (3.7.3) of §3.7.3 (solid lines).

Except the Spectral patch scheme, the estimated coupling compute times $T_C = 0.58, 1.8, 7.4, 23, 63 \mu\text{s}$ for the viscous shallow water flows are about the same as the coupling compute times $T_C = 0.44, 1.8, 7.6, 24, 63 \mu\text{s}$ of the general linear wave (p. 139 of §3.7.4). There are additional layers of edge nodes in the staggered patch grid for the viscous shallow water flows (Fig. 4.1.2b) compared to the general linear wave (Fig. 4.1.2a). But as the coupling compute times T_C are average patch coupling compute time *per edge node*, the T_C of the viscous shallow water flows and that of the general linear wave are about the same. Yet, as the total patch coupling time $n_p^E T_C$ depends on the number of edge nodes, the total compute time for one iteration T_p in (3.7.3) (in p. 136 of §3.7.3) is larger for the viscous shallow water flows compared to that of the general linear wave. For example, the compute times for one iteration T_p in Fig. 4.7.2 for the viscous shallow water flows are about 15 to 40% larger (depending upon the patch scheme) compared to the T_p in Fig. 3.7.2 of §3.7.4 for the general linear wave.

As in §3.7.4 for the general linear wave, the smallest coupling compute time $T_C = 0.58 \mu\text{s}$ for the spectral patch scheme is because Algorithm 1 efficiently calculates the edge values for all the $h/u/v$ -centred patches in one shot using the fast Fourier transform via the Fourier shift property. As in §3.7.4, for the polynomial patch schemes, the coupling compute time per edge node T_C increases monotonically from $1.8 \mu\text{s}$ to $63 \mu\text{s}$ with increase in the order p of interpolation from two to eight.

Figure 4.7.3. Ratio $T_p/T_{m\delta}$ of the measured compute time of the staggered patch schemes (viscous shallow water flows) to that of the fine-grid full-domain model, for different n , r . Solid lines represent expression (4.7.2) for $T_p/T_{m\delta}$ using the estimated model compute time $T_M = 0.19 \mu s$ and the respective estimated coupling compute times T_C for each patch scheme.



The focus of the current patch scheme implementation is on the flexibility to explore a large number of possible designs of the patch grid and a large number of possible patch schemes. So, the current patch scheme implementation, being not computationally efficient, leads to large coupling compute times per edge node T_C from Fig. 4.7.2. Hence, the approximate ratios of the coupling compute times to the model compute times are $T_C/T_M = 3, 9, 39, 120, 326$, for the five staggered patch schemes Spectral, Square-p2, Square-p4, Square-p6, and Square-p8 respectively. Compared to the ratio $T_C/T_M = 7, 29, 123, 381, 1020$ in §3.7.4 for the general linear wave, ratio T_C/T_M of the coupling compute times to the model compute times for the viscous shallow water flows is about three times lesser. Compared to the general linear wave, the smaller ratio T_C/T_M for the viscous shallow water flows is because the coupling compute times T_C are about the same as the general linear wave but the model compute time is about three times larger (due to relatively larger complexity and computations of the microscale model as in p. 264 of this §4.7.4).

Figure 4.7.3 plots the ratio $T_p/T_{m\delta}$ of the measured compute time of the fine-grid full-domain model to that of the staggered patch schemes, for different number of sub-patch micro-grid intervals n and patch scale ratio r . Solid lines represent expression (4.7.2) for $T_p/T_{m\delta}$ using the estimated model compute time $T_M = 0.19 \mu\text{s}$ and the respective estimated coupling compute times T_C for each patch scheme. As in §4.7.4, for $r = 0.001$ we compute $T_p/T_{m\delta}$ (plusses in Fig. 4.7.3) using the measured T_p of the patch schemes and the estimated $T_{m\delta}$ of the full-domain model using expression (4.7.2). The measured compute time ratio $T_p/T_{m\delta}$ reasonably closely follow the trend of expression (4.7.2) (solid lines) for the five staggered patch schemes (with the respective T_C).

In Fig. 4.7.3, the compute time ratio $T_p/T_{m\delta}$ for the viscous shallow water flows is about half of the compute time ratio $T_p/T_{m\delta}$ of the general linear wave in Fig. 3.7.3 of §3.7.4. The preceding paragraph reports that the ratio T_C/T_M of the coupling compute times to the model compute times for the viscous shallow water flows is about three times lesser than that of the general linear wave. Due to the additional layers of edge nodes in the staggered patch grid for the viscous shallow water flows (Fig. 4.1.2b) compared to the general linear wave (Fig. 4.1.2a), expression (4.7.2) for $T_p/T_{m\delta}$ has $+64r^2/(3n^2)$ as opposed to $-64r^2/(3n^2)$ in the corresponding expression (3.7.6) of $T_p/T_{m\delta}$ for the general linear wave (p. 136 of §3.7.3). Overall, the combined effect of the three times lesser T_C/T_M and the more edge nodes for the viscous shallow water flows, leads to a lesser compute time ratio $T_p/T_{m\delta}$, which is about half of the compute time ratio $T_p/T_{m\delta}$ of the general linear wave.

Figure 4.7.3 shows that despite the estimated large T_C/T_M (between 3 and 326 for the five patch schemes), for sufficiently small patch scale ratio $r = 0.01, 0.001$ the compute time ratios $T_p/T_{m\delta}$ are about $10^{-2}, 10^{-4}$. That is, despite the large T_C/T_M , for small patch scale ratios, the compute times of the multiscale patch schemes are about 100 to 10 000 times smaller than the corresponding fine-grid full-domain microscale model. These patch scheme computational savings for the viscous shallow water flows are about twice as those for the general linear wave.

As in p. 140 of §4.7.4 for the general linear wave, for patch scheme simulations with fixed grid geometry, the patch coupling coefficients can be precomputed as a sparse matrix, which gives the patch edge values when multiplied by the patch centre values at each instant in time. Using the sparse matrix multiplication for the patch coupling of the five staggered patch schemes, Fig. 4.7.4 plots the measured compute time T_p for computing the time derivative of the state vector (i.e., the compute time for one iteration in time simulation), for different N and n . We measured 10 000 samples of compute times T_p for each of the four Reynolds num-

Figure 4.7.4. Measured compute times T_p , with *patch coupling via sparse matrix multiplication*, for the five staggered patch schemes with different N and n . Solid lines represent expression (3.7.3) (in p. 136 of §3.7.3) using the estimated model compute time $T_M = 0.19 \mu\text{s}$ and the respective estimated coupling compute times T_C for the five patch schemes.

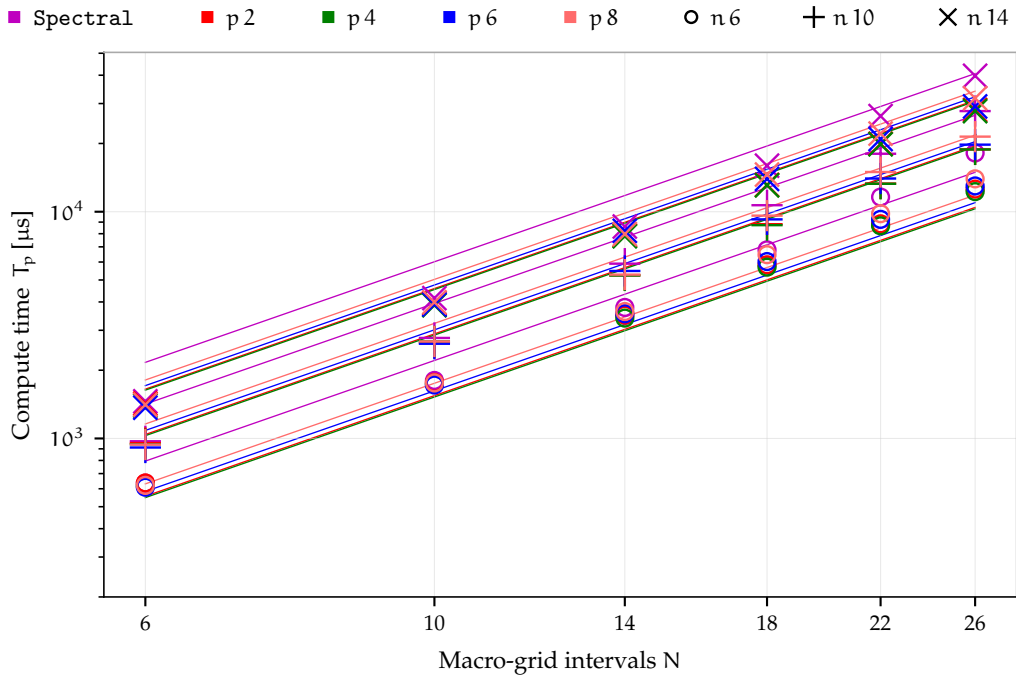
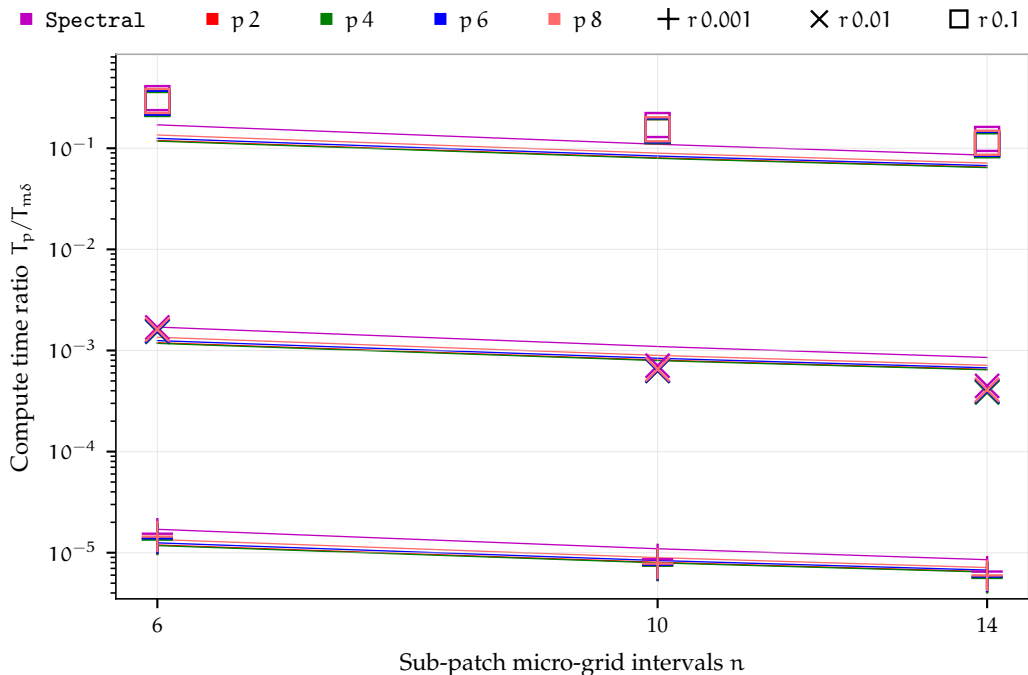


Figure 4.7.5. Ratio $T_p/T_{m\delta}$ of the measured compute time of the staggered patch schemes with *patch coupling via sparse matrix multiplication* to that of the fine-grid full-domain model, for different n , r . Solid lines represent expression (4.7.2) for $T_p/T_{m\delta}$ using the estimated $T_M = 0.19 \mu\text{s}$ and the respective estimated coupling compute times T_C for each patch scheme.



bers $Re \in \{10, 50, 250, 1250\}$. Each point in Fig. 4.7.4 is the mean over the four Reynolds numbers Re .

Similar to §3.7.4 for the measured compute times T_p in Fig. 3.7.4, fitting a power law curve (solid lines in Fig. 3.7.4) using the model compute time $T_M = 0.19 \mu\text{s}$ in expression (3.7.3) (in p. 136 of §3.7.3), we estimate the approximate coupling compute times per edge node $T_C = 0.62, 0.41, 0.4, 0.43, 0.47 \mu\text{s}$ for the five staggered patch schemes Spectral, Square-p2, Square-p4, Square-p6, and Square-p8 respectively. The patch coupling via sparse matrix multiplication reduces the coupling compute time T_C by as large as 170 times compared to the direct coupling compute times.

Figure 4.7.5 plots the ratio $T_p/T_{m\delta}$ of the measured compute time of the staggered patch schemes with *patch coupling via sparse matrix multiplication* to that of the fine-grid full-domain model, for different number of sub-patch micro-grid intervals n and patch scale ratio r . Solid lines represent expression (4.7.2) for $T_p/T_{m\delta}$ using the estimated $T_M = 0.19 \mu\text{s}$ and the respective estimated coupling compute times T_C for each patch scheme. As discussed in the paragraph before (for direct coupling), the computation for the fine-grid full-domain model corresponding to a patch grid with a small patch scale ratio, requires large memory. Hence, for $r = 0.001$ we compute $T_p/T_{m\delta}$ (plusses in Fig. 4.7.5) using the measured T_p of the patch schemes and the estimated $T_{m\delta}$ of the full-domain model using expression (4.7.2). The measured compute time ratio $T_p/T_{m\delta}$ reasonably closely follow the trend of expression (4.7.2) (solid lines) for the five staggered patch schemes (through the respective T_C). As in §3.7.4 for the general linear wave, compared to the compute time ratios $T_p/T_{m\delta}$ in Fig. 4.7.3 via direct coupling, the compute time ratios $T_p/T_{m\delta}$ in Fig. 4.7.5 with patch coupling via sparse matrix multiplication, do not have strong dependence on the specific patch schemes nor the patch scale ratio r . Compared to the compute time ratios $T_p/T_{m\delta}$ in Fig. 4.7.3 via direct coupling, the *patch coupling via sparse matrix multiplication (for fixed grid) reduces the compute time ratios $T_p/T_{m\delta}$ by about ten times* as in Fig. 4.7.5, especially for higher order patch schemes.

As for the direct coupling (p. 268 of this §4.7.4), in Fig. 4.7.5 the compute time ratio $T_p/T_{m\delta}$ for the viscous shallow water flows with patch coupling via sparse matrix multiplication is about half as that of the general linear wave in Fig. 3.7.5 of §3.7.4. As for the direct coupling (p. 268 of this §4.7.4), the combined effect of the lesser T_C/T_M and the more edge nodes for the viscous shallow water flows leads to lesser compute time ratio $T_p/T_{m\delta}$, which is about half of the compute time ratio $T_p/T_{m\delta}$ of the general linear wave.

As in the previous paragraph, due to the overall combined effect of the larger complexity of the microscale model and the more edge nodes for the viscous shallow water flows, the ratio T_C/T_M (of coupling compute time to model compute time) for the viscous shallow water flows is about half as that of the general linear wave. Yet, even for the viscous shallow water flows, the ratio $T_C/T_M > 1$ (between two and three). Figure 4.7.5 shows that despite $T_C/T_M > 1$, for sufficiently small patch scale ratio $r = 0.01, 0.001$ the compute time ratios $T_p/T_{m\delta}$ are about $10^{-3}, 10^{-5}$. That is, for small patch scale ratios, *the compute times of the multiscale patch schemes are about 1000 to 10^5 times smaller than the corresponding fine-grid full-domain microscale model.* This ratio of compute time is roughly about the same as for the general linear wave in §3.7.4. Yet, the patch scheme computational saving for the viscous shallow water flows is twice as that of the general linear wave in §3.7.4.

The demonstrated large computational savings of the patch schemes via compute time ratio $T_p/T_{m\delta}$ in Figs. 4.7.3 and 4.7.5 are for the case of ratio of coupling compute time to model compute time $T_C/T_M > 1$. As explained at the end of §3.7.4 for the general linear wave, even larger computational savings of the patch schemes are possible with smaller ratio T_C/T_M .

4.7.5 Patch scheme time simulations of viscous shallow water flows

This subsection demonstrates the accuracy and the effectiveness of the staggered patch schemes by numerically simulating a viscous roll wave (e.g., Balmforth and Mandre 2004). The patch schemes accurately simulate the localised nearly discontinuous macroscale viscous roll wave emerging from the initial condition of a simple progressive wave within the small sparsely located patches.

As in §3.7.5 for the general linear wave, for the viscous shallow water flows *this subsection uses the BS3 ODE integrator* (Bogacki and L. Shampine 1989; L. F. Shampine and Reichelt 1997) for all the time simulations with the relative and absolute error tolerances of 10^{-3} and 10^{-6} respectively.

Figures 4.7.6 to 4.7.8 show the time evolution of a viscous roll wave (height h and velocities u, v) for Reynolds number $Re = 10$ over a bed inclined 10° downwards along positive x -direction, emerging from the

Figure 4.7.6. Height h for time evolution of a roll wave for $t = 0$ to 10π , emerging from the initial condition of simple progressive wave (4.7.4), using Square-p4 patch scheme (colour-coded ribbons, with $N = 14$, $n = 6$, and $r = 0.1$) agrees reasonably with that of the fine-grid full-domain model (grey mesh). Black circles on h -centred patches show the discrepancy.

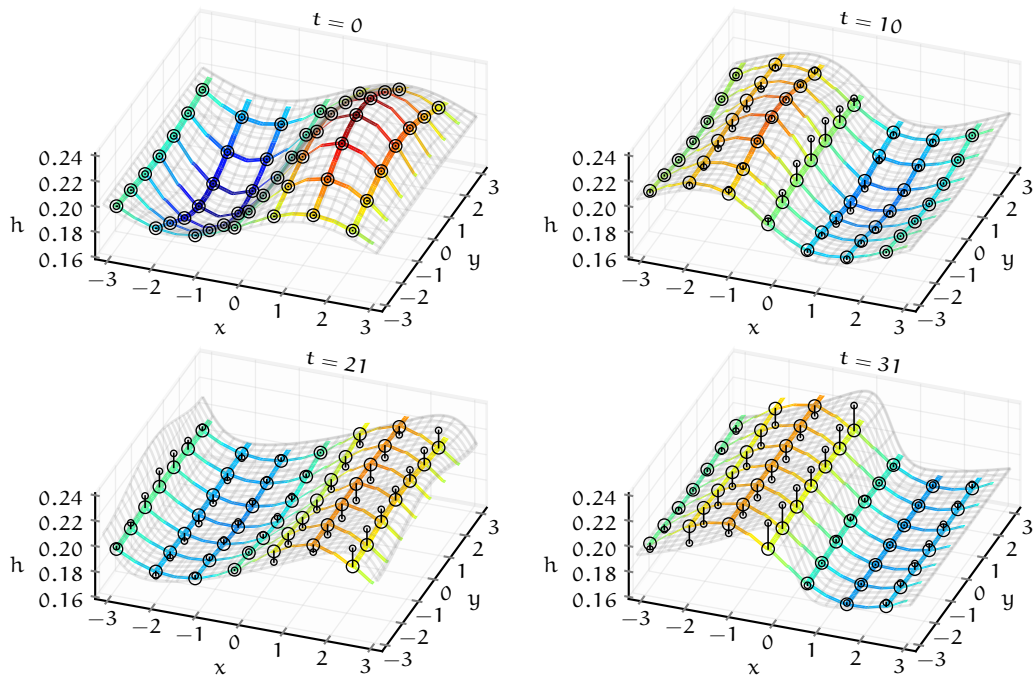


Figure 4.7.7. Velocity u for the time evolution of a roll wave for $t = 0$ to 10π , for the same patch scheme simulation detailed in Fig. 4.7.6, agrees reasonably with that of the fine-grid full-domain model (grey mesh). Black circles on u -centred patches show the discrepancy.

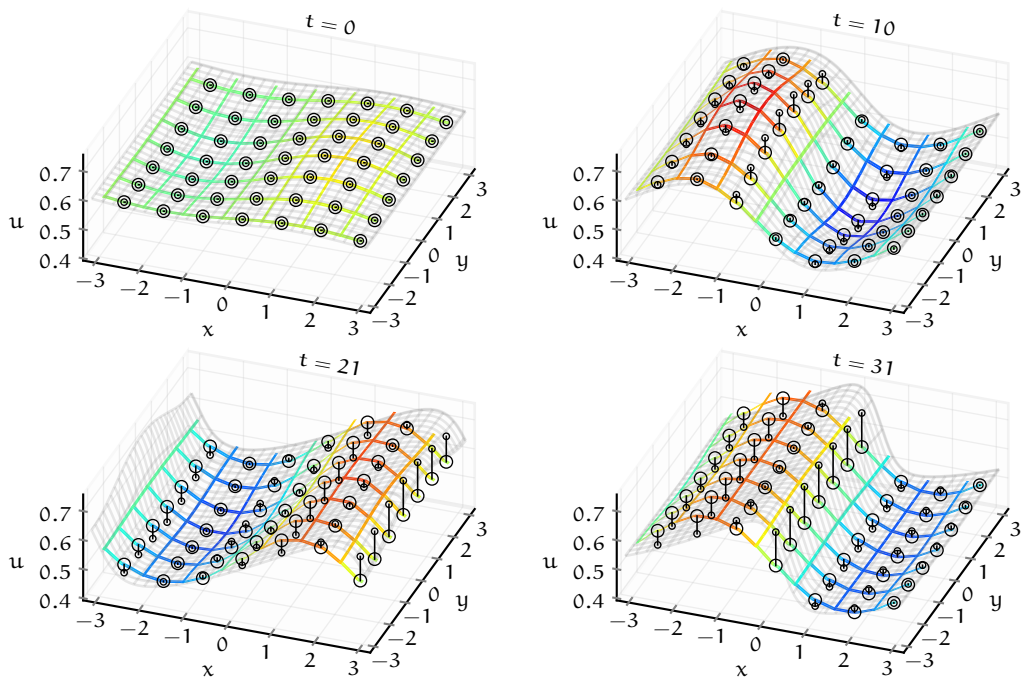
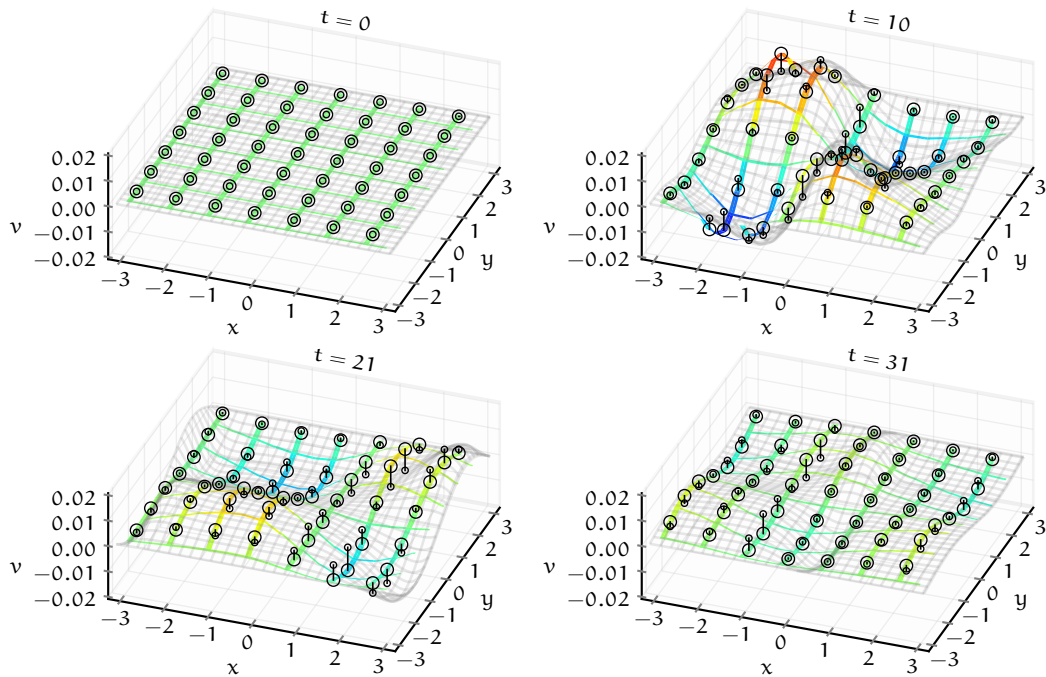


Figure 4.7.8. Velocity v for time evolution of a roll wave for $t = 0$ to 10π , for the same patch scheme simulation detailed in Fig. 4.7.6, agrees reasonably with that of the fine-grid full-domain model (grey mesh). Black circles on h -centred patches show the discrepancy.



initial condition of a simple progressive wave

$$h_0(x, y) = 0.2 + 0.05 \sin(x) \exp[-y^2/4^2], \quad (4.7.4a)$$

$$u_0(x, y) = 0.6 + (0.05/\sqrt{2}) \sin(x) \exp[-y^2/4^2], \quad (4.7.4b)$$

$$v_0(x, y) = 0, \quad (4.7.4c)$$

which is superimposed over approximate equilibrium mean flow $h_M = 0.2$, $u_M = 0.6$, $v_M = 0$. In each of Figs. 4.7.6 to 4.7.8, the subfigures from top-left sub-plot to bottom-right correspond to simulation time $t = 0, 10, 21, 31$. The regions where the colour-coded ribbons cross are patches; the patches are much smaller than illustrated in the figure for visual clarity. The staggered patch schemes compute only within patches, a small fraction of the area of the full domain (§4.7.1).

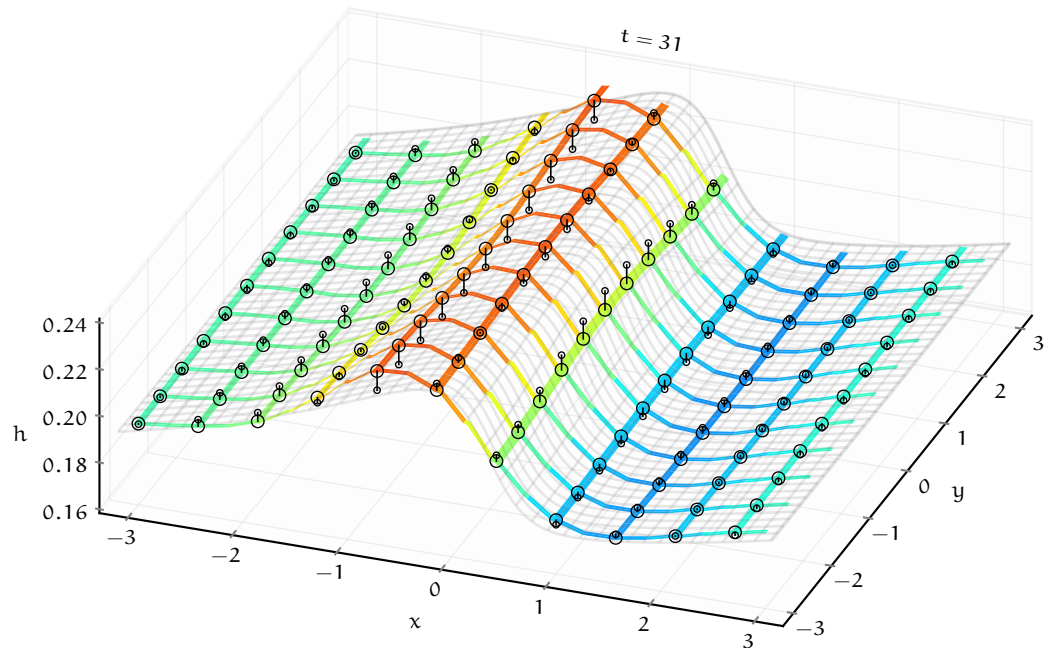
Figures 4.7.6 to 4.7.8 show that the time evolution using the Square-p4 patch scheme (colour-coded ribbons, with $N = 14$, $n = 6$, and $r = 0.1$) agrees reasonably with that of the 420×420 fine-grid full-domain model (grey mesh) with the same full-domain grid interval as the sub-patch micro-grid interval $\delta = 2(2\pi)r/(Nn) = 2\pi/420$ (for the non-dimensional domain

size 2π). Despite the small number of macro-grid intervals ($N = 14$) and a low order patch coupling (fourth order polynomial interpolation), the Square-p4 patch scheme captures the localised nearly discontinuous macroscale roll wave. Figures 4.7.6 and 4.7.7 show that the lateral (i.e., along y axis) local initial disturbance (4.7.4) to the mean flow spreads side-ways while emerging as a roll wave.

In Figs. 4.7.6 to 4.7.8 for the viscous roll wave simulation, the fine-grid full-domain microscale model (grey mesh) uses the same micro-grid interval as the sub-patch micro-grid interval $\delta = 2(2\pi)r/(Nn)$ (for the non-dimensional domain size 2π). But the grey mesh of the full-domain model plots only 27×27 grid instead of all the 421×421 grid lines, skipping many lines for visual clarity. The colour-coded ribbons of the patch scheme in Fig. 4.7.6 consist of all the lines (along the coordinate axes x and y) passing through all the h nodes within all the patches; similarly Figs. 4.7.7 and 4.7.8 for u, v nodes within all the patches respectively. Although the patch scale ratio is $r = 0.1$, the patches are enlarged here for visual clarity so that the ribbons appear wider. In Figs. 4.7.6 to 4.7.8, the solutions $h/u/v$ of fine-grid full-domain microscale model are linearly interpolated using nearest four values to the centres of the respective $h/u/v$ -centred patches, illustrated by small black circles. The large circles are the patch scheme solution $h/u/v$.

With a sufficient number of macro-grid intervals and accurate patch coupling, patch schemes accurately simulate the viscous shallow water flows. Figures 4.7.6 to 4.7.8 show that for small number of macro-grid intervals ($N = 14$) and a low order patch coupling (fourth order polynomial interpolation), the Square-p4 patch scheme reasonably accurately simulates the localised nearly discontinuous macroscale roll wave. Figure 4.7.9 compares the Square-p4 patch scheme patch scheme solution for larger $N = 22$ ($n = 6, r = 0.1$), with the full-domain solution for the same grid interval as the sub-patch micro-grid interval $\delta = 2(2\pi)r/(Nn) = 2\pi/660$ (for the non-dimensional domain size 2π). Increasing the number of macro-grid intervals sufficient enough to resolve the localised roll wave, leads to a more accurate multiscale patch scheme simulation. Increasing the order p of the patch coupling interpolation also increases the accuracy of the patch scheme simulations. Figure 4.7.9 visually shows that the discrepancy between the patch scheme and fine-grid full-domain model is small, non concentric black circles are offset only slightly. This small discrepancy at $t = 31$ (distance between centres of non concentric black circles) also includes the accumulation of the ODE integrator error due to several time iterations before $t = 31$. Thus, with a sufficient number of macro-grid intervals and accurate patch coupling, *patch schemes accurately simulate the viscous shallow water flows.*

Figure 4.7.9. The emergent viscous roll wave (height h at $t = 31$), from the initial condition of simple progressive wave (4.7.4), using Square-p6 patch scheme (colour-coded ribbons, with $N = 22$, $n = 6$, and $r = 0.1$) agrees very closely with that of the fine-grid full-domain model (grey mesh). Black circles on h -centred patches show the discrepancy.



4.7.6 Some practical issues in staggered patch scheme simulations of viscous shallow water flows

Section 4.7.5 (e.g., Fig. 4.7.9) qualitatively shows that for sufficient number of macro-grid intervals and accurate patch coupling, patch schemes accurately simulate the viscous shallow water flows. This subsection establishes the accuracy of the staggered patch scheme simulations more quantitatively and explains some subtle details of the practical issues in the patch scheme simulations.

As in §3.7.5 for the general linear wave, to numerically quantify the discrepancy, we compute the solutions $h_{m\delta}^c$, $u_{m\delta}^c$, $v_{m\delta}^c$ of the fine-grid full-domain microscale model, at the positions of the respective $h/u/v$ -centred patches, by a bilinear interpolation using the four nearest full-domain node values. For example, Figs. 4.7.6 to 4.7.8 of §4.7.5 indicate the full-domain solutions at the respective patch centres as small black circles.

Figure 4.7.10. Convergence of patch scheme time solution h using BS3 *non-stiff* ODE integrator, in terms of simulation error $\epsilon_{2\pi}^h$ of (3.7.9a) for the roll wave (e.g., in Fig. 4.7.6) at $t = 2\pi$. With a sufficient number of macro-grid intervals N and accurate patch coupling, *patch schemes accurately simulate the viscous shallow water flows.*

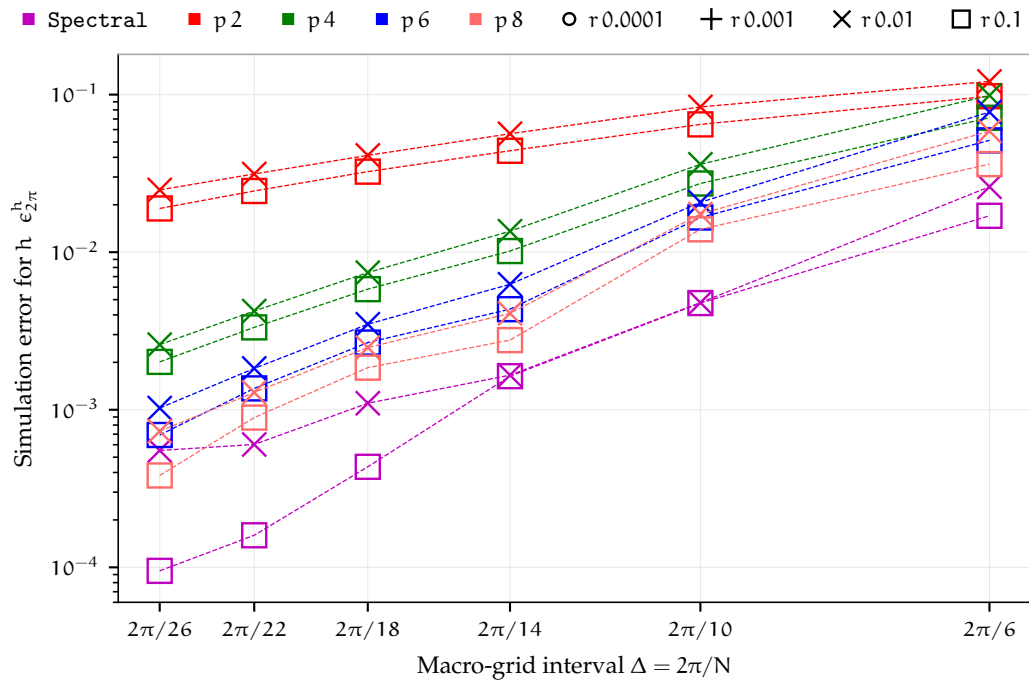


Figure 4.7.11. Patch scheme simulations using QNDF *stiff* ODE integrator gives with almost the same accuracy as the BS3 *non-stiff* ODE integrator (Fig. 4.7.10). For small patch scale ratio $r \lesssim 0.01$, the QNDF *stiff* integrator takes about ten to hundred times less compute time compared to the *non-stiff* BS3 (Fig. 4.7.12) due to fewer function evaluations (Fig. 4.7.13).

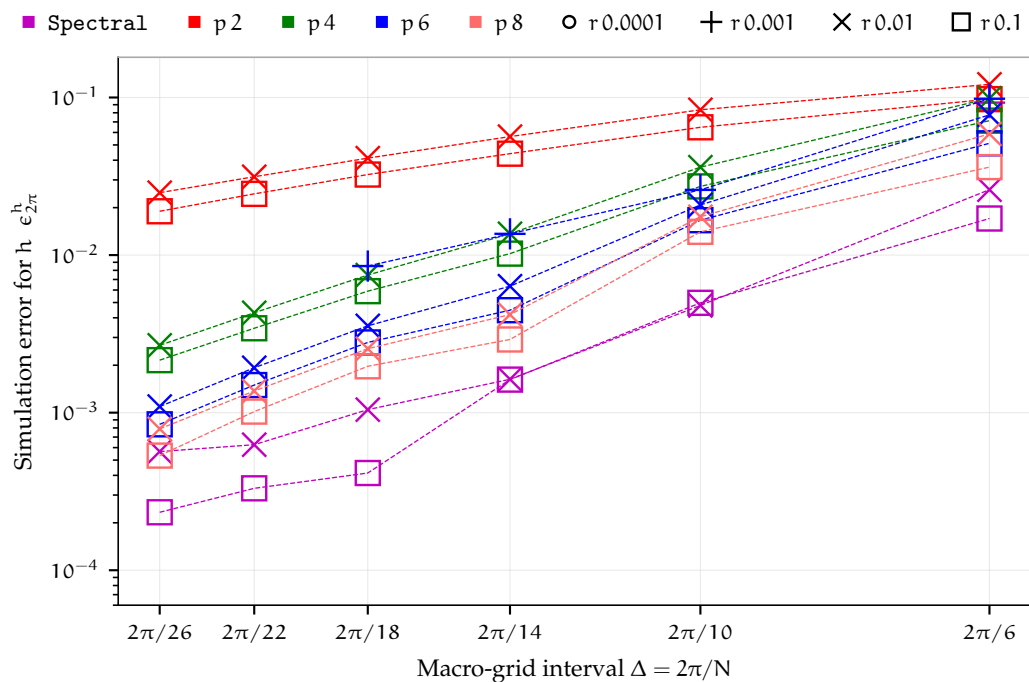


Figure 4.7.10 plots the *solution convergence* of the staggered patch schemes with decreasing macro-grid interval Δ , for the relatively complex nearly discontinuous roll wave simulation visualised in §4.7.5. Figure 4.7.10 shows the convergence via the relative *simulation error* (3.7.9a) (of §3.7.5) for height h . In Fig. 4.7.10, except for the range of macro-grid intervals N and patch scale ratio r , all other parameters are the same as in Figs. 4.7.6 to 4.7.9 of §4.7.5. Figure 4.7.10 shows that, in general, the simulation error $\epsilon_{2\pi}^h$ decreases with decreasing macro-grid intervals $\Delta = 2\pi/N$ (for the non-dimensional domain size 2π) A smaller patch scale ratio ($r \lesssim 0.01$) leads to small degradation in accuracy (about 10–50%) compared to $r = 0.1$, yet the solution errors decrease with decreasing number of macro-grid intervals N , roughly with the same order p as the polynomial interpolation for patch coupling. This decreasing simulation error with decreasing macro-grid intervals, that is the solution convergence similar to the eigenvalue convergence in §4.5, quantitatively establishes the accuracy of the staggered patch scheme time simulations.

The accuracy of the Spectral patch scheme does not deteriorate for large macro-grid interval Δ for the viscous shallow water flows. Figures 3.7.12 to 3.7.14 (of §3.7.5) for the general linear wave show that the simulation errors of the Spectral patch scheme are small (about 10^{-3}), without any dependence on the macro-grid interval Δ . In contrast to the general linear wave, the convergence of the Spectral patch scheme solution for the viscous roll wave in Fig. 4.7.10 shows that the simulation error of the Spectral patch scheme increases with increasing macro-grid interval Δ . But, this increasing error is not due to any deficiency of the Spectral patch scheme, instead simulating this localised nearly discontinuous roll wave requires resolving a large number of wavenumbers, which is achieved by a large number of macro-grid intervals (small macro-grid interval Δ). For simulation of macroscale smooth solutions, such as a simple progressive wave, the simulation error of the Spectral patch scheme does not increase with increasing macro-grid interval Δ . For example, Fig. 4.5.1 of §4.5.1 for the Spectral patch scheme shows that the eigenvalue error corresponding to the wavenumber $(k_x, k_y) = (1, 0)$ is small for a range of macro-grid intervals, with little dependence on the macro-grid intervals Δ . Similarly, the Spectral patch scheme solution is exact (within numerical roundoff errors) for all the wavenumbers resolved by a patch grid. Thus, the accuracy of the Spectral patch scheme does not deteriorate for large macro-grid interval Δ . On the other hand, increasing the number of macro-grid intervals resolves increasingly large macroscale wavenumbers as required by any specific simulation such as roll wave, leading to improving accuracy with decreasing macro-grid interval Δ .

Figure 4.7.12. Compute times of three ODE integrators (*non-stiff* BS3, *stiff* CVODE_BDF, and *stiff* QNDF) for Square-p6 patch scheme simulation in Fig. 4.7.6 for different system dimension n_p^1 and patch scale ratio r . For $r \lesssim 0.01$, compute times of *stiff* integrators are about ten to hundred times lesser than *non-stiff* BS3 due to fewer function evaluations (Fig. 4.7.13).

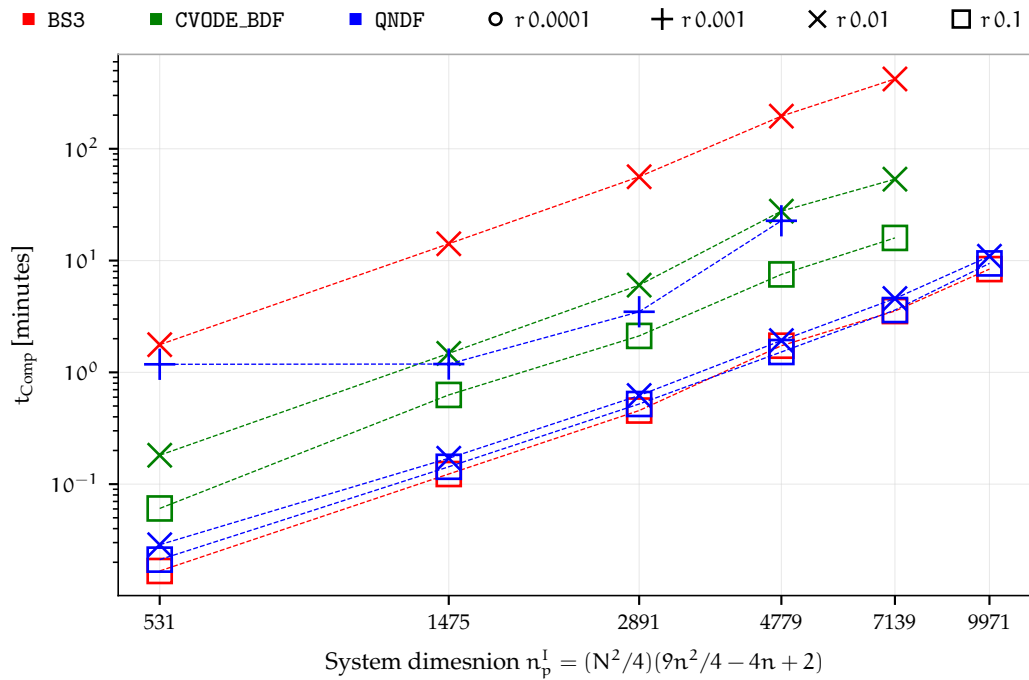
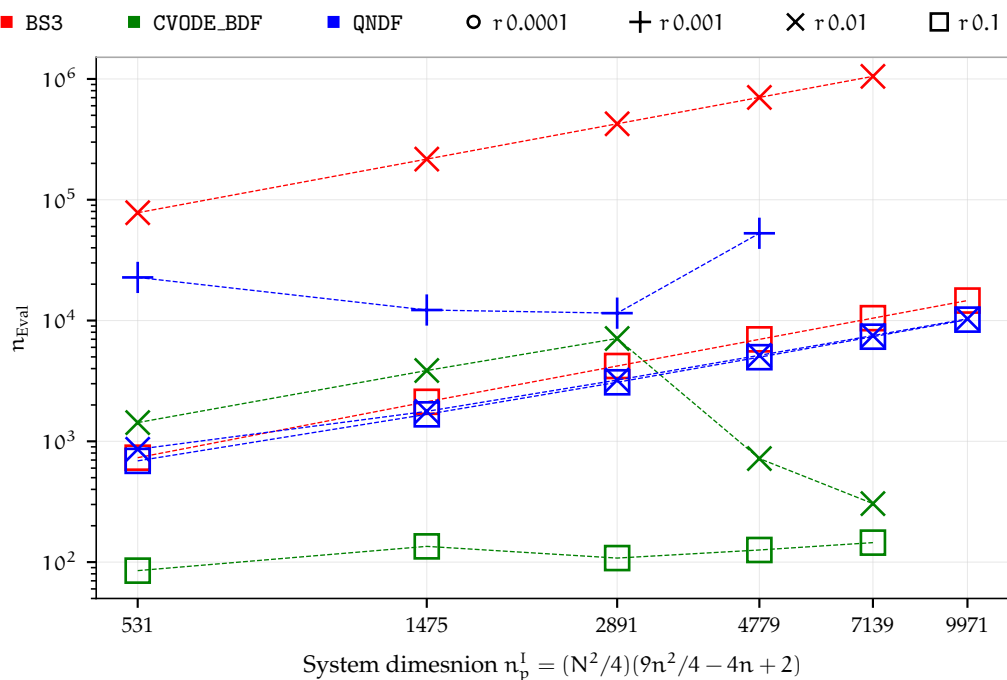


Figure 4.7.13. Number of function evaluations of three ODE integrators (*non-stiff* BS3, *stiff* CVODE_BDF, and *stiff* QNDF) for Square-p6 patch scheme simulation in Fig. 4.7.6 for different system dimension n_p^1 and patch scale ratio r . For small patch scale ratio $r \lesssim 0.01$, *stiff* integrators perform about ten to hundred times less function evaluations than *non-stiff* BS3.



Compute times of non-stiff ODE integrators for the patch scheme simulations increase with decreasing patch scale ratio r . The solution convergence plot in Fig. 4.7.10 does not have data points for patch scale ratio $r \lesssim 0.001$ (no plusses or circles). That is because the patch scheme simulation for small patch scale ratio using non-stiff ODE integrators (e.g., BS3 in Fig. 4.7.10) requires a large compute time. For $N = 10, n = 6$, keeping all other parameters the same as in Fig. 4.7.10, using BS3 non-stiff ODE integrator, the roll wave patch scheme simulation with patch scale ratios $r = 0.1, 0.01$, complete in about 0.1 minute and 14 min respectively. The same roll wave patch scheme simulation with a patch scale ratio $r = 0.001$ ($N = 10, n = 6$) using BS3 non-stiff ODE integrator does not complete even after five days. On the other hand, the same roll wave patch scheme simulation (i.e., $r = 0.001, N = 10, n = 6$) using QNDF stiff ODE integrator completes in 1.2 min. The QNDF stiff integrator of the Julia package DifferentialEquations.jl (2021) is a quasi-constant time step variable-order NDF (numerical differentiation) method, roughly equivalent to the common variable-step, variable-order (VSVO) ode15 integrator (L. F. Shampine and Reichelt 1997, p. 4) of MATLAB (with the default option to use NDF).

For the patch scheme simulations with small patch scale ratio $r \lesssim 0.001$, stiff ODE integrators are much faster yet as accurate as the non-stiff ODE integrators. Figure 4.7.12 plots the compute times of three ODE integrators (non-stiff BS3, stiff CVODE_BDF, and stiff QNDF) for Square-p6 patch scheme simulation in Fig. 4.7.6 for different system dimension n_p^1 (size of state vector) and patch scale ratio r . A plot of compute times versus system dimension n_p^1 for all the other four staggered patch schemes have identical trend and approximately same magnitudes as in Fig. 4.7.12. Figure 4.7.12 shows that for both the stiff (BS3) and the non-stiff (CVODE_BDF, and stiff QNDF) ODE integrators, the compute times increase with decreasing patch scale ratio r , for all system dimensions $n_p^1 = (N^2/4)(9n^2/4 - 4n + 2)$ corresponding to the macro-grid intervals $N \in \{6, 10, 14, 18, 22, 26\}$. Specifically, comparing the red crosses with the green and blue crosses in Fig. 4.7.12 shows that for small patch scale ratio $r \lesssim 0.01$, the compute times of stiff integrators are about ten to hundred times lesser than non-stiff BS3. Figure 4.7.11 plots the solution convergence using the QNDF stiff ODE integrator for the same relative and absolute error tolerances (10^{-3} and 10^{-6}) and other parameters as used by BS3 non-stiff ODE in Fig. 4.7.10. Comparing Figs. 4.7.10 and 4.7.11 shows that both the stiff and non-stiff ODE integrators, give same accuracy, except a small deviation for the Spectral patch scheme for small macro-grid interval $\Delta \lesssim 2\pi/22$ (for the non-dimensional domain size 2π). With a smaller relative and absolute error tolerances of 10^{-7} and 10^{-6} respectively, a convergence plot using the QNDF stiff ODE integrator

is identical to Fig. 4.7.10, also for the Spectral patch scheme for small macro-grid interval $\Delta \lesssim 2\pi/22$. That is, despite the large differences in the compute times among the stiff and non-stiff ODE integrators, both give reasonably the same accuracy. Especially, for the patch scheme simulations with small patch scale ratio $r \lesssim 0.001$, stiff ODE integrators are must faster (ten to hundred times) yet as accurate as the non-stiff ODE integrators.

Patch scheme simulations for small patch scale ratio $r \lesssim 0.001$ require ODE integrator that can handle stiff systems. Figure 3.7.7 of §3.7.5 for the general linear wave shows that the compute times of the stiff ODE integrators (sp.BDF, sp.Radau) are ten to hundred times larger compared the non-stiff ode integrators (BS3, DP5, Tsit5, Vern7). Similarly, for an even simpler linear system $du/dt = Au + b$, Maclean et al. (2021b, p. 1742, Fig.4) comment that “The stiff integrator is fast and reasonably accurate at low system dimension, but performs poorly at dimension 60 and above.” In contrast, the preceding paragraph shows that for the patch scheme simulations with a small patch scale ratio $r \lesssim 0.001$, stiff ODE integrators are much faster yet as accurate as the non-stiff ODE integrators. From Figs. 4.7.10 and 4.7.11 and Fig. 4.7.12, it is evident that this trend of stiff ODE integrators being much faster also holds for different system dimensions as small as about five hundred to as large as ten thousand *for viscous shallow water flows*. Based on study for a simple linear system $du/dt = Au + b$, Maclean et al. (2021b, §3.1.4) find that projective ODE integrator (Gear and Kevrekidis 2003) which specifically utilises the spectral gap in a system outperforms the stiff ODE integrator both in accuracy and compute times. A detailed comparative study of different ODE integrators including the projective ODE integrator, for complex viscous shallow water flows, is left as future work. The current work shows that for nonlinear microscale models (e.g., viscous shallow water flows) patch scheme simulations for small patch scale ratio $r \lesssim 0.01$ require a ODE integrator that can handle stiff systems efficiently.

The following paragraphs investigate why the compute times (ODE integration times) of the patch scheme simulations increase with decreasing patch scale ratio r , and hence necessitating a ODE integrator that can handle stiff systems efficiently.

For the patch scheme simulations, the *increasing compute times with decreasing patch scale ratio is not due to patch scheme computations, but due to the need for non-stiff ODE integrators to take smaller time steps for stability.* (Moler 2004, pp. 202–206; Quarteroni et al. 2014, pp. 319–325; Lomax et al. 2011, pp. 149–150; Pulliam and Zingg 2014, p. 57; Schiesser and G. W. Griffiths 2009, p. 22–23). Such smaller time steps require correspondingly more function evaluations. Figure 4.7.13 plots the number of function evaluations to compute the time derivative of a patch system corresponding to the

compute times in Fig. 4.7.12, for different system dimension n_p^I and patch scale ratio r . Figure 4.7.13 shows that, except some deviations, in general the number of function evaluation increases with decreasing patch scale ratio r . On the other hand, as §4.7.4 (e.g., Fig. 4.7.5) shows, the compute time to compute the time derivative of a patch scheme system (one iteration of simulation) is much smaller by several orders of magnitude compared to the corresponding full-domain microscale model. That is, the increasing total compute times of the patch scheme simulations are not due to the patch schemes per iteration, but due to the ODE integrators calling the function to compute the time derivative of a patch scheme many times.

The patch schemes become increasingly stiff with decreasing patch scale ratio r . For a patch grid with a fixed number of macro-grid intervals N and sub-patch micro-grid intervals n , decreasing the patch scale ratio r leads to large wavenumber structures within the patches for the same smooth macroscale structure in the solution. For example, consider the patch scheme complex plane eigenvalue plot in Figs. 4.2.11 and 4.2.12 for patch scale ratio $r = 0.1, 0.001$ respectively, keeping all other parameters the same. Figures 4.2.11 and 4.2.12 show that with decreasing patch scale ratio r , the microscale eigenvalues (blue circles on the left) both moves to the left (taking larger negative real part values) and spreads up and down (taking large magnitudes of imaginary parts) without any change to the macroscale eigenvalues on the right. That is, decreasing the patch scale ratio r leads to increasing wavenumber for the sub-patch microscale modes. This *intrinsic tendency of a patch scheme* (for both the usual collocated and the present staggered patch scheme) *makes the system of ODEs increasingly stiff with decreasing patch scale ratio*, necessitating a ODE integrator that can handle stiff systems efficiently.

Chapter 5

Patch schemes accurately simulate turbulent shallow water flows

The multiscale staggered patch schemes' ability to accurately model the macroscale waves with large computational savings is an enabling feature for accurate simulation and prediction of large-scale waves like floods and tsunamis. This chapter shows that the staggered patch schemes accurately simulate the macroscale dynamics of the Smagorinski-based turbulent shallow water flows, using the PDEs derived by Cao and Roberts (2016) as the microscale model within the patches.

For example, Fig. 1.0.1 shows the accurate patch scheme simulation (colour-coded ribbons) in comparison with the full-domain simulation (grey mesh) of a nearly discontinuous turbulent roll wave; §5.5 gives further details. The regions where the colour-coded ribbons cross are patches; the patches are much smaller than illustrated in the figure for visual clarity. The staggered patch schemes compute only within patches, a small fraction of the area of the full domain (e.g., §4.7.1).

Cao and Roberts (2016) derive Smagorinski-based turbulent 2D shallow water PDEs, in terms of the depth-averaged variables, but without depth-averaging the PDEs. Instead, from the 3D Reynolds averaged Navier–Stokes (RANS) equation and the Smagorinski turbulence model, they derive the 2D turbulent shallow water PDEs using the centre manifold theory, in terms of the depth-averaged variables.

Section 5.1 first non-dimensionalises the turbulent shallow water PDEs of Cao and Roberts (2016) slightly differently to facilitate extensive analysis of the staggered patch schemes. Subsequently, §5.1 derives a discrete full-domain microscale model and a generic staggered patch scheme corresponding to the turbulent shallow water flows. Throughout this chapter, we use this full-domain microscale model as a reference to assess various

characteristics (accuracy, stability, consistency, etc.) of the multiscale staggered patch schemes we develop. [Section 5.1.3](#) chooses a set of values for the non-dimensional parameters towards exploration of patch schemes for turbulent shallow water PDEs.

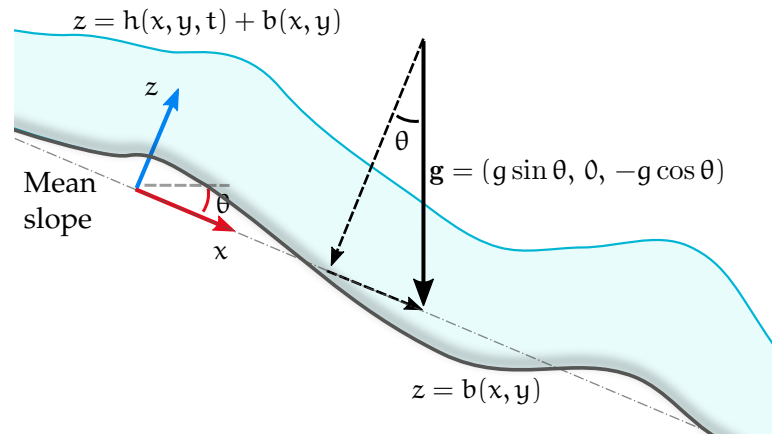
[Section 5.2](#) shows that the developed five staggered patch schemes are accurate for the turbulent shallow water flows by comparing the eigenvalues of the staggered patch schemes with the eigenvalues of the fine-grid full-domain microscale model. [Section 5.2](#) establishes the accuracy of the staggered patch schemes in general (as opposed to one specific initial condition) by comparing the eigenvalues of the staggered patch schemes with the eigenvalues of fine- and coarse-grid full-domain microscale model. [Sections 5.2.1 to 5.2.3](#) derives the eigenvalues of the turbulent shallow water PDEs, full-domain microscale model, and that of the staggered patch schemes. [Section 5.2.4](#) illustrates the structure of the patch scheme eigenvalues in the complex plane and explains the corresponding dynamical modes via eigenvector plots. The eigenvalue analysis in [§5.2.4](#) visually demonstrates the accuracy (in the complex plane eigenvalue plots) for a representative subset of the physical parameters and grid parameters. [Section 5.4](#) on the consistency of the patch schemes establishes the accuracy over a wider range of parameters.

[Section 5.3](#) shows that the staggered patch schemes do not have any artificial instability for appropriate patch grids and explores the dependence of the patch scheme stability on various aspects like grid symmetry, physical parameters, and grid parameters. [Section 5.4](#) shows that the staggered patch schemes are consistent with the given microscale model for increasingly finer patch grids. [Section 5.5](#) demonstrates the accuracy and effectiveness of the patch schemes via time simulation of a turbulent roll wave.

5.1 PDEs, Full-domain microscale model, and staggered patch schemes

This section first non-dimensionalises the turbulent shallow water PDEs of Cao and Roberts (2016) slightly differently to facilitate extensive analysis of the staggered patch schemes. Subsequently, this section derives a discrete full-domain microscale model and a generic staggered patch scheme corresponding to the turbulent shallow water flows.

Figure 5.1.1. Shallow turbulent flow over an inclined smooth non-flat bed. The non-dimensional gravity vector $\mathbf{g}' = \mathbf{g}/(g \cos \theta)$, that is, $\mathbf{g}' = (\tan \theta, 0, -1)$ where g is gravitational acceleration and θ is the mean bed inclination angle.



Section 5.1.1 non-dimensionalises the turbulent shallow water PDEs and the boundary conditions using a reference length in terms of domain size as opposed to the characteristic height used by Cao and Roberts (2016). Section 5.1.2 derives a discrete full-domain microscale model and a generic staggered patch scheme corresponding to the turbulent shallow water PDEs of §5.1.1. Throughout this chapter, we use this full-domain microscale model as a reference to assess various characteristics (accuracy, stability, consistency, etc.) of the multiscale staggered patch schemes we develop. Section 5.1.3 chooses a set of values for the non-dimensional parameters towards exploration of patch schemes for turbulent shallow water PDEs.

5.1.1 Non-dimensionalise the PDEs to keep same domain size

Consider the non-dimensional *comprehensive* Smagorinski-based turbulent shallow water PDEs (27a)–(27c) in the article by Cao and Roberts (2016) for the flow schematic in Figure 5.1.1. With the magnitude of horizontal velocity $q = \sqrt{u^2 + v^2}$, the same PDEs, after dropping the over bar for depth-averaged dependent variables, omitting the sediment concentra-

tion $c(x, y, t)$, and setting bed height $b(x, y) = 0$, are

$$\frac{\partial h}{\partial t} \approx -\frac{\partial hu}{\partial x} - \frac{\partial hv}{\partial y}, \quad (5.1.1a)$$

$$\begin{aligned} \frac{\partial u}{\partial t} \approx & -0.003 \frac{uq}{h} + 0.993 \left[\tan \theta - \frac{\partial h}{\partial x} \right] - 1.030u \frac{\partial u}{\partial x} - 1.020v \frac{\partial u}{\partial y} \\ & - 0.008 \left(\frac{u^2}{h} \frac{\partial h}{\partial x} - \frac{uv}{h} \frac{\partial h}{\partial y} \right) + 0.094 \frac{q}{h} \left[\frac{\partial}{\partial x} \left(h^2 \frac{\partial u}{\partial x} \right) + \frac{\partial}{\partial y} \left(h^2 \frac{\partial u}{\partial y} \right) \right] \\ & + 0.084 \frac{u^2 - v^2}{hq} \left[\frac{\partial}{\partial x} \left(h^2 \frac{\partial u}{\partial x} \right) - \frac{\partial}{\partial y} \left(h^2 \frac{\partial u}{\partial y} \right) \right], \end{aligned} \quad (5.1.1b)$$

$$\begin{aligned} \frac{\partial v}{\partial t} \approx & -0.003 \frac{vq}{h} - 0.993 \frac{\partial h}{\partial y} - 1.030v \frac{\partial v}{\partial y} - 1.020u \frac{\partial v}{\partial x} \\ & - 0.008 \left(\frac{uv}{h} \frac{\partial h}{\partial x} - \frac{v^2}{h} \frac{\partial h}{\partial y} \right) + 0.094 \frac{q}{h} \left[\frac{\partial}{\partial x} \left(h^2 \frac{\partial v}{\partial x} \right) + \frac{\partial}{\partial y} \left(h^2 \frac{\partial v}{\partial y} \right) \right] \\ & + 0.084 \frac{u^2 - v^2}{hq} \left[\frac{\partial}{\partial x} \left(h^2 \frac{\partial v}{\partial x} \right) - \frac{\partial}{\partial y} \left(h^2 \frac{\partial v}{\partial y} \right) \right]. \end{aligned} \quad (5.1.1c)$$

The PDEs (5.1.1) have been non-dimensionalised using the characteristic height H and the long wave speed $\sqrt{g_z H}$, which leads to different non-dimensional domain sizes for different characteristic water heights. We want to explore patch schemes for the same dimensional domain size with different characteristic water height H , and in doing so *we also want to keep the non-dimensional domain size the same, to reuse some of the patch scheme computations*. Hence, following exactly the same non-dimensionalisation rescaling as in §4.1.1 for the viscous shallow water flows, non-dimensionalising the 2D space by a reference length $L/(2\pi)$ gives *our* non-dimensional *comprehensive Smagorinski-based turbulent shallow water* PDEs

$$\frac{1}{h_M} \frac{\partial h}{\partial t} \approx -\frac{\partial hu}{\partial x} - \frac{\partial hv}{\partial y}, \quad (5.1.2a)$$

$$\begin{aligned} \frac{1}{h_M} \frac{\partial u}{\partial t} \approx & -0.003 \frac{uq}{h} + \frac{0.993}{h_M} \left[\tan \theta - \frac{\partial h}{\partial x} \right] - \left[1.030u \frac{\partial u}{\partial x} + 1.020v \frac{\partial u}{\partial y} \right] \\ & - 0.008 \left[\frac{u^2}{h} \frac{\partial h}{\partial x} - \frac{uv}{h} \frac{\partial h}{\partial y} \right] + 0.094 \frac{q}{h} \left[\frac{\partial}{\partial x} \left(h^2 \frac{\partial u}{\partial x} \right) + \frac{\partial}{\partial y} \left(h^2 \frac{\partial u}{\partial y} \right) \right] \\ & + 0.084 \frac{u^2 - v^2}{hq} \left[\frac{\partial}{\partial x} \left(h^2 \frac{\partial u}{\partial x} \right) - \frac{\partial}{\partial y} \left(h^2 \frac{\partial u}{\partial y} \right) \right], \end{aligned} \quad (5.1.2b)$$

$$\frac{1}{h_M} \frac{\partial v}{\partial t} \approx -0.003 \frac{vq}{h} - \frac{0.993}{h_M} \frac{\partial h}{\partial y} - \left[-1.030v \frac{\partial v}{\partial y} - 1.020u \frac{\partial v}{\partial x} \right]$$

$$\begin{aligned}
& -0.008 \left[\frac{uv}{h} \frac{\partial h}{\partial x} - \frac{v^2}{h} \frac{\partial h}{\partial y} \right] + 0.094 \frac{q}{h} \left[\frac{\partial}{\partial x} \left(h^2 \frac{\partial v}{\partial x} \right) + \frac{\partial}{\partial y} \left(h^2 \frac{\partial v}{\partial y} \right) \right] \\
& + 0.084 \frac{u^2 - v^2}{hq} \left[\frac{\partial}{\partial x} \left(h^2 \frac{\partial v}{\partial x} \right) - \frac{\partial}{\partial y} \left(h^2 \frac{\partial v}{\partial y} \right) \right]. \tag{5.1.2c}
\end{aligned}$$

As in §4.1.1 for the viscous shallow water flows, also for the turbulent shallow water PDEs (5.1.3), the dimensional domain $[0, L] \times [0, L]$ corresponds to the non-dimensional domain $[0, 2\pi] \times [0, 2\pi]$ irrespective of the characteristic height H .

Neglecting a few small terms in the comprehensive turbulent shallow water PDEs (5.1.2), using “=” instead of “ \approx ”, and simplifying, we get the following *simplified Smagorinski-based turbulent shallow water* PDEs (with magnitude of horizontal velocity $q = \sqrt{u^2 + v^2}$),

$$\frac{1}{h_M} \frac{\partial h}{\partial t} = -\frac{\partial hu}{\partial x} - \frac{\partial hv}{\partial y}, \tag{5.1.3a}$$

$$\begin{aligned}
\frac{1}{h_M} \frac{\partial u}{\partial t} = & -0.003 \frac{uq}{h} + \frac{0.993}{h_M} \left[\tan \theta - \frac{\partial h}{\partial x} \right] - 1.030u \frac{\partial u}{\partial x} - 1.020v \frac{\partial u}{\partial y} \\
& + 0.094qh \nabla^2 u, \tag{5.1.3b}
\end{aligned}$$

$$\frac{1}{h_M} \frac{\partial v}{\partial t} = -0.003 \frac{vq}{h} - \frac{0.993}{h_M} \frac{\partial h}{\partial y} - 1.030v \frac{\partial v}{\partial y} - 1.020u \frac{\partial v}{\partial x} + 0.094qh \nabla^2 v. \tag{5.1.3c}$$

The PDE (5.1.3a) represents the mass conservation, and the PDEs (5.1.3b) and (5.1.3c) represent the momentum equations in the x and y directions respectively. The PDEs represent the key physical mechanisms of quasi-hydrostatic acceleration, advection, and nonlinear bed drag and eddy diffusion. Simplified Smagorinski-based turbulent shallow water PDEs (5.1.3) are equations (11a)–(11c) of Bunder et al. (2020), but non-dimensionalised using $L/(2\pi)$ as reference length scale instead of their reference length H .

We use the non-dimensional simplified Smagorinski-based turbulent shallow water PDEs (5.1.3) as the microscale model within the patches in our study of the staggered patch schemes. In all our further use “turbulent shallow water PDEs” means these *simplified* Smagorinski-based turbulent shallow water PDEs (5.1.3). For the turbulent shallow water PDEs (5.1.3), throughout this chapter, we consider the boundary conditions that the three fields h , u , and v are 2π -periodic in both x and y (for the non-dimensional domain size 2π), and an appropriate initial condition $h(x, y, 0)$, $u(x, y, 0)$, and $v(x, y, 0)$.

5.1.2 Full-domain microscale model and staggered patch schemes

This subsection derives a full-domain microscale finite difference system for the turbulent shallow water PDEs (5.1.3) of §5.1.1. In Fig. 1.0.1, the full-domain simulation (grey mesh) of a the turbulent roll wave uses the microscale model developed in this subsection.

Approximating the spatial derivatives in the turbulent shallow water PDEs (5.1.3) by central finite differences on the nodes of the full-domain staggered grid (filled circles in Fig. 4.1.1) with the micro-grid interval δ gives the *full-domain microscale model* corresponding to the PDEs (5.1.3).

$$\bullet \frac{1}{h_M} \frac{dh_{i,j}}{dt} = - \frac{(h_{i,j} + h_{i+2,j}) u_{i+1,j} - (h_{i-2,j} + h_{i,j}) u_{i-1,j}}{4\delta} - \frac{(h_{i,j} + h_{i,j+2}) v_{i,j+1} - (h_{i,j-2} + h_{i,j}) v_{i,j-1}}{4\delta} \quad (5.1.4a)$$

for $i, j \in \{0, 2, 4, \dots, n-2\}$,

$$\bullet \frac{1}{h_M} \frac{du_{i,j}}{dt} = -0.003 u_{i,j} \frac{\sqrt{u_{i,j}^2 + [(v_{i-1,j-1} + v_{i+1,j-1} + v_{i-1,j+1} + v_{i+1,j+1})/4]^2}}{(h_{i+1,j} + h_{i-1,j})/2} + \frac{0.993}{h_M} \left[\tan \theta - \frac{h_{i+1,j} - h_{i-1,j}}{2\delta} \right] - 1.03 u_{i,j} \frac{u_{i+2,j} - u_{i-2,j}}{4\delta} - 1.02 [(v_{i-1,j-1} + v_{i+1,j-1} + v_{i-1,j+1} + v_{i+1,j+1})/4] \frac{(u_{i,j+2} - u_{i,j-2})}{4\delta} + 0.094 \sqrt{u_{i,j}^2 + [(v_{i-1,j-1} + v_{i+1,j-1} + v_{i-1,j+1} + v_{i+1,j+1})/4]^2} \frac{h_{i-1,j} + h_{i+1,j}}{2} \left(\frac{u_{i-2,j} - 2u_{i,j} + u_{i+2,j}}{4\delta^2} + \frac{+u_{i,j-2} - 2u_{i,j} + u_{i,j+2}}{4\delta^2} \right) \quad (5.1.4b)$$

for $i \in \{1, 3, 5, \dots, n-1\}$, $j \in \{0, 2, 4, \dots, n-2\}$,

$$\bullet \frac{1}{h_M} \frac{dv_{i,j}}{dt} = -0.003 v_{i,j} \frac{\sqrt{v_{i,j}^2 + [(u_{i-1,j-1} + u_{i+1,j-1} + u_{i-1,j+1} + u_{i+1,j+1})/4]^2}}{(h_{i,j+1} + h_{i,j-1})/2} - \frac{0.993 (h_{i,j+1} - h_{i,j-1})}{h_M} - 1.03 v_{i,j} \frac{(v_{i,j+2} - v_{i,j-2})}{4\delta} - 1.02 [(u_{i-1,j-1} + u_{i+1,j-1} + u_{i-1,j+1} + u_{i+1,j+1})/4] \frac{(v_{i+2,j} - v_{i-2,j})}{4\delta}$$

$$\begin{aligned}
& + 0.094 \sqrt{[(\mathbf{u}_{i-1,j-1} + \mathbf{u}_{i+1,j-1} + \mathbf{u}_{i-1,j+1} + \mathbf{u}_{i+1,j+1})/4]^2 + v_{i,j}^2} \\
& \frac{h_{i,j-1} + h_{i,j+1}}{2} \left(\frac{v_{i-2,j} - 2v_{i,j} + v_{i+2,j}}{4\delta^2} + \frac{v_{i,j-2} - 2v_{i,j} + v_{i,j+2}}{4\delta^2} \right)
\end{aligned} \tag{5.1.4c}$$

for $i \in \{0, 2, 4, \dots, n-2\}$, $j \in \{1, 3, 5, \dots, n-1\}$.

Analogous to the PDEs (5.1.3), the three fields $h_{i,j}$, $u_{i,j}$, $v_{i,j}$ are n -periodic in both i and j where $n = 2\pi/\delta$ (for the non-dimensional domain size 2π), with an appropriate initial condition $h_{i,j}(0)$, $u_{i,j}(0)$, and $v_{i,j}(0)$. Due to the “missing” nodes on the staggered grid (Fig. 4.1.1), some of the terms in the full-domain microscale model (5.1.4) involves averaging the node values. Section 4.1.2 for the viscous shallow water flows explains the discretisation involving averaging on the staggered grids for some of the similar terms.

Substituting the solution of a steady uniform flow $h_{i,j} = h_M$, $u_{i,j} = u_M$, $v_{i,j} = v_M$ with mean height h_M and horizontal mean velocity u_M, v_M into the full-domain microscale model (5.1.4) and setting the time derivatives to zero gives the fixed points or the *equilibrium solution*

$$h_{i,j} = h_M, \quad u_{i,j} = \sqrt{0.993 \tan \theta / 0.003}, \quad v_{i,j} = 0, \tag{5.1.5}$$

for the full-domain microscale model (5.1.4) for the turbulent shallow water flows. The equilibrium solution (5.1.5) is also the equilibrium solution for the turbulent shallow water PDEs (5.1.3). The velocity $v = 0$ in the fixed point (5.1.5) is due to that the bed is sloping down only along x direction (e.g., Fig. 5.1.1). For a bed with a positive slope (downward inclination along x), the turbulent shallow water flows reach the equilibrium velocity of the fixed point (5.1.5) when the bed drag and gravitational force are in balance. The larger the inclination, larger the equilibrium velocity; for a horizontal bed, the only fixed point is stagnant water with $u = 0, v = 0$.

A full-domain microscale simulation (e.g., the grey mesh Fig. 1.0.1) is performed by numerical time-integration of the ODEs (5.1.4) on the nodes of the microscale staggered grid (filled circles in Fig. 4.1.1 of §4.1.2), with the discrete macroscale n -periodic boundary conditions in i, j .

Similar to the full-domain microscale model (4.1.11) of the viscous shallow water flows, the full-domain microscale model (5.1.4) of the turbulent shallow water flows also has terms involving the average of the neighbouring values on the staggered grid. Based on the terms in the full-domain microscale model, p. 168 of §4.1.3 discusses the requirement of the number of layers of the edge nodes for a staggered patch grid, for the viscous shallow water flows. A similar study shows that, to use the finite difference

equations (5.1.4) of the turbulent shallow water flows as the microscale model within the patches, a staggered patch grid requires two layers of edge nodes in the normal direction to the edges, and one layer of edge nodes in the tangential direction to the edges, as in Fig. 4.1.2b (same patch grid required for the viscous shallow water flows). Throughout this chapter, *for the turbulent shallow water flows, the staggered patch schemes use the patch grid in Fig. 4.1.2b.*

Using the full-domain microscale model (5.1.4) within the patches of a suitable staggered patch grid (e.g., the patch grid in Fig. 4.1.2b with $n = 6$), gives the *staggered patch scheme* on the patch interior nodes, whose equations are same as (5.1.4) with patch index I, J as the superscript in each of the terms (similar to the patch scheme (4.1.15) for viscous shallow water flows). Analogous to the full-domain microscale model (5.1.4), the three fields $h_{i,j}^{I,J}$, $u_{i,j}^{I,J}$, $v_{i,j}^{I,J}$ in the patch scheme are macroscale N -periodic in both I and J where $N = 2\pi/\Delta$ (for the non-dimensional domain size 2π), with an appropriate initial condition $h_{i,j}^{I,J}(0)$, $u_{i,j}^{I,J}(0)$, and $v_{i,j}^{I,J}(0)$. For the staggered patch grid in Fig. 4.1.2b, the left and right edge values are $\circ h_{i,j}^{I,J}$, $\circ u_{i,j}^{I,J}$, $\circ v_{i,j}^{I,J}$, for $i \in \{-1, 0, n, n+1\}$ and $j \in \{0, 1, 2, \dots, n-1, n\}$. Similarly the bottom and top edge value indices are $i \in \{0, 1, 2, \dots, n-1, n\}$ and $j \in \{-1, 0, n, n+1\}$. A specific patch coupling (e.g., Square-p4) computes patch edge values ($\circ h_{i,j}^{I,J}$, $\circ u_{i,j}^{I,J}$, $\circ v_{i,j}^{I,J}$ in Fig. 4.1.2a) from the centre values of neighbouring patches ($\bullet h_{i,j}^{I,J}$, $\bullet u_{i,j}^{I,J}$, $\bullet v_{i,j}^{I,J}$ with $i = j = n/2$ in Fig. 4.1.2a). The patch coupling provides a mechanism whereby patches influence each other, §2.2 discusses various details of different patch couplings.

Patch scheme simulation is performed by numerical time-integration of the ODEs (5.1.4) with patch index I, J in superscript for each term, on the interior nodes of the staggered patch grid (filled circles in Fig. 4.1.2b), with the discrete macroscale N -periodic boundary conditions in both I and J . As in §2.1.2, evaluating the time derivatives in the staggered patch scheme is done in two steps: first, edge values $x^E(x^I)$ are computed via patch coupling; second, using both interior and edge values of each patch in the staggered patch grid, the time derivatives of x^I are computed for the full-domain microscale model (5.1.4) of turbulent shallow water flows.

5.1.3 Selection of parameter regime for patch scheme exploration

Table 5.1.1 lists the dimensional parameter ranges we choose to explore the patch schemes for turbulent shallow water flows. We propose that large-scale turbulent waves of floods and tsunamis are important appli-

Table 5.1.1. Approximate dimensional parameter ranges relevant for the turbulent shallow water equations for simulating floods and tsunamis. The domain size L is constrained to be within the shallow water regime $H/L \in [1/100, 1/20]$.

Parameter	Range of values
characteristic mean water height H	1 to 10 m
characteristic flow velocity U	0.1 to 5 m/s
domain size L , depending on H (i.e., $H/L \in [1/100, 1/20]$)	20 m to 1000 m

cation areas of the multiscale staggered patch schemes. The characteristic parameter values (such as the mean water height H , flow velocity U and the bed inclination angle θ) of the floods are within the range of the parameters of tsunamis; for example Cohen et al. (2019) gives a typical range of flood water heights. Hence we choose the range of parameters primarily based on the relevant parameters of tsunamis.

- Ghobarah et al. (2006) reports various the field investigations of the 26 December 2004 tsunami in Thailand and Indonesia. In page 314, they list various wave run-up heights approximately ranging 1 m to 49 m. R bke and V tt (2017, p.298) and IOC (2014, p.4) present the various depths (characteristic mean height H) and instantaneous velocities relevant for the Tsunami wave shoaling from deep sea to the shore. With our focus on the tsunami waves near the shore, and based on the range of the heights in these articles (Ghobarah et al. 2006, p.314; R bke and V tt 2017, p.298; IOC 2014, p.4), we choose the range of characteristic mean heights H from 1 m to 10 m.
- Based on the typical instantaneous velocity of the Tsunami wave near the shore from R bke and V tt (2017, p.298) and IOC (2014, p.4), our focus is on the range of instantaneous velocities from 1 m/s to 10 m/s. Hence we choose the range of characteristic mean velocities U to from 0.1 m/s to 5 m/s to cover both floods and tsunamis.

Table 5.1.1 lists the dimensional parameter ranges we choose for the turbulent shallow water equations. The non-dimensional parameter ranges we choose roughly corresponding to the dimensional parameters in Table 5.1.1 are listed in Table 5.1.2:

- Characteristic non-dimensional mean height $h_M = 2\pi H/L$ is so as to be within the shallow water regime ($H/L \in [1/100, 1/20]$).

Table 5.1.2. Approximate non-dimensional parameter ranges for the general study of the patch schemes for turbulent shallow water equations corresponding to the dimensional parameter ranges in Table 5.1.1.

Parameter	Range of values
characteristic mean non-dimensional mean height $h_M = 2\pi H/L$	$0.05 \approx 2\pi/100$ to $0.3 \approx 2\pi/20$
characteristic mean non-dimensional velocity $u_M = U/\sqrt{g_z H}$	0.03 to 0.5
bed inclination angle θ	-10° to 10°

- Characteristic non-dimensional velocity $u_M = U/\sqrt{g_z H}$ is computed by non-dimensionalising using the long wave speed $\sqrt{g_z H}$ (Cao and Roberts 2016, p.190) for the respective dimensional mean water heights H .
- We choose the range of bed inclination angle θ (positive downwards) to be from -10° to 10° , mainly for exploring the patch scheme simulations in the time domain. But, as θ enters into the turbulent shallow water PDEs via a constant term, the Jacobian of the linearised turbulent shallow water PDEs is independent of the bed inclination angle θ . Hence, for our study of eigenvalues for stability and consistency of the patch schemes, we use the simple case of a horizontal bed with $\theta = 0$.

5.2 Staggered patch schemes are accurate

Following §4.2 for the viscous shallow water flows, this §5.2 shows that the developed five staggered patch schemes are accurate for the turbulent shallow water PDEs (5.1.3). As in §4.2, we establish the accuracy of the staggered patch schemes in general (as opposed to one specific initial condition) by comparing the eigenvalues of the staggered patch schemes with the eigenvalues of fine- and coarse-grid full-domain microscale model, and for completeness also compare with the eigenvalues of the turbulent shallow water PDEs (5.1.3). The eigenvalue analysis for accuracy in this section is done for a representative subset of the physical parameters (mean flow h_M, u_M, v_M) and the grid parameters (macro-grid intervals N , sub-patch micro-grid intervals n , patch scale ratio r). Section 5.4 on the consistency of the patch schemes establishes the accuracy over a wider range of parameters.

The approach to studying the accuracy of the staggered patch schemes and the conventions are the same as discussed in §4.2 for the viscous

shallow water flows. As defined in §4.2, the staggered patch schemes are accurate when the macroscale eigenvalues (defined in p. 52 of §3.2) of that patch scheme agree closely with the corresponding macroscale eigenvalues of the full-domain microscale model. Hence, in the eigenvalue analysis for accuracy in this section, we compare in the complex plane the eigenvalues of the staggered patch schemes with the eigenvalues of the full-domain microscale model.

As in §4.2, we follow the method of substituting an arbitrary Fourier mode into the governing partial/ordinary differential equations to derive the eigenvalues in §§5.2.1 to 5.2.3. Sections 5.2.1 to 5.2.3 derive the eigenvalues for

1. the 2D turbulent shallow water PDEs (5.1.3),
2. the full-domain microscale model (5.1.4), and
3. the staggered patch scheme.

To numerically compute the eigenvalues of the numerical staggered patch scheme, which includes any instabilities and inaccuracies due to the numerical roundoff errors, we numerically differentiate the evolution function as discussed in §§4.2.4 and 4.2.5 for the viscous shallow water flows.

Section 5.2.4 compares and contrasts various eigenvalues (e.g., analytic and numerical eigenvalues of the PDEs, full-domain microscale model, and patch schemes) to demonstrate the accuracy of the patch schemes. We use the same notational convention as in §4.2 to identify the various eigenvalues.

5.2.1 Eigenvalue analysis of the PDEs

Following the same approach of §4.2.1 for the viscous shallow water flows, substituting the Fourier mode (4.2.1) with perturbations proportional to $\exp[i(k_x x + k_y y)]$, into the turbulent shallow water PDEs (5.1.3), followed by linearisation and algebraic simplifications gives an eigensystem with the Jacobian $\mathbf{J}(\mathbf{x}_M)$ about the linearisation point of mean flow $\mathbf{x}_M = (h_M, u_M, v_M)$. The elements of the 3×3 Jacobian $\mathbf{J}(\mathbf{x}_M)$ of the 2D turbulent shallow water PDEs (5.1.3) are

$$\mathbf{J}_{1,1} = -i h_M u_M k_x - i h_M v_M k_y, \quad (5.2.1a)$$

$$\mathbf{J}_{1,2} = -i h_M^2 k_x, \quad (5.2.1b)$$

$$\mathbf{J}_{1,3} = -i h_M^2 k_y, \quad (5.2.1c)$$

$$\mathbf{J}_{2,1} = -0.993 i k_x + \frac{0.003 u_M q_M}{h_M}, \quad (5.2.1d)$$

$$\begin{aligned} \mathbf{J}_{2,2} = & -0.094 h_M^2 q_M k_x^2 - 0.094 h_M^2 q_M k_y^2 \\ & - 1.030 i h_M u_M k_x - 1.020 i h_M v_M k_y \\ & - 0.003 q_M - \frac{0.003 u_M^2}{q_M}, \end{aligned} \quad (5.2.1e)$$

$$\mathbf{J}_{2,3} = -\frac{0.003 u_M v_M}{q_M}, \quad (5.2.1f)$$

$$\mathbf{J}_{3,1} = -0.993 i k_y + \frac{0.003 v_M q_M}{h_M}, \quad (5.2.1g)$$

$$\mathbf{J}_{3,2} = -\frac{0.003 u_M v_M}{q_M}, \quad (5.2.1h)$$

$$\begin{aligned} \mathbf{J}_{3,3} = & -0.094 h_M^2 q_M k_x^2 - 0.094 h_M^2 q_M k_y^2 \\ & - 1.020 i h_M u_M k_x - 1.030 i h_M v_M k_y \\ & - 0.003 q_M - \frac{0.003 v_M^2}{q_M}. \end{aligned} \quad (5.2.1i)$$

Similar to the Jacobian in the eigensystem (4.2.4) for the viscous shallow water flows, the Jacobian $\mathbf{J}(\mathbf{x}_M)$ for the nonlinear turbulent shallow water flows depends on the wavenumber (k_x, k_y) and the linearisation point $\mathbf{x}_M = (h_M, u_M, v_M)$, which is the mean flow state.

We compute the eigenvalues $\lambda_{\text{PDE}}^{\text{NEI}}$ of the numerically evaluated Jacobian $\mathbf{J}(\mathbf{x}_M)$, and compare (for sanity check) with the eigenvalues of the full domain microscale model and the patch schemes for assessing the accuracy of the patch schemes in §5.2.4.

5.2.2 Eigenvalue analysis of staggered grid full-domain model

Following the same approach of §4.2.2 for the full-domain microscale model of the viscous shallow water flows, substituting the discrete Fourier mode (4.2.6) with perturbations proportional to $\exp[i(k_x i\delta + k_y j\delta)]$, into the full-domain microscale model (5.1.4) of turbulent shallow water flows, followed by linearisation and algebraic simplifications gives an eigensystem with the Jacobian $\mathbf{J}(\mathbf{x}_M)$ about the linearisation point of mean flow $\mathbf{x}_M = (h_M, u_M, v_M)$. The elements of the 3×3 Jacobian $\mathbf{J}(\mathbf{x}_M)$ of the full-domain microscale model (5.1.4) are

$$\mathbf{J}_{1,1} = -i h_M u_M \frac{\sin(2\delta k_x)}{2\delta} - i h_M v_M \frac{\sin(2\delta k_y)}{2\delta}, \quad (5.2.2a)$$

$$\mathbf{J}_{1,2} = -i h_M^2 \frac{\sin(\delta k_x)}{\delta}, \quad (5.2.2b)$$

$$\mathbf{J}_{1,3} = -i h_M^2 \frac{\sin(\delta k_y)}{\delta}, \quad (5.2.2c)$$

$$\mathbf{J}_{2,1} = -0.993 i \frac{\sin(\delta k_x)}{\delta} + \frac{0.003 u_M q_M}{h_M} \cos(\delta k_x), \quad (5.2.2d)$$

$$\begin{aligned} \mathbf{J}_{2,2} = & -0.094 h_M^2 q_M \left[\frac{\sin(\delta k_x)}{\delta} \right]^2 - 0.094 h_M^2 q_M \left[\frac{\sin(\delta k_y)}{\delta} \right]^2 \\ & - 1.030 i h_M u_M \frac{\sin(2\delta k_x)}{2\delta} - 1.020 i h_M v_M \frac{\sin(2\delta k_y)}{2\delta} \\ & - 0.003 q_M - \frac{0.003 u_M^2}{q_M}, \end{aligned} \quad (5.2.2e)$$

$$\mathbf{J}_{2,3} = -\frac{0.003 u_M v_M}{q_M} \cos(\delta k_x) \cos(\delta k_y), \quad (5.2.2f)$$

$$\mathbf{J}_{3,1} = -0.993 i \frac{\sin(\delta k_y)}{\delta} + \frac{0.003 v_M q_M}{h_M} \cos(\delta k_y), \quad (5.2.2g)$$

$$\mathbf{J}_{3,2} = -\frac{0.003 u_M v_M}{q_M} \cos(\delta k_x) \cos(\delta k_y), \quad (5.2.2h)$$

$$\begin{aligned} \mathbf{J}_{3,3} = & -0.094 h_M^2 q_M \left[\frac{\sin(\delta k_x)}{\delta} \right]^2 - 0.094 h_M^2 q_M \left[\frac{\sin(\delta k_y)}{\delta} \right]^2 \\ & - 1.020 i h_M u_M \frac{\sin(2\delta k_x)}{2\delta} - 1.030 i h_M v_M \frac{\sin(2\delta k_y)}{2\delta} \\ & - 0.003 q_M - \frac{0.003 v_M^2}{q_M}. \end{aligned} \quad (5.2.2i)$$

As in §4.2.2, as the grid interval $\delta \rightarrow 0$ and/or the wavenumber $(k_x, k_y) \rightarrow (0, 0)$, the Jacobian elements (5.2.2) of the full-domain microscale model converge to the Jacobian elements (5.2.1) of the turbulent shallow water PDEs. Hence, the eigenvalues of the full-domain microscale model (5.1.4) converge to the analytic eigenvalues of the PDEs (5.1.3) as we decrease the grid interval δ and/or wavenumber (k_x, k_y) .

We compute the eigenvalues λ_m^{NE1} of the numerically evaluated Jacobian $\mathbf{J}(\mathbf{x}_M)$ for specific wavenumber and the linearisation point \mathbf{x}_M . As in §4.2.2, when we compute the eigenvalues λ_m^{NE1} of the full-domain microscale model,

- for the same grid-spacing δ as the sub-patch micro-grid interval (also called δ), we call the eigenvalues $\lambda_{m\delta}^{NE1}$,
- for the same grid-spacing Δ as the inter-patch distance Δ , we call the eigenvalues $\lambda_{m\Delta}^{NE1}$.

For various macroscale wavenumbers, we compute the eigenvalues of the numerically evaluated Jacobian $\mathbf{J}(\mathbf{x}_M)$, and compare with the eigenvalues of the turbulent shallow water PDEs and the patch schemes for assessing the accuracy (§5.2.4) and stability (§5.3) of the patch schemes.

5.2.3 Analytic eigenvalue analysis of staggered patch schemes

This subsection derives analytic eigenvalues of a generic staggered patch scheme over a staggered patch grid, for the 2D turbulent shallow water PDEs (5.1.3). We use the patch scheme eigenvalues to assess accuracy (§5.2.4), stability (§5.3), and consistency (§5.4) of the staggered patch schemes.

The staggered patch schemes for turbulent shallow water flows use the same patch grid as viscous shallow water flows, as in Fig. 4.1.2b, with two layers of edge nodes in the normal direction to the edges, one layer of edge nodes in the tangential direction to the edges. Page 168 of §4.1.3 discusses why the staggered patch grid with such edge node arrangement is required for the viscous shallow water flows, the same arguments apply for the turbulent shallow water flows.

Following the same approach of §4.2.3 for the viscous shallow water flows, substituting the patch scheme Fourier mode (4.2.10) with perturbations proportional to $\exp[i(k_x I\Delta + k_y J\Delta)]$, into the patch scheme (equations (5.1.4) with patch index I, J in superscript for each term) for the turbulent shallow water flows, followed by linearisation and algebraic simplifications gives an eigensystem (e.g., (4.2.14)) with the one-cell analytic Jacobian $\mathbf{J}(\mathbf{x}_M)$ for the patch scheme about the linearisation point of mean flow $\mathbf{x}_M = (h_M, u_M, v_M)$. The only physical parameter in the patch scheme for turbulent shallow water flows is the bed inclination angle θ . The physical parameter θ occurs only as a the constant term $0.993 \tan \theta$ (without being multiplied by a state value) in the equations (5.1.4b) and (5.1.4c). Hence, none of the Jacobian elements depends on the physical parameter θ .

For example, similar to the case of general linear wave and viscous shallow water flows, for $n = 6$ sub-patch grid intervals, the one-cell Jacobian $\mathbf{J}(\mathbf{x}_M)$ for the turbulent shallow water flows, is a 59×59 sparse matrix generally with only 318 of the 3481 elements being nonzero irrespective of the particular patch coupling interpolation of the staggered patch schemes (i.e., same for both the spectral patch scheme and all the polynomial patch schemes). For some particular combinations of numerical values of the parameters, the sparsity is higher. The 318 nonzero elements of the one-cell

Jacobian of a staggered patch scheme (for $n = 6$) contain all the information about the underlying microscale model and the patch coupling, for the macroscale wave of wavenumber (k_x, k_y) . The elements of a staggered patch scheme one-cell Jacobian for turbulent shallow water flows are similar to the expressions in p. 185 of §4.2.3 for viscous shallow water flows, with differences due to the different nonlinearities. In the one-cell Jacobian elements for turbulent shallow water flows, the increasing complexity with the order of interpolation is also the same as that of the viscous shallow water flows.

Due to the large Jacobian size (e.g., 59×59 for $n = 6$) and the long expressions in their elements, all the CAS packages we tried (SymPy, Reduce and Maple) fail to compute the analytic eigenvalues of the one-cell Jacobian, even for the simplest staggered patch scheme Square-p2 with $n = 6$ sub-patch micro-grid intervals. So we numerically evaluate the one-cell Jacobian for numerical values of $\Delta, \delta, h_M, u_M, v_M, k_x, k_y$ and compute the eigenvalues λ_p^{NE1} . We compare with the eigenvalues λ_p^{NE1} of the numerically evaluated one-cell Jacobian of the patch schemes, with the eigenvalues of the full domain microscale model and the eigenvalues of the general linear wave PDEs, for assessing the accuracy (§5.2.4) and stability (§5.3) of the patch schemes.

5.2.4 Staggered patch schemes are accurate for macroscale waves

Similar to §§3.2.6 and 4.2.6 for the general linear wave and viscous shallow water flows, this section explains the qualitative structure of the staggered patch scheme eigenvalues and eigenvectors, and qualitatively demonstrates the accuracy of the staggered patch schemes for the *turbulent shallow water flows* for few representative cases. Section 5.4 on the consistency of the staggered patch schemes, quantitatively establish the patch scheme accuracy in more detail, over a much broader range of parameters.

Similar to §§3.2.6 and 4.2.6, this section demonstrates the accuracy of the developed five staggered patch schemes (Spectral, Square-p2, Square-p4, Square-p6, and Square-p8) by comparing the following eigenvalues in the complex plane plots.

1. Eigenvalues λ_p^N of the numerical Jacobian of a staggered patch scheme on a finite domain (e.g., §4.2.5).
2. Eigenvalues λ_p^{NE1} of the numerically evaluated one-cell Jacobian in §5.2.3, of a staggered patch scheme on an infinite domain.

3. Eigenvalues $\lambda_{m\delta}^{\text{NE1}}$ of the numerically evaluated analytic Jacobian in §5.2.2, of fine-grid full-domain microscale model, with micro-grid interval equal to the sub-patch micro-grid interval δ .
4. Eigenvalues $\lambda_{m\Delta}^{\text{NE1}}$ of the numerically evaluated analytic Jacobian in §5.2.2, of coarse grid version of the full-domain microscale model, with $\delta = \Delta$.
5. Eigenvalues $\lambda_{\text{PDE}}^{\text{NE1}}$ of the numerically evaluated analytic Jacobian in §5.2.1, of turbulent shallow water PDEs (5.1.3). Comparison with the eigenvalues $\lambda_{\text{PDE}}^{\text{NE1}}$ is only for completeness.

All the analytic eigenvalues ($\lambda_p^{\text{NE1}}, \lambda_{m\delta}^{\text{NE1}}, \lambda_{m\Delta}^{\text{NE1}}, \lambda_{\text{PDE}}^{\text{NE1}}$) are numerically evaluated for all the $N^2/4$ *macroscale wavenumbers* (k_x, k_y) resolved on a corresponding finite staggered patch grid with $N \times N$ macro-grid intervals. To illustrate the complete structure of eigenvalues (i.e., for all wavenumbers) of the full-domain microscale model and to cross-verify analytic and numerical computation of the full-domain microscale model eigenvalues, we also compute the eigenvalues of the numerical Jacobian of the full-domain microscale model for few cases (e.g., Figs. 5.2.1 and 5.2.2).

The sets of eigenvalues (e.g., $\lambda_p^{\text{N}}, \lambda_p^{\text{NE1}}, \lambda_{m\delta}^{\text{N}}, \lambda_{m\Delta}^{\text{N}}, \lambda_{\text{PDE}}^{\text{NE1}}$), in all the complex plane plots, are numbered in the legend entries on the left. In all the complex plane plots, physical parameters for each of these eigenvalues are listed in groups *below the legend entries*. Page 68 of §3.2.6 explains with an example, the conventions of this parameter listing.

Figures 5.2.1 and 5.2.2 plot the eigenvalues ($\lambda_p^{\text{N}}, \lambda_p^{\text{NE1}}$) of the Spectral patch scheme on a staggered patch grid with 6×6 macro-grid intervals ($N = 6$) and each patch containing 6×6 sub-patch micro-grid intervals ($n = 6$). Also plotted are the eigenvalues $\lambda_{m\delta}^{\text{N}}, \lambda_{m\Delta}^{\text{N}}$ of respectively the fine- and coarse-grid versions of the full-domain microscale model (5.1.4) and the eigenvalues $\lambda_{\text{PDE}}^{\text{NE1}}$ of the PDE (5.1.3). Similar to Figs. 5.2.1 and 5.2.2, in all the complex plane eigenvalue plots, eigenvalues are grouped within clusters based on eigenvalues λ_p^{NE1} of the staggered patch scheme Jacobian. Each cluster is annotated with the number of eigenvalues λ_p^{NE1} in the cluster and the cluster number in the superscript.

Page 71 of §3.2.6 explains the rationale and utility of the arcsinh scaling used in Fig. 5.2.2. For example, the clusters of macroscale eigenvalues on arcsinh scaling (i.e., clusters 1–7 in Fig. 5.2.2) reveal more details, compared to the clusters of macroscale eigenvalues on linear scaling (i.e., cluster 1 in Fig. 5.2.1). Hence, *most complex plane eigenvalue plots in this thesis are on arcsinh scaling*. Specifically, the complex plane plots on arcsinh scaling, plot an eigenvalue λ as a point on a 2D space with coordinates

Figure 5.2.1. Spectral staggered patch scheme ($N = 6, n = 6$) eigenvalues ($\lambda_p^N, \lambda_p^{NE1}$) on complex plane (*linear scale*) for turbulent shallow water flows. Due to the large range of magnitudes of eigenvalues, details of eigenvalues for macroscale modes (mid-right cluster 1) are not discernable.

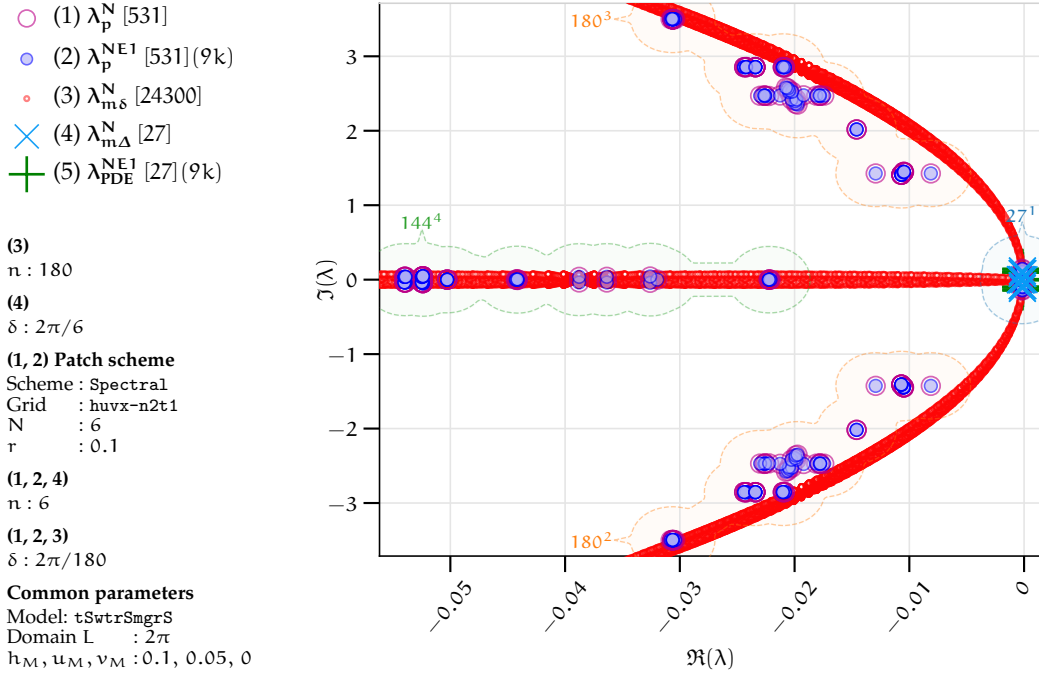
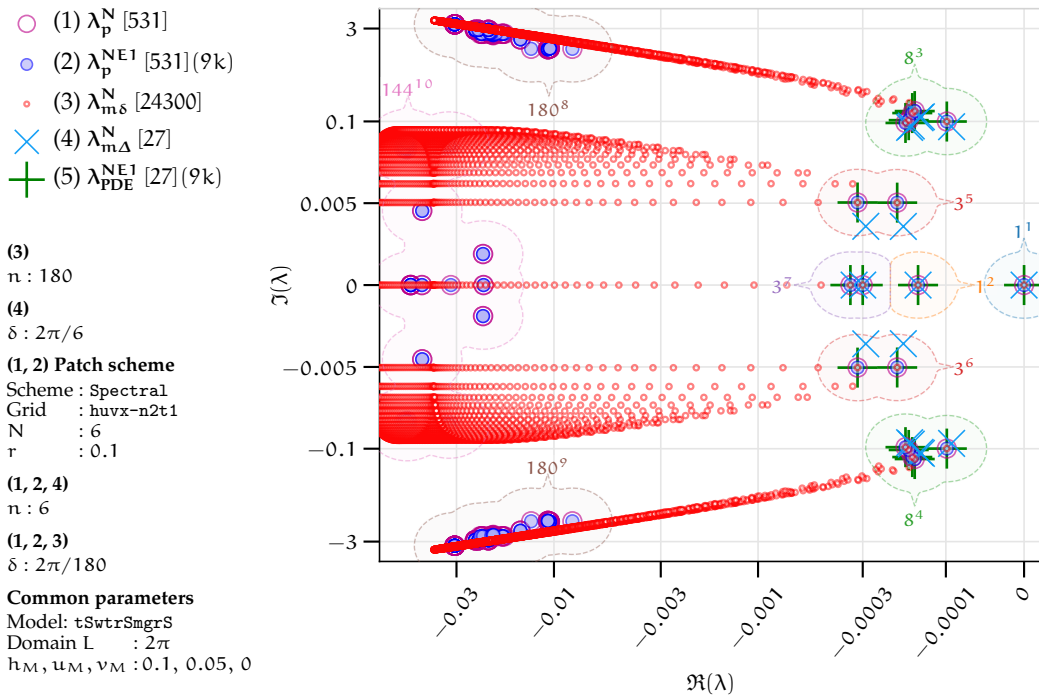


Figure 5.2.2. Spectral staggered patch scheme ($N = 6, n = 6$) eigenvalues ($\lambda_p^N, \lambda_p^{NE1}$) on complex plane (*arcsinh nonlinear scale*) for turbulent shallow water flows. The arcsinh scaling zooms out the eigenvalues of macroscale modes (mid-right cluster 1 in Fig. 5.2.1 to clusters 1–7 here).



($\text{arcsinh}[S_h \Re(\lambda)]/S_h$, $\text{arcsinh}[S_v \Im(\lambda)]/S_v$), where S_h, S_v are the horizontal and vertical scale factors and $(0, 0)$ is the centre of zoom. In this chapter, most plots on arcsinh scaling use the scale factors $S_h = 10^4$, $S_v = 5 \cdot 10^4$ (different from those in §3.2.6 for general linear wave and §4.2.6 for viscous shallow water flows).

As Page 80 of §3.2.6 defines, a *staggered patch scheme is accurate* when the macroscale eigenvalues (e.g., $\lambda_p^N, \lambda_p^{NE1}$) of the staggered patch schemes are close to the macroscale eigenvalues (e.g., $\lambda_{m\delta}^{NE1}$) of the corresponding fine-grid full-domain microscale model with the same grid interval as the sub-patch micro-grid interval. Figure 5.2.2 shows that, within the clusters 1–7 on the right, the numerical macroscale eigenvalues λ_p^N of the patch scheme (large magenta circles) and the numerical macroscale eigenvalues $\lambda_{m\delta}^N$ (small red circles) visually agree. That is the Spectral patch scheme accurately resolves the macroscale waves.

As Fig. 5.2.2 shows, for both microscale and macroscale modes, the patch scheme eigenvalues λ_p^{NE1} of the numerically evaluated one-cell analytic Jacobian (§5.2.3) and the patch scheme eigenvalues λ_p^N of the numerical Jacobian (e.g., §4.2.5), agree (i.e., the large magenta and blue circles). Hence, to avoid large computational effort and as the primary focus is on the macroscale eigenvalues, *all other complex plane plots in this subsection §5.2.4 use eigenvalues $\lambda_{m\delta}^{NE1}$ of the numerically evaluated analytic Jacobian (§5.2.2), as opposed to the numerical eigenvalues $\lambda_{m\delta}^N$.*

The qualitative structure of the eigenvalues (e.g., in Fig. 5.2.2) of the turbulent shallow water flows are same as those of the viscous shallow water flows explained in p. 193 of §4.2.6. The patch scheme eigenvectors of the turbulent shallow water flows are also qualitatively same as the eigenvectors in Figs. 3.2.13 to 3.2.18 (general linear wave) and Figs. 4.2.13 and 4.2.14 (viscous shallow water flows).

Sections 4.4 and 5.3 on patch scheme stability define *artificial instability* as a characteristic of a patch scheme to be *more unstable* than the corresponding full-domain microscale model. That is, a patch scheme is artificially unstable when the maximum real part of the patch scheme eigenvalues is positive and larger than the maximum real part of the corresponding full-domain microscale model is stable. Unlike the general linear wave and the viscous shallow water flows, for $n = 6$ sub-patch micro-grid intervals, the staggered patch schemes for the turbulent shallow water flows have artificial instability for many combinations of the mean height h_M and horizontal mean velocities u_M, v_M . Figure 5.3.4 in p. 308 of §5.3 shows that $n = 10$ avoids such artificial instability. Hence, all the following complex plane plots in this subsection use $n = 10$ sub-patch micro-grid intervals.

Comparing macroscale eigenvalues λ_p^{NE1} and $\lambda_{m\delta}^{NE1}$ the following two

paragraphs show that the patch schemes are accurate for macroscale turbulent shallow water flows for different linearisation points (h_M, u_M, v_M) , assuming $v_M = 0$ without loss of generality (§4.6 shows that the staggered patch schemes are invariant to flow direction).

The *staggered patch schemes are accurate for macroscale turbulent shallow water flows of different mean velocity u_M* . Except for the quantitative parameter dependence, *all the following points about the qualitative dependence of the turbulent shallow water flows on the mean velocity, are the same as those of the viscous shallow water flows in p. 197 of §4.2.6*. Figures 5.2.3 to 5.2.6 plot the Spectral patch scheme ($N = 10, n = 10$) eigenvalues for different mean velocity $u_M = 10^{-5}, 0.05, 3, 5$ respectively, keeping $h_M = 0.1$ and $v_M = 0$. Whereas the following points are based on the Spectral patch scheme eigenvalues, they also hold for the four polynomial patch schemes (§2.2.2).

- Figures 5.2.3 to 5.2.6 show that for the different mean velocity of $u_M = 10^{-5}, 0.05, 3, 5$, the macroscale eigenvalues λ_p^{NE1} of the Spectral patch scheme (large blue circles within macroscale clusters identified in figure caption), agree with the macroscale eigenvalues $\lambda_{m\delta}^{NE1}$ (small red circles) of the fine-grid full-domain microscale model. This macroscale agreement of eigenvalues $\lambda_p^{NE1}, \lambda_{m\delta}^{NE1}$ indicates that the *patch schemes are accurate for macroscale turbulent shallow water flows for different mean velocity*.
- While increasing u_M from 10^{-5} to 5, as the previous paragraph explains, first the vortex modes (cluster 4 in Fig. 5.2.3) split into vortex modes and advecting shear flow modes (clusters 4 and clusters 5, 6 respectively in Fig. 5.2.4), next the clusters of advecting shear flow modes distort and overlap with the clusters of the (dynamical/oscillatory) wave mode (clusters 5, 6 in Figs. 5.2.5 and 5.2.6).
- The *spectral gap* (between the microscale and macroscale patch scheme eigenvalues) *decreases with increasing mean velocity u_M* . For example, in Figs. 5.2.3 to 5.2.6 for mean velocities $u_M = 10^{-5}, 0.05, 3, 5$, the corresponding spectral gaps are 4841, 4661, 35, 11. Physically, increasing u_M , increases the bed drag (macroscale eigenvalues move to left) faster than the eddy viscosity increases (microscale eigenvalues move to left), leading to decreasing spectral gap. This decreasing spectral gap with increasing u_M is the most prevalent trend among the various combinations of u_M , mean height h_M and patch scale ratio r . But, for some combinations of the grid parameters (N, n, r) and physical parameters (Re, h_M, u_M), as for the viscous shallow water flows (p. 198 of §4.2.6), a small subset of the microscale eigenvalues in the complex

Figure 5.2.3. Spectral staggered patch scheme ($N = 10, n = 10$) eigenvalues λ_p^{NE1} for turbulent shallow water flows for $(h_M, u_M, v_M) = (0.1, 10^{-5}, 0)$. Eigenvalues λ_p^{NE1} and $\lambda_{m\delta}^{NE1}$ of the fine-grid full-domain micro-scale model agree for macroscale wavenumbers in clusters 1, 2, 3.

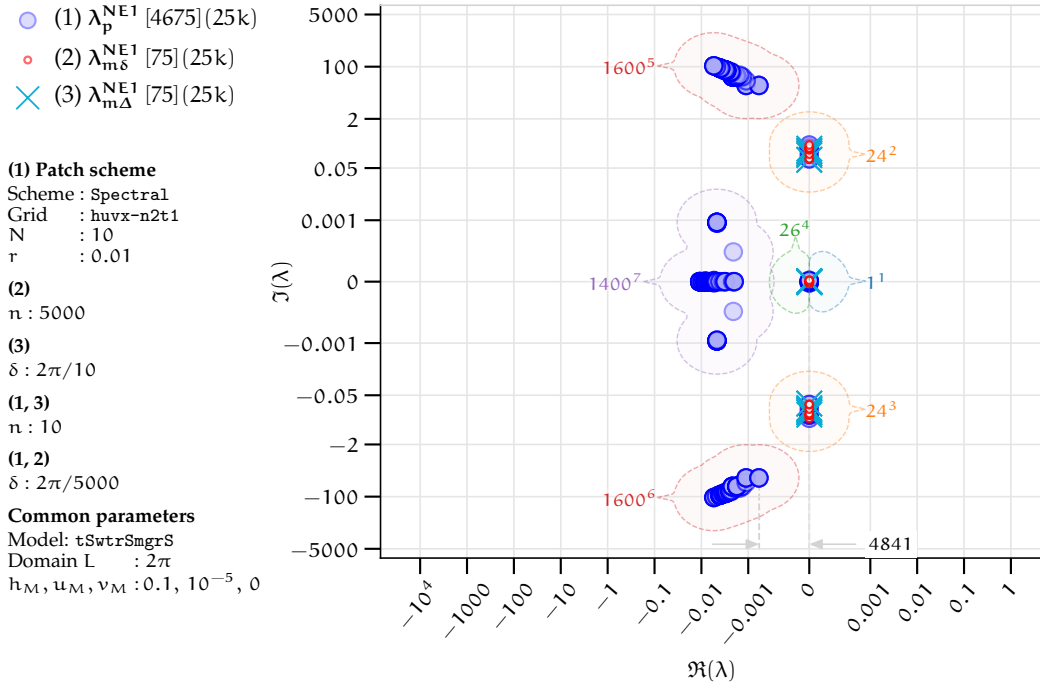


Figure 5.2.4. Spectral staggered patch scheme ($N = 10, n = 10$) eigenvalues λ_p^{NE1} for turbulent shallow water flows for $(h_M, u_M, v_M) = (0.1, 0.05, 0)$. Eigenvalues λ_p^{NE1} and $\lambda_{m\delta}^{NE1}$ of the fine-grid full-domain micro-scale model agree for macroscale modes in clusters 1–6.

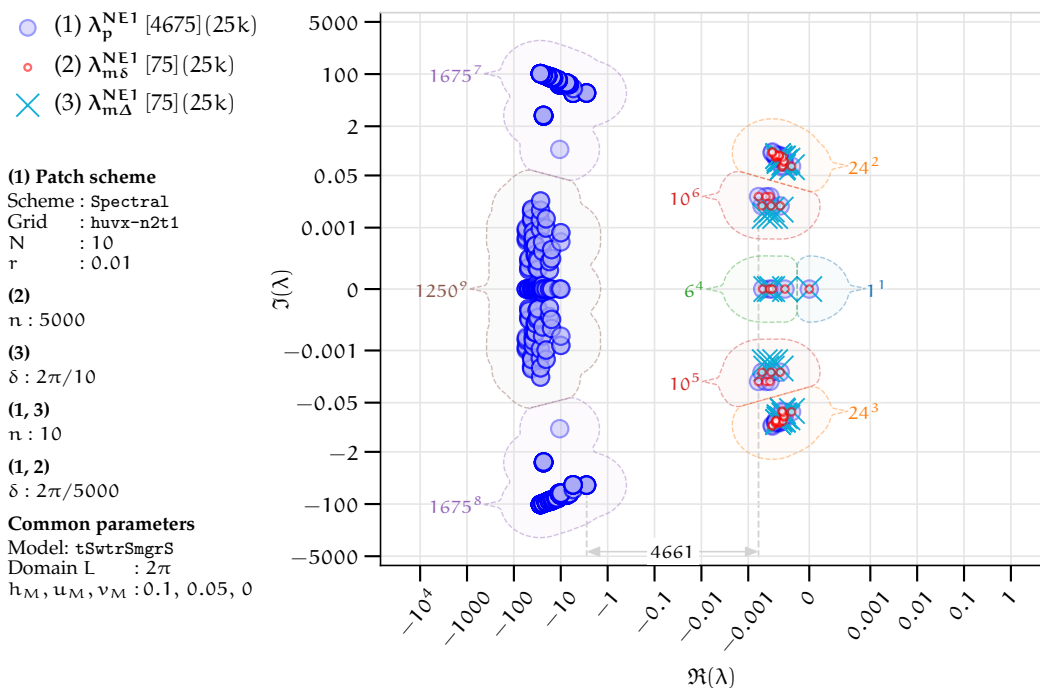


Figure 5.2.5. Spectral staggered patch scheme ($N = 10, n = 10$) eigenvalues λ_p^{NE1} for turbulent shallow water flows for $(h_M, u_M, v_M) = (0.1, 3, 0)$. Eigenvalues λ_p^{NE1} and $\lambda_{m\delta}^{NE1}$ agree for macroscale modes in clusters 1–6. *Physically* unstable macroscale wave modes in clusters 1, 2.

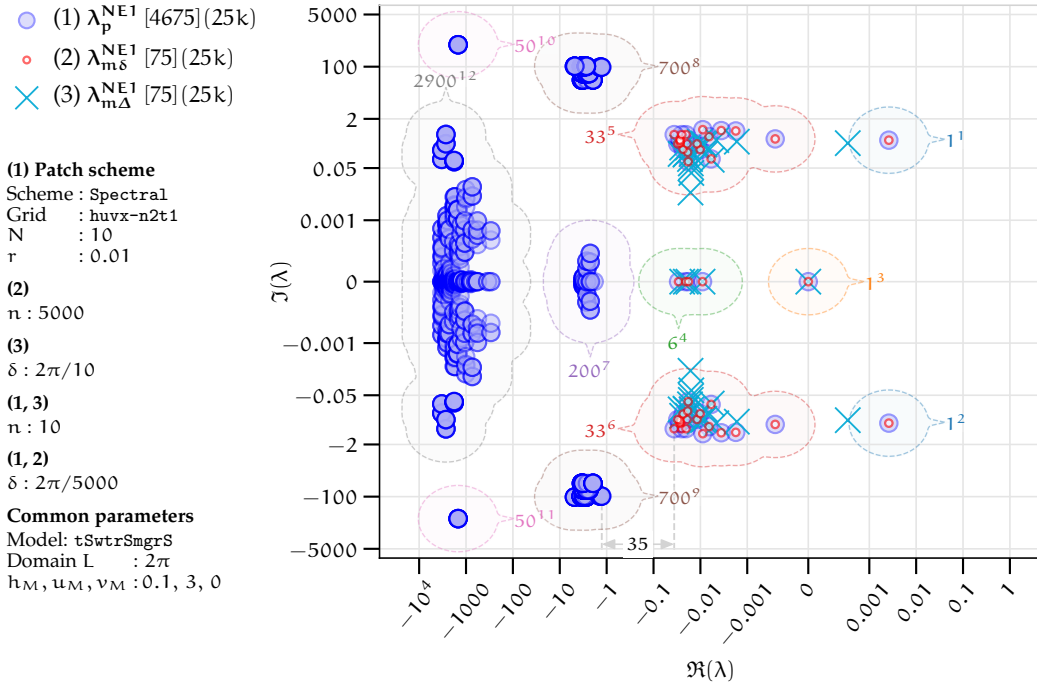
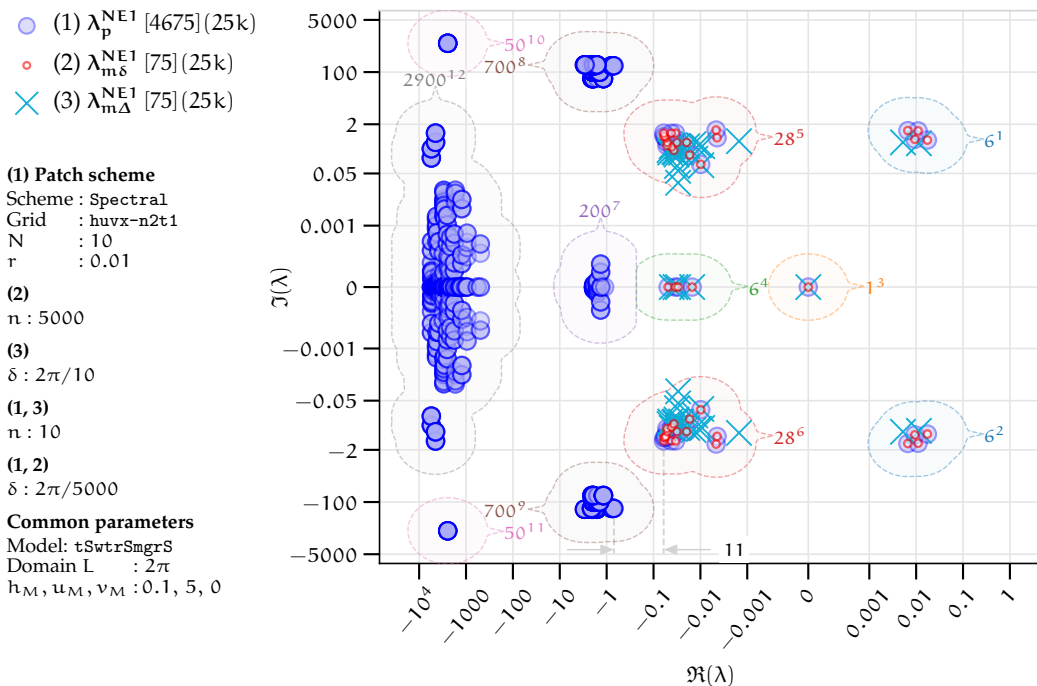


Figure 5.2.6. Spectral staggered patch scheme ($N = 10, n = 10$) eigenvalues λ_p^{NE1} for turbulent shallow water flows for $(h_M, u_M, v_M) = (0.1, 5, 0)$. Eigenvalues λ_p^{NE1} and $\lambda_{m\delta}^{NE1}$ agree for macroscale modes in clusters 1–6. *Physically* unstable macroscale wave modes in clusters 1, 2.



plane move to the right with increasing u_M , leading to decreasing the spectral gap. For example, the clusters 7–9 in Figs. 5.2.5 and 5.2.6 contain such eigenvalues of sub-patch microscale modes.

- Compared to the viscous shallow water flows in p. 197 of §4.2.6, increasing u_M decreases the spectral gap more rapidly. This rapid decrease in spectral gap is due to increasing real parts of the eigenvalues for some of the *weakly dissipating microscale modes* such as clusters 7, 8, 9 in Figs. 5.2.5 and 5.2.6
- For large mean velocity $u_M \gtrsim 2$, the turbulent shallow water flows have inherent *physical instability*, (i.e., the full-domain microscale model itself is unstable). Such physical instability is evident from the positive real part eigenvalues of the full-domain microscale model in Figs. 5.2.5 and 5.2.6 (clusters 1, 2). Section 4.4.1 for viscous shallow water flows, shows the detailed trends of similar physical instabilities as captured by the patch scheme for a wide range of parameters h_M, u_M, N, r, n .

The *staggered patch schemes are accurate for macroscale viscous shallow water flows for different mean height h_M* . Figs. 5.2.5, 5.2.7 and 5.2.8 plot the Spectral patch scheme ($N = 10, n = 10$) eigenvalues for different mean heights $h_M = 0.1, 0.2, 0.3$ respectively, keeping $u_M = 3$ and $v_M = 0$. The following points summarise the key dependence of the patch scheme eigenvalues on increasing mean height h_M . All the characteristics in the following listing also hold for the four polynomial patch schemes (§2.2.2).

- Figures 5.2.5, 5.2.7 and 5.2.8 show that for the different mean heights of $h_M = 0.1, 0.2, 0.3$, the macroscale eigenvalues λ_p^{NE1} of the Spectral patch scheme (large blue circles within macroscale clusters identified in figure caption), agree with the macroscale eigenvalues $\lambda_{m\delta}^{NE1}$ (small red circles) of the fine-grid full-domain microscale model. This macroscale agreement of eigenvalues $\lambda_p^{NE1}, \lambda_{m\delta}^{NE1}$ indicates that the *patch schemes are accurate for macroscale turbulent shallow water flows for different mean heights*.
- As with the viscous shallow water flows, while increasing h_M from 0.1 to 0.3, both the microscale and macroscale eigenvalues move to the left, taking larger negative real parts. That is, increasing h_M increases both the microscale and macroscale dissipation.
- *In contrast to the viscous shallow water flows, the spectral gap decreases with increasing mean height h_M* . Similar to the viscous shallow water

Figure 5.2.7. Spectral staggered patch scheme ($N = 10, n = 10$) eigenvalues for turbulent shallow water flows for $(h_M, u_M, v_M) = (0.2, 1, 0)$. The macroscale eigenvalues λ_p^{NE1} clusters 1–6 agree with macroscale eigenvalues $\lambda_{m\delta}^{NE1}$. Increasing h_M decreases spectral gap (Figs. 5.2.5, 5.2.7 and 5.2.8).

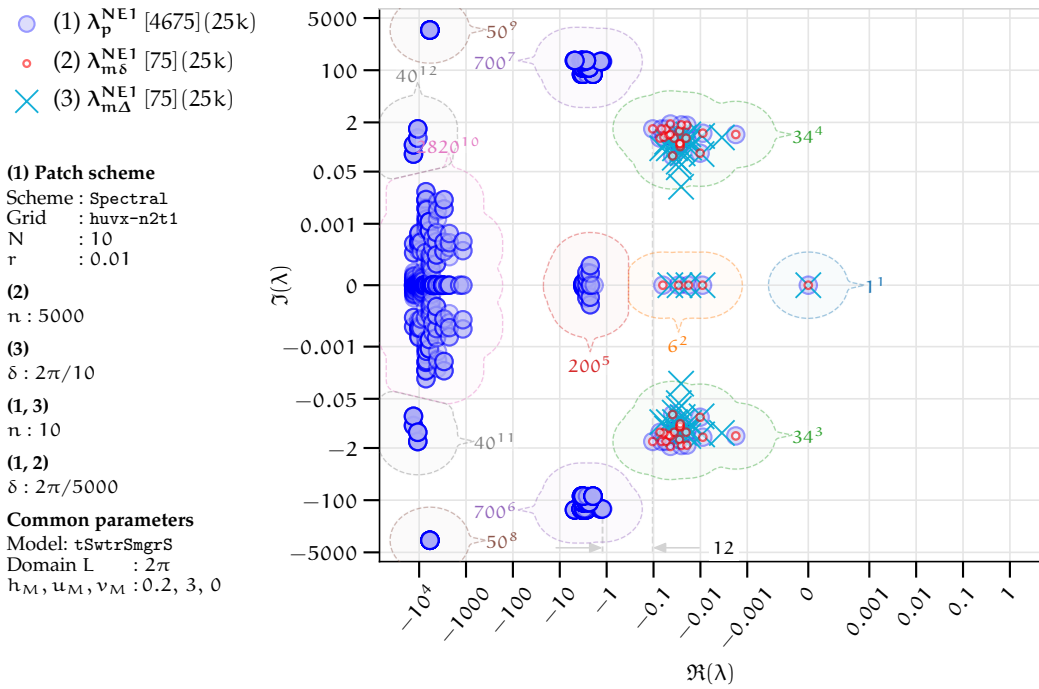
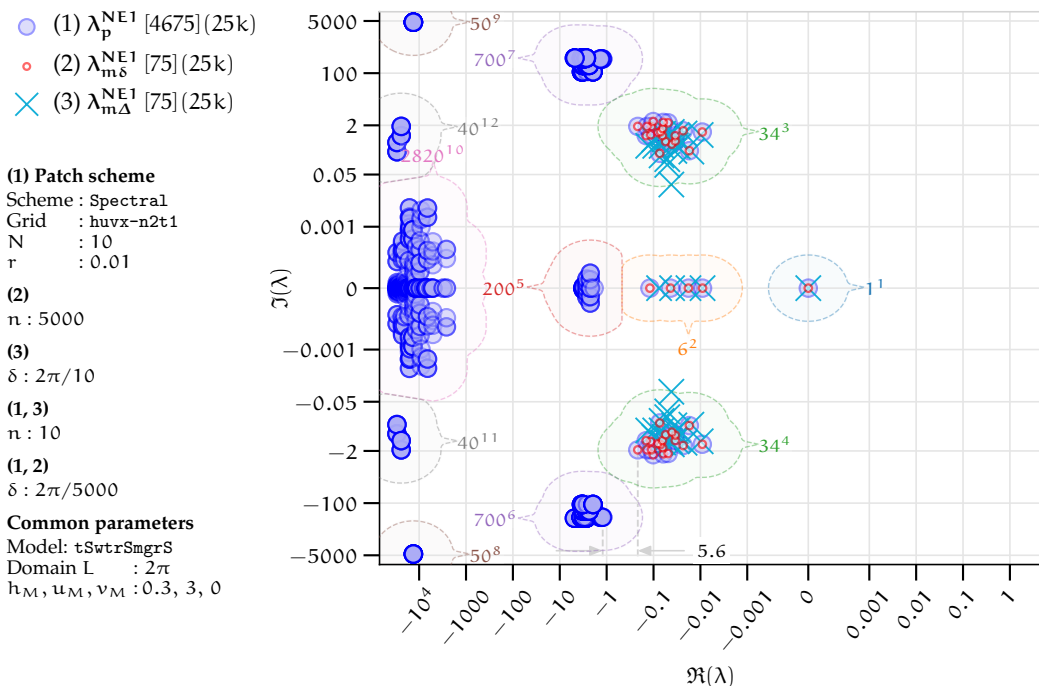


Figure 5.2.8. Spectral staggered patch scheme ($N = 10, n = 10$) eigenvalues for turbulent shallow water flows for $(h_M, u_M, v_M) = (0.3, 1, 0)$. The macroscale eigenvalues λ_p^{NE1} in clusters 1–6 agree with macroscale eigenvalues $\lambda_{m\delta}^{NE1}$. Increasing h_M decreases spectral gap (Figs. 5.2.5, 5.2.7 and 5.2.8).



flows, both the microscale and macroscale dissipation increase with increasing h_M ; yet, the microscale dissipation increases at a larger rate. This is possibly due to the increasing turbulent mixing with increasing mean height h_M , whereas the bed drag remains nearly constant. But, increasing h_M also pushes some of the microscale eigenvalues (weakly dissipating microscale modes) to the right (e.g., clusters 5, 6, 7 in Figs. 5.2.7 and 5.2.8). Hence, the spectral gap decreases with increasing mean height h_M . For example, in Figs. 5.2.5, 5.2.7 and 5.2.8 for mean heights $h_M = 0.1, 0.2, 0.3$, the corresponding spectral gaps are 35, 12, 5.6.

The last two paragraphs demonstrate that for different linearisation points (h_M, u_M, v_M) , the macroscale eigenvalues λ_p^{NE1} of the Spectral patch scheme agree with the macroscale eigenvalues $\lambda_{m\delta}^{NE1}$ of the fine-grid full-domain microscale model. This agreement of the Spectral patch scheme macroscale eigenvalues with those of the fine-grid full-domain model, is exact (within numerical roundoff errors). The polynomial patch scheme macroscale eigenvalues also agree with those of the fine-grid full-domain model, but to a varying degree of accuracy (§5.4 on consistency gives more details). Thus, the *staggered patch schemes are accurate for macroscale turbulent shallow water flows, about different linearisation points*. Section 5.4 on the consistency of the staggered patch schemes, establishes the accuracy for wider range of parameters h_M, u_M, N, r, n .

5.3 Staggered patch schemes are not artificially unstable for appropriate patch grids

Similar to §4.4 for viscous shallow water flows, a detailed study of the patch scheme eigenvalues shows that the staggered patch schemes are not artificially unstable for appropriate grid parameters. This section explains some notable trends.

For a sufficiently large number of sub-patch micro-grid intervals $n \geq 10$, and a sufficiently small patch scale ratio $r \lesssim 0.01$, the patch schemes do not have any artificial instability.

- Figures 5.3.1 and 5.3.2 show the patch scheme eigenvalues for patch scale ratio $r = 0.01, 0.1$ respectively, keeping all other parameters the same. Figures 5.3.1 and 5.3.2 illustrate that using appropriately small patch scale ratio removes artificial instability. With few exceptions, the trend of decreasing artificial instability with decreasing patch scale ratio r holds in general.

Figure 5.3.1. Spectral staggered patch scheme ($N = 10, n = 10, r = 0.01$) eigenvalues λ_p^{NE1} for turbulent shallow water flows for $(h_M, u_M, v_M) = (0.1, 0.5, 0)$. Eigenvalues λ_p^{NE1} and $\lambda_{m\delta}^{NE1}$ agree for macroscale modes in clusters 1–8. *No artificial instability* as in Fig. 5.3.2 for $r = 0.1$.

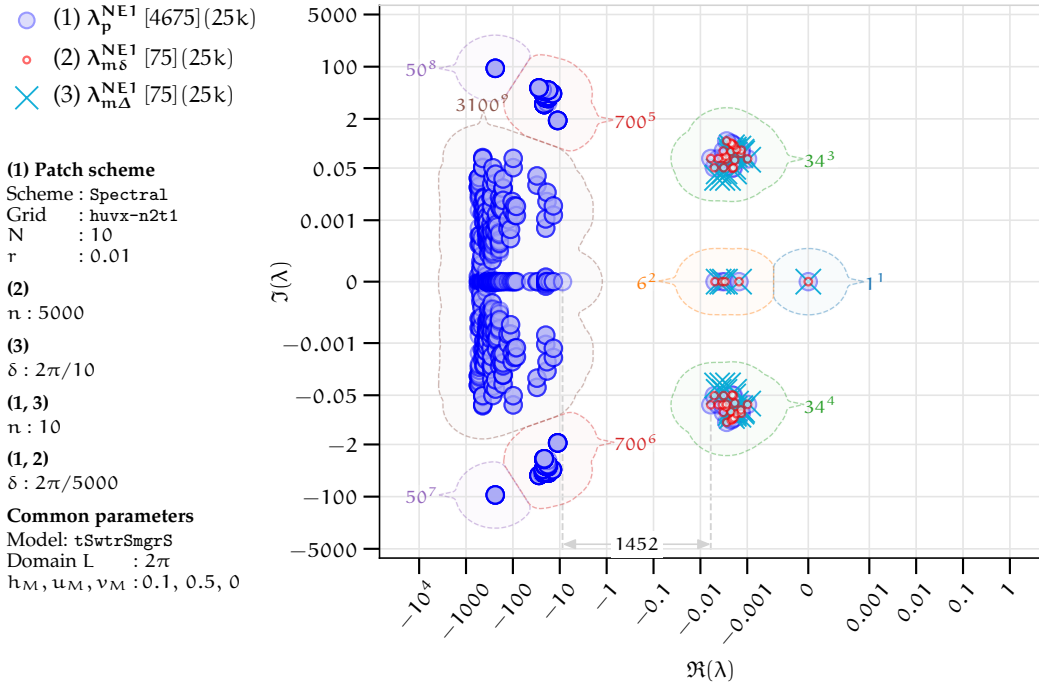
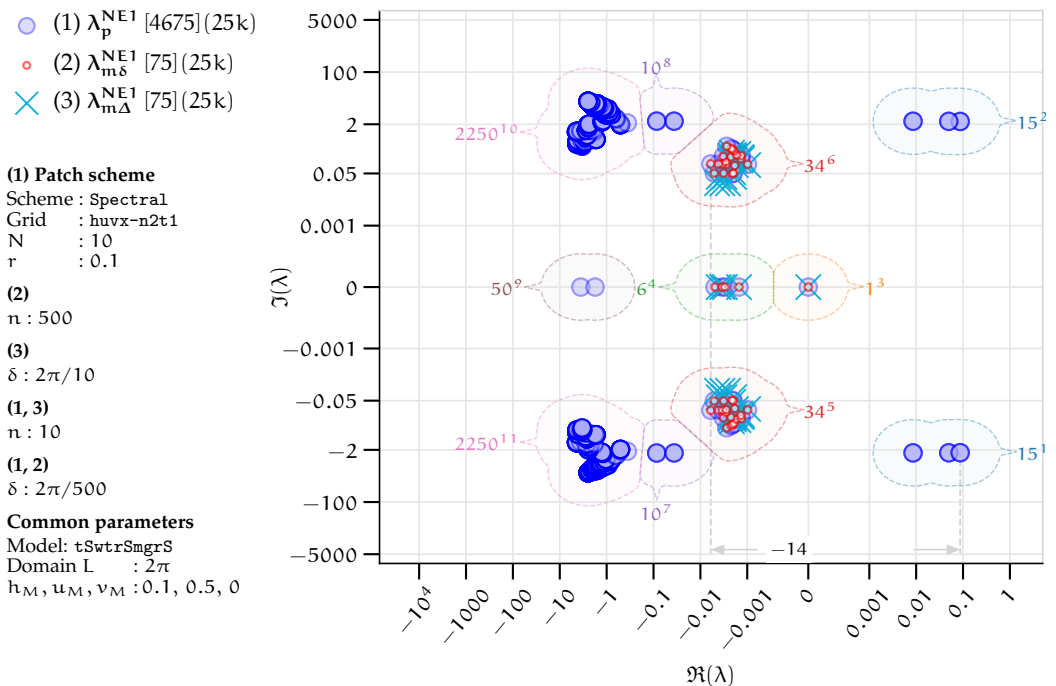


Figure 5.3.2. Spectral staggered patch scheme ($N = 10, n = 10, r = 0.1$) eigenvalues λ_p^{NE1} for turbulent shallow water flows for $(h_M, u_M, v_M) = (0.1, 0.5, 0)$. *Artificially unstable sub-patch microscale wave modes* in the clusters 1, 2.



- Unlike for the viscous shallow water flows in §4.4, for $n = 6$ sub-patch micro-grid intervals, decreasing patch scale ratio $r \in [0.0001, 0.1]$ does not remove the artificial instability of staggered patch schemes. That is, *for the turbulent shallow water flows, the staggered patch schemes require at least $n = 6$ sub-patch micro-grid intervals.* For example, Fig. 5.3.3 for $n = 6$ shows the eigenvalues of the artificially unstable modes in clusters 1–3; there is no such artificially unstable modes in Fig. 5.2.6 (of §5.2.4) for $n = 10$, keeping all other parameters the same.

The previous paragraph shows two examples of the stability trends of the patch schemes for the turbulent shallow water flows via two specific mean flows (linearisation points). Figure 5.3.4 plots the maximum real parts of the Spectral patch scheme for $n = 10$ (left) and $n = 6$ (right) for different mean flow (h_M, u_M) where $h_M \in \{0.025, 0.05, \dots, 0.4\}$ and $u_M \in \{0.05, 0.5, \dots, 6\}$. Figure 5.3.4 shows that the Spectral patch scheme is artificially unstable for $n = 6$, that is, $\max \Re(\lambda_p^N) > \max \Re(\lambda_{m\delta}^{NE1}) \geq 0$ for $u_M \gtrsim 1.5$; but there is no such artificial instability for $n = 10$. This trend of being artificially unstable for $n = 6$, but not for $n = 10$, holds for different patch scale ratio $r \in \{0.0001, 0.001, 0.01\}$ and also for the polynomial patch schemes. That is, for $n \geq 10$ and sufficiently small patch scale ratio $r \lesssim 0.01$, *the staggered patch schemes do not have any artificial instability.*

Figure 5.3.3. Spectral staggered patch scheme ($N = 10, n = 6, r = 0.01$) eigenvalues λ_p^{NE1} for turbulent shallow water flows for $(h_M, u_M, v_M) = (0.1, 5, 0)$. Artificially unstable sub-patch microscale wave modes in clusters 1–3; but Fig. 5.2.6 for $n = 10$ shows no such artificially unstable modes.

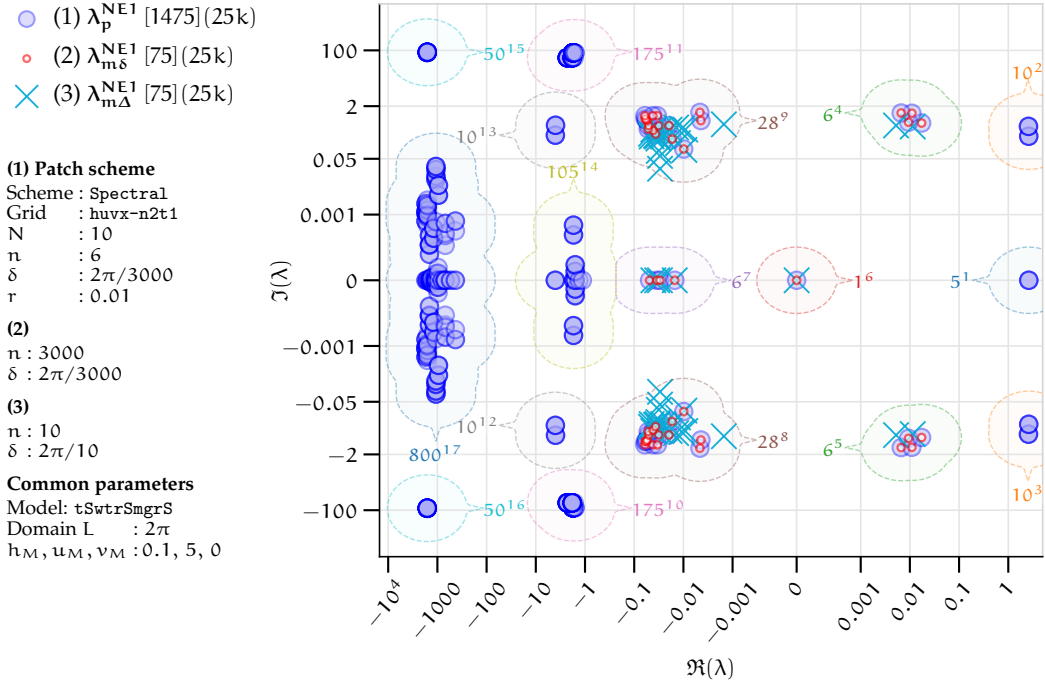
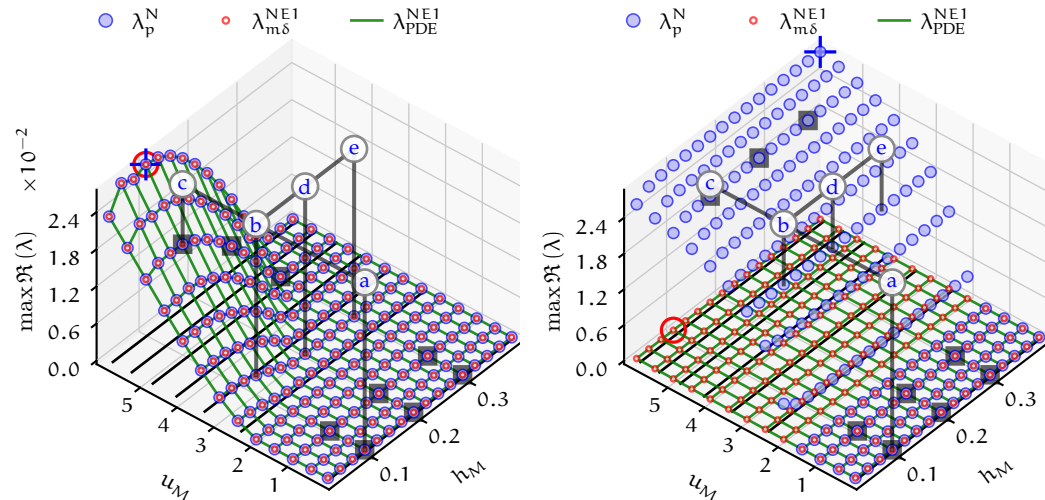


Figure 5.3.4. Maximum real part of eigenvalues for λ_p^N of Spectral patch scheme ($N = 10, r = 0.01$), $\lambda_{m\delta}^{NE1}$ of full-domain model, and λ_{PDE}^{NE1} of the turbulent shallow water PDEs, about mean flow h_M, u_M with $v_M = 0, \theta = 0^\circ$. For $n = 6$ (right), patch scheme has artificial instability for $u_M \gtrsim 1.5$. Seven black lines along h_M indicate equilibrium (5.1.5) for $\theta = 0, 1, \dots, 7$. §5.4 establishes patch scheme consistency for h_M, u_M indicated by black squares. Points a-e correspond to complex plane plots Figs. 5.2.4 to 5.2.8.

(a) No artificial instability for $n = 10$; **(b)** Artificial instability for $n = 6$; that is, $\max \Re(\lambda_p^N) \approx \max \Re(\lambda_{m\delta}^{NE1}) \geq 0$. Peak values (blue plus and red circle) are $\max \Re(\lambda_p^N) = 0.027 = \max \Re(\lambda_{m\delta}^{NE1})$. and $\max \Re(\lambda_{PDE}^{NE1}) = 0.027$ (red circle).



5.4 Staggered patch schemes are consistent

This section shows that the staggered patch schemes are consistent with the full-domain microscale model of turbulent shallow water flows, with decreasing macro-grid interval Δ , via the convergence of the patch scheme eigenvalues. Similar to §4.5 for viscous shallow water flows, we performed a detailed study of the eigenvalue convergence with decreasing macro-grid interval Δ using the eigenvalues for the 2 160 combinations of the parameters listed in Table 5.4.1. Based on the detailed study, omitting the eigenvalues convergence plots such as Fig. 4.5.3 in §4.5, the following two paragraphs summarise the overall key characteristics.

The last two paragraphs in §5.2.4 show that for turbulent shallow water flows about different linearisation points (h_M, u_M, v_M) , the macroscale eigenvalues λ_p^{NE1} of the Spectral patch scheme agree with the macroscale eigenvalues $\lambda_{m\delta}^{\text{NE1}}$ of the fine-grid full-domain microscale model. Except for two extreme cases of very small patch scale ratio $r \lesssim 0.0001$ and nearly stagnant water with very small velocity $u_M \lesssim 0.05$, this agreement of eigenvalues between λ_p^{NE1} and $\lambda_{m\delta}^{\text{NE1}}$ is exact (within numerical roundoff errors), without any dependence on macro-grid interval Δ . That is, as in §4.5.1 for viscous shallow water flows, also for the turbulent shallow water flows, in general, *the Spectral patch scheme is uniformly accurate with the full-domain model, with little dependence on the macro-grid interval Δ .*

Similar to the Spectral patch scheme, the four polynomial patch schemes' macroscale eigenvalues also agree with those of the fine-grid full-domain model but to a varying degree. That is, except for two extreme cases of very small patch scale ratio $r \lesssim 0.0001$ and nearly stagnant water with very small velocity $u_M \lesssim 0.05$, the eigenvalues of the polynomial patch schemes are increasingly accurate, that is, converge to the eigenvalues of the full-domain

Table 5.4.1. Section 5.4 establishes the consistency of the patch schemes using eigenvalues for all the 2 160 combinations of the listed parameters.

Patch schemes	Spectral, Square-p2, Square-p4, Square-p6, and Square-p8
Mean height	$h_M \in \{0.1, 0.2, 0.3\}$
Mean velocity	$u_M \in \{0.05, 1, 5\}, \quad v_M = 0$
Macro-grid intervals	$N \in \{6, 10, 14, 18, 22, 26\}$
Sub-patch micro-grid intervals	$n \in \{6, 10\}$
Patch scale ratio	$r \in \{0.0001, 0.001, 0.01, 0.1\}$

model, with decreasing macro-grid interval Δ . Specifically, as in §4.5.2 for viscous shallow water flows, also for the turbulent shallow water flows, in general, *the four polynomial patch schemes are consistent with the full-domain microscale model to the same order p as the patch coupling interpolation, and with the same order of convergence p for all the physical parameters h_M, u_M .*

5.5 Staggered patch scheme time simulations of turbulent shallow water flows

This subsection demonstrates the accuracy and the effectiveness of the staggered patch schemes by numerically simulating a turbulent roll wave. The patch schemes accurately simulate the localised nearly discontinuous macroscale turbulent roll wave emerging from the initial condition of a moving Gaussian hump.

As in §§3.7.5 and 4.7.5 for the general linear wave and viscous shallow water flows, also for the turbulent shallow water flows *this subsection uses the BS3 ODE integrator for the time simulation* with the relative and absolute error tolerances of 10^{-3} and 10^{-6} respectively. The BS3 is a lower order Bogacki–Shampine 3/2 method (Bogacki and L. Shampine 1989; L. F. Shampine and Reichelt 1997), similar to the `ode23` of MATLAB (DifferentialEquations.jl 2021).

Figures 5.5.1 to 5.5.3 show the time evolution of a turbulent roll wave (height h and velocities u, v) over a bed inclined 1° downwards along downstream, emerging from the initial condition of a moving Gaussian hump

$$h_0(x, y) = 0.1 + 0.05 \exp[-(x + 1)^2 - y^2/4^2], \quad (5.5.1a)$$

$$u_0(x, y) = 2.4 + 0.5 \exp[-(x + 1)^2 - y^2/4^2], \quad (5.5.1b)$$

$$v_0(x, y) = 0, \quad (5.5.1c)$$

which is superimposed over approximate equilibrium mean flow $h_M = 0.1$, $u_M = 2.4$, $v_M = 0$. In each of Figs. 5.5.1 to 5.5.3, the subfigures from top-left sub-plot to bottom-right correspond to simulation time $t = 0, 18, 36, 54$. The regions where the colour-coded ribbons cross are patches; the patches are much smaller than illustrated in the figure for visual clarity. The staggered patch schemes compute only within patches, a small fraction of the area of the full domain (e.g., §4.7.1).

Figure 5.5.1. Height h for time evolution of a turbulent roll wave, emerging from the initial condition of a moving Gaussian hump (5.5.1), using Spectral patch scheme (colour-coded ribbons, with $N = 26$, $n = 10$, and $r = 0.1$) agrees reasonably with that of the fine-grid full-domain model (grey mesh).

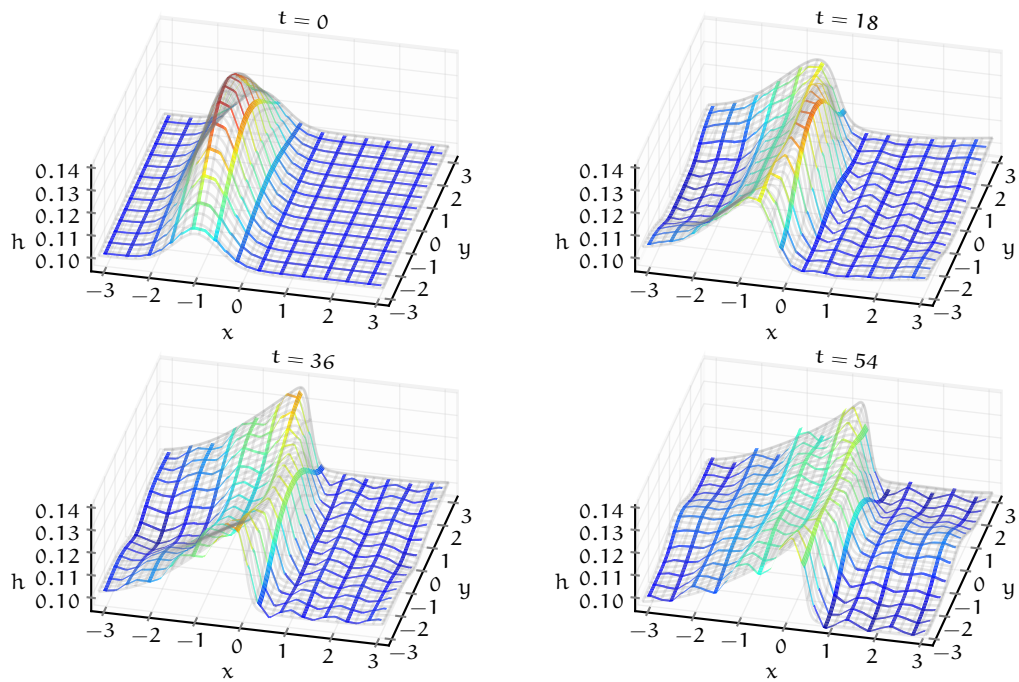


Figure 5.5.2. Velocity u for time evolution of a turbulent roll wave, for the same patch scheme simulation detailed in Fig. 5.5.1 (colour-coded ribbons) agrees reasonably with that of the fine-grid full-domain model (grey mesh).

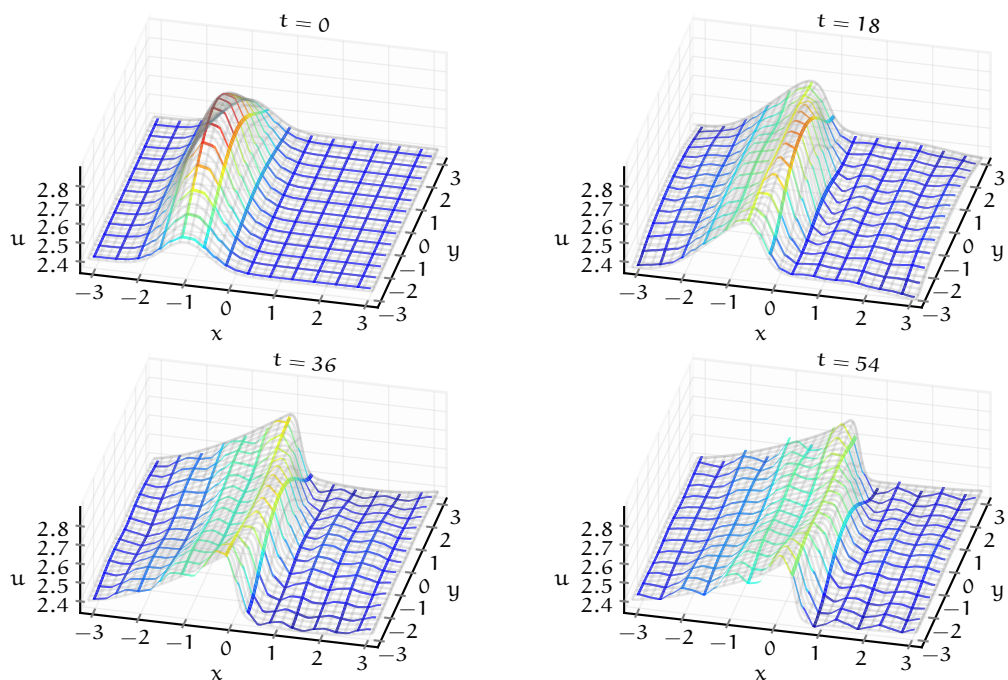
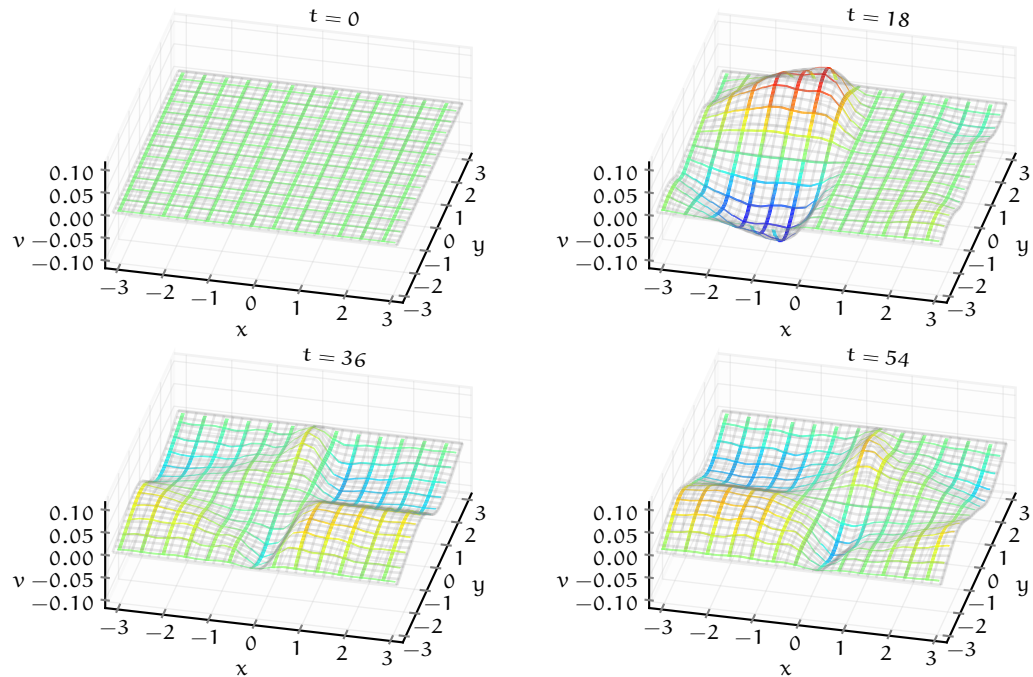


Figure 5.5.3. Velocity v for time evolution of a turbulent roll wave, for the same patch scheme simulation detailed in Fig. 5.5.1 (colour-coded ribbons) agrees reasonably with that of the fine-grid full-domain model (grey mesh).



Figures 5.5.1 to 5.5.3 show that the time evolution using the Spectral patch scheme (colour-coded ribbons, with $N = 26$, $n = 10$, and $r = 0.1$) agrees reasonably with that of the 1300×1300 fine-grid full-domain model (grey mesh). The fine-grid full-domain microscale model (grey mesh) uses the same micro-grid interval as the sub-patch micro-grid interval $\delta = 2(2\pi)r/(Nn)$ (for the non-dimensional domain size 2π). But the grey mesh of the full-domain model plots only 32×32 grid instead of all the 1301×1301 grid lines, skipping many lines for visual clarity. The colour-coded ribbons of the patch scheme in Fig. 5.5.1 consist of all the lines (along the coordinate axes x and y) passing through all the h nodes within all the patches; similarly Figs. 5.5.2 and 5.5.3 for u , v nodes within all the patches respectively. Although the patch scale ratio is $r = 0.1$, the patches are enlarged here for visual clarity so the ribbons appear wider.

Figure 1.0.1 of Chapter 1 shows an enlarged snapshot of the same roll wave as in left-bottom of Fig. 5.5.1 at $t = 36$, with more visual detail and clarity. In Fig. 1.0.1, the solution h of the fine-grid full-domain microscale model are linearly interpolated using nearest four values to the centres of the respective $h/u/v$ -centred patches, illustrated by small black circles. The large circles are the patch scheme solution $h/u/v$. That the non-concentric large

and small black circles are offset only slightly, shows that the discrepancy between the solutions of the patch scheme and the fine-grid full-domain model is small. The undulations in the patch scheme solution, away from the steep rise of the roll wave are due to the nearly discontinuous jump in the height. These undulations decrease with increasing the number of patches (macro-grid intervals). In Fig. 1.0.1, the small discrepancy at $t = 36$ (distance between centres of non concentric black circles) also includes the accumulation of the ODE integrator error. Thus, for a sufficient number of macro-grid intervals and accurate patch coupling, *patch schemes accurately simulate the turbulent shallow water flows.*

Patch scheme simulations of turbulent shallow water flows require a larger number of sub-patch micro-grid intervals n , compared to the viscous shallow water flows. As opposed to $n = 6$ sub-patch micro-grid intervals in the time simulations of §§4.7.5 and 4.7.6 for the viscous shallow water flows, the time simulation in the previous paragraphs of this subsection use $n = 10$ sub-patch micro-grid intervals. This larger $n = 10$ is a necessity for the turbulent shallow water flows for mean velocity $u_M \gtrsim 1.5$ to avoid artificial instability of the staggered patch schemes. Figure 5.3.4 in p. 308 of §5.3 shows the artificial instability of the patch scheme for $n = 6$, via the maximum real parts of the patch scheme eigenvalues.

The practical issues of patch scheme simulation explained in §4.4.1 for the viscous shallow water flows also apply for the turbulent shallow water flows, perhaps more strongly. For example, the patch schemes for the turbulent shallow water flows are stiffer compared to the viscous shallow water flows. The impacts of the stiffness and the artificial instability of the patch schemes for the turbulent shallow water flows are relatively more severe than the viscous shallow water flows, especially for small patch scale ratio $r \lesssim 0.1$.

Thus, for a broad range of parameters, this chapter shows that the patch scheme can accurately and effectively simulate and predict the Smagorinsky-based turbulent shallow water flows.

Chapter 6

Conclusion

Many important phenomena exhibit multiscale emergent behaviour. For example, the length scales in the fluid dynamics of Earth's atmosphere and oceans range from a few millimetres to several thousands of kilometres. The main interest generally lies in large-scale dynamics, yet the effect of the smallest scales needs to be accounted for its emergent large-scale dynamics. Detailed simulation over such a large space is impractical. To address this issue, many multiscale modelling techniques have been developed for dissipative systems. The equation-free multiscale modelling framework is particularly attractive due to its flexibility. The equation-free multiscale *patch schemes* accurately model emergent macroscale spatial dynamics using a given microscale model within small sparsely located coupled patches. Such patch schemes have been developed and applied successfully for dissipative systems. The weak inherent dissipation in wave-like systems poses significant challenges for developing patch schemes that are stable and accurate for wave-like systems, especially in multiple dimensions. The recent works of Cao and Roberts (2013, 2015) extend the patch scheme to 1D wave-like systems. This PhD thesis develops the equation-free multiscale staggered patch schemes for 2D wave-like systems (small dissipation) and explores the schemes more thoroughly.

6.1 Multiscale staggered patch schemes enable accurate large-scale simulation of wave-like systems

We designed two staggered patch grids that constitute stable and accurate staggered patch schemes for wave-like systems. Over a computationally efficient patch grid, we developed two novel families of equation-free

multiscale staggered patch schemes for accurate large-scale simulation of wave-like systems: a spectral patch scheme, and four polynomial patch schemes. The spectral patch scheme is the best for accuracy, requiring an equispaced patch grid over simple domain geometry and periodic boundary conditions. Polynomial patch schemes are best suited for complex domain geometry and boundary conditions.

The developed multiscale staggered patch schemes *enable accurate simulation of macroscale waves for many specific application areas* over large space, yet computing only within small sparsely located patches. As a concrete example, the current work mainly focuses on water waves. This work shows that the staggered patch schemes accurately simulate the macroscale waves using three microscale models within the patches, namely, general 2D linear waves (Chapter 3), nonlinear viscous shallow water flows (Chapter 4), and nonlinear turbulent shallow water flows (Chapter 5). The three respective chapters (Chapters 3 to 5) show that the developed multiscale staggered patch schemes

1. are accurate over a wide range of system and grid parameters,
2. do not have any artificial instabilities (for appropriate grid parameters), and
3. are consistent with the full-domain microscale simulation (with decreasing macro-grid interval).

Despite the attractive characteristics, if the staggered patch schemes are very sensitive to numerical roundoff errors, then they would not be suitable for practical numerical simulations using finite precision floating-point representations, for example, the common 64 bit format of IEEE754. From both qualitative and quantitative arguments, §§3.4 and 4.3 shows that the staggered patch schemes are not sensitive to numerical roundoff errors for the general linear wave.

The staggered patch schemes accurately model the macroscale waves with large computational savings, via detailed microscale simulations only within the patches, that is, within a small fraction (e.g., millionth) of the whole space. The staggered patch schemes compute only for a small number of dynamical state variables, for example, one-millionth of the number of state variables in the corresponding full-domain model. For time-varying grid geometry, the measured compute times of the multiscale patch schemes are up to 10 000 times smaller than the corresponding full-domain model. For fixed patch grids, the measured compute times of the multiscale staggered patch schemes are potentially 10^5 times smaller than the corresponding full-domain model. A

reduction of 10^5 times is equivalent to reducing the compute time from one week to six seconds. The user can choose how much computational savings to achieve depending on the scales of interest in the modelling. The patch schemes' ability to accurately model the macroscale waves with large computational savings is an enabling feature for accurate simulation and prediction of large-scale wave phenomena like floods and tsunamis.

6.2 Further research directions

Study the staggered patch schemes for depth resolved turbulent microscale physics. In shallow water waves, the back and forth material motion near the solid bed (despite being small compared to the wave speed) reflects oscillating pressure in the horizontal direction (Zirker 2013, p. 19). Towards a more realistic application, applying the staggered patch schemes to depth-resolved turbulent models such as the full Navier–Stokes equation is an important further research.

A generic 3D staggered patch schemes. Extending the developed 2D staggered patch schemes to full 3D-space simulations will expand the utility of the staggered patch schemes more generically to a wide number of systems such as general large-scale fluid dynamics.

Combine projective time integration with the staggered patch schemes. Section 4.7.6 of Chapter 4 outlines some practical issues in integrating the ODEs of the staggered patch schemes for small patch scale ratios. One of the major issues is the highly stiff ODEs of patch schemes, especially for nonlinear waves. Based on study for a simple linear system $du/dt = Au + b$, Maclean et al. (2021b, §3.1.4) find that projective ODE integrator (Gear and Kevrekidis 2003) which specifically utilises the spectral gap in a system outperforms the stiff ODE integrator both in accuracy and compute times. Combining the projective time integration with the developed staggered patch schemes will extend the practical applicability of the patch schemes to wider parameter combinations. Such an extension is challenging because of the long-lasting microscale waves.

Patch schemes for sediment transport. Another challenging multiscale problem closely related to the large-scale wave-like systems, is modelling the sediment transport in environmental fluid dynamics. Extending and studying the effectiveness of the staggered patch schemes will enable efficient multiscale modelling of sediment transport in coastal engineering.

Patch schemes for flows and waves in heterogeneous media. There are two classes of heterogeneity: macroscale and microscale. The smallest macroscale structures a staggered patch scheme can resolve is twice the inter-

patch distance (Divahar et al. 2022, p.34, §4.3). Hence, we expect that staggered patch schemes must cater for macroscale heterogeneity on scales of about twice the inter-patch distance and larger. First, apply the equation-free multiscale staggered patch schemes for flows and waves in heterogeneous media with slowly varying material properties (i.e, with slow spatial variation of the coefficients in the governing PDEs). A patch scheme for microscale heterogeneity, for example, with more rapid spatial variation of material properties requires more careful treatment. Some recent works (Bunder et al. 2021, 2017; Maclean et al. 2021a) have proven that the patch scheme is accurate and efficient for microscale heterogeneity in dissipative systems. Outstanding research is to prove similar properties for staggered patch schemes of wave-like systems.

Adaptive and moving patch grids for unsteady and discontinuous problems. The recent work of Maclean et al. (2021a) adaptively refines the patch grid to accurately capture shock waves. Maclean et al. (2021a, p. 14) also discuss the utility of including moving meshes to adaptively both create and merge patches. Extending the 2D staggered patch schemes to adaptive and moving meshes will improve both the accuracy and efficiency in the multiscale patch schemes simulation of localised structures such as a turbulent bore.

Practically relevant complex macroscale boundary conditions for the multidimensional patch schemes. All the studies in this work use simple periodic boundary conditions (BCs). As Cao and Roberts (2015, §5.2, Fig.12) explain for the 1D space, there are at least two ways of imposing a simple Dirichlet BCs: imposing on the patch edges (microscale); imposing on the patch centre (macroscale). Boundary conditions in multiple dimensions, and Neumann and other complex BCs require more careful treatment (e.g., patch edge alignment to the boundary, additional patches outside the domain, possible degradation of stability and consistency). As a next step, extending the staggered patch schemes to complex macroscale boundary conditions will enable solving challenging real-world practical problems.

Extend patch schemes to other continuum modelling methods. All the studies of the 2D staggered patch schemes in this work use finite difference microscale models within the patches. Extending the staggered patch schemes to multidimensional finite volume, finite element, and other continuum modelling methods will improve the flexibility and utility of the multiscale patch schemes.

Develop wrappers of staggered patch schemes for industrial scale simulation software. Implementing the staggered patch schemes as thin wrappers for industrial scale simulation software such as OpenFOAM, Ansys, SU2, FEniCS, deal.II is also a relevant next step. Such wrappers will enable quick adaptation and hence allow both solving and testing the patch schemes on

multiscale modelling within various application areas.

Generalise staggered patch schemes to macroscale unstructured patch grids. All the current works on the multidimensional multiscale patch schemes (both the collocated and staggered) are based on structured patch grids both in microscale and macroscale. Generalising the staggered patch schemes to macroscale unstructured patch grids will enable multiscale patch scheme simulation over complex real-world geometry such as simulating tsunami over complex terrains.

Bibliography

- Anderson, John D. (1995). *Computational fluid dynamics. The basics with applications*. McGraw-Hill. ISBN: 0070016852 (cit. on p. 12).
- Arakawa, Akio and Vivian R. Lamb (1977). “Computational Design of the Basic Dynamical Processes of the UCLA General Circulation Model”. In: *General Circulation Models of the Atmosphere*. Vol. 17. Methods in Computational Physics: Advances in Research and Applications. Elsevier, pp. 173–265. DOI: [10.1016/B978-0-12-460817-7.50009-4](https://doi.org/10.1016/B978-0-12-460817-7.50009-4) (cit. on p. 13).
- Babuška, I. and J. E. Osborn (1983). “Generalized Finite Element Methods: Their Performance and Their Relation to Mixed Methods”. In: *SIAM Journal on Numerical Analysis* 20.3, pp. 510–536. DOI: [10.1137/0720034](https://doi.org/10.1137/0720034) (cit. on p. 1).
- Balmforth, N. J. and S. Mandre (2004). “Dynamics of roll waves”. In: *Journal of Fluid Mechanics* 514, pp. 1–33. DOI: [10.1017/S0022112004009930](https://doi.org/10.1017/S0022112004009930) (cit. on pp. 159, 261, 271).
- Berlyand, Leonid and Volodymyr Rybalko (2018). *Getting Acquainted with Homogenization and Multiscale*. Birkhäuser. DOI: [10.1007/978-3-030-01777-4](https://doi.org/10.1007/978-3-030-01777-4) (cit. on p. 1).
- Bezanson, Jeff, Alan Edelman, Stefan Karpinski, and Viral B. Shah (2017). “Julia: A Fresh Approach to Numerical Computing”. In: *SIAM Review* 59.1, pp. 65–98. DOI: [10.1137/141000671](https://doi.org/10.1137/141000671) (cit. on p. 15).
- Bogacki, P. and L.F. Shampine (1989). “A 3(2) pair of Runge - Kutta formulas”. In: *Applied Mathematics Letters* 2.4, pp. 321–325. ISSN: 0893-9659. DOI: [10.1016/0893-9659\(89\)90079-7](https://doi.org/10.1016/0893-9659(89)90079-7) (cit. on pp. 146, 271, 310).
- Bullo, Francesco and Andrew D Lewis (2019). *Geometric Control of Mechanical Systems. Modeling, Analysis, and Design for Simple Mechanical Control Systems*. Springer. DOI: [10.1007/978-1-4899-7276-7](https://doi.org/10.1007/978-1-4899-7276-7) (cit. on p. 106).

- Bunder, J. E., J. Divahar, I. G. Kevrekidis, Trent W. Mattner, and A.J. Roberts (2020). “Large-scale simulation of shallow water waves via computation only on small staggered patches”. In: *International Journal for Numerical Methods in Fluids*. DOI: [10.1002/flid.4915](https://doi.org/10.1002/flid.4915) (cit. on pp. 5, 7, 27, 143, 286).
- Bunder, J. E., I. G. Kevrekidis, and A. J. Roberts (Oct. 2021). “Equation-free patch scheme for efficient computational homogenisation via self-adjoint coupling”. In: *Numerische Mathematik* 149.2, pp. 229–272. DOI: [10.1007/s00211-021-01232-5](https://doi.org/10.1007/s00211-021-01232-5) (cit. on p. 317).
- Bunder, J. E., A. J. Roberts, and I. G. Kevrekidis (2017). “Good coupling for the multiscale patch scheme on systems with microscale heterogeneity”. In: *Journal of Computational Physics* 337, pp. 154–174. DOI: [10.1016/j.jcp.2017.02.004](https://doi.org/10.1016/j.jcp.2017.02.004) (cit. on pp. 5, 6, 317).
- Cain, John W. and Angela M. Reynolds (2010). *Ordinary and Partial Differential Equations: An Introduction to Dynamical Systems*. Virginia Commonwealth University. ISBN: 9780982406236 (cit. on pp. 52, 175).
- Cao, M. and A. J. Roberts (2013). “Multiscale modelling couples patches of wave-like simulations”. In: *ANZIAM Journal* 54.0, pp. C153–C170. DOI: [10.21914/anziamj.v54i0.6137](https://doi.org/10.21914/anziamj.v54i0.6137) (cit. on pp. ix, 6, 11, 314).
- (Oct. 2015). “Multiscale modelling couples patches of non-linear wave-like simulations”. In: *IMA Journal of Applied Mathematics* 81.2, pp. 228–254. DOI: [10.1093/imamat/hxv034](https://doi.org/10.1093/imamat/hxv034) (cit. on pp. ix, 6, 11, 314, 317).
- (June 2016). “Modelling suspended sediment in environmental turbulent fluids”. In: *Journal of Engineering Mathematics* 98.1, pp. 187–204. ISSN: 1573-2703. DOI: [10.1007/s10665-015-9817-7](https://doi.org/10.1007/s10665-015-9817-7) (cit. on pp. 9, 282–284, 291).
- Chicone, C. (2006). *Ordinary differential equations with applications*. 2nd ed. Texts in Applied Mathematics. Springer. DOI: [10.1007/0-387-35794-7](https://doi.org/10.1007/0-387-35794-7) (cit. on p. 105).
- Chorin, Alexandre J. and Panagiotis Stinis (2005). *Problem reduction, renormalization, and memory*. Tech. rep. DOI: [10.48550/ARXIV.MATH/0503612](https://doi.org/10.48550/ARXIV.MATH/0503612) (cit. on p. 1).
- Cisternas, J., C. W. Gear, S. Levin, and I. G. Kevrekidis (2004). “Equation-free modelling of evolving diseases: coarse-grained computations with individual-based models”. In: *Proceedings of the Royal Society of London A: Mathematical, Physical and Engineering Sciences* 460.2050, pp. 2761–2779. DOI: [10.1098/rspa.2004.1300](https://doi.org/10.1098/rspa.2004.1300) (cit. on p. 5).

- Cohen, S., A. Raney, D. Munasinghe, J. D. Loftis, A. Molthan, J. Bell, L. Rogers, J. Galantowicz, G. R. Brakenridge, A. J. Kettner, Y.-F. Huang, and Y.-P. Tsang (2019). “The Floodwater Depth Estimation Tool (FwDET v2.0) for improved remote sensing analysis of coastal flooding”. In: *Natural Hazards and Earth System Sciences* 19.9, pp. 2053–2065. DOI: [10.5194/nhess-19-2053-2019](https://doi.org/10.5194/nhess-19-2053-2019) (cit. on p. 290).
- Constantin, A. (2017). “Nonlinear water waves: introduction and overview”. In: *Philosophical Transactions of the Royal Society A* 376. DOI: [10.1098/rsta.2017.0310](https://doi.org/10.1098/rsta.2017.0310) (cit. on p. 9).
- Dean, Robert G and Robert A Dalrymple (1991). *Water Wave Mechanics for Engineers and Scientists*. World Scientific. DOI: [10.1142/1232](https://doi.org/10.1142/1232) (cit. on p. 46).
- DifferentialEquations.jl (Aug. 27, 2021). *Solver Algorithms: ODE Solvers*. Version 6.19. URL: https://diffeq.sciml.ai/v6.19/solvers/ode_solve/ (cit. on pp. 15, 144, 146, 279, 310).
- Divahar, J., A. J. Roberts, Trent W. Mattner, J. E. Bunder, and Ioannis G. Kevrekidis (July 2022). *Staggered grids for multidimensional multiscale modelling*. Tech. rep. University of Adelaide, Johns Hopkins University. DOI: [10.48550/arXiv.2207.12623](https://doi.org/10.48550/arXiv.2207.12623) (cit. on pp. 108, 317).
- Dolbow, J., M. A. Khaleel, and J. Mitchell (2004). *Multiscale Mathematics Initiative: A Roadmap*. 3rd DoE Workshop on Multiscale Mathematics. Tech. rep. Department of Energy, Washington, DC. URL: https://science.osti.gov/-/media/ascr/pdf/research/am/docs/Multiscale_math_workshop_3.pdf (cit. on p. 1).
- Dorobantu, Mihai and Björn Engquist (1998). “Wavelet-Based Numerical Homogenization”. In: *SIAM Journal on Numerical Analysis* 35.2, pp. 540–559. DOI: [10.1137/S0036142996298880](https://doi.org/10.1137/S0036142996298880) (cit. on p. 1).
- E, Weinan and Engquist Björn (Mar. 2003). “The Heterogenous Multiscale Methods”. In: *Communications in Mathematical Sciences* 1.1, pp. 87–132. ISSN: 1945-0796. DOI: [10.4310/CMS.2003.v1.n1.a8](https://doi.org/10.4310/CMS.2003.v1.n1.a8) (cit. on p. 1).
- (2005). “The Heterogeneous Multi-Scale Method for Homogenization Problems”. In: *Multiscale Methods in Science and Engineering*. Springer, pp. 89–110. DOI: [10.1007/3-540-26444-2_4](https://doi.org/10.1007/3-540-26444-2_4) (cit. on p. 1).
- E, Weinan, Engquist Björn, and Zhongyi Huang (Mar. 2003). “Heterogeneous multiscale method: A general methodology for multiscale mod-

- eling". In: *Phys. Rev. B* 67 (9), p. 092101. DOI: [10.1103/PhysRevB.67.092101](https://doi.org/10.1103/PhysRevB.67.092101) (cit. on p. 1).
- Edwards, C .H., D. E. Penney, and D. Calvis (2017). *Differential Equations and Linear Algebra*. 4th ed. Pearson. ISBN: 9780134497181 (cit. on pp. [52](#), [105](#), [175](#)).
- Efendiev, Yalchin, Juan Galvis, and Thomas Y. Hou (2013). "Generalized multiscale finite element methods (GMsFEM)". In: *Journal of Computational Physics* 251, pp. 116–135. DOI: [10.1016/j.jcp.2013.04.045](https://doi.org/10.1016/j.jcp.2013.04.045) (cit. on p. 1).
- Ei, Shin-Ichiro, Kazuyuki Fujii, and Teiji Kunihiro (2000). "Renormalization-Group Method for Reduction of Evolution Equations; Invariant Manifolds and Envelopes". In: *Annals of Physics* 280.2, pp. 236–298. DOI: [10.1006/aphy.1999.5989](https://doi.org/10.1006/aphy.1999.5989) (cit. on p. 1).
- Emereuwa, Chigoziem A. (2020). "Mathematical homogenization and stochastic modeling of energy storage systems". In: *Current Opinion in Electrochemistry*. DOI: [10.1016/j.coelec.2020.01.009](https://doi.org/10.1016/j.coelec.2020.01.009) (cit. on p. 4).
- Ferziger, Joel H., Milovan Peric, and Robert L. Street (2020). *Computational Methods for Fluid Dynamics*. Springer International Publishing, p. 596. DOI: [10.1007/9783319996936](https://doi.org/10.1007/9783319996936) (cit. on pp. [121](#), [244](#)).
- Feyel, Frédéric and Jean-Louis Chaboche (2000). "FE2 multiscale approach for modelling the elastoviscoplastic behaviour of long fibre SiC/Ti composite materials". In: *Computer Methods in Applied Mechanics and Engineering* 183.3, pp. 309–330. DOI: [10.1016/S0045-7825\(99\)00224-8](https://doi.org/10.1016/S0045-7825(99)00224-8) (cit. on p. 1).
- Fletcher, Steven J. (2020). *Semi-Lagrangian Advection Methods and Their Applications in Geoscience*. Walthm, MA, USA: Elsevier. DOI: [10.1016/C2018-0-02183-0](https://doi.org/10.1016/C2018-0-02183-0) (cit. on pp. [31](#), [32](#), [41](#)).
- Foias, C., M. S. Jolly, I. G. Kevrekidis, G. R. Sell, and E. S. Titi (1988a). "On the computation of inertial manifolds". In: *Physics Letters A* 131.7, pp. 433–436. ISSN: 0375-9601. DOI: [10.1016/0375-9601\(88\)90295-2](https://doi.org/10.1016/0375-9601(88)90295-2) (cit. on p. [25](#)).
- Foias, C., G. R Sell, and R. Temam (1988b). "Inertial manifolds for nonlinear evolutionary equations". In: *Journal of Differential Equations* 73.2, pp. 309–353. DOI: [10.1016/0022-0396\(88\)90110-6](https://doi.org/10.1016/0022-0396(88)90110-6) (cit. on p. [25](#)).

- Fornberg, Bengt (1990). "High-Order Finite Differences and the Pseudospectral Method on Staggered Grids". In: *SIAM Journal on Numerical Analysis* 27.4, pp. 904–918. DOI: [10.1137/0727052](https://doi.org/10.1137/0727052) (cit. on p. 13).
- Fornberg, Bengt and Michelle Ghrist (1999). "Spatial Finite Difference Approximations for Wave-Type Equations". In: *SIAM Journal on Numerical Analysis* 37.1, pp. 105–130. DOI: [10.1137/S0036142998335881](https://doi.org/10.1137/S0036142998335881) (cit. on p. 13).
- Franci, Alessandro, Massimiliano Cremonesi, Umberto Perego, and Eugenio Oñate (2020). "A Lagrangian nodal integration method for free-surface fluid flows". In: *Computer Methods in Applied Mechanics and Engineering* 361, p. 112816. DOI: [10.1016/j.cma.2019.112816](https://doi.org/10.1016/j.cma.2019.112816) (cit. on p. 5).
- Gear, C. W. and I. G. Kevrekidis (2003). "Projective Methods for Stiff Differential Equations: Problems with Gaps in Their Eigenvalue Spectrum". In: *SIAM Journal on Scientific Computing* 24.4, pp. 1091–1106. DOI: [10.1137/S1064827501388157](https://doi.org/10.1137/S1064827501388157) (cit. on pp. 280, 316).
- Ghobarah, Ahmed, Murat Saatcioglu, and Ioan Nistor (2006). "The impact of the 26 December 2004 earthquake and tsunami on structures and infrastructure". In: *Engineering Structures* 28.2, pp. 312–326. DOI: [10.1016/j.engstruct.2005.09.028](https://doi.org/10.1016/j.engstruct.2005.09.028) (cit. on p. 290).
- Goldberg, David (1991). "What every computer scientist should know about floating-point arithmetic". In: *ACM Computing Surveys (CSUR)* 23.1, pp. 5–48 (cit. on pp. 96, 102, 208).
- Griffiths, David F. and Desmond J. Higham (2010). *Numerical Methods for Ordinary Differential Equations Initial Value Problems*. 1st ed. Springer. DOI: [10.1007/978-0-85729-148-6](https://doi.org/10.1007/978-0-85729-148-6) (cit. on p. 106).
- Griffiths, Graham W. and William E. Schiesser (2011). *Traveling Wave Analysis of Partial Differential Equations: Numerical and Analytical Methods with Matlab and Maple*. 1st ed. Academic Press. DOI: [10.1016/C2009-0-64536-0](https://doi.org/10.1016/C2009-0-64536-0) (cit. on pp. 54, 55).
- Grooms, Ian and Keith Julien (Nov. 2018). "Multiscale models in geophysical fluid dynamics". In: *Earth and Space Science*. DOI: [10.1029/2018EA000439](https://doi.org/10.1029/2018EA000439) (cit. on pp. 3, 4).
- Gupta, Rajesh Kumar (2019). *Numerical Methods. Fundamentals and Applications*. Cambridge University Press. DOI: [10.1017/9781108685306](https://doi.org/10.1017/9781108685306) (cit. on pp. 31, 32, 41).

- Harlow, Francis H. and J. Eddie Welch (1965). "Numerical Calculation of Time-Dependent Viscous Incompressible Flow of Fluid with Free Surface". In: *The Physics of Fluids* 8.12, pp. 2182–2189. DOI: [10.1063/1.1761178](https://doi.org/10.1063/1.1761178) (cit. on p. 13).
- Haynes, W.M., David R. Lide, and Thomas J. Bruno (2016). *CRC Handbook of Chemistry and Physics*. Ed. by W.M. Haynes, David R. Lide, and Thomas J. Bruno. 97th. ISBN: 9781498754293 (cit. on p. 173).
- Heister, Timo, Leo G. Rebholz, and Fei Xue (2019). *Numerical Analysis*. De Gruyter. DOI: [doi:10.1515/9783110573329](https://doi.org/10.1515/9783110573329) (cit. on p. 102).
- Hinch, E. J. (2020). *Think Before You Compute. A Prelude to Computational Fluid Dynamics*. Cambridge University Press. DOI: [10.1017/9781108855297](https://doi.org/10.1017/9781108855297) (cit. on pp. 12, 54, 55).
- Hirsch, M. W. and S. Smale (1974). *Differential Equations, Dynamical Systems, and Linear Algebra*. Pure and Applied Mathematics 60. Elsevier. ISBN: 0123495504 (cit. on p. 106).
- Hirsch, M. W., S. Smale, and R. L. Devaney (2013). *Differential Equations, Dynamical Systems, and an Introduction to Chaos*. 3rd ed. Academic Press. DOI: [10.1016/B978-0-12-382010-5.00001-4](https://doi.org/10.1016/B978-0-12-382010-5.00001-4) (cit. on p. 105).
- Hou, Thomas and Yalchin Efendiev (2009). *Multiscale Finite Element Methods. Theory and Applications*. Springer. DOI: [10.1007/978-0-387-09496-0](https://doi.org/10.1007/978-0-387-09496-0) (cit. on p. 1).
- Hughes, Thomas J.R., Gonzalo R. Feijóo, Luca Mazzei, and Jean-Baptiste Quincy (1998). "The variational multiscale method—a paradigm for computational mechanics". In: *Computer Methods in Applied Mechanics and Engineering* 166.1, pp. 3–24. DOI: [10.1016/S0045-7825\(98\)00079-6](https://doi.org/10.1016/S0045-7825(98)00079-6) (cit. on p. 1).
- Hyman, J. M. (May 2005). "Patch dynamics for multiscale problems". In: *Computing in Science Engineering* 7.3, pp. 47–53. DOI: [10.1109/MCSE.2005.57](https://doi.org/10.1109/MCSE.2005.57) (cit. on p. 4).
- Intergovernmental Oceanographic Commission, International Tsunami Information Centre (2014). *Tsunami, The Great Waves, Revised Edition*. URL: http://itic.ioc-unesco.org/images/stories/awareness_and_education/great_waves/great_waves_en_low_v14.pdf (cit. on p. 290).
- Jain, M.K., Iyengar S.R.K., and M.K. Jain (2004). *Numerical Methods. Problems and Solutions*. 2nd ed. New Age International (cit. on pp. 31, 32, 41).

- Jordan, Dominic and Peter Smith (2007). *Nonlinear Ordinary Differential Equations. An introduction for Scientists and Engineers*. Oxford University Press, USA. ISBN: 9780199208258 (cit. on p. 105).
- Kevrekidis, I. G., C. W. Gear, and G. Hummer (2004). "Equation-free: The computer-aided analysis of complex multiscale systems". In: *AIChE Journal* 50.7, pp. 1346–1355. DOI: [10.1002/aic.10106](https://doi.org/10.1002/aic.10106) (cit. on pp. 4, 5, 25).
- Kevrekidis, I. G., C. W. Gear, J. M. Hyman, P. G. Kevrekidis, O. Runborg, and C. Theodoropoulos (2003). "Equation-free, coarse-grained multiscale computation: enabling microscopic simulators to perform system-level analysis". In: *Commun. Math. Sci.* 1.4, pp. 715–762 (cit. on p. 5).
- Kevrekidis, I. G. and G. Samaey (2009). "Equation-Free Multiscale Computation: Algorithms and Applications". In: *Annual Review of Physical Chemistry* 60.1, pp. 321–344. DOI: [10.1146/annurev.physchem.59.032607.093610](https://doi.org/10.1146/annurev.physchem.59.032607.093610) (cit. on p. 4).
- Lauritzen, Peter, Christiane Jablonowski, Mark Taylor, and Ramachandran Nair (2011). *Numerical Techniques for Global Atmospheric Models*. Springer. DOI: [10.1007/978-3-642-11640-7](https://doi.org/10.1007/978-3-642-11640-7) (cit. on p. 14).
- Lomax, Harvard, Thomas H Pulliam, and David W Zingg (2011). *Fundamentals of computational fluid dynamics*. 1st ed. Scientific Computation. Springer-Verlag Berlin Heidelberg. DOI: [10.1007/9783662046548](https://doi.org/10.1007/9783662046548) (cit. on p. 280).
- Lorenz, E. N. (1986). "On the Existence of a Slow Manifold". In: *Journal of the Atmospheric Sciences* 43.15, pp. 1547–1558. DOI: [10.1175/1520-0469\(1986\)043<1547:OTEQAS>2.0.CO;2](https://doi.org/10.1175/1520-0469(1986)043<1547:OTEQAS>2.0.CO;2) (cit. on p. 25).
- Lynch, Stephen (2018). *Dynamical Systems with Applications using Python*. Birkhäuser. DOI: [10.1007/9783319781457](https://doi.org/10.1007/9783319781457) (cit. on p. 105).
- Maclean, J., J. E. Bunder, I. G. Kevrekidis, and A. J. Roberts (2021a). "An Equation Free Algorithm Accurately Simulates Macroscale Shocks Arising From Heterogeneous Microscale Systems". In: *IEEE Journal on Multiscale and Multiphysics Computational Techniques* 6, pp. 8–15. DOI: [10.1109/JMMCT.2021.3054012](https://doi.org/10.1109/JMMCT.2021.3054012) (cit. on p. 317).
- Maclean, J., J. E. Bunder, and A. J. Roberts (Aug. 2021b). "A toolbox of equation-free functions in Matlab/Octave for efficient system level simulation". In: *Numerical Algorithms* 87.4, pp. 1729–1748. DOI: [10.1007/s11075-020-01027-z](https://doi.org/10.1007/s11075-020-01027-z) (cit. on pp. 5, 6, 280, 316).

- Makeev, A. G. and I. G. Kevrekidis (2004). “Equation-free multiscale computations for a lattice-gas model: coarse-grained bifurcation analysis of the NO+CO reaction on Pt(100)”. In: *Chemical Engineering Science* 59.8, pp. 1733–1743. DOI: [10.1016/j.ces.2004.01.029](https://doi.org/10.1016/j.ces.2004.01.029) (cit. on p. 5).
- Målqvist, Axel and Daniel Peterseim (Sept. 2014). “Localization of elliptic multiscale problems”. In: *Mathematics of Computation* 83.290, pp. 2583–2603. DOI: [10.1090/S0025-5718-2014-02868-8](https://doi.org/10.1090/S0025-5718-2014-02868-8) (cit. on p. 1).
- Manneville, Paul (2004). *Instabilities, Chaos and Turbulence*. World Scientific. DOI: [10.1142/p349](https://doi.org/10.1142/p349) (cit. on pp. 52, 175).
- Marsden, Jerrold E. and Tudor S. Ratiu (1999). *Introduction to Mechanics and Symmetry. A Basic Exposition of Classical Mechanical Systems*. 2nd. Texts in Applied Mathematics. Springer. ISBN: 9780387986432 (cit. on p. 106).
- Maruskin, Jared (2018). *Dynamical Systems and Geometric Mechanics*. De Gruyter. DOI: [10.1515/9783110597806](https://doi.org/10.1515/9783110597806) (cit. on pp. 52, 175).
- Mehaute, Bernard Le (1976). *An Introduction to Hydrodynamics and Water Waves*. 1st ed. Springer Study Edition. Springer Berlin Heidelberg. DOI: [10.1007/9783642855672](https://doi.org/10.1007/9783642855672) (cit. on p. 46).
- Mei, Chiang C. and Bogdan Vernescu (2010). *Homogenization Methods for Multiscale Mechanics*. World Scientific. DOI: [10.1142/7427](https://doi.org/10.1142/7427) (cit. on p. 1).
- Meiss, James D. (2017). *Differential Dynamical Systems. Revised Edition*. Dynamical Systems. Society for Industrial and Applied Mathematics. DOI: [10.1137/1.9781611974645](https://doi.org/10.1137/1.9781611974645) (cit. on p. 106).
- Mellodge, Patricia (2016). *A practical approach to dynamical systems for engineers*. Elsevier. DOI: [10.1016/C2014-0-03574-5](https://doi.org/10.1016/C2014-0-03574-5) (cit. on p. 106).
- Moler, Cleve B. (2004). *Numerical Computing with Matlab*. Society for Industrial and Applied Mathematics. DOI: [10.1137/1.9780898717952](https://doi.org/10.1137/1.9780898717952) (cit. on p. 280).
- Johansson, Fredrik et al. (Dec. 2018). *mpmath: a Python library for arbitrary-precision floating-point arithmetic (version 1.2.1)*. URL: <http://mpmath.org/> (cit. on p. 250).
- Mudavanhu, B. and R. E. O’Malley (2003). “A New Renormalization Method for the Asymptotic Solution of Weakly Nonlinear Vector Systems”. In: *SIAM Journal on Applied Mathematics* 63.2, pp. 373–397. DOI: [10.1137/S0036139901394311](https://doi.org/10.1137/S0036139901394311) (cit. on p. 1).

- Ólafsson, Haraldur and Jian-Wen Bao (2021). *Uncertainties in Numerical Weather Prediction*. Elsevier. DOI: [10.1016/C2017-0-03301-3](https://doi.org/10.1016/C2017-0-03301-3) (cit. on p. 14).
- Patankar, S.V and D.B Spalding (1972). “A calculation procedure for heat, mass and momentum transfer in three-dimensional parabolic flows”. In: *International journal of heat and mass transfer* 15.10, pp. 1787–1806 (cit. on p. 13).
- Perko, Lawrence (2001). *Differential Equations and Dynamical Systems | Lawrence Perko | Springer*. Springer-Verlag New York. DOI: [10.1007/9781461300038](https://doi.org/10.1007/9781461300038) (cit. on pp. 105, 106).
- Pulliam, Thomas H and David W. (auth.) Zingg (2014). *Fundamental Algorithms in Computational Fluid Dynamics*. 1st ed. Scientific Computation. Springer International Publishing. ISBN: 9783319050539 (cit. on p. 280).
- Quarteroni, Alfio, Fausto Saleri, and Paola Gervasio (2014). *Scientific Computing with MATLAB and Octave*. 4th ed. Springer. DOI: [10.1007/978-3-642-45367-0](https://doi.org/10.1007/978-3-642-45367-0) (cit. on p. 280).
- Rackauckas, Christopher and Qing Nie (2017). “DifferentialEquations.jl—a performant and feature-rich ecosystem for solving differential equations in julia”. In: *Journal of Open Research Software* 5.1. DOI: [10.5334/jors.151](https://doi.org/10.5334/jors.151) (cit. on pp. 15, 18, 144).
- Raju, Karthikayen, Tong-Earn Tay, and Vincent Beng Chye Tan (Mar. 2021). “A review of the FE2 method for composites”. In: *Multiscale and Multidisciplinary Modeling, Experiments and Design* 4.1, pp. 1–24. DOI: [10.1007/s41939-020-00087-x](https://doi.org/10.1007/s41939-020-00087-x) (cit. on p. 1).
- Roberts, A. J. (1988). “The application of centre-manifold theory to the evolution of system which vary slowly in space”. In: *The Journal of the Australian Mathematical Society. Series B. Applied Mathematics* 29.4, pp. 480–500. DOI: [10.1017/S0334270000005968](https://doi.org/10.1017/S0334270000005968) (cit. on p. 25).
- (2003). “Low-Dimensional Modelling of Dynamical Systems Applied to Some Dissipative Fluid Mechanics”. In: *Nonlinear Dynamics: From Lasers to Butterflies*, pp. 257–313. DOI: [10.1142/9789812791252_0007](https://doi.org/10.1142/9789812791252_0007) (cit. on p. 25).
- Roberts, A. J. and I. G. Kevrekidis (2005). “Higher order accuracy in the gap-tooth scheme for large-scale dynamics using microscopic simulators”. In: *ANZIAM Journal* 46.0, pp. 637–657. URL: <https://journal.austms.org.au/ojs/index.php/ANZIAMJ/article/view/981> (cit. on pp. 4, 6).

- Roberts, A. J. and I. G. Kevrekidis (2007). “General Tooth Boundary Conditions for Equation Free Modeling”. In: *SIAM Journal on Scientific Computing* 29.4, pp. 1495–1510. DOI: [10.1137/060654554](https://doi.org/10.1137/060654554) (cit. on pp. 4–6).
- Roberts, A. J. and Zhenquan Li (2006). “An accurate and comprehensive model of thin fluid flows with inertia on curved substrates”. In: *Journal of Fluid Mechanics* 553, pp. 33–73. DOI: [10.1017/S0022112006008640](https://doi.org/10.1017/S0022112006008640) (cit. on pp. 8, 9, 157, 159, 160, 162).
- Röbke, B.R. and A. Vött (2017). “The tsunami phenomenon”. In: *Progress in Oceanography* 159, pp. 296–322. DOI: [10.1016/j.pocean.2017.09.003](https://doi.org/10.1016/j.pocean.2017.09.003) (cit. on p. 290).
- Samaey, G., A. J. Roberts, and I. G. Kevrekidis (2009). “Equation-Free Computation: An Overview of Patch Dynamics”. In: *Multiscale Methods. Bridging the Scales in Science and Engineering*. Oxford University Press. DOI: [10.1093/acprof:oso/9780199233854.003.0008](https://doi.org/10.1093/acprof:oso/9780199233854.003.0008) (cit. on p. 5).
- Schiesser, William E. and Graham W. Griffiths (2009). *A Compendium of Partial Differential Equation Models: Method of Lines Analysis with Matlab*. Cambridge University Press. DOI: [10.1017/CB09780511576270](https://doi.org/10.1017/CB09780511576270) (cit. on p. 280).
- Shampine, Lawrence F. and Mark W. Reichelt (1997). “The MATLAB ODE Suite”. In: *SIAM Journal on Scientific Computing* 18.1, pp. 1–22. DOI: [10.1137/S1064827594276424](https://doi.org/10.1137/S1064827594276424) (cit. on pp. 15, 146, 271, 279, 310).
- Siettos, C. I., C. W. Gear, and I. G. Kevrekidis (2012). “An equation-free approach to agent-based computation: Bifurcation analysis and control of stationary states”. In: *EPL (Europhysics Letters)* 99.4. DOI: [10.1209/0295-5075/99/48007](https://doi.org/10.1209/0295-5075/99/48007) (cit. on p. 5).
- Strogatz, Steven H. (2018). *Nonlinear Dynamics and Chaos*. 2nd ed. CRC Press. DOI: [10.1201/9780429492563](https://doi.org/10.1201/9780429492563) (cit. on p. 106).
- Temam, R. (Sept. 1990). “Inertial manifolds”. In: *The Mathematical Intelligencer* 12.4, pp. 68–74. DOI: [10.1007/BF03024036](https://doi.org/10.1007/BF03024036) (cit. on p. 25).
- Tsoumanis, A. C., C. I. Siettos, G. V. Bafas, and I. G. Kevrekidis (2010). “Equation-Free Multiscale Computations In Social Networks: From Agent-Based Modeling To Coarse-Grained Stability And Bifurcation Analysis”. In: *International Journal of Bifurcation and Chaos* 20.11, pp. 3673–3688. DOI: [10.1142/S0218127410027945](https://doi.org/10.1142/S0218127410027945) (cit. on p. 5).
- Welsh, Zachary, Matthew J. Simpson, Md Imran H. Khan, and M. A. Karim (2018). “Multiscale Modeling for Food Drying: State of the Art”. In:

- Comprehensive Reviews in Food Science and Food Safety* 0.0. DOI: [10.1111/1541-4337.12380](https://doi.org/10.1111/1541-4337.12380) (cit. on p. 4).
- Wiggins, Stephen (2003). *Introduction to Applied Nonlinear Dynamical Systems and Chaos*. 2nd ed. Texts in Applied Mathematics. Springer-Verlag New York. DOI: [10.1007/b97481](https://doi.org/10.1007/b97481) (cit. on pp. 105, 106).
- Zagaris, Antonios, C. William Gear, Tasso J. Kaper, and I. G. Kevrekidis (2009). "Analysis of the accuracy and convergence of equation-free projection to a slow manifold". In: *ESAIM: Mathematical Modelling and Numerical Analysis* 43.4, pp. 757–784. DOI: [10.1051/m2an/2009026](https://doi.org/10.1051/m2an/2009026) (cit. on p. 25).
- Zikanov, Oleg (2010). *Essential Computational Fluid Dynamics*. Wiley. ISBN: 9780470423295 (cit. on p. 12).
- Zirker, J. B. (2013). *The science of ocean waves. ripples, tsunamis, and stormy seas*. Johns Hopkins University Press. ISBN: 1421410796 (cit. on p. 316).